Xiao-Zi Yuan
Chaojie Song
Haijiang Wang
Jiujun Zhang

Electrochemical Impedance Spectroscopy in PEM Fuel Cells

Fundamentals and Applications

Springer

Electrochemical Impedance Spectroscopy in PEM Fuel Cells

Xiao-Zi Yuan · Chaojie Song · Haijiang Wang
Jiujun Zhang

Electrochemical Impedance Spectroscopy in PEM Fuel Cells

Fundamentals and Applications

Springer

Dr. Xiao-Zi Yuan
National Research Council of Canada
Institute for Fuel Cell Innovation
4250 Wesbrook Mall
Vancouver BC V6T 1W5
Canada
Xiao-Zi.Yuan@nrc-cnrc.gc.ca

Dr. Haijiang Wang
National Research Council of Canada
Institute for Fuel Cell Innovation
4250 Wesbrook Mall
Vancouver BC V6T 1W5
Canada
Haijiang.Wang@nrc-cnrc.gc.ca

Dr. Chaojie Song
National Research Council of Canada
Institute for Fuel Cell Innovation
4250 Wesbrook Mall
Vancouver BC V6T 1W5
Canada
Chaojie.Song@nrc-cnrc.gc.ca

Dr. Jiujun Zhang
National Research Council of Canada
Institute for Fuel Cell Innovation
4250 Wesbrook Mall
Vancouver BC V6T 1W5
Canada
jiujun.zhang@nrc.gc.ca

ISBN 978-1-84882-845-2 e-ISBN 978-1-84882-846-9
DOI 10.1007/978-1-84882-846-9
Springer London Dordrecht Heidelberg New York

British Library Cataloguing in Publication Data
A catalogue record for this book is available from the British Library

Library of Congress Control Number: 2009940583

Cover design: eStudioCalamar, Figueres/Berlin

Printed on acid-free paper

Springer is part of Springer Science+Business Media (www.springer.com)

Preface

Proton exchange membrane (PEM) fuel cells hold the promise of environmentally friendly power generation due to their low/zero emissions in comparison with internal combustion engines. PEM fuel cells also have several other advantages over conventional energy converting devices, including both high efficiency and power density, which make them unique across a wide range of portable, stationary, and transportation power applications. However, several challenges remain, including cost and reliability/durability. Intensive R&D is therefore still needed to address these challenges in order to achieve sustainable commercialization. In this ongoing R&D, fuel cell testing and diagnostics play a critical role in material characterization, performance optimization, design validation, and fundamental understanding for further development. Among the testing and diagnostic tools used in fuel cell R&D, AC impedance spectroscopy (or electrochemical impedance spectroscopy, EIS) is regarded by scientists and engineers as a powerful technique.

In recent years, EIS has been widely used in studies of electrochemical systems, including batteries and materials corrosion, and is also being increasingly employed by researchers in PEM fuel cell studies. During the last few decades this technique has emerged as a primary tool in PEM fuel cell diagnosis.

Because PEM fuel cells are being developed at an increasingly rapid rate, with many new researchers entering the field, an overview of EIS methods is warranted to describe the basic principles, measurement techniques, and applications of this tool. Current researchers may or may not be electrochemists. Indeed, as fuel cells grow in popularity among students in mechanical, chemical, and electrical engineering, in environmental studies and engineering, as well as in materials science and engineering, fuel cell courses are being offered worldwide at many universities and research institutes, as well as in industry settings. The need for a text or reference book on fuel cell EIS has motivated the writing of this volume.

Each of the authors is closely involved in PEM fuel cell technology, including the areas of design, materials, components, operation, diagnostics, and systems. The present publication is therefore a direct result of many years' experience working on EIS diagnosis of PEM fuel cells. The authors hope this book will provide a general understanding of EIS techniques, as well as detailed guidance in the application of this technology to PEM fuel cells. The volume is also designed with the intention that other potential readers, especially non-electrochemists, will find it an accessible and useful introduction to EIS techniques, will gain basic knowledge of EIS testing, and after reading it will be well prepared for

experimental result analysis. Although the book's primary audience is intended to be fuel cell researchers and practising engineers in universities, research institutes, and industries who perform PEM fuel cell testing and diagnostics, some undergraduate students, as well as M.Sc. and Ph.D. candidates in mechanical engineering, chemical and electrochemical engineering, environmental engineering, and materials science and engineering may also find this book a very useful reference source.

The book comprises six chapters and contains comprehensive information on the fundamentals of PEM fuel cells, as well as the basic principles of EIS electronics, measurements, and applications. Chapter 1 introduces readers to the general field of PEM fuel cells, including an overview of fuel cell history, the different types of fuel cells, and electrochemical approaches in fuel cell studies. Chapter 2 provides the electrical fundamentals that are the foundation for understanding spectra analysis based on electric equivalent circuits. Chapter 3 gives a brief overview of EIS fundamentals, covering topics such as impedance and its physical and chemical processes, and the relationships between impedance spectroscopy and other electrochemical techniques. Chapter 4 describes the equivalent circuits frequently used in PEM fuel cell diagnosis and their corresponding AC impedance spectra. Following this coverage of fundamentals in the first four chapters, progress in EIS techniques and applications is reviewed in Chapters 5 and 6, accompanied by some typical example analyses. These two chapters are more related to the practice and state-of-the-art development of EIS applications in PEM fuel cells. Literature published in scientific journals has been cited in this book up to the time of writing the final draft for each specific chapter.

We would like to take this opportunity to thank the many outstanding engineers and scientists who made direct contributions to the writing of this book at the National Research Council of Canada's Institute for Fuel Cell Innovation. Special thanks go to Dr. Yanghua Tang for his constructive contribution to Chapter 2, to Mr. Jason Ng Cheng Hin for his efficient editing of all the images, and to Dr. Dania Sheldon for her effective editing and indexing services. We also wish to thank the family members of all the authors for their continued patience, understanding, encouragement, and support throughout the writing of this monograph. Finally, it is our pleasure to acknowledge with gratitude the financial support provided by the NRC-Helmholtz Project, which made possible the editing and publication of this work.

If technical errors are found, all of the authors would deeply appreciate readers' constructive comments for correction and further improvement.

Vancouver, BC, Canada
May 2009

Xiao-Zi Yuan, Chaojie Song, Haijiang Wang, and Jiujun Zhang

Contents

Acronyms and Abbreviations xi

1 PEM Fuel Cells and their Related Electrochemical Fundamentals 1
1.1 Fuel Cell Description 1
1.2 Fuel Cell Types 4
1.2.1 H_2/Air Fuel Cells 5
1.2.2 Direct Liquid Fuel Cells 8
1.2.3 Alkaline Fuel Cells 10
1.2.4 Phosphoric Acid Fuel Cells 11
1.3 Fuel Cell Challenges 12
1.4 PEM Fuel Cell Electrochemistry 13
1.4.1 Electrochemistry Fundamentals 13
1.4.2 Polarization Curves 20
1.4.3 Current Interruption 20
1.4.4 Chronoamperometry 21
1.4.5 Cyclic Voltammetry 22
1.4.6 Electrochemical Impedance Spectroscopy 26
1.5 Fuel Cell Analysis 28
1.5.1 Open Circuit Voltage 29
1.5.2 Cell Voltage Under Load 31
1.5.3 Ohmic Drop 34
1.5.4 Mass Transfer Drop 34
1.5.5 Fuel Cell Efficiencies 35
1.6 Chapter Summary 36
References 36

2 Electrical Fundamentals 39
2.1 Introduction 39
2.2 Direct Current Circuits 40
2.2.1 Ohm's Law 40
2.2.2 Series and Parallel Circuits 41
2.2.3 Kirchhoff's Laws 42
2.2.4 Resistors in DC Circuits 43
2.2.5 Capacitors in DC Circuits 45
2.2.6 Inductors in DC Circuits 49
2.3 Alternating Current Circuits 50
2.3.1 Sinusoidal Systems 50
2.3.2 Resistors in AC Circuits 52

2.3.3 Capacitors in AC Circuits 53
2.3.4 Inductors in AC Circuits 53
2.4 Complex Algebra and Impedance 54
2.4.1 AC Impedance of a Resistor–Capacitor Circuit 56
2.4.2 AC Impedance of a Resistor–Inductor Circuit 59
2.4.3 AC Impedance of a Capacitor–Inductor Circuit 61
2.4.4 AC Impedance of a Resistor–Capacitor–Inductor Circuit 63
2.5 Network Circuit Analysis 72
2.5.1 Topological Features of a Network 72
2.5.2 Network Theorems 73
2.5.3 Transient Network Analysis 78
2.6 Basic Knowledge for Understanding EIS 81
2.6.1 Introduction 81
2.6.2 Nyquist and Bode Plots 82
2.6.3 Equivalent Circuit Models 84
2.6.4 Data Fitting of EIS 89
2.6.5 Applications 92
2.7 Chapter Summary 93
References 93

3 Impedance and its Corresponding Electrochemical Processes 95
3.1 Electrode/Electrolyte Interfaces 95
3.1.1 Introduction 95
3.1.2 Equivalent Circuit of an Electrode/Electrolyte Interface 96
3.1.3 Differences Between Solid State and Aqueous Electrochemistry 97
3.2 Faradaic Impedance 98
3.2.1 Calculation of the Faradaic Impedance at the Equilibrium Electrode Potential 98
3.2.2 Kinetic Parameters from Z_f 104
3.2.3 Vectorgraphs of Faradaic Impedance 108
3.3 Total Impedance of an Electrochemical System 109
3.3.1 Calculated Z_f Based on Experimental Measurements 109
3.3.2 Graphic Presentations of the Total Impedance 112
3.3.3 Impedance Plots of Real Electrochemical Systems Using the Complex Plane 116
3.3.4 Semicircle Rotation of the Impedance 118
3.4 Correlation of EIS with Other Electrochemical Techniques 123
3.4.1 EIS and the Polarization Curve 123
3.4.2 EIS and Current Interruption 128
3.5 EIS Measurements 129
3.6 Advantages and Limitations of EIS 133
3.6.1 EIS Advantages 133
3.6.2 EIS Limitations 134
3.7 Chapter Summary 135
References 136

4 EIS Equivalent Circuits 139
4.1 Electrochemical Elements 139
4.1.1 Lumped Elements 139
4.1.2 Frequency-Dependent Elements 140
4.1.3 Bounded Frequency-Dependent Elements 142
4.2 Basic Equivalent Circuits 143
4.2.1 Simple Combinations of Electrical Elements 143
4.2.2 Randles Cell 154
4.2.3 Structural Circuits 168
4.2.4 Other Circuits 177
4.3 Brief Discussion of Equivalent Circuits in PEM Fuel Cells 180
4.3.1 Gas Diffusion Layers 180
4.3.2 Catalyst Layers 180
4.3.3 Proton Exchange Membranes 184
4.3.4 Conductive Polymers 184
4.3.5 Membrane Electrode Assemblies 191
4.4 Chapter Summary 191
References 191

5 EIS Diagnosis for PEM Fuel Cell Performance 193
5.1 Ex Situ Diagnosis 193
5.1.1 Electrode Characterization 193
5.1.2 Membrane Characterization 202
5.1.3 Comparison of Ex Situ and In Situ EIS Methods 212
5.2 In Situ Diagnosis 213
5.2.1 Different Gas Feeding Modes 214
5.2.2 Measurement Modes 237
5.2.3 Operating Conditions 239
5.2.4 Reference Electrodes 243
5.3 EIS Under Heavy Duty 250
5.3.1 Introduction 250
5.3.2 Grounded Mode 251
5.3.3 Floating Mode 254
5.4 Fast EIS 255
5.4.1 Principles and Measurements 255
5.4.2 Differences Between Frequency Domain and Time Domain 256
5.5 Chapter Summary 257
References 258

6 EIS Applications 263
6.1 EIS Applications in PEMFCs 263
6.1.1 Optimization of MEA Structure 264
6.1.2 Ionic Conductivity 288
6.1.3 Contamination 295
6.1.4 Stack and Individual Cell Impedance 298
6.1.5 Localized EIS 307
6.1.6 EIS at High Temperatures 313

6.2 EIS Applications in DMFCs 323
6.2.1 Ex Situ Methanol Oxidation 323
6.2.2 In Situ Anode Reaction 335
6.2.3 Determination of the Ionic Resistance 338
6.2.4 In Situ Cathode Reaction 339
6.3 Chapter Summary 342
References 342

Appendix A: Fourier Transform 347
Appendix B: Laplace Transform 353
Appendix C: Kramers–Kronig Transform 363
Appendix D: Effects of Equivalent Circuit Parameters on Nyquist Plots 371

Contributor Biographies 411

Index 413

Acronyms and Abbreviations

AC	Alternating current
AFC	Alkaline fuel cell
BCPE	Bounded constant phase element
BW	Bounded Warburg element
CB	Carbon black
CE	Counter electrode
CFE	Carbon fibre electrode
CL	Catalyst layer
CNLS	Complex non-linear least squares
CNT	Carbon nanotube
CPE	Constant phase element
DC	Direct current
DEFC	Direct ethanol fuel cell
DFAFC	Direct formic acid fuel cell
DFT	Discrete Fourier transform
DHE	Dynamic hydrogen electrode
DMFC	Direct methanol fuel cell
EDL	Electrical double layer
EIS	Electrochemical impedance spectroscopy
FFT	Fast Fourier transform
FRA	Frequency response analyzer
FT-EIS	Fourier transform EIS
GDE	Gas diffusion electrode
GDL	Gas diffusion layer
HF	High frequency
HFR	High-frequency resistance
HOR	Hydrogen oxidation reaction
IAE	Ionized air reference electrode
KCL	Kirchhoff's current law
K–K	Kramers–Kronig
KVL	Kirchhoff's voltage law
LANL	Los Alamos National Laboratory

LST	Linear systems theory
MCFC	Molten carbonate fuel cell
MEA	Membrane electrode assembly
NHE	Normal hydrogen electrode
NLLS	Non-linear least squares
OCV	Open circuit voltage
ORR	Oxygen reduction reaction
Ox	Oxidant
PAFC	Phosphoric acid fuel cell
PBI	Polybenzimidazole
PEFC	Polymer electrolyte fuel cell
PEM	Proton exchange membrane
PEMFC	Polymer electrolyte membrane fuel cell
PEO	Polyethylene oxide
PPY-PSS	Polypyrrole polystyrene sulfonate
PTFE	Polytetrafluoroethylene
RC	Resistor-capacitor
RCL	Resistor-capacitor-inductor
Rd	Reductant
RDE	Rotating disk electrode
RDS	Rate-determining step
RE	Reference electrode
RHE	Reversible hydrogen electrode
RL	Resistor-inductor
RRDE	Rotating ring-disk electrode
SCE	Saturated calomel electrode
SHE	Standard hydrogen reference electrode
SOFC	Solid oxide fuel cell
SWCNT	Single-walled carbon nanotube
TDS	Thermal desorption spectroscopy
W	Warburg
WE	Working electrode
XPS	X-ray photoelectron spectroscopy

1

PEM Fuel Cells and their Related Electrochemical Fundamentals

1.1 Fuel Cell Description

The history of fuel cells begins 170 years ago, when Sir William Grove invented the first fuel cell in 1839 [1, 2]. In the first step of his experiment, Grove embedded two platinum electrodes inside two separate glass tubes and then placed these in a dilute sulphuric acid solution, as shown in the left part of Figure 1.1. He then passed an electric current through the electrodes, causing the electrolysis of water. The resulting oxygen and hydrogen were accumulated in the two glass tubes. In the second step, the power supply was replaced with an ammeter, which detected a small electric current arising from the reduction of oxygen and the oxidation of hydrogen on the individual Pt electrodes.

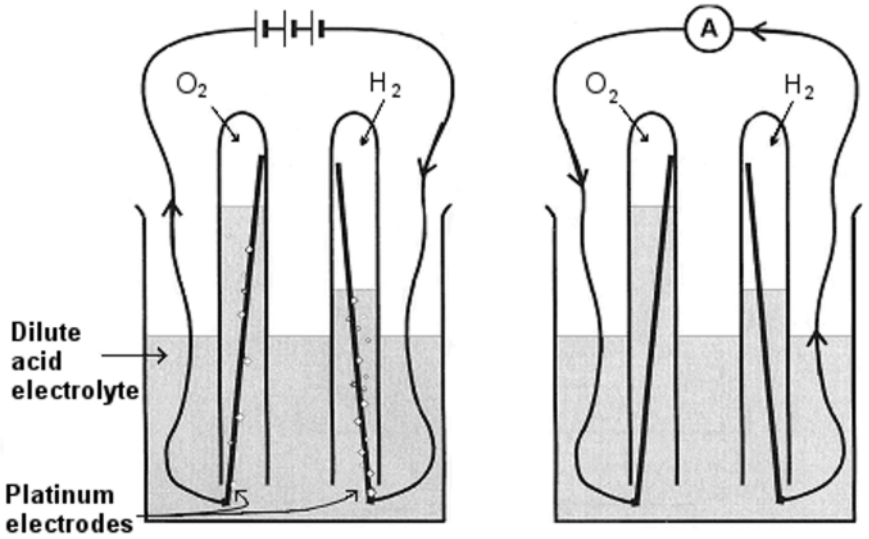

Figure 1.1. Schematic representation of the first fuel cell [3]. (From Larminie J, Dicks A. Fuel cell systems explained. ©2003 John Wiley & Sons Limited. Reproduced with permission of the publisher and the authors.)

The electrochemical reactions for electrolysis and the fuel cell processes can be described as follows:

Electrolysis process:

$$\text{Anode: } H_2O \rightarrow 2H^+ + 1/2O_2 + 2e^- \quad (1.1)$$

$$\text{Cathode: } 2H^+ + 2e^- \rightarrow H_2 \quad (1.2)$$

$$\text{Total reaction: } H_2O \rightarrow H_2 + 1/2O_2 \quad (1.3)$$

Fuel cell process:

$$\text{Anode: } H_2 \rightarrow 2H^+ + 2e^- \quad (1.4)$$

$$\text{Cathode: } O_2 + 4H^+ + 4e^- \rightarrow H_2O \quad (1.5)$$

$$\text{Total reaction: } H_2 + 1/2O_2 \rightarrow H_2O \quad (1.6)$$

In addition to this fuel cell experiment, Grove three years later published his idea of fuel cell stacks comprised of multiple single cells. After this, fuel cell research attracted some attention, but unfortunately, fuel cell development proceeded very slowly and little progress was made. However, several important innovations were developed. For example, in 1889, L. Mond and C. Langer [4] established the prototype of modern acid fuel cells by using electrolyte-immersed porous materials such as earthenware and asbestos as membranes, Pt black as catalyst, hydrogen and oxygen as fuel and oxidant (respectively), and perforated Pt foil or gold foils as current collectors. These fuel cells could provide a current density of 3.5 mA/cm^2 at a cell voltage of 0.73 V. In addition, the cells could be combined side by side or on top of each other, forming fuel cell stacks. This design was similar to that of modern fuel cells but with different materials. Mond's and Langer's invention thus established the foundation for phosphoric acid and proton exchange membrane (PEM) fuel cells.

Other fuels were also tried in the early stages of fuel cell development. Coal, the major fuel at that time, was considered as a candidate. Attempts to replace hydrogen with coal resulted in the invention of alkaline fuel cells (AFCs) and molten carbonate fuel cells (MCFCs). Mond used reformate gas from coal, which contained abundant hydrogen, as the fuel, with the intention of scaling up Grove's fuel cell to produce electric power. However, impurities poisoned the catalyst and made Mond's design impractical.

Jacques [5] was the first person to succeed in making large fuel cell systems. In 1895, he built a 1.5 kW battery consisting of about 100 small single fuel cells. Later, he also designed a stack with 30 kW of power. This was the first alkaline fuel cell, and it used molten KOH as the electrolyte and coke as the fuel. This AFC could provide 100 mA/cm^2 at 1.0 V.

Direct coal fuel cells were also tried, using molten carbonate as the electrolyte [6]. However, ash formation, poor conductivity, and technical problems in continuously feeding the fuel made the process impractical and uneconomical. The subsequent successful development of the internal combustion engine, and the

abundance of fossil fuels led the energy industry elsewhere, and fuel cell development was eclipsed in this period. Nonetheless, these pioneering endeavours built the foundation for modern fuel cells, including fuel cell concepts and a variety of cell types.

In the quest to improve fuel cell performance, the concept of fuel cell reactions requiring a three-phase interface was first proposed by Grove. In his initial experiment, he noticed that the reaction sped up when the three-phase area was large. In 1923, Schmid [7] developed the first gas diffusion electrode, which significantly increased the electrode active surface area and revolutionized fuel cell electrodes. The electrode contained a coarse-pore graphite gas-side layer and a fine porous platinum electrolyte layer.

Combining the essences of previous researchers' work, a new alkaline fuel cell that could operate at 200°C was successfully designed in the 1940s [8, 9]. The fuel cell provided a current density of 1 A/cm^2 at a cell voltage of 0.8 V, a significant jump in progress. Based on this prototype, Bacon in 1952 successfully developed a 5 kW AFC power plant, which resulted in the construction of alkaline fuel cell power plants by Pratt & Whitney, who designed and developed the fuel cell system as part of the power supply system for the Apollo aircraft.

Molten carbonate fuel cell technology was developed based on the work of Bauers and Ehrenberg, Davytan, and Broers and Ketelaar in the 1940s [8]. The electrolyte is a molten salt such as sodium carbonate, borax, or cryolite. This type of fuel cell requires a high temperature to keep the electrolyte in a molten state. The following 30–40 years saw great successes, with the development of MCFCs and MCFC stacks that could be operated for over 5000 hours.

In the 1960s, the General Electric Company successfully developed solid polymer electrolyte fuel cells, or polymer electrolyte membrane fuel cells (PEMFCs), which were used as the power source for NASA's Gemini space vehicles. PEMFCs were superior to other power converting devices because of the former's high power and energy densities, simple design, minimum noise and vibration, and reliability. The system produced no waste: the product was water, which could be drunk by the astronauts. Although the PEMFC developed by General Electric passed 57,000 hours in a lifetime test, its cost was too high, hindering its use in applications.

Fuel cell research and development then remained dormant for about 20 years due to technological obstacles and cost issues. However, with the world oil crisis came revitalization, as high fossil fuel prices and panic over depletion of fossil fuels forced researchers to switch their attention back to fuel cells. Fears about air pollution and global warming also played important roles in the fuel cell renaissance. Since the 1980s, fuel cells have attracted renewed attention and are close to commercialization. The introduction of a perfluorosulfonated polymer electrolyte has significantly improved PEMFC performance and lifetime. The most popular such membrane used in today's PEMFCs is Nafion®, developed by DuPont in the 1960s for the chloro-alkali industry. Since the 1980s, many fuel cell companies have been founded, and demonstration PEMFC vehicles are in the testing process. Figure 1.2 shows a Mercedes-Benz Citaro bus, operated in Perth, Australia, powered with Ballard® fuel cell technology.

Figure 1.2. Ballard Power Systems fuel cell bus [10]. (Image courtesy of Ballard Power Systems.)

1.2 Fuel Cell Types

Several types of fuel cells have been developed and are classified according to the electrolytes used: alkaline fuel cells, molten carbonate fuel cells, phosphoric acid fuel cells (PAFCs), PEMFCs, and solid oxide fuel cells (SOFCs). As shown in Figure 1.3, the optimum operation temperatures of these fuel cells are different, and each type has different advantages and disadvantages.

In this book the focus is on PEMFCs; therefore, in the following sections we will only discuss several major types of PEMFCs, such as H_2/air (O_2) fuel cells, direct liquid fuel cells, PAFCs, and alkaline fuel cells. PEMFCs, also called solid polymer electrolyte fuel cells, use a polymer electrolyte membrane as the electrolyte. They are low-temperature fuel cells, generally operating below 300°C.

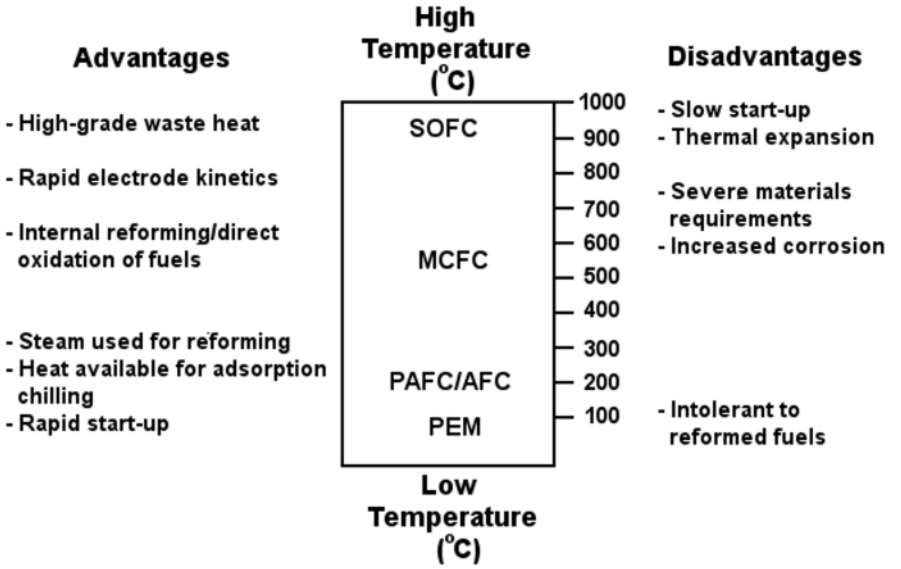

Figure 1.3. Fuel cell types and their advantages and disadvantages [8]. (Reproduced by permission of ECS–The Electrochemical Society, from Perry ML, Fuller TF. A historical perspective of fuel cell technology in the twentieth century.)

1.2.1 H_2/Air Fuel Cells

Figure 1.4 shows schematic sets for a single H_2/air fuel cell and its corresponding stack. In a single fuel cell, the electrochemical reactions at both electrodes are as follows:

$$\text{Anode: } H_2 \rightarrow 2H^+ + 2e^- \tag{1.7}$$

$$\text{Cathode: } O_2 + 4H^+ + 4e^- \rightarrow 2H_2O \tag{1.8}$$

The total reaction is

$$O_2 + 2H_2 \rightarrow 2H_2O \tag{1.9}$$

The theoretical cell voltage is 1.23 V at 25°C and standard conditions. Low-temperature operation of PEMFCs requires noble metal catalysts such as Pt to catalyze the H_2 oxidation and O_2 reduction reactions. In the early stages of development, Pt black was used as both cathode and anode catalyst, which meant a large catalyst loading and high cost. Later, carbon-supported Pt was used, so the catalyst loading could be reduced significantly and at the same time, the fuel cell performance was also greatly improved. Carbon supports play an important role in dispersing the catalyst, conducting electrons, facilitating gas and water

transportation, as well as improving catalyst utilization. This development resulted in a ten-fold decrease in catalyst loading (from 4 mg/cm^2 to 0.4 mg/cm^2).

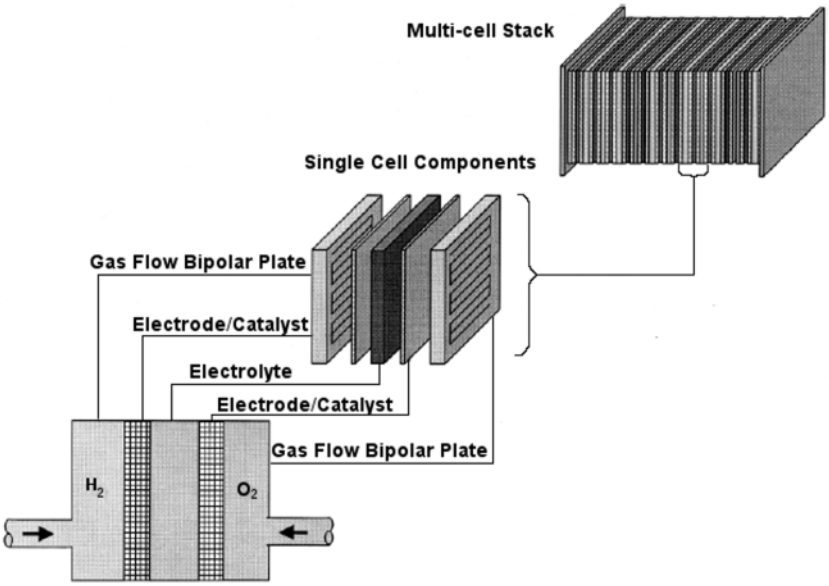

Figure 1.4. PEM fuel cells, from single cell to multi-cell stack [11]. (Reprinted, with permission, from the *Annual Review of Environment and Resources*, Volume 24, ©1999 by Annual Reviews, www.annualreviews.org, and with the permission of the authors.)

Carbon-supported Pt can also be used as the anode catalyst. However, this requires pure H_2. Contaminants such as carbon monoxide (CO) poison the catalyst, because CO can strongly adsorb on Pt, blocking the catalytic sites and reducing platinum's catalytic activity. In H_2 produced from the reforming of other fuels, CO is always present. Thus, to improve contaminant tolerance, carbon-supported PtRu was developed and now is always used as the anode catalyst. Ru can facilitate the oxidation of CO, releasing the catalytic sites on Pt through the following reactions:

$$Pt + CO \rightarrow Pt\text{-}CO_{ads} \tag{1.10}$$

$$Ru + H_2O \rightarrow Ru\text{-}OH_{ads} + H^+ + e^- \tag{1.11}$$

$$Pt\text{-}CO_{ads} + Ru\text{-}OH_{ads} \rightarrow Pt + Ru + CO_2 + H^+ + e^- \tag{1.12}$$

In a H_2/air fuel cell, the protons produced at the anode side need to be transferred to the cathode side to react with O_2. This requires a proton transport electrolyte. Nafion® membranes, composed of a perfluorosulfonated polymer, are the most commonly used polymer electrolyte membranes to conduct protons. The structure of the Nafion® membrane is shown in Figure 1.5. Nafion® can take on a

significant amount of water, and its proton conductivity is dependent on its water content: the higher the water content, the higher the conductivity. Thus, gas transport and water management are two important factors affecting PEMFC performance. Protons transferring inside the membrane from anode to cathode usually transport in a hydrated form, which is called electroosmotic drag. The water brought by this electroosmotic drag plus the water formed at the cathode via the oxygen reduction reaction (ORR) may flood the cathode compartment, blocking O_2 transport to the catalyst surface and resulting in lower performance. A positive effect is water back-diffusion: the water gradient created inside the membrane between the cathode and anode sides can lead to water back-diffusion from cathode to anode, which can decrease cathode flooding and alleviate the drying out of the anode caused by electroosmotic drag. A humidifying system is normally needed to maintain these requirements and achieve high performance.

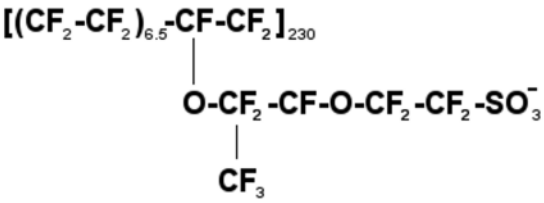

Figure 1.5. Molecular structure of Nafion® 117 [12]. (Reprinted from Electrochimica Acta, 46(10–11), Haubold HG, Vad Th, Jungbluth H, Hiller P, Nano structure of NAFION: a SAXS study, 1559-63, © 2001, with permission from Elsevier.)

Because the conductivity of Nafion® membranes is dependent on water content, they cannot be used at temperatures higher than 100°C, which limits the operating temperature. Normally, PEMFCs are operated at low temperatures, less than 80°C. Problems hindering their commercialization and obstructing performance improvement include slow reaction kinetics, low contamination tolerance, poor heat rejection, and water management problems. High-temperature operation is needed to overcome these challenges. Currently, the most effort is being focused on developing high-temperature membranes. Acid-doped polybenzimidazole (PBI) membranes can operate up to 300°C.

As shown in Figure 1.6, the optimized cathode and anode structures in PEMFCs include carbon paper or carbon cloth coated with a carbon–PTFE (polytetrafluoroethylene) sub-layer (or diffusion layer) and a catalyst layer containing carbon-supported catalyst and Nafion® ionomer. The two electrodes are hot pressed with the Nafion® membrane in between to form a membrane electrode assembly (MEA), which is the core of the PEMFC. Other methods, such as catalyst coated membranes, have also been used in the preparation of MEAs.

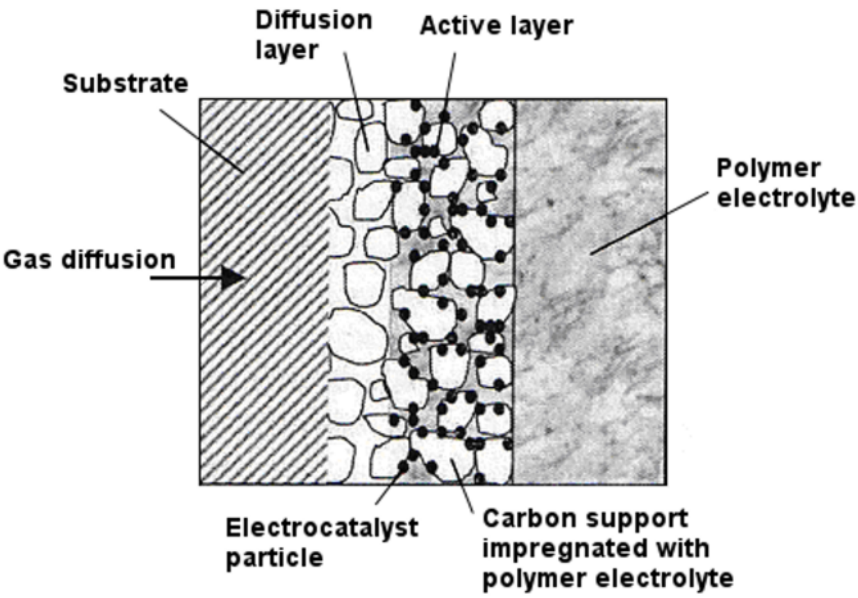

Figure 1.6. PEM fuel cell catalyst layer structure [13]. (Reproduced from Journal of Power Sources, 102, Costamagna P, Srinivasan S, Quantum jumps in the PEMFC science and technology from the 1960s to the year 2000: Part II. Engineering, technology development and application aspects, 253–69 ©2001, with permission from Elsevier.)

Other components used in PEMFCs include bipolar plates with gas flow channels, current collectors, and end plates. A heating/cooling system is also required to maintain the fuel cell at a certain operating temperature. The commonly used bipolar plate material is graphite, which has good electric and thermal conductivity. Other bipolar plates, such as metals and composites, have also been investigated, the goal being to find cheaper, lighter, but durable plates that can reduce the weight–power density and improve the bipolar plate's and the cell's lifetime.

1.2.2 Direct Liquid Fuel Cells

There are several types of direct liquid fuel cells, such as direct methanol fuel cells (DMFCs), direct formic acid fuel cells (DFAFCs), and direct ethanol fuel cells (DEFCs), the most popular being the DMFC, which is the focus of this section. A schematic DMFC system is shown in Figure 1.7.

The storage, transportation, and handling of H_2 are difficult. It has been reported that between H_2 production and H_2 application, a 15% loss due to leakage is unavoidable. Liquid methanol has advantages over H_2 in this respect, and direct methanol fuel cells are presently believed to be the ideal energy converting alternatives to hydrogen PEMFCs.

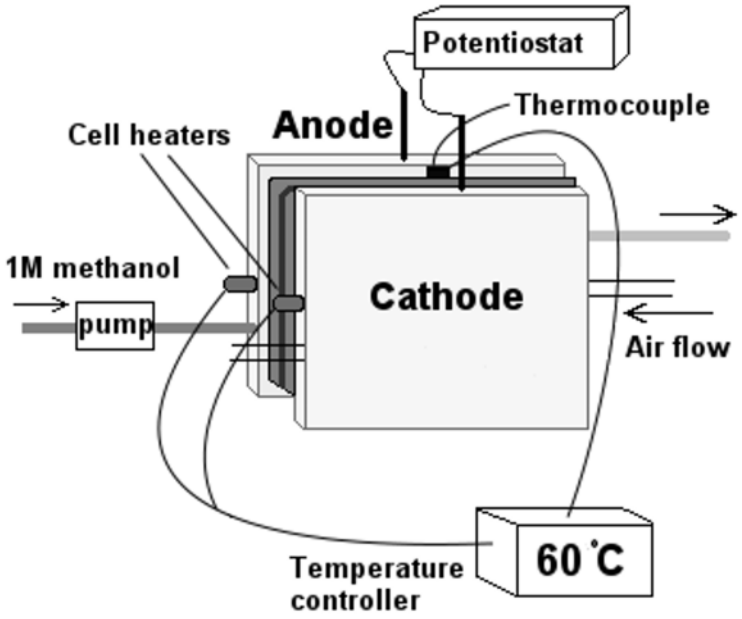

Figure 1.7. Schematic representation showing a DMFC testing system

The electrochemical reaction in a DMFC is as follows:

$$\text{Anode: } CH_3OH + H_2O \rightarrow CO_2 + 4H^+ + 6e^- \tag{1.13}$$

$$\text{Cathode: } O_2 + 4H^+ + 4e^- \rightarrow 2H_2O \tag{1.14}$$

The overall reaction is

$$3/2O_2 + CH_3OH \rightarrow 2H_2O + CO_2 \tag{1.15}$$

The theoretical cell voltage of a DMFC at standard conditions is 1.20 V. The materials used in DMFCs are similar to those in PEMFCs. Pt, PtRu, and Nafion® membrane are used as cathode catalyst, anode catalyst, and proton transfer membranes, respectively. However, the catalyst loading in a DMFC is much higher than the loading used in H_2/air fuel cells, because both side reactions are slow (Pt loadings: 4 mg/cm^2 for a DMFC, 0.8 mg/cm^2 for a H_2/air fuel cell).

Methanol oxidation in a DMFC is more difficult than H_2 oxidation in a PEMFC, and the kinetics is slow, even using state-of-the-art PtRu catalysts. The role of Ru in methanol oxidation is to provide oxygenated species to oxidize the CO formed on Pt catalytic sites at low potentials. The mechanism can be written as follows:

$$Pt + CH_3OH \rightarrow Pt\text{-}CO_{ads} + 4H^+ + 4e^- \tag{1.16}$$

$$Ru + H_2O \rightarrow Ru\text{-}OH_{ads} + H^+ + e^- \quad (1.17)$$

$$Pt\text{-}CO_{ads} + Ru\text{-}OH_{ads} \rightarrow Pt + Ru + CO_2 + H^+ + e^- \quad (1.18)$$

In addition to the slow methanol oxidation kinetics, methanol that crosses over from the anode to the cathode side through the membrane can react with O_2 at the cathode catalyst, leading to a mixed potential at the cathode side and thereby reducing cell performance. To solve this problem, methanol-tolerant catalysts as well as membranes with low methanol permeability have been investigated. However, these materials are still in the research stages and commercial applications have not been developed.

1.2.3 Alkaline Fuel Cells

Alkaline fuel cells (AFCs) were the first type of fuel cell to be widely used in space exploration applications–for example, in NASA's Apollo and space shuttle flights. Figure 1.8 shows a schematic of an AFC structure. AFCs use H_2 and O_2 as fuel and oxidant, respectively. The electrolyte is a concentrated KOH solution absorbed into an asbestos matrix. The temperature for AFCs ranges from 100–250°C and the efficiency can be > 60%. OH^- ions are transported through the electrolyte from cathode to anode. The reactions are as follows:

$$\text{Cathode: } O_2 + 2H_2O + 4e^- \rightarrow 4\ OH^- \qquad E^0 = 0.401\ V \quad (1.19)$$

$$\text{Anode: } H_2 + 2OH^- \rightarrow\ 2H_2O + 2e^- \qquad E^0 = -0.828\ V \quad (1.20)$$

$$\text{Overall: } O_2 + 2H_2 \rightarrow\ 2H_2O \quad (1.21)$$

In alkaline conditions, the oxygen reduction reaction is much faster in AFCs while the hydrogen oxidation reaction (HOR) is slower, compared with acidic fuel cells (H_2/air and direct methanol fuel cells).

A wide range of catalysts can be used in AFCs, including Ni, Ag, and noble metals. At present, Pt/C gas diffusion electrodes are generally used for both anode and cathode. The fuel supplied to AFCs must be pure hydrogen, as any impurities such as CO and CO_2 will contaminate the electrolyte, converting potassium hydroxide to potassium carbonate.

The KOH electrolyte used in AFCs is in a stabilized matrix, usually a gel-like material. It has also been found that a much longer operating lifetime can be obtained by circulating the KOH. A circulating electrolyte provides a good barrier against gas leakage and can also be used as a cooling liquid in the cell or stack. Other advantages include using the electrolyte circulation to clean the cell and remove the water produced at the anode. An early demonstration of an AFC with circulating electrolyte was made by Kordesch et al. [15] in the 1970s.

An AFC combined with a lead acid battery has been used in a hybrid vehicle. Between operating times the cell was shut down by using the battery to drain the KOH electrolyte. This technique can improve the life expectancy enormously by protecting the fuel cell from a high open circuit voltage, which otherwise could induce carbon oxidation processes to produce carbonates that would destroy the matrix electrolyte.

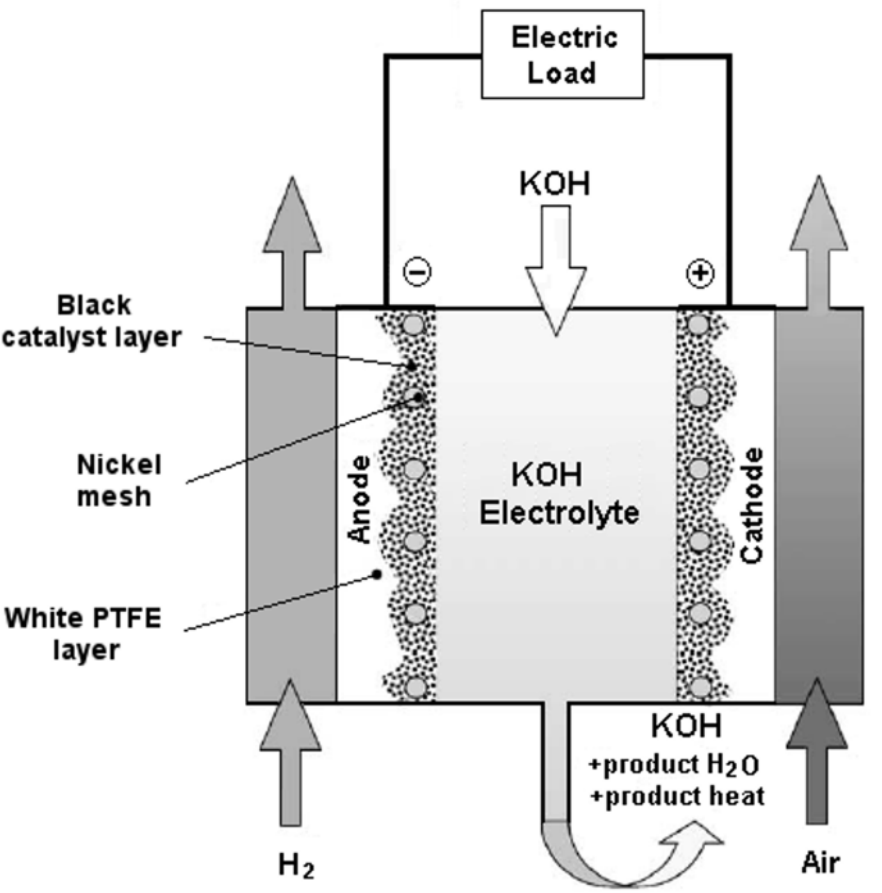

Figure 1.8. Alkaline fuel cell structure [14]. (Reproduced from International Journal of Hydrogen Energy, 27(5), McLean GF, Niet T, Prince-Richard S, Djilali N, An assessment of alkaline fuel cell technology, 507–26, ©2000, with permission from the International Association of Hydrogen Energy.)

1.2.4 Phosphoric Acid Fuel Cells

Both the half-electrode reactions and the total reactions in a PAFC are the same as those in a H_2/air fuel cell. Figure 1.9 shows the schematic of a PAFC, in which the

electrolyte (as the name indicates) is phosphoric acid. The cell operating temperature is between 150 and 200°C. The several advantages of phosphoric acid include high stability in the electrochemical environment, high electrolyte conductivity in the temperature range, and efficient rejection of water and waste heat, all of which make it attractive as an electrolyte. In actuality, high-temperature PEMFCs using phosphoric acid-doped PBI membranes are similar to PAFCs in some respects.

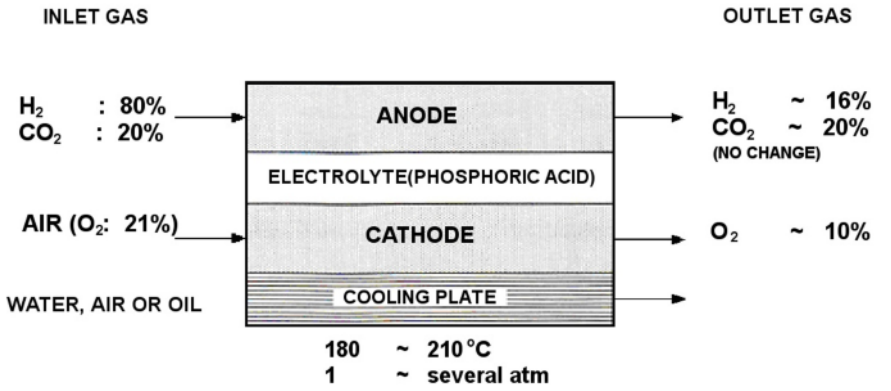

Figure 1.9. Schematic presentation showing PAFC structure and reactions with an anode efficiency of 80% [16]. (With kind permission from Springer Science+Business Media: Blomen MJ, Mugerwa MN, eds., Fuel cell systems, ©1993 Springer.)

The catalysts and electrode materials used in PAFCs are also similar to those in acidic H_2/air fuel cells. Carbon-supported Pt is used as the catalyst at both anode and cathode, porous carbon paper serves as the electrode substrate, and graphite carbon forms the bipolar plates. Since a liquid electrolyte is used, an efficient water removal system is extremely important. Otherwise, the liquid electrolyte is easily lost with the removed water. An electrolyte matrix is needed to support the liquid phosphoric acid. In general, a Teflon®-bonded silicon carbide is used as the matrix.

1.3 Fuel Cell Challenges

Fears of rapid fossil fuel depletion and concerns over accelerated emissions of global warming gases have revitalized the area of fuel cell research and development. Currently, fuel cells are considered the most efficient energy converting devices, with low or zero pollution emissions. However, despite more than 26 years of contemporary development and 170 years of history, fuel cells are still not ready for commercialization. Indeed, the concept of “clean energy” may not be as clean as people have thought. First, hydrogen is not a naturally occurring resource, so once fuel cells are commercialized, hydrogen production will be a major problem. Even though hydrogen is a by-product of some industries, the productivity is not great enough to support a fully developed hydrogen fuel cell

industry. Hydrogen can also be obtained by reforming fossil fuels or by electrolyzing water. But the former results in CO_2 emissions and certainly requires additional energy, while the latter requires electric energy and so far, water electrolysis efficiency remains low.

Currently developed low-temperature fuel cells still require a noble metal as the catalyst. To carry out both the HOR and the ORR, Pt-based catalysts must be used. As is well known, Pt is a rare metal; not enough is available on Earth to replace existing vehicles with fuel-cell-powered ones. The concomitant high cost of using Pt is thus the largest barrier to overcome.

The reliability/durability of these fuel cells is another major barrier hindering commercialization. Developing durable catalysts, membranes, gas diffusion layers, and bipolar plates are currently the major areas of concentration in the search for technical breakthroughs.

1.4 PEM Fuel Cell Electrochemistry

1.4.1 Electrochemistry Fundamentals

1.4.1.1 Nernst Equation

For an electrochemical reaction,

$$\mathrm{O} + \mathrm{n\,e^-} \rightarrow \mathrm{R} \tag{1.22}$$

the Gibbs free energy is obtained by the following equation:

$$\Delta G = \Delta G^0 + RT \ln \frac{[R]}{[O]} \tag{1.23}$$

where ΔG^0 is the standard free energy, $[R]$ is the activity of the product (R), and $[O]$ is the activity of the reactant (O) at equilibrium.

The electrical work done through this reaction is nFE, where F is the Faraday constant and E is the electrode potential. This electrical work equals the Gibbs free energy release:

$$\Delta G = -nFE \tag{1.24}$$

Thus,

$$E = E^0 + \frac{RT}{nF} \ln \frac{[O]}{[R]} \tag{1.25}$$

where E^0 is the standard thermodynamic potential at 25 ºC and the activities of both reactant and product are 1.

For an electrochemical reaction involving gases, the electrode potential is related to the pressure of the gases. In H_2/O_2 fuel cells, the electrode potentials at both anode and cathode sides are given by the following equations:

$$\text{Anode: } H_2 \rightarrow 2H^+ + 2e^- \tag{1.26}$$

$$E_a = E_a^0 + \frac{RT}{2F}\ln\frac{[H^+]^2}{P_{H_2}} \tag{1.27}$$

$$\text{Cathode: } O_2 + 4H^+ + 4e^- \rightarrow 2H_2O \tag{1.28}$$

$$E_c = E_c^0 - \frac{RT}{4F}\ln\frac{[H_2O]}{P_{O_2}[H^+]^4} \tag{1.29}$$

In Equations 1.27 and 1.29, E_a is the anode potential, E_c is the cathode potential, E_a^o is the anode standard potential, E_c^o is the cathode standard potential, P_{H_2} is the partial pressure of H_2 gas, P_{O_2} is the partial pressure of O_2 gas, while R, F, and T have their usual meanings.

Here, the cathode potential is dependent on the water phase. If the water is liquid, its activity is usually considered to be 1. In this case, the fuel cell voltage (E_{cell}) can be written as

$$E_{cell} = E_{cell}^0 + \frac{RT}{2F}\ln P_{H_2}P_{O_2}^{1/2} \tag{1.30}$$

If water vapour is produced, the activity of water will be the water vapour pressure (P_{H_2O}), and the cell potential is represented by the following equation:

$$E_{cell} = E_{cell}^0 + \frac{RT}{2F}\ln\frac{P_{H_2}P_{O_2}^{1/2}}{P_{H_2O}} \tag{1.31}$$

where E_{cell}^o is the theoretical open circuit voltage of the fuel cell.

The potential of an electrochemical reaction is temperature-dependent, since the free energy is dependent on temperature according to the following equation:

$$\Delta G = \Delta H - T\Delta S \tag{1.32}$$

In H_2/O_2 fuel cells, an increase in temperature leads to a decrease in theoretical cell voltage.

1.4.1.2 The Butler–Volmer Equation

The Nernst equation is a thermodynamic expression of the equilibrium state of an electrochemical reaction. It can give the value of the thermodynamic electrode potential for electrochemical reactions as well as point out the reaction direction. However, it cannot show the reaction rate. To connect the reaction rate and the electrode potential, one needs to use the Butler–Volmer equation.

For an elementary reaction,

$$O + e^- \leftrightarrow R \tag{1.33}$$

the forward reaction rate can be expressed as

$$i_f = i_0 \exp(-\frac{\alpha F \eta}{RT}) \tag{1.34}$$

Similarly, the backward reaction rate can also be expressed as

$$i_b = i_0 \exp(\frac{(1-\alpha) F \eta}{RT}) \tag{1.35}$$

where i_f is the forward current density, i_b is the backward current density, η is the overpotential (which will be discussed in detail in the following sections), and α is the symmetry factor, indicating the proportion of applied overpotential exerted for the forward reaction. The value of this parameter is usually in the 0.3–0.7 range and in most cases, the number is 0.5. The symmetry factor is different from the normally used transfer coefficient [17]. First, the symmetry factor applies to an elementary reaction, whereas the transfer coefficient is for a complex reaction involving several steps, which reflects the impact of each step on the whole reaction rate. Second, the transfer coefficient can be larger than 1, depending on the reaction mechanism. However, the symmetry factor never exceeds 1 [17].

The net rate of the elementary reaction is obtained by deducting the backward reaction from the forward reaction. This is called the Butler–Volmer equation:

$$i = i_c - i_a = i_0(\exp(-\frac{\alpha F \eta}{RT}) - \exp(\frac{(1-\alpha) F \eta}{RT})) \tag{1.36}$$

where i_o is the exchange current density, which will be discussed in the following section. For a multi-electron reaction ($O + ne^- \rightarrow R$), the reaction mechanism consists of several elementary reactions. Some of these involve electron transfer, so the Butler–Volmer equation can be used, while some might be purely chemical reactions to which the Butler–Volmer equation does not apply. The whole reaction rate will be the combination of all the elementary reaction rates. Thus, there is no simple expression of the Butler–Volmer equation for a multi-electron reaction. Indeed, a multi-electron elementary reaction is not realistic because having several electrons transfer in one step is impossible. In electrochemistry, many electrochemical reactions do involve multi-electron transfers; for example, the

HOR and the ORR involve two and four electrons, respectively. Since the Butler–Volmer equation is important for expressing the relationship between the current density of an electrochemical reaction and the overpotential, the rate-determining step (RDS) of a multi-electron reaction can be simplified as a pseudo-elementary reaction involving multiple electrons. The Butler–Volmer equation for this reaction is usually written as follows:

$$i = i_0(\exp(-\frac{\alpha n_\alpha F\eta}{RT}) - \exp(\frac{(1-\alpha)n_\alpha F\eta}{RT})) \tag{1.37}$$

This is only an approximate representation, in which α is the transfer coefficient and n_α is the apparent electron number involved in the pseudo-elementary reaction. This n_α is different from the total electron transfer number of the reaction (n).

1.4.1.3 Electrochemical Parameters

Overpotential

For an electrochemical reaction, $O + ne^- \leftrightarrow R$, at equilibrium, the forward reaction rate equals the backward reaction rate, the net reaction rate is 0, and no net electric current is produced. The potential at equilibrium is the Nernst potential or thermodynamic potential as expressed in Equations 1.30 and 1.31. To obtain a net current from the reaction, as shown in Equation 1.37, the potential applied to the electrode surface should shift away from the Nernst potential; the difference between the applied potential and the Nernst potential is called overpotential:

$$\eta = E - E^0 \tag{1.38}$$

where E is the applied potential and E^0 is the Nernst potential. The relationship between the overpotential and the current follows Equation 1.37. The higher the overpotential, the bigger the current. Bockris has provided a theoretical explanation of overpotential in [18].

Exchange Current Density (i_0)

In a chemical reaction at equilibrium, the concentrations of reactants and products do not change and no net reaction occurs. However, this does not mean that no reaction takes place in the system. Rather, it means that the forward reaction rate equals the backward reaction rate, and the consumption speed of the reactants in the forward reaction equals the production rate of the reactants in the backward reaction, resulting in no net concentration change for reactants and products.

In an electrochemical reaction ($O + ne^- \leftrightarrow R$), both forward and backward reactions can occur simultaneously. At equilibrium, no net current flows out of or draws into the system, and the current density of the forward reaction equals the current density of the backward reaction. This current density is called the exchange current density, as described above in Equations 1.34 to 1.37. The exchange current density is a kinetic parameter that depends on the reaction and on the electrode surface upon which the electrochemical reaction occurs.

The magnitude of the exchange current density determines how easily the electrochemical reaction can occur on the electrode surface. A small exchange current means that a high overpotential is required to achieve a high current flow, while a large exchange current density indicates that only a small overpotential is needed to produce a large current flow. For example, on a Pt surface, the exchange current density of H_2 oxidation is 5–6 magnitudes larger than that of O_2 reduction. Thus, at a very small overpotential, the HOR could be very fast. However, to reach the same current density, the ORR requires a higher overpotential. This is the problem in H_2/O_2 fuel cells: most of the voltage loss is due to the cathode ORR, so an efficient cathode catalyst is necessary to speed up the reaction.

Apparent Exchange Current Density ($i_0^{apparent}$)

In a fuel cell, the exchange current density can be estimated using alternating current (AC) impedance spectroscopy at open circuit voltage (OCV), and can be obtained from the charge-transfer resistance measured in the AC impedance spectra, as will be described in Section 1.4.6. This calculated exchange current density is dependent on reactant concentration, electroactive catalyst surface area, and temperature, and is called the apparent exchange current density. Unfortunately, the apparent exchange current density may not be useful because the reactant concentration and the electroactive catalyst surface area can be significantly different, as shown in the following equation:

$$i_0 = nFAKC_O\left(\frac{C_O}{C_R}\right)^{-\alpha} \tag{1.39}$$

where A is the electroactive catalyst surface area, K is the electrochemical reaction rate, C_O is the oxidant concentration, C_R is the reduction product concentration, α is the transfer coefficient of the reaction, while n and F and have their usual meanings.

Intrinsic Exchange Current Density ($i_0^{intrinsic}$)

To make a valid comparison, one should calculate the intrinsic exchange current density, which can be done using the following equation:

$$i_0^{intrinsic} = nFK = \frac{i_0}{AC_O^{1-\alpha}C_R^{\alpha}} \tag{1.40}$$

The intrinsic exchange current density is very important in fuel cells because the electroactive Pt surface area is significantly different from its geometric area, and the former changes with temperature.

Tafel Slope

In 1905, Julius Tafel found that overpotential was related to current density (i) by the following equation:

$$\eta = a \log \frac{i}{i_0} \tag{1.41}$$

where a is constant. In a certain current density range, overpotential is linearly dependent on the logarithmic of current density. The exchange current density can be obtained from the intercept at the current density axis. The slope of the line is called the Tafel slope. The higher the Tafel slope, the slower the electrode reaction kinetics.

Taking Equation 1.37, when the overpotential is large enough that the other reaction can be neglected, the equation can be simplified for the forward reaction as

$$i_f = i_0 \exp(-\frac{\alpha n_a F \eta}{RT}) \tag{1.42}$$

and for the backward reaction as

$$i_b = i_0 \exp(\frac{(1-\alpha) n_a F \eta}{RT}) \tag{1.43}$$

Rearrangement of the two equations gives a forward reaction of

$$\eta = -\frac{2.303RT}{\alpha n_\alpha F} \log \frac{i_f}{i_0} \tag{1.44}$$

and a backward reaction of

$$\eta = \frac{2.303RT}{(1-\alpha) n_\alpha F} \log \frac{i_b}{i_0} \tag{1.45}$$

Equations 1.44 and 1.45 are called Tafel equations. Figure 1.10 shows the Tafel plots for both forward and backward electrode reactions.

The terms $-\frac{2.303RT}{\alpha n_\alpha F}$ and $\frac{2.303RT}{(1-\alpha) n_\alpha F}$ in Equations 1.44 and 1.45 are the Tafel slopes for the forward and backward reactions, respectively.

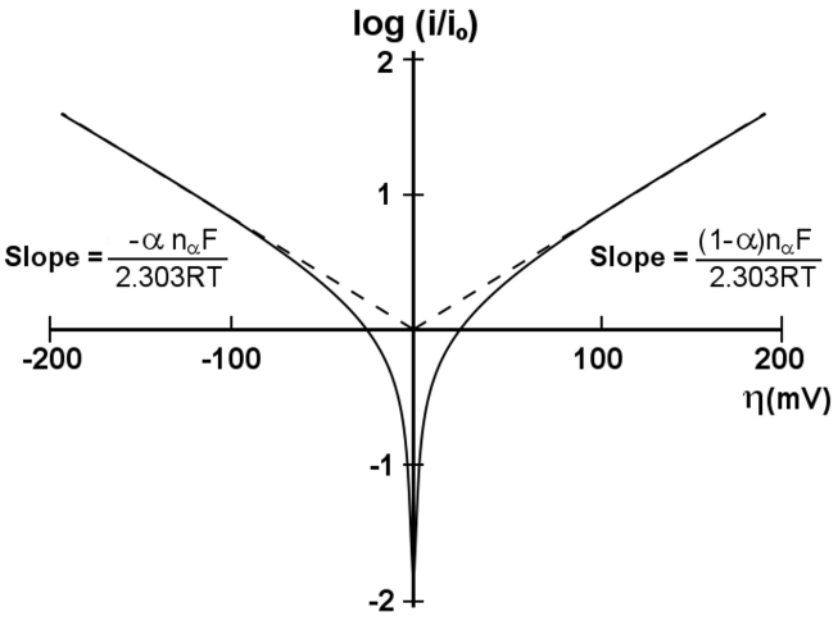

Figure 1.10. Tafel plot for cathode and anode branches of the current–voltage curve [19]. (From Wang J. Analytical electrochemistry. ©2006 Wiley-VCH. Reproduced with permission.)

Charge-Transfer Resistance (R_{ct})

R_{ct} is the charge-transfer resistance for electrochemical reactions. This resistance refers to the barrier through which the electron must pass across the electrode surface to the adsorbed species, or from the adsorbed species to the electrode. The resistance is related to the electrode potential, or more precisely, related to the overpotential. As the overpotential becomes larger, the resistance diminishes.

At a very small overpotential, the relationship between the R_{ct} and the exchange current density can be deduced from Equation 1.37, which can be simplified as

$$i = i_0 \frac{n_\alpha F \eta}{RT} \tag{1.46}$$

Thus, charge-transfer resistance (R_{ct}) can be expressed as

$$R_{ct} = \frac{RT}{n_\alpha F i_0} \tag{1.47}$$

Again, the electron number is only for the electrons involved in the rate-determining step. For a multi-electron, multi-step reaction, n_α does not equal the total number of electrons involved in the whole reaction. For example, in the ORR, the total number of electrons is four; however, the apparent electron number

changes with the Tafel slope. In a low current density range (low overpotential), a Tafel slope of 60 mV/decade has been observed, indicating that the apparent electron number in the rate-determining step is 2 [20].

1.4.2 Polarization Curves

Polarization means that the potential of the electrode surface shifts away from its equilibrium value, leading to an electrochemical reaction. Polarization curves record the voltage change with current density, which is important data for characterizing fuel cell performance. A good fuel cell should display a polarization curve with high current density at high cell voltage, indicating high power output. Figure 1.11 shows typical polarization curves for a PEMFC.

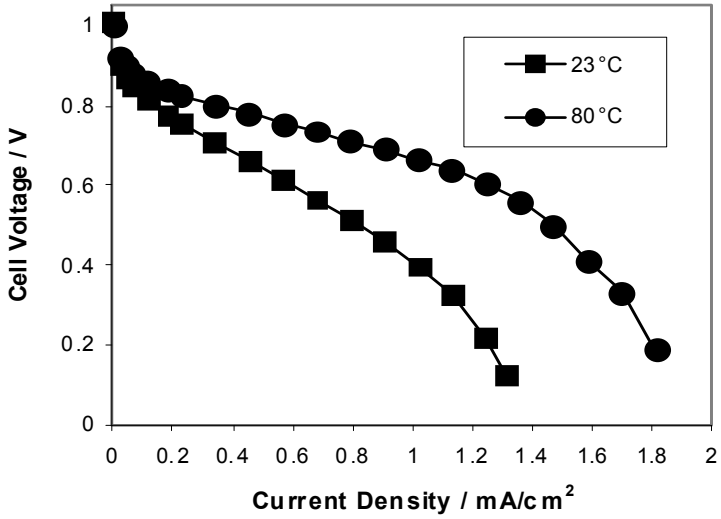

Figure 1.11. Polarization curves obtained at 23°C and 80°C with a back-pressure of 30 psig. MEA active area: 4.4 cm^{-2}. H_2/air gases with 100% relative humidity [20]. (Adapted from Electrochimica Acta, 52, Song C, Tang Y, Zhang J, Zhang J, Wang H, Shen J, et al., PEM fuel cell reaction kinetics in the temperature range of 23–120ºC, 2552–61. ©2007, with permission from Elsevier.)

1.4.3 Current Interruption

The current interruption method is used to measure the internal resistance of an electrochemical system. In a fuel cell, it is usually used to measure the membrane resistance.

According to this method, a certain current is forced to pass through the electrochemical system, then the current is suddenly set to 0. The voltage change due to the disappearance of the ohmic drop can be observed immediately, while the voltage change due to the electrochemical overpotential gradually disappears, as shown in Figure 1.12. The resistance can be obtained by dividing the voltage

change by the current. This method can eliminate voltage change caused by electrochemical overpotential.

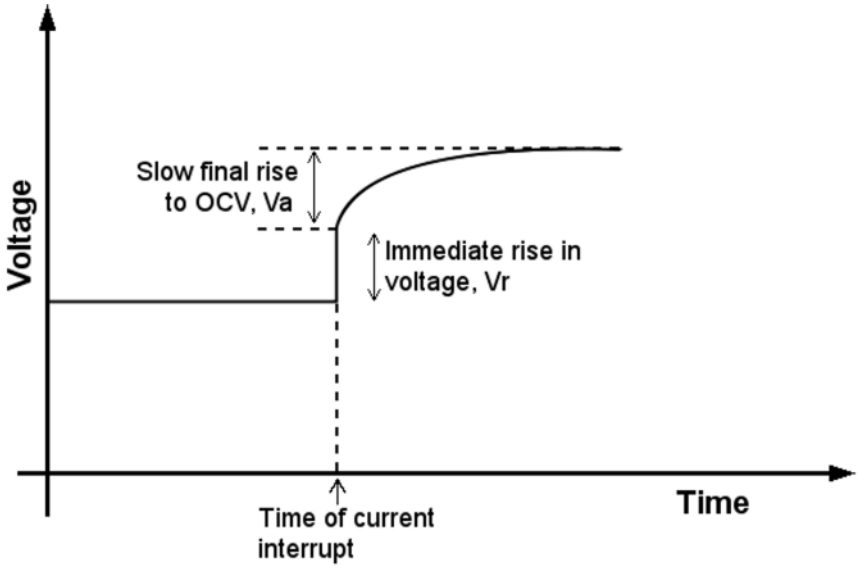

Figure 1.12. Current interruption method showing the voltage change with time [3]. (From Larminie J, Dicks A. Fuel cell systems explained. ©2003 John Wiley & Sons Limited. Reproduced with permission of the publisher and the authors.)

1.4.4 Chronoamperometry

In an electrochemical system with a stationary working electrode and a quiescent solution, when the potential of the working electrode is increased from a value at which no electrochemical reaction is occurring to a value at which the electrochemical reaction is diffusion controlled, the current will decay with time, as shown in Figure 1.13. This technique is called chronoamperometry. At this potential the surface concentration of the electroactive species decreases according to the potential, and the diffusion layer expands with time and according to the depletion of the reactant, which causes the current decay. The Cottrell equation can be used to express current decay with time:

$$i(t) = \frac{nFACD^{1/2}}{\pi^{1/2} t^{1/2}} \tag{1.48}$$

where C is the reactant concentration, D is the diffusion coefficient of the reactant species, t is time, A is the electrode area, n is the electron number, and F is the Faraday constant. This method is usually used to determine the diffusion coefficient. In fuel cells, this technique is used to measure fuel crossover.

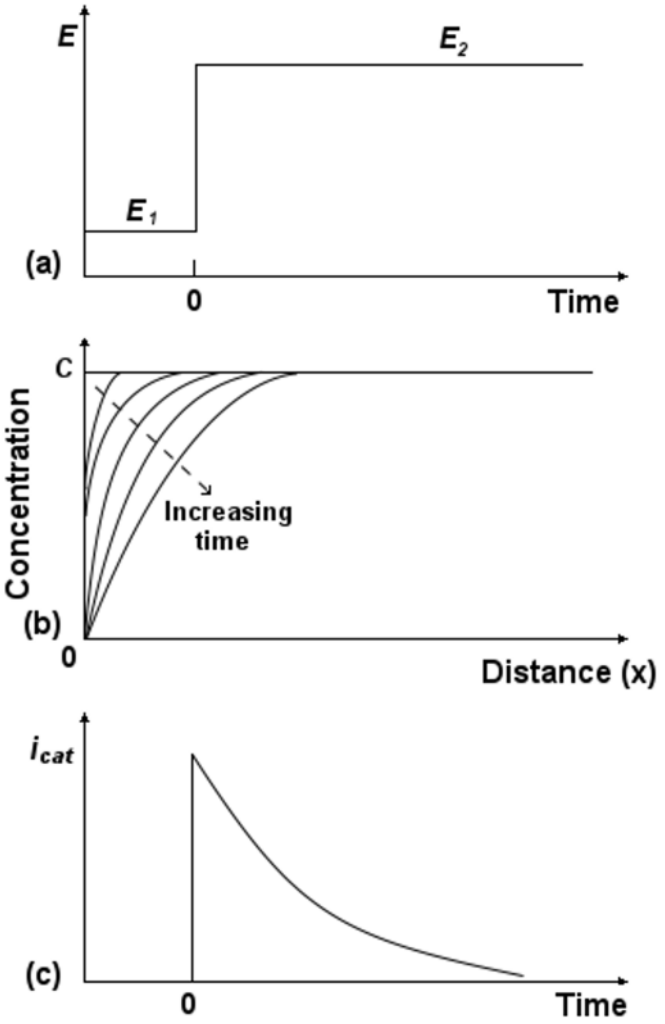

Figure 1.13. Chronoamperometric experiment: (*a*) potential-time waveform; (*b*) change in concentration profiles as time progresses; (*c*) the resulting current-time response [19]. (From Wang J. Analytical electrochemistry. ©2006 Wiley-VCH. Reproduced with permission.)

1.4.5 Cyclic Voltammetry [19, 21]

Cyclic voltammetry is the most useful technique in electrochemistry. It can rapidly provide qualitative information about electrochemical reactions, such as thermodynamics and kinetics.

In cyclic voltammetry, the potential of the working electrode is scanned linearly from an initial to a vertex value, and then the scan is reversed. The electrochemical response of the target species with applied potential during the forward and reverse scans can be obtained from the scan cycle. Figure 1.14 shows

a schematic illustration of the potential changes in cyclic voltammetric experiments.

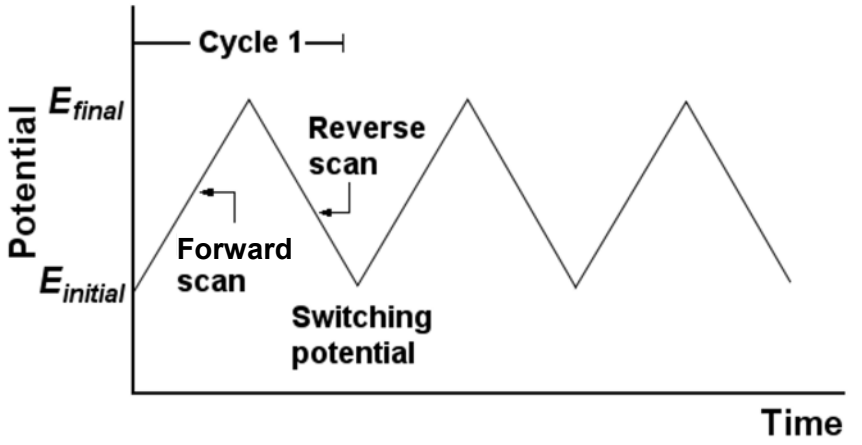

Figure 1.14. Potential–time excitation signals in a cyclic voltammetric experiment [19]. (From Wang J. Analytical electrochemistry. ©2006 Wiley-VCH. Reproduced with permission.)

Assuming that a redox species exists only in oxidized form (O) in the solution, as the potential scans from being more positive than the thermodynamic potential of the redox species to being a negative potential, there is initially no Faradaic current flow. As the electrode potential approaches E^0, reduction of O starts and the reduction current begins to flow. As the potential continues to become more negative, the cathodic current increases until it reaches a peak and then starts to decrease. At the peak current, the reaction speed is determined by the mass transfer rate of O to the electrode surface. The decline of the current after the peak is due to the expansion of the diffusion layer near the electrode surface. As time passes, the diffusion layer became much thicker, leading to a decrease in the cathodic current. The current decline is $t^{-½}$-dependent, in accordance with Equation 1.48 in Section 1.4.4. After the potential is scanned at least 90/n mV negative to the peak potential, the scan is reversed. In the reverse cycle, the reduced species R, formed in the forward potential sweep, is oxidized back to O. Again, an oxidation peak and a decline of the peak can be observed. The visually represented response of current versus potential is called a cyclic voltammogram.

Figure 1.15 shows a potential sweep cycle, the electrochemical response with the cycle, and the surface concentration profile in the potential sweep. A cyclic voltammogram can give information about the thermodynamic potential, diffusion coefficient, kinetics, and reversibility of the reaction.

The extent to which qualitative parameters can be extracted from the cyclic voltammogram is dependent on its reversibility. Different equations have been obtained for different systems.

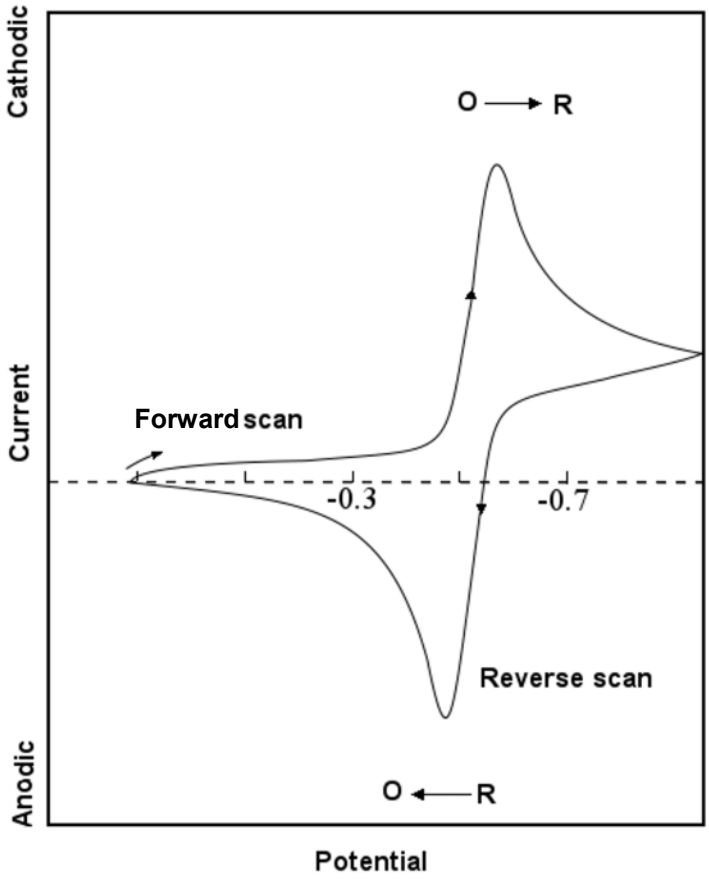

Figure 1.15. Typical cyclic voltammogram for a reversible redox process [19]. (From Wang J., Analytical electrochemistry. ©2006 Wiley-VCH. Reproduced with permission.)

For a reversible system, the Randles–Sevcik equation gives the peak current (i_p) for a reversible couple:

$$i_p = 0.2263(\frac{F^3}{RT})^{1/2} n^{3/2} A D_O^{1/2} C_O v^{1/2} \tag{1.49}$$

where F, R, and T have their usual meanings, n is the electron number, A is the electrode area, D_O is the diffusion coefficient of O, C_O is the concentration of O in the solution, and v is the potential scan rate.

At 25°C, with A in cm^2, D_O in cm^2/s, C_O in mol/cm^3, v in V/s, and i_p in A, the equation becomes

$$i_p = (2.69\times10^5) n^{3/2} A D_o^{1/2} C_O v^{1/2} \tag{1.50}$$

The reversible electrochemical process is characterized by the following features:

1. The peak current is proportional to $v^{1/2}$, and $i_{P_c}/i_{P_a} = 1$.
2. The peak position does not change with the scan rate.
3. Peak separation between the cathodic peak potential and the anodic potential (ΔE_p) is a constant given by the following equation:

$$\Delta E_p = E_{p,a} - E_{p,c} = 2.3\frac{RT}{nF} = \frac{0.059}{n} \text{ V (at 25°C)} \tag{1.51}$$

where $E_{p,a}$ and $E_{p,c}$ are the anodic and cathodic peak potential, respectively. Thus, from a cyclic voltammogram, the electron number, diffusion coefficient, electrode area, and electroactive species concentration can be obtained.

The thermodynamic potential of the redox reaction can also be obtained by averaging the anodic peak potential and the cathodic peak potential. However, for a reversible system, kinetic parameters such as reaction rate cannot be obtained because the reaction rates for both forward and backward reactions are extremely fast.

For an irreversible system ($O + ne^- \rightarrow R$), the peak current is reduced and given by the following equation:

$$i_p = (2.99\times10^5)n(\alpha n_a^{1/2})AD_o^{1/2}C_O v^{1/2} \tag{1.52}$$

where α is the charge transfer coefficient and n_a is the electron number involved in the charge transfer step. The peak current is proportional to the square root of the scan rate. However, it is only about 80% of its reversible counterpart, assuming an α of 0.5. The αn_a value can be obtained from the peak separation between the peak potential and the half-wave potential ($E_{p/2}$). In the irreversible system,

$$\left|E_p - E_{p/2}\right| = \frac{1.857RT}{\alpha n_a F} = \frac{47.7}{\alpha n_a} \text{ mV at 25°C} \tag{1.53}$$

The peak potential is dependent on the scan rate, as given in the following equation:

$$E_p = E^0 - \frac{RT}{\alpha n_a F}[0.78 - \ln\frac{k^0}{D^{1/2}} + \ln(\frac{\alpha n_a F v}{RT})^{1/2}] \tag{1.54}$$

where k^0 is the electrochemical reaction rate. It can be seen clearly that a cathodic shift of E_p by an amount $1.15RT/\alpha n_a F$ or $30/\alpha n_a$ mV can be obtained from the slope of E_p versus $\log v$.

The relationship between the peak current and the peak potential is given by the following equation:

$$i_p = 0.227nFACk^0 \exp[\frac{-\alpha n_a F}{RT}(E_p - E^0)] \quad (1.55)$$

The parameters αn_a and k^0 can be obtained from the plot of $\ln(i_p)$ versus E_p–E^0 determined at different scan rates from the slope and intercept, respectively.

For a quasi-reversible process, both charge transfer and mass transfer affect the current. The shape of the cyclic voltammogram is a function of $k^0/\sqrt{\pi aD}$ (where $a = nF\nu/RT$). The peak separation between the anodic and cathodic peaks can give information about k^0.

The reversibility of electrochemical reactions is determined by the reaction rates: for a reversible reaction, $k^0 \geq 0.3\nu^{1/2}$ cm/s, for a quasi-reversible reaction, $0.3\nu^{1/2} > k^0 \geq 2 \times 10^{-5}\nu^{1/2}$ cm/s, while for an irreversible reaction, $k^0 < 2 \times 10^{-5}\nu^{1/2}$ cm/s. Figure 1.16 shows the cyclic voltammograms for irreversible and quasi-reversible redox processes.

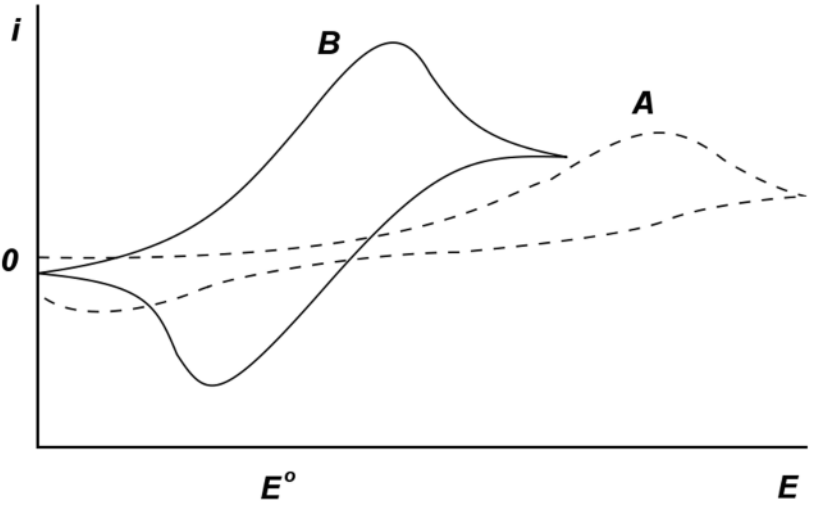

Figure 1.16. Cyclic voltammograms for irreversible (*A*) and quasi-reversible (*B*) redox processes [19]. (From Wang J. Analytical electrochemistry. ©2006 Wiley-VCH. Reproduced with permission.)

1.4.6 Electrochemical Impedance Spectroscopy

Electrochemical reactions consist of electron transfer at the electrode surface. These reactions mainly involve electrolyte resistance, adsorption of electroactive species, charge transfer at the electrode surface, and mass transfer from the bulk solution to the electrode surface. Each process can be considered as an electric component or a simple electric circuit. The whole reaction process can be represented by an electric circuit composed of resistance, capacitors, or constant phase elements combined in parallel or in series. The most popular electric circuit for a simple electrochemical reaction is the Randles–Ershler electric equivalent

circuit model, which includes electrolyte resistance, charge-transfer resistance at the electrode/electrolyte interface, double-layer capacitance, and mass transfer resistance.

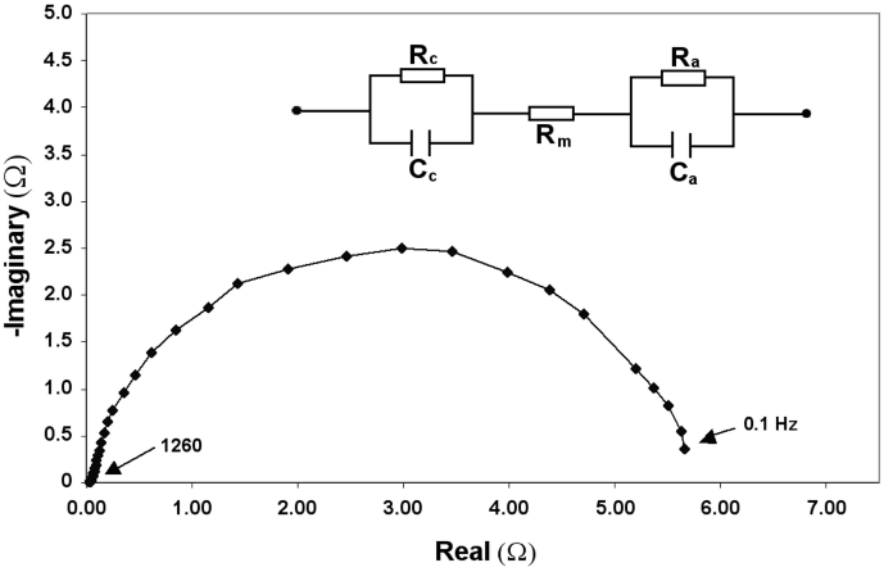

Figure 1.17. Nyquist plot for a fuel cell operated at OCV, 80°C, 3.0 atm, and 100% RH [20]. (Reproduced from Electrochimica Acta, 52, Song C, Tang Y, Zhang J, Zhang J, Wang H, Shen J, et al., PEM fuel cell reaction kinetics in the temperature range of 23–120ºC, 2552–61. ©2007, with permission from Elsevier.)

AC impedance spectroscopy is an effective technique to extract each component in an electric circuit. Applying AC impedance in electrochemical systems can also provide detailed information about the electrochemical reactions. In this technique, a small AC amplitude perturbation is added to a constant direct current (DC) signal with a changing frequency. By scanning the frequency, the impedance change can be recorded and each component value can be obtained. For example, if a fuel cell is in the OCV condition, mass transfer resistance is negligible and the anode can be neglected due to the fast anodic kinetics. The impedance of the electric circuit ($Z(\omega)$) of such a fuel cell is given by the following equation:

$$Z(\omega) = R_m + R_{ct}/(1+\omega^2 R_{ct}^2 C_{ct}^2) - j\omega R_{ct}^2 C_{ct}/(1+\omega^2 R_{ct}^2 C_{ct}^2) \tag{1.56}$$

where R_m is the membrane resistance, R_{ct} is the charge-transfer resistance, C_{ct} is the charge transfer related capacity, and ω is the AC frequency. The plot with the real resistance as the X axis and the imaginary resistance as the Y axis is called the Nyquist plot. Figure 1.17 shows a typical Nyquist plot of the ORR in a PEMFC, and the equivalent circuit of the MEA. At high frequencies, the imaginary impedance is zero and the resistance equals R_m, the electrolyte resistance. At low frequencies, the resistance is the sum of R_m and R_{ct}, from which the charge-transfer

resistance can be extracted. From the frequency showing the maximum imaginary impedance, the product of R_cC_c can be calculated. Thus, all the parameters can be obtained using the AC impedance spectrum.

AC impedance spectra provide a large amount of information about the electrochemical system being investigated. However, the analysis of AC impedance spectra and the correlation of AC impedance spectra with a specific parameter are still not fully understood. For example, for electrochemical reactions under load (or with a certain reaction rate), how the charge-transfer resistance relates to the reaction rate is not clear. More work is needed to deduce electrochemical reaction parameters from these spectra. In a later part of this book, impedance derived from reaction mechanisms and its correlation with electric circuit components will be discussed.

1.5 Fuel Cell Analysis

A fuel cell is an electrochemical device that converts the chemical energy of a fuel directly into electricity. The cell consists of three main parts: the fuel compartment, the oxidant compartment, and an electrolyte membrane separating the fuel and oxidant. At the fuel side, the fuel is oxidized and electrons are released. At the oxidant side, the oxidant is reduced by accepting the electrons released from the fuel side. The electrons flowing through the fuel side to the oxidizer side can be harnessed, producing electric power. For an H_2/air fuel cell, the reactions are:

$$H_2 \rightarrow 2H^+ + 2e^- \tag{1.57}$$

$$O_2 + 4H^+ + 4e^- \rightarrow 2H_2O \tag{1.58}$$

The overall reaction is

$$2H_2 + O_2 \rightarrow 2H_2O \tag{1.59}$$

To obtain electric current, an electronic insulating and proton-conducting membrane is needed to separate these two half-reactions. The electrons flow through the external electric circuit, while the protons pass through the membrane to complete the reaction. Both H_2 oxidation and O_2 reduction reactions are very slow processes, and catalysts are required to harness the reactions in a practical way. So far, the best catalyst for these two reactions is Pt, which is expensive and in limited supply on Earth. Figure 1.18 shows a membrane electrode assembly, with O_2 passing the cathode, H_2 passing the anode, and electrical load connected in the electric circuit.

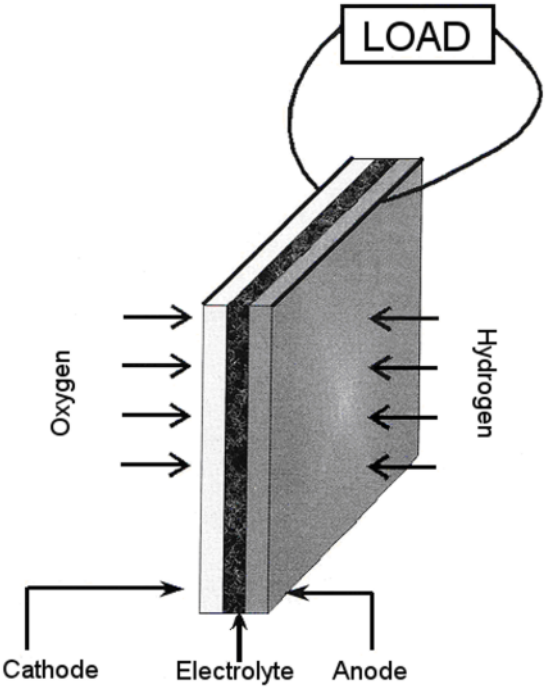

Figure 1.18. Membrane electrode assembly in a fuel cell [3]. (From Larminie J, Dicks A. Fuel cell systems explained. ©2003 John Wiley & Sons Limited. Reproduced with permission from the publisher and the authors.)

1.5.1 Open Circuit Voltage

Open circuit voltage (OCV) is the cell voltage at an electric current of 0, with no load and no power output. The fuel cell voltage is the difference between cathode potential and anode potential. In principal, at an electric current of 0, the cell voltage should be the difference in thermodynamic potential between the cathode and the anode, which are related to the Gibbs free energy via $\Delta G = -nFE^0$. At 25°C and 1 atm, if liquid water is produced, the Gibbs free energy oxygen reduction reaction is –237 kJ/mol. Thus, under standard conditions, the thermodynamic cell voltage for a H_2/air (O_2) fuel cell is 1.23 V.

If water vapour instead of liquid water is produced in the reaction, matters are different. For the reaction:

$$O_2 + 4H^+ + 4e^- \rightarrow 2H_2O_{(g)} \qquad \Delta G = -229 \text{ kJ/mol} \tag{1.60}$$

the thermodynamic cell voltage will be smaller at 1.19 V.

In a fuel cell, the H_2 and O_2 pressures are not limited to 1 atm. Change in these pressures leads to deviation from the theoretical cell voltage. The relationships between the gas pressures, the anode and cathode potentials, and the cell voltage

are given in Equations 1.27 to 1.31. For clarity, Equations 1.30 and 1.31 are rewritten here as 1.61 and 1.62:

$$E_{cell} = E_c - E_a = E_{cell}^0 + \frac{RT}{2F}\ln(\frac{P_{O_2}^{1/2}P_{H_2}}{P_{H_2O}}) \tag{1.61}$$

while in the case of liquid water production, the activity of liquid water is usually considered to be 1, thus Equation 1.61 becomes Equation 1.62:

$$E_{cell} = E_c - E_a = E_{cell}^0 + \frac{RT}{2F}\ln(P_{O_2}^{1/2}P_{H_2}) \tag{1.62}$$

It can be seen that increasing either oxygen or hydrogen pressure leads to an increase in theoretical cell voltage. For example, in the case of H_2/air fuel cells, at room temperature and if the pressure is 1 atm on both sides, the theoretical cell voltage is 1.22 V. If the pressure for both sides is 3 atm, the theoretical cell voltage becomes 1.24 V, 20 mV higher.

Under theoretical cell voltage conditions, for both half-cell reactions (HOR and ORR) there is no net reaction. In other words, both half-electrochemical reactions are in equilibrium, and no net current passes through the external circuit. The cell voltage can be considered the OCV. At 25 ºC, if the pressures of both H_2 and O_2 are 1 atm, the OCV should be 1.23 V. However, in reality the OCV is normally lower and an OCV of 1.23 V is never observed. This is due to the mixed potential at the cathode side, and hydrogen crossover from the anode side to the cathode side [22, 23]. At 1.23 V, Pt is not stable so oxidation of Pt occurs:

$$Pt + H_2O \rightarrow PtO + 2H^+ + 2e^- \qquad E = 0.88\ V \tag{1.63}$$

The deviation of electrode potential from the theoretical potential also leads to oxygen reduction. Thus, at the cathode side, three reactions occur at OCV: Pt oxidation, H_2 oxidation, and O_2 reduction. The two oxidation reactions release electrons and O_2 reduction accepts electrons. At OCV, the net current is zero. Thus,

$$I_{O_2}^{OCV} = I_{H_2}^{crossover} + I_{Pt}^{OCV} \tag{1.64}$$

Under this condition, the cell voltage is the OCV. It has been widely reported that in a half-cell with only Pt, O_2, and electrolyte, the mixed potential is 1.06 V. In a real fuel cell, the OCV may be lower due to the presence of hydrogen crossover, which will drag the cell voltage down. In a recent paper we reported an investigation of OCV across a wide temperature range. Figure 1.19 shows the experimental OCV and the theoretical OCV. After correction for hydrogen crossover and mixed potential, it was found that the theoretical OCV was in agreement with the experimental value.

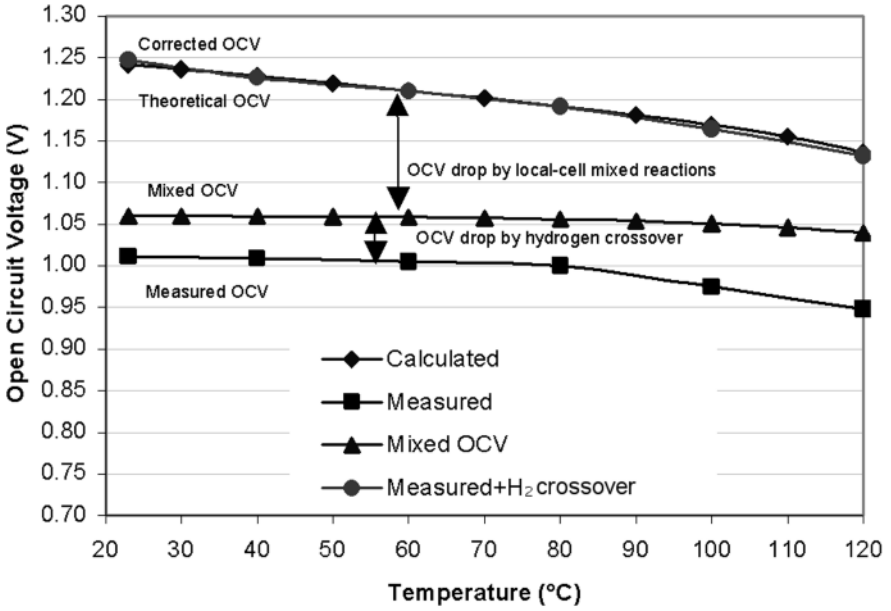

Figure 1.19. Experimental OCV and theoretical OCV corrected for mixed potential and H_2 crossover [22]. (Adapted from Journal of Power Sources, 163, Zhang J, Tang Y, Song C, Zhang J, Wang H. PEM fuel cell open circuit voltage (OCV) in the temperature range of 23ºC to 120ºC, 532–7, ©2006, with permission from Elsevier.)

1.5.2 Cell Voltage Under Load

The OCV seems to be of less practical use. It is much more useful for a fuel cell to work under a load, with power being delivered to the users. With the electric energy output, the fuel cell voltage will decrease as the electric current load increases. A popular way to evaluate a fuel cell is to measure its polarization curve (abbreviated as "I–V curve"), which is a plot showing the cell voltage change with current or current density. Figure 1.20 shows a typical polarization curve obtained with a PEMFC.

In the polarization curve, three parts can be observed: kinetic, ohmic, and mass transfer. In the kinetic part, the cell voltage drop is due to the charge-transfer kinetics, i.e., the O_2 reduction and H_2 oxidation rate at the electrode surface, which is dominated by the kinetic I–η equation (Equation 1.37). In the ohmic part, the cell voltage drop is mainly due to the internal resistance of the fuel cell, including electrolyte membrane resistance, catalyst layer resistance, and contact resistance. In the mass transfer part, the voltage drop is due to the transfer speed of H_2 and O_2 to the electrode surface.

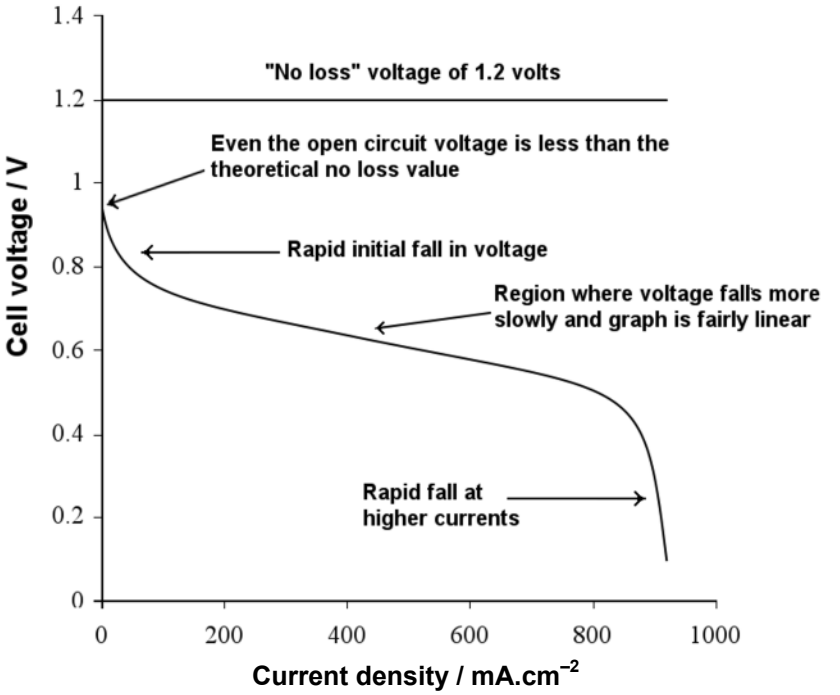

Figure 1.20. A typical polarization curve in a fuel cell [3]. (From Larminie J, Dicks A. Fuel cell systems explained. ©2003 John Wiley & Sons Limited. Reproduced with permission from the publisher and the authors.)

1.5.2.1 Cell Voltage Drop Due to Reaction Kinetics [20]

When a fuel cell is under operation, the electric current passes through both anode and cathode sides, and the electrode potentials of both deviate from their equilibrium values. These deviations are called anode and cathode overpotentials, respectively. At both sides, Equation 1.37 holds. Thus, at the anode side,

$$I_a = i_0^{H_2}\left(e^{\frac{n_{aH}\alpha_H F\eta_a}{RT}} - e^{-\frac{n_{aH}(1-\alpha_H)F\eta_a}{RT}}\right) \tag{1.65}$$

where $i_0^{H_2}$ is the exchange current of the HOR, n_{aH} is the electron number at the rate-determining step, a_H is the electron transfer coefficient, η_a is the anode overpotential, while R and T have their usual meanings.

In Equation 1.65, the first part in the parentheses of the equation represents the forward reaction rate, indicating hydrogen oxidation; the second part represents the backward reaction rate, indicating the hydrogen evolution reaction. The net hydrogen oxidation rate equals the forward reaction rate minus the backward reaction rate.

In the literature, the cathode Pt electrode surface of a fuel cell is considered to be pure Pt. However, from the above-mentioned OCV argument it can be seen that

the electrode surface status is actually related to the electrode potential. In our recent paper investigating PEMFC reaction kinetics, two cathode surfaces were considered. If the Pt electrode potential is higher than ~ 0.8 V, Pt oxidation occurs and the electrode surface will be a mixture of Pt/PtO_x. Otherwise, the Pt electrode will be a pure Pt surface. For the ORR at low current densities, the electrode potential is high, the electrode surface is mixed, and the observed kinetics is the ORR on Pt/PtO_x. At high current densities, the potential is low and the electrode surface is pure Pt; therefore, the ORR kinetics is different from that at low current densities. Two sets of kinetic parameters, including two Tafel slopes and two exchange current densities, should be obtained. This has been reported extensively in the literature on half-cell investigations of the ORR on Pt electrodes.

At low current densities, the previous anode reaction equation also holds true for the cathode, and the equation becomes

$$I_c = i_0^{O_2-Pt/PtO}\left(e^{\frac{n_{\alpha O-Pt/PtO}\alpha_{O-Pt/PtO}F\eta_c}{RT}} - e^{-\frac{n_{\alpha O-Pt/PtO}(1-\alpha_{O-Pt/PtO})F\eta_c}{RT}}\right) \tag{1.66}$$

The parameters in this equation have similar meanings to those for the hydrogen oxidation reaction, as applied to the cathode.

In a fuel cell, the overpotential for the HOR is defined as $\eta_a = E_a - E_a^0$, while the overpotential for the ORR is defined as $\eta_c = E_c^0 - E_c$; here, $E_a^0 = 0$ and $E_c^0 = 1.23$ under standard conditions.

In a fuel cell, I_a should equal I_c, and then the fuel cell voltage (V_{cell}) can be expressed as

$$V_{cell} = E_{OCV} - \eta_c - \eta_a - I_{cell}R_{el} \tag{1.67}$$

where E_{OCV} is the open circuit voltage, I_{cell} is the fuel cell current density, and R_{el} is the polymer electrolyte membrane resistance.

At high current densities, the backward reactions for both anode and cathode can be omitted, and the mass transfer process in both reactions should be considered. The cathode and anode current densities can be expressed as Equations 1.68 and 1.69:

$$I_c = i_0^{O_2}\left[\left(1-\frac{I_c}{I_{dc}^f}\right)e^{\frac{n_{\alpha O}\alpha_O F\eta_c}{RT}}\right] \tag{1.68}$$

$$I_a = i_0^{H_2}\left[\left(1-\frac{I_a}{I_{da}^f}\right)e^{\frac{n_{\alpha H}\alpha_H F\eta_a}{RT}}\right] \tag{1.69}$$

The relationship between the cell voltage and the cell current density can be simply written as the following equation if the fuel cell polarization is larger than 60 mV:

$$V_{cell} = E_{OCV} + \frac{RT}{0.001678Tn_{\alpha O}F}\ln(i_0^{O_2}) + \frac{RT}{0.5n_{\alpha H}F}\ln(i_0^{H_2}) - \frac{RT}{0.001678Tn_{\alpha O}F}\ln(\frac{I_{cell}I_{dc}^f}{I_{dc}^f - I_{cell}}) - \frac{RT}{0.5n_{\alpha H}F}\ln(\frac{I_{cell}I_{da}^f}{I_{da}^f - I_{cell}}) - I_{cell}R_{el} \quad (1.70)$$

where $i_0^{O_2}$ is the apparent exchange current density for the cathodic ORR on a pure Pt surface, which should be a different value from that on a Pt/PtO surface. The electron number (n_{aO}) should accordingly be taken as 1.0 rather than 2.0. I_{da} and I_{dc} are the diffusion limiting current densities of the anode and cathode reactions, respectively, and $0.001678T$ indicates the temperature-dependent transfer coefficient for the ORR. It is believed that $i_0^{H_2}$ should have the same value as that obtained at low current densities because in both low and high current density ranges only the pure Pt surface is involved.

In a very rough treatment, the statuses of the cathode electrode surface at low and high current densities are considered to be the same, as reported in most of the literature. A simple empirical expression can then be given:

$$V_{cell} = E_{OCV} - b\log I_{cell} - I_{cell}R_m - m\exp(I_{cell}n) \quad (1.71)$$

where b is the Tafel slope, and m and n are transfer coefficient related parameters, as discussed below.

1.5.3 Ohmic Drop

At the mid-point of the polarization curve (Figure 1.20), the cell voltage drop is dominated by the drop caused by internal resistance. This internal resistance is also called ohmic resistance. The drop can be calculated as $\Delta E_{ohmic} = I_{cell}R_{el}$.

The internal resistance of a fuel cell includes the electric contact resistance among the fuel cell components, and the proton resistance of the proton-conducting membrane. In PEMFCs, the proton resistance of the polymer electrolyte membrane contributes the most to the total ohmic resistance.

1.5.4 Mass Transfer Drop

Electrochemical reactions in fuel cells occurring on an electrode surface involve several steps. The electroactive species need to reach the electrode surface and adsorb on it, and then the electron transfer occurs at the electrode/electrolyte interface. The first step is mass transfer, and the second and third steps are electrode kinetics. If the mass transfer is fast, and the absorption and charge transfer are slow, the total reaction rate is determined by the electrochemical reaction kinetics. However, in the case of slow mass transfer and fast electrochemical kinetics, the mass transfer limits the whole reaction speed. In other words, the reactant that can reach the electrode surface will be consumed immediately, and the problem will be insufficient reactant on the electrode surface.

In a fuel cell, as the cell current becomes high, which indicates the electrochemical reaction rate on the electrode surface is fast, the mass transfer rate of the reactants is not fast enough to provide enough reactants to the electrode surface. Depletion of reactants at the electrode surface leads to a drop in cell voltage. The calculation of the cell voltage drop in this part is difficult, and a semi-empirical equation is usually used to estimate the mass transfer drop. The most popular expression for the mass transfer drop is

$$\Delta E_{masstransfer} = m\exp(nI) \tag{1.72}$$

where m and n are the mass transfer parameters simulated from the polarization curves.

1.5.5 Fuel Cell Efficiencies

In an internal combustion engine, the efficiency of the engine is given by a Carnot efficiency equation:

$$\varepsilon_{ice}^{thermal} = 1 - \frac{T_2}{T_1} \tag{1.73}$$

where T_1 and T_2 represent the absolute temperatures inside and outside the internal combustion engine, respectively. In principle, T_2 can be infinitely low, while T_1 can be very high. For example, combustion of fossil fuel can reach two to three thousand degrees Celsius, while the coolant temperature can be several hundred degrees. In practice, the durability of materials limits the engine's efficiency, which is usually less than 50%.

However, the efficiency of a fuel cell is determined by the thermodynamic equation of Gibbs free energy:

$$\Delta G = \Delta H - T\Delta S \tag{1.74}$$

ΔG is the electric energy that can be converted from the system and ΔH is the enthalpy change of the electrochemical reaction, indicating that if the fuel was burned, this amount of heat could be produced in the reaction. However, not all the enthalpy change from the reaction can be converted to electric energy, as some is lost due to the change in entropy. Thus, the maximum efficiency (ε_r^{cell}) can be calculated by

$$\varepsilon_r^{cell} = \frac{\Delta G}{\Delta H} = 1 - \frac{T\Delta S}{\Delta H} \tag{1.75}$$

According to this equation, the maximum efficiency change with increasing temperature depends on the entropy change of the fuel cell reactions. For example, for H_2/air (O_2) fuel cells, the thermodynamic efficiency decreases with increasing

temperature. At 25 ºC, the maximum efficiency is 83%. At 120 ºC, it decreases to 79%.

Figure 1.21 shows a comparison between the efficiencies of a fuel cell and an internal combustion engine. It can be seen that in a temperature range of less than 700°C, the fuel cell has a greater efficiency than the internal combustion engine.

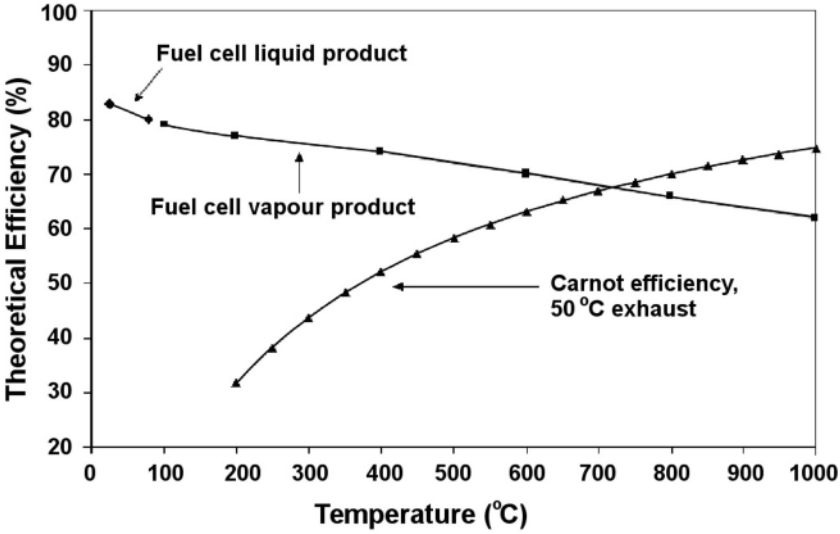

Figure 1.21. Comparison of fuel cell efficiency with Carnot efficiency, assuming the coolant temperature is 50°C [3]. (From Larminie J, Dicks A. Fuel cell systems explained. ©2003 John Wiley & Sons Limited. Reproduced with permission from the publisher and the authors.)

1.6 Chapter Summary

This chapter has presented a brief history of fuel cell evolution, the electrochemical fundamentals of PEM fuel cells, PEM fuel cell concepts and terminology, as well as performance analysis. Its main purpose has been to provide readers with some introductory and background information for a fundamental understanding of fuel cell AC impedance, to facilitate their journey through the next several chapters.

References

1. Grove WR (1839) On voltaic series and the combination of gases by platinum. Philos Mag Third Ser 14:127–30
2. Grove WR (1843) On a gaseous voltaic battery. Philos Mag Third Ser 21:417–20
3. Larminie L, Dicks A (2000) Fuel cell systems explained. Wiley, Chichester, England
4. Mond L, Langer C (1889) A new form of gas battery. Proc R Soc London 46:296–304

5. Jacques WW (1897) Electricity direct from coal. Harper's New Monthly Magazine 94:144–50
6. Appleby AJ (1990) From Sir William Grove to today: fuel cells and the future. J Power Sources 29:3–11, and references therein.
7. Schmid A (1923) Die Diffusionsgaselektrode. Enke, Stuttgart
8. Perry ML, Fuller TF (2002) A historical perspective of fuel cell technology in the twentieth century. J Electrochem Soc 149:S59–67
9. Bacon FT (1969) Fuel cells, past, present, and future. Electrochim Acta 14:569–85
10. Ballard Power Systems (2009) Fuel cell buses in Perth, Australia. www.ballard.com/About_Ballard/News_Events_Press_Room/Image_Gallery/details.aspx?gID=98. Accessed 30 May 2009
11. Srinivasan S, Mosdale R, Stevens P, Yang C (1999) Fuel cells: reaching the era of clean and efficient power generation in the twenty-first century. Annu Rev Energy Environ 24:281–328
12. Haubold HG, Vad Th, Jungbluth H, Hiller P (2001) Nano structure of NAFION: a SAXS study. Electrochim Acta 46(10–11):1559–63
13. Costamagna P, Srinivasan S (2000) Quantum jumps in the PEMFC science and technology from the 1960s to the year 2000: part II. Engineering, technology development, and application aspects. J Power Sources 102:253–69
14. McLean GF, Niet T, Prince-Richard S, Djilali N (2000) An assessment of alkaline fuel cell technology. Int J Hydrogen Energy 27(5):507–26
15. Kordesch K, Hacker V, Gsellmann J, Cifrain M, Faleschini G, Enzinger P, Fankhauser R, Ortner M, Muhr M, Aronson RR (2000) Alkaline fuel cells applications. J Power Sources 86:162–5
16. Blomen MJ, Mugerwa MN (eds) (1993) Fuel cell systems. Plenum Press, New York
17. Bockris JO'M, Nagy Z (1973) Symmetry factor and transfer coefficient: a source of confusion in electrode kinetics. J Chem Edu 50:839–43
18. Bockris JO'M (1971) Overpotential: a lacuna in scientific knowledge. J Chem Educ 48:352–7
19. Wang J (2006) Analytical electrochemistry. Wiley-VCH, Hoboken, NJ
20. Song C, Tang Y, Zhang J, Zhang J, Wang H, Shen J, et al. (2007) PEM fuel cell reaction kinetics in the temperature range of 23–120ºC. Electrochim Acta 52:2552–61
21. Bard AJ, Faulkner LR (1980) Electrochemical methods: fundamentals and applications. Wiley, New York
22. Zhang J, Tang Y, Song C, Zhang J, Wang H (2006) PEM fuel cell open circuit voltage (OCV) in the temperature range of 23 ºC to 120 ºC. J Power Sources 163:532–7

2

Electrical Fundamentals

In order to understand electrochemical impedance spectroscopy (EIS), we first need to learn and understand the principles of electronics. In this chapter, we will introduce the basic electric circuit theories, including the behaviours of circuit elements in direct current (DC) and alternating current (AC) circuits, complex algebra, electrical impedance, as well as network analysis. These electric circuit theories lay a solid foundation for understanding and practising EIS measurements and data analysis.

2.1 Introduction

An electric circuit or electric network is an integration of electrical elements (also known as circuit elements). Each element can be expressed as a general two-terminal element, as shown in Figure 2.1. The terminals “a” and “b” are accessible for connections with other elements. These circuit elements can be interconnected in a specified way, forming an electric circuit. Figure 2.2 demonstrates an example of an electric circuit.

Circuit elements can be classified into two categories, passive elements and active elements. The former consumes energy and the latter generates energy. Examples of passive elements are resistors (measured in ohms), capacitors (measured in farads), and inductors (measured in henries). The two typical active elements are the current source (measured in amperes), such as generators, and the voltage source (measured in volts), such as batteries.

Two major parameters used to describe and measure the circuits and elements are current (I) and voltage (V). Current is the flow, through a circuit or an element, of electric charge whose direction is defined from high potential to low potential. The current may be a movement of positive charges or of negative charges, or of both moving in opposite directions. For example, in a metallic resistor the current is the movement of electrons, whereas in an electrolyte solution the current is the movement of ions, and in a proton exchange polymer it is the movement of protons. Voltage is the difference in electrical potential between two points of an electric circuit or an element, expressed in volts. As shown in Figure 2.1, the potential difference between terminal “a” and terminal “b” is the voltage, which drives current through the element [1, 2].

Figure 2.1. A general two-terminal electrical element

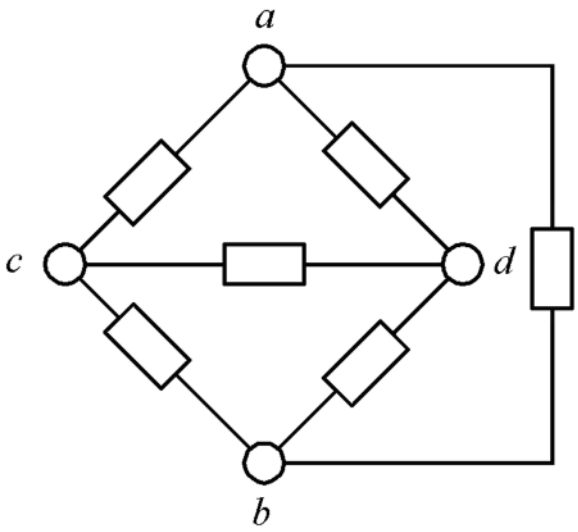

Figure 2.2. An example of an electric circuit

2.2 Direct Current Circuits

If the independent sources in a circuit are constant sources, such as batteries, all the currents and voltages remain constant and the circuit reaches its steady state. In this case, we say that the circuit is in a DC steady state.

2.2.1 Ohm's Law

The relationship between voltage and current in the circuit can be described by Ohm's law, which states that the current passing through a conductor between two points is directly proportional to the voltage across the two points, and inversely proportional to the resistance between them. The mathematical equation that describes this relationship is

$$V = IR \tag{2.1}$$

where V is the driving voltage in volts (V), R is the resistance in ohms (Ω), and I is the current in amperes (A).

Two common concepts are relevant to resistance. One is the short circuit, which is the direct connection externally between two nodes using an electrically conductive wire that has a theoretical resistance of zero. The opposite of a short circuit is an open circuit, in which the two nodes have no external connection or an infinite resistance connection [3]. Note that a point of connection of two or more circuit elements is called a node, as seen in Figure 2.3*b*.

Another important quantity, known as conductance, is defined by

$$G = 1/R \tag{2.2}$$

where G is the conductance in siemens (S). Obviously, in this case Ohm's law can also be expressed as

$$I = GV \tag{2.3}$$

2.2.2 Series and Parallel Circuits

There are two basic circuit connections: series circuit and parallel circuit. If two or more circuit components are connected end to end, as shown in Figure 2.3*a*, they are connected in series. A series circuit has only one path for the electric current to run through all of its components. If two or more circuit components are connected like the rungs of a ladder, as shown in Figure 2.3*b*, they are connected in parallel. A parallel circuit has different paths for the electric current through each of its components, with the same voltage across.

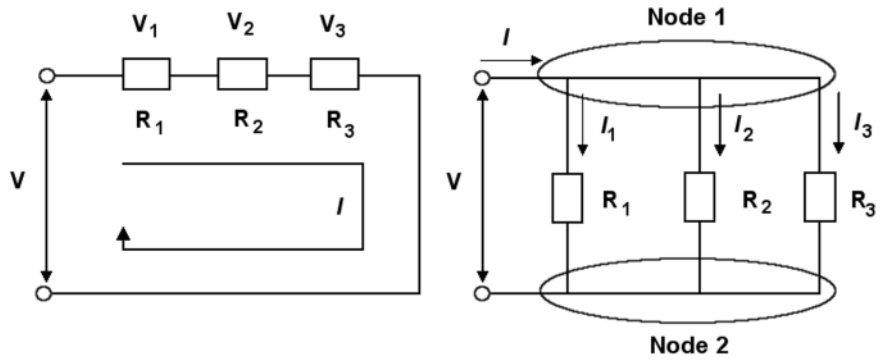

a *b*

Figure 2.3. *a* Series and *b* parallel circuits

2.2.3 Kirchhoff's Laws

Electric circuits can be very complicated. For example, they may include series-connected sections, parallel-connected sections, or both. No matter how complex they are, the behaviours of these sections are governed by fundamental laws, which provide basic tools for the analysis of all the circuits.

The fundamental laws for circuit analysis are Ohm's law and Kirchhoff's laws. Ohm's law, described above, can be used to find the current, voltage, and power associated with a resistor. However, in some cases Ohm's law by itself cannot analyze the circuit. Analytical solutions for most electric networks need to combine Ohm's law and Kirchhoff's laws, the latter being also known as Kirchhoff's current law (KCL) and Kirchhoff's voltage law (KVL).

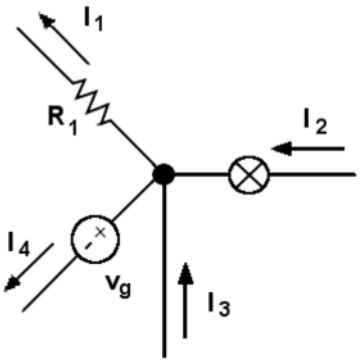

Figure 2.4. Principle schematic of Kirchhoff's current law

Kirchhoff's current law states that the algebraic sum of the currents entering a node is equal to the algebraic sum of the currents leaving the node. The principle schematic of KCL is shown in Figure 2.4, and the mathematical equation that describes KCL in Figure 2.4 is

$$I_1 + I_4 = I_2 + I_3 \tag{2.4}$$

More commonly, the current has a reference direction indicating entrance to or exit from the node. If the current enters the node, the arrow points to the node and a positive value is denoted for this current. Conversely, if the current leaves the node, the arrow points away from the node and a negative value is assigned to this current. So, KCL can also be expressed as

$$\sum I = 0 \tag{2.5}$$

Applying KCL to the circuit in Figure 2.3*b*, we have

$$I - I_1 - I_2 - I_3 = 0 \tag{2.6}$$

Kirchhoff's voltage law states that the algebraic sum of the voltage over the circuit elements around any closed circuit loop must be zero. The principle schematic of KVL is shown in Figure 2.5. The mathematical equation that describes KVL in Figure 2.5 can be expressed as

$$V_1 + V_2 + V_3 + V_4 = 0 \tag{2.7}$$

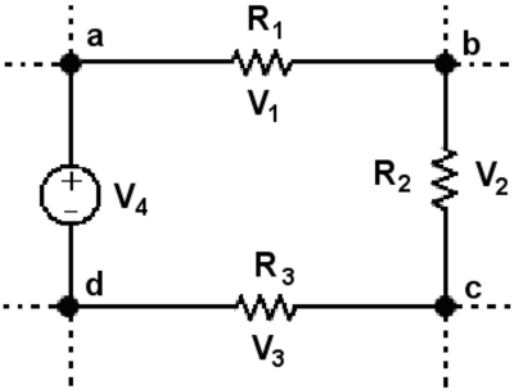

Figure 2.5. Principle schematic of Kirchhoff's voltage law

More commonly, KVL can be expressed as

$$\sum V = 0 \tag{2.8}$$

According to KVL, in a closed circuit loop, the sum of the voltage drops caused by the current across the elements, such as the resistor, capacitor, or inductor, is equal to the sum of the driving voltages produced by a voltage source such as a battery or a generator:

$$\sum \text{Driving voltages} = \sum \text{Voltage drops} \tag{2.9}$$

2.2.4 Resistors in DC Circuits

Electric circuits or networks can be analyzed using both Ohm's law and Kirchhoff's laws. For a circuit of resistors in series, as shown in Figure 2.6, the current flow in each resistor is the same (I_R).

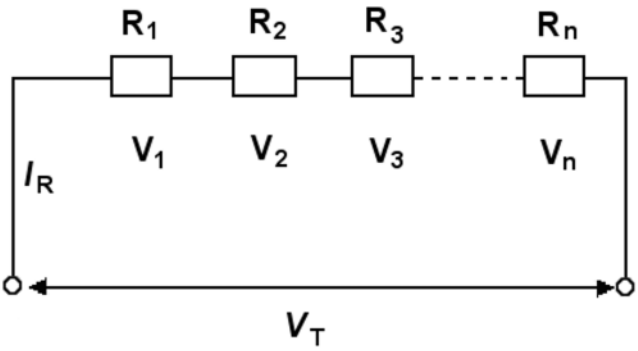

Figure 2.6. Resistors in series

Applying KVL to the circuit in Figure 2.6, we have

$$V_T = V_1 + V_2 + V_3 + ... + V_n \tag{2.10}$$

Applying Ohm's law to Equation 2.10, we can obtain

$$V_T = I_R R_1 + I_R R_2 + I_R R_3 + \ldots + I_R R_n \tag{2.11}$$

Equation 2.10 can be rearranged as Equation 2.12:

$$V_T = I_R (R_1 + R_2 + R_3 + ... + R_n) \tag{2.12}$$

Thus, the equivalent resistance R of n resistors connected in series can be expressed as

$$R = \frac{V_T}{I_R} = R_1 + R_2 + R_3 + ... + R_n \tag{2.13}$$

For a circuit of resistors in parallel, as shown in Figure 2.7, the voltage across each resistor is the same (V_T). Applying KCL to the circuit in Figure 2.7, we have

$$I_T = I_1 + I_2 + I_3 + ... + I_n \tag{2.14}$$

Then,

$$I_T = (\frac{V_T}{R_1} + \frac{V_T}{R_2} + \frac{V_T}{R_3} + ... + \frac{V_t}{R_n}) \tag{2.15}$$

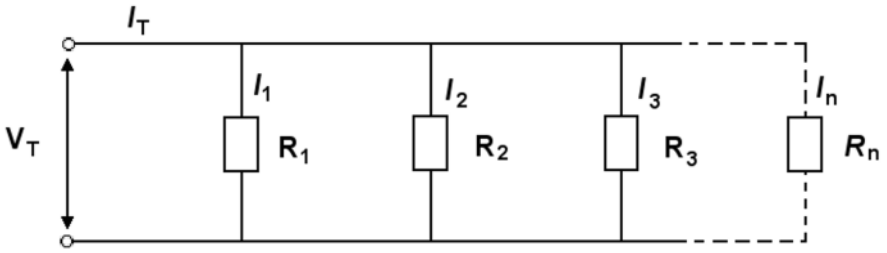

Figure 2.7. Resistors in parallel

Therefore, the equivalent resistance of the parallel combination of *n* resistors is

$$R = \frac{V_T}{I_T} = \left(\frac{1}{R_1} + \frac{1}{R_2} + \frac{1}{R_3} + ... + \frac{1}{R_n} \right)^{-1} \tag{2.16}$$

The equivalent conductance of *n* resistors in parallel, *G*, can be expressed as

$$G = \frac{I_T}{V_T} = G_1 + G_2 + G_3 + ... + G_n = \frac{1}{R_1} + \frac{1}{R_2} + \frac{1}{R_3} + ... + \frac{1}{R_n} \tag{2.17}$$

2.2.5 Capacitors in DC Circuits

Capacitance represents the energy-storing capability of a capacitor. The most common form of charge storage device is a two-plate capacitor, as shown in Figure 2.8. A parallel-plate capacitor is a circuit element with two conducting plates at the terminals and a nonconductive material, known as the dielectric material, to separate them. When a charge source, such as a battery, transfers charges to a capacitor, the voltage builds up across the two conductive terminals. The charges accumulate at the two plates of the capacitor, and can be expressed as

$$q = CV \tag{2.18}$$

where *C* is the capacitance in farads (F), *q* is the accumulated charge in coulombs (C), and *V* is the voltage measured between the two conducting plates in volts (V). The capacitance value (*C*) of a parallel-plate capacitor is related to the geometry of the capacitor and to the dielectric constant of the nonconductive material in the capacitor by the following equation:

$$C = \frac{KA(8.854 \times 10^{-12})}{d} \tag{2.19}$$

where *C* is the capacitance in farads (F), *K* is the dielectric constant of the insulating material, *A* is the surface area in square metres (m^2), and *d* is the thickness of the dielectric material in metres (m).

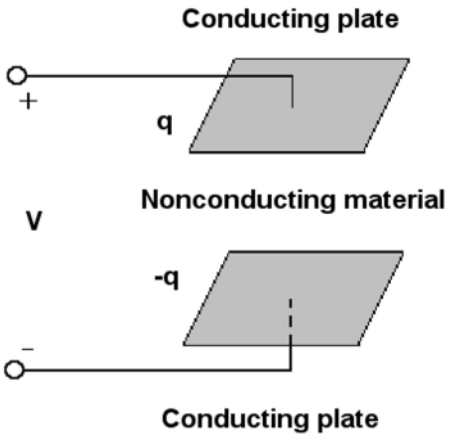

Figure 2.8. A parallel-plate capacitor

Some representative dielectric constants are 1.0 for air, 5 for mica, 6 for glass, and 7500 for ceramic.

In a DC circuit, a capacitor behaves like an open circuit. In other words, the current through it is zero when the circuit reaches its steady state. However, if a current or voltage source is impressed on or switched out of the circuit with a capacitor (or capacitors), as shown in Figure 2.9, there will be a transitory change in the current and voltage. Between the moment of switching and the steady state, the current passing through the capacitor is not zero. The time dependence of the voltage across the capacitor during the transient state in a DC circuit like Figure 2.9 can be obtained using Laplace transforms (for these, please refer to Appendix B).

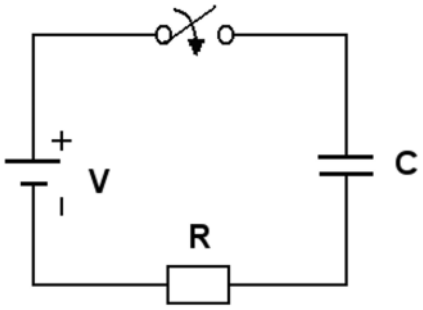

Figure 2.9. A DC circuit containing a capacitor and a switch

Since the current is defined as the change rate of the charge, by differentiating Equation 2.18 we can obtain

$$I(t) = C\frac{dV(t)}{dt} \tag{2.20}$$

Equation 2.20 is the current–voltage relation for a capacitor.

Figure 2.10 shows the transient process of a capacitor when charging. In the charging process, the electric field in the nonconductive material changes due to the charge increase in the conductive terminals of the capacitor. The charging process stops when the voltage V across the capacitor is equal to the DC charge source.

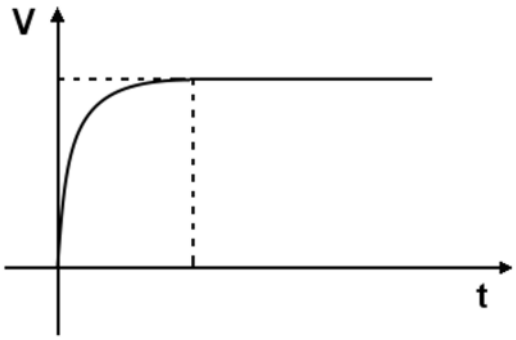

Figure 2.10. Voltage build-up versus charging time in a capacitor

2.2.5.1 Equivalent Capacitance of Capacitors in Series

Applying KVL to the circuit in Figure 2.11, we have

$$V_T = V_1 + V_2 + V_3 + ... + V_n \tag{2.21}$$

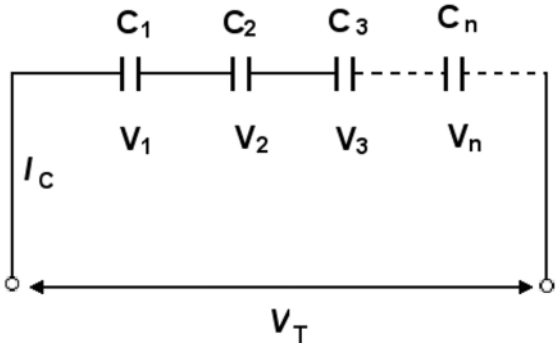

Figure 2.11. Capacitors in series

Substituting voltages according to Equation 2.18, we obtain

$$V_T = \frac{q_1}{C_1} + \frac{q_2}{C_2} + \frac{q_3}{C_3} + \ldots + \frac{q_n}{C_n} \tag{2.22}$$

Since the current to all the elements in a series circuit is the same, the accumulation of charge in every capacitor must be the same. Thus,

$$q_1 = q_2 = q_3 = q_n = q \tag{2.23}$$

Equation 2.22 becomes

$$V_T = q(\frac{1}{C_1} + \frac{1}{C_2} + \frac{1}{C_3} + \ldots + \frac{1}{C_n}) \tag{2.24}$$

Then, the equivalent capacitance of *n* capacitors in series, C_s, is determined by

$$\frac{1}{C_s} = \frac{V_T}{q} = \frac{1}{C_1} + \frac{1}{C_2} + \frac{1}{C_3} + \ldots + \frac{1}{C_n} \tag{2.25}$$

In other words, the total capacitance of capacitors in series is equal to the reciprocal of the sum of the reciprocals of the individual capacitances.

2.2.5.2 Equivalent Capacitance of Capacitors in Parallel
Applying KCL to the circuit in Figure 2.12, we have

$$I_T = I_1 + I_2 + I_3 + ... + I_n \tag{2.26}$$

As the voltage across each element in a parallel circuit is the same, by substituting currents using Equation 2.20 we can obtain

$$I_T = C_1 \frac{dV}{dt} + C_2 \frac{dV}{dt} + C_3 \frac{dV}{dt} + \ldots + C_n \frac{dV}{dt} \tag{2.27}$$

Therefore,

$$I_T = (C_1 + C_2 + C_3 + ... + C_n) \frac{dV}{dt} \tag{2.28}$$

Thus, the equivalent capacitance of *n* parallel capacitors, C_p, is simply the sum of the individual capacitances:

$$C_p = C_1 + C_2 + C_3 + ... + C_n \tag{2.29}$$

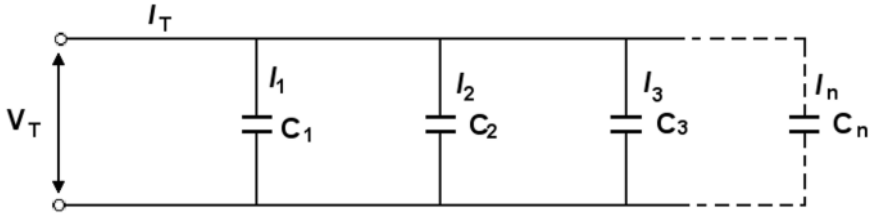

Figure 2.12. Capacitors in parallel

2.2.6 Inductors in DC Circuits

An inductor is commonly a coiled conducting wire wrapped around a core (e.g., ferromagnetic material) with two terminals. When current passes through the inductor, magnetic flux is produced, resulting in inductance. The number of loops, the size of each loop, and the core material all affect the inductance value.

In a DC circuit, an inductor is like a short circuit, which means the voltage across it is zero when the circuit reaches its steady state. However, if a current or voltage source is impressed on or switched out of the circuit with an inductor, as shown in Figure 2.13, there will be a transitory change in the current and voltage. During the time period from the moment of switching to the steady state, the voltage across the inductor is not zero.

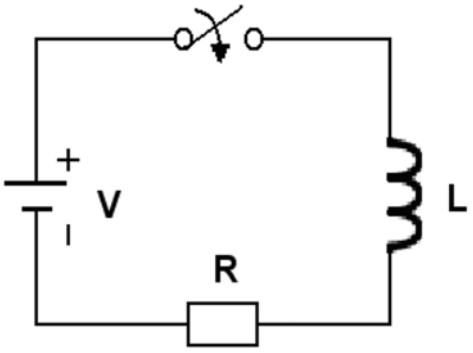

Figure 2.13. A DC circuit containing an inductor and a switch

While a capacitor delays changes in voltage, an inductor delays changes in current. Generally, the relationship between the time-varying voltage $V(t)$ across an inductor with an inductance of L and the time-varying current $I(t)$ passing through it can be written as the differential equation:

$$V(t) = L\frac{dI(t)}{dt} \tag{2.30}$$

where L is the inductance (measured in henries).

Inductors in series and in parallel are shown in Figures 2.14 and 2.15, respectively. While the voltage across each inductor may be different, the current through inductors in series stays the same. Since the sum of the voltages is equal to the total voltage, the total inductance of inductors in series, L_s, can be expressed as

$$L_s = L_1 + L_2 + L_3 + ... + L_n \tag{2.31}$$

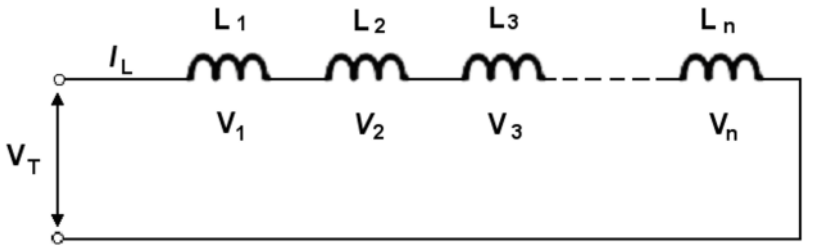

Figure 2.14. Inductors in series

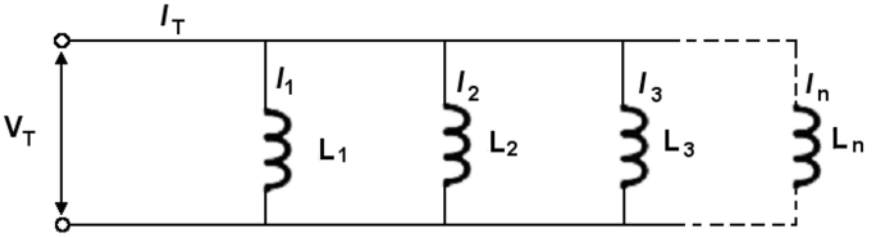

Figure 2.15. Inductors in parallel

In a parallel configuration of inductors, as shown in Figure 2.15, each inductor has the same voltage. Therefore, the total equivalent inductance of inductors in parallel, L_p, can be obtained:

$$\frac{1}{L_p} = \frac{1}{L_1} + \frac{1}{L_2} + \frac{1}{L_3} + \ldots + \frac{1}{L_n} \tag{2.32}$$

2.3 Alternating Current Circuits

2.3.1 Sinusoidal Systems

Alternating current or voltage (AC) refers to current or voltage that varies with time in a periodic manner. Figure 2.16 shows three examples of periodic voltage waves. As shown there, one cycle is a complete set of the periodic wave, the frequency of which, f (Hz), is the number of cycles completed in one second (one cycle per second is one hertz). The period of the periodic wave, T (s), is the time required to complete one cycle. Thus, the relation between the frequency and the period is as follows:

$$T = \frac{1}{f} \tag{2.33}$$

Among the periodic waves, the sinusoidal wave is extremely important, being the easiest to work with mathematically. The general mathematical expression for the sinusoidal wave (voltage) is given by

$$V(t) = V_m \sin(\omega t + \theta) \tag{2.34}$$

where $V(t)$ is the instantaneous voltage value at the instant of time t, V_m is the peak amplitude of the sinusoidal voltage wave (V), θ is the phase angle, ω is the angular frequency (rad/s), and T is the time (s).

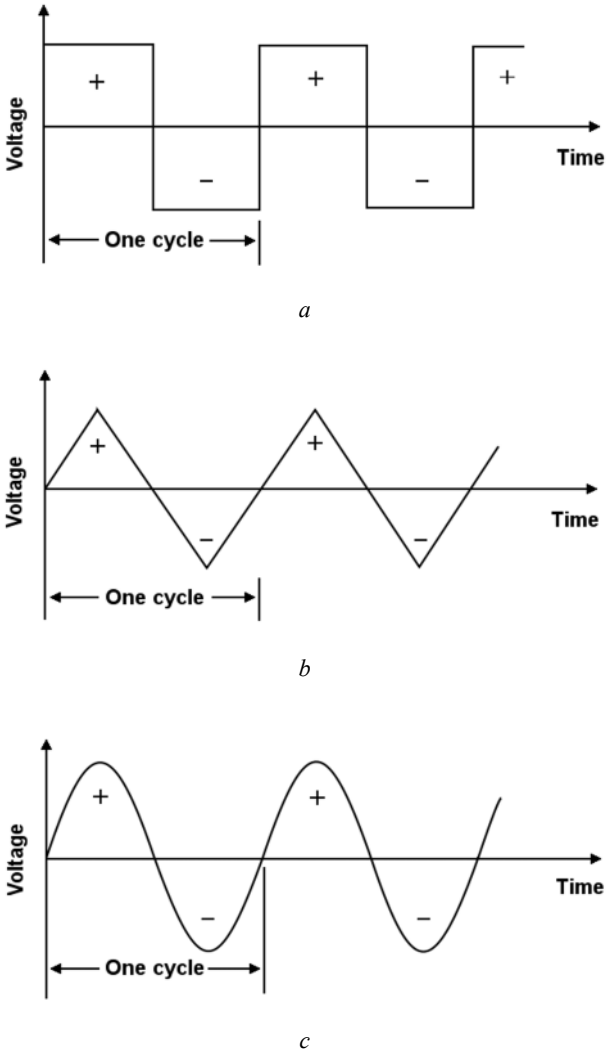

Figure 2.16. Periodic voltage waves: *a* rectangular, *b* triangular, *c* sinusoidal

Since the angle spun in one cycle is 2π radians, we have

$$\omega = 2\pi f \tag{2.35}$$

Thus,

$$T = \frac{2\pi}{\omega} \tag{2.36}$$

Substituting for ω using Equation 2.35, we obtain

$$V(t) = V_m \sin(2\pi ft + \theta) \tag{2.37}$$

Similarly, the equation for a sinusoidal current wave is

$$I(t) = I_m \sin(2\pi ft + \phi) \tag{2.38}$$

where $I(t)$ is the instantaneous current value at the instant of time t; I_m is the amplitude or the maximum value of the sinusoidal current wave (A); ϕ is the phase angle; f is the frequency (Hz); and T is the time (s).

Direct current or voltage can be considered a special type of sinusoidal current wave or sinusoidal voltage wave whose frequency is at the lower limit of zero hertz.

2.3.2 Resistors in AC Circuits

In an AC circuit, assuming the voltage across the resistor is described by a sinusoidal wave (as shown in Equation 2.37), the current through the resistor, based on Ohm's law, is

$$I_R(t) = \frac{V_R(t)}{R} = \frac{V_m \sin(2\pi ft + \theta)}{R} = \frac{V_m}{R}\sin(2\pi ft + \theta) \tag{2.39}$$

As can be seen in Equation 2.39, both $I_R(t)$ (the current through the resistor) and $V_R(t)$ (the voltage across the resistor) have the same frequency and phase.

According to Equation 2.38, we have

$$I_R(t) = I_m \sin(2\pi ft + \phi) \tag{2.40}$$

Comparing Equations 2.39 and 2.40, we can obtain

$$I_m = \frac{V_m}{R} \tag{2.41}$$

Since there is no angular difference between the current in a resistor and the voltage across it, we have

$$\phi = \theta \tag{2.42}$$

2.3.3 Capacitors in AC Circuits

In a sinusoidal AC circuit, the current through a pure capacitor leads the voltage drop across this capacitor by 90°. The 90° phase relationship between $I_C(t)$ (the current through the capacitor) and $V_C(t)$ (the voltage across the capacitor) can be written as

$$I_C(t) = C\frac{dV_C(t)}{dt} \tag{2.43}$$

For example, if the voltage across the capacitor, $V_C(t)$, is

$$V_C(t) = V_m \sin 2\pi ft \tag{2.44}$$

then substituting $V_C(t)$ in Equation 2.43 with Equation 2.44, we have

$$I_C(t) = C\frac{d(V_m \sin 2\pi ft)}{dt} = CV_m(2\pi f)\cos 2\pi ft = \omega CV_m \sin(2\pi ft + 90°) \tag{2.45}$$

The current through the capacitor, $I_C(t)$, will be

$$I_C(t) = I_m \sin(2\pi ft + 90°) \tag{2.46}$$

where

$$I_m = \omega CV_m \tag{2.47}$$

2.3.4 Inductors in AC Circuits

In a sinusoidal AC circuit, the voltage drop across a pure inductor advances the current through it by 90°. The 90° phase relationship between $I_L(t)$ (the current through the inductor) and $V_L(t)$ (the voltage across the inductor) is expressed by

$$V_L(t) = L\frac{dI_L(t)}{dt} \tag{2.48}$$

For example, if the current through the inductor, $I_L(t)$, is

$$I_L(t) = I_m \sin 2\pi ft \tag{2.49}$$

then substituting $I_L(t)$ from Equation 2.49 into Equation 2.48, we have

$$V_L(t) = L\frac{d(I_m \sin 2\pi ft)}{dt} = LI_m(2\pi f)\cos 2\pi ft = \omega LI_m \sin(2\pi ft + 90°) \tag{2.50}$$

The voltage across the inductor, $V_L(t)$, will be

$$V_L(t) = V_m \sin(2\pi ft + 90°) \tag{2.51}$$

where

$$V_m = \omega LI_m \tag{2.52}$$

2.4 Complex Algebra and Impedance

Complex algebra is a powerful tool for solving problems in AC electric circuits, including sinusoidal systems. The complex number Z can be written in the rectangular form

$$Z = Z_{re} + iZ_{im} \tag{2.53}$$

where Z_{re} (or Z') and Z_{im} (or Z'') are the real and imaginary parts of Z, respectively, and $i = \sqrt{-1}$.

The complex number Z can also be expressed in the polar form

$$Z = |Z|e^{i\phi} \tag{2.54}$$

or

$$Z = |Z|(\cos\phi + i\sin\phi) \tag{2.55}$$

where $|Z|$ is the magnitude of Z:

$$|Z| = \sqrt{(Z_{re})^2 + (Z_{im})^2} \tag{2.56}$$

and ϕ is called the argument or the angle of Z:

$$\phi = \tan^{-1}\frac{Z_{im}}{Z_{re}} \tag{2.57}$$

Complex algebra is associated with a two-dimensional plane, called the complex plane. The complex plane of the complex number Z is presented in Figure 2.17. As can be seen there, the horizontal and vertical axes are called the real and imaginary axes, respectively. Complex algebra applications will be employed in the following sections and in Chapter 4.

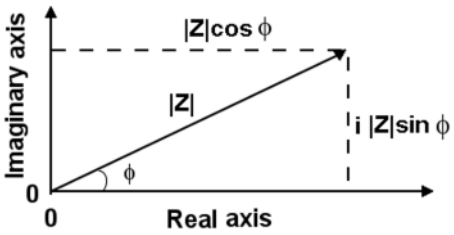

Figure 2.17. Complex plane of the complex number Z

Let us recall the general sinusoidal voltage and current:

$$V(t) = V_m \sin(2\pi ft + \theta) \tag{2.58}$$

$$I(t) = I_m \sin(2\pi ft + \phi) \tag{2.59}$$

These can be displayed in related complex numbers:

$$\boldsymbol{V} = V_m e^{i\theta} = V_m \angle \theta \tag{2.60}$$

$$\boldsymbol{I} = I_m e^{i\phi} = I_m \angle \phi \tag{2.61}$$

which are defined as phasors, or phasor representations. To distinguish them from other complex numbers, phasors are printed in bold.

Having introduced complex algebra, we are now able to go further, to the concept of electrical impedance or simply impedance. Electrical impedance extends the concept of resistance to AC circuits and therefore is also called AC impedance. As impedance is a complex quantity, the term complex impedance may also be used. Based on the definition of resistance described by Ohm's law, the current–voltage relationship in impedance can be expressed as

$$Z = \frac{V(t)}{I(t)} \tag{2.62}$$

where $V(t)$ and $I(t)$ are measurements of voltage and current in an AC system.

For a sinusoidal system, the AC impedance of a resistor, Z_R, in the complex plane can be expressed as

$$Z_R = R \tag{2.63}$$

The AC impedance of a capacitor, Z_C, in the complex plane can be expressed as

$$Z_C = \frac{1}{i\omega C} \tag{2.64}$$

because

$$Z_C = \frac{V_m e^{i0^0}}{I_m e^{i90^0}} = \frac{V_m e^{i0^0}}{\omega C V_m e^{i90^0}} = \frac{e^{i(-90^0)}}{\omega C} \tag{2.65}$$

Applying Euler's formula, we have

$$e^{i(-90°)} = \cos(-90°) + i\sin(-90°) \tag{2.66}$$

Therefore,

$$Z_C = \frac{e^{i(-90^0)}}{\omega C} = \frac{-i}{\omega C} = \frac{1}{i\omega C} \tag{2.67}$$

The AC impedance of an inductor, Z_L, in the complex plane can be expressed as

$$Z_L = i\omega L \tag{2.68}$$

because

$$Z_L = \frac{V_m e^{i90^0}}{I_m e^{i0^0}} = \frac{\omega L I_m e^{i90^0}}{I_m e^{i0^0}} = \omega L e^{i90^0} \tag{2.69}$$

Again, applying Euler's formula, we obtain

$$Z_L = \omega L e^{i90^0} = i\omega L \tag{2.70}$$

2.4.1 AC Impedance of a Resistor–Capacitor Circuit

In a parallel resistor–capacitor (RC) circuit (R/C), the overall AC impedance of the circuit is denoted as $Z_{R/C}$. Since

$$\frac{1}{Z_{R/C}} = \frac{1}{Z_R} + \frac{1}{Z_c} \tag{2.71}$$

$Z_{R/C}$ can be expressed as

$$Z_{R/C} = \left(\frac{1}{R} + \frac{1}{(i\omega C)^{-1}} \right)^{-1} = (\frac{1}{R} + i\omega C)^{-1} \tag{2.72}$$

Then we have

$$Z_{R/C} = \frac{R}{1 + i\omega RC} \tag{2.73}$$

Ultimately, Equation 2.73 can be transferred to the standard form of a complex number:

$$Z_{R/C} = \frac{R}{1 + (\omega RC)^2} - i\frac{\omega R^2 C}{1 + (\omega RC)^2} \tag{2.74}$$

Therefore, the real and imaginary components, Z_{re} and Z_{im}, in the AC impedance of the parallel RC circuit are given by

$$Z_{re} = \frac{R}{1 + (\omega RC)^2} \tag{2.75}$$

$$Z_{im} = -\frac{\omega R^2 C}{1 + (\omega RC)^2} \tag{2.76}$$

while the phase angle ϕ is given by

$$\tan\phi = -\omega RC \tag{2.77}$$

At low frequency ($\omega RC << 1$, $Z_{re} \approx R$ and $Z_{im} \approx 0$), this RC circuit acts as a resistor, and at high frequency ($\omega RC >> 1$, $Z_{re} \approx 0$ and $Z_{im} \approx \frac{1}{\omega C}$), as a capacitor. The time constant τ of this circuit is equal to *RC*.

Combining Equation 2.77 with Equations 2.75 and 2.76 yields

$$\left(Z_{re} - \frac{R}{2} \right)^2 + Z_{im}{}^2 = \left(\frac{R}{2} \right)^2 \tag{2.78}$$

Equation 2.78 represents a half-circle in the fourth quadrant of the complex plane, with a radius of *R*/2 and circle centre of (*R*/2, 0), as shown in Figure 2.18. Note that the frequency range in Figure 2.18 is from 1 MHz to 0.001 Hz. The same frequency range is kept for the following figures in this chapter, unless otherwise stated.

It can be seen from Figure 2.18 that at $\omega \to 0$, the plot crosses the real axis at (R, 0). At $\omega \to \infty$, the plot crosses the origin. The frequency at $\frac{\partial(Z_{im})}{\partial \omega} = 0$ is designated the characteristic frequency, ω_C. At the characteristic frequency, $\omega_C \tau_C$ is equal to one.

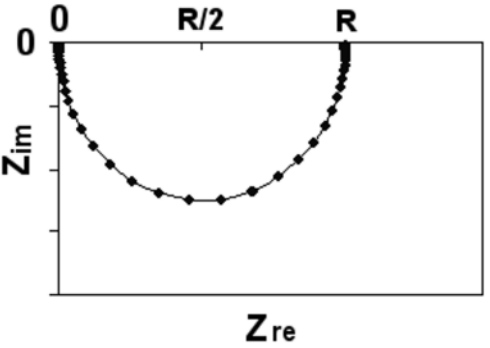

Figure 2.18. Graphical representation of the AC impedance of a parallel RC circuit

In a series RC circuit (R-C), according to the primary rules, the overall impedance, Z_{R-C}, is expressed as

$$Z_{R-C} = R + (i\omega C)^{-1} \tag{2.79}$$

Then we have

$$Z_{R-C} = R - i(\omega C)^{-1} \tag{2.80}$$

The real and imaginary components Z_{re}, Z_{im} in the AC impedance of the series RC circuit are given by

$$Z_{re} = R \tag{2.81}$$

$$Z_{im} = -(\omega C)^{-1} \tag{2.82}$$

The phase angle ϕ is given by

$$\tan\phi = -\frac{(\omega C)^{-1}}{R} \tag{2.83}$$

According to the above calculations, a graphical representation of the AC impedance of a series RC circuit is presented in Figure 2.19. As shown in the complex plane of Figure 2.19, the AC impedance of a series RC circuit is a straight vertical line in the fourth quadrant with a constant Z' value of R.

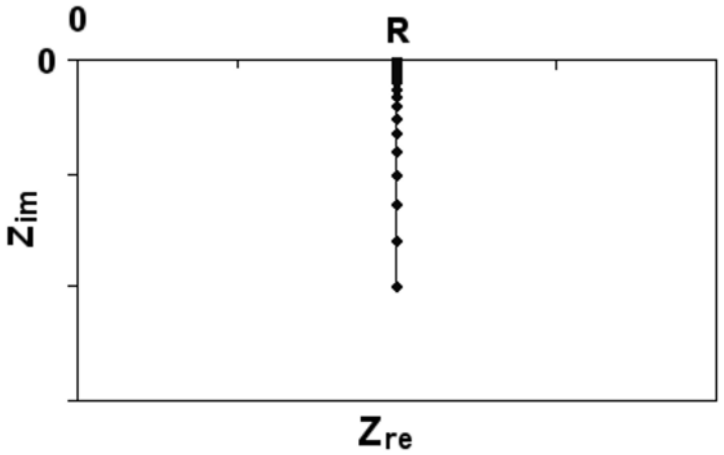

Figure 2.19. Graphical representation of the AC impedance of a series RC circuit

2.4.2 AC Impedance of a Resistor–Inductor Circuit

In a parallel resistor–inductor (RL) circuit (R/L), the overall AC impedance, $Z_{R/L}$, can be expressed as

$$Z_{R/L} = [(R^{-1} + (i\omega L)^{-1}]^{-1} \tag{2.84}$$

Then, we have

$$Z_{R/L} = \frac{\omega^2 RL^2}{R^2 + \omega^2 L^2} + i\frac{\omega R^2 L}{R^2 + \omega^2 L^2} \tag{2.85}$$

So, the real and imaginary components in the AC impedance of a parallel RL circuit are given by

$$Z_{re} = \frac{\omega^2 RL^2}{R^2 + \omega^2 L^2} \tag{2.86}$$

$$Z_{im} = \frac{\omega R^2 L}{R^2 + \omega^2 L^2} \tag{2.87}$$

and the impedance phase angle is given by

$$\tan\phi = \frac{R}{\omega L} \tag{2.88}$$

In the complex plane, the AC impedance of a parallel RL circuit is represented by a semicircle in the first quadrant with a radius of R/2 and the centre at (R/2, 0), as

shown in Figure 2.20. The curve crosses the real axis at R and 0 at the frequencies of $\omega \to \infty$ and $\omega = 0$, respectively.

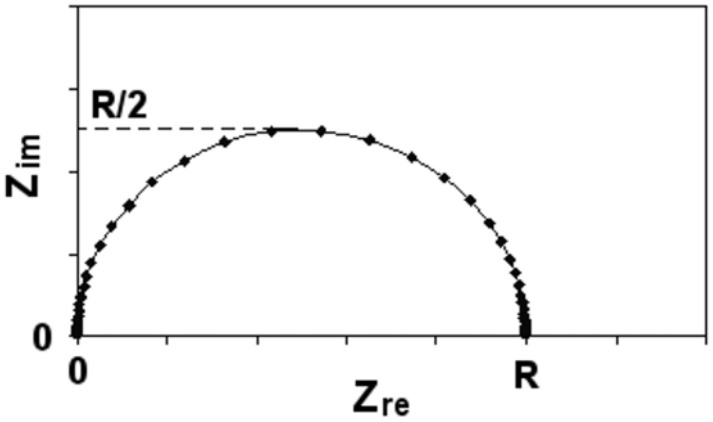

Figure 2.20. Graphical representation of the AC impedance of a parallel RL circuit

In a series RL circuit (R-L), the overall impedance of the RL circuit in series, Z_{R-L}, is written as

$$Z_{R-L} = R + i\omega L \tag{2.89}$$

The real and imaginary components, Z_{re} and Z_{im}, in the AC impedance can be obtained:

$$Z_{re} = R \tag{2.90}$$

$$Z_{im} = \omega L \tag{2.91}$$

The phase angle ϕ is as follows

$$\tan\phi = \frac{\omega L}{R} \tag{2.92}$$

A graphical representation of the AC impedance of a series RL circuit, according to the above calculations, is shown in Figure 2.21. In the complex plane of this figure, the AC impedance of a series RL circuit is a straight vertical line in the first quadrant with a constant Z' value of R.

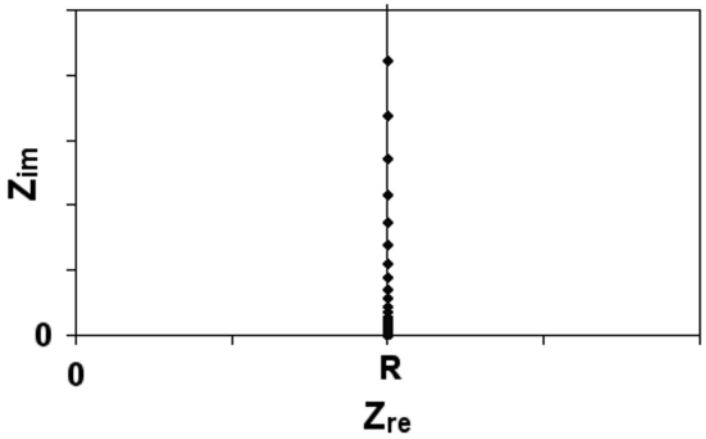

Figure 2.21. Graphical representation of the AC impedance of a series RL circuit

2.4.3 AC Impedance of a Capacitor–Inductor Circuit

In a parallel capacitor–inductor (CL) circuit (C/L), the overall AC impedance, $Z_{C/L}$, can be expressed as

$$Z_{C/L} = [(i\omega L)^{-1} + i\omega C]^{-1} \tag{2.93}$$

Then

$$Z_{C/L} = \left(\frac{1}{\frac{1}{\omega L} - \omega C}\right) i \tag{2.94}$$

So, the real and imaginary components of the AC impedance of the parallel CL circuit are given by

$$Z_{re} = 0 \tag{2.95}$$

$$Z_{im} = \frac{1}{\frac{1}{\omega L} - \omega C} \tag{2.96}$$

and the phase angle is 90°.

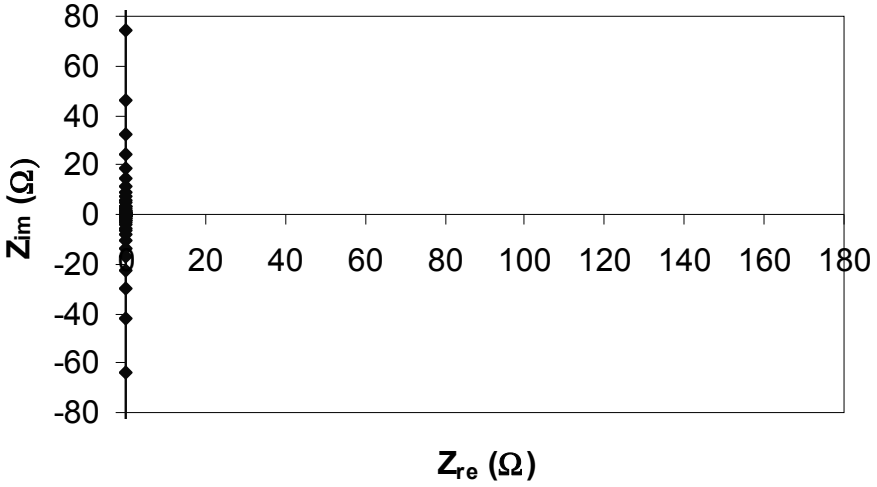

Figure 2.22. Graphical representation of the AC impedance of a simple parallel CL circuit (L = 0.04 H, C = 0.00001 F)

According to the above calculations, a graphical representation of the AC impedance of a parallel CL circuit is depicted in Figure 2.22. In the complex plane, the AC impedance of the parallel CL circuit is represented by a straight vertical line on the Z''-axis with a constant Z' value of zero.

In a series CL circuit (C-L), according to the primary rules, the overall AC impedance of a CL circuit in series, Z_{C-L}, is expressed as

$$Z_{C-L} = (i\omega C)^{-1} + i\omega L \tag{2.97}$$

Therefore,

$$Z_{C-L} = (\omega L - \frac{1}{\omega C})i \tag{2.98}$$

The real and imaginary components, Z_{re} and Z_{im}, in the AC impedance can then be obtained:

$$Z_{re} = 0 \tag{2.99}$$

$$Z_{im} = \omega L - \frac{1}{\omega C} \tag{2.100}$$

and the phase angle is again 90°.

According to the above calculations, a graphical representation of the AC impedance of a series CL circuit is given in Figure 2.23. As shown in the complex

plane, the AC impedances of a series CL circuit are also located on the Z''-axis with a constant Z' value of zero.

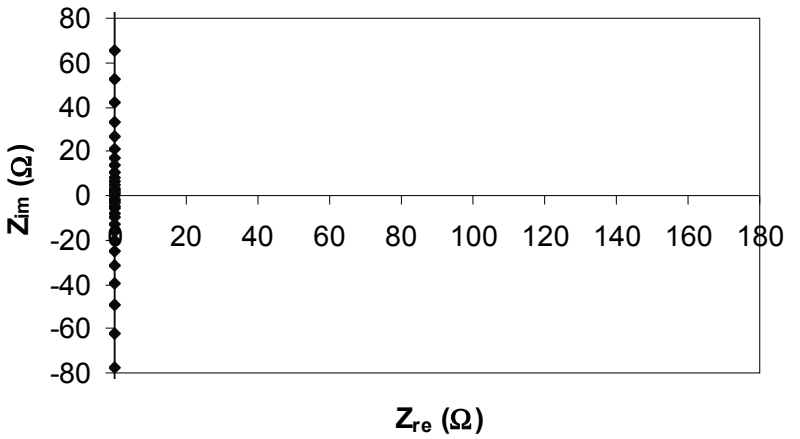

Figure 2.23. Graphical representation of the AC impedance of a series CL circuit (L = 0.04 H, C = 0.01 F)

2.4.4 AC Impedance of a Resistor–Capacitor–Inductor Circuit

2.4.4.1 R-(C/L) Circuit

If a circuit of parallel CL is in series with R (R-(C/L)), the overall AC impedance, $Z_{R-(C/L)}$, can be expressed as

$$Z_{R-(C/L)} = R + [(i\omega L)^{-1} + i\omega C]^{-1} \tag{2.101}$$

Then, we have

$$Z_{R-(C/L)} = R + \left(\frac{1}{\frac{1}{\omega L} - \omega C}\right)i \tag{2.102}$$

So, the real and imaginary components of the AC impedance of the R-(C/L) circuit are given by

$$Z_{re} = R \tag{2.103}$$

$$Z_{im} = \frac{1}{\frac{1}{\omega L} - \omega C} \tag{2.104}$$

and the phase angle ϕ is given by

$$\tan\phi = \frac{1}{R(\frac{1}{\omega \mathrm{L}} - \omega C)} \tag{2.105}$$

Based on these equations, Figure 2.24 gives a graphical representation of the AC impedance of the R-(C/L) circuit. In the complex plane, the AC impedance of the circuit is represented by a straight vertical line with a constant Z' value of R.

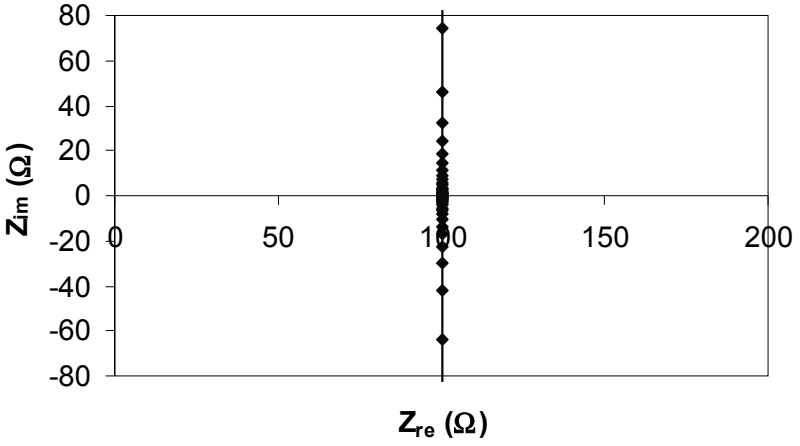

Figure 2.24. Graphical representation of the AC impedance of the R-(C/L) circuit (L = 0.04 H, C = 0.00001 F, R = 100 Ω)

2.4.4.2 R-C-L Circuit

In a series RCL circuit (R-C-L), the overall impedance, Z_{R-C-L}, is expressed as

$$Z_{R-C-L} = R + (i\omega C)^{-1} + i\omega L \tag{2.106}$$

Then we obtain

$$Z_{R-C-L} = R + (\omega L - \frac{1}{\omega C})i \tag{2.107}$$

The real and imaginary components, Z_{re} and Z_{im}, in the AC impedance of the R-C-L circuit in series are given by

$$Z_{re} = R \tag{2.108}$$

$$Z_{im} = \omega L - \frac{1}{\omega C} \tag{2.109}$$

The phase angle ϕ is then described by

$$\tan\phi = \frac{\omega L - \frac{1}{\omega C}}{R} \tag{2.110}$$

Based on these equations, a graphical representation of the AC impedance of the (R-C-L) circuit is given in Figure 2.25. As shown in the complex plane of this figure, the AC impedance of the series RCL circuit is a straight line with a constant Z' value of R.

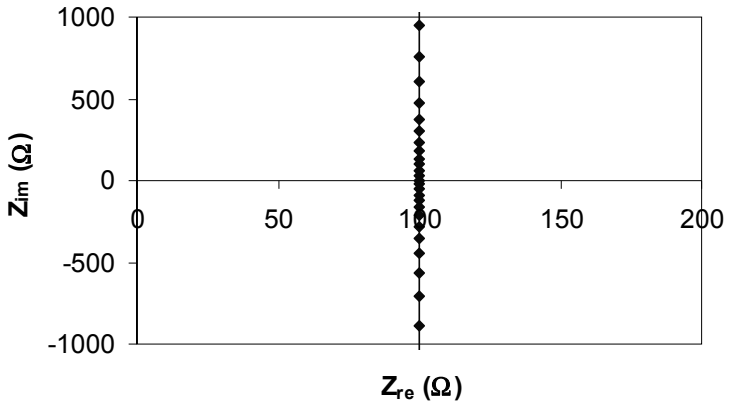

Figure 2.25. Graphical representation of the AC impedance of a series RCL circuit (L = 0.04 H, C = 0.00001 F, R = 100 Ω)

2.4.4.3 R/C/L Circuit

In a circuit of parallel RCL (R/C/L), the overall AC impedance, $Z_{R/C/L}$, can be expressed as

$$Z_{R/C/L} = [R^{-1} + (i\omega L)^{-1} + i\omega C]^{-1} \tag{2.111}$$

After a series of transformations, the standard form of the impedance is obtained:

$$Z_{R/C/L} = \frac{\frac{1}{R}}{(\frac{1}{R})^2 + (\omega C - \frac{1}{\omega L})^2} - \frac{\omega C - \frac{1}{\omega L}}{(\frac{1}{R})^2 + (\omega C - \frac{1}{\omega L})^2} i \tag{2.112}$$

Thus, the real and imaginary components of the AC impedance of the parallel RCL circuit are given by

$$Z_{re} = \frac{\frac{1}{R}}{(\frac{1}{R})^2 + (\omega C - \frac{1}{\omega L})^2} \tag{2.113}$$

$$Z_{im} = -\frac{\omega C - \frac{1}{\omega L}}{(\frac{1}{R})^2 + (\omega C - \frac{1}{\omega L})^2} \tag{2.114}$$

and the phase angle ϕ is given by

$$\tan\phi = R(\omega C - \frac{1}{\omega L}) \tag{2.115}$$

Based on these equations, Figure 2.26 gives a graphical representation of the AC impedance of the (R/C/L) circuit.

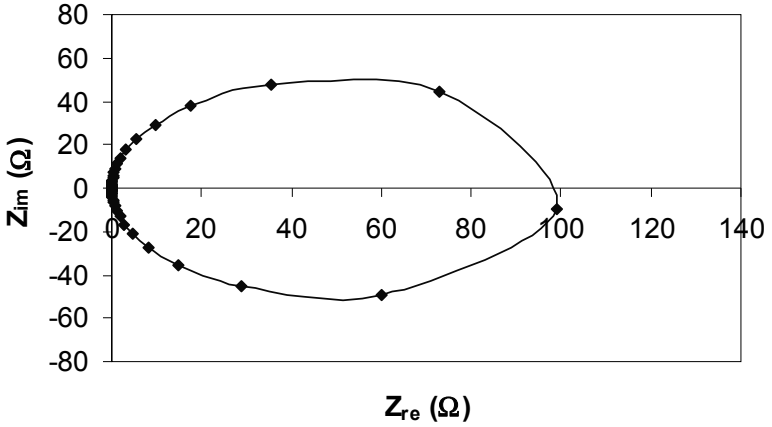

Figure 2.26. Graphical representation of the AC impedance of a simple parallel RCL circuit (L = 0.04 H, C = 0.00001 F, R = 100 Ω)

2.4.4.4 R/(C-L) Circuit

If a series CL is in parallel with R (R/C-L) in a circuit, the overall impedance, $Z_{R/(C-L)}$, is expressed as

$$Z_{R/(C-L)} = [R^{-1} + ((i\omega C)^{-1} + i\omega L)^{-1}]^{-1} \tag{2.116}$$

Then, we have

$$Z_{R/(C-L)} = \frac{\frac{1}{R}}{(\frac{1}{R})^2 + (\frac{\omega C}{\omega^2 CL - 1})^2} + \frac{\frac{\omega C}{\omega^2 CL - 1}}{(\frac{1}{R})^2 + (\frac{\omega C}{\omega^2 CL - 1})^2} i \tag{2.117}$$

Thus, the real and imaginary components, Z_{re} and Z_{im}, in the AC impedance of the R/C-L circuit are:

$$Z_{re} = \frac{\frac{1}{R}}{(\frac{1}{R})^2 + (\frac{\omega C}{\omega^2 CL - 1})^2} \tag{2.118}$$

$$Z_{im} = \frac{\frac{\omega C}{\omega^2 CL - 1}}{(\frac{1}{R})^2 + (\frac{\omega C}{\omega^2 CL - 1})^2} \tag{2.119}$$

The phase angle ϕ is then given by

$$\tan\phi = \frac{\omega CR}{\omega^2 CL - 1} = R(\omega L - \frac{1}{\omega C})^{-1} \tag{2.120}$$

Based on these, a graphical representation of the AC impedance of the R/C-L circuit can be calculated and is depicted in Figure 2.27.

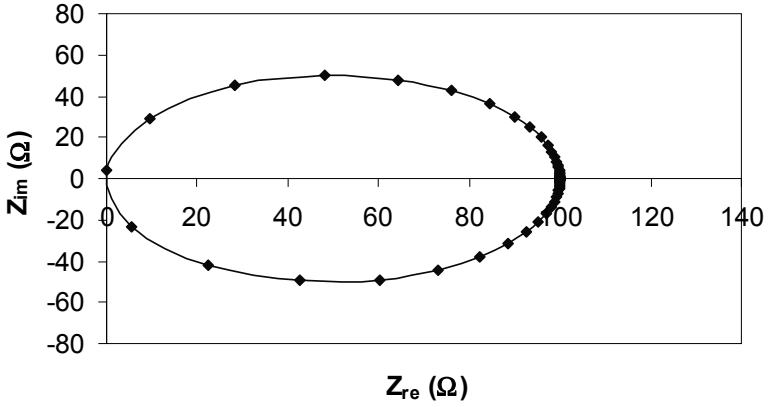

Figure 2.27. Graphical representation of the AC impedance of the R/(C-L) circuit (L = 0.04 H, C = 0.00001 F, R = 100 Ω)

2.4.4.5 C-(R/L) Circuit

In a circuit of a parallel RL in series with C (C-R/L), the overall AC impedance, $Z_{C-(R/L)}$, can be expressed as

$$Z_{C-(R/L)} = (i\omega C)^{-1} + [(R^{-1} + (i\omega L)^{-1}]^{-1} \tag{2.121}$$

Based on the previous calculation in Equation 2.85, we have

$$Z_{C-(R/L)} = (i\omega C)^{-1} + \frac{\omega^2 RL^2}{R^2 + \omega^2 L^2} + i\frac{\omega R^2 L}{R^2 + \omega^2 L^2} \tag{2.122}$$

Then

$$Z_{C-(R/L)} = \frac{\omega^2 RL^2}{R^2 + \omega^2 L^2} + i\left(\frac{\omega R^2 L}{R^2 + \omega^2 L^2} - \frac{1}{\omega C}\right) \tag{2.123}$$

So, the real and imaginary components of the AC impedance of the C-R/L circuit are given by

$$Z_{re} = \frac{\omega^2 RL^2}{R^2 + \omega^2 L^2} \tag{2.124}$$

$$Z_{im} = \frac{\omega R^2 L}{R^2 + \omega^2 L^2} - \frac{1}{\omega C} \tag{2.125}$$

and the phase angle is written as

$$\tan\phi = \frac{\omega^2 R^2 LC - R^2 - \omega^2 L^2}{\omega^3 RL^2 C} \tag{2.126}$$

In the complex plane, an example of the AC impedance of the C-(R/L) circuit is shown in Figure 2.28.

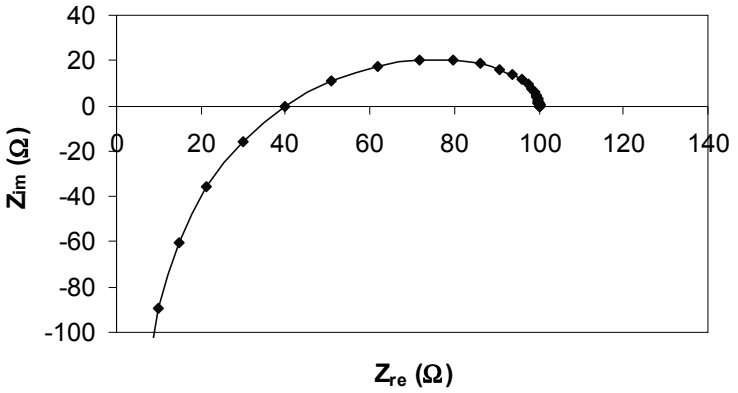

Figure 2.28. Graphical representation of the AC impedance of the C-(R/L) circuit (L = 0.04 H, C = 0.00001 F, R = 100 Ω)

2.4.4.6 C/(R-L) Circuit

In a circuit of a series RL in parallel with C (C/(R-L)), the overall impedance, $Z_{C/(R-L)}$, is expressed as

$$Z_{C/(R-L)} = [(i\omega C) + (R + i\omega L)^{-1}]^{-1} \tag{2.127}$$

Then, we have

$$Z_{C/(R-L)} = \frac{R}{(1-\omega^2 LC)^2 + (R\omega C)^2} + \frac{\omega L(1-\omega^2 LC) - R^2\omega C}{(1-\omega^2 LC)^2 + (R\omega C)^2} i \tag{2.128}$$

The real and imaginary components, Z_{re} and Z_{im}, of the AC impedance of the C/(R-L) circuit are then written as

$$Z_{re} = \frac{R}{(1-\omega^2 LC)^2 + (R\omega C)^2} \tag{2.129}$$

$$Z_{im} = \frac{\omega L(1-\omega^2 LC) - R^2\omega C}{(1-\omega^2 LC)^2 + (R\omega C)^2} \tag{2.130}$$

The phase angle ϕ is given by

$$\tan\phi = \frac{\omega L(1-\omega^2 LC) - R^2\omega C}{R} \tag{2.131}$$

An example, in the complex plane, of the AC impedance of the C/(R-L) circuit is presented in Figure 2.29.

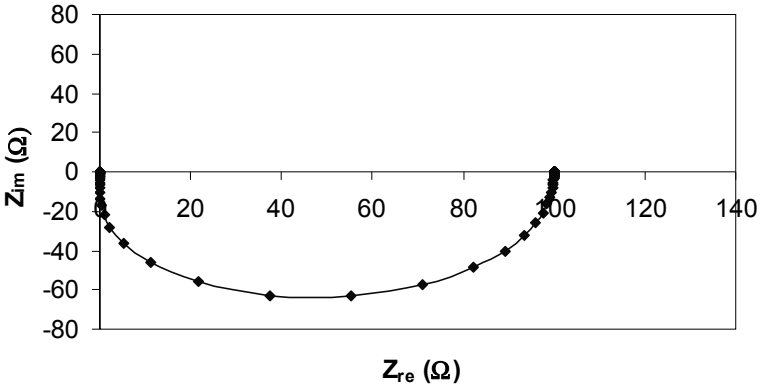

Figure 2.29. Graphical representation of the AC impedance of the C/(R-L) circuit (L = 0.04 H, C = 0.00001 F, R = 100 Ω)

2.4.4.7 L-(R/C) Circuit

In a circuit of a parallel RC in series with L (L-R/C), the overall AC impedance, $Z_{L-(R/C)}$, can be expressed as

$$Z_{L\text{-}(R/C)} = i\omega L + \left(R^{-1} + i\omega C\right)^{-1} \tag{2.132}$$

Based on Equation 2.74, we have

$$Z_{L-(R/C)} = i\omega L + \frac{R}{1+(\omega RC)^2} - i\frac{\omega R^2 C}{1+(\omega RC)^2} \tag{2.133}$$

Then

$$Z_{L-(R/C)} = \frac{R}{1+(\omega RC)^2} + i(\omega L - \frac{\omega R^2 C}{1+(\omega RC)^2}) \tag{2.134}$$

The real and imaginary components, Z_{re} and Z_{im}, of the AC impedance of the L-R/C circuit are written as

$$Z_{re} = \frac{R}{1+(\omega RC)^2} \tag{2.135}$$

$$Z_{im} = \omega L - \frac{\omega R^2 C}{1+(\omega RC)^2} \tag{2.136}$$

The phase angle ϕ is given by

$$\tan\phi = \frac{\omega L + \omega^3 R^2 L C^2 - \omega R^2 C}{R} \tag{2.137}$$

In the complex plane, an example of the AC impedance of the L-(R/C) circuit is depicted in Figure 2.30.

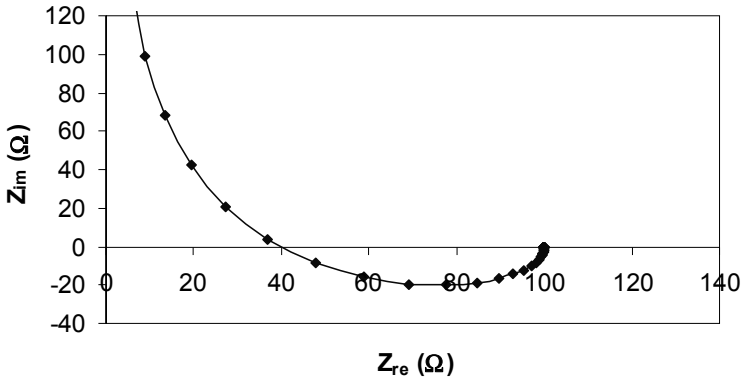

Figure 2.30. Graphical representation of the AC impedance of the L-(R/C) circuit (L = 0.04 H, C = 0.00001 F, R = 100 Ω)

2.4.4.8 L/(R-C) Circuit

In a circuit of a series RC in parallel with L (L/(R-C)), the overall impedance, $Z_{L/(R-C)}$, is expressed as

$$Z_{L/(R-C)} = [(i\omega L)^{-1} + (R + (i\omega C)^{-1})^{-1}]^{-1} \tag{2.138}$$

Then we have

$$Z_{L/(R-C)} = \frac{R}{(1-\frac{1}{\omega^2 LC})^2 + (\frac{R}{\omega L})^2} + \frac{\frac{R^2}{\omega L} - \frac{1}{\omega C}(1-\frac{1}{\omega^2 LC})}{(1-\frac{1}{\omega^2 LC})^2 + (\frac{R}{\omega L})^2} i \tag{2.139}$$

The real and imaginary components, Z_{re} and Z_{im}, of the AC impedance of the L/(R-C) circuit are given by

$$Z_{re} = \frac{R}{(1-\frac{1}{\omega^2 LC})^2 + (\frac{R}{\omega L})^2} \tag{2.140}$$

$$Z_{im} = \frac{\frac{R^2}{\omega L} - \frac{1}{\omega C}(1-\frac{1}{\omega^2 LC})}{(1-\frac{1}{\omega^2 LC})^2 + (\frac{R}{\omega L})^2} \tag{2.141}$$

The phase angle ϕ is given by

$$\tan\phi = \frac{R^2 - \frac{L}{C} + \frac{1}{\omega^2 C^2}}{R\omega L} \tag{2.142}$$

In the complex plane, an example of the AC impedance of the L/(R-C) circuit is shown in Figure 2.31.

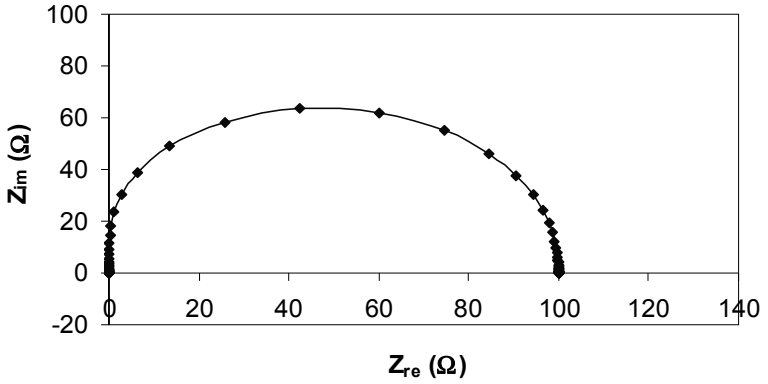

Figure 2.31. Graphical representation of the impedance of the L/(R-C) circuit (L = 0.04 H, C = 0.00001 F, R = 100 Ω)

2.5 Network Circuit Analysis

To construct an equivalent circuit of a complicated electrode process (e.g., a porous electrode) and calculate its impedance, more knowledge about the network circuit may be necessary. In this section, we will spend some time discussing network circuit analysis.

2.5.1 Topological Features of a Network

Two major factors shape an electric network: the type of elements it contains and the manner in which the elements are connected. The latter is called the network topology. To analyze an electric network, one needs to know the number of independent voltage and current variables. To facilitate the following discussion of a network topology, we keep the nodes and replace the elements with lines in the network circuit, thus simplifying the network topology, as depicted in Figure 2.32. Figure 2.32*a* shows a regular network circuit while the configuration in Figure 2.32*b* is called the line graph of a network.

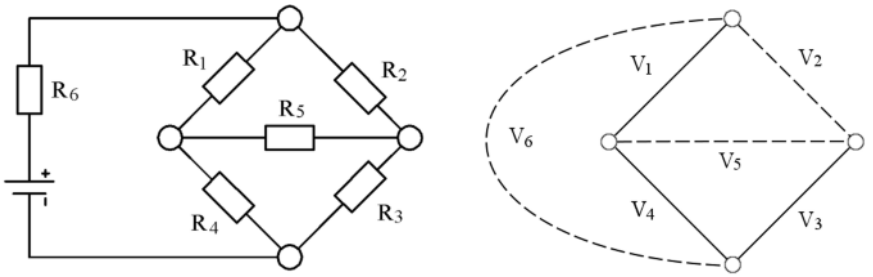

Figure 2.32. A regular circuit and its network line graph: *a* circuit diagram; *b* line graph of circuit

2.5.1.1 Some Terms Used in Network Topology

Several terms are frequently used in network analysis: node, branch, tree, link, loop, and mesh.

A *node* is a terminal or junction at which two or more circuit elements are connected.

A *branch* is a portion of a network which contains either a single element or a certain connection of elements between two nodes.

A *tree* is a connected portion or sub-graph of the entire graph that contains all the nodes but no loops. For example, the solid lines in Figure 2.32*b* form a tree, which consists of all the four nodes in the graph; there are no loops within the tree.

In Figure 2.32*b*, the dashed lines are called *links*, i.e., the branches which are not in the chosen tree. A graph usually has more than one tree, and the entire graph is the sum of the links and tree branches. Assuming that there are N nodes in a network, the number of tree branches is N–1.

A *loop* comprises a set of branches that form a closed path in a network. This set of branches passes through no node or element more than once.

A *mesh* is a loop which contains no other loops within the contour of its closed path. Basically, the term "loop" is applicable to a closed path in both planar and non-planar circuits, whereas "mesh" is only applicable to planar circuits. The meshes in a planar circuit are in fact the contours of the "windows" seen in the circuit diagram. For example, Figure 2.32*a* has three windows, and thus the circuit is a three-mesh circuit.

A *planar network* or *circuit* is one that can be drawn on a plane surface without any of the branches crossing each other. Conversely, a non-planar network or circuit cannot be drawn on a plane surface without the crossing of branches.

2.5.1.2 Independent Voltages

Assuming that there are N nodes and B branches in a network, if all the branch voltages of any tree are made zero by short-circuiting the branches, all the nodes of the circuit are at the same potential, and thus all the voltages of the links are zero. In other words, the link voltages depend on the tree branch voltages. Assuming that there is one link voltage independent of the tree branch voltages, it could not be forced to zero by short-circuiting the tree branches. Consequently at least one node voltage is different from the voltage of the rest of the nodes. Therefore, we conclude that the (N–1) tree branch voltages are independent and can be used to obtain the link voltages. For example, there are four nodes and three independent voltages, namely V1, V3, and V4 in Figure 2.32*b*. The link voltages V2, V5, and V6 can be calculated from the three independent voltages.

2.5.1.3 Independent Currents

Since a tree in a graph contains no loops, all the tree branch currents depend on the link currents. In other words, all the tree branch currents can be expressed in terms of the link currents. Assuming the number of branches in a circuit is B, there will be B–(N–1) link currents, which are independent. Therefore, B–(N–1) independent equations are needed to analyze the circuit. For example, Figure 2.32*b* needs three independent current equations.

2.5.2 Network Theorems [4]

Although the application of Kirchhoff's laws offers basic tools to analyze a network, knowledge of certain network theorems, use of network equivalence, and use of reduction procedures simplify the process of network analysis. Basically, these theorems are applicable for linear networks.

2.5.2.1 Network Reduction

One of the most important strategies to simplify or reduce a linear circuit is superposition. The superposition theorem states that the response of a linear network to a number of simultaneously applied sources is equal to the sum of the individual responses due to each source acting alone.

By analyzing separately a single-input circuit, superposition allows us to analyze linear circuits with more than one independent source. For example, Figure

2.33*a* shows one voltage source and one current source. According to the superposition theorem, the current flowing through resistor R_1 is the sum of the individual response to the voltage source and current source. By replacing the voltage source with a short circuit, as depicted in Figure 2.33*b*, the current through resistor R_1 is the response of R_1 to the current source. To find the response of R_1 to the voltage source, we can replace the current source with an open circuit, as depicted in Figure 2.33*c*. Then the current flowing through resistor R_1 with a voltage source and a current source can be obtained. Compared with the straight analysis of the current through resistor R_1, superposition simplifies the circuit.

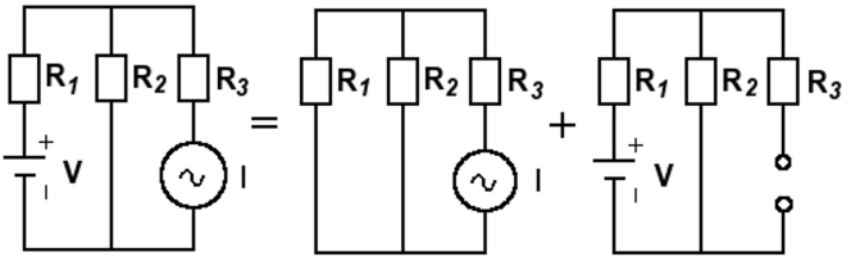

a *b* *c*

Figure 2.33. Superposition of a linear circuit

Other methods to simplify the circuit are Thevenin's and Norton's theorems. These two theorems can be used to replace the entire circuit by employing equivalent circuits. For example, Figure 2.34 shows a circuit separated into two parts. Circuit A is linear. Circuit B contains non-linear elements. The essence of Thevenin's and Norton's theorems is that no dependent source in circuit A can be controlled by a voltage or current associated with an element in circuit B, and vice versa.

Thevenin's theorem states that a section of a linear circuit containing one or more sources and impedances can be replaced with an equivalent circuit model containing only one voltage source and one series-connected impedance, as shown in Figure 2.35.

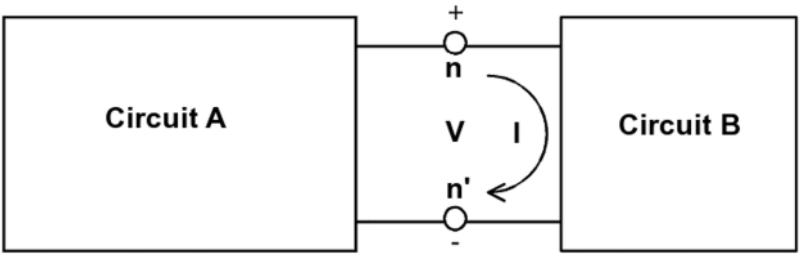

Figure 2.34. Partitioned circuit

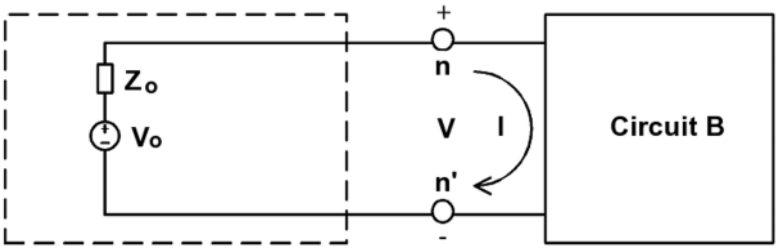

Figure 2.35. Graphical presentation of Thevenin's theorem

To determine V_o, we can remove circuit B and calculate the voltage drop across the terminals n and n'. This voltage drop is the Thevenin voltage. To determine the impedance Z_o, we can kill all the sources in circuit A, as we did in Figure 2.33, and then calculate the impedance from n-n' terminals by looking back into circuit A. This impedance Z_o is the Thevenin impedance, which is also called the output impedance of circuit A.

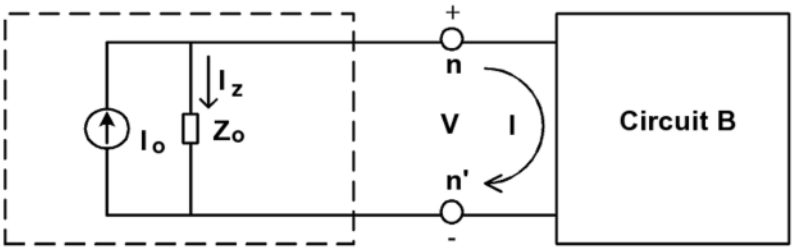

Figure 2.36. Graphical presentation of Norton's theorem

Similar to Thevenin's theorem, Norton's theorem states that a section of a linear circuit containing one or more sources and impedances can be replaced with an equivalent circuit model containing only one constant current source and one parallel-connected impedance, as shown in Figure 2.36.

To determine the Norton equivalent impedance Z_o in Figure 2.36, we can kill all the sources in circuit A and then calculate the impedance from n-n' terminals by looking back into circuit A. Thus, the Norton impedance Z_o is equal to the Thevenin impedance. The Norton current I_o is a constant current that remains the same regardless of the impedance of circuit B. It can be determined by

$$I_o = \frac{V_o}{Z_o} \tag{2.143}$$

Note that only at the output terminals n-n' are the Thevenin and Norton equivalents the same. In other words, at the output terminals n-n' the voltage and current of the Thevenin equivalent circuit and the Norton equivalent circuit are identical.

2.5.2.2 Loop and Mesh Analysis

A commonly used network analysis method is loop and mesh analysis, which is generally based on KVL. As defined previously, loop analysis refers to the general method of current analysis for both planar and non-planar networks, whereas mesh analysis is reserved for the analysis of planar networks. In loop or mesh analysis, the circulating currents are selected as the unknowns, and a circulating current is assigned to each independent loop or mesh of the network. Then a series of equations can be formed according to KVL.

The series of equations in the form of $[Z][I]=[V]$ can be established by equating the sum of the externally applied voltage sources acting in each loop to the sum of the voltage drops across the branches forming the loop. The number of equations is equal to the number of independent loops in the network. The general equation in loop or mesh analysis is given by

$$\begin{pmatrix} Z_{11} & Z_{12} & Z_{13} & \cdots & Z_{1N} \\ Z_{21} & Z_{22} & Z_{23} & \cdots & Z_{2N} \\ Z_{31} & Z_{32} & Z_{33} & \cdots & Z_{3N} \\ \cdots & \cdots & \cdots & \cdots & \cdots \\ Z_{N1} & Z_{N2} & Z_{N3} & \cdots & Z_{NN} \end{pmatrix} \bullet \begin{pmatrix} I_1 \\ I_2 \\ I_3 \\ \cdots \\ I_N \end{pmatrix} = \begin{pmatrix} V_1 \\ V_2 \\ V_3 \\ \cdots \\ V_N \end{pmatrix} \tag{2.144}$$

where the impedance matrix [*Z*] is an $N \times N$ matrix, as described in Equation 2.144. The following rules describe how to determine the values of the voltages, currents, and impedances in Equation 2.144.

1. The voltages in Equation 2.144 are equal to the voltage sources in a given loop. If the direction of the current caused by the voltage is the same as that of the assigned current, the voltage is positive. Otherwise, the voltage is negative.
2. The series of mesh impedances, known as the self-mesh impedances, Z_{11}, Z_{22}, Z_{33}, …, Z_{NN}, are given by the sum of all impedances through the loop in which the circulating current flows.
3. Each mesh mutual impedance, denoted by Z_{ik} ($i \neq k$), is given by the sum of the impedances through which both mesh currents I_i and I_k flow. In other words, the mesh mutual impedances are equal to the sum of the impedances shared by meshes *i* and *k*. If the direction of the current I_i in loop *i* is opposite to that of the current I_k in the adjacent loop *k*, the mutual impedance equals the negative sum of the impedances, whereas if the direction of the current I_i is the same as that of the current I_k, then the mutual impedance equals the positive sum. In a linear network, the following can be obtained:

$$Z_{ik} = Z_{ki} \tag{2.145}$$

A linear matrix equation can be solved by the application of Cramer's rule. Assuming the determinant Δ of the matrix *Z* is non-zero, the solution of the current can be expressed as

$$[I] = [Z]^{-1}[V] \tag{2.146}$$

where $[Z]^{-1}$ is the inverse of [Z], which can be expressed as

$$[Z]^{-1} = \frac{1}{\Delta}(\Delta_{ik})^T = \frac{1}{\Delta}\Delta_{ki} \tag{2.147}$$

where Δ_{ik} is the matrix cofactor and $(\Delta_{ik})^T = \Delta_{ki}$ represents the matrix transpose. Δ and Δ_{ki} can be expressed as follows:

$$\Delta = |[Z]| = \begin{vmatrix} Z_{11} & Z_{12} & \ldots & Z_{1i} & \ldots & Z_{1N} \\ Z_{21} & Z_{22} & \ldots & Z_{2i} & \ldots & Z_{2N} \\ \ldots & \ldots & \ldots & \ldots & \ldots & \ldots \\ Z_{N1} & Z_{N2} & \ldots & Z_{Ni} & \ldots & Z_{NN} \end{vmatrix} \tag{2.148}$$

$$\Delta_{ki} = \begin{bmatrix} \Delta_{11} & \Delta_{21} & \Delta_{31} & \ldots & \Delta_{N1} \\ \Delta_{12} & \Delta_{22} & \Delta_{32} & \ldots & \Delta_{N2} \\ \Delta_{13} & \Delta_{23} & \Delta_{33} & \ldots & \Delta_{N3} \\ \ldots & \ldots & \ldots & \ldots & \ldots \\ \Delta_{1N} & \Delta_{2N} & \Delta_{3N} & \ldots & \Delta_{NN} \end{bmatrix} \tag{2.149}$$

where |[Z]| is the determinant of [Z].

2.5.2.3 Nodal Analysis

In nodal analysis, the voltages between adjacent nodes of the network are chosen as the unknowns. This can commonly be achieved by selecting a reference node from the graph of the network. Equations are then formed if KCL is employed. By equating the sum of the currents flowing through admittances associated with one node to the sum of the currents flowing out of the current sources associated with the same node, a set of equations can be established with the form of $[Y][V] = [I]$:

$$\begin{pmatrix} Y_{11} & Y_{12} & Y_{13} & \ldots & Y_{1,N-1} \\ Y_{21} & Y_{22} & Y_{23} & \ldots & Y_{2,N-1} \\ Y_{31} & Y_{32} & Y_{33} & \ldots & Y_{3,N-1} \\ \ldots & \ldots & \ldots & \ldots & \ldots \\ Y_{N-11} & Y_{N-12} & Y_{N-13} & \ldots & Y_{N-1,N-1} \end{pmatrix} \begin{pmatrix} V_1 \\ V_2 \\ V_3 \\ \ldots \\ V_{N-1} \end{pmatrix} = \begin{pmatrix} I_1 \\ I_2 \\ I_3 \\ \ldots \\ I_{N-1} \end{pmatrix} \tag{2.150}$$

where the admittance matrix [*Y*] is an $(N-1)\times(N-1)$ matrix given in Equation 2.150. The following rules describe how to determine the values in Equation 2.150.

1. The currents in Equation 2.150 are equal to the sum of the source currents associated with one given node. The currents are positive if they go into the nodes. Otherwise, the currents are negative.
2. Y_{11}, Y_{22}, Y_{33}, …, $Y_{N\text{-}1,N\text{-}1}$, known as the self node admittances, are given by the sum of all admittances directed to a given node with all other nodes shorted to the reference node.
3. Each node mutual admittance Y_{ik} $(i \neq k)$ is the sum of the admittances between two given nodes *i* and *k*. The current $Y_{ik}V_i$ in the mutual admittances between nodes *i* and *k* is negative if the voltages of nodes *i* and *k* have the same assumed polarity relative to the reference node. The current $Y_{ik}V_i$ is positive if the voltages of nodes *i* and *k* have the opposite assumed polarity relative to the reference node. In a linear network, we have

$$Y_{ik} = Y_{ki} \tag{2.151}$$

2.5.3 Transient Network Analysis

If a generator is imposed on a network or switched out of the circuit with capacitors and/or inductors, there will be a transitory change in the currents and voltages until a new equilibrium state is established. These changing currents and voltages are defined as transients. The time period from the moment of switching to the time equilibrium established is called the transient state. In transient analysis, we always come across linear differential, integral, or integro-differential equations of either the first or the second order when Kirchhoff's laws are applied. In this section, we will solve these equations using a classical method.

The first order circuit with one storage element is described by

$$\frac{dx}{dt} + a_0 x = f(t) \tag{2.152}$$

The second order circuit with two storage elements can be described by

$$\frac{d^2x}{dt^2} + a_1\frac{dx}{dt} + a_0 = f(t) \tag{2.153}$$

In Equations 2.152 and 2.153, a_1 and a_0 are the constant coefficients; *x* may be either voltage, current, or charge; $f(t)$ is the driving voltage or current; and *t* is time. The solution of these equations consists of two parts:

$$x = x_n + x_f \tag{2.154}$$

where x_n is the natural response and x_f is the forced response. The natural response is the general solution of the differential equation with the driving function $f(t)$ set to zero. The forced response is a particular solution of the differential equation for a given driving function. For example, the complete solution of Equation 2.152 can be derived as follows.

The characteristic equation of Equation 2.153 can be expressed as

$$s^2 + a_1 s + a_0 = 0 \tag{2.155}$$

Providing s_1 and s_2 are the two eigenvalues of Equation 2.155, the two natural responses can be obtained:

$$x_{n1} = A_1 e^{s_1 t} \tag{2.156}$$

$$x_{n2} = A_2 e^{s_2 t} \tag{2.157}$$

where A_1 and A_2 are arbitrary constants.

As this is a linear equation, the natural response x_n can simply be summed up as

$$x_n = A_1 e^{s_1 t} + A_2 e^{s_2 t} \tag{2.158}$$

The eigenvalues are also known as the natural frequencies of the circuit, which are the reciprocals of the circuit response time constant. The eigenvalues of Equation 2.155 could be real or complex numbers. If the natural frequencies are complex, we have

$$s_{1,2} = \alpha \pm i\beta \tag{2.159}$$

The natural response is given by

$$x_n = A_1 e^{(\alpha + i\beta)t} + A_2 e^{(\alpha - i\beta)t} \tag{2.160}$$

Based on Euler's formula, the above equation can be rewritten as

$$x_n = \left[B_1 \cos \beta t + i B_2 \sin \beta t \right] e^{\alpha t} \tag{2.161}$$

where

$$B_1 = A_1 + A_2 \tag{2.162}$$

$$B_2 = A_1 - A_2 \tag{2.163}$$

In a circuit, if the real part in the eigenvalues is negative, then the response decays with time. The imaginary part in the eigenvalues implies that this decayed response is accompanied by oscillation.

If there are two real and equal roots for Equation 2.155, the natural response is given by

$$x_n = \left(A_1 + A_2 t\right) e^{st} \tag{2.164}$$

This demonstrates that the response is the superposition of two parts: the linear response and the exponential decayed response.

One solution of the forced response x_f is the undetermined coefficient method. Assuming the forced response has the same form of source function $f(t)$ but a different coefficient, putting this trial forced response into the differential equation yields the coefficients in the forced response x_f.

For a higher order equation, the general form is given by

$$a_n \frac{d^n x}{dt^n} + a_{n-1} \frac{d^{n-1} x}{dt^{n-1}} + \ldots + a_r \frac{d^r x}{dt^r} + \ldots + a_1 \frac{dx}{dt} + a_0 x = f(t) \tag{2.165}$$

The characteristic equation of the above equation is given by

$$a_n s^n + a_{n-1} s^{n-1} + \ldots + a_r s^r + \ldots + a_1 s + a_0 = 0 \tag{2.166}$$

The eigenvalues of s_1, …, s_n are the natural frequencies of this circuit, otherwise known as the poles of the circuit network. If the poles are all different, the natural response is given by

$$x_n = A_1 e^{s_1 t} + A_2 e^{s_2 t} + \ldots + A_r e^{s_r t} + \ldots + A_n e^{s_n t} \tag{2.167}$$

If r poles are equal, then we have

$$x_n = \left(A_1 + A_2 t + \ldots + A_r t^{r-1}\right) e^{s_r t} + A_{r+1} e^{s_{r+1} t} + \ldots + A_n e^{s_n t} \tag{2.168}$$

where A_1 ... A_n are arbitrary constants.

In general, x_n satisfies

$$a_n \frac{d^n (x_n)}{dt^n} + a_{n-1} \frac{d^{n-1} (x_n)}{dt^{n-1}} + \ldots + a_r \frac{d^r (x_n)}{dt^r} + \ldots + a_1 \frac{d(x_n)}{dt} + a_0 x_n = 0 \tag{2.169}$$

and x_f is a solution of

$$a_n \frac{d^n (x_f)}{dt^n} + a_{n-1} \frac{d^{n-1} (x_f)}{dt^{n-1}} + \ldots + a_r \frac{d^r (x_f)}{dt^r} + \ldots + a_1 \frac{d(x_f)}{dt} + a_0 x_f = f(t) \tag{2.170}$$

Summing the above two equations, we have

$$a_n \frac{d^n(x_n + x_f)}{dt^n} + a_{n-1} \frac{d^{n-1}(x_n + x_f)}{dt^{n-1}} + \ldots + a_r \frac{d^r(x_n + x_f)}{dt^r} + \ldots + a_1 \frac{d(x_n + x_f)}{dt} + a_0(x_n + x_f) = f(t) \tag{2.171}$$

Thus, $x = x_n + x_f$ is the complete solution of Equation 2.165.

2.6 Basic Knowledge for Understanding EIS

2.6.1 Introduction

Ohm's law defines the resistance, R, in terms of the ratio between voltage V and current I. Its use is limited to the ideal resistor for a DC system, which is independent of frequency. The relationship between the resistance, current, and voltage can be expressed as

$$R = \frac{V}{I} \tag{2.172}$$

However, real electrochemical systems exhibit much more complex behaviours. They are not simply resistive. The electrochemical double layer adds a capacitive term. Other electrode processes, such as diffusion, are time and/or frequency dependent. Therefore, for an actual electrochemical system, impedance is used instead of resistance. The impedance of an electrochemical system (defined as $Z(\omega)$) is the AC response of the system being studied to the application of an AC signal (e.g., sinusoidal wave) imposed upon the system. The form of the current–voltage relationship of the impedance in an electrochemical system can also be expressed as

$$Z(\omega) = \frac{V(t)}{I(t)} \tag{2.173}$$

where $V(t)$ and $I(t)$ are the measurements of voltage and current in an AC system.

The technique that measures the AC impedance of a circuit element or an electric circuit is called *AC impedance spectroscopy*. As described in Section 2.4, the impedances of a resistor (Z_R), a capacitor (Z_C), and an inductor (Z_L) for a sinusoidal system can be expressed, respectively, as follows:

$$Z_R(\omega) = \frac{V(t)}{I(t)} = R \tag{2.174}$$

$$Z_C(\omega) = \frac{V(t)}{I(t)} = \frac{1}{i\omega C} \tag{2.175}$$

$$Z_L(\omega) = \frac{V(t)}{I(t)} = i\omega L \tag{2.176}$$

If AC impedance spectroscopy is used in an electrochemical system, this technique is generally called *electrochemical impedance spectroscopy*, known as EIS. The impedance of an electrochemical system can also be expressed typically in Cartesian coordinates:

$$Z(\omega) = Z_{re} + iZ_{im} \tag{2.177}$$

where Z_{re} (or Z') and Z_{im} (or Z'') are the real and imaginary parts of the impedance, respectively. In polar coordinates, this becomes

$$Z(\omega) = |Z|e^{i\theta} \tag{2.178}$$

where $|Z| = \sqrt{(Z_{re}^2 + Z_{im}^2)}$ is the modulus and θ is the phase corresponding to a given frequency.

2.6.2 Nyquist and Bode Plots

Generally, the impedance spectrum of an electrochemical system can be presented in Nyquist and Bode plots, which are representations of the impedance as a function of frequency. A Nyquist plot is displayed for the experimental data set $Z(Z_{re,i}, Z_{im,i}, \omega_i)$, ($i$ = 1, 2, …, n) of n points measured at different frequencies, with each point representing the real and imaginary parts of the impedance $(Z_{re,i} \sim Z_{im,i})$ at a particular frequency ω_i.

A Bode plot is an alternative representation of the impedance. There are two types of Bode diagram, $\log|Z| \sim \log\omega$ (or $|Z| \sim \log\omega$) and $\theta \sim \log\omega$, describing the frequency dependencies of the modulus and phase, respectively. A Bode plot is normally depicted logarithmically over the measured frequency range because the same number of points is collected at each decade. Both plots usually start at a high frequency and end at a low frequency, which enables the initial resistor to be found more quickly.

Figure 2.37 shows an example impedance spectrum of an electrochemical system with two time constants. Figure 2.37*a*, *b*, and *c* are the equivalent circuit, simulated Nyquist diagram, and Bode plot, respectively.

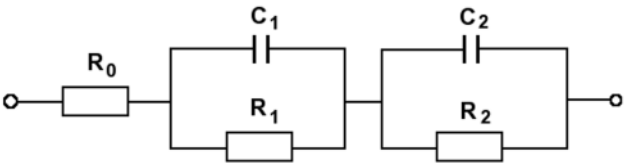

a

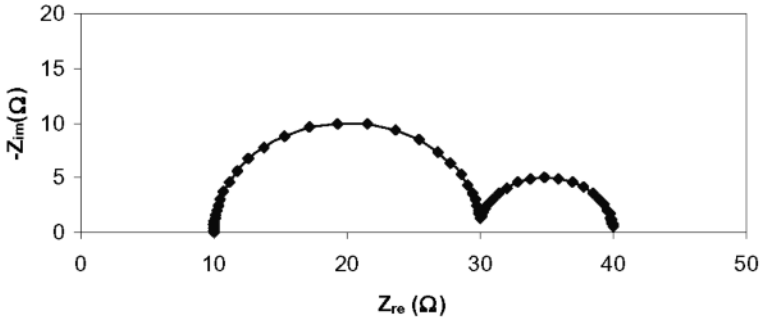

b

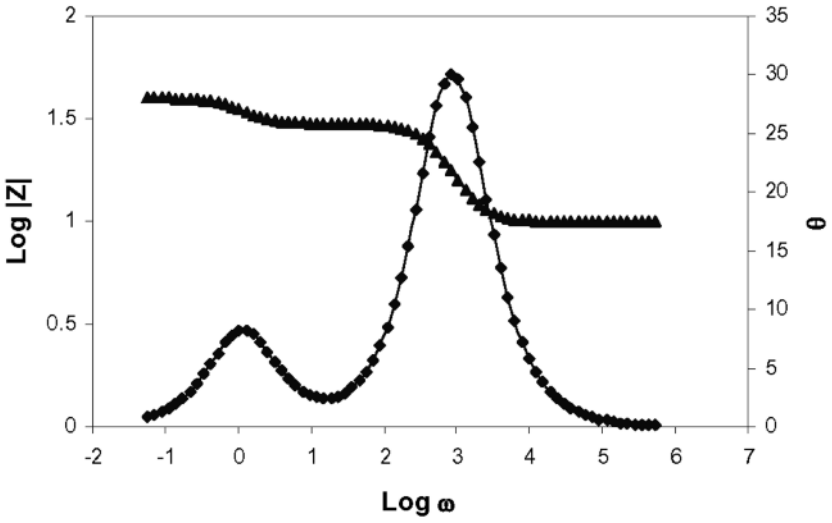

c

Figure 2.37. *a* The equivalent circuit of an electrochemical system with two time constants; *b* Nyquist diagram of a two time constants model simulated over the frequency range 100 kHz–0.0 1Hz (R_0 = 10 Ω, R_1 = 20 Ω, C_1 = 0.0001 F, R_2 = 10 Ω, C_2 = 0.1 F); *c* Bode plot of a two time constants model simulated over the frequency range 100 kHz–0.01 Hz (R_0 = 10 Ω, R_1 = 20 Ω, C_1 = 0.0001 F, R_2 = 10 Ω, C_2 = 0.1 F) (◆) $\log|Z| \sim \log\omega$, (▲) $\theta \sim \log\omega$.

The most common graphical representation of experimental impedance is a Nyquist plot (complex-plane diagram), which is more illustrative than a Bode plot. However, a Bode plot sometimes can provide additional information.

Some typical Nyquist plots for an electrochemical system are shown in Figure 2.38. The usual result is a semicircle, with the high-frequency part giving the solution resistance (for a fuel cell, mainly the membrane resistance) and the width of the semicircle giving the charge-transfer resistance.

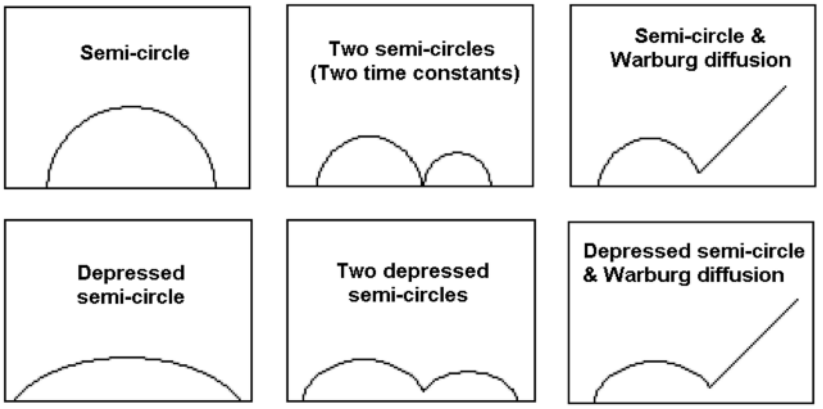

Figure 2.38. Typical Nyquist plots for electrochemical systems

2.6.3 Equivalent Circuit Models

EIS data analysis is commonly carried out by fitting it to an equivalent electric circuit model. An equivalent circuit model is a combination of resistances, capacitances, and/or inductances, as well as a few specialized electrochemical elements (such as Warburg diffusion elements and constant phase elements), which produces the same response as the electrochemical system does when the same excitation signal is imposed. Equivalent circuit models can be partially or completely empirical. In the model, each circuit component comes from a physical process in the electrochemical cell and has a characteristic impedance behaviour. The shape of the model's impedance spectrum is controlled by the style of electrical elements in the model and the interconnections between them (series or parallel combinations). The size of each feature in the spectrum is controlled by the circuit elements' parameters.

However, although powerful numerical analysis software, e.g., Zview, is available to fit the spectra and give the best values for equivalent circuit parameters, analysis of the impedance data can still be troublesome, because specialized electrochemical processes such as Warburg diffusion or adsorption also contribute to the impedance, further complicating the situation. To set up a suitable model, one requires a basic knowledge of the cell being studied and a fundamental understanding of the behaviour of cell elements.

The equivalent circuit should be as simple as possible to represent the electrochemical system and it should give the best possible match between the model's impedance and the measured impedance of the system, whose equivalent circuit contains at least an electrolyte resistance, a double-layer capacity, and the impedance of the Faradaic or non-Faradaic process. Some common equivalent circuit elements for an electrochemical system are listed in Table 2.1. A detailed description of these elements will be introduced in Section 4.1.

Table 2.1. Common circuit elements used in equivalent circuit models

Equivalent element	Name
R	Resistance
C	Capacitance
L	Inductance
W	Infinite Warburg
BW	Finite Warburg (Bounded Warburg)
CPE	Constant phase element
BCPE	Bounded CPE

The following are two examples of the standard equivalent circuits used in electrochemical systems.

2.6.3.1 The Randles Cell

The simplest and most common model of an electrochemical interface is a Randles circuit. The equivalent circuit and Nyquist and Bode plots for a Randles cell are all shown in Figure 2.39. The circuit includes an electrolyte resistance (sometimes solution resistance), a double-layer capacitance, and a charge-transfer resistance. As seen in Figure 2.39*a*, R_{ct} is the charge-transfer resistance of the electrode process, C_{dl} is the capacitance of the double layer, and R_{el} is the resistance of the electrolyte. The double-layer capacitance is in parallel with the charge-transfer resistance.

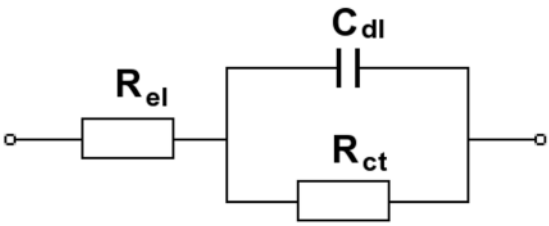

a

Figure 2.39. Graphic presentations of the Randles cell: *a* equivalent circuit, *b* Nyquist plot, *c* Bode magnitude plot, *d* Bode phase plot (R_{el} = 20 Ω, R_{ct} = 80 Ω, C_{dl} = 0.001 F)

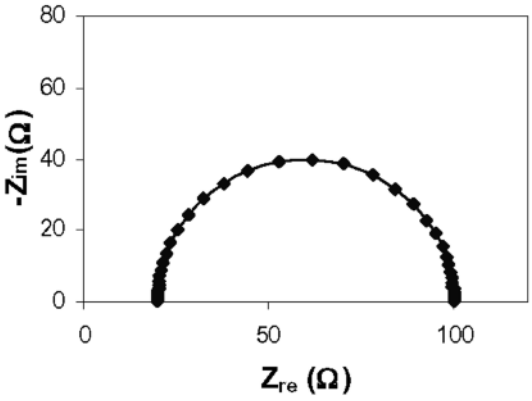

b

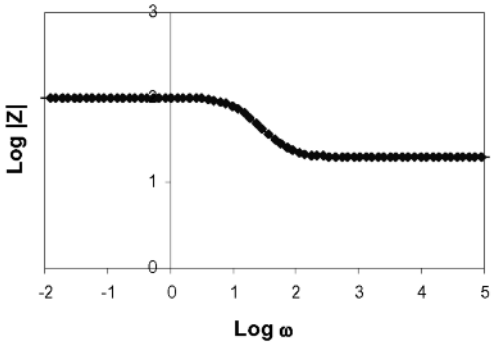

c

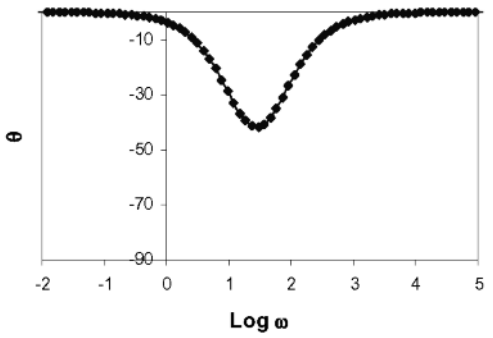

d

Figure 2.39. (continued)

The Nyquist plot of a Randles cell is always a semicircle. At high frequencies the impedance of C_{dl} is very low, so the measured impedance tends to R_{el}. At very low frequencies the impedance of C_{dl} becomes extremely high, and thus, the measured impedance tends to $R_{ct} + R_{el}$. Accordingly, at intermediate frequencies, the impedance falls between R_{el} and $R_{ct} + R_{el}$. Therefore, the high-frequency intercept is associated with the electrolyte resistance, while the low-frequency intercept corresponds to the sum of the charge-transfer resistance and the electrolyte resistance. The diameter of the semicircle is equal to the charge-transfer resistance.

The Bode plot contains a magnitude plot and a phase angle plot. For a Randles cell, the values of the electrolyte resistance and the sum of the electrolyte resistance and the polarization resistance can easily be identified from the horizontal line in the magnitude plot. At high or low frequencies, the phase angles are close to 0°. Otherwise, at intermediate frequencies, the phase angles fall between 0° and 90°.

The Randles cell model is not only useful but also serves as a starting point for more complex models, created by adding more components.

2.6.3.2 Mixed Kinetic and Diffusion Control

In a situation where a charge transfer is also influenced by diffusion to and from the electrode, the Warburg impedance will be seen in the impedance plot. This circuit model presents a cell in which polarization is controlled by the combination of kinetic and diffusion processes. The equivalent circuit and the Nyquist and Bode plots for the system are all shown in Figure 2.40. It can be seen that the Warburg element is easily recognizable by a line at an angle of 45° in the lower frequency region.

When investigating an electrochemical system using EIS, the equivalent circuit model that has been constructed must be verified. An effective way to do so is to alter a single cell component and see if the expected changes in the impedance spectrum occur, or to keep adding components to the circuit to see if a suitable circuit can be achieved, until reaching a perfect fit. Nevertheless, empirical models should use as few components as possible.

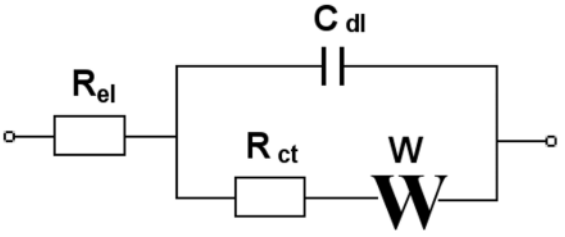

a

Figure 2.40. Graphic presentations of a mixed kinetic and diffusion control circuit: *a* equivalent circuit, *b* Nyquist plot, *c* Bode magnitude plot, *d* Bode phase plot (R_{el} = 100 Ω, R_{ct} = 100 Ω, C_{dl} = 0.001 F, σ = 20 $\Omega s^{-1/2}$)

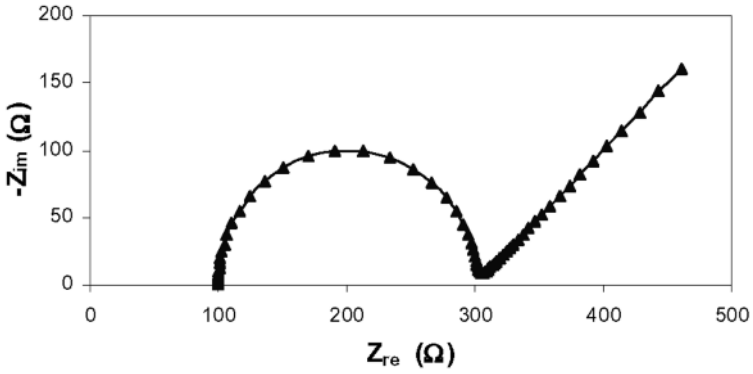

b

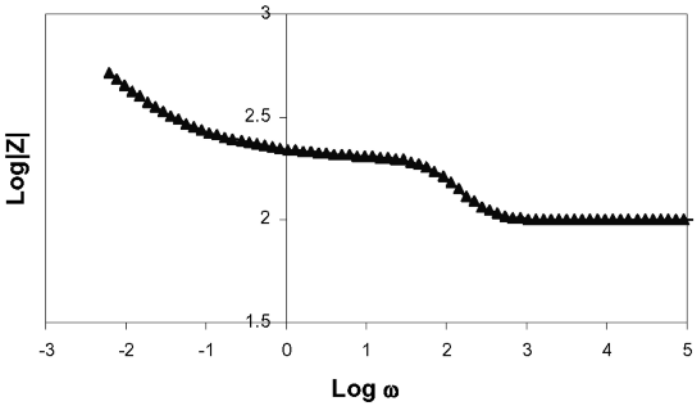

c

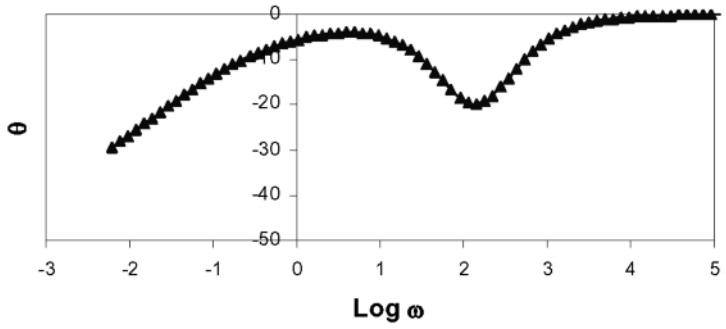

d

Figure 2.40. (continued)

It should also be pointed out that an equivalent circuit is not unique. In describing the same AC impedance spectrum, several circuits may exhibit the same result. For example, a model that includes elements without any chemical basis and practical meaning can demonstrate a perfect fit. Various equivalent circuit models used in PEM fuel cells will be discussed in detail in Chapter 4.

2.6.4 Data Fitting of EIS

It has been recognized that the analysis of EIS spectra is not straightforward. An effective approach is to fit the data using equivalent circuit models. Different methods for data fitting exist, such as the graphic method, the non-linear least square method, and the deconvolution approach. Although the graphic method is extremely simple and sufficiently accurate, with the rapid development of computer technology fewer people are using it. Here we briefly introduce the widely used non-linear least squares (NLLS) method and the deconvolution approach.

2.6.4.1 Non-Linear Least Squares Method

The rapid development of computer technology has yielded powerful tools that make it possible for modern EIS analysis software not only to optimize an equivalent circuit, but also to produce much more reliable system parameters. For most EIS data analysis software, a non-linear least squares fitting method, developed by Marquardt and Levenberg, is commonly used. The NLLS Levenberg–Marquardt algorithm has become the basic engine of several data analysis programs.

The core of the NLLS Levenberg–Marquardt algorithm is the use of the chi-squared parameter, χ^2, which is defined as follows

$$\chi^2 = \sum_{i=1}^{n} \left[(y_i - f(x_i)) / \sigma_i \right]^2 \tag{2.179}$$

where σ_i, y_i, and $f(x_i)$ represent the standard deviation of measurement, the data, and the known function, respectively. By minimizing the object function, χ^2, this method makes it possible to measure the "goodness of fit".

For the complex non-linear least squares (CNLS) method, the object function, S, is defined as [5, 6]

$$S = \sum_{i=1}^{n} w_i \left\{ \left[Z_{re,i} - Z_{re}(\omega_i, \alpha_k) \right]^2 + \left[Z_{im,i} - Z_{im}(\omega_i, \alpha_k) \right]^2 \right\} \tag{2.180}$$

where

$Z_{re,i} + jZ_{im,i}$ is the measured impedance at frequency ω_i (here, $j = \sqrt{-1}$ is used for differentiation);

$Z(\omega_i, a_k) = Z_{re}(\omega_i, a_k) + jZ_{im}(\omega_i, a_k)$ is the model function, which can be altered using the adjustable parameters; the model function can often be presented by an equivalent circuit, involving such elements as resistance, capacitance, and Warburg in series and/or in parallel;

α_k ($k = 1 \ldots M$) is the adjustable parameters; and

w_i is the weight factor, which is the inverse of the square of the vector length of the impedance.

Other parameters, such as CNLS-fit residuals (Δ_{re} and Δ_{im}), also indicate the "goodness of fit". They are defined as

$$\Delta_{re} = \frac{Z_{re,i} - Z_{re}(\omega_i, a_k)}{\left|Z(\omega_i, a_k)\right|} \tag{2.181}$$

$$\Delta_{im} = \frac{Z_{im,i} - Z_{im}(\omega_i, a_k)}{\left|Z(\omega_i, a_k)\right|} \tag{2.182}$$

For an optimum fit, the residuals should distribute over the full range of frequencies.

NLLS or CNLS starts with the selection of the equivalent circuit, followed by the initial value estimation for all the model parameters. Estimation of the initial values is one of the most difficult tasks in the analysis of an equivalent circuit model. A good initial value estimation needs a solid understanding of the element behaviours in the circuit. If the initial estimations are far from the "real values", the optimum fit may not be found. An estimated value within a factor of ten of the true value is a good start for determining a model parameter [7].

The simplest case for estimating the initial values of the circuit parameters is when the semicircle arcs in the impedance spectrum are not overlapping. In this situation the charge-transfer resistance, R_{ct}, can be estimated using the intercepts of the arc with the real axis, and the associated double-layer capacitance, C_{dl}, is then obtained from $\omega_{\max} = (R_{ct}C_{dl})^{-1}$, where $\omega_{\max}$ is the peak value of the frequency.

Experimental arcs in the spectrum are not always ideal semicircles, and this complicates parameter estimation. Nevertheless, there are still basic rules for estimating the initial values [8, 9]. The key is to identify the region of the spectrum in which one element dominates and then estimate the value of the element in this region. For example, the resistor's impedance dominates the spectrum at a low frequency, while the impedance of a capacitor approaches zero at a high frequency and infinity at a low frequency; also, individual resistors can be recognized based on the horizontal regions in a Bode plot.

Using the estimated initial values of the parameters, the software will adjust several or all of the parameters and evaluate the resulting fit. The process is repeated again and again until the goodness of fit is satisfactory. Generally speaking, the NLLS algorithm optimizes the fit over the entire frequency range rather than over a small section of the spectrum. Sometimes the fit looks poor due to an inappropriate choice of model, or poor estimates of the initial values, or noise. In such cases, the model should be adjusted and the procedure repeated.

2.6.4.2 Deconvolution

Assuming that the Nyquist plot of the impedance does not display an ideal semicircle (e.g., it shows a depressed semicircle or a wide arc), it might be described using two or more discrete time constants or a continuous distribution of time constants. In the former case, the equivalent circuit may involve two or more parallel RCs in series. In the latter case, it may involve one or more parallel CPEs and Rs in series. As mentioned, one solution could be to use several CNLS fittings; however, a more direct method would be the deconvolution of the imaginary part of the impedance data.

One of the advantages of the deconvolution method is to make it possible to decide whether the Nyquist plot of the impedance is describable by discrete time constants or by a continuous distribution of time constants, according to the width of the individual relaxation. Also, from the values of the peak relaxation time, τ_p, one may calculate the approximate frequency region as well, from $\omega_p = \tau_p^{-1}$. These results may then be used to build an appropriate equivalent circuit and estimate the initial values of the parameters for subsequent CNLS fittings.

Starting with Equation 2.183, the basic equations for attaining the distribution of relaxation times, $g_z(\tau)$, can be derived:

$$Z(\omega) = R_0 \int_0^{\infty} \frac{g_z(\tau)dt}{1 + i\omega\tau} \tag{2.183}$$

where R_0 is the $\omega \to 0$ value of $Z(\omega)$.

Assuming that ω_0 is approximately the central value of all frequencies measured, the following transformations can be performed:

$$\omega_0 \equiv 2\pi f_0 \tag{2.184}$$

$$\tau_0 \equiv \omega_0^{-1} \tag{2.185}$$

$$\omega\tau_0 \equiv \exp(-z) \tag{2.186}$$

$$\tau \equiv \tau_0 \exp(s) \tag{2.187}$$

$$G_z(s) \equiv \tau g_z(\tau) \tag{2.188}$$

where s and z are the new logarithmic variables. Then, the relation presented in Equation 2.183 can be transferred into the convolution form

$$Z(z) = R_0 \int_{-\infty}^{\infty} \frac{G_z(s)ds}{1 + i\exp[-(z-s)]} \tag{2.189}$$

The standard convolution forms can be obtained by separating Equation 2.189 into real and imaginary parts, each having an expression related to $G_z(s)$. Normally, it is

preferable to calculate the imaginary part of the impedance Z, denoted as Z_{im}, instead of the real part denoted as Z_{re}, since the imaginary part shows more structure than the real part. The imaginary part of Z is then expressed in the following form:

$$Z_{im}(z) = -(R_0 / 2)\int_{-\infty}^{\infty} G_z(s)\sec h(z-s)ds \tag{2.190}$$

The deconvolution process is basically complicated, but using modern computer techniques, calculating $G_z(s)$ and $g_z(\tau)$ is quite easy [8].

2.6.5 Applications

EIS has proven to be a useful technique for the analysis of electrochemical systems, such as corrosion systems and batteries. In comparison with DC electrochemical techniques, EIS has tremendous advantages, as it can provide a wealth of information about the system being studied. Also, due to the small perturbation in the AC signal, the electrode response is in a linear potential region, causing no destructive damage to the electrode. Therefore, EIS can be used to evaluate the time relation of interface parameters.

EIS thus has been demonstrated to be a powerful technique for investigating the electrical properties of materials, including gaseous, liquid, and solid materials, and the interfaces of conducting electrodes in different research areas. Miscellaneous applications of EIS are listed below:

- Mechanisms, such as reaction mechanisms, electrode kinetics, state of charge, change of active surface area
- Processes, such as complicated corrosion, crystallization, sintering, transport through membranes
- Interfaces, including blocked interfaces, liquid/liquid interfaces, electrode/solid electrolyte interfaces, etc.

In recent decades, research has intensified to develop commercially viable fuel cells as a cleaner, more efficient source of energy, due to the global shortage of fossil fuels. The challenge is to achieve a cell lifetime suitable for transportation and stationary applications. Among the possible fuel cell types, it is generally believed that PEM fuel cells hold the most promise for these uses [10, 11]. In order to improve fuel cell performance and lifetime, a suitable technique is needed to examine PEM fuel cell operation. EIS has also proven to be a powerful technique for studying the fundamental components and processes in fuel cells [12], and is now widely applied to the study of PEM fuel cells as well as direct methanol fuel cells (DMFCs), solid oxide fuel cell (SOFCs), and molten carbonate fuel cells (MCFCs).

2.7 Chapter Summary

This chapter has provided basic electrical fundamentals, including concepts and definitions for circuit elements, and their relationships within electric circuits. Various basic AC electric circuits were also presented. Following upon primary circuit theories, the concept of electrochemical impedance spectroscopy and basic information about EIS was introduced. This chapter lays a foundation for readers to expand their study of EIS and its applications in PEM fuel cell research and development.

References

1. Johnson DE, Johnson JR, Hilburn JL (1992) Electric circuit analysis. 2nd edn. Prentice-Hall, Englewood Cliffs, NJ
2. Hubert CI (1982) Electric circuits AC/DC: an integrated approach. McGraw-Hill, New York
3. Wikipedia (2009) Short circuit. http://en.wikipedia.org/wiki/Short_circuit. Accessed 4 May 2009
4. Meadows RG (1972) Electric network analysis. Athlone Press, University of London
5. Boukamp BA (2004) Impedance spectroscopy, strength and limitations. Technisches Messen 71(9):454–9
6. Boukamp BA (2004) Electrochemical impedance spectroscopy in solid state ionics: recent advances. Solid State Ionics 169(1–4):65–73
7. Raistrick ID (1986) Application of impedance spectroscopy to materials science. Ann Rev Mater Sci 16:343–70
8. Barsoukov E, Macdonald JR (2005) Impedance spectroscopy theory, experiment, and applications. 2nd edn. John Wiley & Sons, Hoboken, NJ
9. Research Solutions & Resources (2008) Fitting EIS data to equivalent circuits. http://www.consultrsr.com/resources/eis/eiscrkts.htm. Accessed 1 December 2008
10. Healy J, Hayden C, Xie T, Olson K, Waldo R, Brundage M, et al. (2005) Aspects of the chemical degradation of PFSA ionomers used in PEM fuel cells. Fuel cells 5(2):302–8
11. Knights SD, Colbow KM, St-Pierre J, Wilkinson DP (2004) Aging mechanisms and lifetime of PEFC and DMFC. J Power Sources 127(1–2):127–34
12. Li G, Pickup PG (2003) Ionic conductivity of PEMFC electrodes: effect of Nafion loading. J Electrochem Soc (11):C745–52

3

Impedance and its Corresponding Electrochemical Processes

When we begin to investigate an electrochemical system, we normally know little about the processes or mechanisms within the system. Electrochemical impedance spectroscopy (EIS) can be a powerful approach to help us establish a hypothesis using equivalent circuit models. A data-fitted equivalent circuit model will suggest valuable chemical processes or mechanisms for the electrochemical system being studied. From Chapter 1, we know that a fuel cell is actually an electrochemical system involving electrode/electrolyte interfaces, electrode reactions, as well as mass transfer processes. Therefore, EIS can also be a powerful tool to diagnose fuel cell properties and performance.

The purpose of this chapter is to provide background information on electrochemical interfaces and on the relationship between impedance spectra and interfaces in electrochemical systems, including fuel cells. Two major references for some sections of this chapter are [1] and [2].

3.1 Electrode/Electrolyte Interfaces

3.1.1 Introduction

As Schmickler states [3], "Electrochemistry is the study of structures and processes at the interface between an electronic conductor (the electrode) and an ionic conductor (the electrolyte) or at the interface between two electrolytes". The electrode/electrolyte or electrolyte/electrolyte interface is the region whose properties differ from the two adjoining phases, and/or the place where reactant adsorption and electrochemical reactions occur. Commonly, it is recognized as the interface between an electronic conductor (e.g., metals and semiconductors) and an ionic conductor (e.g., electrolyte solutions, molten salts, and solid electrolytes), known as an electrochemical interface. In a narrow region of an electrode/electrolyte interface, an electrical double layer (EDL) exists. The EDL is believed to be extremely thin, and is an important component of the interface.

Fuel cell researchers deal primarily with interfaces between solid electrolyte materials and solid metallic electrodes. The characterization of electrochemical systems with solid–solid interfaces has become a major issue in the study of fuel cells. It is generally believed that the interface of a solid electrode and solid electrolyte is similar to the electrode/liquid electrolyte interface but more complicated [4].

Although EIS characterizes many of the electrical properties of materials and their interfaces, to begin with we focus on a typical electrochemical system: a metal–solution interface.

3.1.2 Equivalent Circuit of an Electrode/Electrolyte Interface

Any electrochemical interface (or cell) can be described in terms of an electric circuit, which is a combination of resistances, capacitances, and complex impedances (and inductances, in the case of very high frequencies). If such an electric circuit produces the same response as the electrochemical interface (or cell) does when the same excitation signal is imposed, it is called the equivalent electric circuit of the electrochemical interface (or cell). The equivalent circuit should be as simple as possible to represent the system targeted.

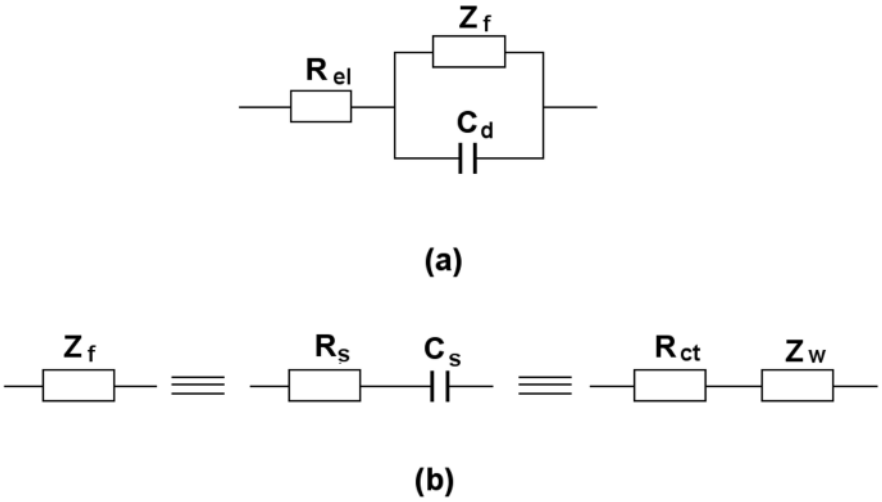

Figure 3.1. *a* Equivalent circuit of an electrochemical cell; *b* subdivision elements of Z_f

Figure 3.1 shows a typical equivalent circuit of an electrochemical cell. R_{el} represents the electrolyte resistance between the working electrode surface and the point of reference electrode; C_d is a pure capacitor of the capacity associated with the double layer of the electrode/electrolyte interface; and Z_f refers to the Faradaic impedance, which corresponds to the impedance of the charge transfer at the electrode/electrolyte interface. The connection of Z_f and C_d in Figure 3.1 is in parallel. The impedance Z_f can be subdivided in two equivalent ways, as seen in Figure 3.1*b*:

1. A resistance, R_s, in series with a pseudo-capacitance, C_s.
2. A charge-transfer resistance, R_{ct}, and an impedance called Warburg impedance, Z_w, which describes the mass transport of the electroactive

species. Thus, for kinetically favoured reactions ($R_{ct} \to 0$), Z_w predominates, whereas for slow reactions ($R_{ct} \to \infty$), R_{ct} predominates.

Figure 3.1 represents only the simplest electrode process occurring at the electrode/electrolyte interface. When more processes are included or more steps are involved in the electrode process, more complicated circuits have to be constructed. Other types of equivalent circuits representing different electrochemical cells, including fuel cells, will be introduced in Chapter 4.

3.1.3 Differences Between Solid State and Aqueous Electrochemistry

In general, hydrogen–oxygen fuel cells use solid electrolytes, unlike conventional electrochemical systems, which use liquid electrolytes. The requirements for a PEM fuel cell electrolyte are chemical and physical stability during operation, low/zero permeability to the fuel gases, and minimal thickness to reduce ohmic loss (while still retaining the necessary mechanical strength). Other functions of the membrane are to keep the fuel and oxidant separated, prevent the fuel and oxidant gases from mixing, and withstand harsh conditions such as high temperatures or temperature fluctuations, strong oxidants, and reactive radicals. Therefore, an ideal polymer must have excellent proton conductivity, high chemical and thermal stability, physical strength, high flexibility, low gas permeability, low water drag, low cost, and good availability [5].

For PEMFCs, the solid electrolytes are *polymer membranes*: polymers modified to include ions, usually sulfonic groups. One of the most widely used membranes today is the polymer Nafion®, created by the DuPont company. These membranes have aliphatic perfluorinated backbones with ether-linked side chains ending in sulfonate cation exchange groups [6, 7]. Nafion® is a copolymer of tetrafluoroethylene and sulfonyl fluoride vinyl ether [8] and has a semi-crystalline structure [9]. This structure (which resembles Teflon®) gives Nafion® long-term stability in oxidative or reductive conditions. The sulfonic groups of the polymers facilitate the transport of protons. The polymers consist of hydrophilic and hydrophobic domains that allow the transport of protons from the anode to the cathode [10, 11].

There are some distinctions between solid and liquid electrolytes [4]

1. Liquid electrolytes have negligible electronic conductivity. However, quite a number of solid electrolytes have electronic conductivity.
3. Solid electrolytes can be amorphous, polycrystalline, or single-crystal.
4. The dissociated charges in a liquid electrolyte or molten salt are mobile.
5. In solid electrolytes, if the steric effect is permitted, the mobile ions are able to move to the electrode.

Thus, capacitative effects in electrode interface regions can be considerably different between solid and liquid electrolyte systems. However, EIS has been successfully applied to both solid and liquid electrolyte systems.

3.2 Faradaic Impedance

Faradic impedance (Z_f) is directly related to the rates of charge transfer reactions at and near the electrode/electrode interface. As shown in Figure 3.1, the Faradaic impedance acts in parallel with the double-layer capacitance C_d, and this combination is in series with the electrolyte resistance R_{el}. The parameters R_{el} and C_d in the equivalent circuit are similar to the idea of electrical elements. However, Z_f is different from those normal electrical elements because Faradaic impedance is not purely resistive. It contains a capacitive contribution, and changes with frequency. Faradaic impedance includes both the finite rate of electron transfer and the transport rate of the electroactive reagent to the electrode surface. It is helpful to subdivide Z_f into R_s and C_s, and then seek their frequency dependencies in order to obtain useful information on the electrochemical reaction.

3.2.1 Calculation of the Faradaic Impedance at the Equilibrium Electrode Potential

At a planar electrode, a sinusoidal perturbation is expressed as

$$I = I_m \sin \omega t \tag{3.1}$$

where I_m is the maximum magnitude of the sinusoidal perturbation wave and ω is the perturbation frequency (rad s^{-1}).

Let us assume that the Faradaic impedance can be expressed as a series combination of R_s and C_s. As a sinusoidal current is forced through the circuit, the total voltage drop (V_f) across the Faradaic impedance is [2]

$$V_f = IR_s + q / C_s \tag{3.2}$$

where q is the charge quantity stored inside the capacitance (C_s).

Since

$$\frac{dq}{dt} = I \tag{3.3}$$

by differentiation, Equation 3.2 becomes

$$\frac{dV_f}{dt} = R_s \frac{dI}{dt} + \frac{I}{C_s} \tag{3.4}$$

Thus,

$$\frac{dV_f}{dt} = (R_s I_m \omega)\cos\omega t + \frac{I_m}{C_s}\sin\omega t \tag{3.5}$$

Considering the charge transfer reaction (Ox + n $e^- \Leftrightarrow$ Rd) with both oxidant (Ox) and reductant (Rd) being soluble, the electrode potential can be expressed as an equilibrium electrode potential plus a sinusoidal voltage perturbation:

$$\varphi = \varphi_e + V_f \tag{3.6}$$

where φ_e is the equilibrium electrode potential. The general relation reflecting the charge transfer process, i.e., $\varphi = f[I, C_O(0,t), C_R(0,t)]$, leads to

$$\frac{d\varphi}{dt} = (\frac{\partial\varphi}{\partial I})\frac{dI}{dt} + [\frac{\partial\varphi}{\partial C_O(0,t)}]\frac{dC_O(0,t)}{dt} + [\frac{\partial\varphi}{\partial C_R(0,t)}]\frac{dC_R(0,t)}{dt} \tag{3.7}$$

where $C_o(0,t)$ and $C_R(0,t)$ are the electrode surface concentration of Ox and Rd, respectively, at time *t*.

As φ_e is a constant, we then have

$$\frac{d\varphi}{dt} = \frac{dV_f}{dt} = (\frac{\partial V_f}{\partial I})\frac{\partial I}{\partial t} + [\frac{\partial V_f}{\partial C_O(0,t)}]\frac{dC_O(0,t)}{dt} + [\frac{\partial V_f}{\partial C_R(0,t)}]\frac{dC_R(0,t)}{dt} \tag{3.8}$$

or

$$\frac{dV_f}{dt} = R_{ct}\frac{dI}{dt} + \beta_O\frac{dC_O(0,t)}{dt} + \beta_R\frac{dC_R(0,t)}{dt} \tag{3.9}$$

where

$$R_{ct} = [\frac{\partial V_f}{\partial I}]_{C_O(0,t),C_R(0,t)} \tag{3.10}$$

$$\beta_O = [\frac{\partial V_f}{\partial C_O(0,t)}]_{I,C_R(0,t)} \tag{3.11}$$

$$\beta_R = [\frac{\partial V_f}{\partial C_R(0,t)}]_{I,C_O(0,t)} \tag{3.12}$$

In order to obtain $\frac{dV_f}{dt}$, we need R_{ct}, β_O, β_R, and the three derivatives. These three derivatives describe the kinetics of the reaction. According to Equation 3.1, $\frac{dI}{dt}$ is obvious:

$$\frac{dI}{dt} = (I_m \omega)\cos \omega t \tag{3.13}$$

The other two derivatives in Equation 3.9 can be derived by taking diffusion into consideration. For a reaction Ox + n $e^- \Leftrightarrow$ Rd, the diffusion of the oxidant and reductant can be expressed as

$$\frac{\partial C_O(x,t)}{\partial t} = D_O \frac{\partial^2 C_O(x,t)}{\partial x^2} \tag{3.14}$$

$$\frac{\partial C_R(x,t)}{\partial t} = D_R \frac{\partial^2 C_R(x,t)}{\partial x^2} \tag{3.15}$$

where D_O and D_R are the diffusion coefficiencies of the reactants Ox and Rd, respectively.

The initial conditions are as follows

$$C_O(x,0) = C_O^* \qquad (t = 0) \tag{3.16}$$

$$C_R(x,0) = 0 \qquad (t = 0) \tag{3.17}$$

where C_O^* is the initial concentration or bulk concentration of the oxidant.

The boundary conditions can be written as

$$C_O(x,t) = C_O^* \qquad (t > 0, x \to \infty) \tag{3.18}$$

$$C_R(x,t) = 0 \qquad (t > 0, x \to \infty) \tag{3.19}$$

Assuming the reaction is under current control:

$$D_O[\frac{\partial C_O(x,t)}{\partial x}]_{x=0} = \frac{I(t)}{nFA} \tag{3.20}$$

where A is the reaction area, n is the electron number of the reaction, and F is Faraday's constant.

Based on current balance, we have

$$D_O[\frac{\partial C_O(x,t)}{\partial x}]_{x=0} + D_R[\frac{\partial C_R(x,t)}{\partial x}]_{x=0} = 0 \tag{3.21}$$

Using the Laplace transforms described in Appendix B, we are able to solve the two diffusion equations (3.14) and (3.15) under the given initial conditions (Equations 3.16 and 3.17) and boundary conditions (Equations 3.18 and 3.19). Then we have

$$\overline{C}_O(x,s) = \frac{C_O^*}{s} - \frac{\bar{I}(s)}{nFA\sqrt{D_O s}}\exp(-\sqrt{\frac{s}{D_O}}x) \tag{3.22}$$

$$\overline{C}_R(x,s) = \frac{\bar{I}(s)}{nFA\sqrt{D_R s}}\exp(-\sqrt{\frac{s}{D_R}}x) \tag{3.23}$$

where s is the complex argument of the Laplace transform, and by custom, the reducing current is positive.

For a semi-infinite linear diffusion, we assume

$$C_R(0,t) = C_R^* \tag{3.24}$$

where C_R^* is the initial concentration or bulk concentration of the reductant.

Setting $x = 0$ in Equations 3.22 and 3.23, we obtain (assuming that the oxidizing current is positive in order to be consistent with circuit analysis)

$$\overline{C}_O(0,s) = \frac{C_O^*}{s} + \frac{\bar{I}(s)}{nFA\sqrt{D_O s}} \tag{3.25}$$

$$\overline{C}_R(0,s) = \frac{C_R^*}{s} - \frac{\bar{I}(s)}{nFA\sqrt{D_R s}} \tag{3.26}$$

Then, inverse Laplace transformation using convolution, as introduced in Appendix B, gives

$$C_O(0,t) = C_O^* + \frac{1}{nFA\sqrt{\pi D_O}}\int_0^t \frac{I(t-\tau)}{\sqrt{\tau}}d\tau \tag{3.27}$$

$$C_R(0,t) = C_R^* - \frac{1}{nFA\sqrt{\pi D_R}}\int_0^t \frac{I(t-\tau)}{\sqrt{\tau}}d\tau \tag{3.28}$$

For Equation 3.1, if t is replaced with $t-\tau$, we will have

$$I(t-\tau) = I_m \sin[\omega(t-\tau)] = I_m(\sin\omega t\cos\omega\tau - \cos\omega t\sin\omega\tau) \tag{3.29}$$

Note that AC impedance is a steady-state method. The response signals are measured until the system reaches the steady state. Thus, the integrals in Equations 3.27 and 3.28 can be calculated as

$$\lim_{t\to\infty}\int_0^t \frac{I(t-\tau)}{\sqrt{\tau}}d\tau = I_m \sin\omega t\int_0^\infty \frac{\cos\omega\tau}{\sqrt{\tau}}d\tau \tag{3.30}$$

$$-I_m\cos\omega t\int_0^\infty \frac{\sin\omega\tau}{\sqrt{\tau}}d\tau$$

Using mathematical transformations

$$\int_0^\infty t^{x-1}\cos t dt = \cos(\frac{\pi x}{2})\Gamma(x) \qquad x>0 \tag{3.31}$$

$$\int_0^\infty t^{x-1}\sin t dt = \sin(\frac{\pi x}{2})\Gamma(x) \qquad x>0 \tag{3.32}$$

where $\Gamma(x)$ is the gamma function

$$\Gamma(x) = \int_0^\infty t^{x-1}e^{-t}dt \tag{3.33}$$

we obtain

$$\int_0^\infty \frac{\cos\omega\tau}{\sqrt{\tau}}d\tau = \frac{1}{\sqrt{\omega}}\int_0^\infty (\omega\tau)^{(\frac{1}{2}-1)}\cos\omega\tau d(\omega\tau) \tag{3.34}$$

$$= \frac{1}{\sqrt{\omega}}\cos(\frac{\pi}{2}\cdot\frac{1}{2})\Gamma(\frac{1}{2})$$

$$= \frac{1}{\sqrt{\omega}} \cdot \frac{1}{2} \cdot \sqrt{\pi} = \sqrt{\frac{\pi}{2\omega}}$$

Similarly, we have

$$\int_0^\infty \frac{\sin \omega\tau}{\sqrt{\tau}} d\tau = \sqrt{\frac{\pi}{2\omega}} \tag{3.35}$$

Substituting Equations 3.34 and 3.35 into Equation 3.30, we obtain

$$\lim_{t\to\infty} \int_0^t \frac{I(t-\tau)}{\sqrt{\tau}} d\tau = I_m \sin \omega t \sqrt{\frac{\pi}{2\omega}} - I_m \cos \omega t \sqrt{\frac{\pi}{2\omega}} \tag{3.36}$$

Consequently, Equations 3.27 and 3.28 become

$$C_O(0,t) = C_O^* + \frac{1}{nFA\sqrt{2\omega D_O}} (\sin \omega t - \cos \omega t) \tag{3.37}$$

$$C_R(0,t) = C_R^* + \frac{1}{nFA\sqrt{2\omega D_R}} (\sin \omega t - \cos \omega t) \tag{3.38}$$

Thus,

$$\frac{dC_O(0,t)}{dt} = \frac{I_m}{nFA} \sqrt{\frac{\omega}{2D_O}} (\cos \omega t + \sin \omega t) \tag{3.39}$$

$$\frac{dC_R(0,t)}{dt} = -\frac{I_m}{nFA} \sqrt{\frac{\omega}{2D_R}} (\cos \omega t + \sin \omega t) \tag{3.40}$$

Substituting Equations 3.13, 3.39, and 3.40 into Equation 3.9, we then obtain

$$\frac{dV_f}{dt} = (R_{ct} + \frac{\sigma}{\sqrt{\omega}}) I_m \omega \cos \omega t + I_m \sigma \sqrt{\omega} \sin \omega t \tag{3.41}$$

where

$$\sigma = \frac{1}{nFA\sqrt{2}} (\frac{\beta_O}{\sqrt{D_O}} - \frac{\beta_R}{\sqrt{D_R}}) \tag{3.42}$$

Finally, it is easy to identify the subdivision of Faradaic impedance by comparing Equation 3.41 with Equation 3.4:

$$R_s = R_{ct} + \frac{\sigma}{\sqrt{\omega}} \tag{3.43}$$

$$C_s = \frac{1}{\sigma\sqrt{\omega}} \tag{3.44}$$

Thus, the total Faraday impedance can be expressed as

$$Z_f = R_{ct} + \frac{\sigma}{\sqrt{\omega}} - j\frac{\sigma}{\sqrt{\omega}} \tag{3.45}$$

If the impedance Z_f is subdivided into a charge-transfer resistance, R_{ct}, and the Warburg impedance, Z_w, we easily obtain

$$Z_w = \frac{\sigma}{\sqrt{\omega}} - j\frac{\sigma}{\sqrt{\omega}} \tag{3.46}$$

Note that in this chapter we use j instead of i for the imaginary unit of the complex in order to distinguish j from the current density i.

3.2.2 Kinetic Parameters from Z_f

Equation 3.45 contains the parameters R_{ct}, β_0, and β_R. In order to obtain the kinetic parameters of the electrode reaction, we have to find the relationship between these three parameters and the kinetic parameters.

According to a well-known current density/overpotential relationship in electrochemistry, we have

$$i = i_0\left\{\frac{C_O(0,t)}{C_O^*}\exp(-\alpha nf\eta) - \frac{C_R(0,t)}{C_R^*}\exp[(1-\alpha)nf\eta]\right\} \tag{3.47}$$

where

i = the current density (A/cm^2)
η = the overpotential (V)
i_0 = the exchange current density (A/cm^2)
n = the electron transfer number of the reaction
α = the transfer coefficient

Here we define

$$f = \frac{F}{RT} \tag{3.48}$$

where

R = the universal gas constant (8.314 J/mol· K)

T = the temperature (K)

F = the Faraday constant (96485 C/mol)

The value of α is theoretically between 0 and 1, and most typically for the reactions on a metallic surface it is around 0.5. The relationship between the reduction coefficient, α_R, and the oxidation coefficient, α_O, is as follows:

$$\alpha_R + \alpha_O = 1 \tag{3.49}$$

In Equation 3.47 it is customarily assumed that the cathode current is positive. In order to be consistent with circuit analysis we now assume that the oxidation current is positive. Then we can write

$$-\frac{i}{i_0} = \left\{ \frac{C_O(0,t)}{C_O^*} \exp(-\alpha n f \eta) - \frac{C_R(0,t)}{C_R^*} \exp[(1-\alpha) n f \eta] \right\} \tag{3.50}$$

When the electrolyte concentration at the electrode surface is close to the bulk concentration of the solution, i.e., $C_O(0,t) = C_O^*$ and $C_R(0,t) = C_R^*$, Equation 3.47 can be simplified to

$$-\frac{i}{i_0} = \{\exp(-\alpha n f \eta) - \exp[(1-\alpha) n f \eta]\} \tag{3.51}$$

This is the so-called Butler–Volmer equation.

As the sinusoidal perturbation is very small, the electrode reaction performs near equilibrium, thus,

$$\exp(-\alpha n f \eta) \approx 1 - \alpha n f \eta \tag{3.52}$$

$$\exp[(1-\alpha) n f \eta] \approx 1 + (1-\alpha) n f \eta \tag{3.53}$$

Substituting Equation 3.50 with Equations 3.52 and 3.53, we obtain the expression

$$-\frac{i}{i_0} = \left\{ \frac{C_O(0,t)}{C_O^*} - \frac{C_R(0,t)}{C_R^*} - \alpha n f \eta \frac{C_O(0,t)}{C_O^*} - (1-\alpha) n f \eta \frac{C_R(0,t)}{C_R^*}] \right\} \tag{3.54}$$

In the meantime, the concentrations of Ox and Rd at the electrode surface are also close to the bulk concentration, i.e.,

$$\frac{C_O(0,t)}{C_O^*} \approx 1 \tag{3.55}$$

$$\frac{C_R(0,t)}{C_R^*} \approx 1 \tag{3.56}$$

Then,

$$\alpha nf\eta \frac{C_O(0,t)}{C_O^*} \approx \alpha nf\eta \tag{3.57}$$

$$(1-\alpha)nf\eta \frac{C_R(0,t)}{C_R^*} \approx (1-\alpha)nf\eta \tag{3.58}$$

Substitution of Equations 3.57 and 3.58 into Equation 3.54 yields

$$-\frac{i}{i_0} = \left\{ \frac{C_O(0,t)}{C_O^*} - \frac{C_R(0,t)}{C_R^*} - nf\eta \right\} \tag{3.59}$$

Hence,

$$\eta = \varphi - \varphi_e = \frac{RT}{nF}\left[\frac{C_O(0,t)}{C_O^*} - \frac{C_R(0,t)}{C_R^*} + \frac{i}{i_0}\right] \tag{3.60}$$

Then, we can write

$$R_{ct} = \frac{\partial \varphi}{\partial i} = \frac{\partial \eta}{\partial i} = \frac{RT}{nFi_0} \tag{3.61}$$

$$\beta_O = \frac{\partial \varphi}{\partial C_O(0,t)} = \frac{\partial \eta}{\partial C_O(0,t)} = \frac{RT}{nFC_O^*} \tag{3.62}$$

$$\beta_R = \frac{\partial \varphi}{\partial C_R(0,t)} = \frac{\partial \eta}{\partial C_R(0,t)} = -\frac{RT}{nFC_R^*} \tag{3.63}$$

Substitution of Equations 3.62 and 3.63 into Equation 3.42 gives

$$\sigma = \frac{RT}{\sqrt{2}(nF)^2 A}\left[\frac{1}{\sqrt{D_O}C_O^*} + \frac{1}{\sqrt{D_R}C_R^*}\right] \tag{3.64}$$

As we can see, Equations 3.61 and 3.64 connect the Faradaic impedance, Z_f, with the kinetic parameter, i_0, and the diffusion coefficients, D_O and D_R. If the series values of R_s and $1/\omega C_s$ are measured at different frequencies, by plotting R_s versus $1/\sqrt{\omega}$ and $1/\omega C_s$ versus $1/\sqrt{\omega}$, one can obtain two straight lines, as shown in Figure 3.2. The slopes of the straight lines are σ, and the intercept of R_s at the y-axis is R_{ct}. According to Equation 3.61, the exchange current density is therefore obtained:

$$i_0 = \frac{RT}{nFR_{ct}} \tag{3.65}$$

The information on D_O and D_R can be obtained from the slope.

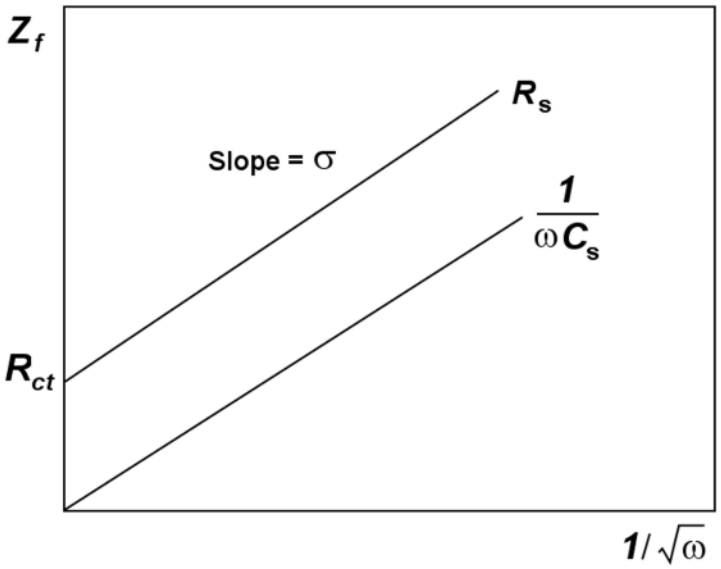

Figure 3.2. Frequency dependence of Faradaic impedance

3.2.3 Vectorgraphs of Faradaic Impedance

According to the complex expression of Z_f and Z_w in Equations 3.45 and 3.46, it is easy to draw their vectorgraphs in the complex plane:

$$tg\theta_w = \frac{\sigma/\sqrt{\omega}}{\sigma/\sqrt{\omega}} = 1 \tag{3.66}$$

$$\theta_w = \pi/4 \tag{3.67}$$

$$tg\theta_f = \frac{\sigma/\sqrt{\omega}}{\sigma/\sqrt{\omega} + R_{ct}} \tag{3.68}$$

$$\theta_f = arctg\frac{\sigma/\sqrt{\omega}}{\sigma/\sqrt{\omega} + R_{ct}} < \pi/4 \tag{3.69}$$

where θ_w and θ_f are the phase angles of Z_w and Z_f, respectively. If the electrode reaction has a large exchange current density, according to Equation 3.61 we have $R_{ct} \approx 0$. Thus, we obtain $Z_w = Z_f$ and $\theta_f = \pi/4$. Conversely, if the exchange current density is very small, the θ_f is also small. Therefore, based on the vectorgraph of the Faradaic impedance, as shown in Figure 3.3, one can roughly estimate the reversibility of the electrode reaction and the reaction rate.

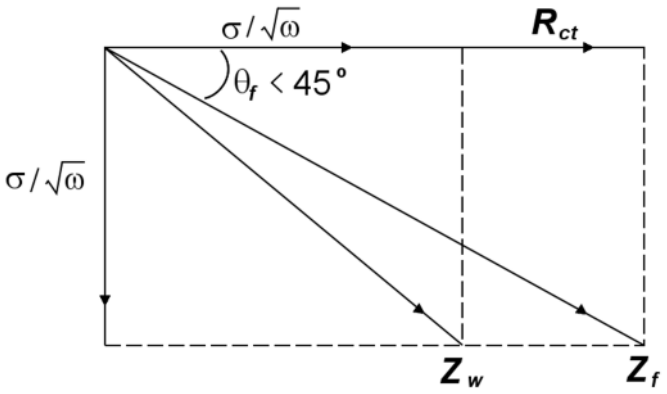

Figure 3.3. Vectorgraph of Faradaic impedance

3.3 Total Impedance of an Electrochemical System

3.3.1 Calculated Z_f Based on Experimental Measurements

We have discussed in the above sections Faradaic impedance and the correlation between Faradaic impedance and kinetic parameters. In general, one desires to separate the Faradaic impedance from R_{el} and C_d. Now we will focus on the extraction of Z_f and the kinetic parameters from direct impedance measurements. This is based on the transformation between equivalent circuits in series and equivalent circuits in parallel.

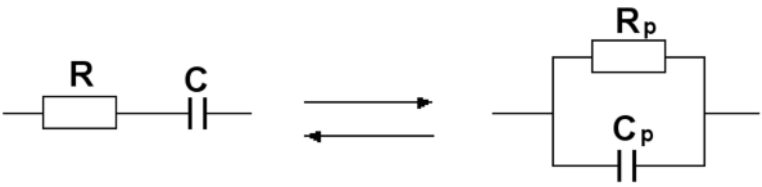

Figure 3.4. Transformation of equivalent circuit from series to parallel or from parallel to series

Figure 3.4 includes an RC circuit in series. We hope that there is an R_PC_P circuit in parallel that has the same impedance as the RC circuit in series. For the parallel circuit, we can write

$$\frac{1}{Z} = \frac{1}{R_P} + j\omega C_P \tag{3.70}$$

For the series, we have

$$Z = R - j\frac{1}{\omega C} \tag{3.71}$$

The reciprocal of Equation 3.71 yields

$$\frac{1}{Z} = \frac{\omega C}{\omega RC - j} = \frac{\omega C(\omega RC + j)}{(\omega RC)^2 + 1} \tag{3.72}$$

Assuming $W \equiv (\omega RC)^2$, Equation 3.72 becomes

$$\frac{1}{Z} = \frac{W/R}{W+1} + \frac{j\omega C}{W+1} \tag{3.73}$$

Comparing the real and imaginary parts in Equations 3.70 and 3.73, we obtain

$$R_P = R(\frac{W+1}{W}) \tag{3.74}$$

$$C_P = \frac{C}{W+1} \tag{3.75}$$

and vice versa, if there is an R_PC_P circuit in parallel we want to have an RC circuit in series that has the same impedance as the R_PC_P circuit in parallel. The transform result is

$$R = \frac{R_P}{W_P+1} \tag{3.76}$$

$$C = (\frac{W_P+1}{W_P})C_P \tag{3.77}$$

where $W_P \equiv (\omega R_P C_P)^2$.

Based on these transform results, it is possible to extract the Faradaic parameters from resistance (R_B) and capacitance (C_B) measured using EIS. The solutions are depicted in Figure 3.5.

(a) As R_{el} is an element in series, we can subtract R_{el} from R_B, and the remainder contains the Faradaic parameters of $R_B^{'}$ and a double-layer capacity of C_B. $R_B^{'}$ can be expressed as

$$R_B^{'} = R_B - R_{el} \tag{3.78}$$

(b) According to the above transform results, it is easy to transform this $R_B^{'}$ C_B series circuit into an R_PC_P parallel circuit. The R_P and C_P obtained can be expressed as Equations 3.79 and 3.80, respectively:

$$R_P = R_B^{'}(\frac{W'+1}{W'}) \tag{3.79}$$

$$C_P = \frac{C_B}{W'+1} \tag{3.80}$$

where $W' \equiv (\omega R_B^{'} C_B)^2$. The capacitance element C_P represents the combination of C_d and a Faradaic capacitance in parallel. Subtracting C_d from C_P yields

$$C_P^{'} = C_P - C_d \tag{3.81}$$

(c) It is clear that $R_P C_P^{'}$ in parallel is equivalent to pure Faradaic impedance. According to the transform Equations 3.76 and 3.77, we can rewrite $R_P C_P^{'}$ in parallel to $R_s C_s$ in series:

$$R_S = \frac{R_P}{W_P^{'} + 1} \tag{3.82}$$

$$C_S = (\frac{W_P^{'} + 1}{W_P^{'}})C_P^{'} \tag{3.83}$$

where $W_P^{'} \equiv (\omega R_P C_P^{'})^2$.

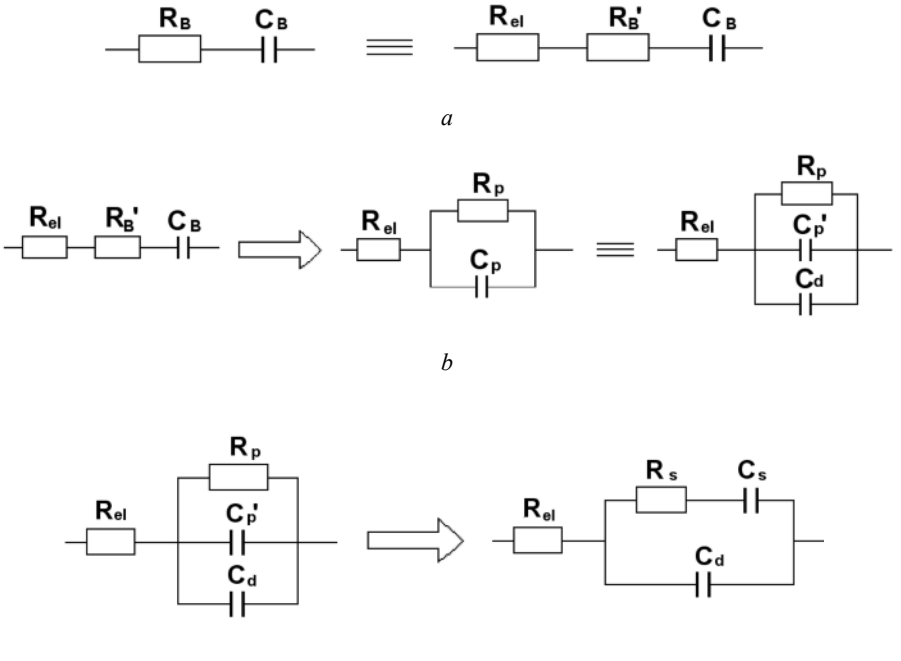

Figure 3.5. The procedure for calculating R_s and C_s from experimental measurements of R_B and C_B

3.3.2 Graphic Presentations of the Total Impedance

As stated in Section 3.3.1, the total measured impedance of the system, Z, is expressed as the series combination of R_B and C_B. These two elements provide the real and imaginary components of Z, i.e., $Z_{re} = R_B$, and $Z_{im} = 1/\omega C_B$. As discussed in Section 3.1.2, the electrochemical system can be described in terms of an equivalent circuit, as shown in Figure 3.1. The Faradaic impedance can be expressed as

$$Z_f = R_S - j\frac{1}{\omega C_S} \tag{3.84}$$

The total impedance is written as

$$Z = R_{el} + \frac{1}{(1/Z_f) + j\omega C_d} = R_{el} + \frac{Z_f}{1 + j\omega C_d Z_f} \tag{3.85}$$

Substituting Equation 3.85 with Equation 3.84, we obtain

$$Z = R_{el} + \frac{R_s - j(1/\omega C_s)}{[1 + (C_d / C_s)] + j\omega C_d R_s} \tag{3.86}$$

Then we have

$$Z = R_{el} + \frac{R_S - j[\frac{1}{\omega C_S}(1 + \frac{C_d}{C_S}) + \omega C_d R_s^2]}{(1 + \frac{C_d}{C_S})^2 + (\omega C_d R_S)^2} \tag{3.87}$$

The real part of the total impedance is

$$Z_{re} = R_B = R_{el} + \frac{R_S}{A^2 + B^2} \tag{3.88}$$

where $A = 1 + (C_d / C_S)$ and $B = \omega C_d R_S$.

The imaginary part of the total impedance is

$$Z_{im} = \frac{1}{\omega C_B} = \frac{A/\omega C_S + B^2/\omega C_d}{A^2 + B^2} \tag{3.89}$$

Substitution of R_s and C_s using Equations 3.43 and 3.44 yields

$$Z_{re} = R_{el} + \frac{R_{ct} + \sigma/\sqrt{\omega}}{(C_d \sigma\sqrt{\omega} + 1)^2 + \omega^2 C_d^2 (R_{ct} + \sigma/\sqrt{\omega})^2} \tag{3.90}$$

$$Z_{im} = \frac{\omega C_d (R_{ct} + \sigma/\sqrt{\omega})^2 + \sigma/\sqrt{\omega}(\sqrt{\omega} C_d \sigma + 1)}{(C_d \sigma\sqrt{\omega} + 1)^2 + \omega^2 C_d^2 (R_{ct} + \sigma/\sqrt{\omega})^2} \tag{3.91}$$

Note that both the real part and the imaginary part change with frequency. Kinetic parameters can be extracted by plotting Z_{im} versus Z_{re} as a function of frequency (ω). Although Equations 3.90 and 3.91 look very complicated, they can be simplified at high and low frequencies. Now let us consider the behaviour for both cases.

3.3.2.1 Low-Frequency Limit

At very low frequencies ($\omega \to 0$), the limiting forms of Equations 3.90 and 3.91 become

$$Z_{re} = R_{el} + R_{ct} + \sigma/\sqrt{\omega} \tag{3.92}$$

$$Z_{im} = \sigma/\sqrt{\omega} + 2C_d\sigma^2 \tag{3.93}$$

Elimination of ω from these two equations yields

$$Z_{im} = Z_{re} - R_{el} - R_{ct} + 2C_d\sigma^2 \tag{3.94}$$

Thus, a plot of Z_{im} versus Z_{re} should be a straight line with a unit slope, as shown in Figure 3.6, and the extrapolated line intersects the real axis at $R_{el} + R_{ct} - 2C_d\sigma^2$. From Equations 3.92 and 3.93, we can see that the frequency dependence at low frequencies comes from Warburg impedance terms; hence, the linear correlation of Z_{im} versus Z_{re} features a diffusion-controlled electrode process. As the frequency rises, the presupposition for Equation 3.94 will not exist. The linear correlation will deviate with increasing frequencies.

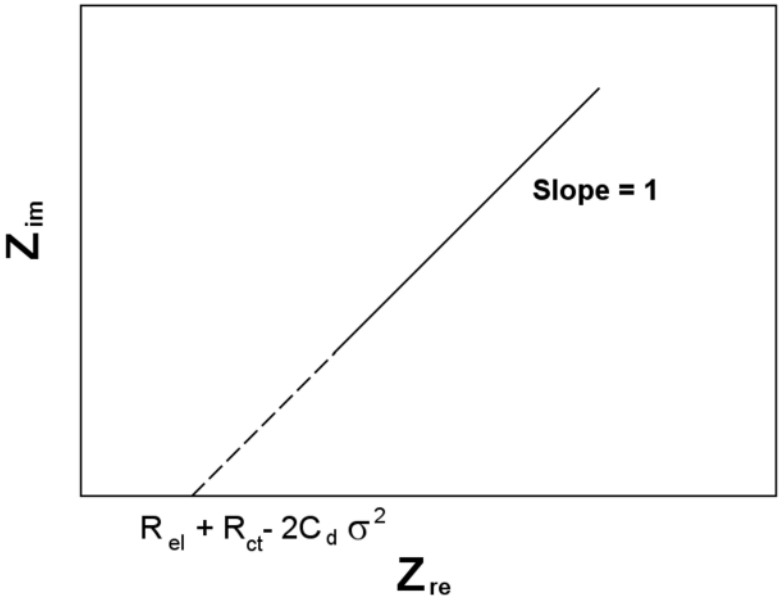

Figure 3.6. Complex plane graph of the total impedance at low frequencies

3.3.2.2 High-Frequency Limit
At very high frequencies ($\omega \to \infty$), from Equation 3.45 we have

$$Z_f = R_{ct} \tag{3.95}$$

In addition, at high frequencies, according to Equations 3.90 and 3.91 we can easily obtain

$$Z_{re} = R_{el} + \frac{R_{ct}}{1+\omega^2 C_d^2 R_{ct}^{\ 2}} \tag{3.96}$$

$$Z_{im} = \frac{\omega C_d R_{ct}^{\ 2}}{1+\omega^2 C_d^2 R_{ct}^{\ 2}} \tag{3.97}$$

Elimination of ω from these two equations gives an equation commonly used in EIS:

$$(Z_{re} - R_{el} - \frac{R_{ct}}{2})^2 + Z_{im}^{\ 2} = (\frac{R_{ct}}{2})^2 \tag{3.98}$$

Hence, Z_{im} versus Z_{re} should be a circular plot centred at $(R_{el} + \frac{R_{ct}}{2}, 0)$ with a radius of $\frac{R_{ct}}{2}$.

This result is presented in Figure 3.7, where the origin of Z_{re} is the double-layer capacitor C_d. When $\omega \to \infty$, the contribution of C_d to the total impedance is close to zero. Therefore, the total impedance becomes R_{el}, as presented by the left intersection of the semicircle and the real axis. As ω decreases, Z_{re} increases. When ω further decreases, C_d becomes very large, resulting in a total impedance of R_{el} + R_{ct}, as presented by the right intersection of the semicircle and the real axis. If ω decreases to an extremely low value, i.e., $\omega \to 0$, the plot becomes the 45° straight line as described in Figure 3.6.

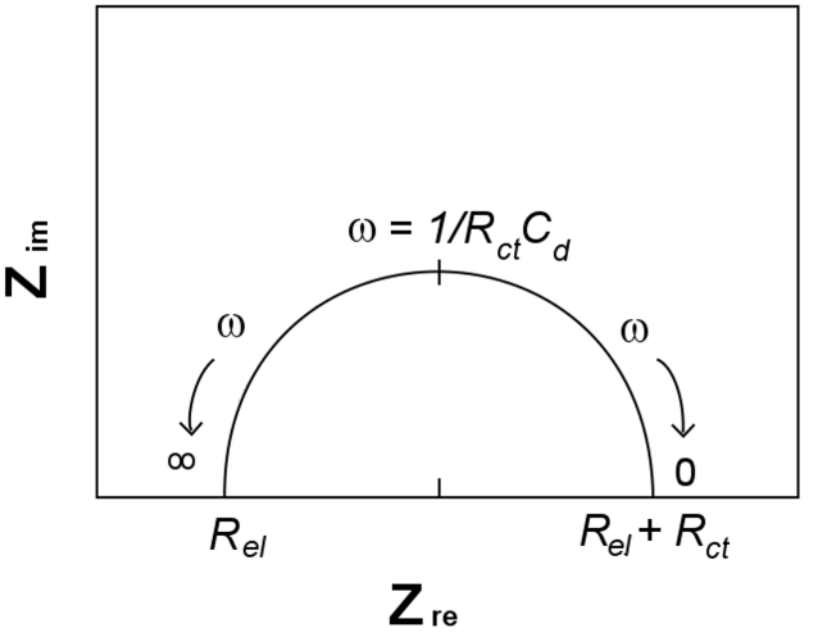

Figure 3.7. Complex plane graph of the total impedance at high frequencies

From the mathematical point of view, if $\omega \to \infty$, then $Z_{re} \to R_{el}$; and if $\omega \to 0$ or $\omega \to \infty$, $Z_{im} \to 0$. Based on Figure 3.7, we can now discuss the change in Z_{im} as ω changes between 0 and ∞, using the following two equations:

$$Z_{im}(\omega) = \frac{\omega C_d {R_{ct}}^2}{1 + \omega^2 C_d^2 {R_{ct}}^2} \tag{3.99}$$

$$\frac{dZ_{im}(\omega)}{d\omega} = R_{ct}^2 C_d \frac{1-(R_{ct}C_d\omega)^2}{[(R_{ct}C_d\omega)^2+1]^2} \tag{3.100}$$

1. If $\omega < 1/(R_{ct}C_d)$, $\frac{dZ_{im}(\omega)}{d\omega} > 0$, $Z_{im}(\omega)$ is an increasing function, i.e., $Z_{im}(\omega)$ increases with increasing ω. This is the right half of the figure.
2. If $\omega = 1/(R_{ct}C_d)$, $\frac{dZ_{im}(\omega)}{d\omega} = 0$, $Z_{im}(\omega)$ has a maximum value of $R_{ct}/2$. This is the peak point of the semicircle.
3. If $\omega > 1/(R_{ct}C_d)$, $\frac{dZ_{im}(\omega)}{d\omega} < 0$, $Z_{im}(\omega)$ is a decreasing function, i.e., $Z_{im}(\omega)$ decreases with increasing ω. This is the left half of the figure.

According to the above analysis, from the semicircle of the impedance measured, one can obtain R_{el}, R_{ct}, and C_d. The interception of the semicircle at $\omega \to \infty$ is R_{el}; the diameter of the semicircle provides R_{ct}; and then by assuming $\frac{dZ_{im}(\omega)}{d\omega} = 0$, C_d can be calculated based on the peak value of the frequency, ω_c (also known as the characteristic frequency):

$$C_d = 1/(R_{ct}\omega_c) \tag{3.101}$$

3.3.3 Impedance Plots of Real Electrochemical Systems Using the Complex Plane

The impedance plot of a real electrochemical system in the complex plane contains both low-frequency and high-frequency portions, as shown in Figure 3.8. In some cases, both features may not be well distinguished. The charge-transfer resistance, R_{ct}, and its relationship to the Warburg impedance, Z_w, will determine the shape of the plot. If the electrochemical system is kinetically sluggish, R_{ct} will be significantly large and the mass transfer feature may not be clearly visible. If the electrochemical reaction is extremely fast, R_{ct} should be very small compared with the ohmic resistance and the Warburg impedance. Thus, mass transfer will play an important role and the semicircular region may not be visible.

In actuality, many electrode processes are more complex than the ones discussed above. For example, Figure 3.9 shows three typical cases controlled by diffusion processes:

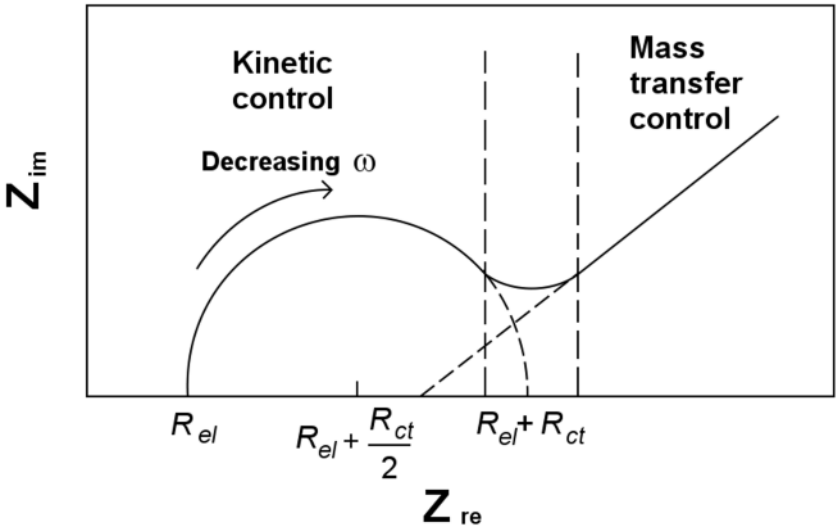

Figure 3.8. Impedance plots of real electrochemical systems in the complex plane

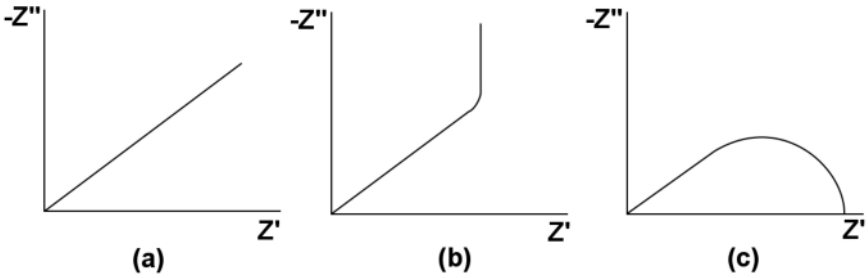

Figure 3.9. Variation of impedance for diffusive systems: *a* semi-infinite diffusion; *b* reflective finite diffusion; *c* transmissive finite diffusion

(a) Semi-infinite diffusion: the impedance is a straight line with a slope of π/4 in the complex plane. This is the Warburg impedance for semi-infinite diffusion.

(b) Reflective finite diffusion: the impedance terminates in an open circuit, which corresponds to reflection. This diffusion is often observed in conducting polymers or porous electrodes.

(c) Transmissive finite diffusion: the impedance terminates in a large resistance. For example, a blocked interface, such as a metal totally covered with oxide, will display this feature. This is sometimes referred to as the finite or bounded Warburg impedance.

The impedance of an interface also depends on its microscopic structure. For example, a porous electrode complicates the impedance of an interface. Nevertheless, although impedance is sometimes very complicated, impedance measurements are still used extensively to study complicated corrosion phenomena, blocked interfaces, the liquid/liquid interface, transport through

membranes, and the electrode/solid electrolyte interface. More complicated cases will be discussed in Chapters 4 and 5.

3.3.4 Semicircle Rotation of the Impedance

In the study of impedance plots, we may observe the depression of semicircles. This is the so-called semicircle rotation of the impedance. This phenomenon is associated with electrode/electrolyte interface double-layer properties. For example, the rough surface of the electrodes or porous electrodes can result in an uneven distribution of the double-layer electric field. This semicircle rotation can be explained using the equivalent circuit presented in Figure 3.10, where R' is inversely proportional to the frequency ω (and b is a constant).

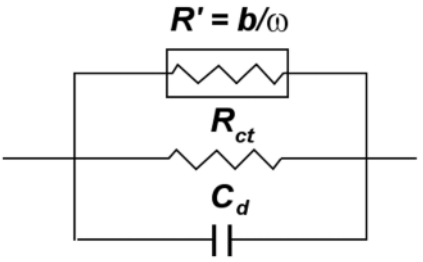

Figure 3.10. Equivalent circuit for explaining the semicircle rotation of the impedance

For the equivalent circuit in Figure 3.10, the total complex admittance Y and complex impedance Z in Cartesian coordinates can be expressed as

$$Y = Y_{re} + jY_{im} = (\frac{\omega}{b} + \frac{1}{R_{ct}}) + j\omega C_d \tag{3.102}$$

$$Z = \frac{1}{Y} \tag{3.103}$$

From Equations 3.102 and 3.103, the real and imaginary parts of the total impedance can be calculated:

$$Z_{re} = \frac{bR_{ct}(\omega R_{ct} + b)}{(\omega R_{ct} + b)^2 + (\omega b R_{ct} C_d)^2} \tag{3.104}$$

$$Z_{im} = \frac{\omega b^2 R_{ct}^2 C_d}{(\omega R_{ct} + b)^2 + (\omega b R_{ct} C_d)^2} \tag{3.105}$$

Then,

$$\frac{Z_{re}}{Z_{im}} = \frac{\omega R_{ct} + b}{\omega R_{ct} b C_d} = \frac{1}{bC_d} + \frac{1}{\omega R_{ct} C_d} \tag{3.106}$$

Thus,

$$\frac{1}{\omega R_{ct} C_d} = \frac{Z_{re}}{Z_{im}} - \frac{1}{bC_d} \tag{3.107}$$

Dividing both denominator and nominator by $(\omega b R_{ct} C_d)^2$, Equation 3.105 becomes

$$Z_{im} = \frac{R_{ct}}{\omega R_{ct} C_d} \cdot \frac{1}{(\frac{\omega R_{ct} + b}{\omega b R_{ct} C_d})^2 + 1} \tag{3.108}$$

Substituting Equations 3.106 and 3.107 into Equation 3.108 provides

$$Z_{im} = R_{ct}(\frac{Z_{re}}{Z_{im}} - \frac{1}{bC_d}) \cdot \frac{1}{(Z_{re}/Z_{im})^2 + 1} \tag{3.109}$$

$$= R_{ct}(Z_{re} - \frac{Z_{im}}{bC_d}) \frac{Z_{im}}{Z_{re}^2 + Z_{rm}^2}$$

Then we can write

$$Z_{re}^2 + Z_{im}^2 = R_{ct} Z_{re} - \frac{R_{ct}}{bC_d} Z_{im} \tag{3.110}$$

Adding $(\frac{R_{ct}}{2})^2 + (\frac{R_{ct}}{2bC_d})^2$ to both sides of the above equation, we obtain

$$(Z_{re} - \frac{R_{ct}}{2})^2 + (Z_{im} + \frac{R_{ct}}{2bC_d})^2 = [\frac{R_{ct}}{2}\sqrt{1 + (\frac{1}{bC_d})^2}\,]^2 \tag{3.111}$$

This is a circular plot centred at $(\frac{R_{ct}}{2}, -\frac{R_{ct}}{2bC_d})$ with a radius of $\frac{R_{ct}}{2bC_d}\sqrt{(bC_d)^2+1}$, as presented in Figure 3.11. The actual impedance is an arc in the first quadrant. Compared with a standard RC circuit in parallel, the centre of the circle shifts down by $\frac{R_{ct}}{2bC_d}$.

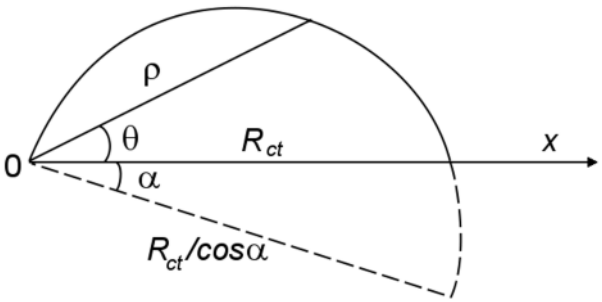

Figure 3.11. Semicircle rotation of the total impedance *Z* in Cartesian coordinates

Now let us calculate the length of the chord using the polar coordinates. The total complex admittance *Y* and complex impedance *Z* in the polar coordinates can be expressed as

$$Y = Y_{re} + jY_{im} = \delta e^{j\theta} \tag{3.112}$$

$$Z = \frac{1}{Y} = \frac{1}{\delta}e^{-j\theta} = \rho e^{-j\theta} \tag{3.113}$$

where δ and ρ are the modulus of the complex admittance *Y* and the complex impedance *Z*, respectively. The polar presentation of complex admittance *Y* is shown in Figure 3.12.

From that figure, we have

$$\delta = \frac{\omega C_d}{\sin\theta} \tag{3.114}$$

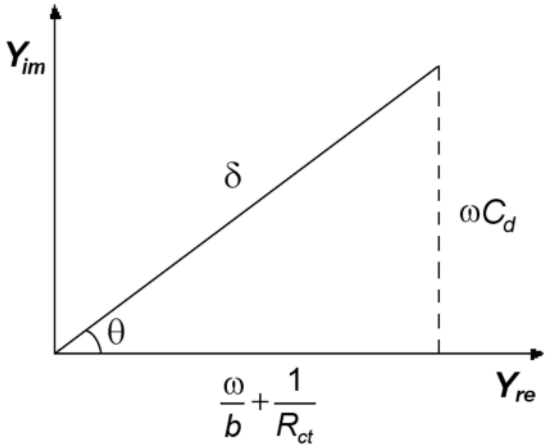

Figure 3.12. Polar presentation of the total complex admittance *Y*

$$tg\theta = \frac{\omega C_d}{\frac{\omega}{b} + \frac{1}{R_{ct}}} = \frac{\omega C_d b R_{ct}}{\omega R_{ct} + b} \tag{3.115}$$

From Equation 3.115, we obtain

$$\omega = \frac{btg\theta}{R_{ct}(bC_d - tg\theta)} \tag{3.116}$$

Substituting Equation 3.116 into Equation 3.114 yields

$$\rho = \frac{1}{\delta} = \frac{\sin\theta}{\omega C_d} = \frac{\sin\theta}{bC_d tg\theta} R_{ct}(bC_d - tg\theta) \tag{3.117}$$

Thus,

$$\rho = R_{ct}(\cos\theta - \frac{1}{bC_d}\sin\theta) \tag{3.118}$$

assuming that

$$tg\alpha = \frac{1}{bC_d} \tag{3.119}$$

Then, we have

$$\rho = R_{ct}(\cos\theta - tg\alpha\sin\theta) = \frac{R_{ct}}{\cos\alpha}(\cos\theta\cos\alpha - \sin\theta\sin\alpha) \quad (3.120)$$

Thus,

$$\rho = \frac{R_{ct}}{\cos\alpha}\cos(\theta + \alpha) \quad (3.121)$$

In the polar coordinates, Equation 3.121 is obviously circular, with a rotation angle of α and a diameter of $R_{ct}/\cos\alpha$. Therefore, it is proved that the length of the chord is R_{ct}, as shown in Figure 3.11, which can be calculated as above.

Now let us consider how to calculate C_d and b. From Equation 3.105, we can write

$$Z_{im}(\omega) = \frac{\omega b^2 R_{ct}^2 C_d}{(\omega R_{ct} + b)^2 + (\omega b R_{ct} C_d)^2} \quad (3.122)$$

Then,

$$\frac{dZ_{im}(\omega)}{d\omega} = \frac{b^2 R_{ct}^2 C_d (b^2 - \omega^2 b^2 R_{ct}^2 C_d^2 - \omega^2 R_{ct}^2)}{[(\omega R_{ct} + b)^2 + (\omega b R_{ct} C_d)^2]^2} \quad (3.123)$$

assuming that

$$\frac{dZ_{im}(\omega)}{d\omega}/_{\omega=\omega_c} = 0 \quad (3.124)$$

where ω_c is the characteristic frequency. Then we have

$$\omega_c^2 R_{ct}^2 (1 + b^2 C_d^2) = b^2 \quad (3.125)$$

$$b^2 = \omega_c^2 R_{ct}^2 (1 + \frac{1}{tg^2\alpha}) = \frac{\omega_c^2 R_{ct}^2}{\sin^2\alpha} \quad (3.126)$$

Thus,

$$b = \frac{\omega_c R_{ct}}{\sin\alpha} \quad (3.127)$$

$$C_d = \frac{\cos\alpha}{\omega_c R_{ct}} \tag{3.128}$$

Knowing ω_c and α, parameters b and C_d can be obtained.

3.4 Correlation of EIS with Other Electrochemical Techniques

Different types of electrochemical techniques are used in PEMFC studies, including polarization curve, AC impedance, and current interruption. It is crucial to choose the right diagnostic technique to find failures and malfunctions, and to model dynamic behaviour. The polarization curve is, nevertheless, the simplest and easiest way of characterizing the fuel cell. EIS is also considered a powerful technique for investigating electrochemical systems, with its ability to distinguish in the frequency domain the individual contributions such as interfacial charge-transfer resistance, and the mass transport resistance in the catalyst layer and backing diffusion layer [12]. It has been proven that different single cells based on similar catalyst and backing layers and operated under similar conditions generate qualitatively similar impedance spectra [13]. The results obtained by EIS must have some correlation with the results from other electrochemical methods.

3.4.1 EIS and the Polarization Curve

The most common method used to characterize the performance of electrochemical systems is to examine current–voltage polarization curves. A polarization curve is the standard electrochemical technique for characterizing performance of fuel cells (both single cells and stacks) [14]. It yields information on the performance losses in the cell or stack under operating conditions. A steady-state polarization curve can be obtained by recording the current as a function of cell voltage or recording the cell voltage as the cell current changes. A non-steady-state polarization curve can be obtained using a rapid current sweep [15]. By measuring polarization curves, we can systematically characterize and compare certain parameters, such as the effects of composition, gas flow rate, temperature, and relative humidity on cell performance.

The typical polarization curve for a single hydrogen/air fuel cell has three major regions, shown in Figure 3.13 [14]. At low current densities (the region of activation polarization), the cell voltage drops sharply and the majority of these losses are due to the sluggish kinetics of the oxygen reduction reaction (ORR). At intermediate current densities (the region of ohmic polarization), the voltage loss caused by ohmic resistance becomes significant. This ohmic loss is mainly caused by ion flow resistance in the electrolyte and electron flow resistance through the electrode [16]. In this region, the cell potential decreases nearly linearly with increasing current density, while the activation polarization reaches a relatively constant value. At high current densities (the region of concentration polarization), gas mass transfer dominates due to the transport limit of the reactant gas through the pore structure of the gas diffusion layers (GDLs) and electrocatalyst layers

(CLs), resulting in a drastic drop in cell performance [17]. Figure 3.13 also shows the difference between the theoretical cell potential (1.23 V) and the thermoneutral voltage (1.4 V), which represents the energy loss under reversible conditions (the reversible loss) [18]. Very often, polarization curves are converted to power density versus current density plots by multiplying the cell voltage by the current density at each point of the curve.

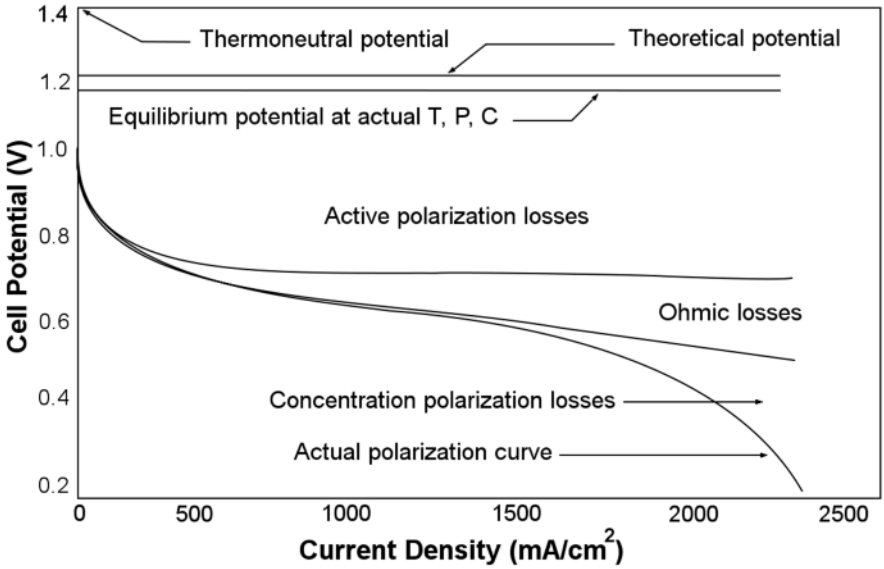

Figure 3.13. Typical polarization curve for a PEMFC [14]. (Modified from Barbir F. PEM fuel cells: theory and practice. New York: Elsevier Academic Press, ©2005, with permission from Elsevier.)

As shown in Figure 3.13, the voltage losses can be analyzed from the polarization curve. Generally, the voltage losses consist of four parts: (1) loss due to gas crossover; this is represented by the open circuit voltage (OCV), which is lower than the thermodynamic voltage; (2) loss due to activation resistance; (3) loss due to ohmic resistance; and (4) loss due to mass transport limitation.

Consequently, the cell voltage of a PEMFC, E_{cell}, can be expressed using the following equation [12]

$$E_{cell} = E_{rev} - \eta_{\text{int}} - \eta_{mix} - \eta_{act} - \eta_{ohm} - \eta_{conc} \tag{3.129}$$

Let us discuss the terms in Equation 3.129 one by one:

1. E_{rev} (reversible cell potential). E_{rev} can be expressed as

$$E_{rev} = 1.229 - 0.85\times10^{-3}(T - 298.15) + 4.3085\times10^{-5}T[\ln(p_{H_2}) + 1/2\ln(p_{O_2})] \quad (3.130)$$

where T, P_{H_2}, and P_{Air} are absolute fuel cell temperature (K), partial pressure of hydrogen (Pa), and partial pressure of air (Pa), respectively. Under standard conditions, E_{rev} equals 1.229 V.

2. η_{int} (internal loss). η_{int} is associated with gas crossover through the membrane. This loss equates to an internal current and remains constant even under open circuit conditions. It does not contribute to the output current or power, and decreases the electron conduction in the membrane.
3. η_{mix} (mixed potential). As discussed in Chapter 1, the mixed potential is composed of both the cathodic O_2/H_2O reaction potential and the Pt/PtO anodic reaction potential. The reported mixed cathode potential is around 1.06 V (versus SHE) at standard conditions (25°C, 1.0 atm) with an O_2 partial pressure dependence of 15 mV/atm [19, 20]. Therefore, the value of $E_{rev} - \eta_{int} - \eta_{mix}$ is what we called open circuit voltage, denoted as E_{OCV}.
4. η_{act} (activation or kinetic loss). η_{act} is associated with the driving force of the electrode reaction. In practice, hydrogen and oxygen must move and attach to the surfaces of the anode and cathode in order to achieve a self-sustaining reaction. This process takes time and limits the current flow.
5. η_{ohm} (ohmic loss). η_{ohm} is mainly caused by proton flow across the membrane and the ionomer inside the catalyst layers. It also includes resistance originating from the non-ideal electrodes and the electrode interconnections.
6. η_{conc} (concentration loss or mass transport loss). η_{conc} is related to the reactant concentration gradients in the gas channels within the catalyst layers. This loss mainly occurs in the high current density range where reactant gas supply becomes the limitation.

The voltage–current curve is a simple and efficient way to evaluate a fuel cell's properties. However, the underlying mechanisms are difficult to analyze by this method because the contributions from different processes overlap. Figure 3.14 shows the percentages of the cell voltage drop caused by membrane, charge transfer, and mass transfer resistances, obtained through EIS measurements [21]. It indicates that at a given current density, the potential loss is the sum of these resistances. At low, medium, and high current density ranges, the dominant processes are kinetic, ohmic, and mass transfer, respectively. For example, the activation loss depends on current density; therefore, it affects the cell voltage not only at low but also at intermediate and high currents, which is not clearly shown from the polarization curve.

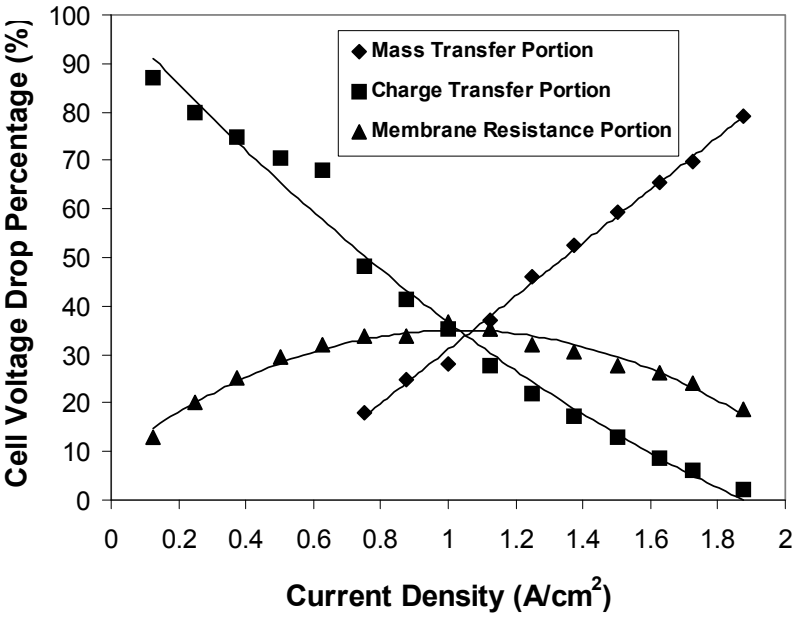

Figure 3.14. Percentage of cell individual voltage drop caused by charger transfer, membrane, and mass transfer resistances at different current densities and 80ºC [21]. (Reproduced by permission of ECS—The Electrochemical Society, from Tang Y, Zhang J, Song C, Liu H, Zhang J, Wang H, Mackinnon S, Peckham T, Li J, McDermid S, Kozak P. Temperature dependent performance and in situ AC impedance of high-temperature PEM fuel cells using the Nafion-112 membrane.)

EIS has the ability to distinguish between influences from different processes, especially when the system involves multiple-step reactions, parallel reactions, or additional processes such as adsorption. Generally speaking, the measurements and analysis of the EIS for a PEMFC are complicated compared with those of the polarization curve. However, the results from both methods are not insular, and some relationships exist between the complicated impedance spectrum and the simple polarization curve [22].

The correlation between the EIS measurements and polarization curves is that the polarization resistance of the cell measured at a certain voltage corresponds to the tangent to the polarization curve at that voltage [23], i.e., a negative slope in the polarization curve equals the polarization resistance in the impedance spectrum. The polarization resistance is the AC impedance when the frequency approaches zero, where only ohmic components attract attention. Obtaining the polarization resistance of a fuel cell requires extrapolation from the simulated EIS impedance at a very low frequency (e.g., 1 nHz) or summing the individual resistances, which are obtained by fitting the measured spectra with an equivalent circuit. The correlation between impedance measurements and polarization curves is illustrated in Figure 3.15.

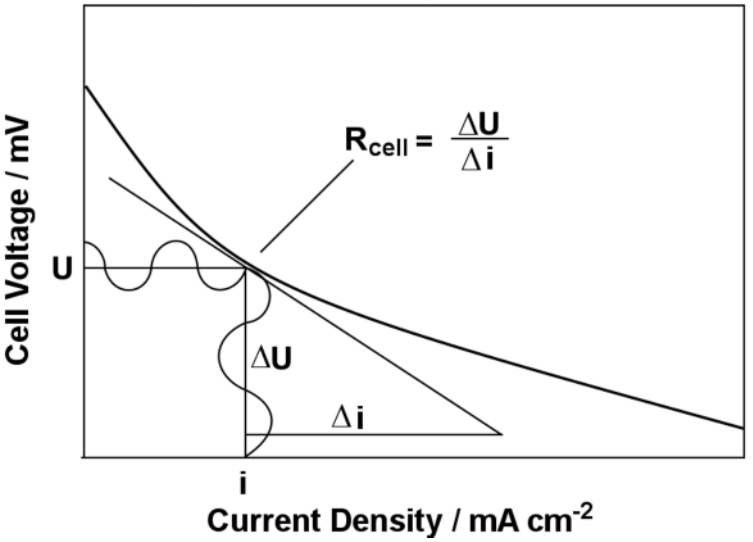

Figure 3.15. Schematic representation of the correlation between fuel cell impedance and polarization curve. (Modified from [23], with kind permission from Springer Science+Business Media: Journal of Applied Electrochemistry, Characterization of membrane electrode assemblies in polymer electrolyte fuel cells using a.c. impedance spectroscopy, 32(8), 2002, 859–63, Wagner N. Figure 4.)

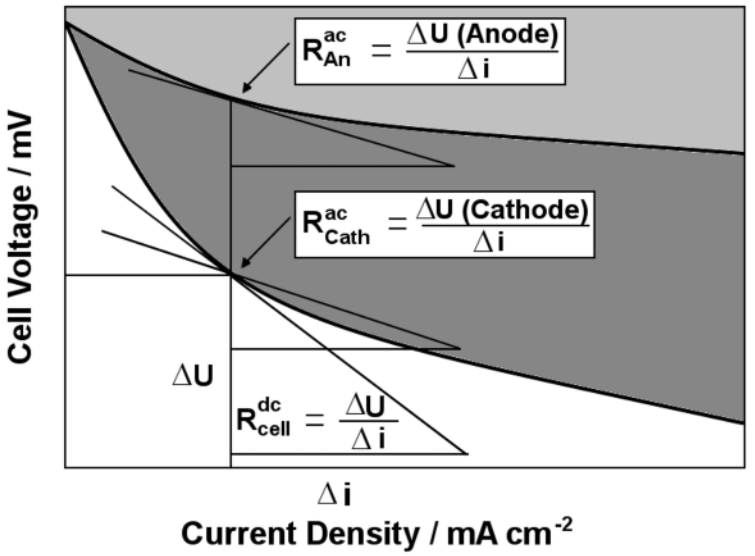

Figure 3.16. Schematic representation of the correlation between polarization resistances (anode, cathode, and cell) and polarization curves [23]. (With kind permission from Springer Science+Business Media: Journal of Applied Electrochemistry, Characterization of membrane electrode assemblies in polymer electrolyte fuel cells using a.c. impedance spectroscopy, 32(8), 2002, 859–63, Wagner N. Figure 6.)

Perry et al. [24] and Jaouen et al. [25] have provided useful diagnostic criteria. They concluded that cathodes controlled by either Tafel kinetics and oxygen diffusion in the agglomerate regions, or by Tafel kinetics and proton transport in the catalyst layer could result in double Tafel slopes. If the cathode was controlled by Tafel kinetics, oxygen diffusion, and proton transport all together, quadruple Tafel slopes would appear.

Using the electrode resistances (R_{anode} and R_{cath}) gained from simulation with an equivalent circuit, the individual cathode and anode polarization curves can be determined, as shown schematically in Figure 3.16 [23].

3.4.2 EIS and Current Interruption

In general, the current interruption method is used to measure ohmic losses (i.e., cell resistance) in a PEM fuel cell. The principle of the technique is that the ohmic losses vanish much more quickly than the electrochemical overpotentials when the current is interrupted [26].

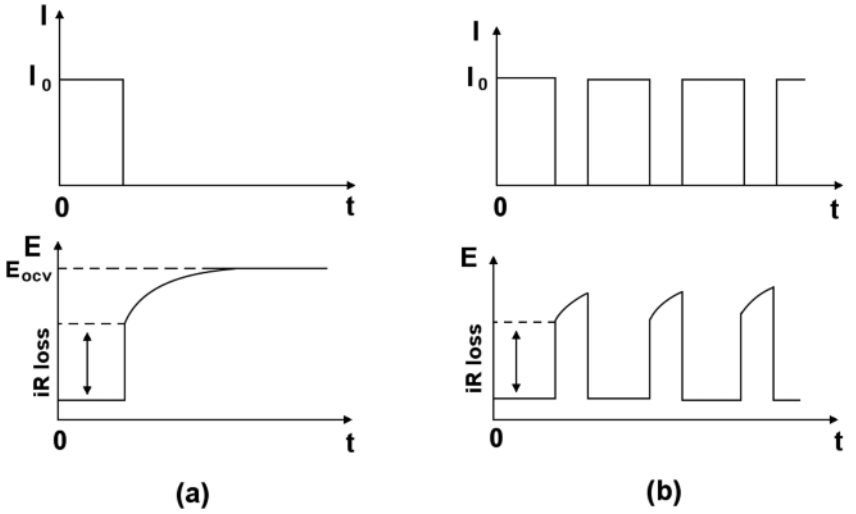

Figure 3.17. An ideal voltage transient in a fuel cell after current interruption: *a* single interruption technique; *b* periodic interruption technique (current pulse)

The current interruption method measures the transient voltage response by abruptly changing the fuel cell current. The ohmic resistance is derived from the change in current and the resulting sudden cell voltage change (a step is usually observed, since the electron flow has a much smaller relaxation time than do other processes). The crucial problem of determining the ohmic resistance for the current interruption method is to separate the ohmic from the charge-transfer and diffusion overpotentials. In the work of Büchi et al. [27, 28], the ideal time window for measuring the ohmic loss was estimated to be 0.5 to 10 ns. Current interruption measurement can be performed by either a single interruption technique or a periodic interruption technique (current pulse), as shown in Figure 3.17. Büchi et

al. [29] measured the ohmic resistance using the current pulse method (5 A amplitude and 10 μs duration) with an ultra-fast switch on the DC current of the cell. Due to the extremely short (less than 10 ns) decay time, their method applied to a fuel cell was very successful. It was also reported that analysis of the voltage relaxation curve after the disappearance of the ohmic losses could yield information on the electrochemical performance of the electrodes. A model containing expressions for Tafel kinetics, electrolyte conductivity, and double-layer capacitance was developed [30], which fitted the experimental data well up to 200 mA/cm^2.

With a fuel cell, the current interruption method differs completely from EIS as a technique for measuring the internal cell resistance (ohmic resistance). Generally speaking, EIS and the current interruption methods will not yield the same results, unless by sheer coincidence. In addition, values estimated from current interruption and EIS do not show the true membrane resistance, but rather the total ohmic drop across the membrane electrode assembly, including the contact resistance, grain-boundary resistance, and bulk membrane resistance, as well as the resistance of the catalyst layers [31]. It has been proven that the ohmic drop values measured by the current pulse method lie below those measured using EIS. However, they do represent a better estimation of the real values [32] because in general, membrane resistances of fuel cells measured with EIS include a non-ohmic contribution due to the limited time resolution [27]. In reality, individual research groups always have their own preferred methods for measuring internal resistance.

Both methods have their advantages and disadvantages for measuring ohmic resistance [22]. Compared with that of EIS, data analysis of the current interruption method is more straightforward. Also, measurement errors associated with magnetic or galvanic couplings, which have significant influences on the transient voltage response, are readily recognizable and can be eliminated. In AC impedance measurements, some side processes can happen at the same frequency as the main process, and unwanted information is difficult to eliminate [27]. However, using current interruption, the voltage transients recorded from fuel cells exhibit non-ideal features. The data analysis also needs to consider the time decay determination. Furthermore, analysis of the non-ohmic part of the voltage response is restricted because the interfacial electrochemical reactions usually have longer characteristic times due to the high values of the double-layer capacities, and are not accessible by this method [32]. In contrast, EIS measurements can provide very rich information, including ohmic loss, charge-transfer resistance, and mass transfer limitation. The membrane resistance is determined from the intercept on the real impedance axis. The reaction resistance is evaluated from the circular arc of the impedance spectra.

3.5 EIS Measurements

A state-of-the-art PEMFC and steady-state current-potential measurements are illustrated in Figure 3.18, which shows a schematic view of the PEMFC geometry, the basic electric circuit of the membrane electrode assembly and the gas diffusion layers at both anode and cathode.

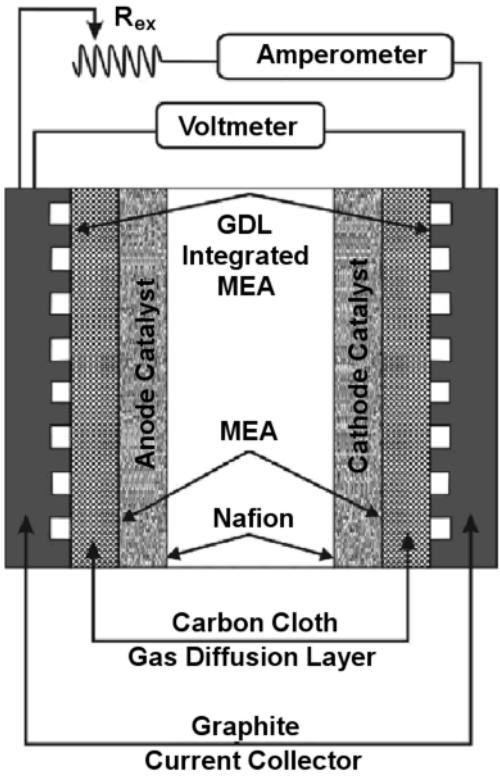

Figure 3.18. Schematic of the PEMFC geometry and basic electric circuit showing the membrane electrode assembly (MEA) and the gas diffusion layers (GDLs) at both anode and cathode [33]. (Reprinted from Electrochimica Acta, 51(13), Tsampas MN, Pikos A, Brosda S, Katsaounis A, Vayenas CG, The effect of membrane thickness on the conductivity of Nafion, 2743–55. ©2006, with permission from Elsevier.)

The impedance can be measured using various instruments and techniques, ranging from a simple oscilloscope display to a fast Fourier transform (FFT) analyzer. The most common instrument used is a frequency response analyzer (FRA), e.g., the Solartron FRA. A potentiostat or a load bank combined with a frequency response analyzer can perform the EIS measurements. The electrical connection between the FRA, the potentiostat (or the load bank), and the fuel cell is illustrated in Figure 3.19.

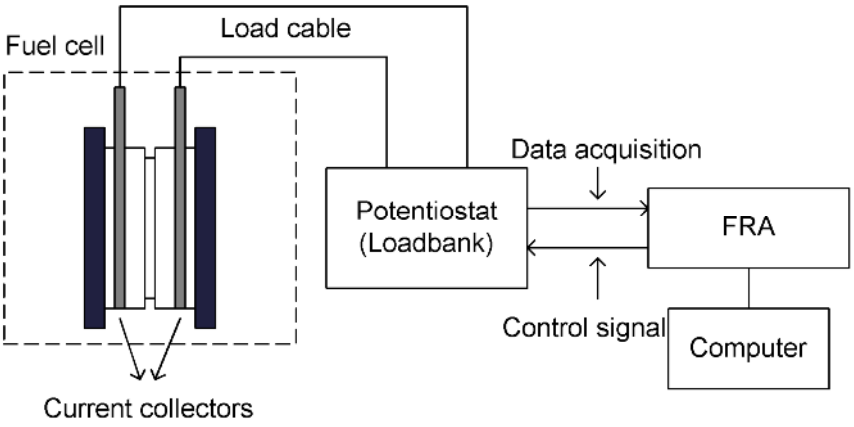

Figure 3.19. Schematic EIS measurement configuration for a fuel cell

There are two options for controlling the perturbation to the measured system: one is to control the current perturbation then record the voltage response from the system; the other is to control the voltage perturbation then record the current response. For a current control measurement, when the leads are all connected the electrical load is set to a DC constant current. The FRA will generate an AC current perturbation and interrupt the fuel cell through a load bank or a potentiostat. The response to the interruption from the fuel cell will enter into the FRA for analysis to obtain the AC impedance spectra.

The FRA is a four-terminal instrument. Two terminals are used for current or voltage signal generation (usually in the form of voltage). The other two accept the voltage or current response. By dividing the response voltage by the perturbation current, the complex impedance (both magnitude and phase) can be obtained at the measured frequency. This procedure is repeated again and again at any desired frequency within the capabilities of the FRA. Ultimately, a full impedance spectrum can be achieved. Suitable software can be chosen to automate the EIS measurements, collect and process the data, and represent them as figures.

It is worthwhile pointing out that a regular potentiostat cannot provide a heavy load in fuel cell testing. Booster technology can help to improve the load capability. Alternatively the fuel cell load bank can be connected directly to the FRA. Sometimes, a power supply may be needed to adapt to the heavy load. Figure 3.20 shows an example of a connection between a TDI load bank and a Solartron 1260. The TDI is a single-channel load bank (RBL 488 series 100-60-400) that can be controlled with signals via an external program; the values of all signals are referred to as S-. When a controlling DC, AC, DC/AC combination, or FRA-generated waveform is connected into the ports of the REM and S- located on the rear panel of the load bank, the load bank will transfer the signal into the fuel cell load. The accuracy of the measurement is limited by the load bank frequency range.

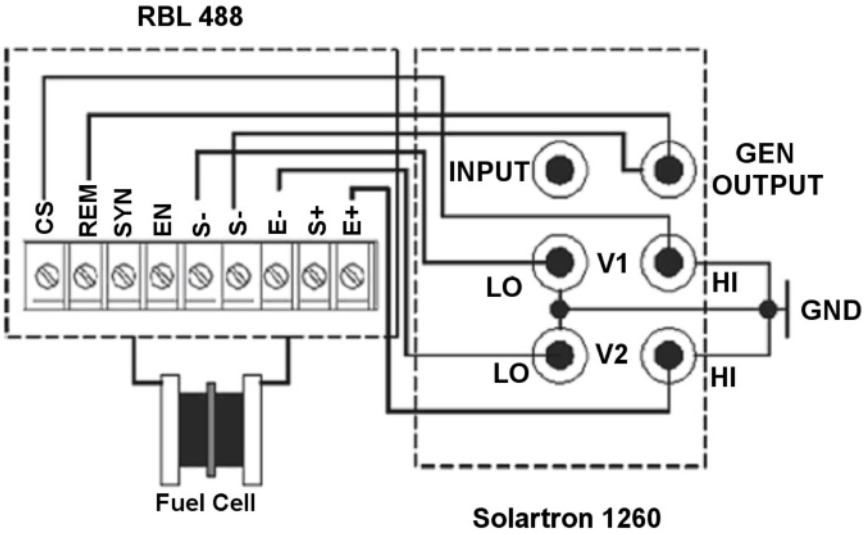

Figure 3.20. AC impedance measurement by TDI RBL 488 load bank and Solartron 1260 [21]. (Reproduced by permission of ECS—The Electrochemical Society, from Tang Y, Zhang J, Song C, Liu H, Zhang J, Wang H, Mackinnon S, Peckham T, Li J, McDermid S, Kozak P. Temperature dependent performance and in situ AC impedance of high-temperature PEM fuel cells using the Nafion-112 membrane.)

In Tang et al.'s [21] impedance experiments, a differential input with a floating ground was chosen to reduce noise and harmonic signals from externally wired circuits. An oscilloscope was connected to the fuel cell current collectors to monitor the noise level. The results showed that this electrical connection could effectively reduce noise. During the measurements, the FRA port, "GEN OUTPUT", gave a software-command signal to the load bank through the ports of "REM" and "S-". The cell voltage response went to FRA "V1" and "V2" for analysis. The impedance information obtained was sent to a computer for data display, and more sophisticated data analysis was performed by powerful software called Z-plot.

To obtain the fuel cell impedance at different frequencies, the frequency of the stimulus sine wave can be swept across the frequency range of interest. However, at high current density, the cell voltage is unstable because of water flooding. This instability could impair the accuracy of the AC impedance measurement, especially for low-frequency measurements. For example, at 10 mHz in one cycle of measurement, which takes about 100 s, it is difficult to obtain accurate AC impedance information at a high current density. More cycles are needed to average the results by integration in the non-linear regime. As we know, the lower the frequency, the longer each frequency point takes for a full impedance spectrum. Therefore, at high frequencies, data collection can be done in the blink of an eye with a high average number, but at very slow frequencies it will slow down dramatically. In terms of the software settings (e.g., Zview), although averaging

more points can improve AC impedance results, to speed up a test below a certain frequency it is preferable to collect fewer points.

3.6 Advantages and Limitations of EIS

3.6.1 EIS Advantages

It has been demonstrated that EIS can serve as a standard analytical *diagnostic tool* in the evaluation and characterization of fuel cells. Scientists and engineers have now realized that the entire frequency response spectrum can provide useful data on non-Faradaic mechanisms, water management, ohmic losses, and the ionic conductivity of proton exchange membranes. EIS can help to identify contributors to PEMFC performance. It also provides useful information for fuel cell optimization and for down-selection of the most appropriate operating conditions. In addition, EIS can assist in identifying problems or predicting the likelihood of failure within fuel cell components.

3.6.1.1 Identifying Contributors
Contributors to the impedance of a PEMFC include interfacial charge-transfer resistance, membrane resistance, contact resistance, oxidant and fuel transport resistance, water transport resistance, proton transport resistance, double-layer capacitance, and Faradaic pseudo-capacitance [34]. The main advantage of EIS as a diagnostic tool is in identifying the individual contributors (e.g., ohmic resistance, interfacial charge-transfer resistance, mass transport resistances in the catalyst layer and back-diffusion layer) in a short period of time. In particular, EIS is able to measure the ohmic resistance (or membrane resistance) at high frequencies, which allows the performance of ohmic compensation during DC tests. By varying fuel cell operating conditions, it is possible to obtain further information about impedance contributors, with the help of an equivalent circuit [23]. For example, Pickup and coworkers [34] investigated the ionic resistance in the catalyst layers of PEMFCs by conducting impedance experiments under a nitrogen atmosphere.

3.6.1.2 Optimizing Performance
Separation of the individual contributors can provide useful information about performance optimization for fuel cells, helping to optimize MEA components, including catalyst layers (e.g., catalyst loading, Nafion® content, and PTFE content), gas diffusion layers, and membranes. It assists in the down-selection of catalysts, composite structure, and MEA fabrication methods. It also helps in selecting the most appropriate operating conditions, including humidification, temperature, back-pressure, and reactant flow rates.

3.6.1.3 Identifying Problems
Performing EIS on fuel cells can help to identify potential problems or failures within the cell, such as catalyst coarsening, membrane degradation, bipolar plate corrosion, gas diffusion layer oxidation, and incorrect operating conditions.

Identifying these problems helps to optimize the cell operating conditions, and to avoid fuel cell performance failure or even collapse.

3.6.2 EIS Limitations

Although EIS offers many advantages for diagnosing fuel cell properties, clear difficulties exist for applying impedance methods and fitting the data to the model to extract the relevant electrochemical parameters. The limitations of the EIS technique derive from the several requirements required to obtain a valid impedance spectrum, because the accuracy of EIS measurement depends not only on the technical precision of the instrumentation but also on the operating procedures. Theoretically, there are three basic requirements for AC impedance measurements: linearity, stability, and causality.

3.6.2.1 Linearity

The amplitude of the AC signal must be low enough to ensure that the response of the electrochemical cell behaves linearly. Perturbation of the electrochemical system using a voltage or current can result in a shift of the steady state. To establish another steady state, the rate at which it proceeds to a new state strongly depends on kinetic parameters, such as charge-transfer resistance, diffusion coefficient, reaction rate constants, and double-layer capacitance. Then, if the shift rate from one state to another is too slow, the system may become non-linear [35]. In a non-linear system, the current change is not proportional to the voltage change, i.e., $\Delta V \neq \Delta IR$, therefore, a plot of voltage change versus current change will not be a straight line. In dynamic analysis, the most troublesome forms are the non-linear behaviours. Often these are severe and may have nothing to do with the system dynamics. When we apply EIS to a system, the response from the system must be a linear or at least quasi-linear function of the applied perturbation in order to gain a meaningful mathematical analysis. However, few systems are in reality linear, so what we measure is a linear approximation by using small amplitude perturbations (e.g., with a potential amplitude of less than 10 mV). Thus, the interface can be treated as a linear system if the amplitude of the perturbation signal is very small.

In practice, we have to consider the trade-off between linearity and accuracy. The perturbation signal amplitude should be small enough to approach quasi-linear conditions for the response. However, it also has to be large enough to be recognized. If the signals are too small, they could be buried in noise, resulting in low accuracy. Therefore, the amplitude should be adjusted to compromise between a high S/N (signal/noise) ratio and the linearity of the system response for any particular case [36].

To know whether or not a system is linear, we may use linear systems theory (LST) [37]. LST is a good time-saving theory for testing whether a system is linear. The two basic tests are homogeneity and additivity.

- *Homogeneity*: If the input signal is doubled, the output response is also doubled. We call this system linear.

- *Additivity*: First, a complex stimulus S1 is input into the system, and then the electrical responses from the system are measured. Next, a second stimulus S2, which is slightly different, is input into the system, and the responses from the system are also measured. Now, suppose the sum of the two stimuli S1 + S2 is input simultaneously. If the system is linear, then the measured response will be just the sum of its responses to each of the two stimuli presented separately.

3.6.2.2 Stability

Measuring an EIS spectrum takes time (sometimes many hours), especially in the low-frequency region. To validate the impedance spectrum, the system must be stable while impedance measurements are being taken. A common cause of problems in EIS measurements and their analysis is drift in the system. The cell can change through adsorption of solution impurities, growth of an oxide layer, build-up of the reaction products in solution, coating degradation, and temperature changes. Standard EIS analysis tools may give wildly inaccurate results for a system that is not at a steady state.

To achieve a steady-state environment, some actions must be taken before starting each impedance measurement for a PEMFC system. For example, Wagner [23] prepolarized the cell for at least 15 min at the measuring potential. The current densities before and after measurement were taken to prove the stability of the cell during measurement times. Guo et al. [38] operated a fuel cell at 0.6 V for 20 h to reach its steady-state operating current. Pickup et al. [34, 39] ran a H_2/O_2 fuel cell for 30 min at 0.5 V before the impedance measurements were performed. In Gode et al.'s work [40], the cell was run galvanostatically for 1 h prior to the impedance measurement.

3.6.2.3 Causality

The output of the system must be caused by the perturbing input. However, absence of linearity or stability does not prevent one from obtaining the output. It is necessary to assess the validity of the obtained impedance data, especially when a new system is being studied.

For a linear system, the phase and amplitude of the impedance relate to each other. Consequently, if we know the frequency dependence of the phase we can calculate the amplitude of the impedance as a function of frequency. Similarly, we can deduce the frequency dependence of the phase from that of the amplitude of the impedance. The calculation can be achieved by the Kramers–Kronig (K–K) transforms. This is a useful check on the validity of a measured impedance spectrum. For information on K–K transforms, see Appendix C.

3.7 Chapter Summary

This chapter has provided background on electrochemical interfaces and the relationships between impedance spectra and electrochemical interface, for fuel cell researchers or engineers who may not be electrochemists but will apply EIS as

a method of analysis. This chapter should also facilitate better understanding of data analysis methods for EIS results.

Electrochemical impedance spectroscopy can yield valuable information. However, experience and knowledge are necessary to conduct EIS measurements for fuel cells. Attention should be paid to the following:

- Noise
- Input impedance of the instrument (which gives systematic errors)
- Bandwidth of the instrument
- Integration time
- Steady-state
- Stability of the combination cell and instrument (no oscillations)
- Amplitude of the signal (linearity of the cell, use the oscilloscope and frequency spectrum window)
- Voltammetric curve measurements
- Data validation (for instance, using the Kramers–Kronig test)

References

1. Bard AJ, Faulkner LR (2001) Electrochemical methods, fundamentals and applications, 2nd edn. Wiley, New York
2. Wu HQ, Li YF (1998) Electrochemical kinetics. China Higher Education Press, Beijing
3. Schmickler W (1996) Interfacial electrochemistry. Oxford University Press, New York
4. Barsoukov E, Macdonald JR (2005) Impedance spectroscopy: theory, experiment, and applications, 2nd edn. Wiley, Hoboken, NJ
5. Breiter MW(1969) Electrochemical process in fuel cells. Springer-Verlag, Berlin
6. LaConti AB, Hamdan M, McDonald RC (2003) Mechanisms of membrane degradation. In: Vielstich W, Lamm A, Gasteiger H (eds) Handbook of fuel cells: fundamentals, technology, and applications. Wiley, Chichester, England
7. Feldheim DL, Lawson DR, Martin CR (1993) Influence of the sulfonate countercation on the thermal stability of Nafion perfluorosulfonate membranes. J Polym Sci Part B: Polym Phys 31(8):953–7
8. Patil YP, Seery TAP, Shaw MT, Parnas RS (2005) In situ water sensing in a Nafion membrane by fluorescence spectroscopy. Ind Eng Chem Res 44(16):6141–7
9. Huang C, Tan KS, Lin J, Tan KL (2003) XRD and XPS analysis of the degradation of the polymer electrolyte in H_2–O_2 fuel cell. Chem Phys Lett 371(1–2):80–5
10. Kadirov MK, Bosnjakovic A, Schlick S (2005) Membrane-derived fluorinated radicals detected by electron spin resonance in UV-irradiated Nafion and Dow ionomers: effect of counterions and H_2O_2. J Phys Chem B 109(16):7664–70
11. Bosnjakovic A, Schlick S (2004) Nafion perfluorinated membranes treated in Fenton media: radical species detected by ESR spectroscopy. J Phys Chem B 108(14):4332–7
12. Brunetto C, Tina G, Squadrito G, Moschetto A (2004) PEMFC diagnostics and modelling by electrochemical impedance spectroscopy. In: Matijasevic M, Pejcinovic B, Tomsic Z, Butkovic Z (eds) Proceedings of the 12th IEEE Mediterranean electrochemical conference. IEEE, Piscataway, NJ
13. Springer TE, Zawodzinski TA, Wilson MS, Gottesfeld S (1996) Characterization of polymer electrolyte fuel cells using AC impedance spectroscopy. J Electrochem Soc 143(2):587–99

14. Barbir F (2005) PEM fuel cells: theory and practice. Elsevier Academic Press, New York
15. Lim CY, Haas HR (2006) A diagnostic method for an electrochemical fuel cell and fuel cell components. WO patent 2006029254
16. Hirschenhofer JH, Stauffer DB, Engleman RR, Klett MG (1998) Fuel cell handbook, 4th edn. Department of Energy/Federal Energy Technology Center-99/1076, Orinda, CA
17. Ju H, Wang CY (2004) Experimental validation of a PEM fuel cell model by current distribution data. J Electrochem Soc 151(11):A1954–60
18. Li X (2006) Principles of fuel cells. Taylor & Francis, New York
19. Hoare JP (1962) Rest potentials in the platinum-oxygen-acid system. J Electrochem Soc 109(9):858–65
20. Thacker R, Hoare JP (1971) Sorption of oxygen from solution by noble metals: I. Bright platinum. J Electroanal Chem 30(1):1–14
21. Tang Y, Zhang J, Song C, Liu H, Zhang J, Wang H, Mackinnon S, Peckham T, Li J, McDermid S, Kozak P (2006) Temperature dependent performance and in situ AC impedance of high-temperature PEM fuel cells using the Nafion-112 membrane. J Electrochem Soc 153(11):A2036–43
22. Yuan XZ, Sun JC, Wang H, Zhang (2007). AC impedance diagnosis of PEM fuel cells. Int J Hydrogen Energy 32(17):4365–80
23. Wagner N (2002) Characterization of membrane electrode assemblies in polymer electrolyte fuel cells using a.c. impedance spectroscopy. J Appl Electrochem 32(8):859–63
24. Perry MI, Newman J, Cairns EJ (1998) Mass transport in gas-diffusion electrodes: a diagnostic toll for fuel cell cathodes. J Electrochem Soc 145(1):5–15
25. Jaouen F, Lindbergh G, Sundholm G (2002) Investigation of mass-transport limitations in the solid polymer fuel cell cathode. J Electrochem Soc 149(4):A437–47
26. Wruck WJ, Machado RM, Chapman TW (1987) Current interruption—instrumentation and applications. J Electrochem Soc 134(3):539–46
27. Büchi FN, Marek A, Scherer GG (1995) In situ membrane resistance measurements in polymer electrolyte fuel cells by fast auxiliary current pulses. J Electrochem Soc 142(6):1895–901
28. Büchi FN, Scherer GG (2001) Investigation of the transversal water profile in Nafion membranes in polymer electrolyte fuel cells. J Electrochem Soc 148(3):A183–8
29. Büchi FN, Scherer GG (1996) In-situ resistance measurements of Nafion® 117 membranes in polymer electrolyte fuel cells. J Electroanal Chem 404(1):37–43
30. Jaouen F, Lindbergh G (2003) Transient techniques for investigating mass-transport limitations in gas diffusion electrodes. J Electrochem Soc 150(1):A1699–710
31. Abe T, Shima H, Watanabe K, Ito Y (2004) Study of PEFCs by AC impedance, current interrupt, and dew point measurements: I. Effect of humidity in oxygen gas. J Electrochem Soc 151(1):A101–5
32. Andreaus B, Scherer GG (2004) Proton-conducting polymer membranes in fuel cells—humidification aspects. Solid State Ionics 168(3–4):311–20
33. Tsampas MN, Pikos A, Brosda S, Katsaounis A, Vayenas CG (2006) The effect of membrane thickness on the conductivity of Nafion. Electrochimica Acta 51(13):2743–55
34. Li G, Pickup PG (2003) Ionic conductivity of PEMFC electrodes: effect of Nafion loading. J Electrochem Soc 150(11):C745–52
35. Retter U, Lohse H (2002) Electrochemical impedance spectroscopy. In: Scholz F (ed) Electroanalytical methods: guide to experiments and applications. Springer, Berlin

36. Popkirov GS, Schindler RN (1995) Effect of sample nonlinearity on the performance of time domain electrochemical impedance spectroscopy. Electrochimica Acta 40(15):2511–17
37. Heeger, D (1999) Linear systems theory handout. http://www.cim.mcgill.ca/~siddiqi/linear-systems.pdf. Accessed 19 April 1999
38. Guo Q, Cayetano M, Tsou Y, De-Castro ES, White RE (2003) Study of ionic conductivity profiles of the air cathode of a PEMFC by AC impedance spectroscopy. J Electrochem Soc 150(11):A1440–9
39. Easton EB, Pickup PG (2005) An electrochemical impedance spectroscopy study of fuel cell electrodes. Electrochim Acta 50(12):2469–74
40. Gode P, Jaouen F, Lindbergh G, Lundblad A, Sundholm G (2003) Influence of the composition on the structure and electrochemical characteristics of the PEFC cathode. Electrochim Acta 48(15):4175–87

4

EIS Equivalent Circuits

4.1 Electrochemical Elements

As discussed in Chapter 3, the electrolyte/interface and associated electrochemical processes can be treated as an electric circuit consisting of electrical elements, including resistance, capacitors, constant phase elements, and so on. Although the commonly used electrical elements have already been described in Chapters 2 and 3, the following section provides a brief review to preface the ensuing discussion of EIS equivalent circuits and their related PEM fuel cell processes.

4.1.1 Lumped Elements

4.1.1.1 Resistance

The electrical element resistance, R, is described in the time domain based on Ohm's law:

$$V = RI \tag{4.1}$$

where V is the voltage drop across R and I is the current passing through R.

In the frequency domain, its impedance has only a real part:

$$Z_R(\omega) = R \tag{4.2}$$

i.e., $Z_{re} = R$ and $Z_{im} = 0$.

In Equation 4.2, ω is the frequency of the AC signal. Resistance in electrochemical systems includes ionic resistance, electronic resistance, charge-transfer resistance, and mass transfer resistance. The ionic resistance is sometimes expressed as ionic conductivity, using the unit of siemens per centimetre (S/cm), which is the reciprocal of the resistivity:

$$\sigma = \frac{1}{\rho} \tag{4.3}$$

where ρ is the resistivity expressed as Ω·cm. This ionic conductivity is normally used to describe the proton transport in perfluorosulfonic acid membranes, such as Nafion® membranes.

Electronic resistance is normally used to describe the movement of electrons within a conducting media, such as metal wires or conducting polymers. In fuel

cells, the electronic resistance is usually omitted because it is very small in comparison with the ionic resistance.

Charge-transfer resistance is the resistance that occurs when electrons transfer at the electrode/electrolyte interface. The charge-transfer resistance is dependent on the reaction, the electrode surface, and the electrode potential. In general, an increase in overpotential leads to a decrease in charge-transfer resistance.

4.1.1.2 Capacitance

If a layer of non-conductive medium is sandwiched between two electrodes and electricity passes through this assembly, electric charge will be stored at both electrodes. This assembly is called a capacitor. The capacitor is measured by its capacitance (C), which is represented by the stored electric charge, divided by the voltage drop across the two electrodes:

$$C = \frac{Q}{V} = \varepsilon_0 \varepsilon_r \frac{A}{d} \tag{4.4}$$

where Q is the charge, V is the voltage difference between the two electrodes, ε_0 is the permittivity of a vacuum, ε_r is the dielectric constant or relative permittivity of the insulator used, A is the electrode area, and d is the distance between the electrodes.

The impedance ($Z_C(\omega)$) of the capacitor is given by the following equation:

$$Z_C(\omega) = \frac{1}{i\omega C} \tag{4.5}$$

where $i = \sqrt{-1}$ and ω is the frequency.

4.1.1.3 Inductance

Inductance (L) is the magnetic field generated when a current is passed through an inductor, typically a wire coil. The strength of the magnetic field is measured in henries (H). The impedance of an inductor ($Z_L(\omega)$) is given as

$$Z_L(\omega) = i\omega L \tag{4.6}$$

In a fuel cell, inductance is usually caused by the adsorbed species on the electrode surface. For example, in a direct methanol fuel cell, adsorption of CO on the anode catalyst can at low frequencies result in an inductance loop.

4.1.2 Frequency-Dependent Elements

4.1.2.1 Warburg Resistance [1]

Warburg resistance represents the resistance related to mass transfer in an electrochemical process. The resistance is frequency dependent, and consists of both resistance and capacitance. As discussed in Chapter 3, the impedance of the Warburg resistance ($Z_w(\omega)$) is written as follows

$$Z_w(\omega) = \sigma\omega^{-1/2} - i(\sigma\omega^{-1/2}) \tag{4.7}$$

where

$$\sigma = \frac{1}{nFA\sqrt{2}}\left(\frac{\beta_o}{D_o^{1/2}} - \frac{\beta_R}{D_R^{1/2}}\right) \tag{4.8}$$

$$i = \sqrt{-1} \tag{4.9}$$

$$\beta_O = \left[\frac{\partial E}{\partial C_O(0,t)}\right]_{iC_R(0,t)} \tag{4.10}$$

$$\beta_R = \left[\frac{\partial E}{\partial C_R(0,t)}\right]_{iC_O(0,t)} \tag{4.11}$$

The meanings of symbols in Equations 4.7 to 4.11 have been defined in Section 3.2 of Chapter 3.

The Warburg impedance can be considered as a resistance ($R_f = \sigma\omega^{-1/2}$) connected with a capacitance ($C_f = \sigma\omega^{-1/2}$) in series. Since the impedance of the real part equals that of the imaginary part, in Nyquist spectra the Warburg impedance is represented by the 45° line following the semicircle (charge transfer and double-layer circuit).

4.1.2.2 Constant Phase Element

The constant phase element (CPE) is a non-intuitive circuit element that was discovered in the course of investigations into responses from real systems. In general, a Nyquist plot (also called a Cole–Cole plot or complex impedance plane plot) should be a semicircle with the centre on the x-axis. However, the observed plot for some real systems was indeed the arc of a circle but with the centre located somewhere below the x-axis. Figure 4.1 shows the impedance spectra of a circuit of a resistor and a constant phase element connected in parallel. The centre of the semicircle is located at (1–n)×90° below the real axis.

A CPE's impedance is given by

$$Z_{CPE}(\omega) = q^{-1}(i\omega)^{-n} \tag{4.12}$$

where q is a factor of proportionality having numerical values, and n is the CPE exponent that characterizes the phase shift. For integral values of n (n = 1, 0, –1), the CPE represents C, R, and L, respectively. For n = 0.5, it gives the Warburg impedance. The physical meanings of the coefficient q for n = 1, 0, –1, and 0.5 are listed in Table 4.1.

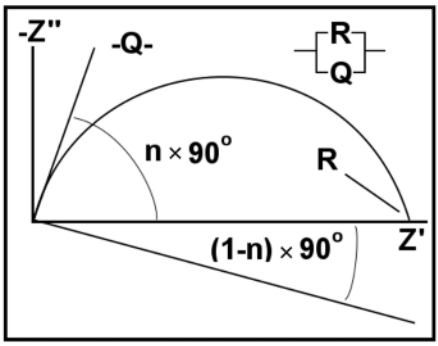

Figure 4.1. Nyquist plot showing the impedance spectra of an R/CPE electric circuit model [2]. (Reproduced with permission from Research Solutions & Resources LLC.)

Table 4.1. Physical meaning of the coefficient Q

n	CPE designation	q (meaning)	units
1	Capacitance	C	$\mathrm{F} = \Omega^{-1}\mathrm{s}$
0	Resistance	R^{-1}	Ω^{-1}
–1	Inductance	L^{-1}	$\mathrm{H}^{-1} = \Omega^{-1}\mathrm{s}^{-1}$
0.5	Warburg element	σ^{-1}	$\Omega\mathrm{s}^{-1/2}$

For n = 1–ε, where $0 < \varepsilon \leq 0.2$, the CPE corresponds to distortion of the capacitance due to electrode surface roughness or distribution/accumulation of charge carriers. For n = 0.5±ε, where $0 < \varepsilon \leq 0.1$, the CPE is related to diffusion, with deviations from Fick's second law. For n = 0±ε, where $0 < \varepsilon \leq 0.2$, the CPE represents distorted resistance. For n < 0, the CPE describes inductive energy accumulation. Therefore, the CPE is a generalized element. Several factors can contribute to the CPE: surface roughness, varying thickness or composition, non-uniform current distribution, and a distribution of reaction rates (non-homogeneous reaction rates on the electrode surface) [3].

4.1.3 Bounded Frequency-Dependent Elements

4.1.3.1 Bounded Warburg [3]

The bounded Warburg element (BW) describes linear diffusion in a homogeneous layer with finite thickness. Its impedance is written as

$$Z_{BW}(\omega) = \sigma(i\omega)^{-1/2} \tanh\left(\frac{i\omega R_0^2}{\sigma^2}\right)^{1/2} \tag{4.13}$$

where σ $(\Omega\mathrm{s}^{-1/2})$ and R_0 (Ω) are two independent structural parameters. At high frequencies ($\omega \to \infty$), the BW demonstrates the behaviour of a Warburg element.

At low frequencies ($\omega \to 0$), it tends to a finite value. The complex-plane impedance of the BW will be shown in Section 4.2.

4.1.3.2 Bounded CPE [3]
A bounded CPE (BCPE) describes the impedance of a bounded homogeneous layer with CPE behaviour. Its impedance is written as

$$Z_{BCPE}(\omega) = q^{-1}(i\omega)^{-n} \tanh R_0 q(i\omega)^n \tag{4.14}$$

where q, n, and R_0 are the structural parameters of the bounded CPE element. The complex-plane impedance of a BCPE will also be covered in Section 4.2.

In summary, the parameters and units of the commonly used equivalent circuit elements described above are listed in Table 4.2.

Table 4.2. Parameters of the equivalent circuit elements

Element	Name	Parameters	Units
R	Resistance	R	Ω
C	Capacitance	C	$\mathrm{F} = \Omega^{-1}\mathrm{s}$
L	Inductance	L	$\mathrm{H} = \Omega\mathrm{s}$
W	Warburg element	σ	$\Omega\mathrm{s}^{-1/2}$
BW	Bounded Warburg	σ	$\Omega\mathrm{s}^{-1/2}$
		R_0	Ω
CPE	Constant phase element	q	$\Omega^{-1}\mathrm{s}^n$
		n	1
BCPE	Bounded CPE	q	$\Omega^{-1}\mathrm{s}^n$
		n	1
		R_0	Ω

4.2 Basic Equivalent Circuits

Impedance models are constructed according to the electrochemical phenomena. The total impedance of an electrochemical system can be expressed by different combinations of the electrical elements. This section covers the features of basic equivalent circuits commonly used in electrochemical systems. In Appendix D, the effect of an element parameter change on a spectrum related to a given equivalent circuit is described in detail.

4.2.1 Simple Combinations of Electrical Elements

The circuit elements can be connected in series or in parallel. The basic rule for the calculation of the circuits is: for an electric circuit with elements in series connection, the total impedance is the sum of the impedances of the individual elements; for an electric circuit with elements in parallel connection, the total

admittance, $Y(\omega)$, which is the inverse of impedance, $1/Z(\omega)$, is the sum of the admittances of the individual elements. This sub-section presents spectra of the simple combination of an element with *R* in series or in parallel.

In Chapter 2, we presented different combinations of electrical elements (resistor, capacitor, and conductor). In this chapter we now present several typical circuits for electrochemical systems, along with their corresponding impedance calculations.

4.2.1.1 Resistance and Capacitance

RC in Series

The simplest model is the connection of resistor and capacitor in either series or parallel. Figure 4.2*a* shows the connection of a resistor and a capacitor in series. This equivalent circuit is the simplest model for an ideal polarizable electrode, with the assumption that neither the charge transfer on the electrode surface nor the diffusion limitations are present.

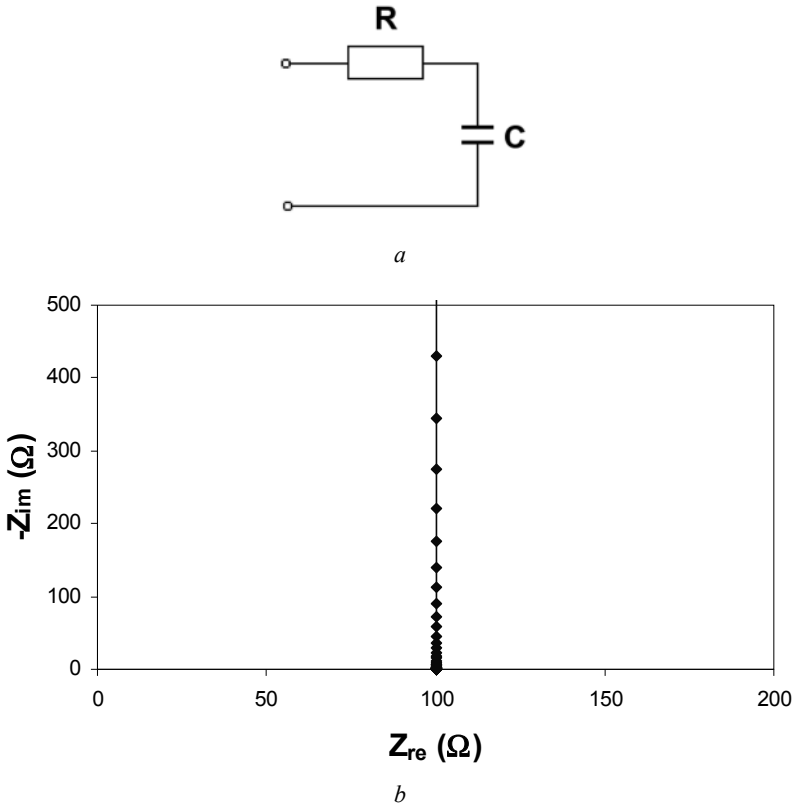

Figure 4.2. *a* Resistor and capacitor in series (Model D1); *b* Nyquist plot of resistor and capacitor in series over the frequency range 1 MHz to 1 mHz (Model D1: R = 100 Ω, C = 0.1 F)

Based on the primary rules, the overall impedance of an RC circuit in series can be expressed as

$$Z(\omega) = R + (i\omega C)^{-1} = R - i(\omega C)^{-1} \tag{4.15}$$

The simulated Nyquist plot of resistance and capacitance in series is a vertical line in the complex-plane impedance diagram, as shown in Figure 4.2(*b*). The effect of the parameter *R* on the position of the line is presented in Appendix D (Model D1).

RC in Parallel

Figure 4.3*a* shows the connection of a resistor and a capacitor in parallel. The total admittance of this RC circuit in parallel is expressed by

$$Y(\omega) = R^{-1} + i\omega C \tag{4.16}$$

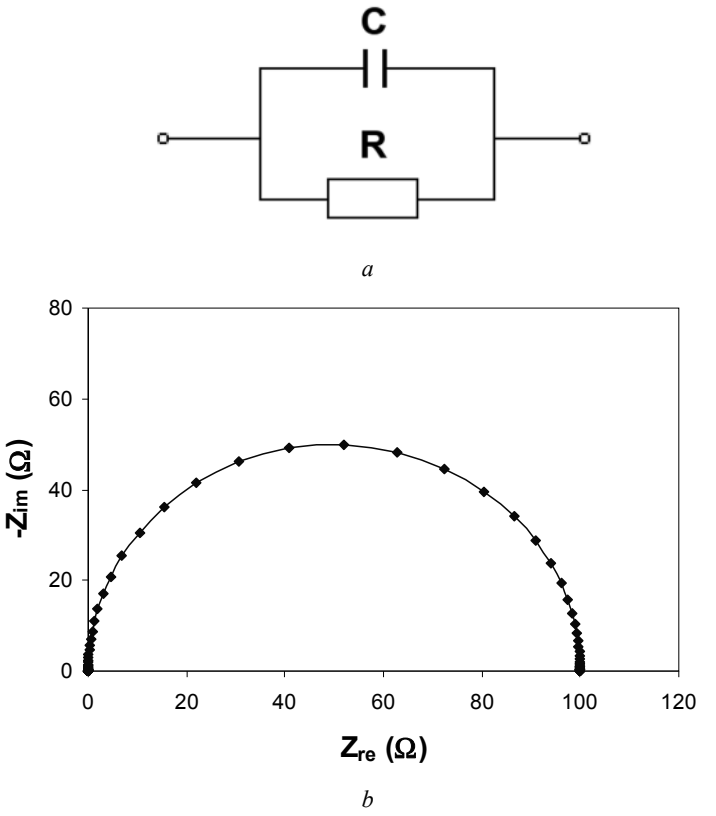

Figure 4.3. *a* Resistor and capacitor in parallel (Model D2); *b* Simulated Nyquist plot of a resistor and a capacitor in parallel over the frequency range 1 MHz to 1 mHz (Model D2: R = 100 Ω, C = 0.001 F)

The impedance can then be expressed as

$$Z(\omega) = \frac{1}{R^{-1} + i\omega C} = \frac{R}{1 + i\omega RC} = \frac{R(1 - i\omega\tau)}{(1 + i\omega\tau)(1 - i\omega\tau)} \tag{4.17}$$

$$Z(\omega) = \frac{R}{1 + \omega^2\tau^2} - i\frac{\omega R\tau}{1 + \omega^2\tau^2} \tag{4.18}$$

where $\tau = RC$ is the time constant, which is considered a measure of the rate of a reaction or process.

In the complex-plane impedance diagram, the Nyquist plot of resistance and capacitance in parallel is an ideal semicircle, as depicted in Figure 4.3*b*. The diameter equals the value of the resistance, *R*. The imaginary part of the impedance reaches a maximum at frequency ω_{max}, denoted as the characteristic frequency:

$$\omega_{max} = (RC)^{-1} = \tau^{-1} \tag{4.19}$$

4.2.1.2 Resistance and CPE

R and CPE in Series

Simulating the double layer of an electrode/electrolyte interface by using a simple capacitance is a simplification, but one that is acceptable if the electrolytes are concentrated and the electrode area is smooth. When the electrode surface is non-uniform or rough and the electrolyte is diluted, the impedance diagram is deformed, mainly due to the geometrical effect. For an ideally polarizable electrode, Model D1 can be modified by replacing capacitance with a capacitive CPE to reflect this geometric effect. Connection of resistance and a CPE in series is shown in Figure 4.4*a*.

The impedance of a CPE can be written as

$$Z_{CPE}(\omega) = q^{-1}(i\omega)^{-n} \tag{4.20}$$

where q is a factor of proportionality and n is the CPE exponent, which characterizes the phase shift. Using De Moivre's formula:

$$[\cos(t) + i\sin(t)]^n = \cos(nt) + i\sin(nt) \tag{4.21}$$

we have

$$i^n = [\cos(\frac{\pi}{2}) + i\sin(\frac{\pi}{2})]^n = \cos(\frac{\pi}{2}n) + i\sin(\frac{\pi}{2}n) \tag{4.22}$$

and

$$i^{-n} = [\cos(\frac{\pi}{2}) + i\sin(\frac{\pi}{2})]^{-n} = \cos(-\frac{\pi}{2}n) + i\sin(-\frac{\pi}{2}n) \tag{4.23}$$

Thus, the impedance of this model is calculated by adding their impedances

$$Z(\omega) = R + q^{-1}(i\omega)^{-n} = R + q^{-1}\omega^{-n}(\cos(-\frac{\pi}{2}n) + i\sin(-\frac{\pi}{2}n)) \tag{4.24}$$

$$Z(\omega) = R + q^{-1}\omega^{-n}\cos(-\frac{\pi}{2}n) + iq^{-1}\omega^{-n}\sin(-\frac{\pi}{2}n) \tag{4.25}$$

Figure 4.4*b* shows the simulated Nyquist plot of resistance and a CPE in series connection, in a complex-plane impedance diagram. More examples of the effect of parameters on the spectra can be found in Appendix D (Model D3).

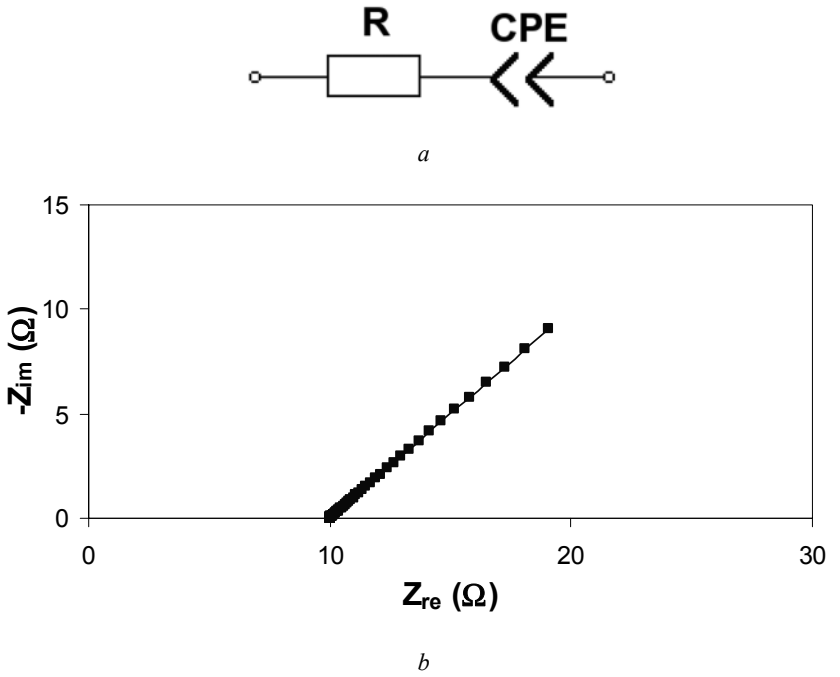

Figure 4.4. *a* Resistor and CPE in series (Model D3); *b* Simulated Nyquist plot of resistor and CPE in series connection over the frequency range 1 MHz to 1 mHz (Model D3: R = 10 Ω, Q = 1 $\Omega^{-1}s^{0.5}$, n = 0.5)

R and CPE in Parallel

Figures 4.5*a* and *b* show the equivalent circuit of a resistor and a CPE in parallel connection, and its simulated Nyquist plot, respectively. More examples of the effect of parameters on the spectra can be found in Appendix D (Model D4).

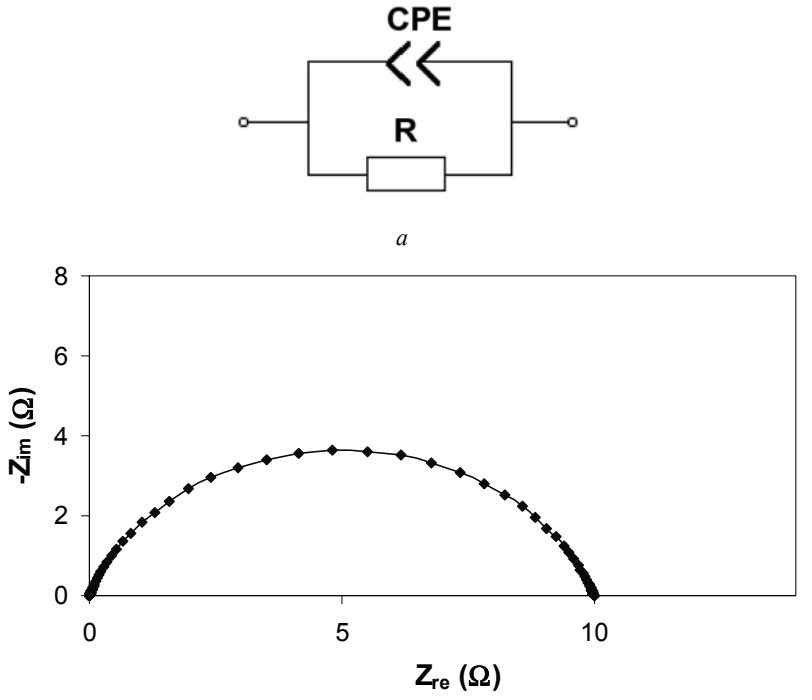

Figure 4.5. *a* Resistor and CPE in parallel (Model D4); *b* Simulated Nyquist plot of resistor and CPE in parallel connection over the frequency range 1 MHz to 1 mHz (Model D4: R = 10 Ω, Q = 0.01 $\Omega^{-1}s^{0.8}$, n = 0.8)

The total admittance of the R-CPE circuit is calculated from

$$Z_{CPE}(\omega)^{-1} = q(i\omega)^n = q\omega^n(\cos(\frac{\pi}{2}n) + i\sin(\frac{\pi}{2}n)) \tag{4.26}$$

$$Z(\omega) = \frac{1}{R^{-1} + q\omega^n(\cos(\frac{\pi}{2}n) + i\sin(\frac{\pi}{2}n))} \tag{4.27}$$

$$Z(\omega) = \frac{R + qR^2\omega^n\cos(\frac{\pi}{2}n)}{1 + 2qR\ \omega^n\cos(\frac{\pi}{2}n) + q^2R^2\omega^{2n}} - i\frac{qR^2\omega^n\sin(\frac{\pi}{2}n)}{1 + 2qR\ \omega^n\cos(\frac{\pi}{2}n) + q^2R^2\omega^{2n}} \tag{4.28}$$

4.2.1.3 Resistance and Inductance

RL in Series

Figure 4.6*a* shows the circuit of a resistor and an inductor in series connection. Based on the primary rules, the overall impedance of this circuit is expressed as

$$Z(\omega) = R + i\omega L \tag{4.29}$$

The simulated Nyquist plot of the circuit is a vertical line in the complex-plane impedance diagram, as depicted in Figure 4.6*b*. The parameter effect of this circuit is provided in Appendix D (Model D5).

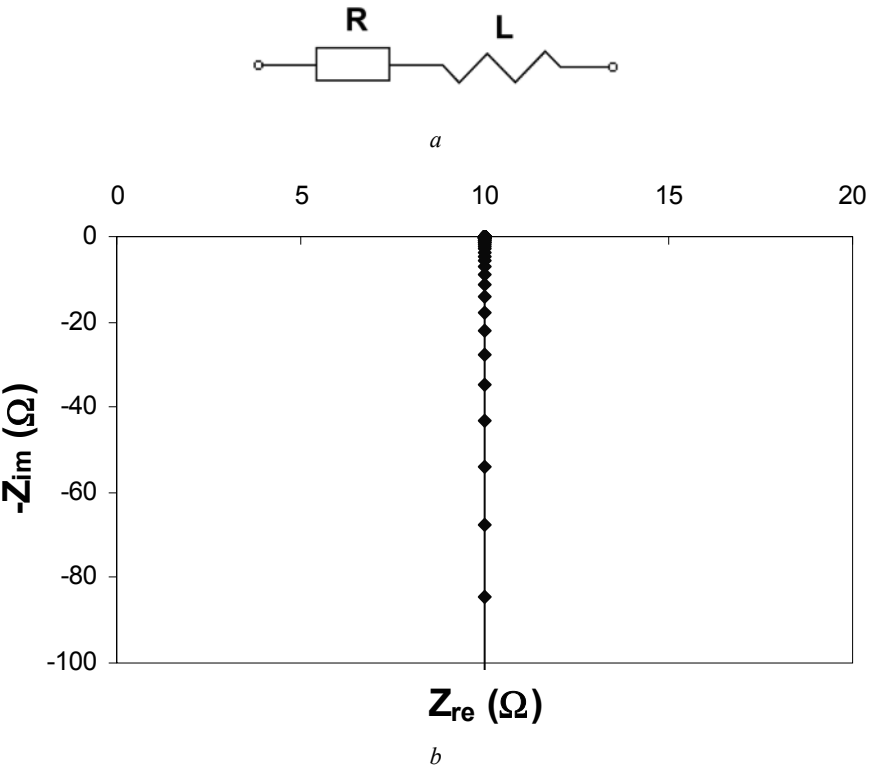

Figure 4.6. *a* Resistor and inductor in series (Model D5); *b* Nyquist plot of resistor and inductor in series connection over the frequency range 1 MHz to 1 mHz (Model D5: R = 10 Ω, L = 0.0001 H)

RL in Parallel

Figure 4.7*a* shows a resistor and an inductor in parallel connection. The impedance of the circuit in parallel is calculated as

$$Z(\omega) = [R^{-1} + (i\omega L)^{-1}]^{-1} \tag{4.30}$$

Then the impedance can be obtained:

$$Z(\omega) = \frac{R\omega^2 L^2 + iR^2\omega L}{\omega^2 L^2 + R^2} \tag{4.31}$$

From Equation 4.31, the simulated Nyquist plot is presented in Figure 4.7*b*.

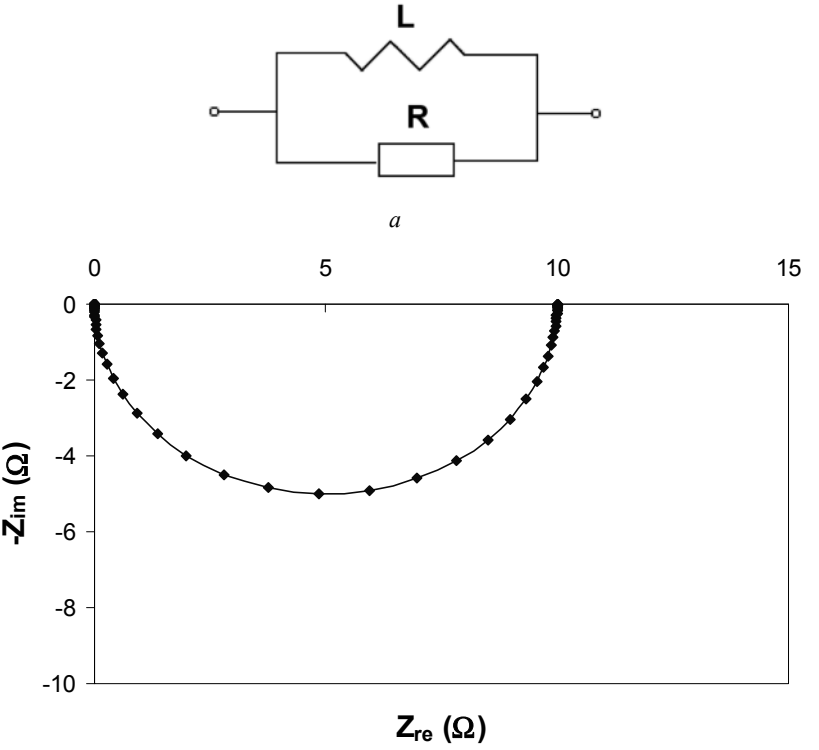

a

b

Figure 4.7. *a* Resistor and inductor in parallel (Model D6); *b* Nyquist plot of resistor and inductor in parallel over the frequency range 1 MHz to 1 mHz (Model D6: R = 10 Ω, L = 0.001 H)

4.2.1.4 Resistance and Warburg

Diffusion can create Warburg impedance. At high frequencies the Warburg impedance is small because the diffusing reactants don't have very far to move. At low frequencies the reactants have to diffuse farther, thereby increasing the Warburg impedance. The impedance for the connection of resistance and "infinite" Warburg impedance in series, depicted in Figure 4.8*a*, can be expressed as

$$Z(\omega) = R + \sigma\omega^{-1/2} - i\sigma\omega^{-1/2} \tag{4.32}$$

where σ is the Warburg coefficient.

Accordingly, the simulated Nyquist plot can be drawn as shown in Figure 4.8*b*. On a Nyquist plot, the infinite Warburg impedance appears as a diagonal line with a slope of 1. More examples can be found in Appendix D (Model D7).

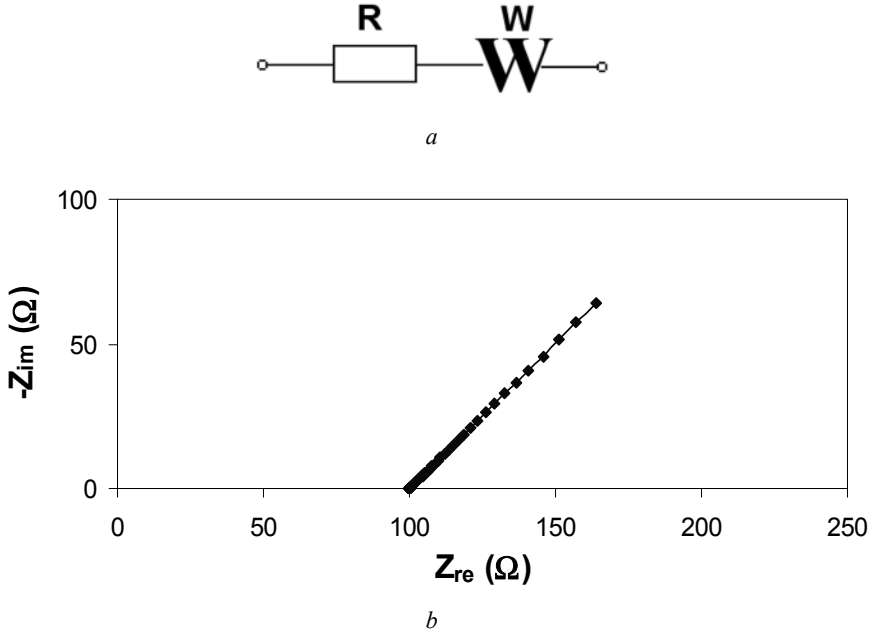

Figure 4.8. *a* Resistor and Warburg element in series (Model D7); *b* Simulated Nyquist plot of resistor and Warburg element in series over the frequency range 1 MHz to 1 mHz (Model D7: $R = 100\ \Omega$, $\sigma = 5\ \Omega s^{-1/2}$)

4.2.1.5 Resistance and Bounded Warburg

The Warburg impedance is only valid if the diffusion layer has an infinite thickness. If the diffusion layer is bounded, the impedance at lower frequencies no longer obeys Equation 4.32. Instead, the "bounded Warburg" element (BW) should be used to replace the Warburg. The impedance of the series connection between the resistance and the BW, shown in Figure 4.9*a*, can be calculated by adding their impedances:

$$Z(\omega) = R + \sigma(i\omega)^{-1/2} \tanh\left(\frac{i\omega R_0^2}{\sigma^2}\right)^{1/2} \tag{4.33}$$

where σ ($\Omega s^{-1/2}$) and R_0 (Ω) are two independent structural parameters. Using one of the solutions of the square root of i:

$$\sqrt{i} = -\left(\frac{\sqrt{2}}{2} + \frac{\sqrt{2}}{2} i\right) \tag{4.34}$$

and Euler's formula:

$$e^{ix} = \cos(x) + i\sin(x) \tag{4.35}$$

the total impedance can be separated into real and imaginary parts:

$$Z(\omega) = R - \frac{\frac{\sqrt{2}}{2}\sigma(e^{2K} + 2e^{K}\sin K - 1)}{\sqrt{\omega}(e^{2K} + 2e^{K}\cos K + 1)} - i\frac{\frac{\sqrt{2}}{2}\sigma(2e^{K}\sin K - e^{2K} + 1)}{\sqrt{\omega}(e^{2K} + 2e^{K}\cos K + 1)} \tag{4.36}$$

where $K = -\frac{R_0\sqrt{2\omega}}{\sigma}$.

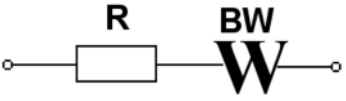

a

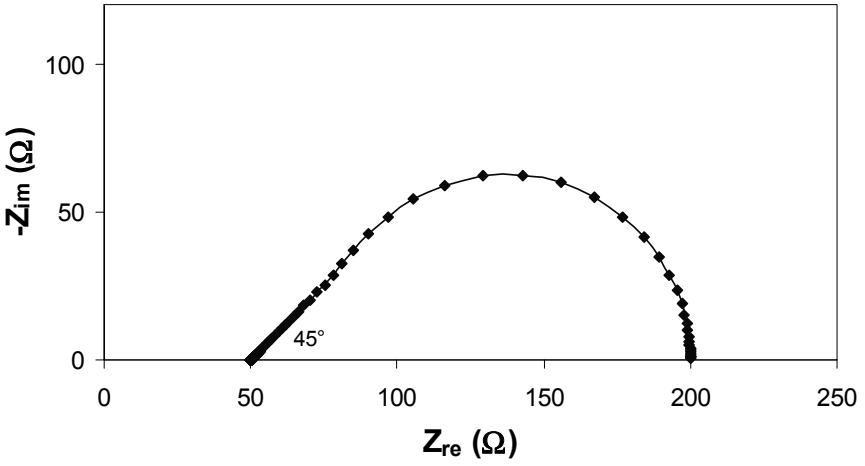

b

Figure 4.9. *a* Resistor and bounded Warburg in series (Model D8); *b* Nyquist plot of resistor and bounded Warburg in series over the frequency range 1 MHz to 1 mHz (Model D8: R = 50 Ω, R_0 = 150 Ω, σ = 100 $\Omega s^{-1/2}$)

The Nyquist plot is presented in Figure 4.9*b*. At high frequencies ($\omega \to \infty$), the curve intercepts the real axis at a value of R. At low frequencies ($\omega \to 0$), it intercepts the real axis at a value of $R+R_0$. Note that the bounded Warburg impedance is easily recognized from its Nyquist plot. At high frequencies, this circuit element looks like a traditional Warburg impedance and shows a 45° line on the Nyquist plot. At low frequencies, it looks like the semicircle of a Randles cell,

which will be discussed in Section 4.2.2. More examples are presented in Appendix D (Model D8).

4.2.1.6 Resistance and Bounded CPE

The impedance of the series connected resistance and bounded CPE element (BCPE), shown in Figure 4.10*a*, is calculated by adding their impedances:

$$Z(\omega) = R + Q^{-1}(i\omega)^{-n} \tanh R_0 Q(i\omega)^n \tag{4.37}$$

where Q, n, and R_0 are the structural parameters of the bounded CPE element.

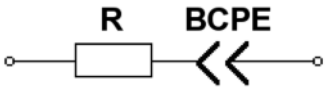

a

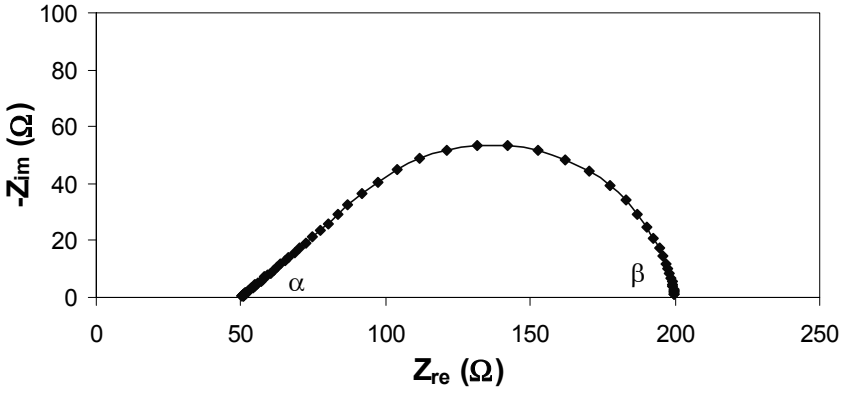

b

Figure 4.10. *a* Resistor and bounded CPE in series (Model D9); *b* Nyquist plot of resistor and bounded CPE in series over the frequency range 12 kHz to 0.1 mHz (Model D9: R = 50 Ω, R_0 = 150 Ω, Q = 0.01 $\Omega^{-1}s^{-0.45}$, n = 0.45)

Based on Euler's formula, the total impedance can be separated into real and imaginary parts:

$$Z(\omega) = R + \frac{cd + fg}{d^2 + g^2} - i\frac{cg - fd}{d^2 + g^2} \tag{4.38}$$

where

$$a = 2R_0 Q\omega^n \cos(\frac{\pi}{2}n),$$

$$b = 2R_0 Q\omega^n \sin(\frac{\pi}{2}n),$$
$$c = (e^a \cos b - 1)\cos(-\frac{\pi}{2}n) - e^a \sin b \sin(-\frac{\pi}{2}n),$$
$$d = Q\omega^n e^a \cos b + Q\omega^n,$$
$$f = (e^a \cos b - 1)\sin(-\frac{\pi}{2}n) + e^a \sin b \cos(-\frac{\pi}{2}n), \text{ and}$$
$$g = Q\omega^n e^a \sin b.$$

Figure 4.10*b* shows the Nyquist plot of the series connection between resistance and a bounded CPE. The angles of α and β are linked by the relationship

$$\beta = 2\alpha \tag{4.39}$$

where α and β are the diagram's asymptotes, corresponding to very high and very low frequencies, respectively. This relationship is also valid for the BW, which can be used to verify impedance behaviour related to the BW or BCPE. More examples are presented in Appendix D (Model D9).

4.2.2 Randles Cell

4.2.2.1 Regular Randles Cell

If a resistor is added in series with the parallel RC circuit, the overall circuit becomes the well-known Randles cell, as shown in Figure 4.11*a*. This is a model representing a polarizable electrode (or an irreversible electrode process), based on the assumptions that a diffusion limitation does not exist, and that a simple single-step electrochemical reaction takes place on the electrode surface. Thus, the Faradaic impedance can be simplified to a resistance, called the charge-transfer resistance. The single-step electrochemical reaction is described as

$$Ox + ne^- \underset{k_b}{\overset{k_f}{\longleftrightarrow}} Red \tag{4.40}$$

where k_f and k_b are the forward and backward redox reaction rate constants and n is the number of electrons. Thus, in Figure 4.11*a* the parameters should have direct physical meanings: R_1 represents the electrolyte resistance (R_{el}), R_2 represents the charge-transfer resistance (R_{ct}), and C represents the double-layer capacitance (C_{dl}). The total impedance can be calculated by

$$Z(\omega) = R_1 + \frac{1}{R_2^{-1} + i\omega C} \tag{4.41}$$

Thus,

$$Z(\omega) = R_1 + \frac{R_2}{1+\omega^2\tau^2} - i\frac{\omega R_2\tau}{1+\omega^2\tau^2} \tag{4.42}$$

where $\tau = R_2C$ is the time constant. The product R_2C (or $R_{ct}C_{dl}$) controls the distribution of the total current between the charging of the double layer and the electrochemical reaction. The Nyquist plot of the Randles cell in a complex-plane diagram is an ideal semicircle, as shown in Figure 4.11*b*. If $\omega \to \infty$, the intercept of the semicircle at the real axis equals R_1, and if $\omega \to 0$, the intercept equals the value $R_1 + R_2$. Complex impedance diagrams with variations in R_1 (or R_{el}) and R_2 (or R_{ct}) are given in Appendix D (Model D10).

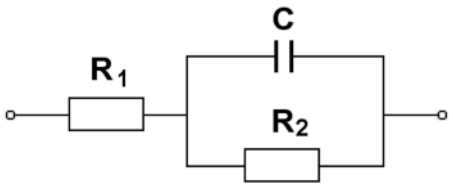

a

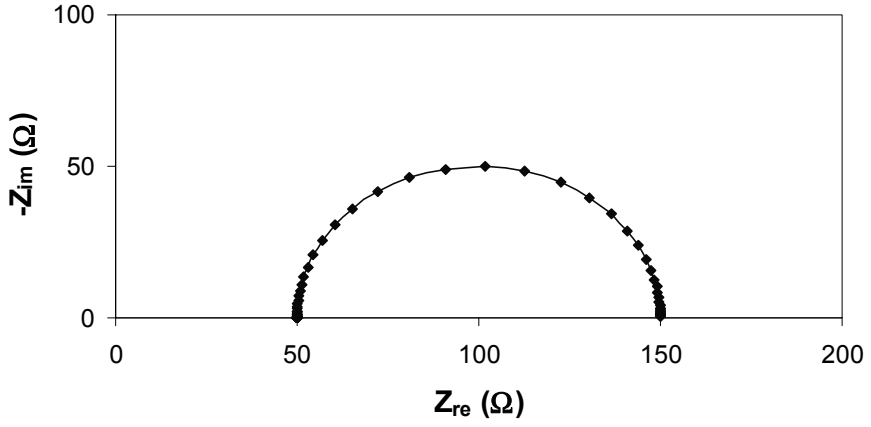

b

Figure 4.11. *a* Randles cell (Model D10); *b* Nyquist plot of Randles cell over the frequency range 1 MHz to 1 mHz (Model D10: R_1 = 50 Ω, R_2 = 100 Ω, C = 0.001 F)

For an electrochemical reaction (Equation 4.40) at open circuit potential, R_{ct} can be expressed as

$$R_{ct} = \frac{RT}{n_\alpha F i_0} \tag{4.43}$$

where i_0 is the exchange current density, n_α is the electron transfer number in the pseudo-rate-determining step, F is the Faradaic constant, and RT is the product of the molar gas constant and the absolute temperature. Thus, i_0 can be obtained from the diameter of the semicircle at open circuit potential. In an ideally reversible process, i_0 is extremely high, so R_{ct} tends to be zero and the total impedance turns into a simple resistance, R_{el}. In this case, the model is called an ideally non-polarizable electrode.

At an electrode potential (E), k_f and k_b can be expressed as Equations 4.44 and 4.45, respectively:

$$k_f = k_f^0 \exp(-\alpha nFE/RT) \tag{4.44}$$

$$k_b = k_b^0 \exp[(1-\alpha)nFE/RT] \tag{4.45}$$

and the exchange current density i_0 becomes

$$i_0 = nFk_f^0 c_O^* \exp(-\alpha nFE_{eq}/RT) = nFk_b^0 c_R^* \exp[(1-\alpha)nFE_{eq}/RT] \tag{4.46}$$

where: k_f^0 and k_b^0 are the forward and backward reaction rate constants, respectively, which are independent of E; α is the transfer coefficient; and c_O^* and c_R^* are the oxidant and reductant concentrations, respectively, at the equilibrium potential E_{eq}. The values of R_{ct} measured at different potentials depend on the rate of the reaction, which means that R_{ct} is potential dependent. At a working equilibrium potential, the value of R_{ct} is

$$R_{ct} = RT(n^2F^2A)^{-1}[\alpha k_f \bar{c}_O + (1-\alpha)k_b \bar{c}_R]^{-1} \tag{4.47}$$

where $\bar{c}_i = c_i(0, t \to \infty)$.

Modification to the Faradaic Resistance

The model of a polarizable electrode (simple Faradaic reaction) can be modified by replacement of R_{ct} with a CPE. The equivalent circuit is shown in Figure 4.12*a*.

The total impedance is calculated by adding the individual impedances of the elements:

$$Z(\omega) = R_{el} + \frac{1}{i\omega C_{dl} + Q\omega^n[\cos(\frac{\pi}{2}n) + i\sin(\frac{\pi}{2}n)]} \tag{4.48}$$

Thus, the real and imaginative parts are separated as

$$Z(\omega) = R_{el} + \frac{Q\omega^n \cos(\frac{\pi}{2}n) - i[\omega C_{dl} + Q\omega^n \sin(\frac{\pi}{2}n)]}{[Q\omega^n \cos(\frac{\pi}{2}n)]^2 + [\omega C_{dl} + Q\omega^n \sin(\frac{\pi}{2}n)]^2} \tag{4.49}$$

The complex-plane impedance diagram is given in Figure 4.12*b*. At both high and medium frequencies the complex-plane impedance is characterized by a well pronounced semicircle, while at the low-frequency range a tail appears. This tail's shape is strongly dependent on the value of the CPE exponent, as can be seen in Appendix D (Model D11).

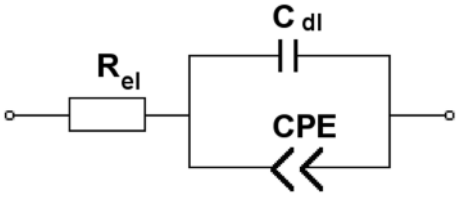

a

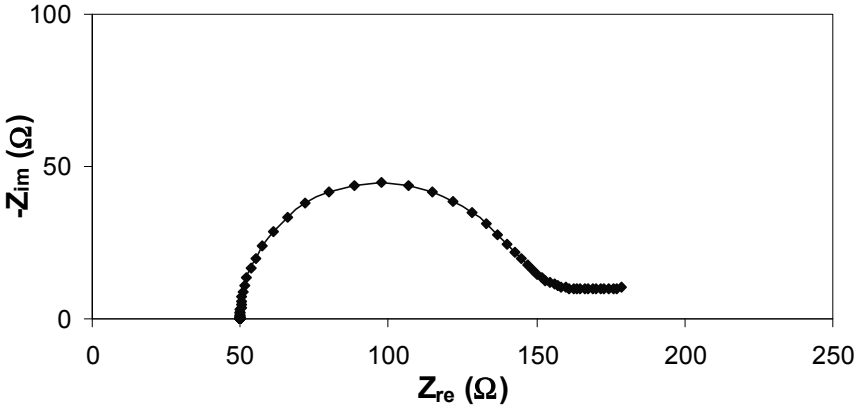

b

Figure 4.12. *a* Randles cell with R_{ct} replaced by CPE (Model D11); *b* Nyquist plot of Randles cell with R_{ct} replaced by CPE over the frequency range 1 MHz to 1 mHz (Model D11: R_{el} = 50 Ω, C_{dl} = 0.001 F, n = 0.05, Q = 0.01 $\Omega^{-1}s^{-0.05}$)

Modified Polarizable Electrode with Capacitive CPE

Figure 4.13*a* shows the most commonly applied model, which represents a polarizable electrode (simple Faradaic reaction) with replacement of the double-layer capacitance by a CPE. All the parameters in the model have direct physical meanings: R_{el} represents the electrolyte resistance and R_{ct} represents the charge-transfer resistance. The CPE describes the depression of the semicircle, which is often observed in real systems. The total impedance can be obtained as follows:

$$Z(\omega) = R_{el} + \frac{1}{R_{ct}^{-1} + Q\omega^n(\cos(\frac{\pi}{2}n) + i\sin(\frac{\pi}{2}n))} \tag{4.50}$$

$$Z(\omega) = R_{el} + \frac{R_{ct} + QR_{ct}^2\omega^n\cos(\frac{\pi}{2}n)}{1 + 2QR_{ct}\omega^n\cos(\frac{\pi}{2}n) + Q^2R_{ct}^2\omega^{2n}} - i\frac{QR_{ct}^2\omega^n\sin(\frac{\pi}{2}n)}{1 + 2QR_{ct}\omega^n\cos(\frac{\pi}{2}n) + Q^2R_{ct}^2\omega^{2n}} \tag{4.51}$$

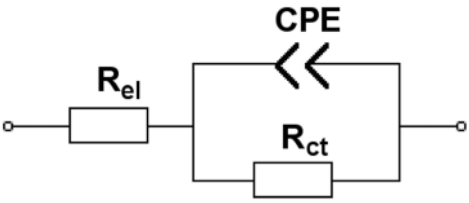

a

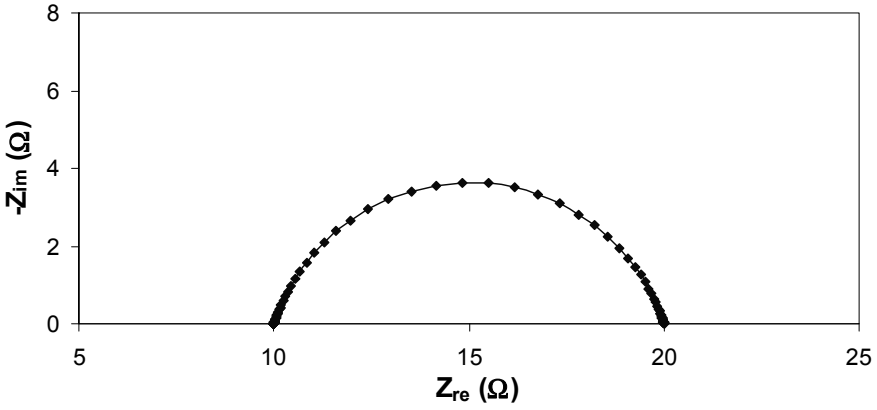

b

Figure 4.13. *a* Randles cell with capacitor replaced by CPE (Model D12); *b* Nyquist plot of Randles cell with capacitor replaced by CPE, over the frequency range 1 MHz to 1 mHz (Model D12: R_{el} = 10 Ω, R_{ct} = 10 Ω, n = 0.8, Q = 0.01 $\Omega^{-1}s^{-0.8}$)

The Nyquist plot in a complex-plane diagram of the Randles cell with capacitor replaced by a CPE is a depressed semicircle, as shown in Figure 4.13*b*. If $\omega \to \infty$, the intercept of the depressed semicircle at the real axis equals R_{el}, and if $\omega \to 0$, the intercept equals the value of $R_{el} + R_{ct}$. The deviation of the n value describes the

deformation of the ideal semicircle in the complex-plane plot. The effect of n on the diagram is shown in Appendix D (Model D12).

4.2.2.2 More Modifications to the Randles Cell

If an extra element is added to a Randles cell, a modified Randles model can be formed.

Adsorption Model

As shown in Figure 4.14*a*, an extra capacitor is added in series with R_{ct}, which assumes that the species transferred through the double layer are adsorbed on the electrode surface. This adsorption model represents the accumulation of species in their adsorbed state. The total impedance can be calculated by

$$Z(\omega) = R_{el} + [i\omega C_{dl} + (R_{ct} + (i\omega C_{ad})^{-1})^{-1}]^{-1}] \tag{4.52}$$

Thus, the impedance can be expressed with real and imaginative parts separated as

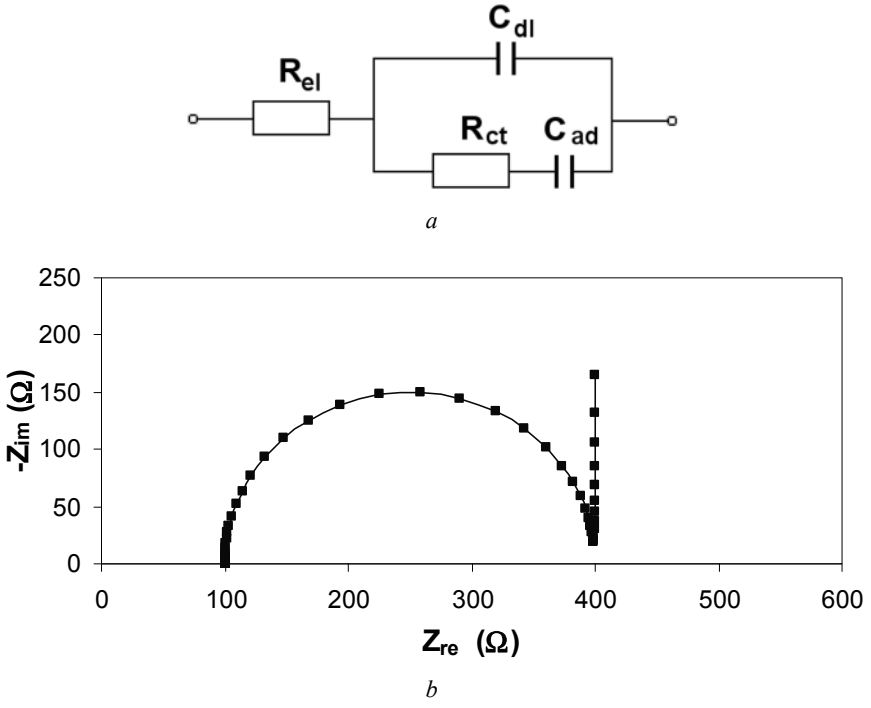

Figure 4.14. *a* Randles cell with an extra capacitor in series with R_{ct} (Model D13); *b* Nyquist plot of Randles cell with an extra capacitor in series with R_{ct} over the frequency range 1 MHz to 1 mHz (Model D13: R_{el} = 100 Ω, R_{ct} = 300 Ω, C_{dl} = 0.001 F, C_{ad} = 1 F)

$$Z(\omega) = R_{el} + \frac{(R_{ct}^2\omega^2 C_{ad}^2 + 1)(\omega^2 C_{ad}^2 R_{ct})}{\omega^4 C_{ad}^4 R_{ct}^2 + (\omega C_{ad} + \omega C_{dl} + R_{ct}^2\omega^3 C_{ad}^2 C_{dl})^2}$$
$$-i\frac{(R_{ct}^2\omega^2 C_{ad}^2 + 1)(\omega C_{ad} + \omega C_{dl} + R_{ct}^2\omega^3 C_{ad}^{\ 2} C_{dl})}{\omega^4 C_{ad}^4 R_{ct}^2 + (\omega C_{ad} + \omega C_{dl} + R_{ct}^2\omega^3 C_{ad}^2 C_{dl})^2} \tag{4.53}$$

or

$$Z(\omega) = R_{el} + \frac{\omega^2 R_{ct} C_{ad}(C_{ad} + C_{dl}) - \omega^2 C_{dl} C_{ad} R_{ct}}{\omega^4 C_{ad}^2 C_{ad}^2 R_{ct}^2 + \omega^2 (C_{ad} + C_{dl})^2}$$
$$-i\frac{\omega^3 C_{ad}^2 C_{dl} R_{ct}^2 + \omega(C_{dl} + C_{ad})}{\omega^4 C_{ad}^2 C_{dl}^2 R_{ct}^2 + \omega^2 (C_{ad} + C_{dl})^2} \tag{4.54}$$

Therefore, the Nyquist plot can be simulated as shown in Figure 4.14*b*. The deformation of the adsorption model caused by the mixing of the parameters is plotted in Appendix D (Model D13).

Diffusion with Infinite Thickness

Figure 4.15*a* shows the structure of a modified Randles cell. This circuit models a cell in which polarization is due to a combination of kinetic and diffusion processes with infinite thickness.

The total impedance can be calculated by

$$Z(\omega) = R_{el} + \left\{ i\omega C_{dl} + [R_{ct} + \sigma\omega^{-1/2} - i\sigma\omega^{-1/2}]^{-1} \right\}^{-1} \tag{4.55}$$

Then, the two parts are separated as

$$Z(\omega) = R_{el} + \frac{(R_{ct}^{\ 2} + 2R_{ct}\sigma\omega^{-1/2} + 2\sigma^2\omega^{-1})(R_{ct} + \sigma\omega^{-1/2})}{(R_{ct} + \sigma\omega^{-1/2})^2 + (R_{ct}^2\omega C_{dl} + 2R_{ct}\sigma C_{dl}\omega^{1/2} + 2\sigma^2 C_{dl} + \sigma\omega^{-1/2})^2}$$
$$-i\frac{(R_{ct}^2 + 2R_{ct}\sigma\omega^{-1/2} + 2\sigma^2\omega^{-1})(R_{ct}^2\omega C_{dl} + 2R_{ct}\sigma C_{dl}\omega^{1/2} + 2\sigma^2 C_{dl} + \sigma\omega^{-1/2})}{(R_{ct} + \sigma\omega^{-1/2})^2 + (R_{ct}^2\omega C_{dl} + 2R_{ct}\sigma C_{dl}\omega^{1/2} + 2\sigma^2 C_{dl} + \sigma\omega^{-1/2})^2} \tag{4.56}$$

or

$$Z(\omega) = R_{el} + \frac{(R_{ct} + \sigma\omega^{-1/2})(\sigma\omega^{1/2} C_{dl} + 1) - \sigma\omega^{1/2} C_{dl}(R_{ct} + \sigma\omega^{-1/2})}{(\sigma\omega^{1/2} C_{dl} + 1)^2 + \omega^2 C_{dl}^2 (R_{ct} + \sigma\omega^{-1/2})^2}$$
$$-i\frac{\sigma\omega^{-1/2}(\sigma\omega^{1/2} C_{dl} + 1) + \omega C_{dl}(R_{ct} + \sigma\omega^{-1/2})^2}{(\sigma\omega^{1/2} C_{dl} + 1)^2 + \omega^2 C_{dl}^{\ 2}(R_{ct} + \sigma\omega^{-1/2})^2} \tag{4.57}$$

Figure 4.15*b* shows the simulated Nyquist plot of the modified Randles cell with a combination of kinetic and diffusion processes plus infinite thickness. As in the example, the Warburg coefficient is assumed to be σ = 5 $\Omega s^{-1/2}$. Other

assumptions are: R_{el} = 100 Ω, R_{ct} = 200 Ω, and C_{dl} = 0.0001 F. Note that the slope approaches 45° at low frequencies. Impedance diagrams with variations in the parameters are included in Appendix D (Model D14).

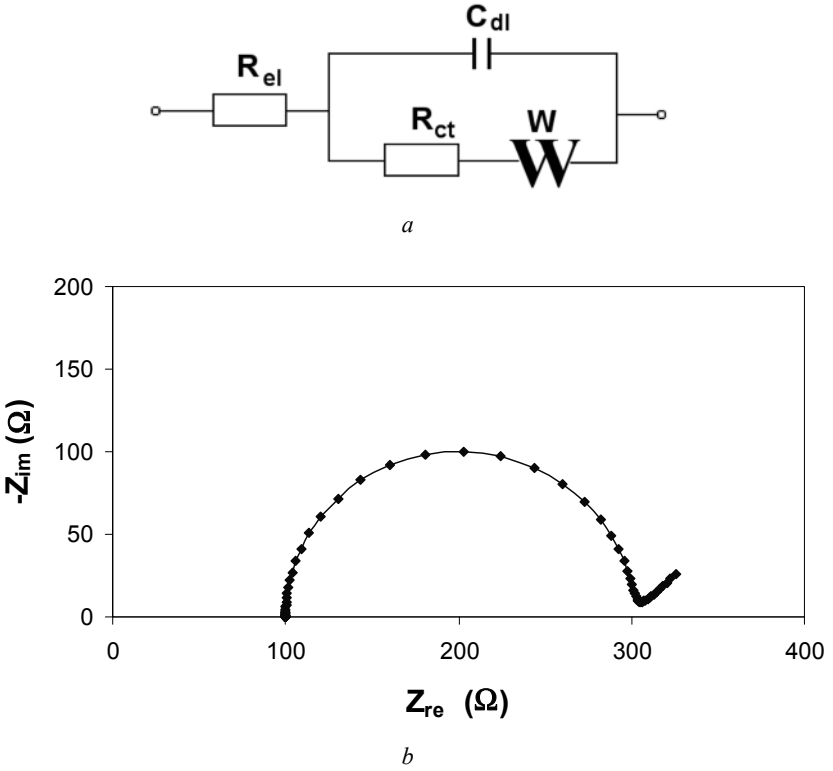

Figure 4.15. *a* Modified Randles cell with a Warburg element in series with R_{ct} (Model D14); *b* Nyquist plot of Randles cell with a Warburg element in series with R_{ct} over the frequency range 1 MHz to 1 mHz (Model D14: R_{el} = 100 Ω, R_{ct} = 200 Ω, C_{dl} = 0.0001 F, σ = 5 $\Omega s^{-1/2}$)

For a porous electrode such as is found in a fuel cell, since the capacitance caused by double-layer charging is distributed along the length of the pores, the conventional double-layer capacitance is often replaced by a CPE. Then the equivalent circuit in Figure 4.15 can be modified to that shown in Figure 4.16*a*.

The total impedance is calculated by

$$Z(\omega) = R_{el} + \left\{ Q\omega^n [\cos(\frac{\pi}{2} n) + i \sin(\frac{\pi}{2} n)] + [R_{ct} + \sigma\omega^{-1/2} - i\sigma\omega^{-1/2}]^{-1} \right\}^{-1} \tag{4.58}$$

Then we have

$$Z(\omega) = R_{el} + \frac{c(ac+bd+1)+d(ad-bc)-i[d(ac+bd+1)-c(ad-bc)]}{(ac+bd+1)^2+(ad-bc)^2} \tag{4.59}$$

where $a = Q\omega^n \cos(\frac{\pi}{2}n)$, $b = Q\omega^n \sin(\frac{\pi}{2}n)$, $c = R_{ct} + \sigma\omega^{-1/2}$, and $d = \sigma\omega^{-1/2}$.

Figure 4.16*b* shows the simulated Nyquist plot of the modified Randles cell shown in Figure 4.16*a*. Impedance diagrams with variations in the CPE parameters are included in Appendix D (Model D15).

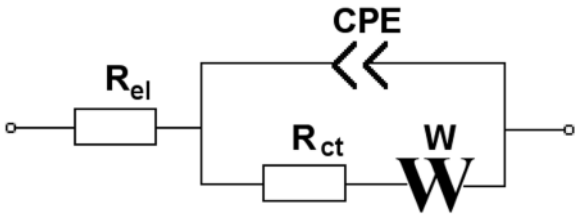

a

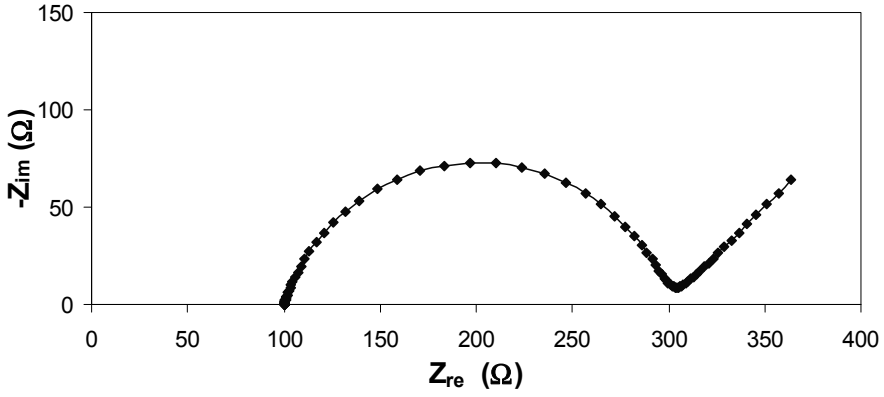

b

Figure 4.16. *a* Modified equivalent circuit of Figure 4.15*a* with CPE in place of capacitor (Model D15); *b* Nyquist plot of circuit, Figure 4.16*a* over the frequency range 1 MHz to 1 mHz (Model D15: R_{el} = 100 Ω, R_{ct} = 200 Ω, Q = 0.0001 $\Omega^{-1}s^{-0.8}$, σ = 5 $\Omega s^{-1/2}$, n = 0.8)

Modified Model to Include Non-Uniform Adsorption

This model is a result of modifying the adsorption model by taking into account the irregularities of C_{ad}. Replacing C_{ad} with CPE represents the non-uniform behaviour of the adsorbed species. The equivalent circuit is shown in Figure 4.17*a*.

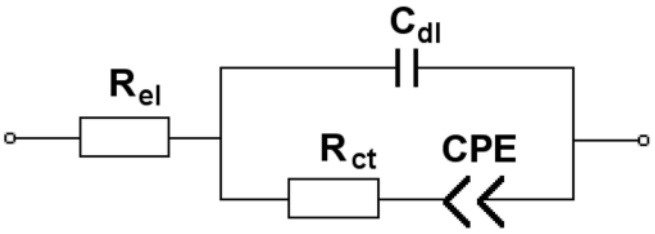

a

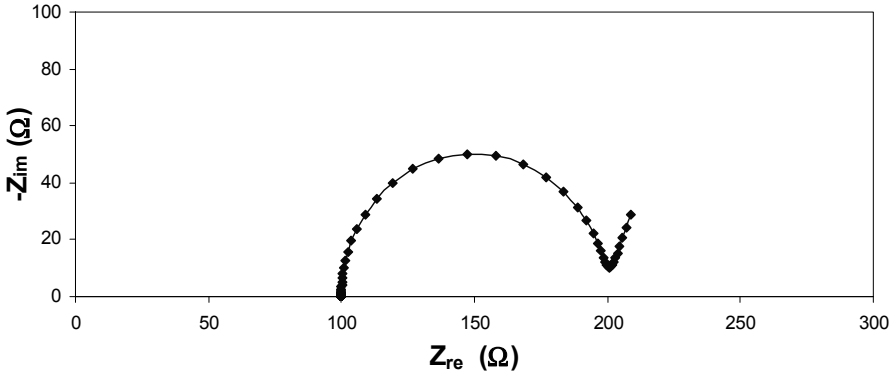

b

Figure 4.17. *a* Modified Randles cell with a CPE in series with R_{ct} (Model D16); *b* Nyquist plot of modified Randles cell having an extra CPE in series with R_{ct}, over the frequency range 1 MHz to 1 mHz (Model D16: R_{el} = 100 Ω, R_{ct} = 100 Ω, C_{dl} = 0.01 F, Q = 2 $\Omega^{-1}s^{0.8}$, n = 0.8)

The total impedance can be calculated by

$$Z(\omega) = R_{el} + [i\omega C_{dl} + [R_{ct} + Q^{-1}\omega^{-n}\cos(-\frac{\pi}{2}n) + iQ^{-1}\omega^{-n}\sin(-\frac{\pi}{2}n)]^{-1}]^{-1} \quad (4.60)$$

Then the two parts are separated:

$$Z(\omega) = R_{el} + \frac{(R_{ct}+a)(1-\omega C_{dl}) + b\omega C_{dl}(R_{ct}+a)}{(1-\omega b C_{dl})^2 + \omega^2 C_{dl}^2 (R_{ct}+a)^2}$$
$$-i\frac{\omega C_{dl}(R_{ct}+a)^2 - b(1-\omega C_{dl})}{(1-\omega b C_{dl})^2 + \omega^2 C_{dl}^2 (R_{ct}+a)^2} \quad (4.61)$$

where $a = Q^{-1}\omega^{-n}\cos(-\frac{\pi}{2}n)$, $b = Q^{-1}\omega^{-n}\sin(-\frac{\pi}{2}n)$.

Or:

$$Z(\omega) = R_{el} +$$

$$\frac{[Q^2\omega^{2n}R_{ct}^2 + 2Q\omega^n R_{ct}\cos(-\frac{\pi}{2}n) + 1][Q^2\omega^{2n}R_{ct} + Q\omega^n\cos(-\frac{\pi}{2}n)]}{[Q^2\omega^{2n}R_{ct} + Q\omega^n\cos(-\frac{\pi}{2}n)]^2 + [Q^2\omega^{2n+1}C_{dl}R_{ct}^2 + 2Q\omega^{n+1}C_{dl}R_{ct}\cos(-\frac{\pi}{2}n) + \omega C_{dl} - Q\omega^n\sin(-\frac{\pi}{2}n)]^2}$$

$$-i\frac{[Q^2\omega^{2n}R_{ct}^2 + 2Q\omega^n R_{ct}\cos(-\frac{\pi}{2}n) + 1][Q^2\omega^{2n+1}C_{dl}R_{ct}^{\ 2} + 2Q\omega^{n+1}C_{dl}R_{ct}\cos(-\frac{\pi}{2}n) + \omega C_{dl} + Q\omega^n\sin(-\frac{\pi}{2}n)]}{[Q^2\omega^{2n}R_{ct} + Q\omega^n\cos(-\frac{\pi}{2}n)]^2 + [Q^2\omega^{2n+1}C_{dl}R_{ct}^2 + 2Q\omega^{n+1}C_{dl}R_{ct}\cos(-\frac{\pi}{2}n) + \omega C_{dl} - Q\omega^n\sin(-\frac{\pi}{2}n)]^2} \tag{4.62}$$

Figure 4.17*b* shows the simulated Nyquist plot of a modified adsorption model with an extra CPE in the Randles circuit. This modification of the adsorption model strongly influences the low-frequency shape of the complex plane impedance diagram. More examples with variations on the CPE exponent are presented in Appendix D (Model D16).

Bounded Randles Cell

The following model is a bounded Randles cell also accounting for a linear but finite diffusion, with a homogeneous layer of finite thickness. The structure of the model is shown in Figure 4.18*a*. The corresponding impedance is

$$Z(\omega) = R_{el} + [i\omega C_{dl} + (R_{ct} + \sigma(i\omega)^{-1/2}\tanh\left(\frac{i\omega R_0^2}{\sigma^2}\right)^{1/2})^{-1}]^{-1} \tag{4.63}$$

Based on the calculated result of Model D8 (Equation 4.36), the total impedance can be expressed as

$$Z(\omega) = R_{el} + [i\omega C_{dl} + (R_{ct} - \frac{a+bi}{d})^{-1}]^{-1} \tag{4.64}$$

where $a = \frac{\sqrt{2}}{2}\sigma(e^{2K} + 2e^K\sin K - 1)$, $b = \frac{\sqrt{2}}{2}\sigma(2e^K\sin K - e^{2K} + 1)$, and $d = \sqrt{\omega}(e^{2K} + 2e^K\cos K + 1)$. Then the real and imaginative parts are separated as

$$Z(\omega) = R_{el} + \frac{(R_{ct}d - a)(d + b\omega C_{dl}) + b\omega C_{dl}(R_{ct}d - a)}{(d + b\omega C_{dl})^2 + [\omega C_{dl}(R_{ct}d - a)]^2}$$
$$-i\frac{b(d + b\omega C_{dl}) + (R_{ct}d - a)^2\omega C_{dl}}{(d + b\omega C_{dl})^2 + [\omega C_{dl}(R_{ct}d - a)]^2} \tag{4.65}$$

or

$$Z(\omega) = R_{el} + \frac{[(R_{ct}d - a)^2 + b^2](d^2R_{ct} - da)}{(d^2R_{ct} - da)^2 + [\omega C_{dl}(R_{ct}d - a)^2 + \omega C_{dl}b^2 + db]^2}$$

$$-i\frac{[(R_{ct}d-a)^2+b^2][\omega C_{dl}(R_{ct}d-a)^2+\omega C_{dl}b^2+db]}{(d^2R_{ct}-da)^2+[\omega C_{dl}(R_{ct}d-a)^2+\omega C_{dl}b^2+db]^2} \tag{4.66}$$

The complex-plane impedance diagram of the bounded Randles cell is given in Figure 4.18*b*. In this example, the parameters of the forward and backward reactions and diffusion coefficients are assumed to be equal. Impedance diagrams with variations in the parameters are presented in Appendix D (Model D17).

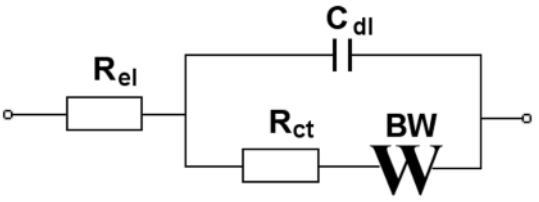

a

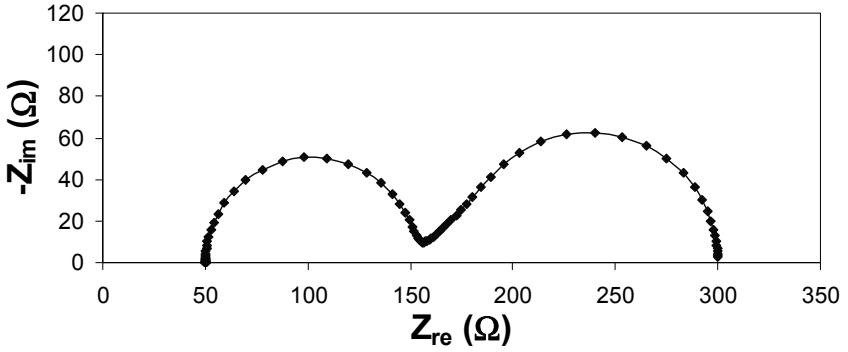

b

Figure 4.18. *a* Modified Randles cell having a bounded Warburg in series with R_{ct} (Model D17); *b* Nyquist plot of modified Randles cell having a bounded Warburg element in series with R_{ct}, over the frequency range 1 MHz to 1 mHz (Model D17: R_{el} = 50 Ω, R_{ct} = 100 Ω, C_{dl} = 0.00001 F, σ = 50 Ωs$^{-1/2}$, R_0 = 150 Ω)

For the porous electrode, the conventional double-layer capacitance is often replaced by a CPE. Then the circuit in Figure 4.18*a* can be changed to that shown in Figure 4.19*a*

The total impedance is calculated by

$$Z(\omega)=R_{el}+\{Q\omega^n[\cos(\frac{\pi}{2}n)+i\sin(\frac{\pi}{2}n)]+[R_{ct}+\sigma(i\omega)^{-1/2}\tanh\left(\frac{i\omega R_0^2}{\sigma^2}\right)^{1/2}]^{-1}\}^{-1} \tag{4.67}$$

Based on the calculation result of Model D8:

$$Z(\omega) = R_{el} + \{Q\omega^n[\cos(\frac{\pi}{2}n) + i\sin(\frac{\pi}{2}n)] + (R_{ct} - \frac{a+bi}{d})^{-1}\}^{-1} \tag{4.68}$$

where

$K = -\frac{R_0\sqrt{2\omega}}{\sigma}$, $a = \frac{\sqrt{2}}{2}\sigma(e^{2K} + 2e^K \sin K - 1)$, $b = \frac{\sqrt{2}}{2}\sigma(2e^K \sin K - e^{2K} + 1)$,
$d = \sqrt{\omega}(e^{2K} + 2e^K \cos K + 1)$.

Then we have

$$Z(\omega) = R_{el} + \frac{f(uf + bv + d) - b(vf - ub) - i[b(uf + bv + d) + f(vf - ub)]}{(uf + bv + d)^2 + (vf - ub)^2} \tag{4.69}$$

where $u = Q\omega^n \cos(\frac{\pi}{2}n)$, $v = Q\omega^n \sin(\frac{\pi}{2}n)$, and $f = dR_{ct} - a$.

Figure 4.19*b* shows the simulated Nyquist plot of the modified Randles cell shown in Figure 4.19*a*. Impedance diagrams with variations in the CPE parameters are included in Appendix D (Model D18).

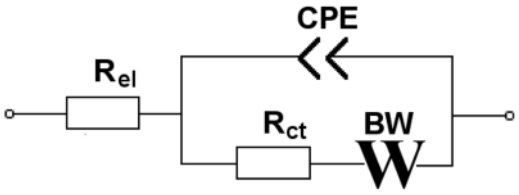

a

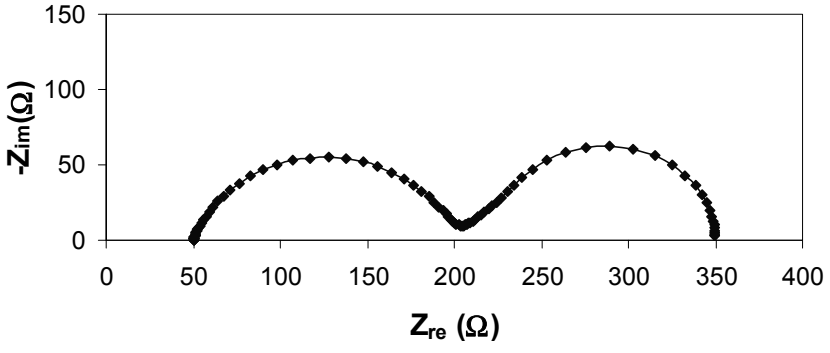

b

Figure 4.19. *a* Modified Randles cell of Model 17 with CPE in place of capacitor (Model D18); *b* Nyquist plot of modified Randles cell depicted in Figure 4.19*a*, over the frequency range 1 MHz to 1 mHz (Model D18: R_{el} = 50 Ω, R_{ct} = 150 Ω, Q = 0.00001 $\Omega^{-1}s^{0.8}$, n = 0.8, σ = 50 $\Omega s^{-1/2}$, R_0 = 150 Ω)

Modified Bounded Randles Cell

If there are deviations from the ideal semi-infinite linear diffusion process, the bounded Randles cell can also be modified by replacing the Warburg impedance with a CPE. The structure of the model is shown in Figure 4.20*a*. This modification is applied when the transport limitations appear in a layer of finite thickness.

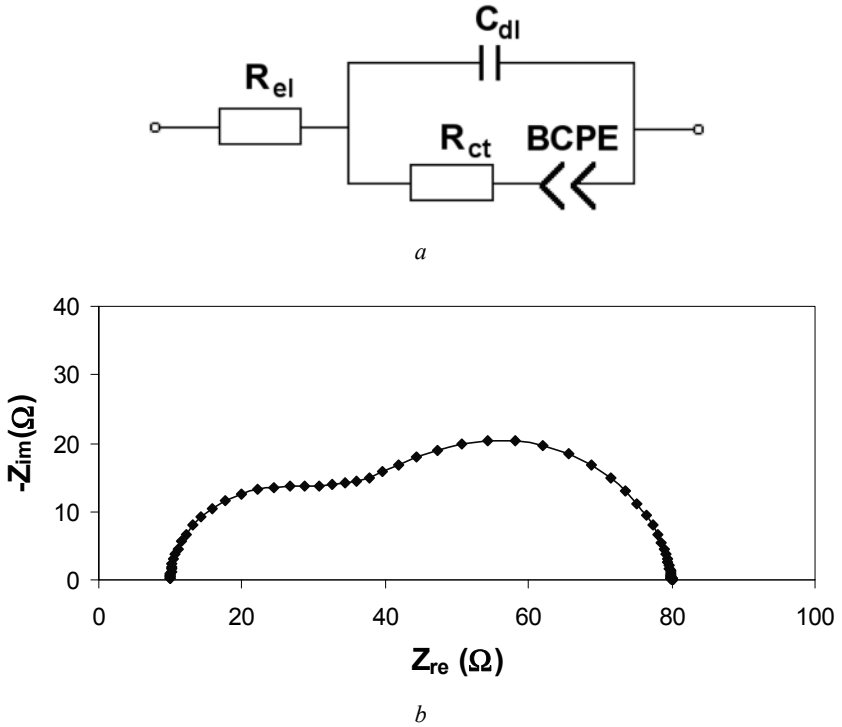

Figure 4.20. *a* Equivalent circuit of modified Randles cell with bounded CPE in series with R_{ct} (Model D19); *b* Nyquist plot of modified Randles cell having a bounded CPE in series with R_{ct} over the frequency range 6 kHz to 1 mHz (Model D19: R_{el} = 10 Ω, R_{ct} = 20 Ω, R_0 = 50 Ω, Q = 0.01 $\Omega^{-1}s^{0.45}$, C_{dl} = 0.0001 F)

The total impedance can be calculated by

$$Z(\omega) = R_{el} + [i\omega C_{dl} + (R_{ct} + Q^{-1}(i\omega)^{-n} \tanh R_0 Q(i\omega)^n)^{-1}]^{-1} \tag{4.70}$$

Based on the impedance of Model D9 (Equation 4.38):

$$Z(\omega) = R_{el} + [i\omega C_{dl} + (R_{ct} + \frac{cd + fg}{d^2 + g^2} - i\frac{cg - fd}{d^2 + g^2})^{-1}]^{-1} \tag{4.71}$$

where

$$a = 2R_0 Q\omega^n \cos(\frac{\pi}{2}n),$$
$$b = 2R_0 Q\omega^n \sin(\frac{\pi}{2}n),$$
$$c = (e^a \cos b - 1)\cos(-\frac{\pi}{2}n) - e^a \sin b \sin(-\frac{\pi}{2}n),$$
$$d = Q\omega^n e^a \cos b + Q\omega^n,$$
$$f = (e^a \cos b - 1)\sin(-\frac{\pi}{2}n) + e^a \sin b \cos(-\frac{\pi}{2}n), \text{ and}$$
$$g = Q\omega^n e^a \sin b.$$

Assuming $s = d^2 + g^2$, $u = cd + fg$, and $v = cg - fd$:

$$Z(\omega) = R_{el} + \frac{[(R_{ct}s+u)^2 + v^2](s^2 R_{ct} + su)}{(s^2 R_{ct} + su)^2 + [\omega C_{dl}(R_{ct}s+u)^2 + \omega C_{dl} v^2 + sv]^2} - i\frac{[(R_{ct}s+u)^2 + v^2][\omega C_{dl}(R_{ct}s+u)^2 + \omega C_{dl} v^2 + sv]}{(s^2 R_{ct} + su)^2 + [\omega C_{dl}(R_{ct}s+u)^2 + \omega C_{dl} v^2 + sv]^2} \quad (4.72)$$

The complex-plane impedance diagram of the modified bounded Randles cell is given in Figure 4.20*b*. If distortions in the double-layer capacitance are assumed, a CPE can be used to replace C_{dl}. More examples of this modified bounded Randles cell can be found in Appendix D (Model D19).

4.2.3 Structural Circuits

4.2.3.1 Maxwell's Structure

Maxwell's structure is often used for modelling parallel processes. As seen in Figure 4.21, Maxwell's structure is basically RC circuits in parallel. The concept of admittance is useful because the overall admittance of parallel elements is simply the sum of the individual admittances, i.e.,

$$Y(\omega) = \sum Y_k(\omega) \quad (4.73)$$

where $Y(\omega)$ denotes the total admittance and $Y_k(\omega)$ denotes the admittances of the individual branches. Therefore, the impedance of Maxwell's structure, presented in Figure 4.21, can be expressed as

$$Z(\omega) = 1/Y(\omega) = \left\{ R_1^{-1} + i\omega C_1 + \sum_{k=2}^{n} \left[R_k + (i\omega C_k)^{-1} \right]^{-1} \right\}^{-1} \quad (4.74)$$

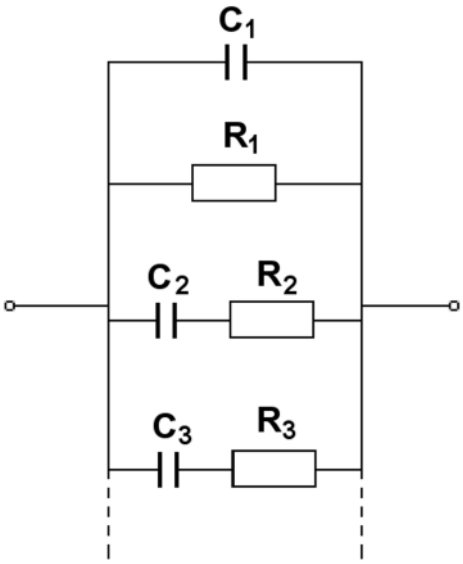

Figure 4.21. Maxwell's structure

A simple example of Maxwell's structure with two parallel processes is shown in Figure 4.22*a*.

The total impedance can be calculated by

$$Z(\omega) = [i\omega C_1 + R_1^{-1} + [(i\omega C_2)^{-1} + R_2]^{-1} + [(i\omega C_3)^{-1} + R_3]^{-1}]^{-1} \tag{4.75}$$

Thus, it can be separated into two parts:

$$Z(\omega) = \frac{R_1 ab[ab + R_1 b\omega^2 C_2^2 R_2 + R_1 a\omega^2 C_3^2 R_3]}{[ab + R_1 b\omega^2 C_2^2 R_2 + R_1 a\omega^2 C_3^2 R_3]^2 + [R_1 ab\omega C_1 + R_1 b\omega C_2 + R_1 a\omega C_3]^2}$$
$$-i\frac{R_1 ab[R_1 ab\omega C_1 + R_1 b\omega C_2 + R_1 a\omega C_3]}{[ab + R_1 b\omega^2 C_2^2 R_2 + R_1 a\omega^2 C_3^2 R_3]^2 + [R_1 ab\omega C_1 + R_1 b\omega C_2 + R_1 a\omega C_3]^2} \tag{4.76}$$

where $a = 1 + (\omega C_2 R_2)^2$ and $b = 1 + (\omega C_3 R_3)^2$.

The complex-plane impedance diagram of this simple Maxwell structure is presented in Figure 4.22*b*. More examples of this model are provided in Appendix D (Model D20).

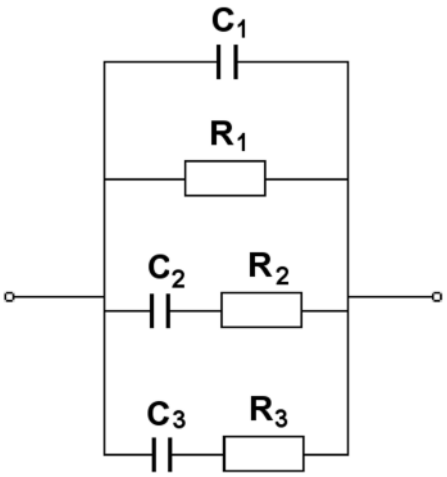

a

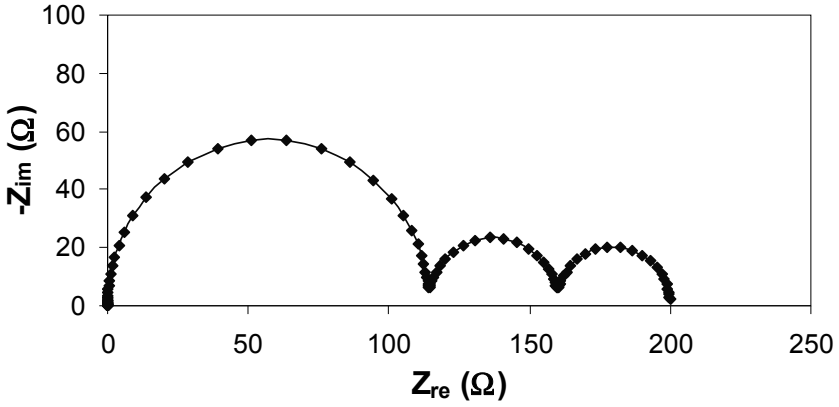

b

Figure 4.22. *a* Simple example of Maxwell's structure with two parallel processes (Model D20); *b* Nyquist plot of a simple Maxwell structure over the frequency range 1 MHz to 1 mHz (Model D20: R_1 = 200 Ω, C_1 = 0.000001 F, R_2 = 400 Ω, C_2 = 0.0001 F, R_3 = 800 Ω, C_3 = 0.01 F)

4.2.3.2 Voigt's Structure

Voigt's structure consists of a number of RC circuits in series, as shown in Figure 4.23. This structure is often applied to the description of solid electrochemical cells. It is known that the electrode/electrolyte interface of a solid electrochemical cell may not have perfect contact between two smooth and clean solid surfaces, and the electrode reaction involves species not only from the electrode and electrolyte but also from the gas phase. Sometimes, the electrolyte resistance produces two arcs in the very high frequency range, corresponding to charge transport through the bulk phase and at the grain boundaries. For polycrystalline

materials with uniform composition of the grains and grain boundaries, only one semicircle will show.

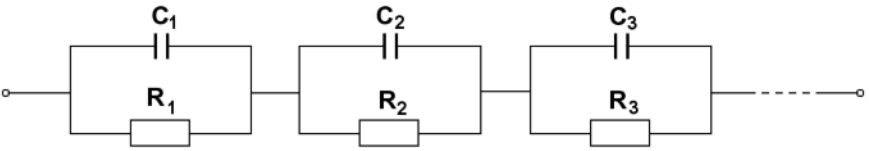

Figure 4.23. Voigt's structure

The overall impedance of elements in series can be calculated by the sum of the individual impedances of the branch, i.e.,

$$Z(\omega) = \sum Z_k(\omega) \tag{4.77}$$

Thus, the impedance with Voigt's structure, which is used to describe the impedance of solid-state bulk samples, is expressed as

$$Z(\omega) = \sum_{k=1}^{n} (R_k^{-1} + i\omega C_k)^{-1} \tag{4.78}$$

Two-RC Circuits

The bulk and grain boundary behaviour of a polycrystalline electroceramic material can be described by a Voigt structure consisting of two RC circuits. This simple Voigt structure is shown in Figure 4.24*a*. The parameters of this model all have direct physical meanings: $R_1 = R_b$, $C_1 = C_b$, $R_2 = R_{gb}$, and $C_2 = C_{gb}$, where *b* refers to bulk and *gb* refers to grain boundary.

The impedance is calculated as follows

$$Z_1(\omega) = \frac{R_1}{1+\omega^2{\tau_1}^2} - i\frac{\omega R_1 \tau_1}{1+\omega^2{\tau_1}^2} \tag{4.79}$$

$$Z_2(\omega) = \frac{R_2}{1+\omega^2{\tau_2}^2} - i\frac{\omega R_2 \tau_2}{1+\omega^2{\tau_2}^2} \tag{4.80}$$

$$\begin{aligned} Z(\omega) = Z_1(\omega) + Z_2(\omega) &= \frac{R_1}{1+\omega^2\tau_1^2} + \frac{R_2}{1+\omega^2\tau_2^2} \\ &\quad -i\left(\frac{\omega R_1\tau_1}{1+\omega^2{\tau_1}^2} + \frac{\omega R_2\tau_2}{1+\omega^2\tau_2^2}\right) \end{aligned} \tag{4.81}$$

where $\tau_1 = R_1C_1$ and $\tau_2 = R_2C_2$.

The complex-plane impedance diagram of the two-RC Voigt structure is depicted in Figure 4.24*b*. It is characterized by two time constants, τ_1 and τ_2. The

mixing of the two semicircles caused by the ratio of the two capacitors for this model can be found in Appendix D (Model D21).

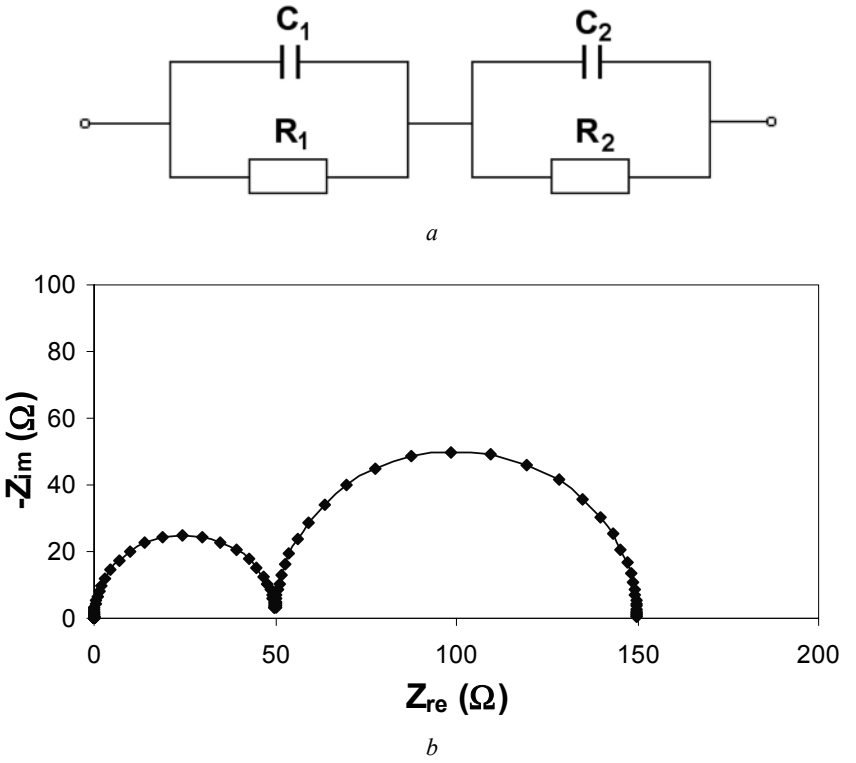

Figure 4.24. *a* Voigt structure with two RC in series (Model D21); *b* Nyquist plot of Voigt structure with two RC in series, over the frequency range 1 MHz to 1 mHz (Model D21: R_1 = 50 Ω, R_2 = 100 Ω, C_1 = 0.00001 F, C_2 = 0.01 F)

Three-RC Circuits

Figure 4.25*a* shows the Voigt structure with three RC circuits in series. The physical meanings of the parameters in Figure 4.25*a* are: $R_1 = R_b$, $C_1 = C_b$, $R_2 = R_{gb}$, $R_3 = R_{ct}$, $C_2 = C_{gb}$, and $C_3 = C_{dl}$.

The total impedance is calculated as

$$Z(\omega) = Z_1(\omega) + Z_2(\omega) + Z_3(\omega) \tag{4.82}$$

$$Z_1(\omega) = \frac{R_1}{1+\omega^2{\tau_1}^2} - i\frac{\omega R_1 \tau}{1+\omega^2{\tau_1}^2} \tag{4.83}$$

$$Z_2(\omega) = \frac{R_2}{1+\omega^2{\tau_2}^2} - i\frac{\omega R_2 \tau}{1+\omega^2{\tau_2}^2} \tag{4.84}$$

$$Z_3(\omega) = \frac{R_3}{1+\omega^2\tau_3{}^2} - i\frac{\omega R_3\tau}{1+\omega^2\tau_3{}^2} \tag{4.85}$$

where $\tau_1 = R_1C_1$, $\tau_2 = R_2C_2$, and $\tau_3 = R_3C_3$.

The complex-plane impedance diagram of the Voigt structure with three RC circuits is depicted in Figure 4.25*b*. It is characterized by three time constants, τ_1, τ_2, and τ_3. More examples of this model can be found in Appendix D (Model D22).

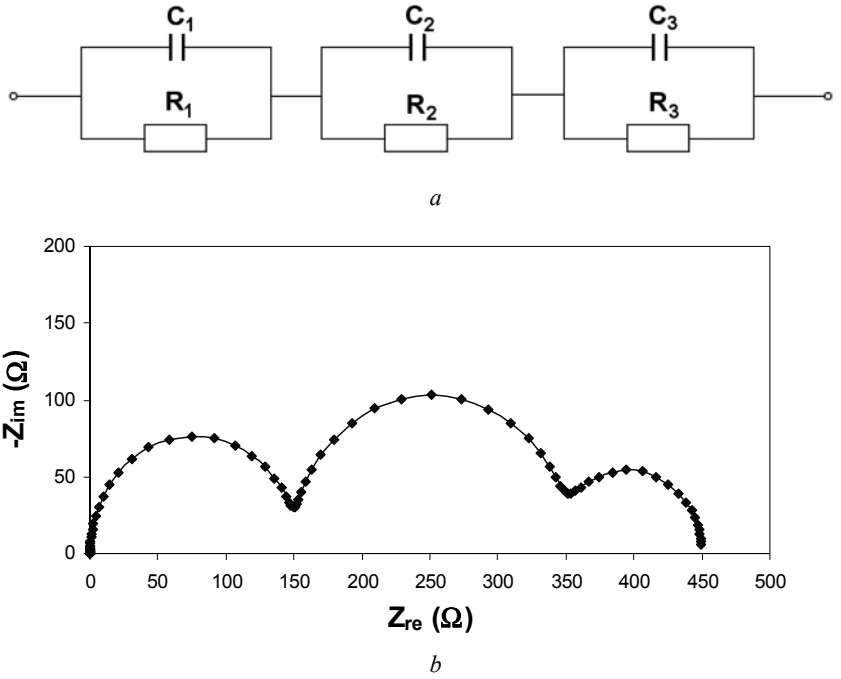

Figure 4.25. *a* Voigt structure with three RC in series (Model D22); *b* Nyquist plot of Voigt structure with three RC in series, over the frequency range 1 MHz to 1 mHz (Model D22: R_1 = 150 Ω, R_2 = 200 Ω, R_3 = 100 Ω, C_1 = 0.00001 F, C_2 = 0.001 F, C_3 = 0.1 F)

4.2.3.3 Ladder Structure

The ladder structure is presented in Figure 4.26. This structure consists of a number of kernels, which occur sequentially. The impedance of the ladder structure is

$$Z(\omega) = Z_1(\omega) + \left\{ Z_2^{-1}(\omega) + \left[Z_3(\omega) + \left(Z_4^{-1}(\omega) + \ldots \right)^{-1} \right]^{-1} \right\}^{-1} \tag{4.86}$$

where $Z_k(\omega)$ is the impedance of the ladder elements. Then the total impedance of this structure can be expressed as

$$Z(\omega) = R_1 + \cfrac{1}{i\omega C_1 + \cfrac{1}{R_2 + \cfrac{1}{i\omega C_2 + \ldots}}} \tag{4.87}$$

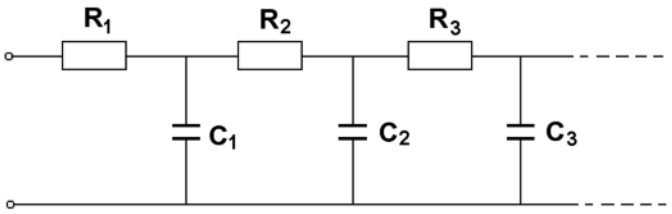

Figure 4.26. Ladder structure

Faradaic Reaction Involving One Adsorbed Species

Figure 4.27*a* shows the equivalent circuit of a simple example of the ladder structure, for electrochemical systems that are known as Faradaic reactions involving one adsorbed species. This heterogeneous reaction occurs in two steps in the absence of diffusion limitation:

$$A \xrightarrow{k_1} B + e^{-1} \tag{4.88}$$

$$B \xrightarrow{k_2} C + e^{-1} \tag{4.89}$$

Species A is transported to the electrode surface where it adsorbs and reacts, producing species C. B is the adsorbed species.

The total impedance of this ladder structure can be calculated as

$$Z(\omega) = R_{el} + \cfrac{1}{i\omega C_{dl} + \cfrac{1}{R_{ct} + \cfrac{1}{i\omega C_2 + \cfrac{1}{R_3}}}} \tag{4.90}$$

Thus,

$$\begin{aligned} Z(\omega) = R_{el} &+ \frac{a(1-\omega^2 bC_{dl}) + \omega^2 b(aC_{dl} + C_2R_3)}{(1-\omega^2 C_{dl}b)^2 + (\omega C_{dl}a + \omega C_2R_3)^2} \\ &-i\frac{a\omega(aC_{dl} + C_2R_3) - \omega b(1-\omega^2 C_{dl}b)}{(1-\omega^2 C_{dl}b)^2 + (\omega C_{dl}a + \omega C_2R_3)^2} \end{aligned} \tag{4.91}$$

or

$$Z(\omega) = R_{el} + \frac{(a^2 + \omega^2 b^2)(a + \omega^2 C_2 R_3 b)}{(a + \omega^2 C_2 R_3 b)^2 + (\omega C_{dl} a^2 + \omega^3 C_{dl} b^2 + \omega C_2 R_3 a - \omega b)^2}$$
$$-i \frac{(a^2 + \omega^2 b^2)(\omega C_{dl} a^2 + \omega^3 C_{dl} b^2 + \omega C_2 R_3 a - \omega b)}{(a + \omega^2 C_2 R_3 b)^2 + (\omega C_{dl} a^2 + \omega^3 C_{dl} b^2 + \omega C_2 R_3 a - \omega b)^2} \quad (4.92)$$

where $a = R_3 + R_{ct}$ and $b = C_2 R_3 R_{ct}$.

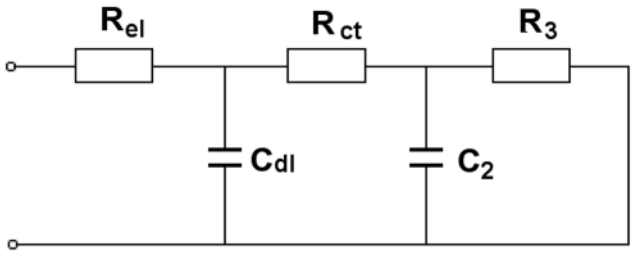

a

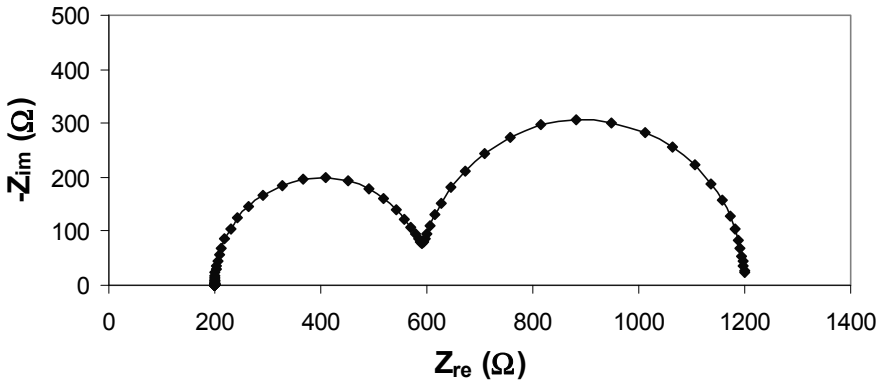

b

Figure 4.27. *a* Ladder structure for electrochemical systems known as Faradaic reactions involving one adsorbed species (Model D23); *b* Nyquist plot of a ladder structure for the Faradaic reaction involving one adsorbed species, over the frequency range 1 MHz to 1 mHz (Model D23: R_{el} = 200 Ω, R_{ct} = 400 Ω, R_3 = 600 Ω, C_{dl} = 0.0001 F, C_2 = 0.01 F)

The simulated complex-plane impedance diagram is shown in Figure 4.27*b*. As can be seen in the figure, this ladder structure is characterized by two semicircles with two time constants, $\tau_1 = R_{ct} C_{dl}$ and $\tau_2 = R_3 C_2$, accounting for the two-step reaction. The element C_2 symbolizes the adsorption capacitance, and τ_2 represents the relaxation of the adsorbing process.

The two semicircles in Figure 4.27*b* may be well pronounced or mixed, depending on the ratio of the two time constants. Note that this characteristic is

quite similar to that of the two-time-constant models with the Voigt structure, described earlier. However, the parameter values can be different. More examples of this ladder structure are presented in Appendix D (Model D23).

Faradaic Reaction Involving Two Adsorbed Species

The electrochemical reaction involving two adsorbed species in the absence of diffusion limitations can also be represented with a ladder type of equivalent circuit. The electrochemical reaction from A to C occurs in three steps involving two adsorbed species, B and C.

$$A \xrightarrow{k_1} B + e^{-1} \tag{4.93}$$

$$B \xrightarrow{k_2} C + e^{-1} \tag{4.94}$$

$$C \xrightarrow{k_3} D + e^{-1} \tag{4.95}$$

This ladder type of equivalent circuit for two adsorbed species is depicted in Figure 4.28*a*.

The total impedance of this ladder structure includes the Faradaic impedance, the double-layer capacitance, and the electrolyte resistance, which can be calculated as

$$Z(\omega) = R_{el} + \cfrac{1}{i\omega C_{dl} + \cfrac{1}{R_{ct} + \cfrac{1}{i\omega C_2 + \cfrac{1}{R_3 + \cfrac{1}{i\omega C_3 + \cfrac{1}{R_4}}}}}} \tag{4.96}$$

Assuming $a = R_3 + R_4$, $b = C_3 R_3 R_4$, $l = a^2 + \omega^2 b^2$, $m = a + \omega^2 C_3 R_4 b$, $n = \omega C_2 a^2 + \omega^3 C_2 b^2 + \omega C_3 R_4 a - \omega b$, and $q = m^2 + n^2$, then the total impedance is given by

$$\begin{aligned} Z(\omega) = R_{el} &+ \frac{(R_{ct}q + lm)(q + \omega C_{dl} nl) - nl\omega C_{dl}(R_{ct}q + lm)}{(q + \omega C_{dl} nl)^2 + [\omega C_{dl}(R_{ct}q + lm)]^2} \\ &- i\frac{nl(q + \omega C_{dl} nl) + (R_{ct}q + lm)\omega C_{dl}(R_{ct}q + lm)}{(q + \omega C_{dl} nl)^2 + [\omega C_{dl}(R_{ct}q + lm)]^2} \end{aligned} \tag{4.97}$$

The complex-plane impedance diagram is displayed in Figure 4.28*b*. The effects of the model parameters on the shape of the spectra can be found in Appendix D (Model D24).

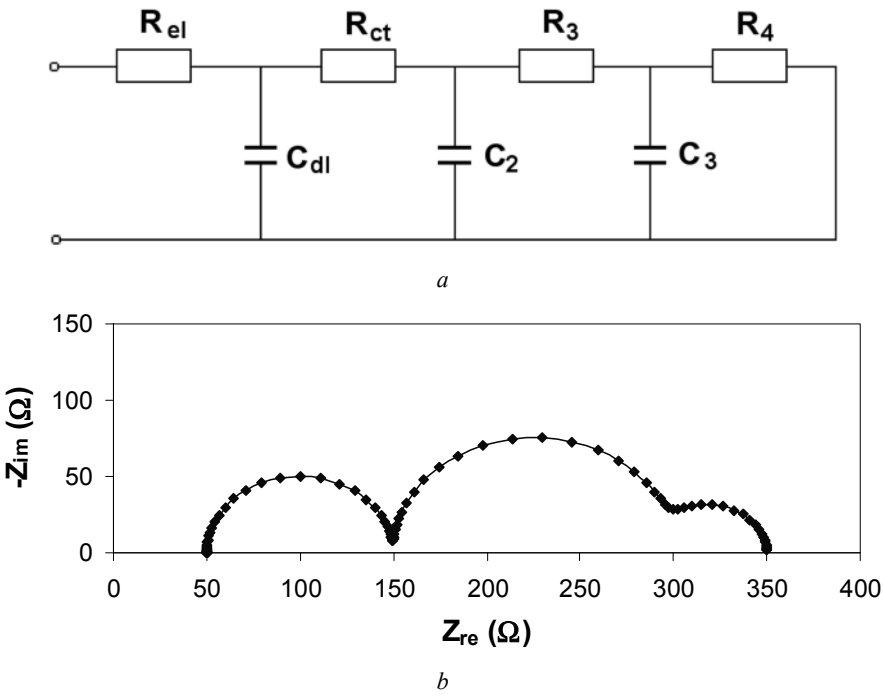

Figure 4.28. *a* Ladder structure with two adsorbed species in the absence of diffusion limitation (Model D24); *b* Nyquist plot of ladder structure with two adsorbed species, over the frequency range 1 MHz to 1 mHz (Model D24: R_{el} = 50 Ω, R_{ct} = 100 Ω, R_3 = 150 Ω, R_4 = 50 Ω, C_{dl} = 0.00001 F, C_2 = 0.001 F, C_3 = 0.1 F)

4.2.4 Other Circuits

4.2.4.1 Modified Voigt Structure

A modified Voigt structure consisting of resistance and two RC circuits in series, and with two Cs replaced by CPEs, is shown in Figure 4.29*a*.

The overall impedance of elements in series can be calculated by the sum of the individual impedances, i.e.,

$$Z(\omega) = R_{el} + Z_1(\omega) + Z_2(\omega) \tag{4.98}$$

$$Z_1(\omega) = \frac{R_1 + Q_1 R_1^2 \omega^{n_2} \cos(\frac{\pi}{2} n_1)}{1 + 2Q_1 R_1 \omega^{n_1} \cos(\frac{\pi}{2} n_1) + {Q_1}^2 R_1^2 \omega^{2n_1}} - i \frac{Q_1 R_1^2 \omega^{n_2} \sin(\frac{\pi}{2} n_1)}{1 + 2Q_1 R_1 \omega^{n_2} \cos(\frac{\pi}{2} n_1) + {Q_1}^2 R_1^2 \omega^{2n_1}} \tag{4.99}$$

$$Z_2(\omega) = \frac{R_2 + Q_2 R_2^2 \omega^{n_2} \cos(\frac{\pi}{2} n_2)}{1 + 2Q_2 R_2 \omega^{n_2} \cos(\frac{\pi}{2} n_2) + {Q_2}^2 R_2^2 \omega^{2n_2}} - i \frac{Q_2 R_2^2 \omega^{n_2} \sin(\frac{\pi}{2} n_2)}{1 + 2Q_2 R_2 \omega^{n_2} \cos(\frac{\pi}{2} n_2) + {Q_2}^2 R_2^2 \omega^{2n_2}} \quad (4.100)$$

Figure 4.29*b* shows the simulated complex-plane diagram of the circuit in Figure 4.29*a*. The effects of the model parameters on the shape of the spectra can be found in Appendix D (Model D25).

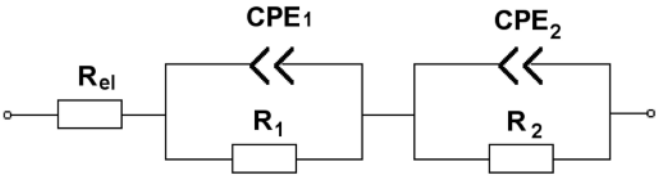

a

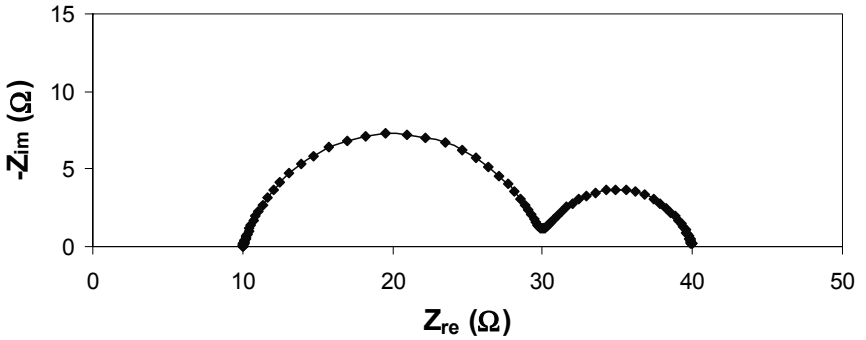

b

Figure 4.29. *a* Resistor and Voigt structure in series, with capacitors replaced by CPE (Model D25); *b* Nyquist plot of the modified Voigt structure over the frequency range 1 MHz to 1 mHz (Model D25: $R_{el} = 10\ \Omega$, $R_1 = 20\ \Omega$, $R_2 = 10\ \Omega$, $Q_1 = 0.0001\ \Omega^{-1}s^{0.8}$, $Q_2 = 0.1\ \Omega^{-1}s^{0.8}$, $n_1 = 0.8$, $n_2 = 0.8$)

4.2.4.2 Solid Cell with Blocking Electrode

For a solid cell with a blocking electrode, the model is often as shown in Figure 4.30*a*. The physical meanings of the parameters in this figure are: $R_1 = R_b$, $C_1 = C_b$, $R_2 = R_{gb}$, and $C_2 = C_{gb}$. C_3 represents the capacitive behaviour of the electrodes.

The impedance is calculated as

$$Z(\omega) = Z_1(\omega) + Z_2(\omega) + (i\omega C_3)^{-1} \tag{4.101}$$

$$Z_1(\omega) = \frac{R_1}{1+\omega^2{\tau_1}^2} - i\frac{\omega R_1 \tau}{1+\omega^2{\tau_1}^2} \tag{4.102}$$

$$Z_2(\omega) = \frac{R_2}{1+\omega^2{\tau_2}^2} - i\frac{\omega R_2 \tau}{1+\omega^2{\tau_2}^2} \tag{4.103}$$

where $\tau_1 = R_1 C_1$ and $\tau_2 = R_2 C_2$.

Figure 4.30*b* shows the simulated Nyquist plot of the above structure over the frequency range 1 MHz to 0.01 Hz. The effects of the model parameters on the shape of the spectra are presented in Appendix D (Model C26).

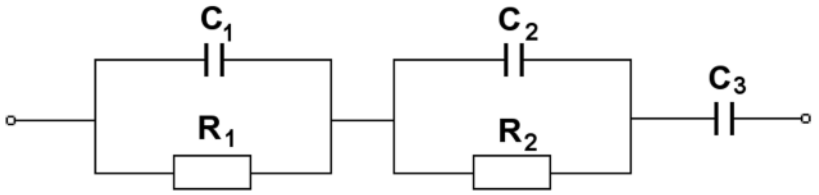

a

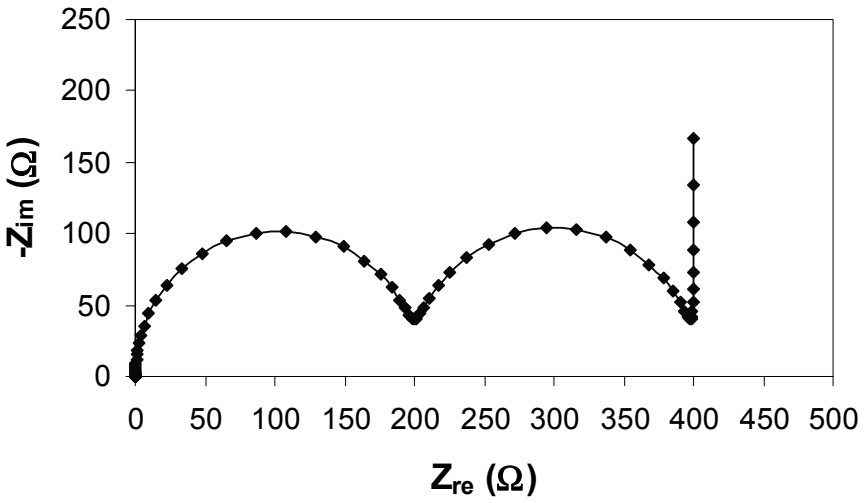

b

Figure 4.30. *a* Capacitor and Voigt structure in series (Model D26); *b* Nyquist plot of a capacitor and a Voigt's structure in series over the frequency range 1 MHz to 1 mHz (Model D26: R_1 = 200 Ω, R_2 = 200 Ω, C_1 = 0.0001 F, C_2 = 0.01 F, C_3 = 1 F)

In summary, simple combinations of elements and basic equivalent circuits for electrochemical systems have been introduced in this section. Although these models are relatively simple, they are commonly employed in the investigation of electrochemical systems, including fuel cells. A real electrochemical system may be much more complicated. However, complicated electrochemical systems can still be constructed from these basic equivalent circuits.

4.3 Brief Discussion of Equivalent Circuits in PEM Fuel Cells

4.3.1 Gas Diffusion Layers

Equivalent circuits for gas diffusion layers (GDLs) in fuel cells have attracted little attention, primarily because of their insignificant role in the system. Despite the importance of the GDL in facilitating gas transport to the electrodes, fuel cell reactions do not occur in the layer. The mass transport resistance, which is related to the gas diffusion, is negligible compared with that in the catalyst layers, and the electronic conductivity can be disregarded because it is several orders higher than the ionic conductivity of the membrane. For example, the electronic conductivity of the GDL is 1250 S/m in the through-plane direction and $1.72–2.13\times10^4$ S/m in the in-plane direction. The membrane conductivity is only about 10 S/m at 100% RH. Recently, several groups have considered the effects of GDL electronic resistances on PEM fuel cell performance, reporting controversial results. Two groups reported that under certain conditions, the electronic resistance of the GDL was significant enough to change the characteristics of the current density distributions [4, 5]. However, another group's recent modelling work showed no significant change in current distribution [6]. Nonetheless, the GDL is basically considered a simple electric resistor.

4.3.2 Catalyst Layers

Equivalent circuits for the catalyst layer are similar to those for porous electrodes, where charge-transfer resistance, capacitance, and Warburg resistance should be considered. The catalyst layer can be conceived of as a whole uniform unit or as a non-uniform circuit. In the case of a uniform unit, the equivalent circuits are similar to the modified ones discussed in Section 4.2.2.2, and the equations in that section apply. In many cases, such as in the presence of adsorbents, the surface is covered by the adsorbed species. For example, in direct methanol fuel cells and in H_2/air fuel cells, CO adsorption should be considered. One example is illustrated in Ciureanu's work [7], as shown in Figure 4.31.

In Figure 4.31, R1 is the charge-transfer resistance, CPE1 represents the double-layer capacitance in the form of a constant phase element, R2 is the adsorption resistance or the diffusion resistance due to slow gas diffusion through the limited porous structure, and CPE2 is the adsorption-related constant phase element or capacitance. In a true case, neither the double-layer nor the adsorption-related capacitance is pure capacitance, and therefore it is more realistic to use CPE instead of capacitance.

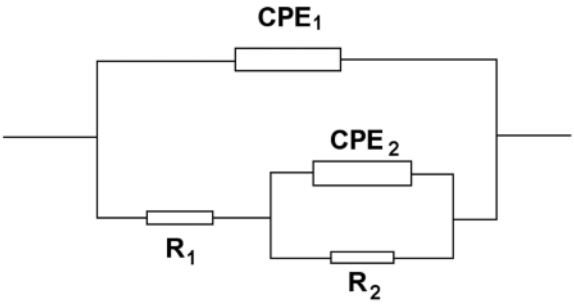

Figure 4.31. Equivalent circuit with adsorption-related electrode surface

The resistance of this equivalent circuit is given by the following equation:

$$Z = \frac{R_1 + R_2 + R_1 R_2 Q_2 (i\omega)^{n_2}}{(R_1 + R_2) Q_1 (i\omega)^{n_1} + R_1 R_2 Q_1 Q_2 (i\omega)^{(n_1+n_2)} + R_2 Q_2 (i\omega)^{n_2} + 1} \tag{4.104}$$

This equation can be reduced to the following:

$$Z = \frac{AC + BD}{A^2 + B^2} + i\frac{AD - BC}{A^2 + B^2} \tag{4.105}$$

where

$$A = (R_1 + R_2) Q_1 \omega^{n_1} \cos(\frac{\pi}{2} n_1) + R_1 R_2 Q_1 Q_2 \omega^{(n_1+n_2)} \cos(\frac{\pi}{2}(n_1 + n_2)) + R_2 Q_2 \omega^{n_2} \cos(\frac{\pi}{2} n_2) + 1 \tag{4.106}$$

$$B = (R_1 + R_2) Q_1 \omega^{n_1} \sin(\frac{\pi}{2} n_1) + R_1 R_2 Q_1 Q_2 \omega^{(n_1+n_2)} \sin(\frac{\pi}{2}(n_1 + n_2) + R_2 Q_2 \omega^{n_2} \sin(\frac{\pi}{2} n_2) \tag{4.107}$$

$$C = R_1 + R_2 + R_1 R_2 Q_2 \omega^{n_2} \cos(\frac{\pi}{2} n_2) \tag{4.108}$$

$$D = R_1 R_2 Q_2 \omega^{n_2} \sin(\frac{\pi}{2} n_2) \tag{4.109}$$

Figure 4.32 shows an impedance spectrum deduced from Equation 4.105. A semicircle is evident, and at low frequencies, the features of inductance are observable.

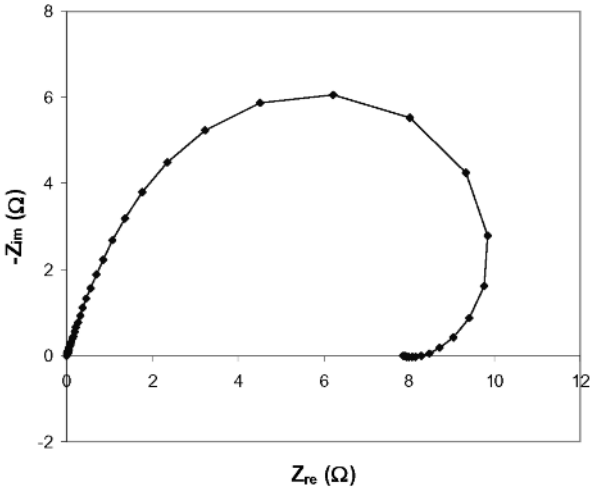

Figure 4.32. Nyquist plot of Figure 4.31 model over the frequency range 30 kHz to 1 mHz (Model D19: $R_1 = 50\ \Omega$, $R_2 = 50\ \Omega$, $Q_1 = 2\ \Omega^{-1}s^{0.9}$, $n_1 = 0.8$, $Q_2 = 1.5\ \Omega^{-1}s^{0.8}$, $n_2 = 0.9$)

It is known that the catalyst layer is far from uniform, especially in the case of a gradient catalyst layer. Thus, profiling properties, such as conductivity, in the catalyst layer are important. Both an electronic conductor (carbon) and an ionic conductor (Nafion®) exist in the catalyst layer, which can be considered a conductive polymer. The conductive polymer electric circuit model has been applied to the catalyst layer, and an ionic conductivity profile was obtained [8], as shown in Figure 4.33.

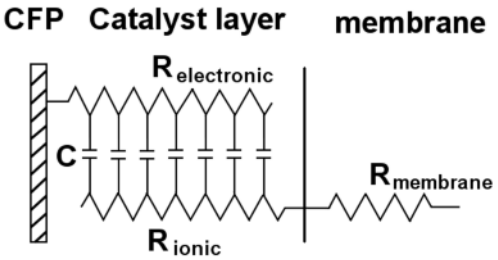

Figure 4.33. Equivalent circuit of a catalyst layer [8]. (Reproduced by permission of the authors and of ECS—The Electrochemical Society, from Lefebvre MC, Martin RB, Pickup PG. Characterization of ionic conductivity within proton exchange membrane fuel cell gas diffusion electrodes by impedance spectroscopy.)

To calculate the impedance of the electric circuit shown in Figure 4.33, an iterative equation should be used. In the calculation process, the membrane resistance is not considered because it only shifts the impedance spectra at the real axis with an $R_{membrane}$ value. The electronic resistance of the carbon support is significantly smaller than the ionic resistance. Thus, the electric circuit could be simplified to a transmission line with capacitance and ionic resistance, as shown in Figure 4.34.

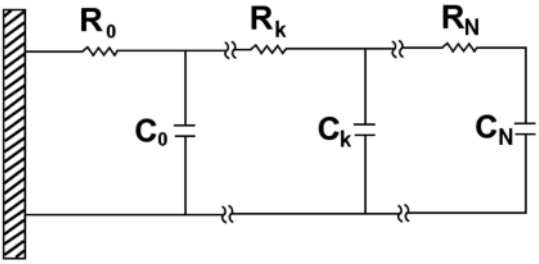

Figure 4.34. Transfer line circuit [9]. (Reproduced by permission of ECS—The Electrochemical Society, from Suchanski MR. AC impedance of the carbon monofluoride electrode.)

Iterated from the right end of the electric circuit (far away from the carbon-fibre paper), the impedance at segments k is related to the circuit impedance from segments (k+1) to the one furthest to the right, by the following equation:

$$Z_k = R_k + 1/(j\omega C_k + 1/Z_{k+1}) \tag{4.110}$$

By the successive substitution of values for R_k and C_k into the equation, the total electrode impedance Z can be obtained.

Assuming $R_{electronic}$ and $R_{membrane}$ are zero, and assuming a total capacitance of 1 F and a total resistance of 0.5 Ω for a uniform ionic resistance profile, a linearly increasing profile was calculated and is shown in Figure 4.35.

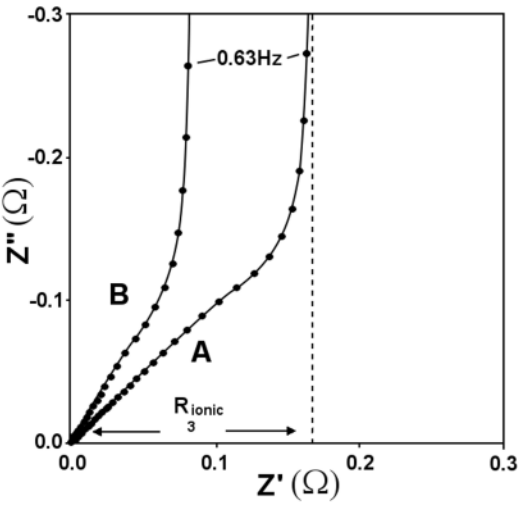

Figure 4.35. A = uniform profile, B = linearly increasing profile [8]. (Reproduced by permission of the authors and of ECS—The Electrochemical Society, from Lefebvre MC, Martin RB, Pickup PG. Characterization of ionic conductivity within proton exchange membrane fuel cell gas diffusion electrodes by impedance spectroscopy.)

A typical profiling of the catalyst layer is shown in Figure 4.36, which compares a Nafion®-impregnated cathode and a cathode without Nafion® impregnation. The former has a much higher ionic conductivity than the latter.

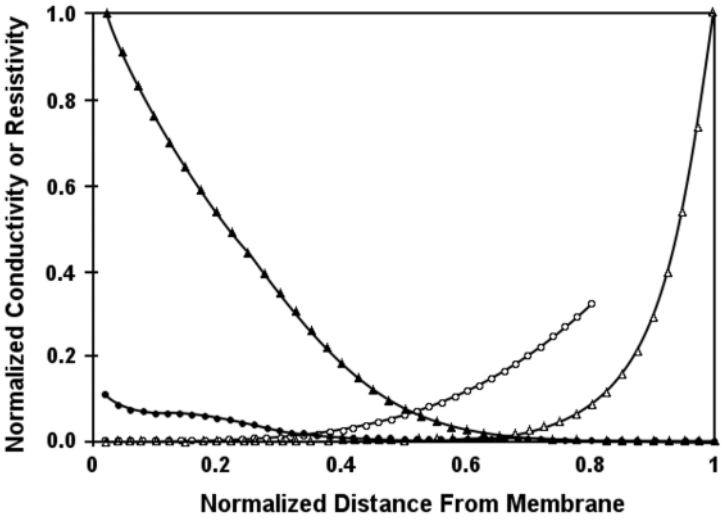

Figure 4.36. Normalized resistivity (open points) and conductivity (solid points) profiles for Pt/C cathodes with (triangles) and without (circles) Nafion® impregnation [8]. (Reproduced by permission of the authors and of ECS—The Electrochemical Society, from Lefebvre MC, Martin RB, Pickup PG. Characterization of ionic conductivity within proton exchange membrane fuel cell gas diffusion electrodes by impedance spectroscopy.)

4.3.3 Proton Exchange Membranes

The proton exchange membranes (PEMs) used in PEM fuel cells consist of two domains: the hydrophobic polymer backbone domain and the hydrophilic ionic cluster domain. The most commonly used membrane is Nafion®, produced by DuPont.

The membrane itself can be considered as a resistance and capacitor in parallel, which will be discussed later in this chapter. The resistance and capacitance can be measured using AC impedance, which yields a semicircle from which the values can be extracted.

In fuel cells, the membrane is considered as a whole unit, and the most important parameter is its ionic conductivity. Thus, the fuel cell membrane is simply treated as a resistor.

4.3.4 Conductive Polymers

Conductive polymers are not used in fuel cells. However, the equivalent circuit of conductive polymers is similar to that of catalyst layers, which may help to understand impedance spectra in fuel cells. In general, the electric circuits of

conductive polymers are based on a transmission line model. There are two types of electric circuit for conductive polymers, depending on the negligibility of the charge-transfer resistance and the double-layer capacitance. If these two factors are negligible, the electric circuit can be constructed by a finite transmission lines as shown in Figure 4.37.

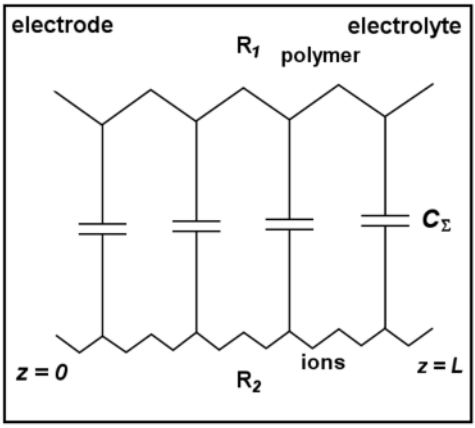

Figure 4.37. Equivalent circuit of conducting polymers [10]. (Albery WJ, Mount AR. Dual transmission line with charge-transfer resistance for conducting polymers. J Chem Soc Faraday Trans 1994;90:1115–9. Reproduced by permission of The Royal Society of Chemistry.)

For this electric circuit, the resistance can be expressed as [11]

$$Z / R_{\Sigma} = \rho + 2\rho f_1 + (1 - 2\rho) f_2 \tag{4.111}$$

where Z is the impedance, $R_{\Sigma} = R_1 + R_2$, R_1 is the electric resistance, R_2 is the ionic resistance, $\rho = R_1 R_2 / R_{\Sigma}^2$:

$$f_1 = \frac{\sinh\theta\cos\theta - \cosh\theta\sin\theta - i[\sinh\theta\cos\theta + \cosh\theta\sin\theta]}{2\theta[\sinh^2\theta\cos^2\theta + \cosh^2\theta\sin^2\theta]} \tag{4.112}$$

and

$$f_2 = \frac{\sinh\theta\cosh\theta - \cos\theta\sin\theta - i[\sinh\theta\cosh\theta + \cos\theta\sin\theta]}{2\theta[\sinh^2\theta\cos^2\theta + \cosh^2\theta\sin^2\theta]} \tag{4.113}$$

where

$$\theta = (\omega R_{\Sigma} C_{\Sigma} / 2)^{1/2} \tag{4.114}$$

and C_{Σ} is the total capacitance of the polymer.

Several important conclusions can be obtained from these equations. At low frequencies, the impedance is expressed approximately as

$$Z = R_{\Sigma}/3 - i/\omega C_{\Sigma} \tag{4.115}$$

The impedance is dominated by the capacitance, and the real impedance is a constant, $R_{\Sigma}/3$.

At high frequencies

$$Z^{-1} = R_1^{-1} + R_2^{-1} \tag{4.116}$$

which is consistent with what is clearly observable in the equivalent circuit. At high frequencies there is no charging and the capacitance is effectively like that of an open circuit; the transmission line is then only two resistances connected in parallel.

If charge-transfer resistance and double-layer capacitance are considered, there are two scenarios: (a) the $R_{ct}C_{dl}$ circuit is at the interface of the electrode and the polymer, or (b) the $R_{ct}C_{dl}$ circuit is at the interface of the polymer and electrolyte solution, as shown in Figure 4.38 [12].

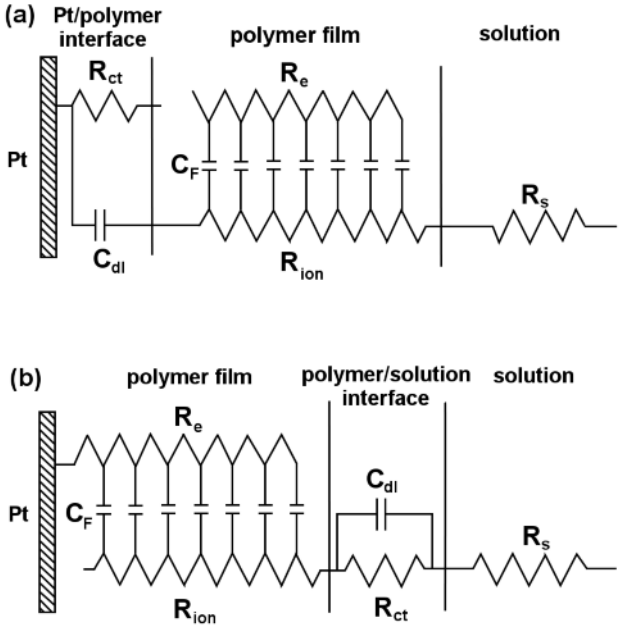

Figure 4.38. Equivalent circuits of conducting polymers with a Randles circuit [12]. (Reprinted from Journal of Electroanalytical Chemistry, 420, Ren X, Pickup PG. An impedance study of electron transport and electron transfer in composite polypyrrole plus polystyrenesulphonate films, 251–7, ©1997 with permission from Elsevier and from the authors.)

The high-to-medium impedance of both cases is given by the following equations [10, 11]:

$$Z = R_1 R_2 / R_\Sigma + R_2^2 / [R_\Sigma (sR_\Sigma C_\Sigma)]^{1/2} + Z_1 \tag{4.117}$$

where

$$\frac{1}{Z_1} = \frac{1 + sC_{dl}(R_{ct} + [c/(a+c)]Z_2)}{R_{ct} + Z_2} \tag{4.118}$$

and

$$Z_2 = R_1^2 / [R_\Sigma (sR_\Sigma C_\Sigma)^{1/2}] \tag{4.119}$$

and where c is the concentration of redox sites in the polymer film, a is the concentration of oxidized redox sites, $s = i\omega$, and ω is the frequency.

When $R_2 >> R_1$, the polymer is more conducting than the pores. The Randles circuit, which is located at the polymer/electrolyte interface (case b), shunts the resistive ionic rail through the polymer. At high frequencies, the equation can be simplified to

$$Z \approx R_1 + (R_2 / C_\Sigma \omega)^{1/2} - i / C_{dl}\omega \tag{4.120}$$

The real impedance is dominated by the transmission line, and the imaginary part is controlled by the double-layer capacitance. Both the double-layer and the transmission-line capacitances must be involved.

In the case $R_1 >> R_2$, the equation can be simplified to

$$Z \approx R_2 + 1/[R_{ct} C_{dl}^2 \omega^2] - i / C_{dl}\omega \tag{4.121}$$

The Randles circuit is at the electrode/polymer interface (case a). The imaginary component of the impedance is dominated by the double-layer capacitance, and the real one is controlled by the double layer. The capacitance of the transmission line is shunted and the transmission line is not involved.

Conductive polymers have been investigated extensively using AC impedance. A typical example, shown here, is from an AC impedance study of reduced polypyrrole polystyrene sulfonate (PPY-PSS), which exhibits different behaviours at different potential ranges [12, 13]. In the potential range 0.1 to –0.6V, the PPY-PSS film shows a simple transfer line, in which the electronic resistance is negligible [13]. Figure 4.39 shows the Nyquist plot of a PPY-PSS film coated on a Pt electrode in aqueous $NaClO_4$ solution. The solution resistance, intercepted at high frequencies, is the same at all investigated potentials. The low-frequency limiting real impedance, R_{low}, is the sum of R_s and $R_{ion}/3$. The ionic resistance decreases with decreasing electrode potential.

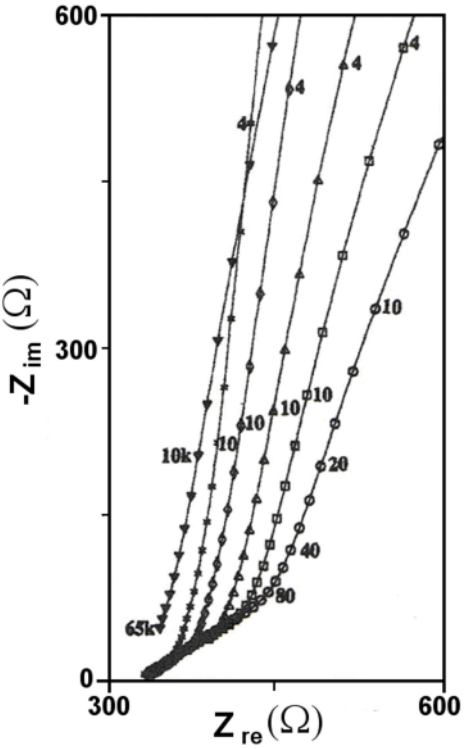

Figure 4.39. Nyquist plot of a Pt and Pt/PPY|PPY/PSS bilayer electrode in 0.2 M $NaClO_4$ solution. Potential: Pt: OCV; conducting polymer: ○, 0.1; □, –0.2; Δ, –0.3; ◊, –0.4, *, –0.5 V [13]. (Reprinted with permission from J Phys Chem 1993;97:3941–3. ©1993 American Chemical Society.)

In the potential range –0.6 to –0.69 V, the high-frequency intercept changes with potential, indicating that the electronic resistance becomes comparable with the ionic resistance [12]. The electronic and ionic resistances can be calculated by the following equations:

$$1/(R_{high} - R_s) = 1/R_e + 1/R_{ion} \tag{4.122}$$

$$3(R_{low} - R_s) = R_{ion} + R_e \tag{4.123}$$

where R_{high} is the real impedance at a high-frequency intercept, R_s is the solution resistance, R_e is the electronic resistance, and R_{ion} is the ionic resistance.

Further decrease in electrode potential leads to the appearance of semicircles as shown in Figures 4.40 and 4.41, indicating that the interfacial charge transfer becomes slow. The plot of the imaginary impedance versus $1/\omega$ is shown in Figure 4.42. A linear relationship is observable, and the capacitance of the double layer is obtained from the slope.

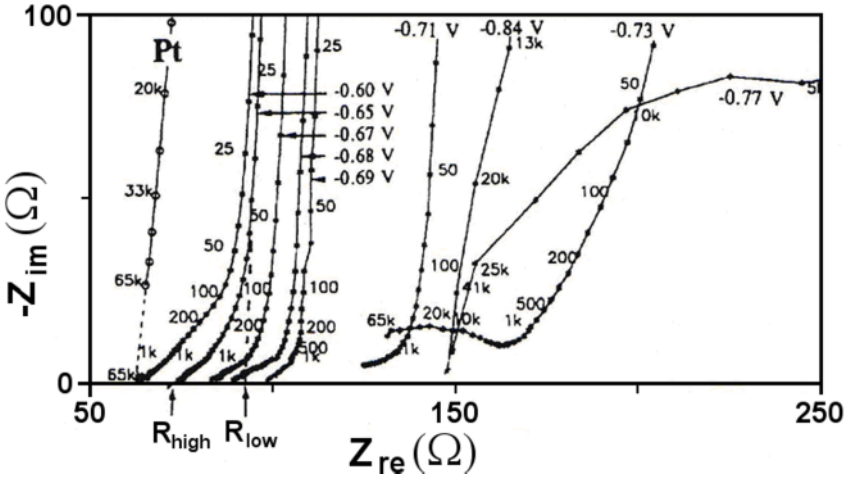

Figure 4.40. Nyquist plot of PPY-PSS film at different potentials [12]. (Reprinted from Journal of Electroanalytical Chemistry, 420, Ren X, Pickup PG. An impedance study of electron transport and electron transfer in composite polypyrrole plus polystyrenesulphonate films, 251–7, ©1997 with permission from Elsevier and from the authors.)

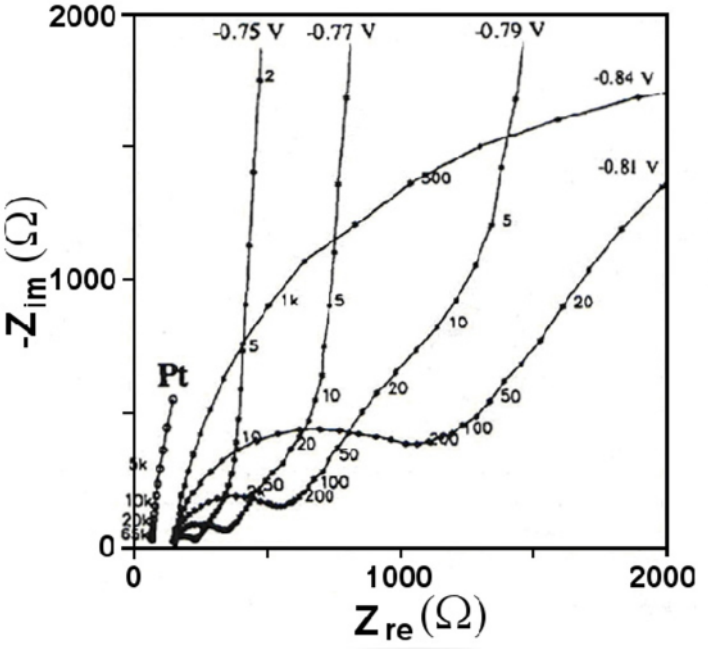

Figure 4.41. Impedance of PPY-PSS in the potential range –0.75 V to –0.84 V [12]. (Reprinted from Journal of Electroanalytical Chemistry, 420, Ren X, Pickup PG. An impedance study of electron transport and electron transfer in composite polypyrrole plus polystyrenesulphonate films, 251–7, ©1997 with permission from Elsevier and from the authors.)

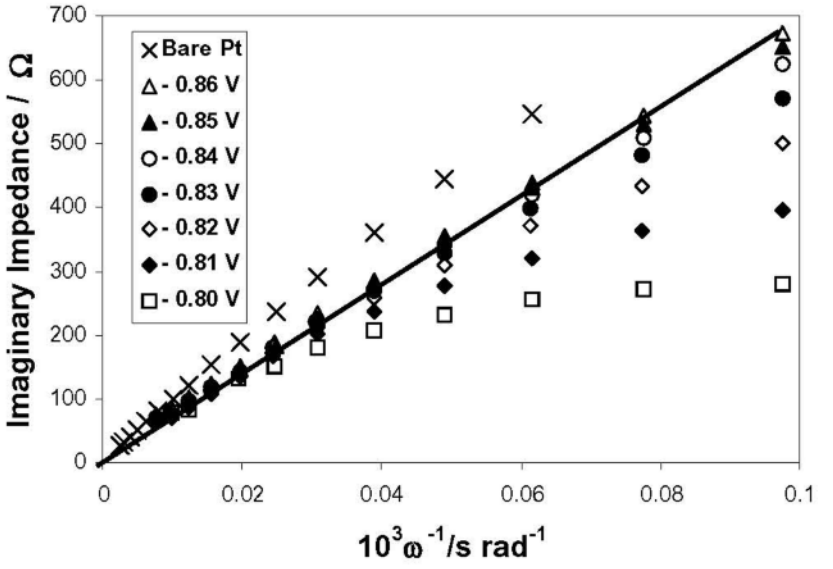

Figure 4.42. Plot of imaginary impedance versus $1/\omega$ for PPY-PSS film coated on Pt [12]. (Reprinted from Journal of Electroanalytical Chemistry, 420, Ren X, Pickup PG. An impedance study of electron transport and electron transfer in composite polypyrrole plus polystyrenesulphonate films, 251–7, ©1997 with permission from Elsevier and from the authors.)

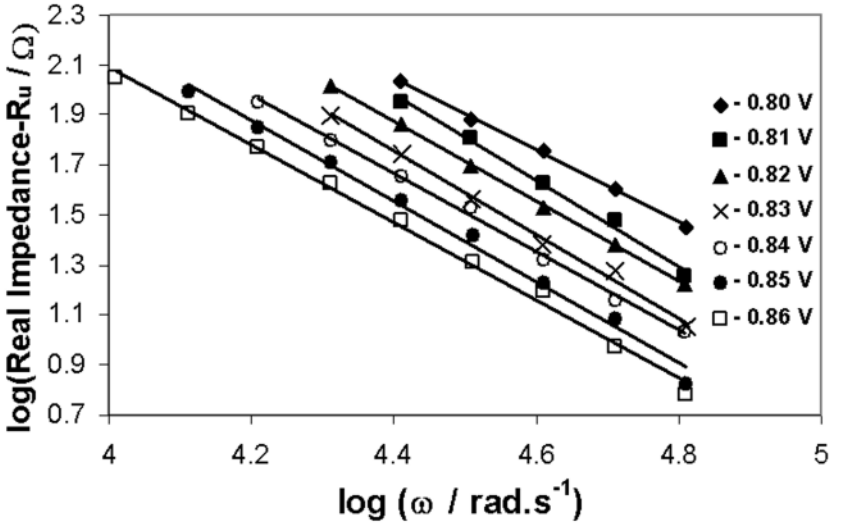

Figure 4.43. Plot of $\log(Z'–R_u)$ versus $\log(\omega)$ [12]. (Reprinted from Journal of Electroanalytical Chemistry, 420, Ren X, Pickup PG. An impedance study of electron transport and electron transfer in composite polypyrrole plus polystyrenesulphonate films, 251–7, ©1997 with permission from Elsevier and from the authors.)

At high frequencies, the plot is linear and the slope is similar to that for a bare Pt electrode. The double-layer capacitance is 28 μF cm^{-2} for the PPY-PSS film and 23 μF cm^{-2} for the bare Pt electrode. The plot of real resistance minus the solution resistance versus log(ω) over the frequency range shown in Figure 4.43 is also linear and fits Equation 4.121 well. This indicates that a Randles circuit is at the electrode/polymer interface.

4.3.5 Membrane Electrode Assemblies

The electric circuit of membrane electrode assemblies is a combination of anode and cathode catalyst layers plus the membrane. In general, the anode catalyst layer is considered an electric circuit, the cathode catalyst layer is considered another electric circuit similar to that of the anode but with different RC values, and the membrane is treated as a resistance. These three electric circuits are connected in series to construct a whole-cell equivalent circuit. A typical impedance spectrum is shown in Chapter 1 as Figure 1.16. Since the anode reaction is significantly faster than the cathode, the RC electric circuit of the anode can be disregarded.

The main impedance in a fuel cell is due to its MEA. Although some resistance exists between the bipolar plates and the MEA, the resistance is mainly electric and effectively negligible.

4.4. Chapter Summary

This chapter has introduced combinations of elements and basic equivalent circuits for electrochemical systems, including PEM fuel cells, and has also provided their corresponding calculations in terms of mathematical expressions and visual plots. The equivalent circuits presented here are those commonly employed in electrochemical and fuel cell research and development. This chapter also has given a brief introduction to fuel cell EIS, including gas diffusion layers, catalyst layers, membranes, as well as membrane electrode assemblies. It is hoped that this chapter will form a strong knowledge base for further reading and for study of the following chapters.

References

1. Bard AJ, Faulkner LR (1980) Electrochemical methods: fundamentals and applications. Wiley, New York
2. Research Solutions and Resources LLC (2009) The constant phase element (CPE). http://www.consultrsr.com/resources/eis/cpe1.htm. Accessed 19 May 2009.
3. Stoynov Z, Vladikova D (2005) Differential impedance analysis. Marin Drinov Academic Publishing House, Bulgaria
4. Meng H, Wang C (2004) Electron transport in PEFCs. J Electrochem Soc 151:A358–67
5. Silertsen BR, Djilali N (2005) CFD-based modelling of proton exchange membrane fuel cells. J Power Sources 141:65–78

6. Zhou T, Liu H (2006) Effects of the electrical resistances of the GDL in a PEM fuel cell. J Power Sources 161:444–53
7. Ciureanu M, Wang H (1999) Electrochemical impedance study of electrode membrane assemblies in PEM fuel cells: I. Electro-oxidation of H_2 and H_2/CO mixtures on Pt based gas diffusion electrodes. J Electrochem Soc 146:4031–40
8. Lefebvre MC, Martin RB, Pickup PG (1999) Characterization of ionic conductivity within proton exchange membrane fuel cell gas diffusion electrodes by impedance spectroscopy. Electrochem Solid-State Lett 2:259–61
9. Suchanski MR (1985) AC impedance of the carbon monofluoride electrode. J Electrochem Soc 132:2059–63
10. Albery WJ, Mount AR (1994) Dual transmission line with charge transfer resistance for conducting polymers. J Chem Soc Faraday Trans 90:1115–19
11. Albery WJ, Elliot CM, Mount AR (1990) A transmission line model for modified electrodes and thin layer cells. J Electroanal Chem 288:15–34
12. Ren X, Pickup PG (1997) An impedance study of electron transport and electron transfer in composite polypyrrole plus polystyrenesulphonate films. J Electroanal Chem 420:251–7
13. Ren X, Pickup PG (1993) Impedance of polypyrrole perchlorate/polypyrrole poly(styrenesulfonate) bilayers. J Phys Chem 97:3941–3

5

EIS Diagnosis for PEM Fuel Cell Performance

Two types of EIS diagnosis exist for PEM fuel cells: material/component evaluation before assembly into a fuel cell and material/component evaluation after assembly into a fuel cell. Normally, the former is evaluated using a half-cell (or an electrochemical cell), while the latter is evaluated in a fuel cell or stack. We define the former as an ex situ diagnosis, and the latter as an in situ diagnosis. In the following sections, we will describe them separately.

5.1 Ex Situ Diagnosis

In general, the performance of PEM fuel cell stacks or single cells is often characterized using commercially available fuel cell test stations. However, these testing stations and their surrounding accessories are usually costly and complex, and the measurements are time consuming. For quick screening of the materials and components, as well as their corresponding performance, ex situ electrochemical diagnosis seems more handy and convenient. It is helpful to evaluate material/component performance functions under conditions that simulate real fuel cell operation. For example, the advantages of such ex situ diagnosis have been demonstrated in catalyst down-selection, in oxygen reduction reaction (ORR) mechanism exploration, as well as in determining the kinetics of carbon monoxide and methanol electrooxidation. With respect to these advantages, many fuel cell researchers prefer the ex situ EIS approach. This section provides an overview or framework for understanding the nature and character of ex situ EIS diagnosis.

5.1.1 Electrode Characterization

Ex situ stationary and transient electrochemical measurements of an electrode are normally carried out using a three-electrode configuration, which includes a working electrode, a reference electrode, and a counter electrode. These measurements can be performed in a conventional three-compartment electrochemical cell operating in half-cell mode using sulphuric acid [1, 2] or alkaline [3, 4] as the electrolyte. The reference electrode can be a saturated calomel electrode (SCE), normal hydrogen electrode (NHE), Ag/AgCl electrode, or Hg/HgO electrode. The counter electrode is normally a Pt wire, mesh, or net. Of course, other stable conducting materials such as gold, carbon, and titanium can also be used as counter electrode materials. Working electrodes can be prepared using different materials and structures, depending on the purpose of the study. Figure 5.1 shows an example of a specially designed electrochemical half-cell and corresponding electrodes. The novel design allows the evaluation of DMFC anodic

activity in an environment close to that of an operating fuel cell. This cell design can be used for catalyst down-selection and catalyst layer optimization [5].

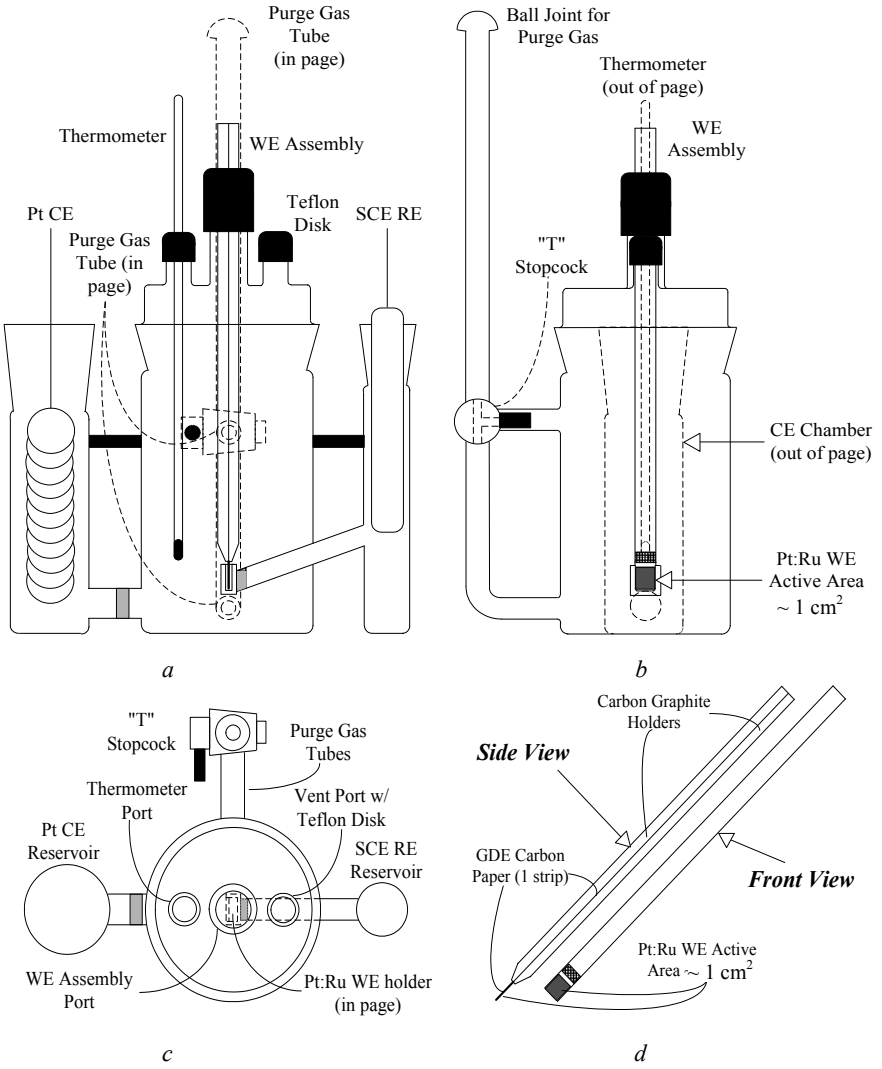

Figure 5.1. *a* Half-cell design, front view. *b* Half-cell, design side view. Note the 1 cm^2 active area. *c* Top view of the half-cell assembly. *c* Side and front views of working electrode assembly with 1 cm^2 active area. (Reproduced from [5] with permission from the author.)

5.1.1.1 Preparation of the Working Electrodes for Catalyst/Catalyst Layer Studies
In fuel cell catalyst/catalyst layer down-selection, the process of preparing the working electrodes includes several steps:

1. Selection of the working electrode substrates, such as glassy carbon or pyrolytic graphite. These substrates have insignificant catalytic activity towards fuel cell reactions (e.g., ORR, hydrogen oxidation reaction [HOR], and methanol oxidation), so they will not interfere with the catalytic activity of the targeted catalyst.
2. Pre-treatment of the electrode substrate, which involves polishing, sonicating, and rinsing. The electrode can be polished using diamond pastes or alumina, followed by ultrasonic cleaning in water, acetone, or ethanol, and is then rinsed to obtain a clean surface.
3. Formation of a thin catalyst layer on the clean electrode surface through surface attachment, such as dropping catalyst ink onto the electrode surface. For either a monolayer or a multilayer of the catalyst on the electrode surface, the bare electrode can be inserted into the soaking solution containing the catalyst, and then taken out and rinsed with water.
4. Installation of the catalyzed electrode into the electrochemical cell for measurement. This process is suitable for stationary electrode measurement, rotating disk electrode (RDE), and/or rotating ring-disk electrode (RRDE).

The coating procedure is critical and can greatly influence accuracy in measuring electrode performance. A typical active coating procedure using Pt/C as catalyst was described by Antoine et al. [6]. In their process, a mixture of Pt/C/Nafion® solution and water was homogenized with ultrasonic waves. A measured volume of this mixture was then dropped onto a glassy carbon support to obtain an RDE active layer. This procedure allowed a very thin active layer with homogeneity in both thickness and composition, and with a known Pt loading. The coated electrode was then dried at room temperature, allowing the low-boiling-point solvents to evaporate, and heated in an oven at 160°C, forming a thin active layer without large gas pores. The resulting glassy carbon electrode coated with a thin active layer was hydrated with ultra-pure water before its use in the RDE study.

5.1.1.2 Gas Diffusion Electrode
Unlike the RDE technique, which is quite popular for characterizing catalyst activities, the gas diffusion electrode (GDE) technique is not commonly used by fuel cell researchers in an electrochemical half-cell configuration. The fabrication of a house-made GDE is similar to the preparation of a membrane electrode assembly (MEA). In this fabrication, Nafion® membrane disks are first hot-washed successively in nitric acid, sulphuric acid, hydrogen peroxide, and ultra-pure water. The membranes are then coated with a very thin active layer and hot-pressed onto the gas diffusion layer (GDL) to obtain a Nafion® membrane assembly. The GDL (e.g., Toray paper) is very thin and porous, and thus the associated diffusion limitation is small enough to be ignored, which makes it possible to study the specific kinetic behaviour of the active layer [6].

A GDE study using an electrochemical cell requires a special cell design that allows the active side (catalyst layer side) of the GDE to be in contact with an

aqueous electrolyte, such as a sulphuric acid solution. A reference electrode (SCE or NHE) is connected close to the GDE active layer using a Luggin capillary. The external carbon paper or cloth side of the GDE is in contact with gas (N_2 or O_2) and connected with a wire for electronic conduction [6]. A schematic design of the GDE technique is illustrated in Figure 5.2.

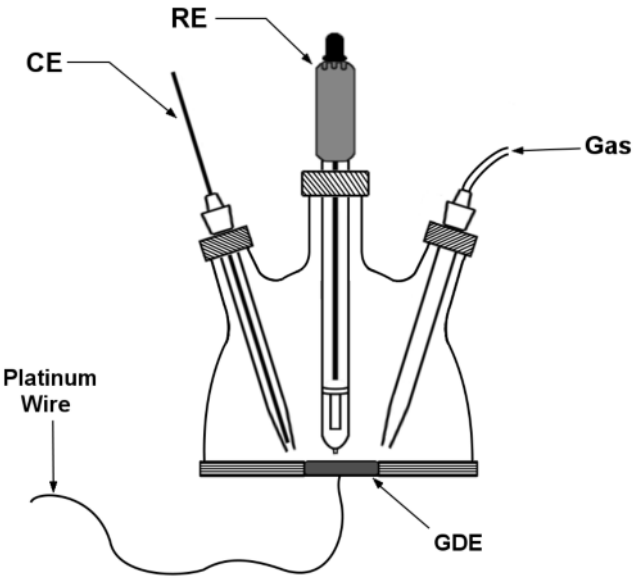

Figure 5.2. The GDE technique in an electrochemical half-cell configuration

Using the GDE technique, Antoine et al. [6] studied the ORR on carbon-supported platinum nanoparticles. An example of the EIS results from the GDE test is shown in Figure 5.3. The ohmic resistance between the Luggin capillary tip and the catalyst layer, which is related to both the aqueous electrolyte and the proton exchange membrane resistance, was subtracted in the figure. Therefore, the interception of the high-frequency end on the x-axis starts from the origination point. The EIS spectra show a high-frequency (HF) and a medium-frequency capacitive loop, and one low-frequency inductive loop. When the electrode overpotential value increases, the polarization resistance decreases, while the HF capacitive loop remains unchanged with potential. This HF loop can be explained as either the electronic contact impedance between the electronic supply and the GDE gas diffusion layer, or the ionic ohmic drop resulting from double-layer charging inside the active layer [6].

The main advantage of the GDE technique is that the electrode structure is similar to the fuel cell membrane electrode assembly. Therefore, the obtained results may be closer to those tested in a real fuel cell. However, the GDE technique is still rarely used in fuel cell studies due to the complicated design of the electrochemical cell, as well as the instability and poor-repeatability of the results. Furthermore, prior to the electrochemical measurements, the GDE needs to

be activated. Different states of activation may result in different electrode responses, creating confusing information for electrode performance evaluation.

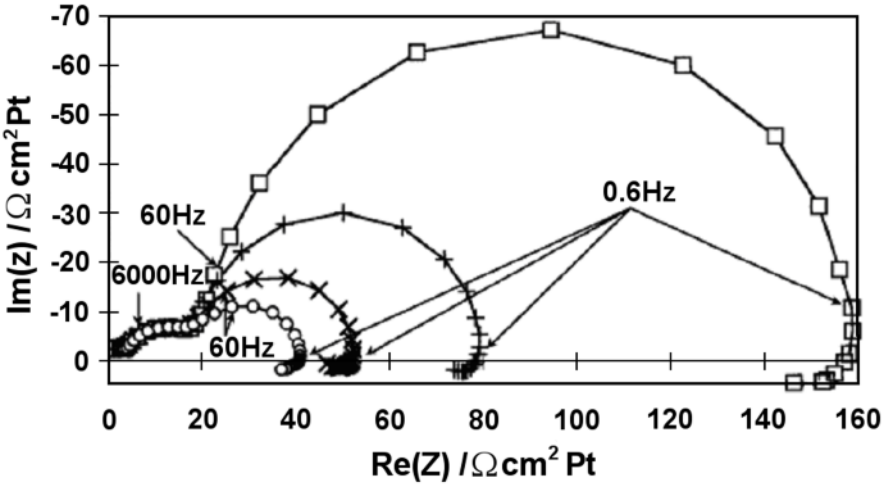

Figure 5.3. Electrode potential effects on ORR impedance spectra using GDE; AC frequency range: 6×10^4 to 6×10^{-3} Hz. Electrode potentials (versus SCE): (□) 0.54 V; (+) 0.49 V; (×) 0.44 V; (○) 0.39 V [6]. (Reprinted from Journal of Electroanalytical Chemistry, 499, Antoine O, Bultel Y, Durand R. Oxygen reduction reaction kinetics and mechanism on platinum nanoparticles inside Nafion®, 85–94, ©2001, with permission from Elsevier.)

5.1.1.3 Examples of Ex situ *Measurements*

Capacitance and Ion Transport Properties of Fuel Cell Catalyst Layers

Ex situ measurements using EIS are normally performed in both acidic and alkaline electrolytes. In Easton and Pickup's work [2], EIS was used to measure the capacitances and ion transport properties of fuel cell catalyst layers. The experiment was carried out at ambient temperature in a typical three-compartment cell using Ag/AgCl as a reference electrode and Pt wire as a counter electrode. Half-cell electrochemical measurements were performed by exposing the electrode to a 0.5 M H_2SO_4 electrolyte. Catalyst ink was prepared by mixing 20% Pt/Vulcan XC72 carbon black and 5% Nafion® solution. Different amounts of catalyst ink were applied with a syringe onto a glassy carbon electrode and allowed to dry before use. Figure 5.4 shows the Nyquist plots obtained with various amounts of catalyst ink applied to the electrode. It can be seen that the ionic resistance increases with the amount of ink applied. In addition, there appears to be a larger increase in resistance for electrodes containing 4 to 6 μL of catalyst ink. The authors clarified that this phenomenon might be due partly to a less homogenous catalyst layer when large amounts of ink are applied.

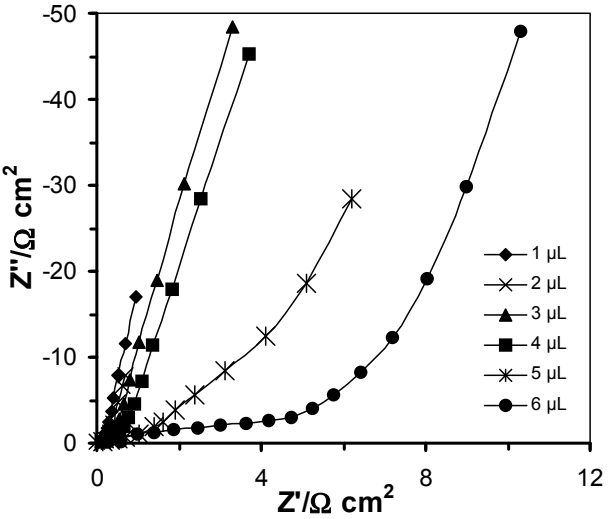

Figure 5.4. Nyquist plots obtained at a DC bias potential of 0.2 V versus Ag/AgCl for electrodes with various amounts of catalyst ink applied [2]. (Reprinted from Electrochimica Acta, 50(12), Easton EB, Pickup PG. An electrochemical impedance spectroscopy study of fuel cell electrodes, 2469–7, ©2005, with permission from Elsevier.)

Kinetics of the ORR and HOR

EIS data were collected by Schulze et al. [1] using a catalyst-coated RDE in a half-cell containing 1 M H_2SO_4 electrolyte. The kinetics of both the ORR and the HOR were studied; for the ORR on a catalyst-coated electrode, the exchange current density was about 2 $\mu A/cm^2$ and the Tafel slope was 92 mV/decade.

Genies et al. [4] also studied the ORR on platinum nanoparticle catalyst using the EIS method performed in alkaline media. They employed a classical glass cell with three electrodes; the working electrode was a glassy carbon RDE embedded inside a Kel-F holder. Catalyst ink was deposited on this RDE surface and dried in air. The counter electrode was a large platinum grid, and the reference electrode was an Hg/HgO electrode in 1 M NaOH (0.100 V/SCE) connected to the cell via a Luggin capillary. The oxygen reduction experiments were conducted in 0.1, 0.5, 1, and 6 M NaOH solutions, separately. The results of the EIS with this RDE are depicted in Figure 5.5, which shows a large capacitive loop (actually two overtopping capacitive loops) with a linear trend (phase angle $\pi/4$) at high frequencies, becoming a semicircle at lower frequencies. Genies et al. attributed the linear trend in the high-frequency range to the charging of the particle double layers through an ohmic resistor network, and the low-frequency behaviour to the control of diffusion inside the solution. At low frequencies, kinetic and mechanistic information (possible inductive loop, etc.) are masked by diffusion limitations inside the aqueous electrolyte. Comparing these results at low frequencies with those observed in acidic media, they proposed a mechanism with a chemical step (5.3) and a final electrochemical step (5.4) by assuming the co-existence of the first step (5.1) (adsorption of O_2) on platinum and the second step (5.2) (first charge transfer reaction). Note that the second step is considered the rate-determining step.

$$O_2 \underset{\overleftarrow{k_A}}{\overset{\overrightarrow{k_A}}{\rightleftarrows}} (O_2)_{ads} \tag{5.1}$$

$$(O_2)_{ads} + e^- \xrightarrow{\overrightarrow{k_B}} (O_2^-)_{ads} \tag{5.2}$$

$$(O_2H)_{ads} + H_2O \underset{\overleftarrow{k_C}}{\overset{\overrightarrow{k_C}}{\rightleftarrows}} 3(OH)_{ads} \tag{5.3}$$

$$(OH)_{ads} + e^- \underset{\overleftarrow{k_D}}{\overset{\overrightarrow{k_D}}{\rightleftarrows}} OH^- \tag{5.4}$$

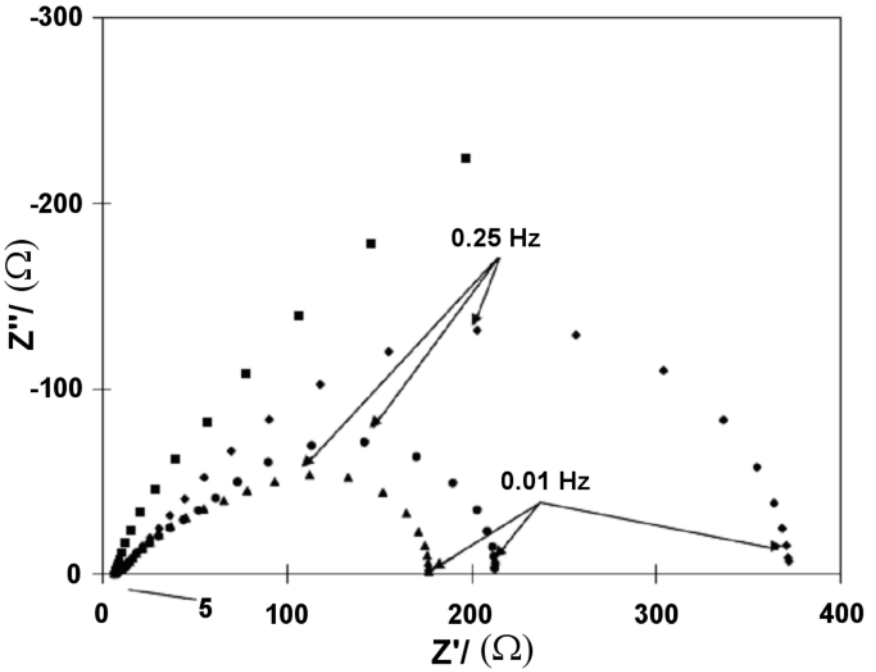

Figure 5.5. Experimental Nyquist diagrams for the ORR on a Pt nanoparticle catalyst (40% Pt/Pt+C) in alkaline solution (1 M NaOH) using an active layer on an RDE at 25°C (EIS frequency range: 5 mHz–10^5 Hz). Electrode potentials (versus Hg/HgO electrode): (■) -0.02 V; (◆) -0.03 V; (▲) -0.06 V; and (●) -0.08 V [4]. (Reprinted from Electrochimica Acta, 48(25–6), Genies L, Bultel Y, Faure R, Durand R. Impedance study of the oxygen reduction reaction on platinum nanoparticles in alkaline media, 3879–90, ©2003, with permission from Elsevier.)

Genies et al. [4] also studied the ORR with a GDE in a half-cell system containing an alkaline electrolyte. The GDE was made by rolling a diffusion layer (Vulcan XC72 + PTFE) onto a nickel mesh current distributor. This diffusion layer was then coated by an active layer (E-TEK Pt/C + 40 wt% Pt/(Pt+C) + PTFE) using a spraying technique. The EIS data obtained using this GDE, as shown in Figure 5.6,

display a large capacitive loop at high and intermediate frequencies, which decreases with increasing current density, and a small inductive loop at low frequencies with the potentials –0.05, –0.08, and –0.10 V versus Hg/HgO, respectively. Moreover, a linear trend (phase angle $\pi/4$) can be observed in the high-frequency region. According to the shape and magnitude of the DC and AC responses of the GDE with respect to the oxygen reduction mechanism, the results were interpreted using their active layer model, and a two-electrochemical-step mechanism was presented:

$$O_2 + 2H_2O + 4e^- \rightarrow 4OH^- \text{ (four-electron pathway)} \tag{5.5}$$

$$O_2 + H_2O + 2e^- \rightarrow HO_2^- + OH^- \text{ (two-electron pathway)} \tag{5.6}$$

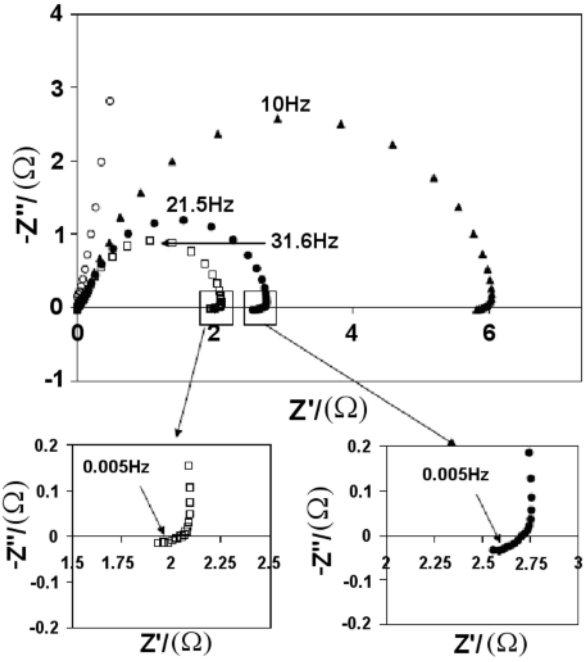

Figure 5.6. Experimental Nyquist diagrams for the ORR on Pt nanoparticle catalyst (40% Pt/(Pt+C)) in an alkaline solution (1 M NaOH) using an active layer in a GDE system at 25°C (frequency range: 5 mHz~10^5 Hz). Electrode potentials (versus Hg/HgO electrode): (○) 0.0 V; (▲) –0.05 V; (●) –0.08 V; (□) –0.10 V [4]. (Reprinted from Electrochimica Acta, 48(25–6), Genies L, Bultel Y, Faure R, Durand R. Impedance study of the oxygen reduction reaction on platinum nanoparticles in alkaline media, 3879–90, ©2003, with permission from Elsevier.)

Carbon Support

It is well known that catalyst support plays an important role in the performance of the catalyst and the catalyst layer. The use of high surface area carbon materials, such as activated carbon, carbon nanofibres, and carbon nanotubes, as new electrode materials has received significant attention from fuel cell researchers. In particular, single-walled carbon nanotubes (SWCNTs) have unique electrical and electronic properties, wide electrochemical stability windows, and high surface areas. Using SWCNTs as support materials is expected to improve catalyst layer conductivity and charge transfer at the electrode surface for fuel cell oxidation and reduction reactions. Furthermore, these carbon nanotubes (CNTs) could also enhance electrocatalytic properties and reduce the necessary amount of precious metal catalysts, such as platinum.

The activities of CNTs have been evaluated by Girishkumar et al. [7] using ex situ EIS. Their study was conducted in a three-compartment electrochemical cell using a GDE electrode (a carbon fibre paper coated with SWCNTs and Pt black as an anode or cathode). Electrophoretic deposition was used to deposit both the commercially available carbon black (CB) for comparison and the SWCNT onto the carbon Toray paper. Commercially available Pt black from Johnson Matthey was used as the catalyst. In both cases, the loading of the electrocatalyst (Pt), the carbon support, and the geometric area of the electrode were kept the same. EIS was conducted in a potentiostatic mode at either an open circuit potential or controlled potentials.

SWCNT/Pt and CB/Pt had close electrochemical active surface area values, which were obtained by cyclic voltammograms. Thus, the EIS data obtained were used to compare the interfacial behaviour of the two supports based on the observed differences in electrode kinetics. Figure 5.7*a* shows the EIS results in the form of a Nyquist plot for the HOR at a carbon fibre electrode (CFE) coated with CB/Pt. The electrode potential was controlled at 0.1 V (versus SCE). Figure 5.7*b* shows the corresponding impedance spectra for the HOR at a CFE coated with SWCNT/Pt. The insets in Figures 5.7*a* and *b* present the impedances under open circuit conditions. The fitting parameters were obtained from the equivalent circuit of the Randle's cell. At an electrode potential of 0.1 V (versus SCE), the charge-transfer resistance for a CFE coated with SWCNT/Pt is about an order of magnitude less than that of a CFE coated with CB/Pt. It also can be seen that the CB/Pt electrode has a very high charge-transfer resistance under open circuit conditions as well, although it drops to 500 Ω at 0.1 V. This behaviour indicates that the interfacial kinetics at the electrode/electrolyte interface of the CB/Pt-coated CFE is slower than that at the interface of SWCNT/Pt-coated CFE. This is explained by the stronger adsorption of H^+ on the surface of the SWCNT/Pt compared with on the CB/Pt, which likely played an important role in facilitating the electron transfer kinetics.

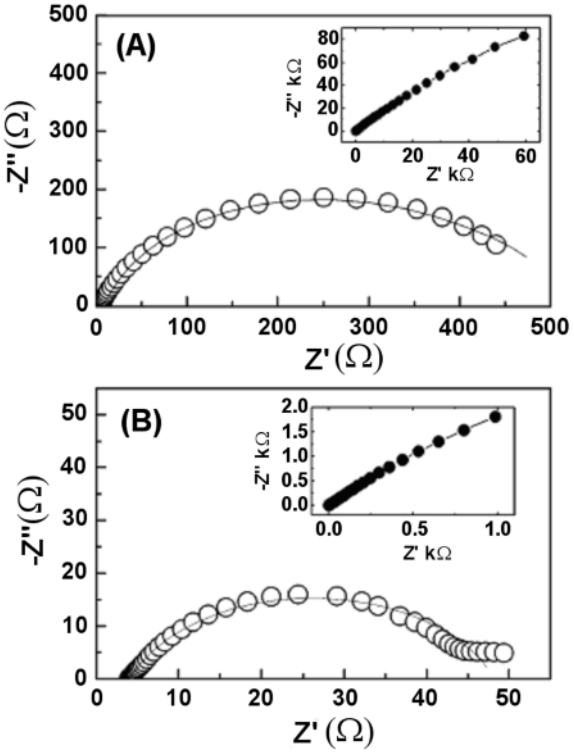

Figure 5.7. Nyquist plots for the hydrogen oxidation reaction at the electrode potential of 0.1 V (versus SCE), at *a* the CFE/CB/Pt electrode and *b* the CFE/SWCNT/Pt electrode. The data under open circuit conditions are shown as insets in both *a* and *b*. Circles indicate experimental data; solid lines indicate the theoretical fits. The area of the electrode is 1 cm^2. AC frequency range: 100 kHz–100 mHz [7]. (Reprinted with permission from Langmuir 2005;21:8487–94. ©2005 American Chemical Society.)

5.1.2 Membrane Characterization

The ionic resistance of a polymer electrolyte membrane is an important parameter in determining the mobility of protons through the membrane and the corresponding voltage loss across the membrane. Currently, the most commonly used membranes in PEM fuel cells are Nafion® membranes produced by DuPont. However, these membranes are limited to low-temperature uses (usually below 80°C) because membrane dehydration at high temperatures can lead to reduced water content and then a lower proton transfer rate, resulting in a significant decrease in conductivity. The relationship between conductivity and the diffusion coefficient of protons can be expressed by the Nernst-Einstein equation:

$$D_{H^+} = \frac{RT}{F^2}\lambda \tag{5.7}$$

where D_{H^+} is the diffusion coefficient of protons, λ is its equivalent conductivity, and R, T, and F are the gas constant, absolute temperature, and Faraday constant, respectively.

Measurement of membrane proton conductivity is important for understanding the membrane properties. Several techniques, such as EIS, current interruption, and nuclear magnetic resonance, have been used to measure the conductivity of membranes. Of these, EIS is the most powerful and popular, and here we will focus only on this technique. In PEMs, protons can transport in two directions, across the membrane and through the membrane. This results in two conductivities, in-plane conductivity and through-plane conductivity. For PEM fuel cells, through-plane conductivity measurement is more important than in-plane because proton transfer occurs in the through-plane direction. In this measurement, the value obtained by the instrument is resistance rather than conductivity. The displayed conductivity is calculated based on measured resistance. Therefore, the terms through-plane resistance and in-plane resistance are also often used. In through-plane conductivity measurement, a small amount of resistance due to a thin membrane can be overwhelmed by the contact resistance between the membrane and the probes, leading to large measurement errors. Therefore, in-plane conductivity measurement is more popular. Nevertheless, if the membrane is isotopic, the through-plane conductivity should be the same as the in-plane conductivity.

The conductivity of the membrane can be calculated based on measured resistance by the following equation:

$$\sigma = \frac{L}{RWT} \tag{5.8}$$

where σ is the membrane conductivity (S/cm), L is the length between the probes, R is the measured resistance, W is the membrane width, and T is the membrane thickness.

5.1.2.1 In-Plane Conductivity Measurement

Two-Probe Method

In the two-probe method, two probes, each measuring both current and voltage, are used to sense the current and voltage passing through the membrane. Figures 5.8*a* and *b* show the schematic diagram of a two-probe cell, and the corresponding equivalent circuit, respectively. Since the voltage and the current are measured from the same probes, the current passing through the whole circuit and the interfacial impedance between the probe and the membrane are also included in the measurement. Although interfacial impedance may lead to large errors in conductivity measurements, our recent study comparing the two- and four-probe methods showed that the two-probe method also gave reliable results [9].

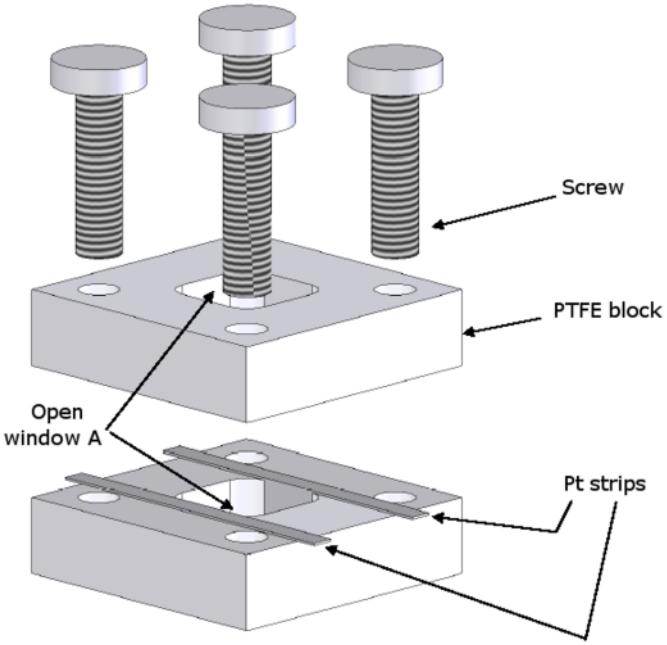

a

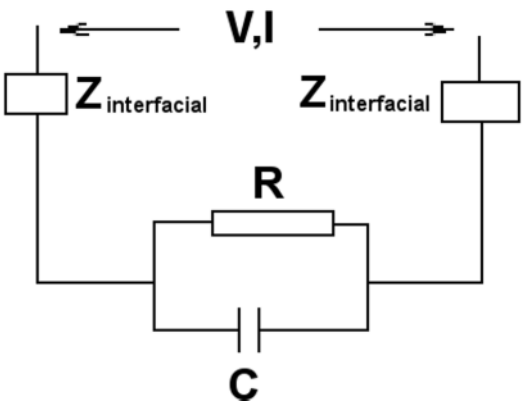

b

Figure 5.8. *a* Schematic diagram of a two-probe conductivity cell [9]. (Reproduced by permission of ECS—The Electrochemical Society, from Xie Z, Song C, Andreaus B, Navessin T, Shi Z, Zhang J, Holdcroft S. Discrepancies in the measurement of ionic conductivity of PEMs using two- and four-probe AC impedance spectroscopy); *b* Equivalent circuit of the two-probe method.

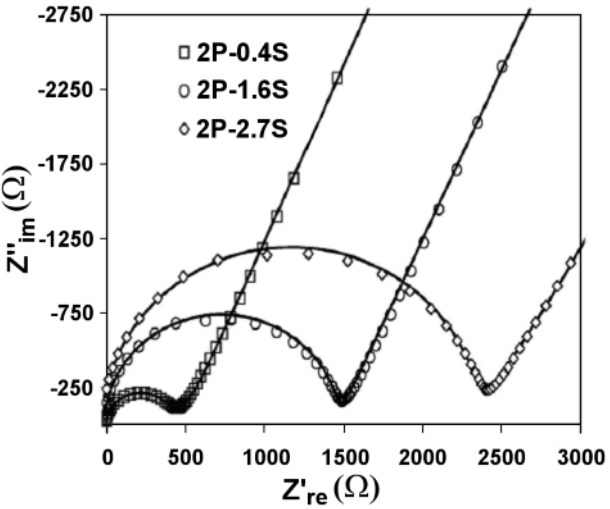

Figure 5.9. AC impedance spectra of Nafion®115 membrane obtained by the two-probe cell method with different probe distances, at room temperature and under fully hydrated conditions [9]. (Reproduced by permission of ECS—The Electrochemical Society, from Xie Z, Song C, Andreaus B, Navessin T, Shi Z, Zhang J, Holdcroft S. Discrepancies in the measurement of ionic conductivity of PEMs using two- and four-probe AC impedance spectroscopy.)

Typical impedance spectra of PEMs measured using the two-probe cell are shown in Figure 5.9, in which a semicircle followed by a 45° line can be observed. The membrane resistance is extracted from the low-frequency intercept of the semicircle. At low frequencies the 45° line is dominated by the blocking behaviour of the Pt/Nafion® interface.

Four-Probe Method

In the four-probe method, the voltage-sensing probe is separated from the current-sensing probe. Two inner voltage probes are added between the two outer current probes. Figure 5.10*a* and *b* show the schematic diagram of a four-probe cell, and the corresponding equivalent circuit, respectively. Since there is no current passing through the voltage probes, the interfacial impedance is not measured with this method. Thus, in principle, the four-probe method is more precise than the two-probe method. Unlike that of the two-probe method, the impedance spectra of the four-probe method showed a geometrically dependent low-frequency feature. Figure 5.11 shows typical spectra obtained with Pt strips as both outer probes and inner probes.

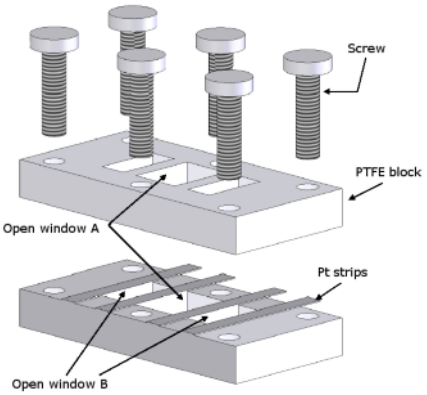

a

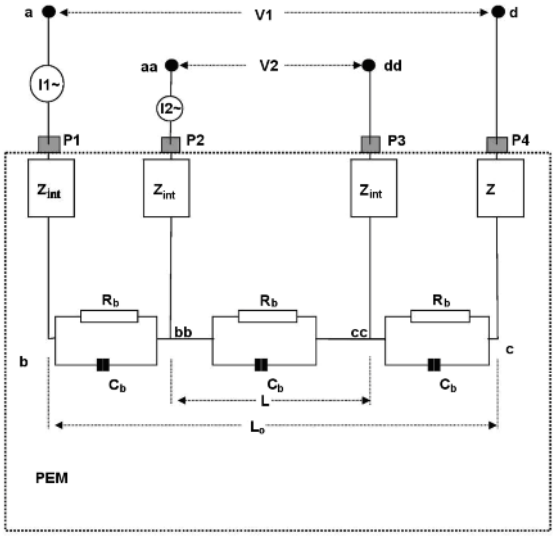

R_b, C_b: Membrane bulk resistance and bulk capacitor
Z_{int}: Pt/membrane interfacial impedance
L: Distance of two voltage-sensing probes in 4-probe
L_o: Distance of two current injectors/ voltage-sensing probes in 2-probe
I1~: ac current applied

I2~: ac current in measuring circuit
V1: ac potential applied
V2: ac potential measured in measuring circuit
a, b, c, d: ac signal applied to circuit
aa, bb, cc, dd: ac signal measuring circuit
P1, P2, P3 and P4: Pt current/voltage probe

b

Figure 5.10. *a* Schematic diagram of a four-probe conductivity cell; *b* Equivalent circuit of the four-probe conductivity measurement cell [9]. (Reproduced by permission of ECS—The Electrochemical Society, from Xie Z, Song C, Andreaus B, Navessin T, Shi Z, Zhang J, Holdcroft S. Discrepancies in the measurement of ionic conductivity of PEMs using two- and four-probe AC impedance spectroscopy.)

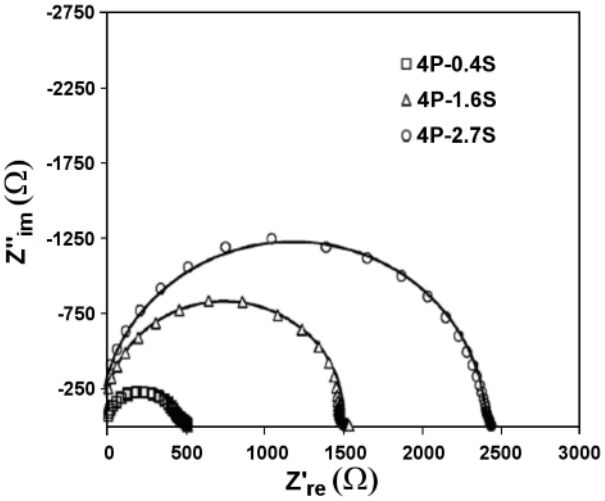

Figure 5.11. AC impedance spectra of Nafion®115 membrane at room temperature under fully hydrated conditions, measured with the four-probe method [9]. (Reproduced by permission of ECS—The Electrochemical Society, from Xie Z, Song C, Andreaus B, Navessin T, Shi Z, Zhang J, Holdcroft S. Discrepancies in the measurement of ionic conductivity of PEMs using two- and four-probe AC impedance spectroscopy.)

Table 5.1 shows the conductivity data measured by the two methods. The results obtained are independent of the method used, but dependent on the distance between the probes. A wide probe distance offers results similar to those reported in the literature [10].

Table 5.1. Conductivity data for Nafion®115 obtained from the two-probe and four-probe methods [9]

Probe distance	**Conductivity (S/cm)**	
	Two-probe method	Four-probe method
0.4 cm	0.071	0.075
1.6 cm	0.086	0.084
2.7 cm	0.090	0.090

Comparison of the Two-Probe and Four-Probe Methods

In principle, the four-probe method is more accurate than the two-probe, because in the former the interface impedance can be eliminated. However, it was reported that in different frequency ranges the membrane resistance and contact resistance could be easily separated. For example, in the two-probe method, the favourite frequency range is 100 to 500 kHz, while in the four-probe method the range becomes 1 to 100 kHz [11]. Thus, both methods can yield reliable results, and the probe distance can affect measurement accuracy. Our experiments using both methods indicated that a large probe distance is required to obtain accurate results.

Coaxial Probe Method [12]

The open-ended coaxial probe method was developed in 1995. This method requires that the gap between the two probes be larger than the membrane thickness, a condition that can easily be met. However, this method did not become popular, possibly due to the complexity of setting up the coaxial probes. The geometry and equivalent circuit of the probe are shown in Figures 5.12*a* and *b*, respectively, where ε^* is the sample permeability. The equivalent circuit consists of an interfacial capacitance in series with a capacitance C_T and a resistance R_T in parallel. A typical impedance spectrum is shown in Figure 5.13. The membrane through-plane resistance R_T can be obtained from the intercept of the impedance semicircle with the real axis. The conductivity then is calculated using the following equation:

$$\sigma = \frac{1}{2\pi R_T h} \ln\left(\frac{b}{a}\right) \tag{5.9}$$

where h is the membrane thickness, R_T is the measured resistance, and a and b are the radii of the inner and outer conductors, respectively, as shown in Figure 5.12*a*.

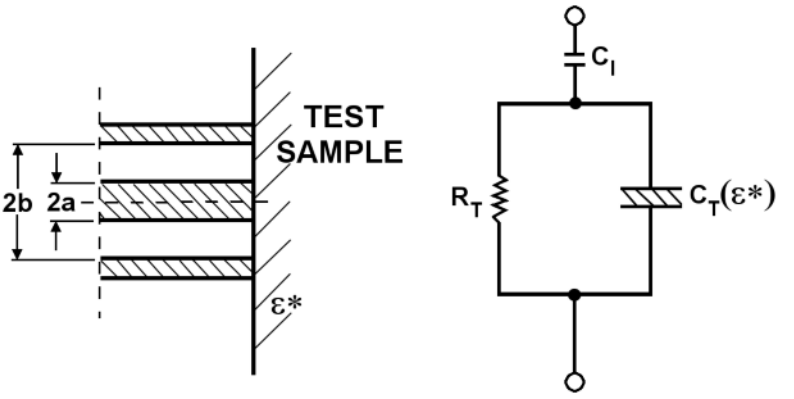

a *b*

Figure 5.12. Open-ended coaxial probe for conductivity measurement: *a* geometry, *b* equivalent circuit [12]. (Reprinted from Journal of Electroanalytical Chemistry, 395, Gardner CL, Anantaraman AV. Measurement of membrane conductivities using an open-ended coaxial probe, 67–73, ©1995, with permission from Elsevier.)

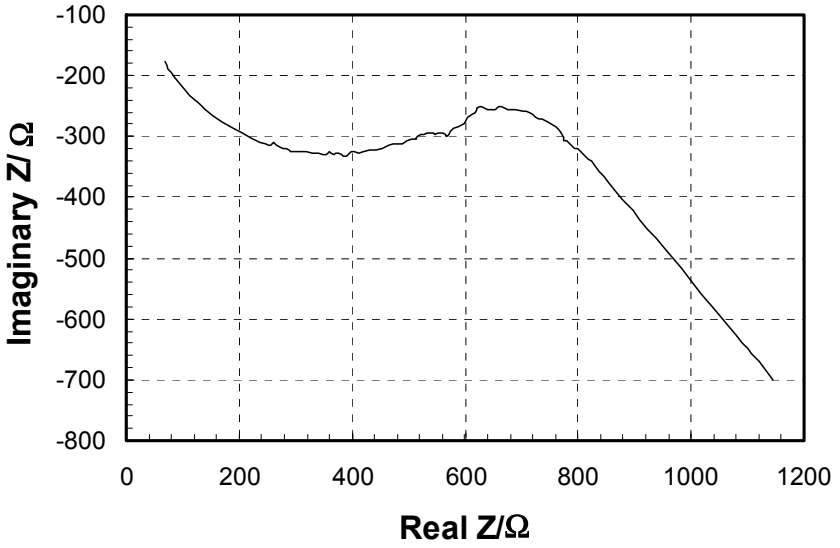

Figure 5.13. Typical impedance spectrum obtained with the coaxial cell [12]. (Reprinted from Journal of Electroanalytical Chemistry, 395, Gardner CL, Anantaraman AV. Measurement of membrane conductivities using an open-ended coaxial probe, 67–73, ©1995, with permission from Elsevier.)

5.1.2.2 Through-Plane Conductivity Measurement

Some membranes are anisotropic, and the conductivity in the through-plane direction is different from that in the in-plane direction. Although Nafion® membrane has been considered isotropic in some cases, it is still debatable whether or not its in-plane conductivity is different from its through-plane conductivity. The difference between the in-plane and through-plane conductivity might be due to a difference in relative humidity. If this is true, the relative humidity can be kept the same for both the in-plane and the through-plane, which should result in the same conductivity in both directions. In a real situation as reported in the literature, it is more likely that the through-plane conductivity will be less than the in-plane conductivity. For example, the membrane resistance measured in fuel cells, which is the through-plane resistance, is much less than the in-plane resistance measured ex situ by the two-probe or four-probe methods.

In fuel cells, through-plane conductivity is more meaningful than in-plane because the proton transfer occurs in the through-plane direction. Several methods have been developed to measure the through-plane conductivity, and these will now be described.

Four-Probe Method [10]

In this method, two saturated calomel reference electrodes (SCEs) are used as the potential probes, Pt gauze is used for both current probes, and 1 M H_2SO_4 is the electrolyte. Figure 5.14 shows the schematic of the hardware and instruments in this method.

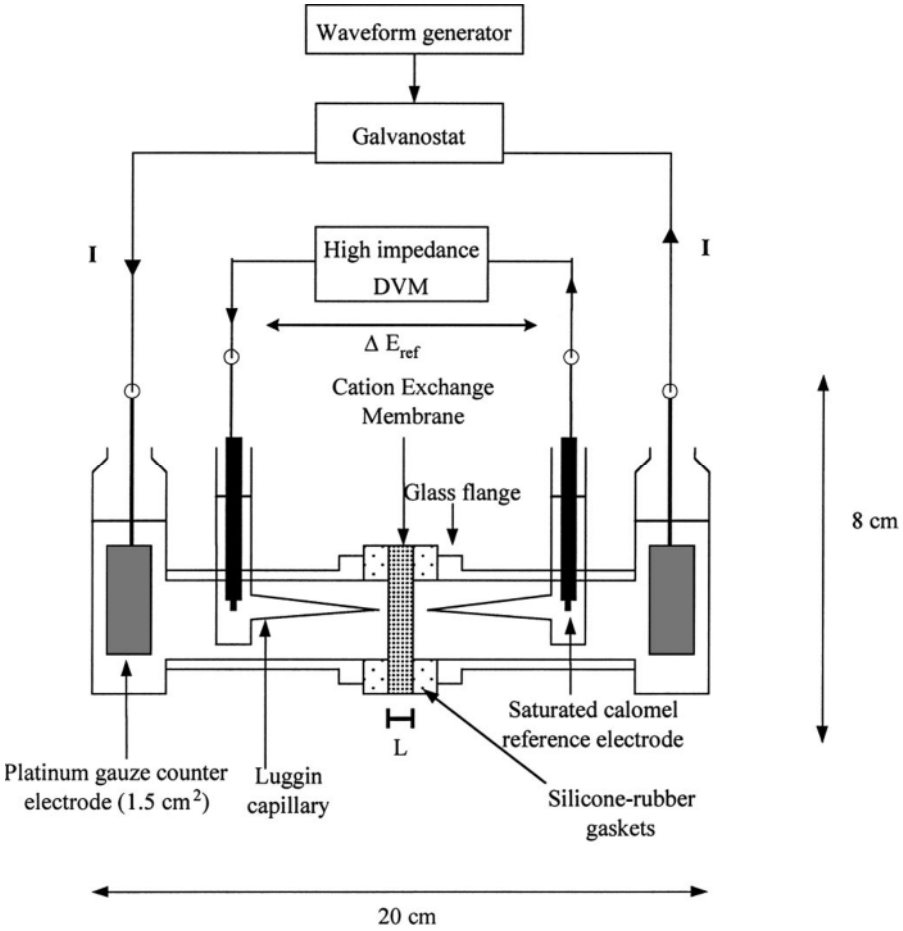

Figure 5.14. Schematic of the four-electrode glass cell used for conductivity measurements on a circular sample of the membrane, using a steady-state linear sweep galvanodynamic technique [10]. (Reproduced by permission of ECS—The Electrochemical Society, from Slade S, Campbell SA, Ralph TR, Walsh FC. Ionic conductivity of an extruded Nafion 1100 EW series of membranes.)

As a current (I) is swept between the two Pt gauze probes, the potential difference between the two sides of the membrane is measured as a function of current density. The plots of the potential difference (ΔE_{ref}) between the two SCEs versus current obey Ohm's law, and the slope of the plot gives the cell resistance (R_{cell}) according to Equation 5.10:

$$\Delta E_{ref} = IR_{cell} \tag{5.10}$$

The cell resistance is the sum of the membrane resistance and the electrolyte resistance. Therefore, the background electrolyte resistance ($R_{electrolyte}$) should be

determined by measuring the potential difference between the two SCE electrodes in the absence of the membrane:

$$\Delta E_{ref} = IR_{electrolyte} \tag{5.11}$$

Thus, the membrane resistance is calculated as follows

$$R_{mem} = R_{cell} - R_{electrolyte}\left(\frac{a-h}{h}\right) \tag{5.12}$$

where a is the distance between the two SCE tips and h is the membrane thickness.

Coaxial Probe Method and Modified Coaxial Probe Method [11, 12]
A coaxial probe can also be used to measure the through-plane conductivity of membranes. Figure 5.15 shows the schematic for a coaxial conductivity measurement cell. In this method, the membrane is cut to the same size as the inner conductor, and the measured resistance is the through-plane resistance. The resulting conductivity, 2.4×10^{-2} S/cm, is close to that reported in the literature.

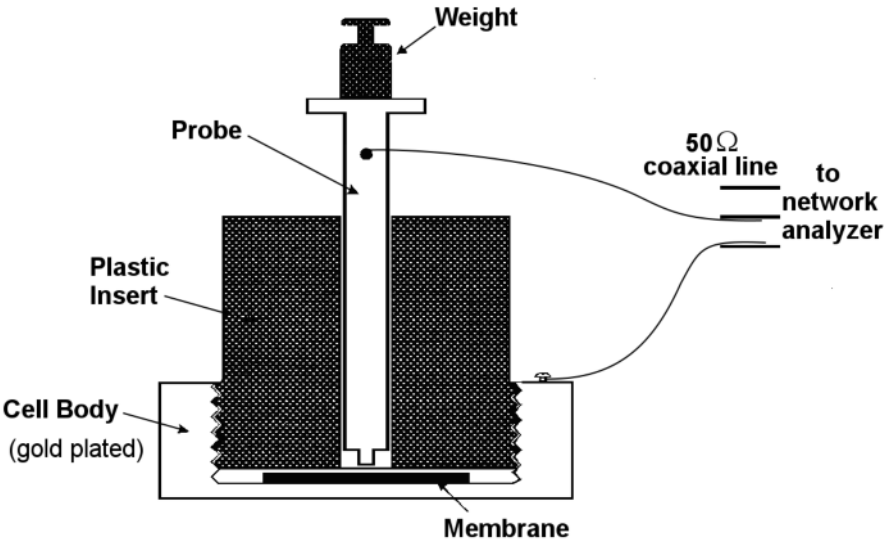

Figure 5.15. Schematic cell for the measurement of through-plane conductivity [13]. (Reprinted from Journal of Electroanalytical Chemistry, 449, Gardner CL, Anantaraman AV. Studies on ion-exchange membranes. II. Measurement of the anisotropic conductance of Nafion®, 209–14, ©1998, with permission from Elsevier.)

The through-plane conductivity (σ_{TPC}) can be calculated according to Equation 5.13:

$$\sigma_{TPC} = \frac{\pi r^2}{R_N h} \tag{5.13}$$

where R_N is the membrane resistance measured in the through-plane direction, h is the membrane thickness, and r is the radius of the probe.

5.1.3 Comparison of Ex situ and In situ EIS Methods

Although a great deal of effort has been put into component characterization using ex situ techniques, the most interesting data are still those obtained from in situ fuel cell experiments (using a single cell or a stack to characterize the materials/components). For measurements in fuel cells, electrochemical experiments can normally be performed on MEAs in a two-electrode configuration (anode and cathode) with hydrogen passing through one electrode coated with Pt catalyst. This hydrogen-fed electrode serves as both counter and reference electrode, while the other electrode is the working electrode. For different purposes, the measurement can be performed in a different gas feed mode.

During the investigation of CO poisoning in PEM fuel cell anodes, Ciureanu and Wang [14] compared in situ and ex situ measurements. They summarized three primary electrochemical methods that could be used for investigating the mechanism by which H_2 and H_2/CO mixtures are oxidized:

(1) Ex situ potentiostatic and potentiodynamic studies in acid solution (1 N H_2SO_4 or $HClO_4$). These two methods are particularly suited to investigating the mechanistic aspects of CO poisoning on well-defined electrodes. However, the kinetic information obtained from these ex situ studies may not always reflect the real situation in a PEM fuel cell.

(2) In situ polarization studies using an entire fuel cell. This method provides information on the behaviour of the electrocatalyst in actual exploitation conditions. However, little data may be available on mechanistic aspects.

(3) In situ stripping voltammetry performed directly on a poisoned GDE. This method provides information only on the oxidation of adsorbed CO in an inert atmosphere, rather than the dynamic equilibrium in an H_2 + CO gas mixture.

For membrane resistance measurements, it is convenient to measure through-plane conductivity using a single fuel cell or stack. The temperature and relative humidity of the membrane can be controlled by heating the fuel cell and humidifying the system. So far, there seem to be no published reports on the systematic investigation of membrane conductivity using this method. In the literature, a similar method was described for measuring Nafion® membrane conductivity [15]. The conductivity measurement cell, shown in Figure 5.16, can be considered a simplified fuel cell but without the catalyst layer. This is actually a two-probe method.

For in-plane membrane resistance measurements, the major error arises from small membrane thickness, as the thickness depends greatly on the relative humidity (RH) of the membrane. For example, the thickness of Nafion®117 changes from 165 μm at 34% RH to 200 μm at 100% RH at room temperature

[16]. Any inaccuracy in RH control can lead to uncertainty in membrane thickness, resulting in a large error in the conductivity results.

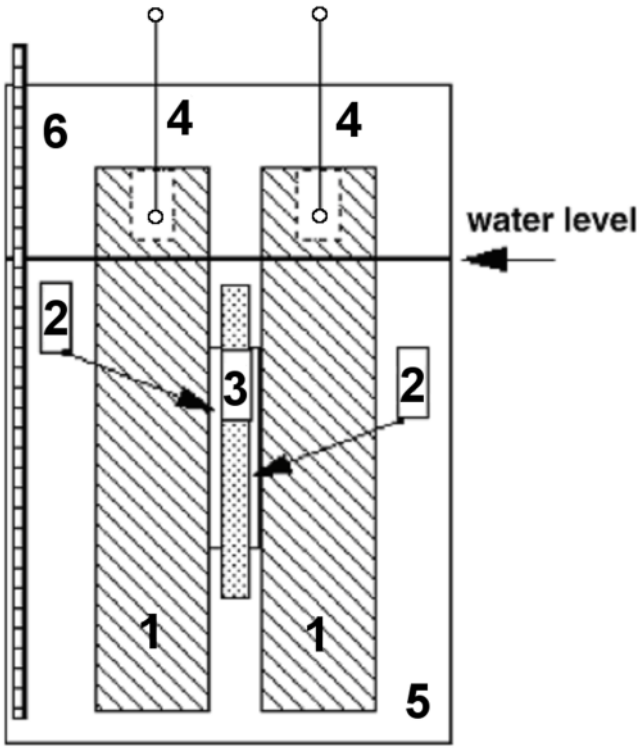

Figure 5.16. Schematic illustration of a conductivity cell for Nafion® membranes: (1) graphite current collectors; (2) carbon paper electrodes; (3) membrane; (4) electrical connections; (5) beaker filled with deionized water; and (6) thermocouple [15]. (Reprinted from Journal of Power Sources, 134, Silva RF, De Francesco M, Pozio A. Tangential and normal conductivities of Nafion® membranes used in polymer electrolyte fuel cells, 18–26, ©2004, with permission from Elsevier.)

5.2 In Situ Diagnosis

The overwhelming majority of reports in the literature on PEM fuel cell EIS measurements use an in situ approach, which offers the most interesting data in EIS research. In situ EIS measurement using a fuel cell assembly enables easier explanation of the fuel cell performance data. However, placing a reference electrode inside the two-electrode fuel cell configuration is a challenge, particularly in the case of solid electrolytes [17]. Fortunately, if the anode side with Pt as catalyst is supplied with a hydrogen stream to form a reference electrode, the measured EIS results for the cathode ORR show negligible difference compared

with those measured using a reversible hydrogen electrode (RHE) [18]. This suggests that the fuel cell performance can be in situ diagnosed using a two-electrode configuration without adding an extra reference electrode inside the assembly.

For in situ measurements with different operation modes (such as potentiostatic [voltage control] and galvanostatic [current control] modes), different gas feed modes (H_2/H_2, O_2/O_2, H_2/O_2, H_2/air, H_2/N_2, etc.), and different operating conditions (such as temperature, pressure, catalyst loading, and humidity [19]), the parameters related to the fuel cell processes (e.g., charge transfer and reactant/product mass transfer) can be obtained. Typically in studies on the effects of operating conditions, EIS measurements were carried out by changing one condition while keeping other conditions constant, in order to gain a better understanding of the effects of each condition on the impedance spectrum [20].

5.2.1 Different Gas Feeding Modes

5.2.1.1 Symmetrical Gas Feeding

In general, EIS is measured in an H_2/O_2 (air) gas feeding mode. In this case, the EIS data contains both the anode and the cathode information. Therefore, it is difficult to reliably distinguish between the individual contributions from anode and cathode. For example, if one were fitting the data using a simple Randles circuit, the apparent charge-transfer resistance would be the sum of both the anode and the cathode charge-transfer resistances, known as $R_{ct,total}$, as shown in Figure 5.17*a* and *b*.

The individual behaviours of the anode and cathode can be investigated using symmetrical single cells (H_2/H_2 or O_2/O_2) operated with an identical hydrogen or oxygen supply in both compartments. Thus, cathode and anode impedance at open circuit voltage (OCV) can be determined directly in two independent experiments without using reference electrodes [19]. For anode impedance measurement, H_2/H_2 gas feeding is used, whereas an O_2/O_2 gas supply is applied to obtain the cathode impedance behaviour. Note that for the symmetrical gas feed cell, measurements can only be performed at OCV.

Figure 5.17*c* shows the equivalent circuit of the PEM fuel cell symmetrical gas supply arrangement. Fitting the spectra of the symmetrical cells for both the anode and the cathode, as seen in Figure 5.17*c*, $R_{ct,anode}$ and $R_{ct,cathode}$ are the half values of the whole charge-transfer resistance obtained using the full H_2/H_2 or O_2/O_2 cell. This is because in a two-electrode arrangement with two identical Pt electrodes, the whole impedance of the cell is double that of each electrode. If the two electrodes are not identical, their impedances should be different. Resolving the individual values for each electrode will then become problematic.

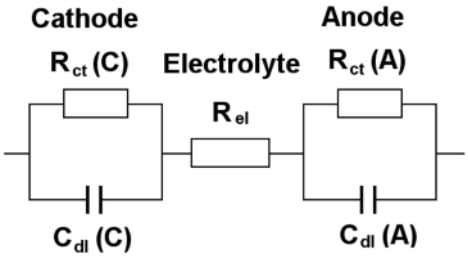

a

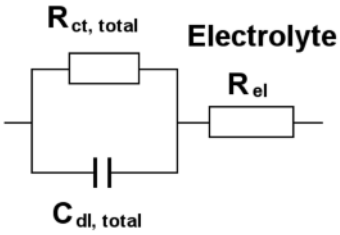

b

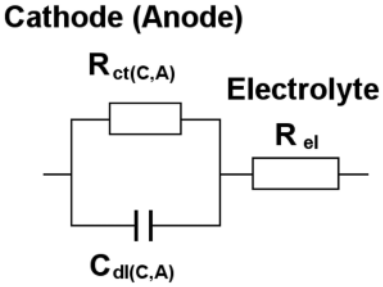

c

Figure 5.17. Equivalent circuit of a PEM fuel cell, with *a* and *b* H_2/O_2 gas supply, and *c* symmetrical gas supply [19]. (With kind permission from Springer Science+Business Media: Journal of Applied Electrochemistry, Characterization of membrane electrode assemblies in polymer electrolyte fuel cells using a.c. impedance spectroscopy, 32, 2002, 859–63, Wagner N, Figure 3, ©2002 Springer.)

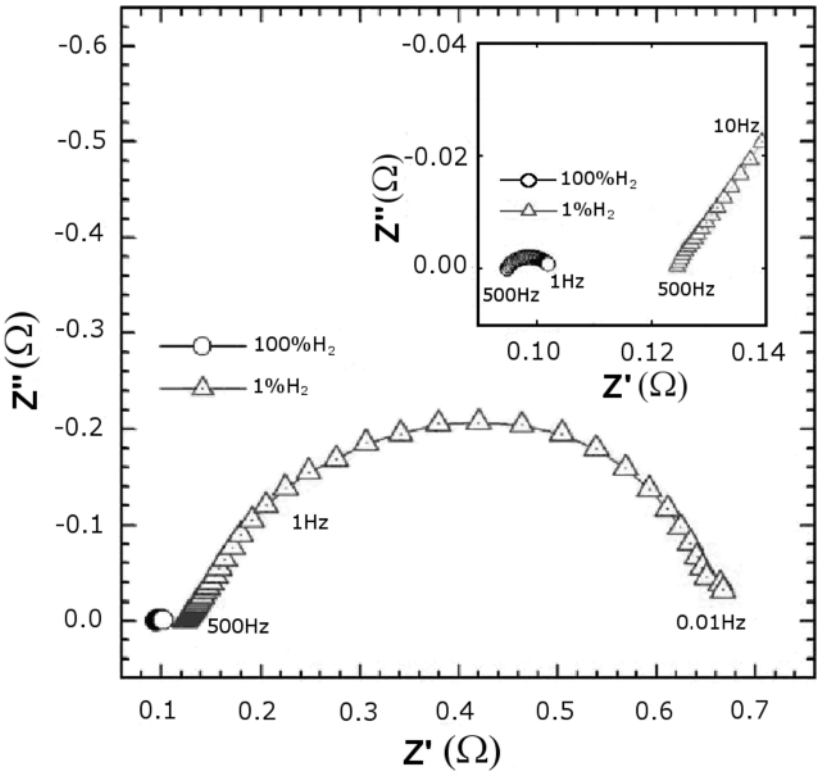

Figure 5.18. Nyquist plots of the symmetric H_2, Pt/Nafion®117/Pt, H_2 cell with P_{H_2} = 1 kPa (Δ) and P_{H_2} = 100 kPa (o). Frequency at the semicircle top was 0.24 and 20 Hz, with a signal amplitude of 5 mV [21]. (Reprinted from Electrochimica Acta, 51, Tsampas MN, Pikos A, Brosda S, Katsaounis A, Vayenas CG. The effect of membrane thickness on the conductivity of Nafion, 2743–55, ©2006, with permission from Elsevier.)

Figure 5.18 presents two typical Nyquist plots obtained at OCV and with both sides fed by hydrogen. The membrane was fully hydrated Nafion®117. Two cases were investigated, with hydrogen partial pressures of P_{H_2} = 1 kPa and P_{H_2} = 100 kPa, respectively. It can be seen from Figure 5.18 that increasing P_{H_2} causes a significant decrease in the total resistance (from 0.67 to 0.1 Ω) and a small increase in the capacitance (from 0.67 to 0.77 F) [21].

Using the charge-transfer resistances of the cathode and anode obtained by Wagner et al. [22], the apparent exchange current densities were calculated as $i^0_{anode} = 0.1\,Acm^{-2}$, and $i^0_{cathode} = 6\,\mu Acm^{-2}$. The results indicated that the cathode impedance dominated the cell impedance at OCV. This can be observed in Figure 5.19, which shows the Bode diagram of the measured EIS with symmetrical gas supply at OCV. It is clear that the cell impedance at OCV is determined by the cathode impedance, and that the contribution of the anode can be ignored [22].

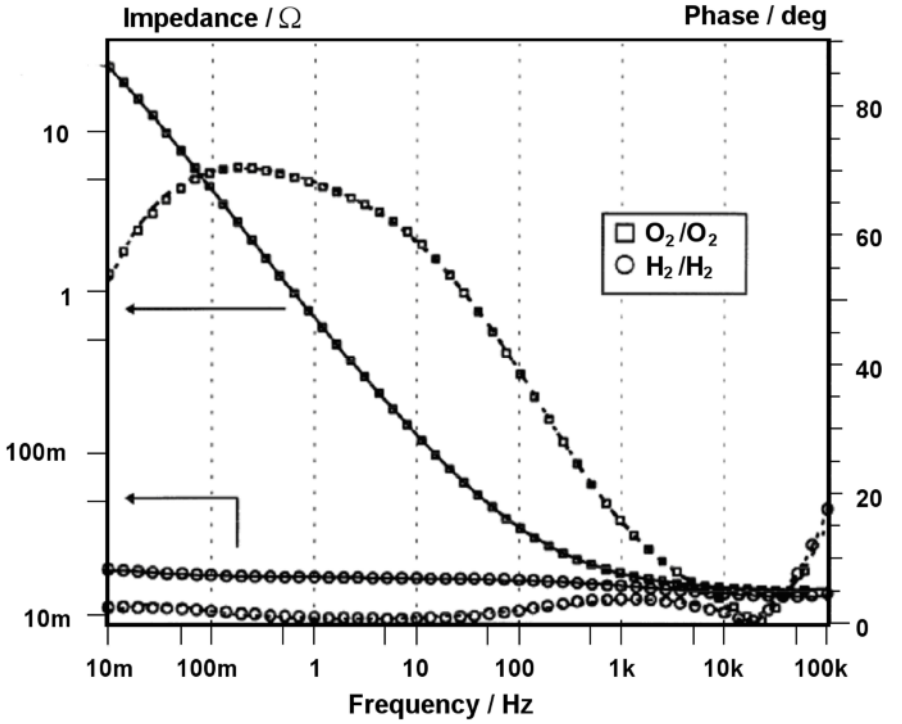

Figure 5.19. Bode diagram of the measured impedance spectra, PEM fuel cell (hot-pressed, Nafion®-impregnated E-TEK electrodes) at 80°C, at both P_{H_2} and P_{O_2} = 1 bar, symmetrical gas supply, and OCV [22]. (Reprinted from Electrochimica Acta, 43, Wagner N, Schnurnberger W, Müller B, Lang M. Electrochemical impedance spectra of solid-oxide fuel cells and polymer membrane fuel cells, 3785–93, ©1998, with permission from Elsevier and from the authors.)

5.2.1.2 H_2/O_2 (Air) Gas Feeding

As discussed above, if the exchange current density of anode hydrogen oxidation is $i^0_{anode} = 0.1\,Acm^{-2}$ and that of the cathode oxygen reduction reaction (ORR) is $i^0_{cathode} = 6\,\mu Acm^{-2}$, the charge transfer resistance obtained by EIS measurements for the overall H_2/O_2 (air) fuel cell reaction will be dominated by the ORR charger transfer resistance. In other words, the impedance spectrum of the whole cell is nearly equal to the cathode impedance, due to the fast hydrogen oxidation reaction [23]. Therefore, when using a H_2/O_2 (air) gas feeding mode, the obtained whole-cell EIS is approximately that of the ORR.

In a H_2/O_2 (air) fuel cell, in general, the spectra, i.e., the Nyquist plots obtained by EIS measurements, very often have three features, which are denoted as high-frequency, medium-frequency, and low-frequency. The high-frequency region of an impedance spectrum is associated with the internal ohmic resistance and the contact capacitance in the granular electrode structure of the membrane electrode assemblies, whereas the medium- and low-frequency regions represent the charge-

transfer resistance and the mass transport resistance, respectively [24]. Mass transport problems in PEM fuel cells can be classified into three categories: (1) depletion of reactants along the flow channel, which can result in a non-uniform current distribution over the whole electrode area, and is particularly severe in a large-scale fuel cell; (2) water flooding, in which liquid water trapped inside the electrodes or flow channels interrupts the flux of reactant/product gases; and (3) dilution of oxidant concentration due to the use of air instead of pure oxygen [25].

Single Impedance Arc

It is very often observed that the Nyquist plot has only a single impedance arc. Here we define this as a medium-frequency feature. Figure 5.20 shows some typical single-arc Nyquist spectra, which were calculated by Springer et al. [18].

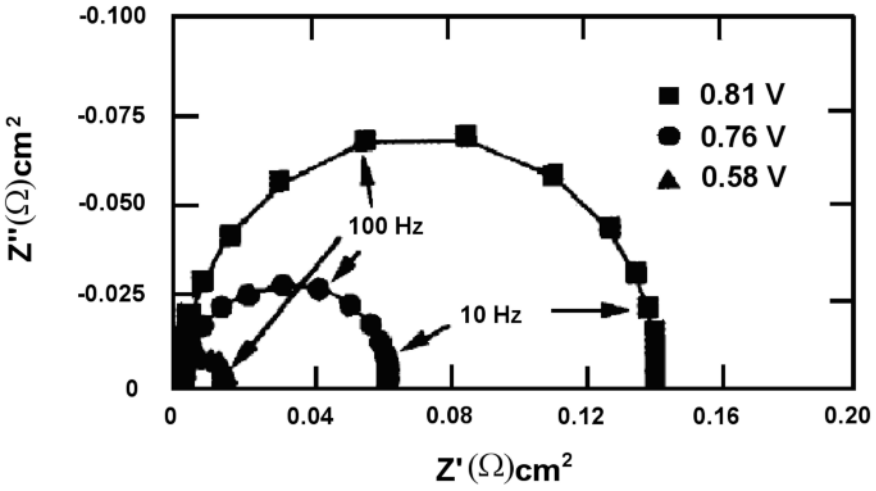

Figure 5.20. Calculated Nyquist plot for a single cell with elimination of the transport barrier in the backing [18]. (Reproduced with modifications by permission of ECS—The Electrochemical Society, from Springer TE, Zawodzinski TA, Wilson MS, Gottesfeld S. Characterization of polymer electrolyte fuel cells using AC impedance spectroscopy.)

A typical single-arc Nyquist plot from experiments is shown in Figure 5.21. Normally, a single semicircle loop that corresponds to one relaxation time (i.e., charge transfer process) occurs when the cathode loss is caused only by the interfacial kinetics of the ORR process. This is the simplest possible behaviour of the impedance spectrum of a PEM fuel cell cathode, and this single loop is called a *kinetic loop*. A typical Bode diagram of the measured single-arc impedance spectra is shown in Figure 5.22.

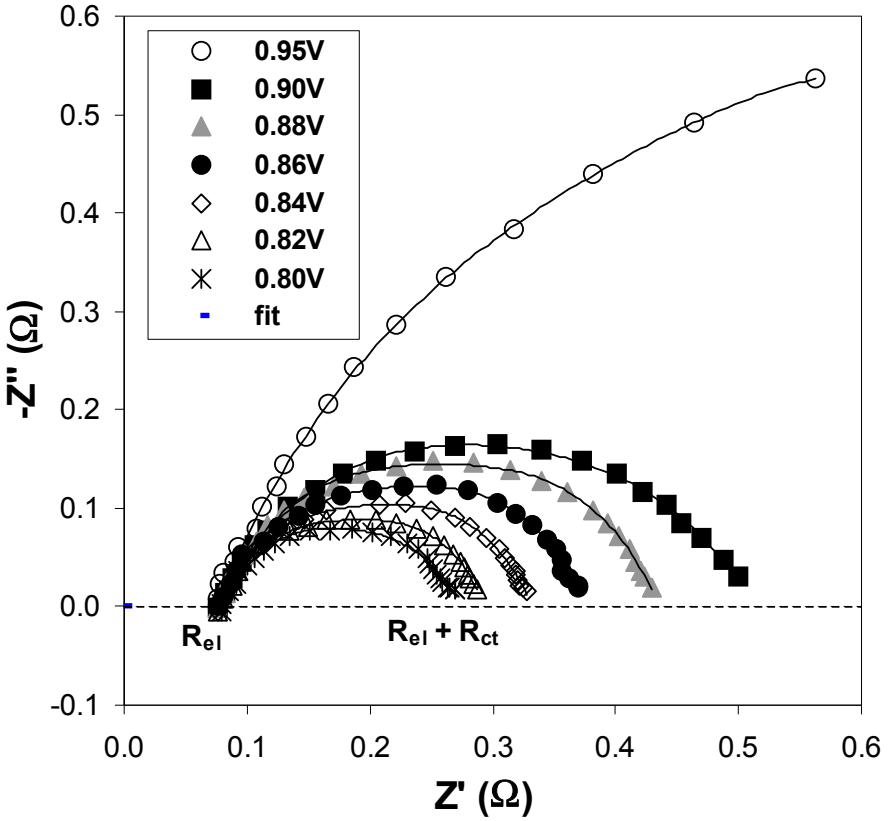

Figure 5.21. Typical Nyquist plot of single arcs from experiments; potential dependence in the range 0.9–0.8 V; t_{cell} = 25°C, ν_{H2}/ν_{air} = 16 sccm/40 sccm, and t_{H2}/t_{air} = 40°C/40°C [26]. (Reprinted with modifications, with permission from Journal of Physical Chemistry B, 2001;105:3531–9. ©2001 American Chemical Society.)

The intercept of the single kinetic arc with the real axis at the high-frequency end, R_{el}, as shown in Figure 5.21, represents the total ohmic resistance. It is generally recognized that this R_{el} is the sum of the contributions from uncompensated contact resistance and the ohmic resistance of cell components such as the membrane, catalyst layer, backing, and end plate, and the resistance between each of them [27]. The dominating contribution is from the membrane proton transport resistance. In the single kinetic loop, the second intercept with the real axis, R_{el} + R_{ct}, is the sum of ohmic resistance (or membrane resistance) and the kinetic resistance (or charger transfer resistance in the ORR) [28]. It can be seen from Figure 5.21 that this R_{ct} is strongly dependent on the fuel cell voltage (or electrode potential) in the range of 0.9 to 0.8 V, giving a trend such that the diameter of the loops decreases with decreasing cell voltage due to the increased driving force at higher overpotentials.

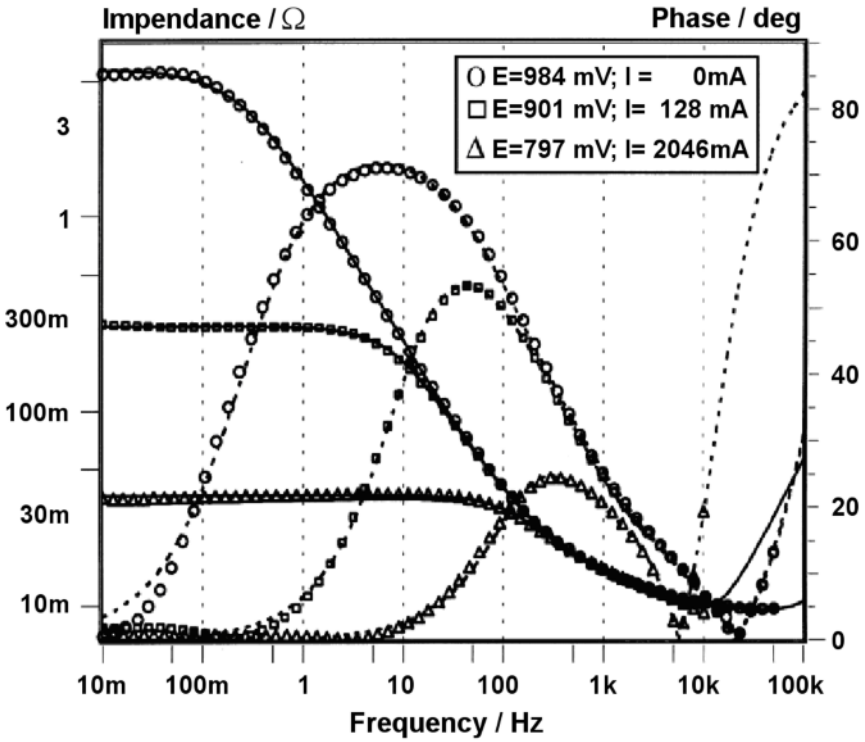

Figure 5.22. Bode diagram of the measured impedance spectra, PEM fuel cell (hot-pressed, as-received E-TEK electrodes) at 80°C, at different cell voltages: (o) OCV (984 mV), (□) 901 mV, (△) 797 mV [22]. (Reprinted from Electrochimica Acta, 43, Wagner N, Schnurnberger W, Müller B, Lang M. Electrochemical impedance spectra of solid-oxide fuel cells and polymer membrane fuel cells, 3785–93, ©1998, with permission from Elsevier and from the authors.)

Springer et al. [18] proved that for a cathode operating on pure oxygen or operating on ample air supply, when the transport barrier in the backing was eliminated completely, only one arc (a medium-frequency feature) appeared in the spectrum. The low-frequency feature was completely absent from the impedance spectrum. The absence of the low-frequency feature at higher overpotentials is a straightforward demonstration that this feature of the impedance spectra arises from a gas-phase, mass transfer barrier in the backing of an air cathode.

Two Impedance Arcs

The diffusion layer inside the MEA can cause the low-frequency end of the impedance to bend over the real axis, giving rise to a double semicircle. These two arcs for the fuel cell cathode process are defined as a medium-frequency feature and a low-frequency feature. Typical two-arc Nyquist plots from simulation (calculated by Springer et al. [18]) and from experiments are presented in Figure 5.23 and Figure 5.24, respectively.

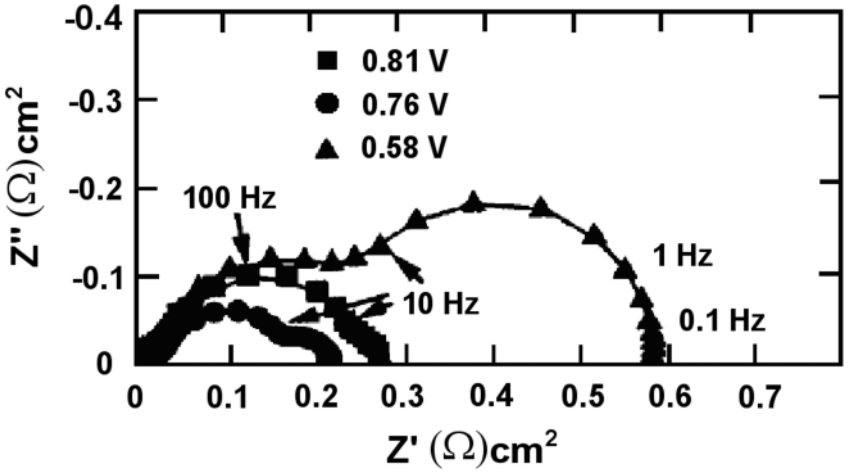

Figure 5.23. Calculated Nyquist plot for single cell with two arcs [18]. (Reproduced with modifications by permission of ECS—The Electrochemical Society, from Springer TE, Zawodzinski TA, Wilson MS, Gottesfeld S. Characterization of polymer electrolyte fuel cells using AC impedance spectroscopy.)

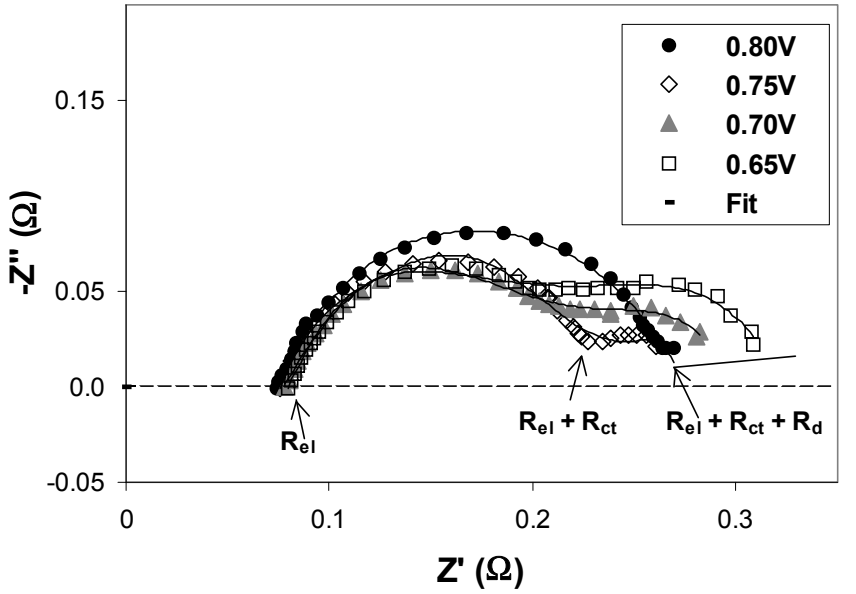

Figure 5.24. Typical Nyquist plot of two arcs from experiments; potential dependence in the range 0.8–0.65 V; t_{cell} = 25°C, ν_{H_2} / ν_{air} = 16 sccm/40 sccm, and t_{H_2} / t_{air} = 40°C/40°C [26]. (Reprinted with modifications, with permission from Journal of Physical Chemistry B, 2001;105:3531–9. ©2001 American Chemical Society.)

As seen in Figure 5.23, when the transport barrier in the backing is not eliminated, two arcs are present instead of a single arc at the same operation potentials shown in Figure 5.21. The experimental result in Figure 5.24 also exhibits two arcs, and with increasing overpotential the second arc increases due to the increased mass transfer limitation. The R_d in Figure 5.24 refers to the diameter of the low-frequency loop.

A typical Bode diagram of the measured impedance spectra with two arcs is depicted in Figure 5.25, and the corresponding equivalent circuit for these two impedance arcs is shown in Figure 5.26. The reason for replacing the capacitor (C) by the constant phase element (CPE) is that the capacitance due to the double-layer charging is distributed along the length of the pores in the porous electrode [26].

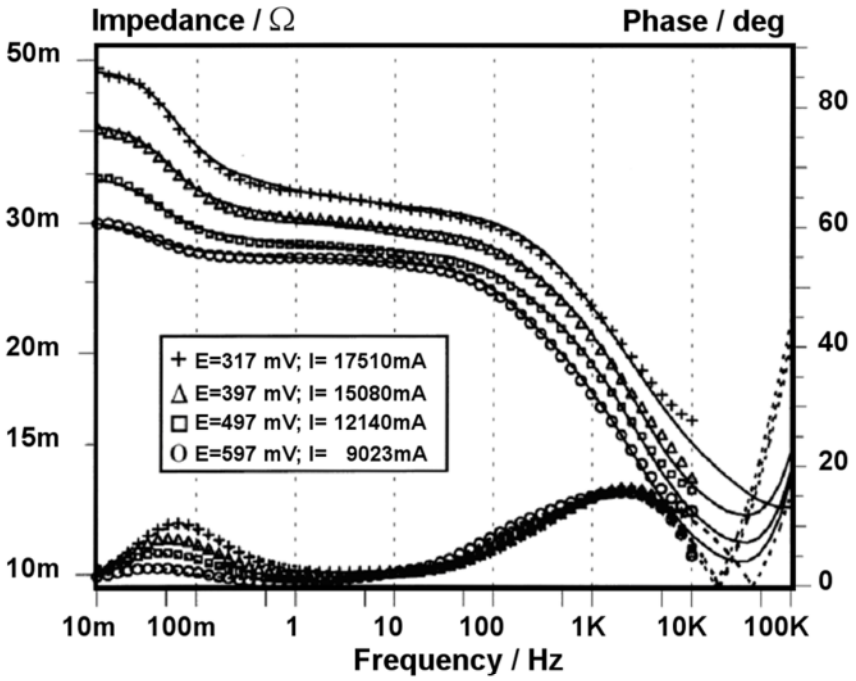

Figure 5.25. Typical Bode diagram of the measured impedance spectra with two arcs, PEM fuel cell (hot-pressed, as-received E-TEK electrodes) at 80°C, at different cell voltages: (o) 597 mV, (□) 497 mV, (Δ) 397 mV, and (+) 317 mV [22]. (Reprinted from Electrochimica Acta, 43, Wagner N, Schnurnberger W, Müller B, Lang M. Electrochemical impedance spectra of solid-oxide fuel cells and polymer membrane fuel cells, 3785–93, ©1998, with permission from Elsevier and from the authors.)

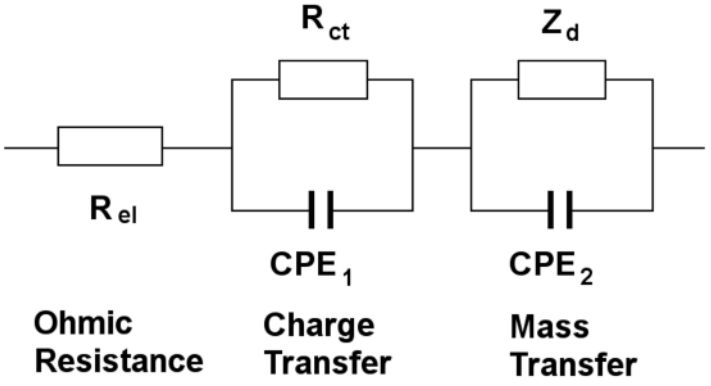

a

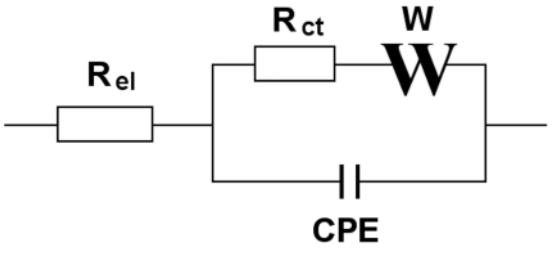

b

Figure 5.26. Two typical equivalent circuits for a two-arc PEMFC system

Two impedance arcs, which correspond to two relaxation times (i.e., charge transfer plus mass transfer) often occur when the cell is operated at high current densities or overpotentials. The medium-frequency feature (kinetic arc) reflects the combination of an effective charge-transfer resistance associated with the ORR and a double-layer capacitance within the catalyst layer, and the low-frequency arc (mass transfer arc), which mainly reflects the mass-transport limitations in the gas phase within the backing and the catalyst layer. Due to its appearance at low frequencies, it is often attributed to a hindrance by finite diffusion. However, other effects, such as constant dispersion due to inhomogeneities in the electrode surface and the adsorption, can also contribute to this second arc, complicating the analysis. Normally, the lower-frequency loop can be eliminated if the fuel cell cathode is operated on pure oxygen, as stated above [18].

For the low-frequency arc, many studies and explanations have been published. Freire and Gonzalez [29] studied the effects of temperature, membrane thickness, and humidification conditions on the impedance response. They suggested that the low-frequency arc has two causes: the effect of liquid water formed at the anode, which affects the transport of oxygen; and the hydration effect, which limits the transport within the membrane. The relative weight of these two effects depends on the thickness of the membrane and the working conditions of the fuel cell. They

concluded that the low-frequency relaxation process is mainly due to water flooding of the cathode. Andreaus et al. [30] attributed this arc to a shortage of oxygen for the ORR, due to the limited diffusivity of oxygen in water. Paganin et al. [31] also observed a low-frequency relaxation process below 0.55 V with increasing overpotentials. They attributed the phenomenon to the water transport characteristics of the membrane.

Freire and Gonzalez [29] gave a further interpretation of the low-frequency arc. They analyzed the arc in terms of the relaxation time, t_{O_2}, which is the reciprocal of the characteristic frequency. The characteristic frequency of the low-frequency arc, ω_2, is defined as $\omega_2 = 1/R_2C_2$, where the subscript 2 represents the low-frequency arc. The relaxation time is related to the recovery rate of the steady-state when a perturbation is applied to the system. This relaxation time is expected to increase with decreasing water content in the membrane because a less hydrated membrane, with narrower channels, can promote more interactions between the moving charges and also between the moving charges and the matrix. In addition, the relaxation time will be larger for fuel cells with thicker membranes. If the values of t_{O_2} are similar, one may conclude that this parameter is not very sensitive to the humidification conditions of the reactant gases.

Furthermore, the characteristic frequency (ω_2) can be used to calculate the thickness of a thin water film formed in the diffusion layer of the cathode:

$$\omega_2 = \frac{D_{eff}}{\delta^2} \tag{5.14}$$

where δ is the thickness of the film and D_{eff} is the effective diffusion coefficient of oxygen in water. In a porous medium, D_{eff} may be given in the form of

$$D_{eff} = \varepsilon D_{O_2} / l \tag{5.15}$$

where ε is the porosity, D_{O_2} is the diffusion coefficient of oxygen, and l is the tortuosity. Taking $D_{O_2} \approx 1.5\times10^{-5}\,\mathrm{cm^2 s^{-1}}$, ε = 0.4, and l(average) = 3 [29], the thickness of the liquid water film can be obtained according to the value of ω_2 measured. Although the calculation is very rough, it gives evidence that under certain conditions, liquid water may flood the diffusion layer of the electrode.

In the Nyquist plots, one can sometimes observe infinite diffusion as a straight line with slope 1 (45°, real part = imaginary part) instead of finite diffusion as an additional loop in the low-frequency range [19]. Comparison of the simulated impedance spectra with and without diffusion at different diffusion lengths is shown in Figure 5.27. It can be seen that: (1) without diffusion only one arc occurs; (2) with a finite diffusion length, two arcs appear, with the low-frequency arc corresponding to the Nernst impedance; and (3) with infinite diffusion length, a 45° straight line can be observed instead of a semicircle at low frequencies, which corresponds to a Warburg impedance.

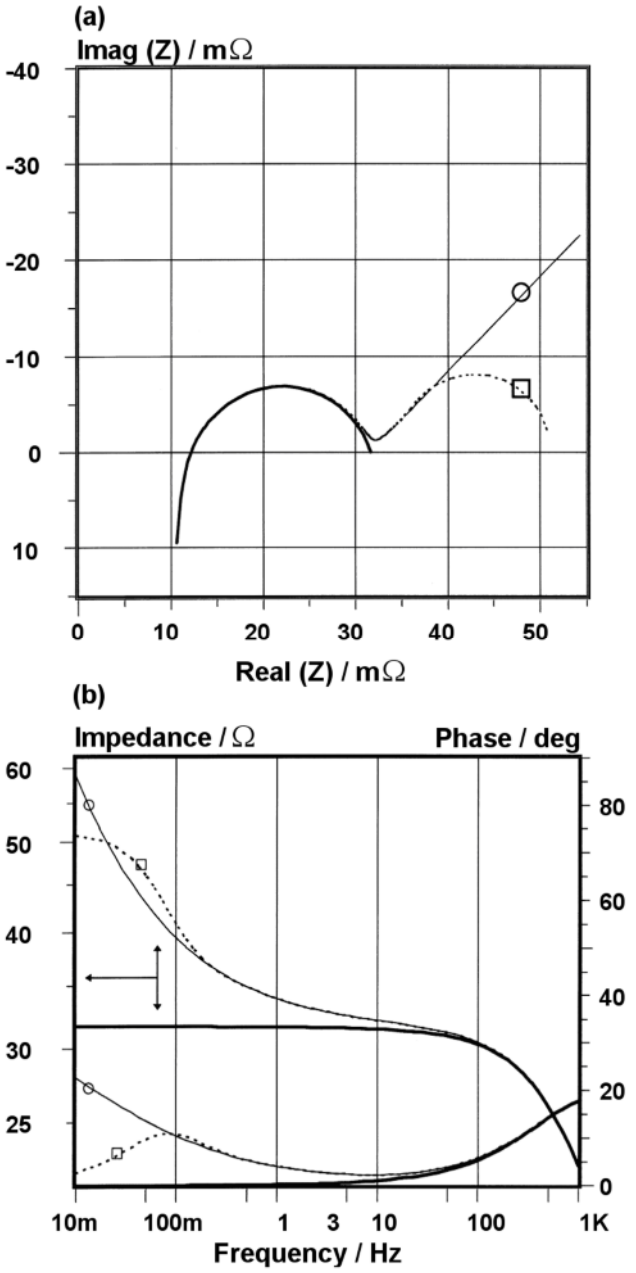

Figure 5.27. *a* Nyquist plots of simulated impedance spectra, PEM fuel cell at 80°C, at cell voltage lower than 700 mV, (—) without diffusion, (□) with finite diffusion length, and (○) infinite diffusion length. *b* The corresponding Bode diagram of simulated impedance spectra [22]. (Reprinted from Electrochimica Acta, 43, Wagner N, Schnurnberger W, Müller B, Lang M. Electrochemical impedance spectra of solid-oxide fuel cells and polymer membrane fuel cells, 3785–93, ©1998, with permission from Elsevier and from the authors.)

High-Frequency Features

Additional Complete or Incomplete Semicircle. In EIS measurements, an additional complete or incomplete semicircle can sometimes be observed at the high-frequency end at different potentials. This high-frequency component does not vary with potential, as shown in Figure 5.28. Fisher et al. [32] attributed the high-frequency loop to the internal ohmic resistance and the contact capacitance in the granular electrode structure. Springer et al. [18] considered this region associated neither with any Faradaic process nor with mass transport limitations on the cathode electrode.

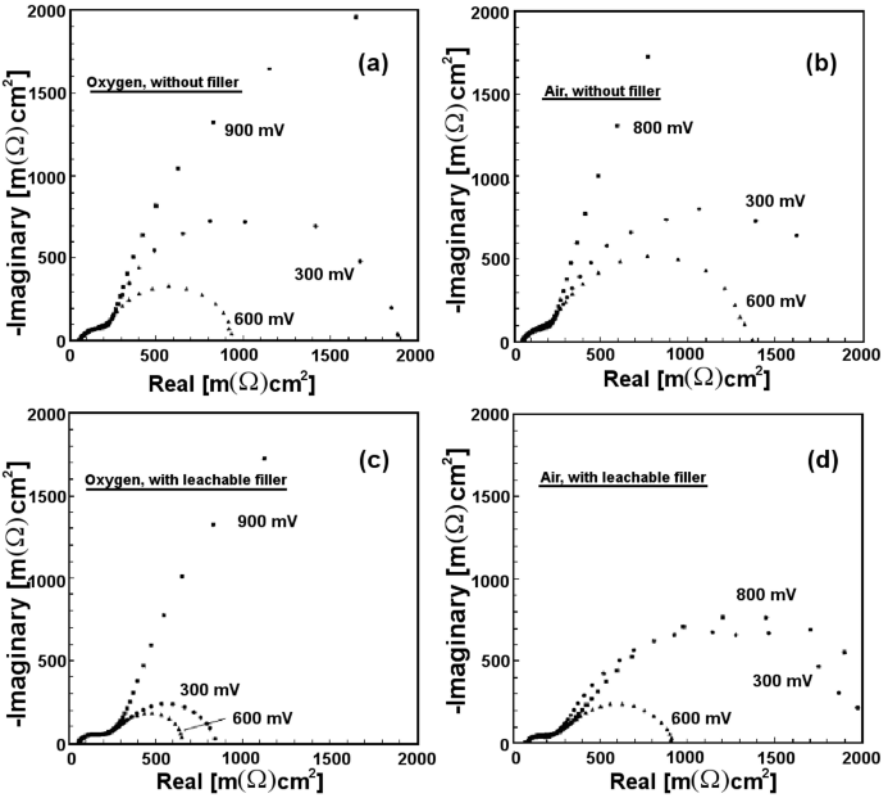

Figure 5.28. Impedance spectra of cells with different cathodes and operated with oxygen or air as the cathode gas. Active cell area 2 cm^2, 0.15 mgPt cm^{-2}, 0.1 MPa H_2. *a* Electrode prepared without filler, 0.1 MPa O_2; *b* electrode prepared without filler, 0.1 MPa air; *c* electrode prepared with leachable filler, 0.1 MPa O_2, and *d* electrode prepared with leachable filler, 0.1 MPa air [32]. (With kind permission from Springer Science+Business Media: Journal of Applied Electrochemistry, Porosity and catalyst utilization of thin layer cathodes in air operated PEM-fuel cells, 28, 1998, 277–82 Fisher A, Jindra J, Wendt H, Figure 5, ©1998 Springer.)

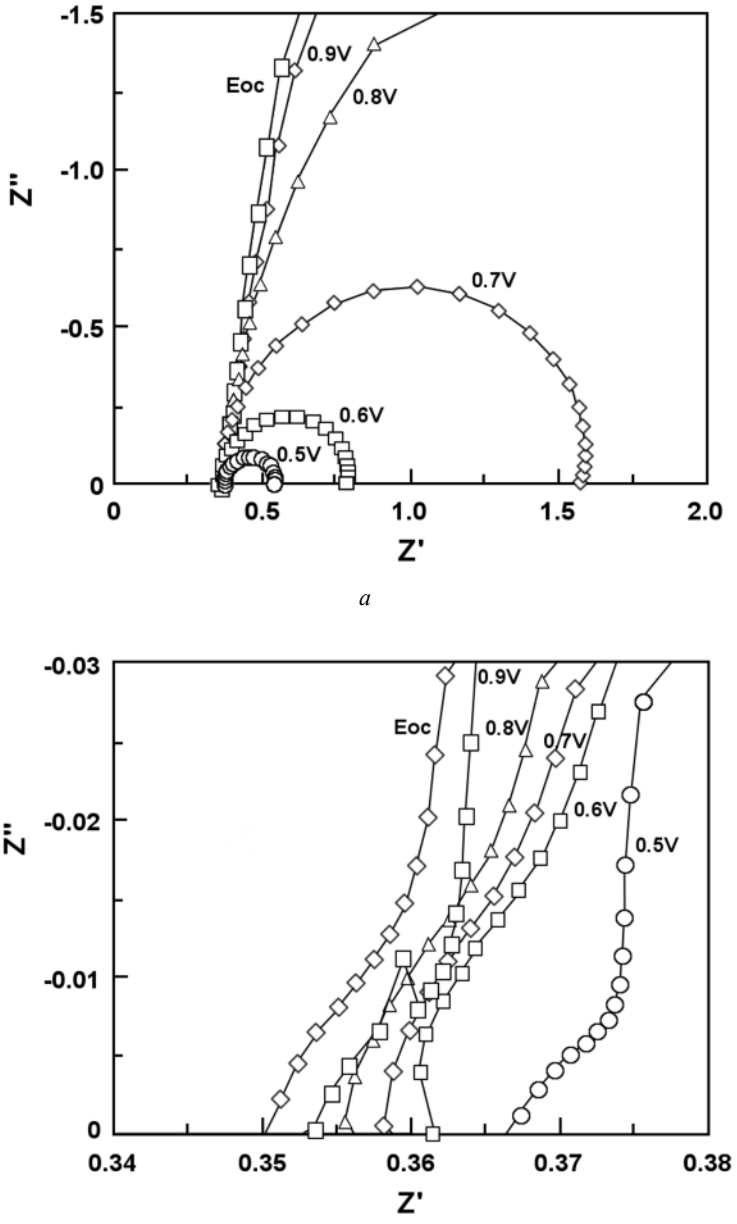

Figure 5.29. Impedance spectra at several cathode potentials for an H_2/O_2 PEM fuel cell. *a* Nyquist plots of the spectra; *b* high-frequency view of the AC impedance spectra [33]. (Reprinted from Journal of Power Sources, 118, Romero-Castanon T, Arriaga LG, Cano-Castillo U. Impedance spectroscopy as a tool in the evaluation of MEA's, 179–82, ©2003, with permission from Elsevier and from the authors.)

Similar phenomena were also observed by Freire and Gonzalez [29], Paganin et al. [31], and Romero-Castanon et al. [33]. The former two attributed the high-frequency relaxation, independent of potential, to the distributed resistance effects in the electrolyte within the catalyst layer. The results from the latter are shown in Figure 5.29*a* and *b*. Figure 5.29*a* shows the Nyquist plots as a function of cell voltage (or cathode potential), obtained using 5 cm^2 of a single fuel cell at room temperature. Figure 5.29*b* illustrates a magnification of the high-frequency region of the Nyquist plots shown in Figure 5.29*a*, from which an incomplete semicircle can be seen at all electrode potentials. Romero-Castanon et al. [33] explained that the MEA structural features could be responsible for this behaviour.

45° Branch. In addition to the complete or incomplete semicircle observed at high frequencies, it is also possible to see another distortion of the high-frequency region in the Cole–Cole representation. This distortion in the high-frequency region presents a straight line at a 45° angle, which resembles a Warburg impedance with a characteristic proportionality of $|Z| \infty \omega^{-1/2}$. According to the one-dimensional transmission-line equivalent circuit, as shown in Figure 5.30, Eikerling and Kornyshev [34] studied this 45° straight line distortion at high frequencies. Their result is presented in Figure 5.31. In this region, Faradaic processes are not significant due to the high frequencies. The double-layer charging effect and proton transport dominate the overall electrode response in this region. The 45° line in the high-frequency region, which is typical for a porous electrode, does not exist for a planar electrode.

The 45° branch distortion has been experimentally observed by many researchers. For example, Figure 5.32 shows impedance plots with a 45° branch for single cells at room temperature, reported by Freire and Gonzalez [29]. They attributed the 45° branch to limited proton transport in the electrode, and considered that the distortion might indicate a lack of protons not only in the thin film of the electrolyte but also inside the agglomerates that contain the catalyst. Springer et al. [18] explained that this 45° branch, which is independent of the electrode potential, could reflect the coupling of the distributed ionic resistance and distributed capacitance in the catalyst layer, and was developed from protonic conductivity limitations within the catalyst layer. The branch disappeared when the catalyst layer resistance was decreased. Lefebvre et al. [35] also observed the Warburg-like response (45° slope) at high frequencies. They regarded this distortion as the consequence of ion migration through the catalyst layer. Further, they predicted that the high angle of the Warburg-like region relative to the theoretical value of 45° could be due to an increase in the ionic resistance profile.

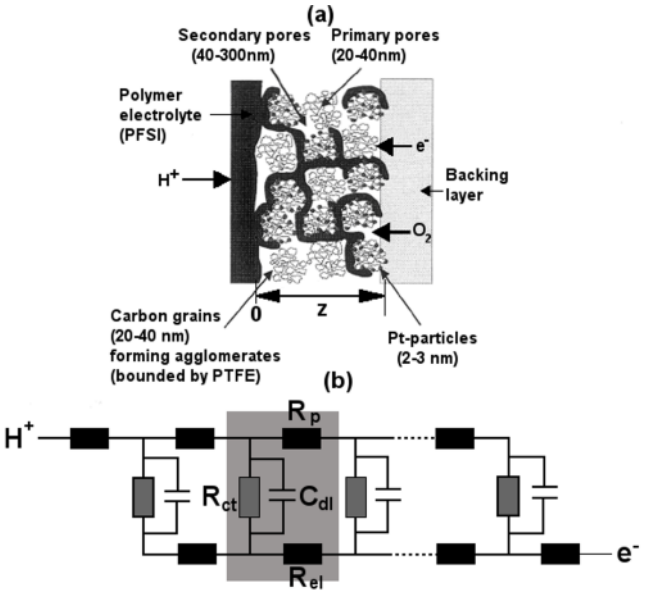

Figure 5.30. Schematic of the catalyst layer geometry and its composition, exhibiting the different functional parts. *a* A sketch of the layer, used to construct a continuous model. *b* A one-dimensional transmission-line equivalent circuit where the elementary unit with protonic resistivity R_p, the charge transfer resistivity R_{ct}, and the double-layer capacitance C_{dl} are highlighted [34]. (Reprinted from Journal of Electroanalytical Chemistry, 475, Eikerling M, Kornyshev AA. Electrochemical impedance of the cathode catalyst layer in polymer electrolyte fuel cells, 107–23, ©1999, with permission from Elsevier.)

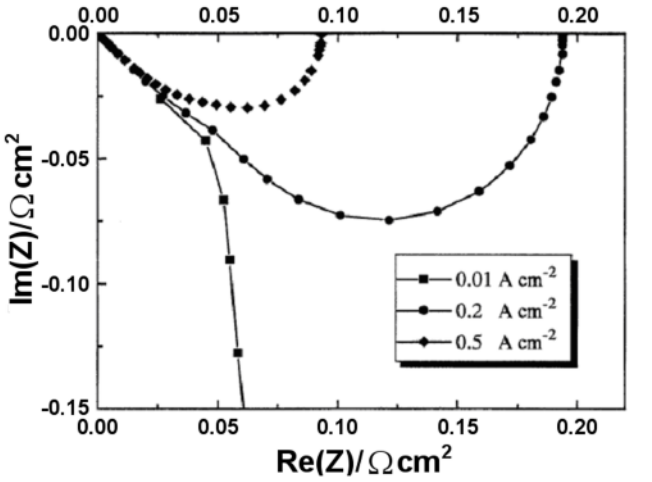

Figure 5.31. Simulation results of the impedance spectra at different current densities [34]. (Reprinted from Journal of Electroanalytical Chemistry, 475, Eikerling M, Kornyshev AA. Electrochemical impedance of the cathode catalyst layer in polymer electrolyte fuel cells, 107–23, ©1999, with permission from Elsevier.)

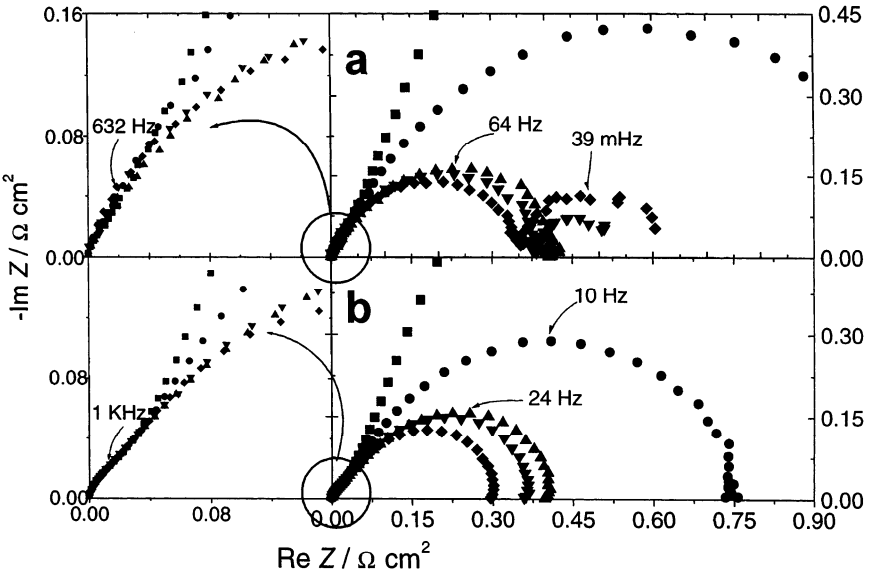

Figure 5.32. Impedance plots for single cells at ambient temperature. *a* Nafion®117. Cell voltage and ohmic drop corrected potential (in parenthesis): (■) 0.9 V (0.9 V); (●) 0.8 V (0.81 V); (▲) 0.70 V (0.76 V); (▼) 0.6 V (0.74 V); (◆) 0.5 V (0.74 V). *b* Nafion®112. Cell voltage and ohmic drop corrected potential (in parenthesis): (■) 0.9 V (0.9 V); (●) 0.8 V (0.81 V); (▲) 0.70 V (0.73 V); (▼) 0.6 V (0.67 V); (◆) 0.5 V (0.61 V). Plots were corrected for the high-frequency resistances. *Left*: detail of the high-frequency regions [29]. (Reprinted from Journal of Electroanalytical Chemistry, 503, Freire TJP, Gonzalez ER. Effect of membrane characteristics and humidification conditions on the impedance response of polymer electrolyte fuel cells, 57–68, ©2001, with permission from Elsevier.)

5.2.1.3 Dilution of the Feeding Gases

Diluted Hydrogen

In a PEM fuel cell, the kinetic resistance of the hydrogen oxidation reaction is much smaller than that of the oxygen reduction reaction. Therefore, the overall impedance response from the whole fuel cell is often solely attributed to the cathode response. In order to study the anode behaviour, a reference electrode has to be positioned inside the fuel cell. Unfortunately, this is not that easy if one wants to obtain reliable results. However, the anode impedance response can be enlarged using dilute hydrogen. It is expected that the anode impedance can be distinguished from the cathode impedance if a high dilution rate and a low flow rate are used at the anode side. In the measurements, pure oxygen rather than air should be used at the cathode side in order to decrease the cathode impedance response [36]. Figure 5.33 shows the Nyquist plots for diluted hydrogen feed. In this figure, the ohmic resistance (found to be about 260 mΩ cm^2) was subtracted from the spectra for easier comparison.

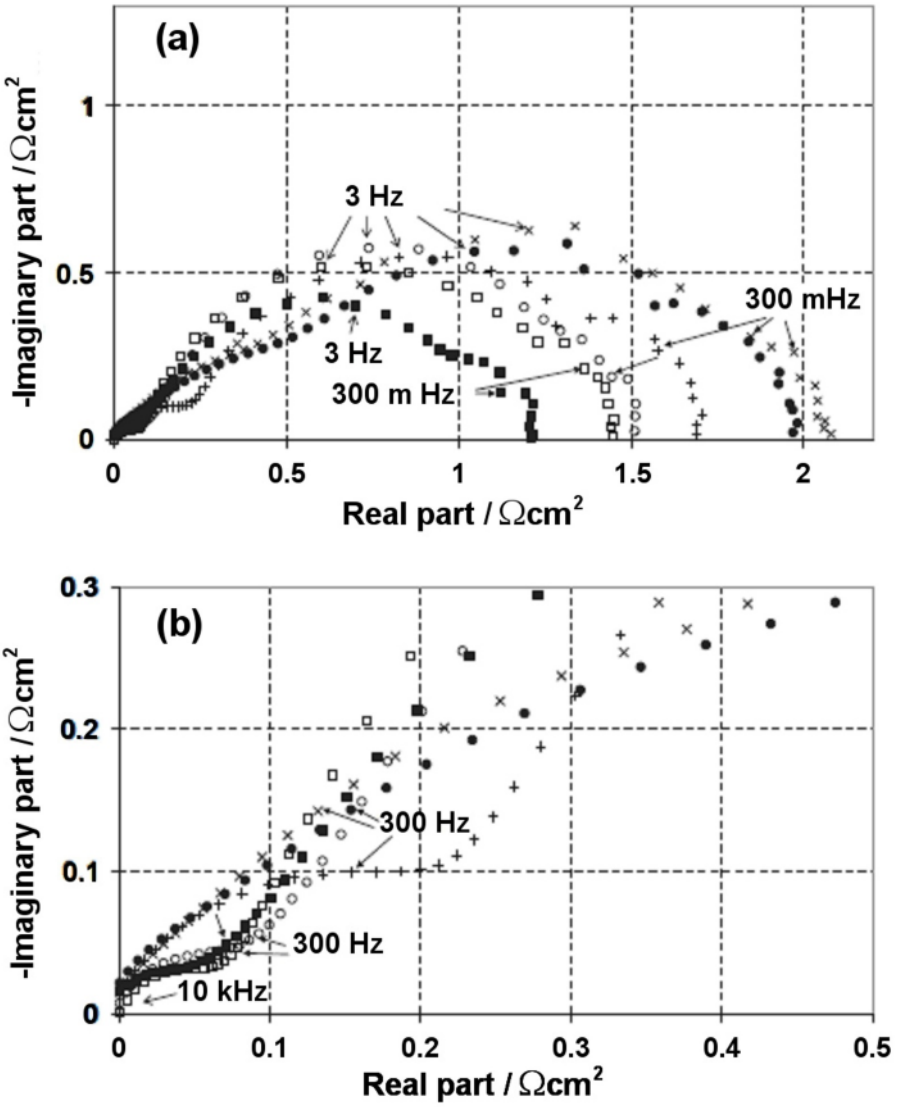

Figure 5.33. Impedance spectra at 160 mA cm^{-2}. Anode feed gases: (□) H_2 (stoichiometry 3); (■) H_2 (stoichiometry 15); (●) 80:20 H_2/CO_2; (○) 80:20 H_2/N_2; (+) 20:80 H_2/N_2; (×) 5:95 H_2/N_2. Cathode feed gas: pure oxygen. *a* Whole range of frequencies. *b* High frequencies [36]. (From Boillot M, Bonnet C, Jatroudakis N, Carre P, Didierjean S, Lapicque F. Effect of gas dilution on PEM fuel cell performance and impedance response. Fuel Cells 2006;6:31–7. Copyright Wiley-VCH Verlag GmbH & Co. KGaA. Reproduced with permission of the publisher and the authors.)

In Figure 5.33, for all scenarios, three more or less distinct loops appear in the spectra, indicated as high-, medium-, and low-frequency loops: (1) the high-

frequency loop becomes larger as the hydrogen dilution rate increases; (2) the large loop at the medium frequency is attributed to the cathode charge-transfer resistance; and (3) the low-frequency loop is related to the mass transfer limitation of oxygen. The latter two loops, corresponding to the charge transfer and mass transfer of oxygen reduction, have been widely discussed in the literature. The high-frequency loop is not observable due to the fast kinetics of hydrogen oxidation under normal fuel cell operating conditions. However, due to the dilution of the feed hydrogen, this loop can be observed for hydrogen oxidation. Therefore, the equivalent circuit for Figure 5.33 can be drawn as Figure 5.34.

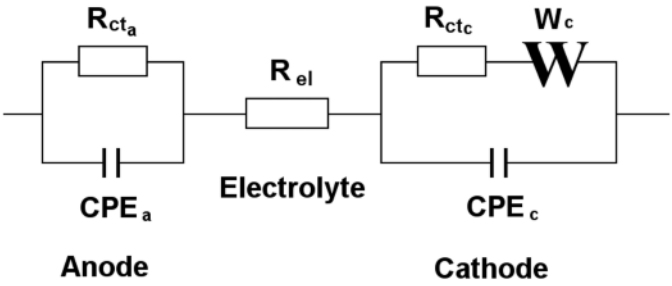

Figure 5.34. Electric equivalent circuit for the impedance spectra in Figure 5.37. R_{el}: ohmic resistance; R_{ct}: charge-transfer resistance; CPE: constant phase element; W: Warburg element. The subscripts a and c denote anode and cathode, respectively [36]. (Modified from Boillot M, Bonnet C, Jatroudakis N, Carre P, Didierjean S, Lapicque F. Effect of gas dilution on PEM fuel cell performance and impedance response. Fuel Cells 2006;6:31–7. ©2006 John Wiley & Sons Limited. Reproduced with permission, and with the permission of the authors.)

In summary, under the circumstance of hydrogen dilution it is possible to observe hydrogen oxidation behaviours in the high-frequency range of the EIS.

Diluted Oxygen

Oxygen dilution happens when an O_2/N_2 mixture or air is used instead of pure oxygen at the cathode side. A typical example of impedance spectra for oxygen dilution is shown in Figure 5.35. The cathode gases fed were air, 50:50 O_2/N_2 mixture, and pure oxygen, with stoichiometric factors of 3.15, 7.5, and 15, whereas pure hydrogen was fed to the anode side with a stoichiometric number of 3. The ohmic resistance was corrected for a clearer comparison. As seen in Figure 5.35, the high-frequency loop does not appear on the spectra because pure hydrogen was used instead of diluted hydrogen. The diameter of the medium-frequency loop decreases with increasing oxygen content at the cathode side. A similar phenomenon was also observed for the low-frequency loop; that is, with increasing oxygen content, the low-frequency loop decreases. When pure oxygen is fed to the cathode, the low-frequency loop vanishes, indicating that there is no mass transfer limitation.

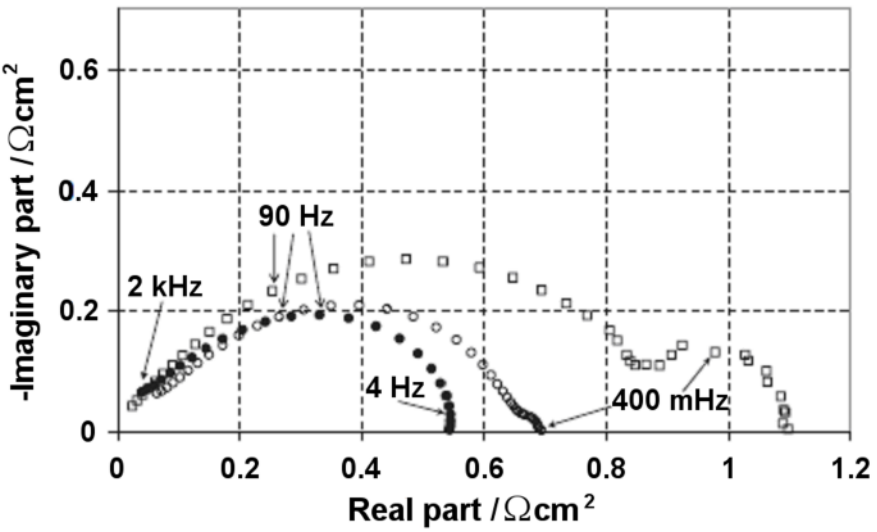

Figure 5.35. Impedance spectra at 160 $mAcm^{-2}$. (●) Pure O_2; (○) 50:50 O_2/N_2; (□) 21:79 O_2/N_2 [36]. (From Boillot M, Bonnet C, Jatroudakis N, Carre P, Didierjean S, Lapicque F. Effect of gas dilution on PEM fuel cell performance and impedance response. Fuel Cells 2006;6:31–7. ©2006 John Wiley & Sons Limited. Reproduced with permission, and with the permission of the authors.)

5.2.1.4 H_2/N_2 Gas Feeding

The performance of an MEA is limited mainly by ORR kinetics and the transport of oxygen to the cathode catalyst surface. Proton conduction, both in the membrane and in the cathode catalyst layer, also makes a significant contribution to the loss of performance. EIS is also used to study the capacitance and ion transport properties of fuel cell catalyst layers by operating the fuel cell in an H_2/N_2 modus. This modus simplifies the impedance response because: (1) when the cell is operated in a H_2/N_2 mode, the anode charge-transfer resistance is negligible and the cathode charge-transfer resistance is infinite; (2) measurement at high frequency will result in total ohmic resistance; and (3) $R_{electronic}$ makes a negligible contribution to the impedance of the electrode, due to the much superior electronic conductivity of carbon as compared to R_{ionic}. Instead of the more common Nyquist plots, Easton and Pickup [2] used capacitance plots to investigate the conductivity variation induced by ionic resistance across the catalyst layer. With a finite transmission-line equivalent circuit, conductivity variation across the catalyst layer can be obtained. The details of this operation modus will be discussed in Chapter 6.

5.2.1.5 Contamination Gas Feeding

Fuel cell systems often include a reformer that converts hydrogen carbon fuel such as methane or methanol to a hydrogen-rich stream of gas. This stream is then fed to a fuel cell, which generates electric power. However, the reforming process also produces some unwanted trace species, such as CO, H_2S, and NH_3, which are considered poisonous to PEM fuel cells. Fuel cell contamination caused by these

impurities adversely affects cell performance and function by degrading the catalyst activity or lowering the conductivity of the membranes.

Ammonia, produced due to the coexistence of H_2 and N_2 at high temperatures in the presence of catalyst, was estimated to be in the concentration range of 30 to 90 ppm [37, 38]. Uribe et al. [39] examined the effects of ammonia trace on PEM fuel cell anode performance and reported that a trace in the order of tens of parts per million could lead to considerable performance loss. They also used EIS in their work. By measuring the high-frequency resistance (HFR, mainly contributed by membrane resistance) with an operation mode of H_2 + NH_3/air (feeding the anode with hydrogen and ammonia), they obtained some information related to membrane conductivity, and found that conductivity reduction due to ammonia contamination is the major cause of fuel cell degradation.

Figure 5.36 shows the high-frequency resistances (HFRs) obtained at different current densities [39]. It can be seen that after 1 hour of exposure to NH_3, the HFRs were nearly the same. However, when NH_3 was kept flowing for longer periods of time, the HFR was affected. After 15 hours of continued H_2/NH_3 flow, the HFR values were much larger than those obtained in the absence of NH_3. This performance loss was irreversible; when the flow of NH_3 was stopped and the cell was allowed to run on pure H_2 for several days, the membrane conductivity did not return to its initial value.

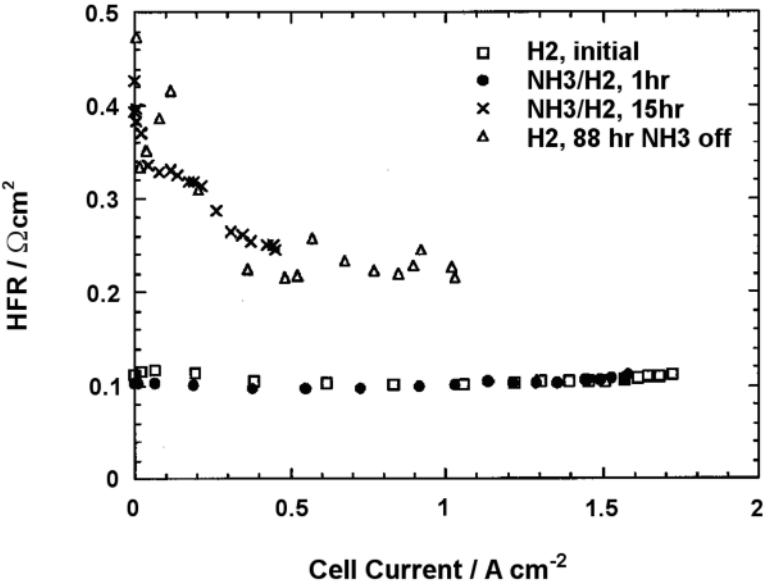

Figure 5.36. Effects that long-term NH_3 exposure has on H_2-air fuel cell high-frequency resistance at 80°C. 30 ppm NH_3 (g) was injected into the anode feed stream [39]. (Reproduced by permission of ECS—The Electrochemical Society, from Uribe FA, Gottesfeld S, Zawodzinski Jr. TA. Effect of ammonia as potential fuel impurity on proton exchange membrane fuel cell performance.)

With respect to H_2S contamination, it has been recognized for many years that the major impact is upon the fuel cell electrode kinetics [40]. When H_2S is added to humidified H_2, EIS can be used to study the H_2S contamination. Information gathered includes the effects of the H_2S concentration, the exposure time, and the reversibility of the contamination. H_2S can strongly adsorb on a Pt catalyst surface, blocking the active sites and then causing irreversible contamination.

CO contamination is widely documented in the literature and recognized as a serious issue in the investigation of PEMFCs; a decline in PEMFC performance is very often due to deactivation of the Pt anode catalyst, caused by traces of CO. Many attempts [14, 41, 42] have been made to use the EIS method to understand the mechanisms of CO poisoning and CO tolerance, by feeding an anode gas mixture of CO and H_2. Examples of such studies will be discussed in detail in Chapter 6.

5.2.1.6 Direct Methanol Fuel Cell Gas Feeding

For EIS measurements of a direct methanol fuel cell (DMFC), the anode is supplied with an aqueous solution of methanol at a concentration such as 1 M and using controlled flow rates. The cathode is operated on either air, oxygen, or hydrogen, with controlled flow rate and pressure [43]. In order to measure the anode EIS, the DMFC is fed with hydrogen gas instead of air or oxygen, to eliminate the contributions of the cathode. This cathode is normally denoted as a dynamic hydrogen electrode (DHE). Thus, the anode impedance spectra between the anode and the DHE can be obtained in a complete fuel cell.

DMFC cathode impedance spectra can be obtained by the following steps:

1. Record the impedance spectrum of a complete DMFC with the cathode operated as usual on air or oxygen.
2. Record the anode spectrum as described above, with the cathode fed by hydrogen.
3. Subtract the anode impedances from the complete cell impedances, thereby obtaining a cathode impedance spectrum [43].

Figure 5.37 illustrates the experimental set-up employed for measuring the EIS of a DMFC. A typical Nyquist plot of the DMFC anode impedance spectrum is presented in Figure 5.38. The spectrum contains three arcs.

1. The high-frequency arc is obviously related to an ohmic process, which can be recognized by the fact that it does not vary with anode potential.
2. The medium-frequency arc, the size of which is strongly dependent on the anode potential, corresponds to methanol electrooxidation kinetics. Note that different anode catalyst compositions and operating conditions of the DMFC can be evaluated by assessing their effects on anode performance.
3. The low-frequency arc is due to mass transfer of methanol in the anode, which can be recognized by the growth of the arc when either the methanol flow rate or the concentration is decreased.

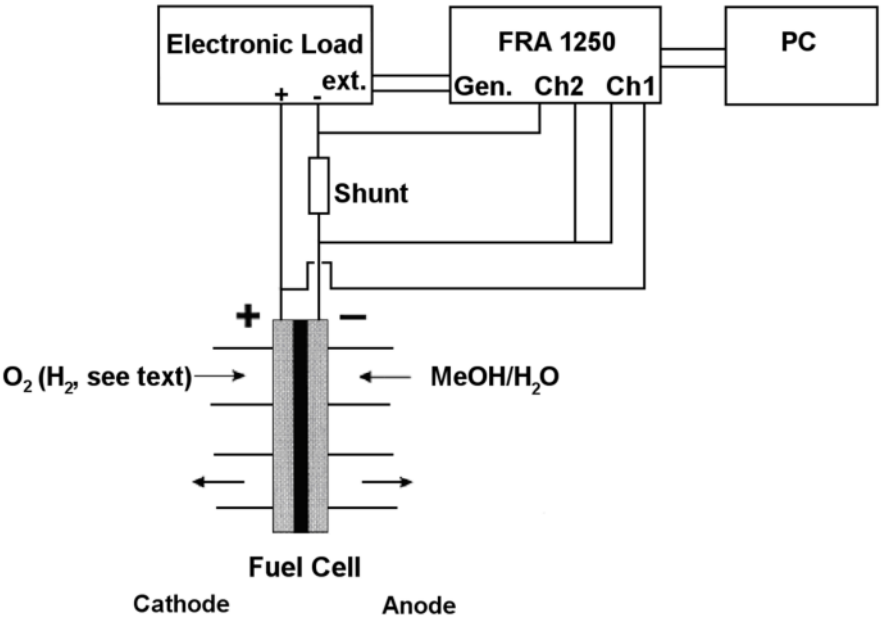

Figure 5.37. Experimental set-up for measuring the impedance spectra of a DMFC or of its anode versus DHE [43]. (Reprinted from Journal of Power Sources, 75, Müller JT, Urban PM. Characterization of direct methanol fuel cells by AC impedance spectroscopy, 139–43, ©1998, with permission from Elsevier and the authors.)

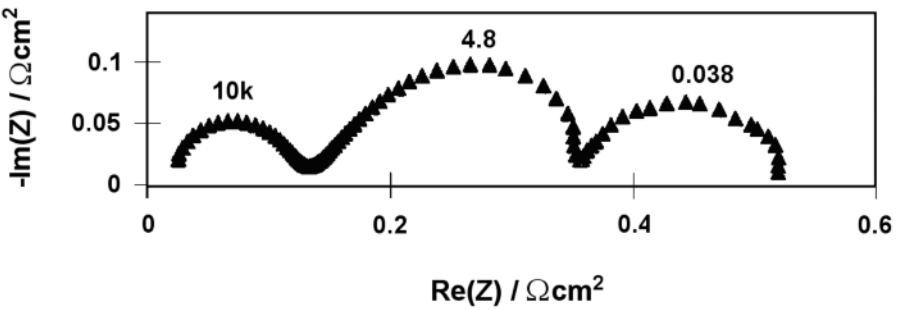

Figure 5.38. Nyquist plot of a typical DMFC anode impedance spectrum [43]. (Reprinted from Journal of Power Sources, 75, Müller JT, Urban PM. Characterization of direct methanol fuel cells by ac impedance spectroscopy, 139–43, ©1998, with permission from Elsevier and the authors.)

Figure 5.39 shows the typical Nyquist plots of the EIS of a DMFC cathode operating on air and pure oxygen, respectively. The low-frequency arc is absent from the cathode spectrum operating on pure oxygen. Two arcs can be observed in the case of operation on air.

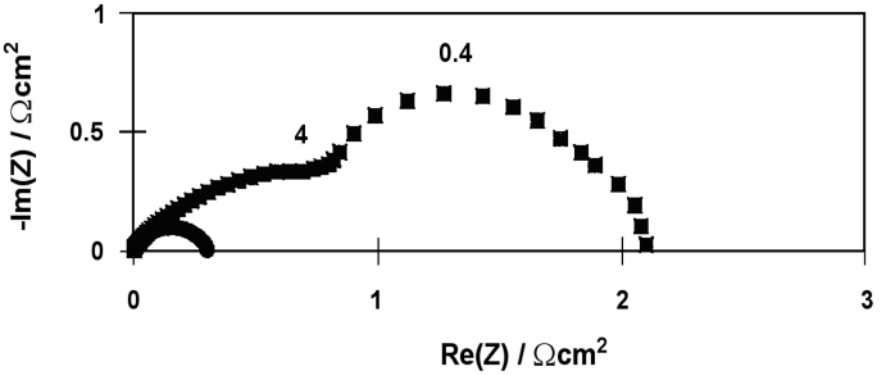

Figure 5.39. Nyquist plots of a typical DMFC cathode impedance spectrum: (■), operation on air; (●), operation on oxygen [43]. (Reprinted from Journal of Power Sources, 75, Müller JT, Urban PM. Characterization of direct methanol fuel cells by AC impedance spectroscopy, 139–43, ©1998, with permission from Elsevier and the authors.)

5.2.2 Measurement Modes

Two modes, galvanostatic and potentiostatic, exist for EIS measurements. Although no major differences are discernible between the results, each mode has its advantages and disadvantages and, depending upon the application, one may be more suitable than the other.

5.2.2.1 Potentiostatic Mode

In a potentiostatic measurement mode, an AC potential perturbation is applied to an electrochemical cell or fuel cell and the current response from the cell is measured. In general, the potentiostatic mode is able to make use of the full bandwidth afforded by the FRA/potentiostat. However, attention must be paid when applying this technique to fuel cells, because a small change in potential may lead to a large difference in current, which can result in overloading the cell and/or the current measurement circuits in the potentiostat. Accordingly, it is necessary to test different AC perturbation voltage amplitudes to ensure that the AC current does not exceed the maximum current range provided by the potentiostat. Furthermore, the cell impedance also changes with the frequency, so a suitable AC voltage level must be found across the frequency range [44].

The amplitude used for the AC perturbation signal plays an important role in obtaining the best possible results. In most potentiostatic measurements for a PEM fuel cell, the AC signal amplitude is between 5 and 15 mV [33, 45, 46]. In Hombrados et al.'s work [47], the AC voltage signal was set at 100 mV because the cell tested had thick collector plates. They suggested that it was necessary to use an AC signal amplitude larger than 25 mV. The impedance spectra were measured by sweeping frequencies over the range from 1 mHz to 100 kHz. The spectra are normally recorded 10 points per decade [46, 48, 49]. Potentiostatic measurements of a PEM fuel cell can be performed either at the OCV or at imposed potentials. EIS of a symmetrical gas-feeding cell can be measured by this

mode only at the OCV. Impedance data at imposed potentials will be more representative of overall electrode performance, including diffusion resistances, than impedance data collected near OCV [50].

Spectra from different overpotentials can give us an overall picture of electrode performance. In order to eliminate interference from the mass transport effect, a potential is normally selected close to the OCV, where the mass transport resistance is not significant and the main contributor to the impedance is the interfacial charge-transfer resistance, which is potential-dependent [2]. In general, the potential-dependent arc is related to the double-layer capacitance of the electrode, combined with the charge-transfer resistance of the ORR. Thus, the obtained radius of the impedance arc (R_{ct}) is mainly contributed by the charge-transfer resistance. The dependency of this arc radius on electrode potential can be described by the Tafel equation ($V \sim \log R_{ct}^{-1}$) [51], and agrees with the typical Tafel slope of approximately 60 mV/decade for the ORR on Pt. As the overpotential increases, the charge-transfer resistance decreases, reflecting an increased driving force for the interfacial ORR process [33]. At medium overpotentials, proton, oxygen, fuel, and water transport can contribute significantly to the total impedance of the cell. At high overpotentials, oxygen diffusion in the backing may become dominant, especially when air is used as the oxidant [24].

5.2.2.2 Galvanostatic Mode

When measuring AC impedance spectroscopies using the galvanostatic mode, an AC current perturbation is applied to an electrochemical cell or fuel cell and the potential response from the cell is measured. In general, galvanostatic mode is a more complex but nonetheless sufficient mode for high-energy applications. Although this operation mode has a more limited bandwidth, it possesses the advantage that the AC and DC current levels can be selected by the operator, which prevents the cell and potentiostat from accidentally overloading. Thus, relatively large AC perturbation currents can be used without significantly changing the cell voltage [44].

The current amplitude chosen for AC impedance measurements in the galvanostatic mode is also very critical. Wagner and Gulzow [41] used 200 mA amplitude for their galvanostatic mode measurements, controlling DC at 5 A or 217 mA/cm^2 to study changes in EIS data over time during CO poisoning of the Pt anode. In Jaouen et al.'s work [52, 53] as well as in ours [54, 55], the amplitude of the AC current was set as 5% of the DC current.

As the galvanostatic mode allows precise control of the current through the cell, it can force a constant conversion rate of the charged species involved in the electrode reactions [41]. This is potentially advantageous. For example, when studying CO poisoning, evaluation of the EIS spectra at a constant voltage during the poisoning of the anode is difficult because both the anode and the cathode impedance change with time [41]. Thus, generally speaking, the galvanostatic mode is suitable for measuring impedance when studying CO contamination.

5.2.3 Operating Conditions

The performance of fuel cell systems can be severely influenced by operating conditions such as temperature, fuel and oxidant flow rates, pressure, and fuel humidity. Performance can drop significantly if the cell is not properly operated. The following sections describe how AC impedance can change under different operating conditions.

5.2.3.1 Temperature Effect

Temperature is one of the most important operating parameters that need to be properly controlled. The major effect of temperature is to change the reaction kinetics of the ORR in the fuel cell; for example, increasing the temperature will speed up the ORR. This is reflected in EIS in such a way that the kinetic arc in a Nyquist plot is larger at low temperatures than at high temperatures, as shown in Figure 5.40. In these graphs, the ohmic drop is corrected by using the high-frequency intercept of the kinetic loop. The other effect is to change the fuel cell's water management. For example, at lower temperatures, the arc radius in a low-frequency range (mass transfer arc) can be significantly reduced by increasing fuel cell temperature as more liquid water may accumulate at the cathode, resulting in a mass transfer problem.

Temperature can also affect proton transport inside the membrane, resulting in membrane conductivity change. For example, at the same water content level, increasing temperature can reduce membrane resistance, thereby improving fuel cell performance. This result is also reflected in an EIS Nyquist plot. The high-frequency intercept value (membrane resistance) of the kinetic loop can be significantly affected by changing fuel cell temperature. Freire and Gonzalez [29] showed that for Nafion®117, the membrane resistance was decreased by increasing the cell temperature. In fact, the influence of temperature on the membrane resistance is more complicated than expected. For example, Mann et al. [56] proposed an empirical expression for Nafion® membrane resistivity, r_M (Ωcm):

$$r_M = \frac{181.6\left[1+0.03\left(\frac{i}{A}\right)+0.062\left(\frac{T}{303}\right)^2\left(\frac{i}{A}\right)^{2.5}\right]}{\left[\lambda-0.634-3\left(\frac{i}{A}\right)\right]\exp\left[4.18\left(\frac{T-303}{T}\right)\right]} \tag{5.16}$$

where λ is the empirical coefficient representing the effective water content of the membrane, and i, A, and T are the current (A), the cell active area (cm^2), and the cell temperature (K), respectively.

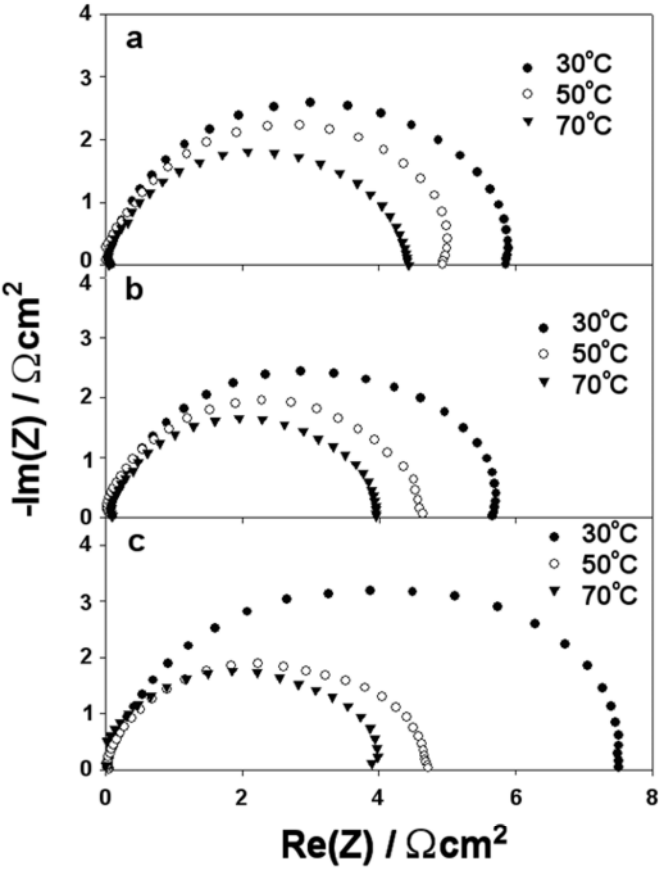

Figure 5.40. Comparison of the ohmic resistance-corrected Nyquist plots of a Ballard Mark V 6-cell stack at different temperatures: *a* 50 A, *b* 100 A, *c* 150 A

5.2.3.2 Flow Rate Effect

It is generally recognized that the oxygen reaction in ORR kinetics is first order with respect to the oxygen concentration. In order to facilitate the ORR, a pressurized gas stream is often used to increase the reactant concentration, especially at high current densities, when mass-transport effects are more dominant than at low current densities [57]. In practice, mass transport limitations can be effectively reduced by using higher reactant flow (corresponding to a high reactant stoichiometry). However, a high flow rate will increase the parasitic power loss in a fuel cell system, resulting in lower efficiency. Young et al. [58] operated a fuel cell at a stoichiometry of over 20, much higher than is usually employed in fuel cell operation, to eliminate the mass transfer effects. Ciureanu [49] used a constant stoichiometry of 4 for the inlet air flow in order to ensure complete removal of the water produced in the cathode compartment. Comparison of EIS spectra at different reactant flow rates provides information on the effect of gas diffusion on mass transport [23]. Thus, we may predict that if a fuel cell stack is operated at a

fixed air flow rate, the impedance spectra of a fuel cell operated at high currents will develop a low-frequency arc due to air shortage.

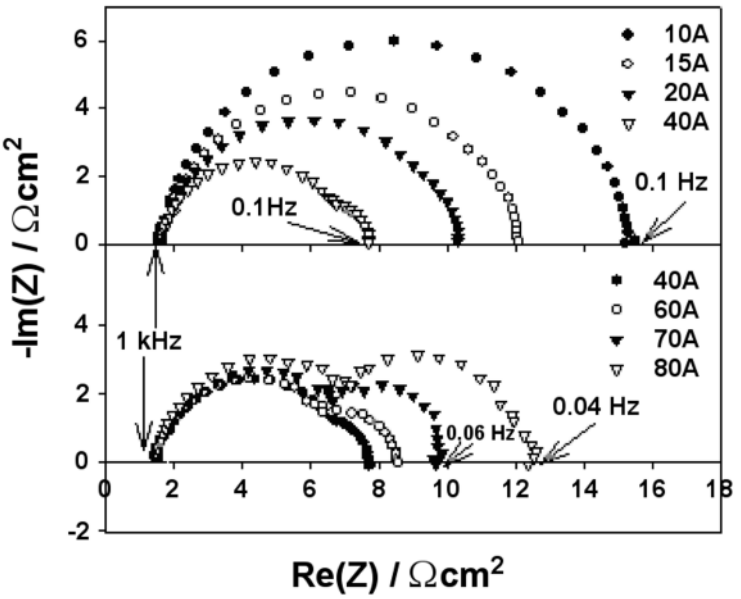

a

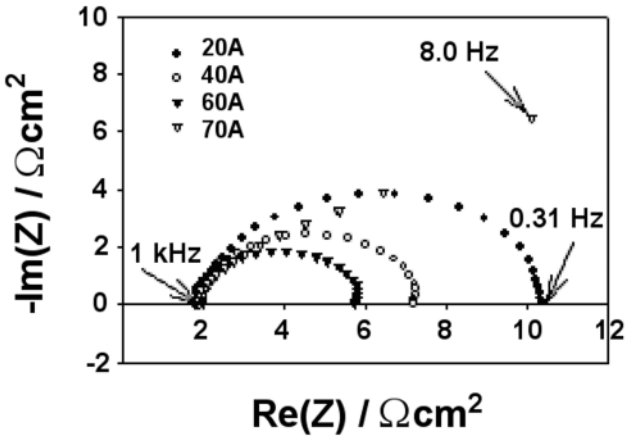

b

Figure 5.41. Effects of flow rate on Nyquist plots of a Ballard Mark V 6-cell stack. *a* Effect of air shortage at 50°C. The air flow rate was 20 L/min. *b* Effect of hydrogen shortage at 50°C. The hydrogen flow rate was 2 L/min

Figure 5.41*a* shows the effect of air shortage on the Nyquist plots of a Ballard Mark V 6-cell stack at 50°C. The fuel cell stack was operated at a fixed air flow rate of 20 standard L/min at the cathode, and a constant hydrogen stoichiometry of 2 at the anode. It can be seen that even at low currents, the impedance spectra of the stack still show an arc caused by mass transfer limitation. With increasing current, the arc becomes progressively larger. If the stack is operated at a fixed hydrogen flow rate of 2 L/min, and the air flow rate remains at a constant stoichiometry of 2.5, the Nyquist plots of the same stack at 50°C show the effect of hydrogen shortage, as illustrated in Figure 5.41*b*. Over the current range of 20 A to 60 A, the kinetic loop decreases with increasing current. When the current reaches 70 A, the stack loses its normal function. By comparing Figures 5.41*a* and 5.41*b* it can be seen that, unlike the case of air shortage, the mass transfer arcs do not appear even under the condition of hydrogen shortage. This is due to the fast reaction kinetics of hydrogen oxidation, so that the spectrum mostly represents the cathode ORR behaviours.

5.2.3.3 Humidity Effect

Water management is an important issue in the performance of PEM fuel cells. Water content at the interface contributes to the transport of the involved species in many different ways. At one extreme, a high water level can block oxygen transport. If water content is elevated due to its generation at the cathode, it can directly affect the ORR kinetics and also contribute indirectly to the state of contact between the Pt catalyst and the ionomer. If there is not enough water at the reaction interface, the ionomer will shrink, reducing both the surface contact of the catalyst with the ionomer and the proton conductivity of the ionomer [59]. In this case, humidified gas streams are necessary for fuel cell feeding. With respect to this, the amount of humidity in the reactant stream may affect the cell performance, which can in turn be reflected by EIS spectra measurements. It is widely reported that humidity can influence the high-frequency intercept at the real axis, which is associated with membrane resistance. The conductivity of the membrane in a PEM fuel cell is directly related to its water content, which depends on: (1) the water carried by the humidified reactant gases; (2) the water generated by the cell reaction at the cathode; (3) the electroosmotic drag – that is, water carried by the protons that are transported from anode to cathode; and (4) back-diffusion of water from the cathode to the anode. In addition, EIS can reveal insufficient humidification of the reactant gases in two other ways: (1) an increase in the resistance of the ionomeric component within the catalyst layer (a significant 45° branch develops), and (2) an increase in the interfacial impedance for the ORR [27].

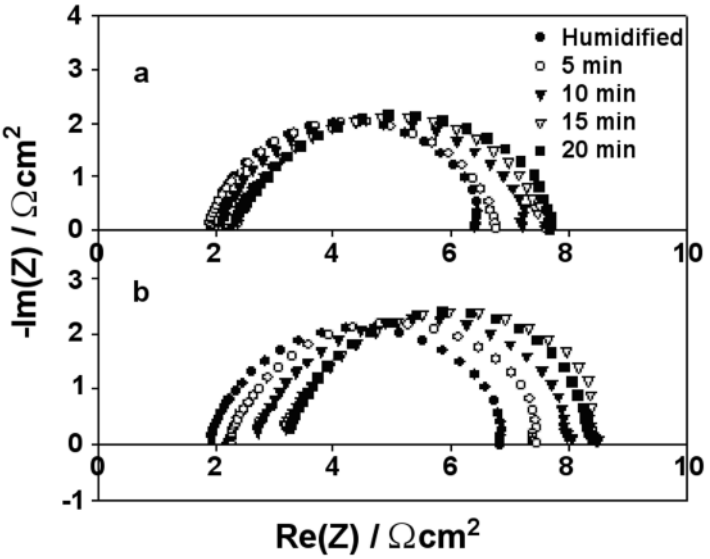

Figure 5.42. Transients of the impedance spectra after interruption of the humidification at 50°C. Initial state is humidified. *a* Cutting off of anode humidification. *b* Cutting off of cathode humidification.

Figure 5.42 shows an example of the effect of humidity on the EIS spectra. It can be seen that the cut-off for anode humidification does not affect the spectra too much compared with the cut-off for cathode humidification. As we know, the fuel cell EIS primarily represents the cathode behaviour. Therefore, cathode humidification can greatly affect the whole impedance spectra. The humidification cut-off at the cathode causes a large difference in both the membrane resistance and the kinetic resistance. Dehydration of the anode also brings about a substantial increase in cathode impedance because a dry anode pulls water away from the cathode and across the membrane, which makes it hard to keep the cathode well hydrated [18].

The sensitivity of the impedance to humidification of the reactant gases also depends on the membrane thickness. It has been reported that a thicker membrane is much more sensitive to humidification conditions. For Nafion®117, membrane resistance normally decreases when the reactant gases are better humidified because the conductivity of Nafion® increases almost linearly with its water content [60]. If the fuel cell is operated with Nafion®112, the effect of humidifying the reactant gases is much less significant because this thin membrane remains well hydrated by the water produced in the fuel cell reaction [29].

5.2.4 Reference Electrodes

In electrochemical studies of fuel cell systems, two-electrode EIS measurements have been applied extensively. However, the results are often difficult to interpret due to superposition of the behaviours at both anode and cathode. In some cases,

such as a DMFC, the anode impedance is significant and comprises a large portion of the entire impedance obtained from anode and cathode. To diagnose fuel cell performance, it is better to understand the individual behaviour of each electrode, in which case a reference electrode may be needed to take EIS measurements of a fuel cell.

As described in Section 5.2.1.1, individual electrode impedance can be obtained by feeding the same gases to both electrode compartments in a symmetrical cell mode. Although impedance spectroscopy can be employed to distinguish the contribution from either anode or cathode, it is not useful when dealing with an asymmetric electrode system. The fuel cell is normally an asymmetric system in which the anode and cathode differ in the type of catalyst, the catalyst loading, and the hydrophilic/hydrophobic properties of the gas diffusion layer, as well as the carbon loading of the microporous layer. Therefore, an alternative is to implement three-electrode EIS measurements. The main goal of using a reference electrode is to measure quantitatively the voltage losses due to the kinetic charge transfer, mass transfer, and ohmic resistance of the individual electrodes.

5.2.4.1 Three-Electrode Configuration

In principle, three-electrode EIS measurement is capable of separating the contributions from the anode and the cathode [61]. In a three-electrode EIS experiment, as shown in Figure 5.43, the potentiostat, with three electrode probes, is applied to measure signals between the working electrode (WE) and the reference electrode (RE). The counter electrode (CE) is used to collect the induced current from the WE. For a fuel cell, if the anode serves as a WE, the cathode will serve as a CE, and vice versa. In this way, the individual electrode impedances can be determined independently.

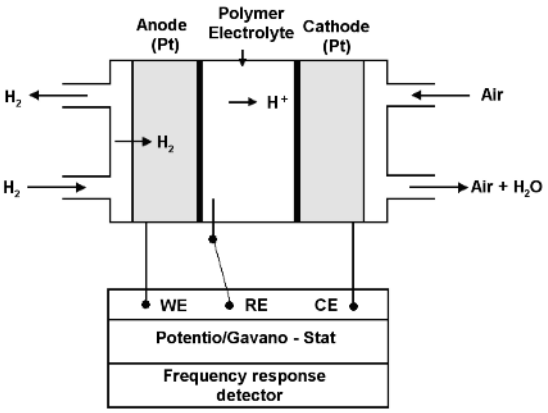

Figure 5.43. Schematic employment of the reference electrode in a PEM fuel cell [62]. (Reprinted from Electrochimica Acta, 47, Song SM, Koo IG, Lee WM, The influence of oxygen additions to hydrogen in their electrode reactions at Pt/Nafion interface, 2413–19. ©2002, with permission from Elsevier.)

In general, the reference electrode should be (1) a reversible electrode that obeys the Nernst equation, (2) stable, and (3) able to respond quickly to changes in environmental conditions [63]. The most commonly used reference electrodes for measuring the AC impedance spectra for fuel cells are the DHE (dynamic hydrogen electrode) and the RHE (reversible hydrogen electrode) [64, 65].

5.2.4.2 Conventional Reference Electrodes

Conventional reference electrodes consist of a solid reversible electrode and an aqueous electrolyte solution. To measure the individual contributions from the anode and the cathode of a PEM fuel cell, the electrolyte solution of the reference electrode must either be in direct contact with one side of the solid proton exchange membrane or be located in a separate compartment with electrical contact between the reference electrode and the solid membrane by means of a salt bridge [66]. As a result, two different types of reference electrode configurations are employed for the study of fuel cells: internal and external.

In the internal type, the reference electrode is in direct contact with the polymer electrolyte membrane of the MEA, as depicted in Figure 5.44. This configuration requires extra attention when assembling and disassembling the fuel cell.

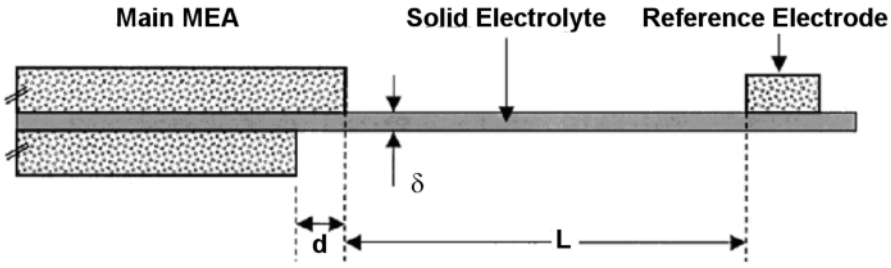

Figure 5.44. Schematic of a PEM fuel cell MEA with an internal reference electrode [67]. (Reproduced by permission of ECS—The Electrochemical Society, from He W, Van Nguyen T. Edge effects on reference electrode measurements in PEM fuel cells.)

The external type of reference electrode is connected to the membrane via a liquid electrolyte bridge, such as a sulphuric acid solution, as shown in Figure 5.45. Compared with the internal reference electrode configuration, the external type is easier to use in a normal PEM fuel cell set-up because it needs minimal modifications. However, attention must also be paid to ensure that the liquid electrolyte has good contact with the membrane and does not flow into the cell. Furthermore, the use of a liquid electrolyte in an acid bridge can induce non-uniform hydration and a proton concentration gradient in the membrane, therefore interfering with the fuel cell electrodes.

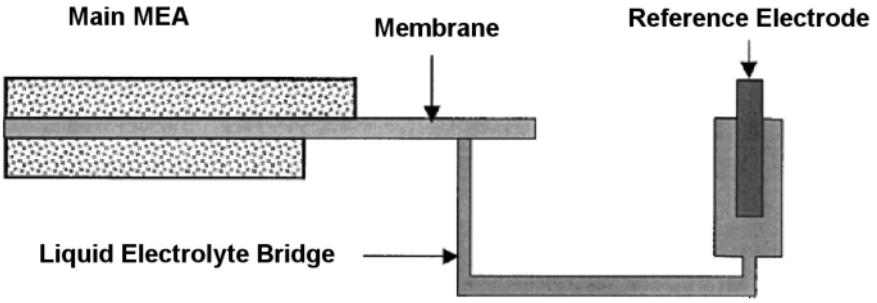

Figure 5.45. Schematic of a PEM fuel cell MEA with an external reference electrode [67]. (Reproduced by permission of ECS—The Electrochemical Society, from He W, Van Nguyen T. Edge effects on reference electrode measurements in PEM fuel cells.)

5.2.4.3 Dynamic Hydrogen Electrode

Since a conventional reference electrode with an aqueous electrolyte is difficult to mount on and connect to the membrane electrolyte, a dynamic hydrogen electrode is considered the most suitable reference electrode in PEM fuel cells [65]. A DHE can be constructed using a pair of platinum (or palladium) thin wires or platinized meshes inserted so as to be in contact with the membrane. In a DHE, if hydrogen can be produced at the Pt or Pd, the hydrogen coverage on the electrode is considered to be constant, and therefore a stable electrode potential can be established. Thus, the DHE has the advantages of minimally contaminating the measured system and not requiring a salt bridge. Compared with the standard hydrogen electrode, which has been utilized widely in electrochemical research as a reference electrode, the DHE is more stable [68].

A DHE can be built as either a sandwich-type or an edge-type [64]. For a sandwich-type configuration, a fine wire reference electrode is inserted between two membranes [61, 69], as shown in Figure 5.46. This configuration does have some disadvantages. First, using two membranes increases the membrane resistance by a factor of two or more. Second, the inserted reference electrode may interfere with the passage of current between the working electrode and the counter electrode, resulting in a non-uniform current distribution. Third, the inserted reference electrode may perturb the water profiles in a fuel cell, which can significantly affect cell performance [30].

For the edge-type configuration, the reference electrode is attached to a region of the polymer electrolyte close to the fuel cell electrodes [65, 68], as shown in Figure 5.47. The fuel cell must be properly designed in order to accommodate the reference electrode. However, the edge-type configuration can be used in a wide variety of cell designs without any modifications, and it does not need a special MEA. Currently, commercially available versions are available. Although dehydration of the membrane outside the active region may cause a significant problem [68], an optimal cell design could mitigate this issue.

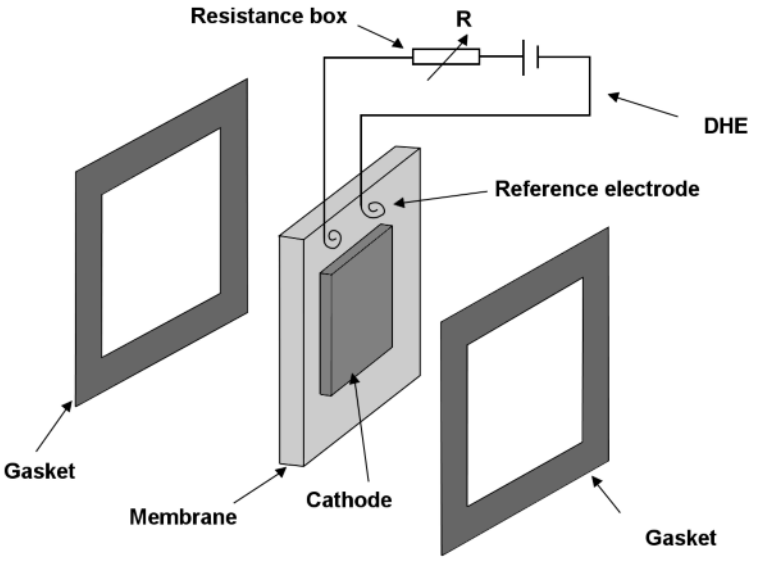

Figure 5.46. Schematic diagram of a cell with a sandwich-type DHE reference electrode [64]. (Reprinted from Electrochimica Acta, 49, Li G, Pickup PG. Measurement of single electrode potentials and impedances in hydrogen and direct methanol PEM fuel cells, 4119–26, ©2004, with permission from Elsevier and the authors.)

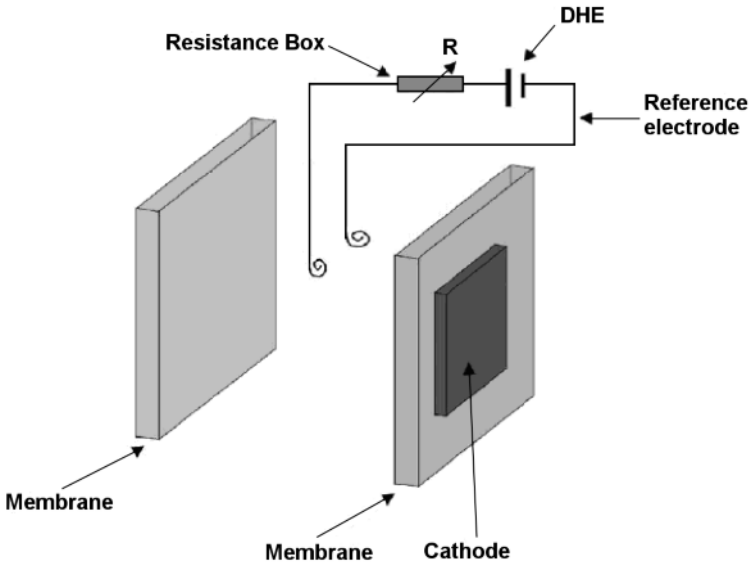

Figure 5.47. Schematic diagram of a cell with an edge-type DHE reference electrode [64]. (Reprinted from Electrochimica Acta, 49, Li G, Pickup PG. Measurement of single electrode potentials and impedances in hydrogen and direct methanol PEM fuel cells, 4119–26, ©2004, with permission from Elsevier and the authors.)

Using an edge-type DHE design, Li and Pickup [64] measured individual electrode potentials and impedances. Figure 5.48 shows the results of the obtained impedance. The complex plane impedance plots were collected at a current density of 0.2 A cm^2. From Figure 5.48, one can observe good agreement between the sum of the individual anode and cathode impedances and the whole cell impedance, which proves that the measurements for individual electrode impedances using an edge-type DHE reference electrode are feasible and accurate. It can also be seen that the anode exhibits significant impedance. Although the cathode impedance dominates that of the whole cell, ignorance of the anode impedance could result in a large measurement error.

Measurements using a DHE reference electrode can be affected by the relative geometry and alignment of the two electrodes. Therefore, designing a DHE for a three-electrode cell configuration requires (1) a uniform current density at the working electrode, which means that the cell geometry should ensure a uniform potential distribution over the entire working electrode [67, 70], and (2) that the cathode and anode be perfectly aligned with each other in a symmetric configuration in order to avoid uneven current distribution [71, 72]. Even with well-designed cell geometry and optimal alignment, there will still be potential-dependent small errors due to minor differences in potential distribution.

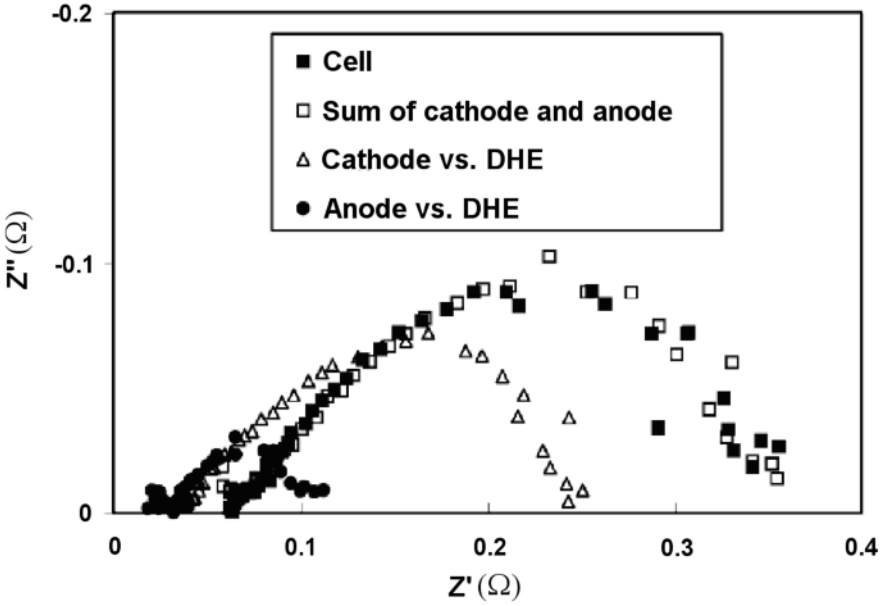

Figure 5.48. Complex plane impedance plots for a 5 cm^2 hydrogen fuel cell at a current density of 0.2 A cm^2. The cell was run at ambient temperature with humidified H_2 and dry air [64]. (Reprinted from Electrochimica Acta, 49, Li G, Pickup PG. Measurement of single electrode potentials and impedances in hydrogen and direct methanol PEM fuel cells, 4119–26, ©2004, with permission from Elsevier and the authors.)

5.2.4.4 Other Reference Electrodes

Fuel cell researchers have also investigated other reference electrodes, such as a pseudo-reference electrode constructed by inserting a micro-sized carbon filament between two polymer electrolyte membranes [73]. The main advantage of pseudo-reference electrodes is their easy implementation, although one disadvantage is that their DC potential is unknown. However, this DC potential may not be that critical because EIS measurements mainly rely on the AC perturbation signal from which the impedance is calculated.

Another alternative, an ionized air reference electrode (IAE), has been described by Foulkes et al. [66] for use with solid polymer electrolytes, in particular Nafion®425. Use of the IAE is achieved by establishing electrical contact with the solid electrolyte from a weak source of ionizing radiation to ionize an air gap. In contrast to conventional reference electrodes, the IAE is a liquid-free device and can make electrical contact with a solid polymer electrolyte without a salt bridge. It is also temperature independent. In view of these special characteristics, the IAE might provide a useful alternative to conventional reference electrodes for use with solid polymer electrolytes.

5.2.4.5 Summary

When conducting individual electrode impedance measurements, it is very useful to place a reference electrode inside a fuel cell. Information separately obtained at the anode and cathode helps to identify problems in the fuel cell; for a DMFC in particular, the magnitude of the anode impedance is comparable to that of the cathode. A reference electrode can also eliminate errors caused by assuming a negligible anode overpotential or impedance. In terms of modelling, the individual information helps to validate the corresponding half-cell modules of a model and to generate more accurate model parameters. Finally, the DHE, an excellent candidate for a fuel cell reference electrode, can be directly mounted very close to the working electrodes of the fuel cell without using a salt bridge or any other electrolyte source, which avoids the introduction of corrosive species and membrane potentials into the system.

Unfortunately, due to technical difficulties, reference electrodes have not been widely employed in fuel cell measurements. The primary cause is the geometric restriction imposed by the thin solid electrolyte (for example, a typical electrolyte thickness is about 50 μm for a Nafion®112 membrane). Additional factors such as the shape and position of the reference electrode must be taken into account in order to obtain reliable and meaningful results. In reality, the requirements for a reference electrode are less stringent than expected, since the main problem is the drift of the reference potential during measurement, which can result in large error due to the strong potential dependence of the impedance.

5.3 EIS Under Heavy Duty

5.3.1 Introduction

Generally speaking, it is easy to carry out EIS measurements at the level of fuel cells with small active areas. However, in the real world, fuel cell stacks are high-powered, and taking EIS measurements of a large fuel cell active area or at stack level is much more challenging [49, 74]. To measure the AC impedance of a larger fuel cell active area, an electrical load (instead of a potentiostat) combined with a frequency response analyzer (FRA) is a feasible option [75, 76]. During measurement, a sinusoidal perturbation wave generated by the FRA is applied to the fuel cell through an electric load bank. This AC signal is superimposed on the DC current, and the AC signals from the fuel cell are then fed back to the FRA to generate the AC impedance.

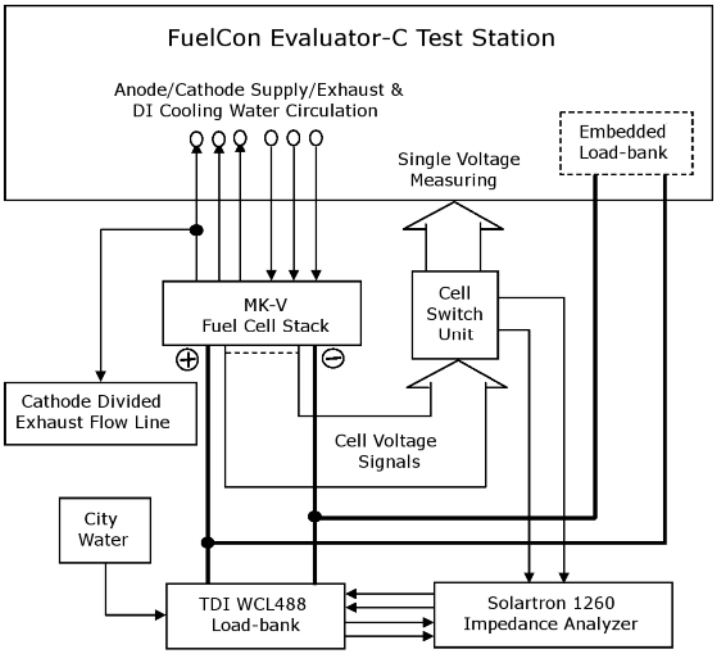

Figure 5.49. Experimental schematic for EIS measurement of a 500 W fuel cell stack [55]. (Reprinted from Journal of Power Sources, 161, Yuan XZ, Sun C, Wang H, Zhang J. AC impedance diagnosis of a 500 W PEM fuel cell stack: part II: individual cell impedance, 929–37, ©2006, with permission from Elsevier.)

When fuel cells work under heavy load conditions, it becomes more difficult to carry out the same measurements of AC impedance. One limitation on the application of EIS to large fuel cell stacks is that most commercially available load banks operating at higher currents do not have good frequency responses (ca. 10

kHz) [77]. Ciureanu [49] determined ohmic resistance by measuring the impedance of a five-cell stack with an active area of 256 cm^2 up to a load of 100 A. Our research group adopted a galvanostatic mode with an amplitude of 5% of the DC current; using a set-up that consisted of a FuelCon test station, a TDI load bank, and a Solartron 1260 FRA, as presented in Figure 5.49, we obtained the EIS of a 500 W Ballard Mark V PEMFC stack with an active area of 280 cm^2. This set-up can measure impedance at up to 1000 A, and we reported data obtained over the frequency range 20 kHz to 0.1 Hz [55]. However, the high-frequency feature may have been strongly affected by the measurement circuit because the load bank did not present an accurate response to the excitation in the high-frequency region. The useful signals began at around 1 kHz, where the kinetic loop started to develop.

Using the above set-up and stack, the effects of temperature, flow rate, and humidification were investigated [54, 55] and are shown in Figures 5.40 to 5.42. Individual cell impedance of the same stack under heavy duty was also studied. Two methods, the grounded mode and the floating mode, were applied in order to measure the impedance spectra of the individual cells; the electrical connection schematics of the EIS measurements for both methods are shown in Figure 5.50. For the grounded-mode method (Figure 5.50*a*), the negative terminal of the stack, as a common point, is always connected to the voltage 2 low input point of the impedance analyzer, using rotary switch #1. For the floating-mode method (Figure 5.50*b*), the voltage 1 and voltage 2 low input points of the impedance analyzer and the S-terminal of the TDI WCL488 load bank are connected together as one of the individual cell voltage measuring points (negative pole) that are floating with the negative terminal of the stack.

5.3.2 Grounded Mode

The common-point electrical connection mode enables one to obtain the AC impedance spectra of the individual cells by measuring impedances in combination (i.e., one cell, two cells, three cells, four cells, five cells, and six cells). At each current density level, the measurements begin with the first cell at the anode side, and then proceed with two cells, three cells, and so on up to six cells, the low potential measurement point remaining unchanged. The advantage of this method is that the instrument can be grounded, and the stack impedance is then measured when the total impedance of all the cells is measured. The disadvantage is that individual cell impedance, except for that of the first cell, is not measured directly. Rather, individual cell impedances are obtained by subtracting the impedance of all the previous cells from the measured impedance. For example, the impedance of the fifth cell is obtained by subtracting the sum impedance of four cells from the sum impedance of five cells. The typical spectra operated at 50 A are presented in Figure 5.51. As the cell numbers increase, the kinetic semicircle and the high-frequency intercept of this kinetic loop also increase [54].

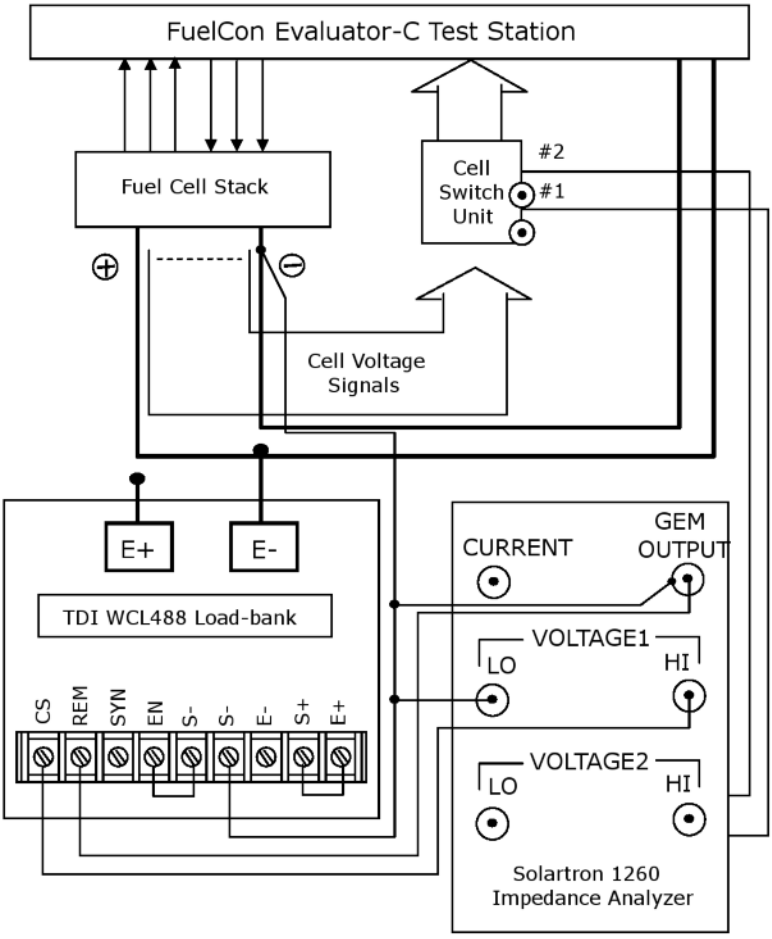

a

Figure 5.50. Electrical connection schematics of EIS measurement. *a* Grounded mode. (Reprinted from Journal of Power Sources, 161, Yuan XZ, Sun C, Wang H, Zhang J. AC impedance diagnosis of a 500 W PEM fuel cell stack: part II: individual cell impedance, 929–37, ©2006, with permission from Elsevier.)

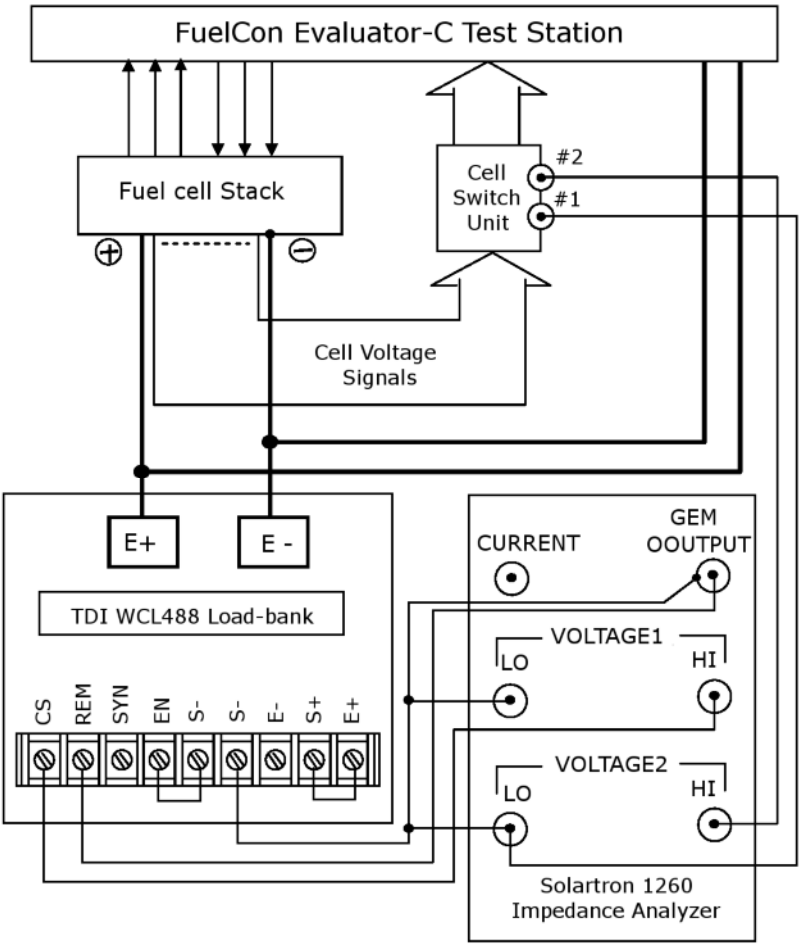

b

Figure 5.50. Electrical connection schematics of EIS measurement. *b* Floating mode [54]. (Reprinted from Journal of Power Sources, 161, Yuan XZ, Sun C, Wang H, Zhang J. AC impedance diagnosis of a 500 W PEM fuel cell stack: part II: individual cell impedance, 929–37, ©2006, with permission from Elsevier.)

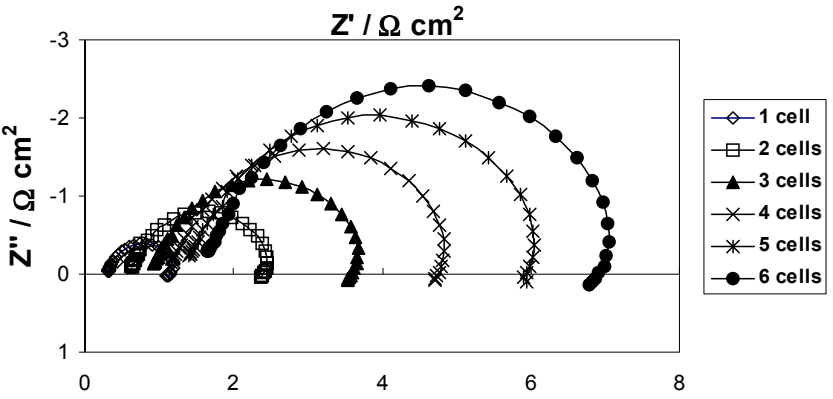

Figure 5.51. Typical impedance spectra for common-point connection at 50 A and 50°C

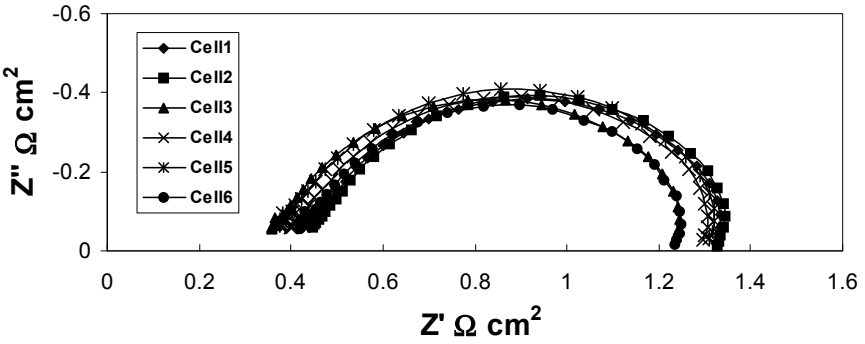

Figure 5.52. Typical impedance spectra in the way of floating-point connection at 50 A and 50°C

5.3.3 Floating Mode

The floating-point electrical connection mode is able to directly measure the AC impedance spectra of each individual cell, one by one. At each current density level, the measurements begin with the whole stack spectrum; then the individual cells are measured, followed by a repeated measurement of the whole stack spectrum. The whole stack measurement is performed before and after the sequence of individual cell measurements, which allows additional insights into the reliability of the measurement system through comparison of the sum of the ohmic losses in the individual cells with the ohmic loss measured across the whole stack. The results of the individual cell impedances are shown in Figure 5.52. The advantage of this method is that data analysis is not as time-consuming as for the grounded-mode method. The disadvantages are that this method undergoes more interference and the stack voltage cannot be displayed on the front panel of the TDI WCL488 load bank because the voltage displayed on the panel depends on the position of rotary switch #1.

5.4 Fast EIS

Measurements at low frequencies take time due to the long AC wave period, and when the cell is not stable, these measurements will be unreliable. To perform quicker measurements, the multi-sine mode can be used. Instead of using single sine waves one by one, a superposition signal containing different frequencies of sine waves can be applied. When we apply signals consisting of several sine waves superimposed on each other, it is possible to extract all of the frequencies or the necessary amplitude and phase information using the Fourier transforms of the voltage and current signals. In this way, the measurement time is significantly shorter than for one-by-one frequency measurements. The method is therefore called fast EIS or time domain EIS. It is also easy to add a random signal source to the instrument since the Fourier transform procedures (see Appendix A) are available for spectral analysis.

5.4.1 Principles and Measurements

In a series of earlier publications, Popkirov and Schindler [78–81] discussed several essential aspects of developing Fourier transform EIS (FT-EIS) as a time-resolved technique that uses a frequency-rich perturbation signal. The system is perturbed by an AC voltage signal composed of a multitude of frequencies, and all frequencies are applied simultaneously. The choice of the perturbation waveform is of crucial importance for reliable EIS measurements based on the Fourier transform. Normally, any type of time domain waveform may be used if it has the necessary frequency content in the desired frequency range. Popkirov and Schindler [78] concluded that a perturbation signal, which is a superposition of sine waves with properly chosen frequencies, provides better accuracy than either a step or a noise signal. When using sine wave signals, both the perturbation signal ($U(t)$) and the current response ($I(t)$), measured in the time domain, can be expressed as follows

$$U(t) = U_0(\omega)\sin(\omega t) \tag{5.17}$$

$$I(t) = I_0(\omega)\sin[\omega t + \theta(\omega)] \tag{5.18}$$

where U_0 and I_0 are the amplitudes of the perturbation signal and the current response, respectively, ω is the frequency, and θ is the phase angle.

By means of a fast Fourier transform (FFT) algorithm, the measured data can be transformed into the frequency domain. This Fourier transform is needed for several reasons. One is comparison with the data that have been measured in the frequency domain. The second is the actual requirement of results at specific frequencies. The third is interpretation of the data [82].

Thus, the sample response at the frequencies of each of the Fourier components can be obtained as follows

$$Z(\omega) = \frac{\hat{U}(\omega)}{\hat{I}(\omega)} \tag{5.19}$$

where $Z(\omega)$ is the complex impedance of the cell, $\hat{U}(\omega)$ is the Fourier transform of the applied AC voltage $U(t)$, and $\hat{I}(\omega)$ is the Fourier transform of the current response $I(t)$.

The time domain method is much faster than the frequency domain method, because the whole spectrum can be obtained from a single set of data. In many practical cases, the long-term stability of the electrochemical system cannot be assured [83]. Thus, this time domain method meets the need for a quick impedance measurement. The frequency resolution and the lowest frequency component are determined by the reciprocal of the total sampling time. Therefore, in order to achieve a wide frequency range for the impedance measurements, long measurement intervals and fast sampling should be carried out. The accuracy depends primarily on the applied perturbation signals and the signal processing [84]. It can be improved by averaging and by using perturbation signals with larger amplitudes. However, this is inappropriate for the linearity requirement of time-dependent systems.

Single sine and FFT techniques are both widely used for AC impedance measurement. In the single sine wave technique, a sine wave with a particular frequency and very low amplitude is superimposed on the DC base signals. If the amplitude of a stimulus sine wave is high, the output signal will be distorted at the non-linear regime, leading to additional frequency components (harmonic distortion). Applying the single sine correlation technique minimizes the harmonic distortion at the non-linear regime. However, to improve the accuracy of the impedance measurement, it is essential to operate with a linear regime and use a low enough amplitude AC stimulus. By increasing the integration cycles, the noises and subharmonics can be reduced.

FFT techniques can measure multiple-frequency AC impedance at the same time as a stimulus waveform containing multiple frequencies. FFT performs very fast AC impedance measurements and can function as a complement to the single sine wave technique. The stimulus waveform, which is constructed by multiple sine waves, should also have as low an amplitude as possible to avoid or decrease the harmonic distortion effects at the non-linear regime. However, if the amplitude of the stimulus wave is too low, each single sine wave will be much lower and may be distorted by noises. Fortunately, some commercially available analyzers have the option of selecting the frequencies for AC impedance measurements. Usually, stimulus frequencies are selected in such a way that each is not coincident with the main harmonics of the lower frequencies. As a result, the main components of the harmonic distortion from each frequency in the stimulus waveform do not interfere with the other stimulus frequencies.

5.4.2 Differences Between Frequency Domain and Time Domain

Time domain and frequency domain EIS are different approaches to impedance spectra measurements. However, from a theoretical point of view they should give

the same results because the two processes are interrelated by the Fourier transform [85]. The methods present both advantages and disadvantages.

The advantages of frequency domain measurements are as follows:

1. A large frequency domain can be achieved, from mHz to GHz and higher, with high accuracy.
2. Data processing is easier since ordinary processes are involved instead of convolution in the time domain [86].
3. Powerful data analysis programs are available (e.g., complex non-linear least square fit or CNLS-fit). Error estimations for model parameters can be obtained.
4. More visual information on various contributing processes is provided [87].

The main disadvantage of frequency domain measurement is that it is a time-consuming process, especially in a wider frequency range. For example, in the low-frequency region, impedance bridges require one to set the frequency and balance the bridge for each of the frequency points [88]. Therefore, obtaining good quality data at very low frequencies is not straightforward.

The advantages of time domain measurements are as follows:

1. Measurement speed is fast
2. Instrumentation is simple and inexpensive
3. Responses can be measured over longer time periods
4. Data acquisition is straightforward, while digital noise filtering can improve long-time data [87]
5. Transient electrochemical processes can be probed [89]

In practice, there are some limitations to this approach, the major one being that it is impossible to separate out the harmonic effects because all harmonics are present in the input signal. In order to reduce the problem of harmonics, one may use several non-harmonically related sine waves. However, the time needed to obtain the results increases due to the increased number of frequencies being measured. As we are concerned with analysis of the results versus log (freq), this approach also gives uniformly spaced output frequencies, thereby providing an unnecessary number of readings at the higher frequencies. Another disadvantage of the time domain method is the complicated data analysis.

As both the frequency domain and the time domain methods have disadvantages, Boukamp [87] recommended that both methods be combined using the CNLS-fit procedure, data validation (Kramers–Kronig transformation), and deconvolution. The Kramers–Kronig transformation can be found in Appendix C.

5.5 Chapter Summary

This chapter has provided the basic knowledge applied in EIS diagnosis for PEM fuel cell systems, including in situ and ex situ techniques. Various gas-feeding

modes for different purposes were presented. EIS under heavy duty conditions as well as fast EIS were also introduced. Equipped with these techniques, even a researcher without an electrochemical background can perform EIS measurements in a PEM fuel cell system. This chapter also lays a foundation for readers to understand the application of EIS in PEM fuel cell research and development, and to further study electrochemical impedance spectroscopy in other fuel cell systems.

References

1. Schulze M, Wagner N, Steinhilber G, Guelzuw E, Woehr M, Bolwin K (1996) Characterization and basic research investigations at PEFC electrodes and MEA. Fuel cell seminar & exposition, 663–7. Courtesy Associates, Washington, DC
2. Easton EB, Pickup PG (2005) An electrochemical impedance spectroscopy study of fuel cell electrodes. Electrochim Acta 50:2469–74
3. Perez J, Gonzalez ER, Ticianelli EA (1998) Impedance studies of the oxygen reduction on thin porous coating rotating platinum electrodes. J Electrochem Soc 145:2307–13
4. Genies L, Bultel Y, Faure R, Durand R (2003) Impedance study of the oxygen reduction reaction on platinum nanoparticles in alkaline media. Electrochim Acta 48(25–6):3879–90
5. Baker R (2008) Substituted iron phthalocyanines: electrocatalytic activity towards O_2 reduction in a proton exchange membrane fuel cell cathode environment as a function of temperature. M.A.Sc. diss. The University of British Columbia, Canada
6. Antoine O, Bultel Y, Durand R (2001) Oxygen reduction reaction kinetics and mechanism on platinum nanoparticles inside Nafion®. J Electroanal Chem 499:85–94
7. Girishkumar G, Rettker M, Underhile R, Binz D, Vinodgopal K, McGinn P, Kamat P (2005) Single-wall carbon nanotube-based proton exchange membrane assembly for hydrogen fuel cells. Langmuir 21:8487–94
8. Gottlieb MH and Sollner K (1968) Failure of the Nernst-Einstein equation to correlate electrical resistances and rates of ionic self-exchange across certain fixed charge membranes. Biophys J 8:515–35
9. Xie Z, Song C, Andreaus B, Navessin T, Shi Z, Zhang J, Holdcroft S (2006) Discrepancies in the measurement of ionic conductivity of PEMs using two- and four-probe AC impedance spectroscopy. J Electrochem Soc 153:E173–8
10. Slade S, Campbell SA, Ralph TR, Walsh FC (2002) Ionic conductivity of an extruded Nafion 1100 EW series of membranes. J Electrochem Soc 149:A1556–64
11. Cahan BD, Wainright JS (1993) AC impedance investigations of proton conduction in Nafion™. J Electrochem Soc 140:L185–6
12. Gardner CL, Anantaraman AV (1995) Measurement of membrane conductivities using an open-ended coaxial probe. J Electroanal Chem 395:67–73
13. Gardner CL, Anantaraman AV (1998) Studies on ion-exchange membranes. II. measurement of the anisotropic conductance of Nafion®. J Electroanal Chem 449:209–14.
14. Ciureanu M, Wang H (2000) Electrochemical impedance study of anode CO-poisoning in PEM fuel cells. J New Mater Electrochem Syst 3:107–19
15. Silva RF, De Francesco M, Pozio A (2004) Tangential and normal conductivities of Nafion® membranes used in polymer electrolyte fuel cells. J Power Sources 134:18–26
16. Anantaraman AV, Gardner CL (1996) Studies on ion-exchange membranes. Part 1. effect of humidity on the conductivity of Nafion®. J Electroanal Chem 414:115–20

17. O'Hayre R, Prinz FB (2004) The air/platinum/Nafion triple-phase boundary: characteristics, scaling, and implications for fuel cells. J Electrochem Soc 151:A756–62
18. Springer TE, Zawodzinski TA, Wilson MS, Gottesfeld S (1996) Characterization of polymer electrolyte fuel cells using AC impedance spectroscopy. J Electrochem Soc 143:587–99
19. Wagner N (2002) Characterization of membrane electrode assemblies in polymer electrolyte fuel cells using a.c. impedance spectroscopy. J Appl Electrochem 32:859–63
20. Brunetto C, Tina G, Squadrito G, Moschetto A (2004) PEMFC diagnostics and modelling by electrochemical impedance spectroscopy. Proceedings of the 12th IEEE Mediterranean electrochemical conference. IEEE Cat. No. 04CH37521, 3:1045–50
21. Tsampas MN, Pikos A, Brosda S, Katsaounis A, Vayenas CG (2006) The effect of membrane thickness on the conductivity of Nafion. Electrochim Acta 51:2743–55
22. Wagner N, Schnurnberger W, Müller B, Lang M (1998) Electrochemical impedance spectra of solid-oxide fuel cells and polymer membrane fuel cells. Electrochim Acta 43:3785–93
23. Kim JD, Park YI, Kobayashi K, Nagai M, Kunimatsu M (2001) Characterization of CO tolerance of PEMFC by ac impedance spectroscopy. Solid state ionics: diffusion and reactions 140:313–25
24. Li G, Pickup PG (2003) Ionic conductivity of PEMFC electrodes. J Electrochem Soc 150:C745–52
25. Kong CS, Kim DY, Lee HK, Shul YG, Lee TH (2002) Influence of pore-size distribution of diffusion layer on mass-transport problems of proton exchange membrane fuel cells. J Power Sources 108:185–91
26. Ciureanu M, Roberge R (2001) Electrochemical impedance study of PEM fuel cells. Experimental diagnostics and modeling of air cathode. J Phys Chem B 105:3531–9
27. Liu F, Yi B, Xing D, Yu J, Hou Z, Fu Y (2003) Development of novel self-humidifying composite membranes for fuel cells. J Power Sources 124:81–9
28. Cha SY, Lee WM (1999) Performance of proton exchange membrane fuel cell electrodes prepared by direct deposition of ultrathin platinum on the membrane surface. J Electrochem Soc 146:4055–60
29. Freire TJP, Gonzalez ER (2001) Effect of membrane characteristics and humidification conditions on the impedance response of polymer electrolyte fuel cells. J Electroanal Chem 503:57–68
30. Andreaus B, McEvoy AJ, Scherer GG (2002) Analysis of performance losses in polymer electrolyte fuel cells at high current densities by impedance spectroscopy. Electrochim Acta 47:2223–9
31. Paganin VA, Oliveira CLF, Ticianelli EA, Springer TE, Gonzalez ER (1998) Modelistic interpretation of the impedance response of a polymer electrolyte fuel cell. Electrochim Acta 43:3761–6
32. Fisher A, Jindra J, Wendt H (1998) Porosity and catalyst utilization of thin layer cathodes in air operated PEM-fuel cells. J Appl Electrochem 28:277–82
33. Romero-Castanon T, Arriaga LG, Cano-Castillo U (2003) Impedance spectroscopy as a tool in the evaluation of MEAs. J Power Sources 118:179–82
34. Eikerling M, Kornyshev AA (1999) Electrochemical impedance of the cathode catalyst layer in polymer electrolyte fuel cells. J Electroanal Chem 475:107–23
35. Lefebvre MC, Martin RB, Pickup PG (1999) Characterization of ionic conductivity profiles within proton exchange membrane fuel cell gas diffusion electrodes by impedance spectroscopy. Electrochem Solid-State Lett 2:259–61
36. Boillot M, Bonnet C, Jatroudakis N, Carre P, Didierjean S, Lapicque F (2006) Effect of gas dilution on PEM fuel cell performance and impedance response. Fuel Cells 6:31–7

37. Khan AR, Zhao J, Polevaya OY (2003) Study of ammonia formation during the autothermal reforming of hydrocarbon based fuels. Mater Res Soc Symp Proc 756:409–14
38. Soto HJ, Woo KL, Van-Zee JW, Murthy M (2003) Effect of transient ammonia concentrations on PEMFC performance. Electrochem Solid-State Lett 6:A133–5
39. Uribe FA, Gottesfeld S, Zawodzinski Jr TA (2002) Effect of ammonia as potential fuel impurity on proton exchange membrane fuel cell performance. J Electrochem Soc 149:A293–6
40. Zhang J, Wang H, Wilkinson DP, Song D, Shen J, Liu ZS (2005) Model for the contamination of fuel cell anode catalyst in the presence of fuel stream impurities. J Power Sources 147:58–71
41. Wagner N, Gulzow E (2004) Change of electrochemical impedance spectra (EIS) with time during CO-poisoning of the Pt-anode in a membrane fuel cell. J Power Sources 127:341–7
42. Ciureanu M, Wang H (1999) Electrochemical impedance study of electrode-membrane assemblies in PEM fuel cells: I. Electro-oxidation of H_2 and H_2/CO mixtures on Pt-based gas-diffusion electrodes. J Electrochem Soc 146:4031–40
43. Müller JT, Urban PM (1998) Characterization of direct methanol fuel cells by ac impedance spectroscopy. J Power Sources 75:139–43
44. Harper J, Rust M, Sayers B, Savage A (2004) High-frequency, high-current impedance spectroscopy: experimental protocols enabling measurement up to 1MHz at high current densities. TB/ANALYTICAL/001. Solartron Analytical, Farnborough, UK
45. Abe T, Shima H, Watanabe K, Ito Y (2004) Study of PEFCs by AC impedance, current interrupt, and dew point measurements. J Electrochem Soc 151:A101–5
46. Silva RF, De-Francesco M, Pozio A (2004) Tangential and normal conductivities of Nafion® membranes used in polymer electrolyte fuel cells. J Power Sources 134:18–26
47. Hombrados AG, Gonzalez L, Rubio MA, Agila W, Villanueva E, Guinea D, Chinarro E, Moreno B, Jurando JR (2005) Symmetrical electrode mode for PEMFC characterisation using impedance spectroscopy. J Power Sources 151:25–31
48. Guo Q, Cayetano M, Tsou Y, De-Castro ES, White RE (2003) Study of ionic conductivity profiles of the air cathode of a PEMFC by AC impedance spectroscopy. J Electrochem Soc 150:A1440–9
49. Ciureanu M (2004) Effects of Nafion® dehydration in PEM fuel cells. J Appl Electrochem 34:705–14
50. Ahn S, Tatarchuk BJ (1990) Composite electrode structures for fuel cell applications. Proceedings of the 25th intersociety energy conversion engineering conference 3:287–92
51. Ihonen J, Jaouen F, Lindbergh G, Lundblad A, Sundholm G (2002) Investigation of mass-transport limitations in the solid polymer fuel cell cathode. J Electrochem Soc 149:A448–54
52. Gode P, Jaouen F, Lindbergh G, Lundblad A, Sundholm G (2003) Influence of the composition on the structure and electrochemical characteristics of the PEFC cathode. Electrochim Acta 48:4175–87
53. Jaouen F, Lindbergh G, Wiezell K (2003) Transient techniques for investigating mass-transport limitations in gas diffusion electrodes. J Electrochem Soc 150:A1711–17
54. Yuan XZ, Sun C, Wang H, Zhang J (2006) AC impedance diagnosis of a 500 W PEM fuel cell stack: part II: individual cell impedance. J Power Sources 161:929–37
55. Yuan XZ, Sun C, Blanco M, Wang H, Zhang J, Wilkinson D (2006) AC impedance diagnosis of a 500 W PEM fuel cell stack: part I: stack impedance. J Power Sources 161:920–8

56. Mann RF, Amphlett JC, Hooper MAI, Jensen HM, Peppley BA, Roberge PR (2000) Development and application of a generalised steady-state electrochemical model for a PEM fuel cell. J Power Sources 86:173–80
57. Perry ML, Newman J, Cairns EJ (1998) Mass transport in gas-diffusion electrodes: a diagnostic tool for fuel-cell cathodes. J Electrochem Soc 145:5–15
58. Young HC, Yong GS, Won CC, Seong IW, Hak SH (2003) Evaluation of the Nafion effect on the activity of Pt–Ru electrocatalysts for the electro-oxidation of methanol. J Power Sources 118:334–41
59. Song JM, Cha SY, Lee WM (2001) Optimal composition of polymer electrolyte fuel cell electrodes determined by the AC impedance method. J Power Sources 94:78–84
60. Halla JD, Mamak M, Williams DE, Ozin GA (2003) Meso-SiO_2-$C_{12}EO_{10}OH$-CF_3SO_3H – a novel proton-conducting solid electrolyte. Adv Funct Mater 13:133–8
61. Dollé M, Orsini F, Gozdz AS, Tarascon JM (2001) Development of reliable three-electrode impedance measurements in plastic Li-ion batteries. J Electrochem Soc 148:A851–7
62. Song SM, Koo IG, Lee WM (2002) The influence of oxygen additions to hydrogen in their electrode reactions at Pt/Nafion interface. Electrochim Acta 47:2413–19
63. Chan SH, Chen XJ, Khor KA (2001) Reliability and accuracy of measured overpotential in a three-electrode fuel cell system. J Appl Electrochem 31:1163–70
64. Li G, Pickup PG (2004) Measurement of single electrode potentials and impedances in hydrogen and direct methanol PEM fuel cells. Electrochim Acta 49:4119–26
65. Ren X, Springer TE, Gottesfeld S (2000) Water and methanol uptakes in Nafion membranes and membrane effects on direct methanol cell performance. J Electrochem Soc 147:92–8
66. Foulkes FR, Archibald GW, Ogumi Z, Takehara Z (1990) An ionized air reference electrode. J Electrochem Soc 137:2022–4
67. He W, Van Nguyen T (2004) Edge effects on reference electrode measurements in PEM fuel cells. J Electrochem Soc 151:A185–95
68. Küver A, Vogel I, Vielstich W (1994) Distinct performance evaluation of a direct methanol SPE fuel cell. A new method using a dynamic hydrogen reference electrode. J Power Sources 52:77–80
69. Büchi FN, Scherer GG (2001) Investigation of the transversal water profile in Nafion membranes in polymer electrolyte fuel cells. J Electrochem Soc 148:A183–8
70. Winkler J, Hendriksen PV, Bonanos N, Mogensen M (1998) Geometric requirements of solid electrolyte cells with a reference electrode. J Electrochem Soc 145:1184–92
71. Adler SB, Henderson BT, Wilson MA, Taylor DM, Richards RE (2000) Reference electrode placement and seals in electrochemical oxygen generators. Solid State Ionics 134:35–42
72. Adler SB (2002) Reference electrode placement in thin solid electrolytes. J Electrochem Soc 149:E166–72
73. Kuhn H, Andreaus B, Wokaun A, Scherer GG (2005) Electrochemical impedance spectroscopy applied to polymer electrolyte fuel cells with a pseudo reference electrode arrangement. Electrochim Acta 51:1622–8
74. Halseid R, Vie PJS, Tunold R (2004) Influence of ammonium on conductivity and water content of Nafion 117 membranes. J Electrochem Soc 51:A381–8
75. Raposa G (2004) Performing ac impedance measurements on fuel cells. Elektron 21:15–16
76. Tang Y, Zhang J, Song C, Liu H, Zhang J, Wang H, Mackinnon S, Peckham T, Li J, McDermid S, Kozak P (2006) Temperature dependent performance and in situ ac impedance of high-temperature PEM fuel cells using the Nafion-112 membrane. J Electrochem Soc 153:A2036–43

77. Brett DJL, Atkins S, Brandon NP, Vesovic V, Vasileiadis N, Kucernak A (2003) Localized impedance measurements along a single channel of a solid polymer fuel cell. Electrochem Solid-State Lett 6:A63–6
78. Popkirov GS, Schindler RN (1992) A new impedance spectrometer for the investigation of electrochemical systems. Rev Sci Instrum 63:5366–72
79. Popkirov GS, Schindler RN (1993) Optimization of the perturbation signal for electrochemical impedance spectroscopy in the time domain. Rev Sci Instrum 64:3111–15
80. Popkirov GS, Schindler RN (1993) Validation of experimental data in electrochemical impedance spectroscopy. Electrochim Acta 38:861–7
81. Popkirov GS, Schindler RN (1995) Effect of sample nonlinearity on the performance of time domain electrochemical impedance spectroscopy. Electrochim Acta 40:2511–17
82. Mopsik FI (1985) The transformation of time-domain relaxation data into the frequency domain. IEEE Transactions on Electrical Insulation EI-20:957–64
83. Popkirov GS (1996) Fast time-resolved electrochemical impedance spectroscopy for investigations under nonstationary conditions. Electrochim Acta 41:1023–7
84. Wiegand G, Neumaier KR, Sackmann E (2000) Fast impedance spectroscopy: general aspects and performance study for single ion channel measurements. Rev Sci Instrum 71:2309-20
85. Metelko D, Jamnik J, Pejovnik S (1992) Comparison between the impedance spectra of $Li/SOCl_2$ batteries obtained using the time and the frequency domain measurement techniques. J Appl Electrochem 22:638–43
86. Gabrielli C, Keddam M, Takenouti H (1990) New trends in the investigation of electrochemical systems by impedance techniques: multi-transfer function analysis. Electrochim Acta 35:1553–7
87. Boukamp BA (2004) Impedance spectroscopy, strength and limitations. Technisches Messen 71:454–9
88. Husimi Y, Wada A (1976) Time-domain measurement of dielectric dispersion as a response to pseudorandom noise. Rev Sci Instrum 47:213–19
89. Garland JE, Pettit CM, Roy D (2004) Analysis of experimental constraints and variables for time resolved detection of Fourier transform electrochemical impedance spectra. Electrochim Acta 49:2623–35

6

EIS Applications

As described in Chapter 1, there are several types of fuel cells. Of these various types, the PEMFC has captured the most attention among fuel cell researchers. The main features of the PEMFC are:

- Low operating temperature (70–100°C)
- High power density (~1.4 kW/kg)
- High electrical efficiency (40–60%)
- Quiet operation
- Zero emissions

These characteristics explain why the PEMFC has become such a promising fuel cell candidate for powering vehicles, and for both stationary and portable power generation [1].

EIS has played an important role in fuel cell technology development, as one of the most important research tools for fuel cell diagnosis. EIS can help to identify the contributions from different components or processes to the total impedance of a PEM fuel cell. Such information is very helpful for understanding the fundamental processes within the fuel cell, the performance–structure relationships, and the contributions of various components to performance loss, as well as the associated failure modes and mechanisms. EIS thus assists with fuel cell design optimization and selection of the most appropriate fuel cell operating conditions. In this chapter, we will present some typical examples of the applications of EIS in PEM fuel cell research, and an overview of EIS spectra analysis.

6.1 EIS Applications in PEMFCs

The membrane electrode assembly (MEA), which consists of three components (two gas diffusion electrodes with a proton exchange membrane in between), is the most important component of the PEMFC. The MEA exerts the largest influence on the performance of a fuel cell, and the properties of each of its parts in turn play significant roles in that performance. Although all the components in the MEA are important, the gas diffusion electrode attracts more attention because of its complexity and functions. In AC impedance spectra, the proton exchange membrane usually exhibits resistance characteristics; the features of these spectra reflect the properties of the gas diffusion electrode. In order to better understand the behaviour of a gas diffusion electrode, we introduce the thin-film/flooded agglomerate model, which has been successfully applied by many researchers to

explain the behaviour of gas diffusion electrodes [2, 3]. The model describes the fuel cell catalyst layer as agglomerates formed by carbon-supported catalyst/particles flooded with electrolyte, in combination with a thin-film diffusion process. According to this model, each gas diffusion electrode is composed of a gas diffusion layer and a catalyst layer that can be described as carbon-supported catalyst agglomerates covered with a thin film of electrolyte. During fuel cell operation, reactant gas reaches the catalyst layer through the hydrophobic channels within the gas diffusion layer, and reaches the reaction sites through diffusion in the thin electrolyte film.

The characteristics of a gas diffusion electrode can also be illustrated by the thin-film/flooded agglomerate model. Paganin et al. [4] summarized the parameters that often appear in the impedance spectra of H_2/O_2 and H_2/air fuel cells:

1. Polarization resistance (R_p) due to the oxygen reduction reaction (ORR), which is in parallel with the double-layer capacitance (C_{dl})
2. Distributed resistance due to the ohmic drop in the electrolyte within the catalyst layer
3. Limiting concentration gradient of oxygen in the flooded agglomerate
4. Limiting concentration gradient in the thin electrolyte film
5. Diffusion of oxygen in the gas diffusion layer of the electrode, particularly when air is used instead of oxygen

6.1.1 Optimization of MEA Structure

Fuel cell performance is affected by MEA composition, including catalyst loading, PTFE content in the gas diffusion layer, and Nafion® content in the catalyst layer and membrane, each of which affects the performance in different ways, yielding distinct characteristics in the electrochemical impedance spectra. Even different fabrication methods may influence a cell's performance and electrochemical impedance spectra. With the help of the model described above, impedance spectra can provide us with a useful tool to probe structure–performance relationships and thereby optimize MEA structure and fabrication methods.

6.1.1.1 Effects of Catalyst Loading

The different behaviours of gas diffusion electrodes with different catalyst loadings were studied by Paganin et al. [4]. EIS measurements of 0.5 and 1 cm^2 single cells were conducted with H_2/O_2 (air) as fuel/oxidant. In their measurements, a Solartron 1250 frequency response analyzer and a 1286 electrochemical interface were employed. The amplitude of the AC signal was 10 mV and the frequency range was typically from 10 mHz to 10 kHz. Representative EIS results are shown in Figures 6.1 and 6.2.

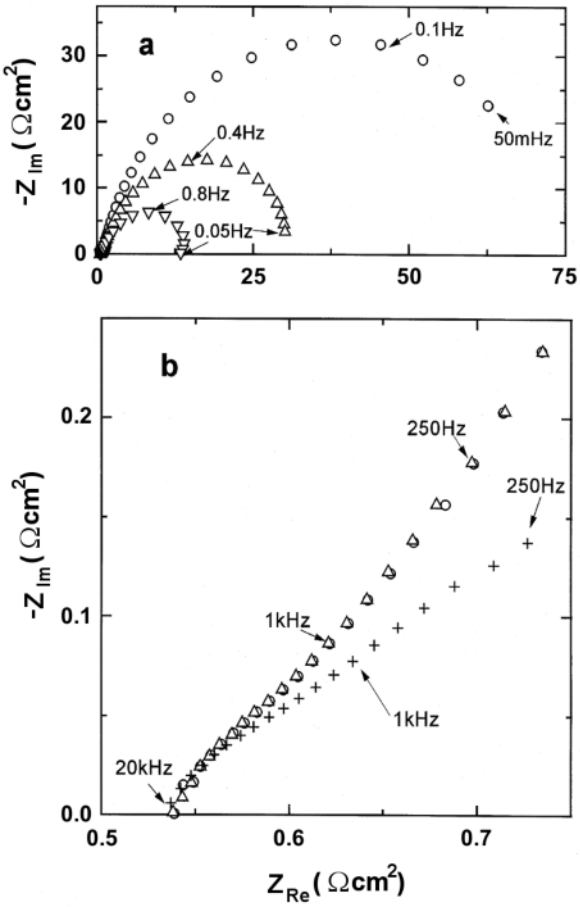

Figure 6.1. Impedance spectra at several electrode potentials for H_2/O_2 PEFCs with 30 wt% Pt/C, 0.4 mg Pt/cm^2 and 0.7 mg Nafion®/cm^2 electrodes, Nafion® 117 membrane at T = 25°C and atmospheric gas pressure: *a* full range of frequency (0.05 Hz to 10 kHz); *b* details of the high-frequency region (○) 0.925 V, (Δ) 0.9 V, (∇) 0.875 V, and (+) 0.65 V [4]. (Reprinted from Electrochimica Acta, 43(24), Paganin VA, Oliveira CLF, Ticianelli EA, Springer TE, Gonzalez ER. Modelistic interpretation of the impedance response of a polymer electrolyte fuel cell, 3761–6, ©1998, with permission from Elsevier and the authors.)

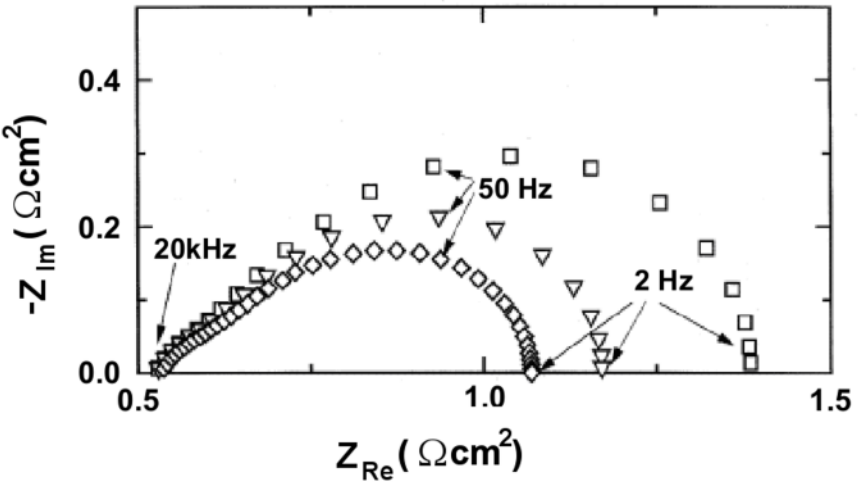

Figure 6.2. Impedance spectra at different potentials: (□) 0.75 V, (∇) 0.7 V, and (◊) 0.65 V for H_2/O_2 PEFCs with 30 wt% Pt/C, 0.4 mg Pt/cm^2 and 0.7 mg Nafion®/cm^2 electrodes, Nafion® 117 membrane at T = 25ºC and atmospheric gas pressure [4]. (Reprinted from Electrochimica Acta, 43(24), Paganin VA, Oliveira CLF, Ticianelli EA, Springer TE, Gonzalez ER. Modelistic interpretation of the impedance response of a polymer electrolyte fuel cell, 3761–6, ©1998, with permission from Elsevier and the authors.)

As can be seen in these figures, the low-frequency arc, which is dependent on electrode potential, is the well-known kinetic arc. But close examination of the high-frequency region (1–20 kHz) in the AC spectra reveals a certain distortion of the kinetic arc from a perfect semicircle, which is the result of superimposition of a small potential-independent impedance branch on the kinetic arc. This behaviour was observed for all types of membranes, experimental conditions, and electrodes employed in Paganin et al.'s [4] work.

According to theoretical models, the potential-dependent arc is related to the charge-transfer resistance (R_p) of the fuel cell reactions and the double-layer capacitance of the electrodes. Since the hydrogen oxidation reaction (HOR) is significantly faster than the ORR (the exchange current of the HOR is 3–4 orders of magnitude greater than that of the ORR), the charge-transfer resistance of the HOR is significantly smaller and can be ignored. Therefore, the charge-transfer resistance measured from AC impedance is mainly that of the ORR. At low overpotentials, the rate-determining step of the fuel cell reaction is the ORR, and the radius of the impedance arc is determined by the charge-transfer resistance. The superimposed 45°-like branch at the high-frequency region reflects coupling of the distributed ionic resistance and distributed capacitance in the catalyst layer, and is developed from protonic conductivity limitation within the catalyst layer, as discussed in Section 5.2.1.2.

Figure 6.3 shows the impedance spectra with catalyst loading of 0.4 and 0.1 mg Pt/cm^2 at different potentials. As can be clearly seen there, the potential-independent branch, which indicates the presence of the distributed resistance inside the catalyst layer of the electrode, is much less prominent for the electrode

with the lower Pt loading of 0.1 mg Pt/cm^2. This can be explained in terms of the thickness of the catalyst layer. In the case of the higher Pt loading of 0.4 mg Pt/cm^2, the catalyst layer is much thicker, which introduces a longer path for the migration of ions, with the result that the distributed resistance effect increases [4].

In Figure 6.3, the diameter of the low-frequency arc with Pt loading of 0.4 mg Pt/cm^2 is much smaller than that for 0.1 mg Pt/cm^2, which represents a smaller charge-transfer resistance with higher catalyst loading. This implies that at higher catalyst loading the electrode has more electrochemical surface area available. As the catalyst layer gets thinner, the spectrum develops much larger arcs as the amount of available electrochemical surface area decreases.

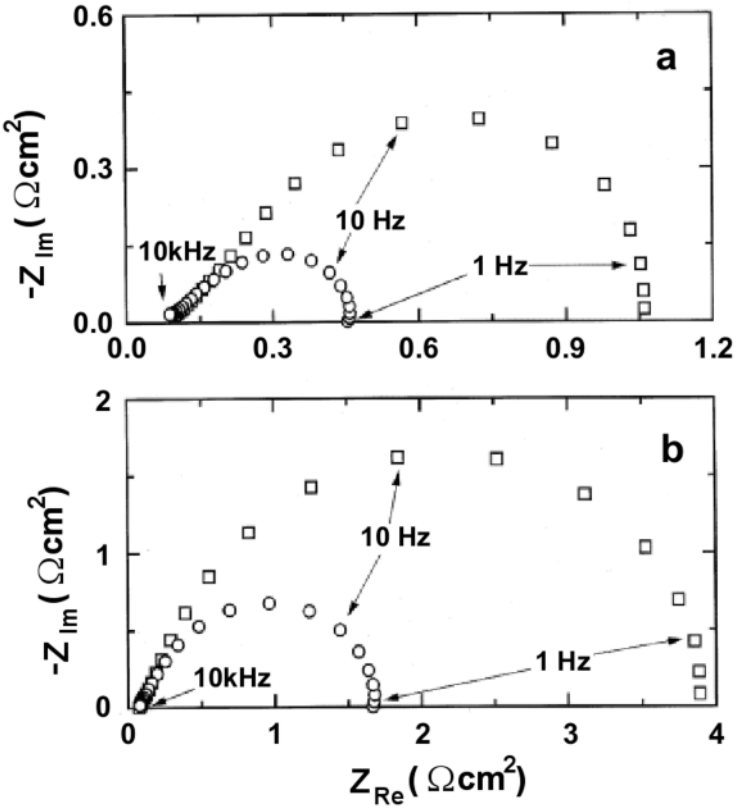

Figure 6.3. Impedance spectra at different potentials: (□) 0.85 V and (○) 0.8 V for H_2/air PEFCs with Nafion® 112 membrane at P_{air} / P_{H_2} = 5/3 atm, T_{cell} = 80°C, T_{air} = 85°C, T_{H_2} = 105°C. The electrodes have 20 wt% Pt/C: *a* 0.4 mg Pt/cm^2 and 1.1 mg Nafion®/cm^2; *b* 0.1 mg Pt/cm^2 and 0.28 mg Nafion®/cm^2 [4]. (Reprinted from Electrochimica Acta, 43(24), Paganin VA, Oliveira CLF, Ticianelli EA, Springer TE, Gonzalez ER. Modelistic interpretation of the impedance response of a polymer electrolyte fuel cell, 3761–6, ©1998, with permission from Elsevier and the authors.)

6.1.1.2 Effects of PTFE Content in the Gas Diffusion Layer

Using both polarization curves and AC impedance methods, Song et al. [5] studied the effect of PTFE content in Teflon®-bonded electrodes on the performance of PEMFCs. PTFE content was optimized based on information gathered using both methods. The fuel cell was operated in a H_2/O_2 gas feed mode with a gas supply pressure of 1 atm at both sides. The electrochemical impedance spectra were measured using a frequency response detector (EG&G Model 1025) and potentiostat/galvanostat (EG&G Model 263A). The frequency range was from 1 mHz to 10 kHz, and the amplitude of the sinusoidal perturbation was within 10 mV.

Figure 6.4 shows the polarization curves of fuel cells with different PTFE content in the gas diffusion layer of the gas diffusion electrodes. The optimal PTFE content in the gas diffusion layer is 30 wt%. The performance of the fuel cell containing a gas diffusion layer with PTFE content of 40 wt% is similar to one with 10 wt% PTFE content.

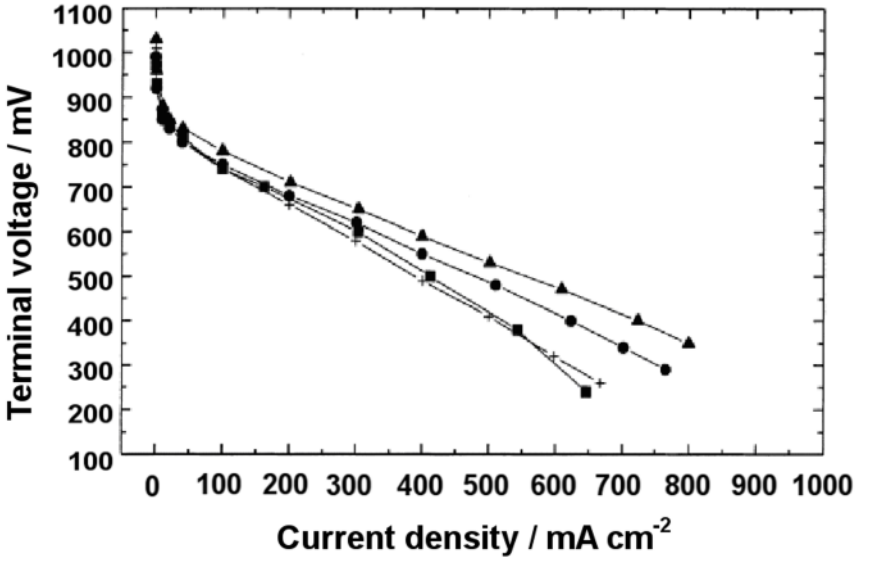

Figure 6.4. The polarization curves of fuel cells with electrodes that contain various PTFE content in the gas diffusion layer: (■) 10; (●) 20; (▲) 30; (+) 40 wt% [5]. (Reprinted from Journal of Power Sources, 94(1), Song JM, Cha SY, Lee WM. Optimal composition of polymer electrolyte fuel cell electrodes determined by the AC impedance method, 78–84, ©2001, with permission from Elsevier and the authors.)

Figure 6.5 shows the AC impedance spectra of the same fuel cells measured at different cathodic potentials. It is evident that as the overpotential increases, the diameter of the kinetic arc decreases due to the increasing kinetic rate. At low overpotential, the kinetics dominates and only the kinetic arc appears. At high overpotentials, the low-frequency region shows additional arcs, which are associated with mass-transport limitations across the gas diffusion layer and within the catalyst layer.

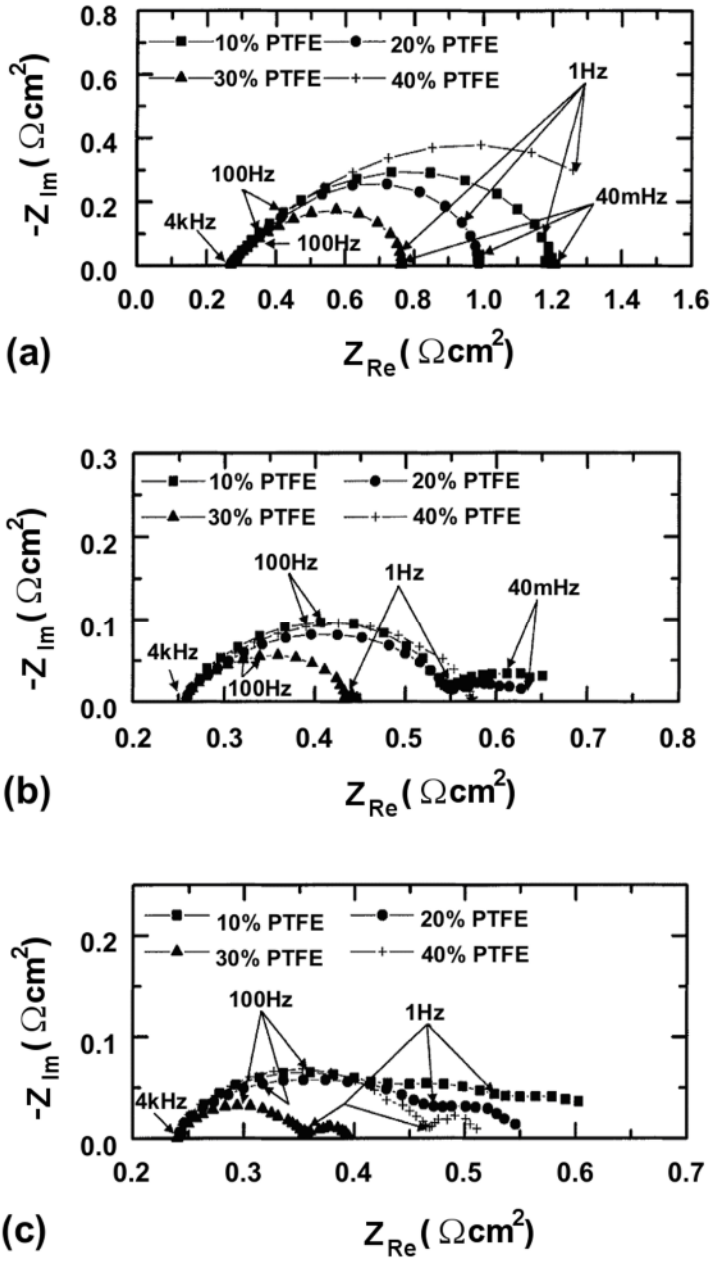

Figure 6.5. Impedance spectra for the oxygen reduction reaction at three different electrode potentials: *a* 0.8 V; *b* 0.7 V; *c* 0.6 V. The microporous layer (loading: 3.5 mg/cm^2) of the electrode has varying PTFE content: (■) 10; (●) 20; (▲) 30; (+) 40 wt% [5]. (Reprinted from Journal of Power Sources, 94(1), Song JM, Cha SY, Lee WM. Optimal composition of polymer electrolyte fuel cell electrodes determined by the AC impedance method, 78–84, ©2001, with permission from Elsevier and the authors.)

In Figure 6.5*a* it can be seen that the kinetic arc for the electrode with 30 wt% PTFE content in the gas diffusion layer has the smallest diameter. Indeed, the spectra for this electrode all have the minimum kinetic loop measured at all three cathode potentials, as seen in Figure 6.5*b* and *c*. This result is in agreement with that from the polarization curve measurements; however, AC impedance spectra provide more information than polarization curves. This figure shows that the impedance arc due to mass transport in the low-frequency region grows with increasing electrode overpotential and is very sensitive to PTFE content in the gas diffusion layer.

Song et al. [5] explained that for the electrode with 40 wt% PTFE content in the gas diffusion layer, the increase in the size of the kinetic arc was attributable to the substantial decrease in the active Pt area caused by low water content at the interface of the catalyst layer and the gas diffusion layer. This explanation has been verified by cyclic voltammetric results. A possible solution to improve the performance of this particular electrode is simply to raise the humidification temperature in order to increase the water content at the interface. The results at higher humidification temperatures are shown in Figures 6.6 and 6.7.

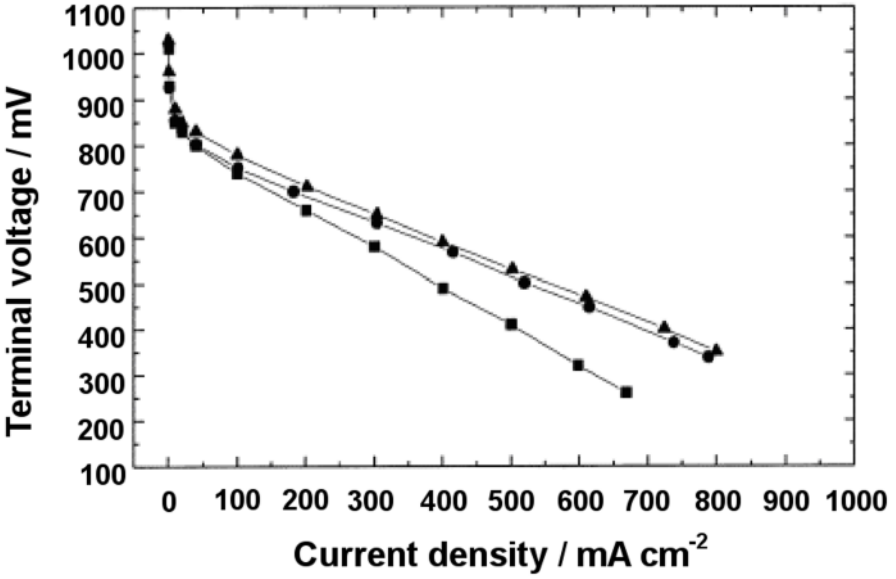

Figure 6.6. Polarization curves of fuel cells with electrodes containing 40 wt% PTFE in the gas diffusion layer. The temperature of the humidifier on the cathode side was maintained at: (■) 65°C and (●) 80°C. For comparison, the polarization curve of the fuel cell with the electrode containing 30 wt% PTFE in the gas diffusion layer is shown at the cathode humidification temperature of 65°C (▲) [5]. (Reprinted from Journal of Power Sources, 94(1), Song JM, Cha SY, Lee WM. Optimal composition of polymer electrolyte fuel cell electrodes determined by the AC impedance method, 78–84, ©2001, with permission from Elsevier and the authors.)

Figure 6.6 proves that increasing the humidification temperature does improve fuel cell performance. Figure 6.7 also confirms that the size of the kinetic arc does decrease with increasing humidification temperature. From these results the authors concluded that it was the reduced water content at the interface that caused the increased charge-transfer resistance of the electrode with excessive PTFE content (40 wt%).

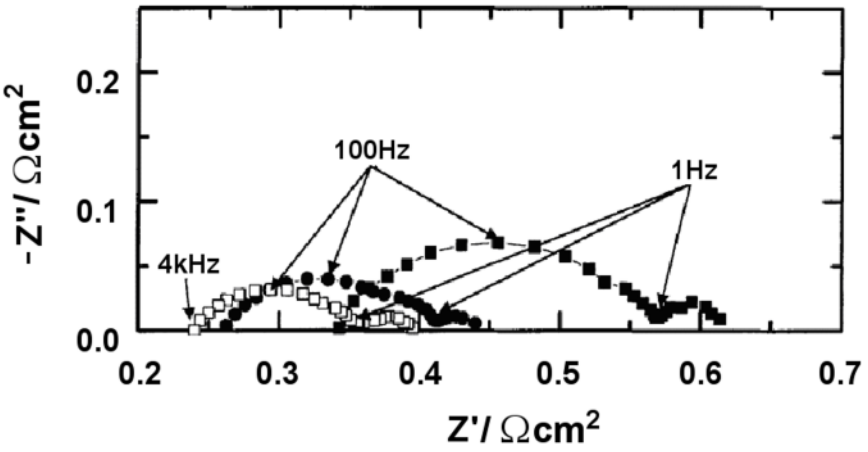

Figure 6.7. Impedance spectra for the oxygen reduction reaction at a cathode potential of 0.6 V. The microporous layer (loading: 3.5 mg/cm^2) of the electrode contained 40 wt% PTFE. The temperature of the humidifier on the cathode side was maintained at: (■) 65°C and (●) 80°C. For comparison, the spectra of the electrode with the microporous layer containing 30 wt% PTFE is shown at the cathode humidification temperature of 65°C (□) [5]. (Reprinted from Journal of Power Sources, 94(1), Song JM, Cha SY, Lee WM. Optimal composition of polymer electrolyte fuel cell electrodes determined by the AC impedance method, 78–84, ©2001, with permission from Elsevier and the authors.)

6.1.1.3 Effects of Nafion® Content

Nafion® content in the catalyst layer plays an important role in electrode performance. Incorporation of Nafion® ionomer into carbon-supported catalyst particles to form the catalyst layer for the gas diffusion electrode can establish a three-dimensional reaction zone, which has been proven by cyclic voltammetric measurements. An optimal Nafion® content in the catalyst layer of the electrode may minimize the performance loss that arises from ohmic resistance and mass transport limitations of the electrode [6].

In Song et al.'s same work [5], the effect that Nafion® content in the catalyst layer had upon electrode performance was also investigated, following their work on the optimization of PTFE content in the gas diffusion layer. The optimization of Nafion® content was done by comparing the performance of electrodes with different Nafion® content in the catalyst layer while keeping other parameters of the electrode at their optimal values. Figures 6.8 and 6.9 show the polarization curves and impedance spectra of fuel cells with electrodes made of catalyst layers containing various amounts of Nafion®.

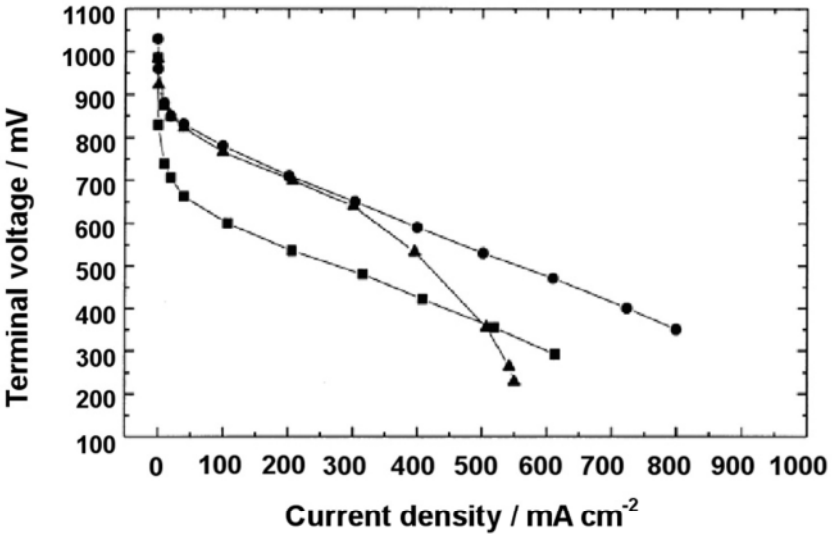

Figure 6.8. Polarization curves of fuel cells with electrodes made of catalyst layers containing various amounts of Nafion®: (■) 0.2; (●) 0.8; (▲) 2.0 mg/cm^2 [5]. (Reprinted from Journal of Power Sources, 94(1), Song JM, Cha SY, Lee WM. Optimal composition of polymer electrolyte fuel cell electrodes determined by the AC impedance method, 78–84, ©2001, with permission from Elsevier and the authors.)

As seen in Figure 6.8, the fuel cell with 0.8 mg/cm^2 Nafion® content in the catalyst layer exhibited the best performance. To the researchers' surprise, the performance of the fuel cell with 2.0 mg/cm^2 Nafion® content dropped sharply when the current was over 300 mA/cm^2. The linear zone of the V–I curve with 2.0 mg/cm^2 Nafion® content is much shorter than that for the other two cases. This certainly would contribute to mass transport limitations within the catalyst layer under high ionomer loading.

As shown in Figure 6.9, the impedance spectra of the fuel cell with 0.8 mg/cm^2 Nafion® content in the catalyst layer have the smallest charge-transfer resistance, which is in agreement with the polarization curve. Among the three fuel cells measured, the fuel cell with the Nafion® content of 2.0 mg/cm^2 displays, in addition to the kinetic arc, another arc in the low-frequency region, which is related to the sharp drop in performance shown in the polarization curve in Figure 6.8. This confirms that high Nafion® content in the catalyst layer retards oxygen transport when the current density is high. Song et al. [5] attribute the mass transport limitation to the increase in the distance across which the gas has to permeate, diffuse, or migrate to the catalyst surface.

The function of a proton-conducting ionomer such as Nafion® in the catalyst layer is to provide an ionic path for proton migration from the membrane to the reaction site at the catalyst surface. Therefore, the content of the proton-conducting ionomer in the catalyst layer will greatly influence the transport of protons to the catalyst sites. The impedance spectra of fuel cells with different Nafion® loadings in the catalyst layers of both the cathode and the anode at OCV were compared by

Guo et al. [7], as shown by the Nyquist plots in Figure 6.10. In their impedance measurements, different amounts of Nafion® ionomer in the catalyst layer, ranging from 0.33 to 1.13 mg/cm^2 (dry weight) were examined. The active area of their fuel cells was 1.0 cm^2. The fuel cells were operated in H_2/air gas feeding mode with a flow rate of 220 cm^3/min (at standard temperature and pressure) for both sides. The cell temperature as well as the humidification temperature for both electrodes were controlled at 70°C. The cell's AC impedance was measured using a Gamry PC4/750-DHC2 potentiostat. The perturbation amplitude was set at 5 mV in potentiostatic mode, and the frequency was scanned from 0.01 Hz to 100 kHz with 10 points per decade.

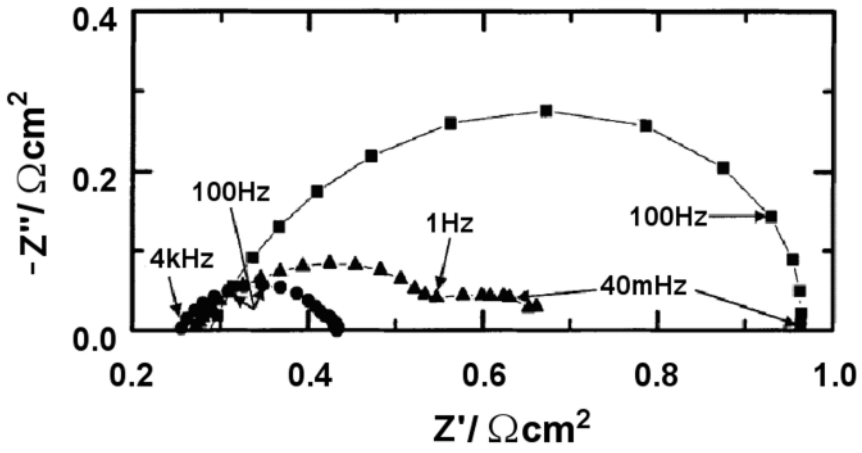

Figure 6.9. Impedance spectra for the oxygen reduction reaction at an electrode potential of 0.6 V. The catalyst layer of the electrode contains various Nafion® loadings: (■) 0.2; (●) 0.8; (▲) 2.0 mg/cm^2 [5]. (Reprinted from Journal of Power Sources, 94(1), Song JM, Cha SY, Lee WM. Optimal composition of polymer electrolyte fuel cell electrodes determined by the AC impedance method, 78–84, ©2001, with permission from Elsevier and the authors.)

As shown in Figure 6.10, each of the curves has the semicircular shape, known as the kinetic loop, associated with the charge-transfer resistance. The fuel cell with 0.33 mg/cm^2 Nafion® loading in the catalyst layer exhibits the largest kinetic impedance loop, which indicates that insufficient Nafion® can result in a less active catalyst layer. It is also notable that excessive Nafion® will also reduce catalyst layer activity. Among the different Nafion® loadings studied, 0.77 mg/cm^2 in the catalyst layer gives the best fuel cell performance, according to the impedance spectra in Figure 6.10.

Antolini et al. [6] have provided empirical equations to calculate the optimal Nafion® loading in the catalyst layer as a function of electrode structure. In the case of a catalyst layer containing Pt/C and Nafion® ionomer, the optimal Nafion® load (in mg/cm^2) is expressed as

$$Nafion \cong 56\frac{L_{Pt}}{P_{Pt}} \tag{6.1}$$

where L_{Pt} is the Pt loading (mg Pt/cm^2) and P_{Pt} is the Pt weight percentage in the carbon-supported Pt catalyst. In the case of electrodes with dual catalyst layers, the presence of PTFE in one of the catalyst layers should be taken into account, and the optimal Nafion® loading then becomes

$$Nafion \cong 56\frac{L_{Pt}}{P_{Pt}}(1 - X_{PTFE}) \tag{6.2}$$

where X_{PTFE} is the PTFE weight fraction in the PTFE catalyst layer.

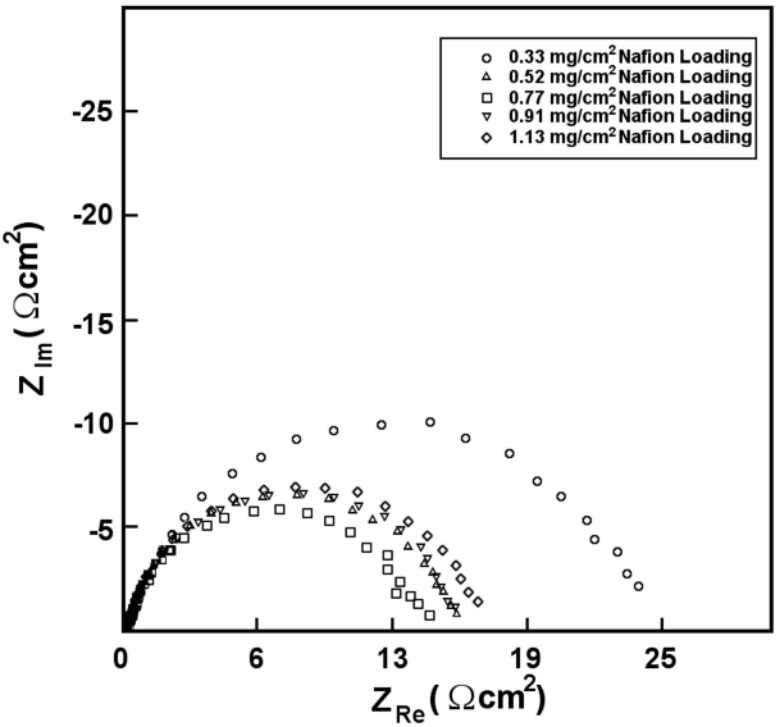

Figure 6.10. Comparison of Nyquist plots of fuel cells with different Nafion® loadings in the catalyst layers of both the cathode and the anode [7]. (Reproduced by permission of ECS—The Electrochemical Society, from Guo Q, Cayetano M, Tsou Y, De-Castro ES, White RE. Study of ionic conductivity profiles of the air cathode of a PEMFC by AC impedance spectroscopy.)

Not only will the loading of the proton-conducting ionomer affect MEA performance, but so will the type of proton-conducting ionomer and the way it is incorporated into the catalyst layer. Ahn et al. [8] developed some new electrodes

for PEMFCs by optimizing the electrode composition to improve the fuel cells' performance without external humidification. A proton-conducting ionomer with low equivalent weight (EW 1000) was used in the electrode to enhance the proton conductivity and thus reduce the ohmic resistance under conditions of insufficient humidification. The results of their impedance measurements are shown in Figure 6.11. In this figure, the legend detail "ic11sc10 MEA" refers to the MEA containing the proton-conducting ionomer of EW 1100 blended in the catalyst layer and the proton-conducting ionomer of EW1000 sprayed on the surface of the catalyst layer, whereas the conventional MEA used the proton-conducting ionomer of EW1100 for the proton-conducting ionomer spray coating on the surface of the catalyst layer. The impedance spectra indicated that the MEA with the EW 1000 proton-conducting ionomer has a much lower (less than half) electrolyte and charge-transfer resistance than the MEA with the EW 1100 proton-conducting ionomer. The authors attributed this phenomenon to the higher ionic conductivity of the EW 1000 proton-conducting ionomer that was sprayed on the catalyst surface. The low electrolyte and charge-transfer resistance of the MEA, along with the EW 1000 proton-conducting ionomer were considered the main factors responsible for this MEA's superior performance.

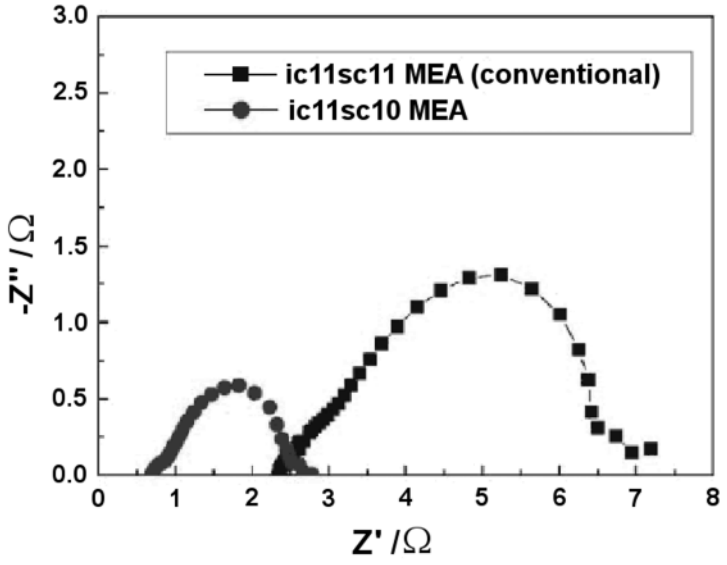

Figure 6.11. Nyquist plots for MEAs containing different proton-conducting ionomers at 0.85 V without external humidification; catalyst loading = 0.4, 0.7 mg Pt/cm^2 for anode and cathode, respectively; T_{cell} = 25°C; Pressure = 1 atm; and H_2/O_2 flow = 400 cm^3/min [8]. (Reprinted from Electrochimica Acta, 50(2–3), Ahn SY, Lee YC, Ha HY, Hong SA, Oh IH. Effect of the ionomers in the electrode on the performance of PEMFC under non-humidifying conditions, 673–6, ©2004, with permission from Elsevier.)

In conclusion, it is possible to achieve high performance with PEMFCs under dry or low-humidity conditions by employing low equivalent weight proton-conducting ionomers in the catalyst layer.

6.1.1.4 Effects of Membrane Thickness

Using the electrochemical impedance method, Freire et al. [9] studied the effect of Nafion® membranes with different thicknesses under different operating conditions. Their fuel cells had an active area of 1 cm^2 and were operated with H_2/O_2 at atmospheric pressure. Four different Nafion® membranes, 117, 115, 1135, and 112, with average thicknesses of 175, 125, 80, and 50 μm, respectively, were used in their study. The impedance measurements were carried out using a Solartron 1250 frequency analyzer with a Solartron 1286 electrochemical interface in the potentiostatic mode. The input signal had an amplitude of 10 mV.

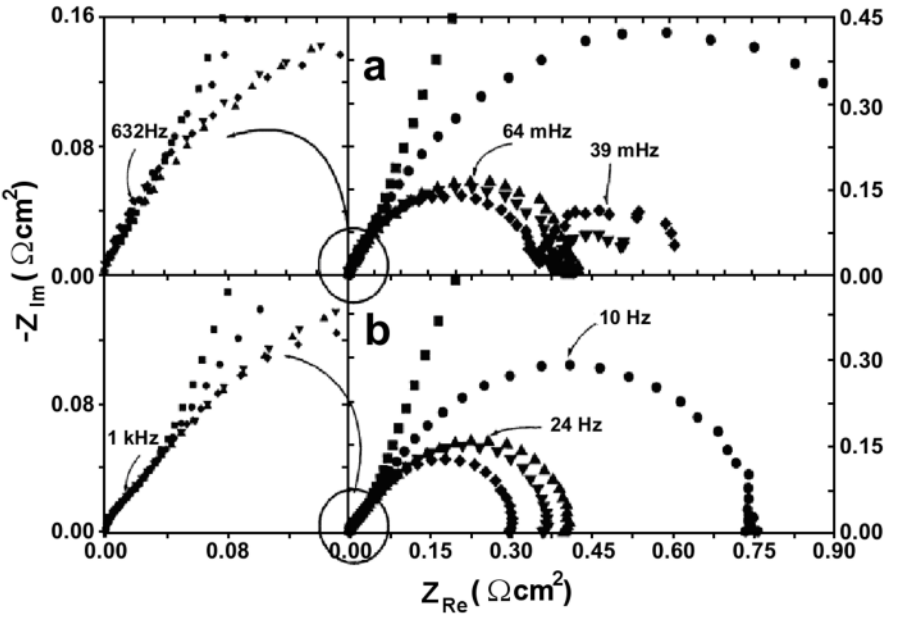

Figure 6.12. Impedance plots for single cells at ambient temperature. *a* Nafion® 117. Cell potential and ohmic drop corrected cell potential (in parentheses): (■) 0.9 V (0.9 V), (●) 0.8 V (0.81 V), (▲) 0.70 V (0.76 V), (▼) 0.6 V (0.74 V), (♦) 0.5 V (0.74 V). *b* Nafion® 112. Cell potential and ohmic drop corrected cell potential (in parentheses): (■) 0.9 V (0.9 V), (●) 0.8 V (0.81 V), (▲) 0.70 V (0.73 V), (▼) 0.6 V (0.67 V), (♦) 0.5 V (0.61 V). Plots were corrected for the high-frequency resistances. Left quadrants: details of the high-frequency regions [9]. (Reprinted from Journal of Electroanalytical Chemistry, 503, Freire TJP, Gonzalez ER. Effect of membrane characteristics and humidification conditions on the impedance response of polymer electrolyte fuel cells, 57–68, ©2001, with permission from Elsevier and the authors.)

The Nyquist impedance plots for the cells with Nafion®117 and Nafion®112 at room temperature with fully humidified reactant gases were shown in Figure 5.32

of Chapter 5, which for ease of discussion is repeated here as Figure 6.12. The plots were corrected for the ohmic drop in the cell using high-frequency resistance. At the high end of the frequency range, the impedance spectra appearing as a 45° branch are independent of the electrode potential. This characteristic has been discussed in detail in the previous sections. What interests us here is the appearance of the new impedance arc at the low end of the frequency range, starting at 0.7 V and increasing in size as the electrode potential becomes lower. Freire et al. ascribed this low-frequency impedance arc to the ineffective mass transport of reactant gases to the catalyst surface, due to flooding of the cathode by the product water.

Therefore, analysis of the full impedance spectra includes: (1) the high-frequency branch, which is independent of electrode potential and is due to the distributed

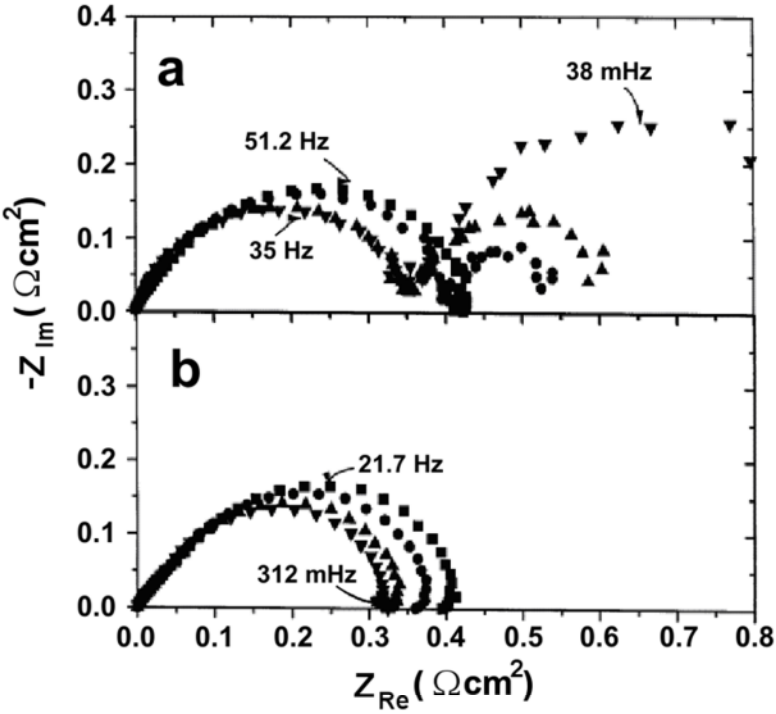

Figure 6.13. Impedance plots for single cells at 80°C with the reactant gases humidified at 95°C for hydrogen and 85°C for oxygen. *a* Nafion®117 membrane. Cell potential and ohmic drop corrected cell potential (in parentheses): (■) 0.70 V (0.75 V), (●) 0.60 V (0.74 V), (▲) 0.50 V (0.73 V), (▼) 0.40 V (0.72 V). *b* Nafion®112 membrane. Cell potential and ohmic drop corrected cell potential (in parentheses): (■) 0.60 V (0.67 V), (●) 0.50 V (0.63 V), (▲) 0.40 V (0.57 V), (▼) 0.30 V (0.50 V). Plots were corrected for the high-frequency resistances [9]. (Reprinted from Journal of Electroanalytical Chemistry, 503, Freire TJP, Gonzalez ER. Effect of membrane characteristics and humidification conditions on the impedance response of polymer electrolyte fuel cells, 57–68, ©2001, with permission from Elsevier and the authors.)

resistance of the electrolyte within the catalyst layer; (2) the kinetic arc in the middle, which is associated with the charge transfer process of the ORR; and (3) the low-frequency arc, which is caused by the mass transport constraint, usually related to flooding of the cathode by the product water.

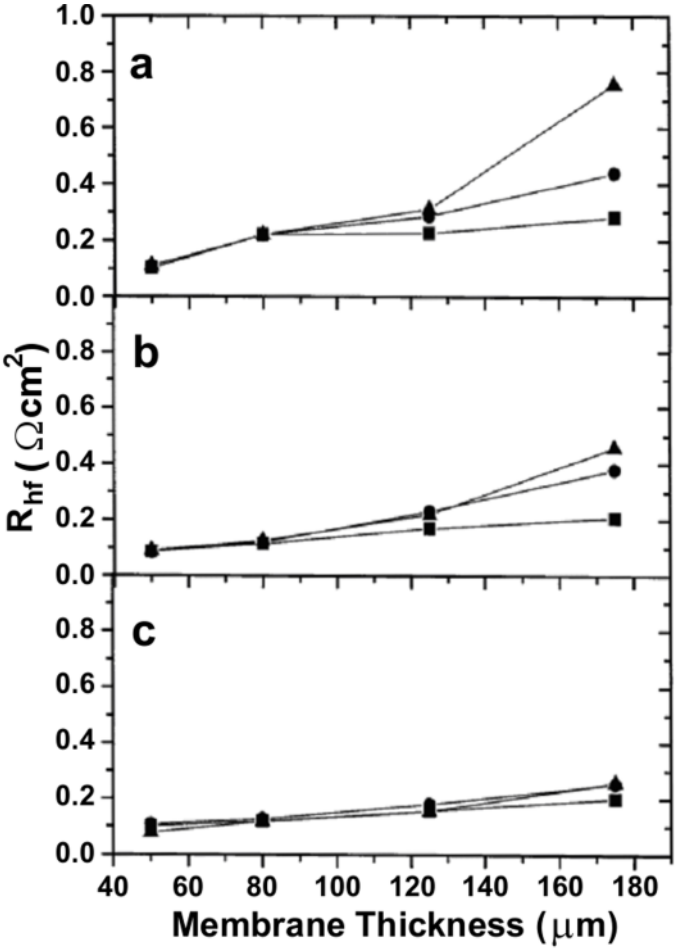

Figure 6.14. Dependence of the high-frequency resistance on membrane thickness at different current densities and: *a* 40°C: (■) 3, (●) 380, (▲) 784 mA/cm^2; *b* 60°C: (■) 54, (●) 706, (▲) 1123 mA/cm^2; and *c* 80°C: (■) 81, (●) 750, (▲) 1500 mA/cm^2 [9]. (Reprinted from Journal of Electroanalytical Chemistry, 503, Freire TJP, Gonzalez ER. Effect of membrane characteristics and humidification conditions on the impedance response of polymer electrolyte fuel cells, 57–68, ©2001, with permission from Elsevier and the authors.)

The Nyquist plots of the impedance spectra for the cell with Nafion® 112 membrane are depicted in Figure 6.12*b*. It is evident that in this case the low-frequency arcs at low electrode potentials disappeared. Freire et al. attributed this

phenomenon to the use of the thinner membrane, which provides better back-diffusion of water to the anode side to reduce product water accumulation at the cathode. This phenomenon also appears at other fuel cell operating conditions. Figure 6.13 shows the impedance plots measured for the single fuel cells at 80°C with the reactant gases humidified at 95°C for hydrogen and 85°C for oxygen. The cells with Nafion® 117 membrane have low-frequency arcs, whereas the cells with Nafion® 112 membrane do not. This is further confirmation that the thicker membrane tends to give rise to cathode flooding by product water due to its ineffective back-diffusion of water, whereas the thinner membrane provides better water management and therefore reduces cathode flooding.

By using the impedance method, Freire et al. also demonstrated that thinner membranes not only show better performance but also are much less sensitive to humidification conditions, cell temperature, and current density. The dependence of the real resistance at high-frequency intercepts on membrane thickness at different current densities is illustrated in Figure 6.14. Linear dependence of the high-frequency resistance, R_{hf}, on the membrane thickness was observed at 80°C, whereas non-linear dependence of R_{hf} on membrane thickness was shown at 40°C and 60°C. They explained that this was due to better hydration of the membrane at higher temperatures. It is also observable that R_{hf} almost does not depend on current density at 80°C and at low current densities; rather, R_{hf} dependence on membrane thickness is almost linear, which indicates that for thicker membranes at high current densities it no longer behaves as a pure resistor due to a capacitive effect caused by less effective back transport of water [9].

6.1.1.5 Effects of the Gas Diffusion Layer (GDL) Structure

It is recognized that GDL structure is very critical to the mass-transport processes within the gas diffusion electrode. For example, by using impedance spectroscopy, Springer et al. [10] proved that at low overpotential, at which the ORR kinetic limitation dominates the electrode process, the cathode performance is somewhat improved when double GDLs are used. At high overpotential, at which mass transfer is limiting the electrode process, the size of the impedance loop when using double GDLs is dramatically larger than when a single GDL is used. Many studies [11–14] have demonstrated the importance of GDL morphology. AC impedance has also indicated that performance loss due to mass transport limitation can be reduced by enlarging the macro volume in the gas diffusion layer. Kong et al. [15] made an effort to understand the influence of GDL pore-size distribution on mass transport. Their experimental results and interpretation of the relationship between GDL pore structure and cell performance are summarized in the remainder of this section.

For the purpose of examining the influence of GDL pore-size distribution on cell performance, a pore-forming step using a pore-former was introduced in the GDL fabrication process. This approach is similar to that of Fisher et al. [16], who improved cell performance by introducing pore-former to the catalyst layer. The effect of the pore-former on mass transport limitation, resulting from the nitrogen gas in air, is attributed to the increased porosity of the catalyst layer. The influence on cell performance of pore-former content in the GDL is shown in Figure 6.15, based on the work of Kong et al. The pore-former content does have a significant

influence on mass transfer, as seen in the high current density region of the curves, and a pore-former loading of 7 mg/cm^2 had the best performance. The results suggested that an optimum amount of pore-former or an appropriate macropore volume of the diffusion layer exists. They explained: (1) decreasing the pore size and porosity increases the overpotential resulting from the mass transport limitation because small pores will be filled with liquid water earlier than large pores, due to water condensation; (2) since macropores produced by the pore-former can provide gas diffusion paths towards the catalytic region, they are capable of reducing the mass transport limitation caused by water flooding; (3) if the macropore volume is too large, the electronic conductivity of the electrode is decreased. Therefore, the optimum pore-former content can be attributed to the effect of the GDL microstructure, where macropores and micropores co-exist in an appropriate ratio.

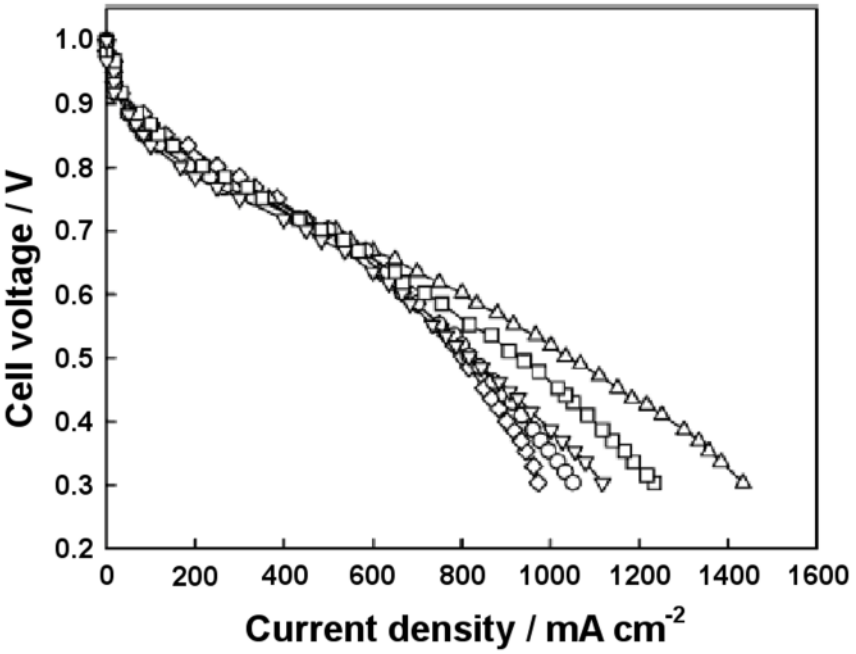

Figure 6.15. Influence of GDL pore-former content on cell performance of a H_2/O_2 single cell: (◊) 0 mg/cm^2, (○) 3 mg/cm^2, (□) 5 mg/cm^2, (Δ) 7 mg/cm^2, and (∇) 10 mg/cm^2 pore-former loading; 5 mg/cm^2 carbon loading in the GDL; and 0.4 mg Pt/cm^2 in the catalyst layer [15]. (Reprinted from Journal of Power Sources, 108(1–2), Kong CS, Kim DY, Lee HK, Shul YG, Lee TH. Influence of pore-size distribution of diffusion layer on mass-transport problems of proton exchange membrane fuel cells, 185–91, ©2002, with permission from Elsevier and the authors.)

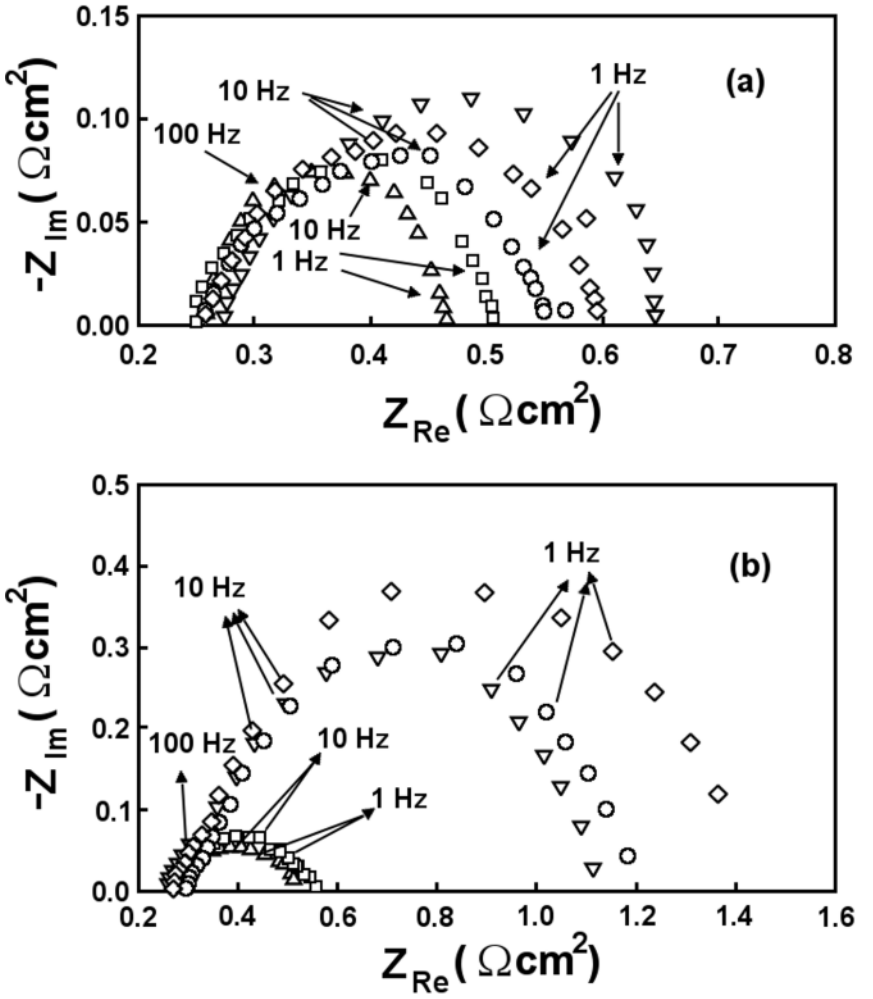

Figure 6.16. Impedance plots as a function of pore-former content in the GDL of a H_2/O_2 single cell at a voltage of *a* 0.7 V and *b* 0.4 V. (◊) 0 mg/cm^2, (○) 3 mg/cm^2, (□) 5 mg/cm^2, (Δ) 7 mg/cm^2, and (∇) 10 mg/cm^2 [15]. (Reprinted from Journal of Power Sources, 108(1–2), Kong CS, Kim DY, Lee HK, Shul YG, Lee TH. Influence of pore-size distribution of diffusion layer on mass-transport problems of proton exchange membrane fuel cells, 185–91, ©2002, with permission from Elsevier and the authors.)

Figure 6.16 shows Nyquist plots at 0.7 V and 0.4 V, which demonstrate the effect of pore-former content on cell performance. An important feature of the plot is the diameter of the semicircle, which corresponds to the polarization resistance R_p (a combination of charge-transfer resistance and diffusion resistance). At 0.7 V, the optimum pore-former loading of 7 mg/cm^2 is indicated by a minimum value of R_p, while excessive pore-former loading results in a larger polarization resistance. At 0.4 V, as the current density increases, the diffusion component becomes more

dominant than the charge transfer component and the magnitude of the impedance grows significantly due to the diffusion effect. The optimum pore-former loading (in this case, 5 mg/cm^2 and 7 mg/cm^2 are both effective) can inhibit the growth of the semicircle resulting from the increasing diffusion resistance. This is attributed to the macropores, which prevent water flooding of the electrodes and enhance the mass transport process within the GDL. Therefore, a GDL modified with a proper pore-former loading is effective for reducing polarization resistance (charge-transfer resistance and mass transfer resistance) at both low and high current density. The reduction of the polarization resistance that resulted from optimum pore-former loading can be clearly seen in Figure 6.17 (0 to 200 wt% of pore-former content corresponds to 0 to 10 mg/cm^2 pore-former loading) [15].

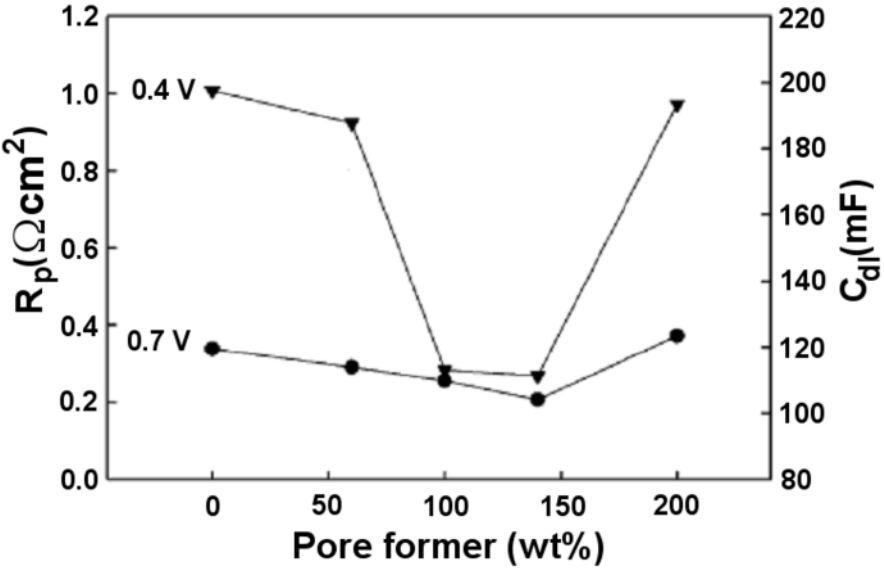

Figure 6.17. Dependence of polarization resistance, R_p, at (●) 0.7 V and (▼) 0.4 V on GDL pore-former content of a H_2/O_2 single cell [15]. (Reprinted from Journal of Power Sources, 108(1–2), Kong CS, Kim DY, Lee HK, Shul YG, Lee TH. Influence of pore-size distribution of diffusion layer on mass-transport problems of proton exchange membrane fuel cells, 185–91, ©2002, with permission from Elsevier and the authors.)

6.1.1.6 Effects of the Electrode Fabrication Method

Electrode preparation methods significantly affect fuel cell performance. A variety of methods have been developed. For example, Bevers et al. [17] produced electrodes using a simple and less costly procedure, a modified rolling technique, formerly used in the production of electrodes for alkaline fuel cells and batteries. With these new electrodes, the same power output was obtained as that using commercial ones.

In Abaoud et al.'s work [18], the details of using polyethylene oxide (PEO) as a suspension agent in the preparation of catalyst ink for PEMFC electrodes were

described for the first time. Two techniques, spraying and screen-printing, were used to prepare the porous carbon electrodes. The performance of the electrodes was evaluated in single cells (13.7 cm^2) with humidified hydrogen and non-humidified oxygen at 80°C, and the electrochemical properties were characterized by polarization and EIS. Figures 6.18 and 6.19 show the Nyquist plots of the electrodes, prepared by both techniques, at different potentials. In both cases, at higher frequencies there appear small incomplete semicircles, which are related to the MEA structure as discussed in Section 5.2.1.2. The semicircle at lower frequencies characterizes the kinetic resistance. It is observable that the impedance varies between 45 and 60 mΩ at 0.82 V and a frequency of 300 mHz. The impedances of the electrodes prepared by both spraying and screen-printing techniques were comparable with those of ETEK standard electrodes. The kinetic parameters of the electrodes indicated an improvement over the results from similar studies, proving that PEO performed better than other conventional suspension agents.

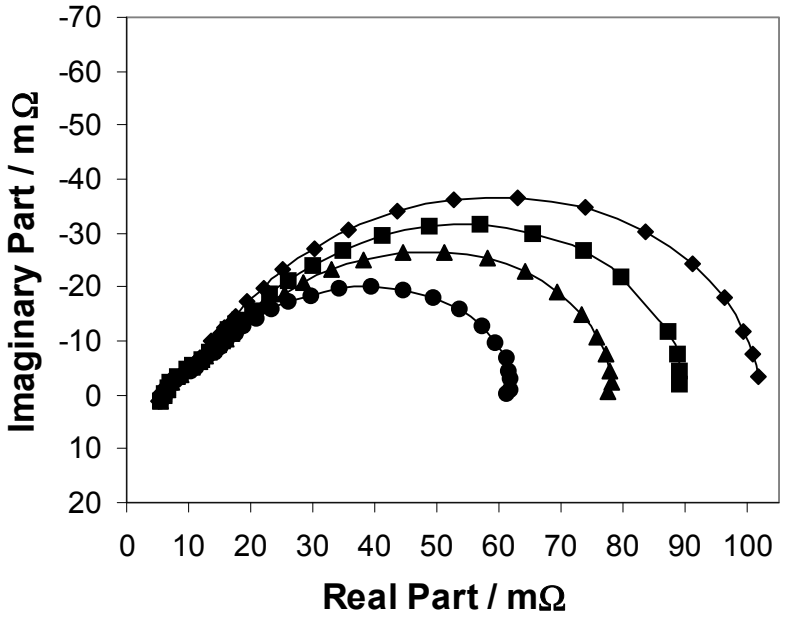

Figure 6.18. Nyquist plots of the sprayed electrode (0.1/0.1 mg $Ptcm^{-2}$) at different voltages [18]. (Reproduced from Abaoud HA, Ghouse M, Lovell KV, Al-Motairy GN, Alternative formulation for proton exchange membrane fuel cell (PEMFC) electrode preparation, Journal of New Materials for Electrochemical Systems 2003;6(3):149–55, with permission from JNMES.)

Wang et al. [19] developed a new method of electrode preparation with a novel silica gel additive (NSGA) instead of the traditional Nafion® polymer additive (TNPA) for PEMFCs. The performance of the two types of electrodes was compared using electrochemical impedance spectroscopy coupled with a polarization curve and constant-current discharge. Figure 6.20 shows the AC

impedance results. Measurement was carried out using a frequency response analyzer (EG&G Model 1025) and potentiostat/galvanostat (EG&G Model 263A) in a potentiostatic mode over the frequency range 10 mHz to 10 kHz. The fuel cell had an active area of 5 cm^2 and was operated in H_2/O_2 mode.

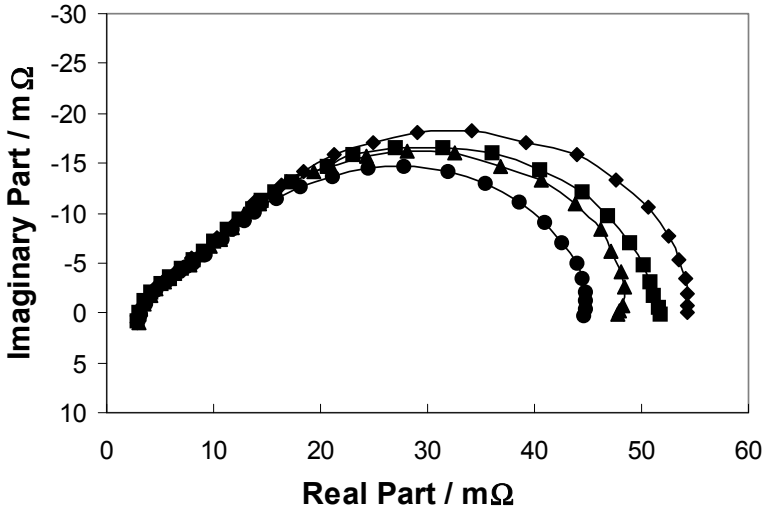

Figure 6.19. Nyquist plots of the screen-printed electrode (0.1/0.15 mg $Ptcm^{-2}$) at different cell voltages [18]. (Reproduced from Abaoud HA, Ghouse M, Lovell KV, Al-Motairy GN, Alternative formulation for proton exchange membrane fuel cell (PEMFC) electrode preparation, Journal of New Materials for Electrochemical Systems 2003;6(3):149–55, with permission from JNMES.)

Generally speaking, there is no significant difference between the SiO_2-gel electrode and the Nafion® latex electrode. At 0.85 V, where the electrode charge-transfer resistance is dominant, the R_{hf} of the TNPA electrode is a bit smaller than that of the NSGA electrode. This can be attributed to the higher conductivity of Nafion®. At 0.5 V, the low-frequency arcs of the NSGA and TNPA electrodes differ significantly due to the low porosity of the latter, a finding which has also been proven by other experiments. The lack of pores in the TNPA electrode explains why it develops a low-frequency arc. According to the above results, the cheaper SiO_2-gel additive can be a substitute for the Nafion® polymer solution in the preparation of electrodes.

The presence of a Pt thin film on the surface of the GDL leads to better performance [20]. Cha and Lee [21] prepared electrodes by direct sputtering of an ultrathin platinum layer onto Nafion®115 membrane. The Pt catalyst was deposited onto both sides of the membrane in several layers using a vacuum sputter. For comparison, electrodes were also fabricated by a conventional method. The AC impedance spectra of the cell (geometric area 1 cm^2) were measured using a potentiostat/galvanostat (EG&G PAR 263A) and a frequency-response detector (EG&G FRD 1025) over a range of frequencies from 10 kHz to 1 mHz at various cell potentials. The cell was operated on H_2 and O_2 feed gases.

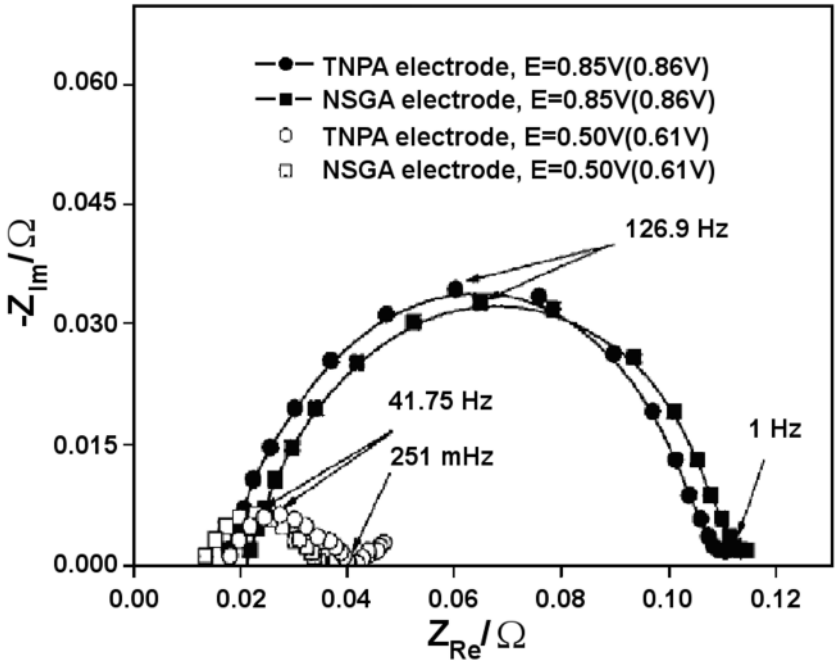

Figure 6.20. Nyquist plots for the electrodes fabricated according to the same preparation procedure [19]. Note: NSGA stands for novel silica gel additive, and TNPA stands for traditional Nafion® polymer additive. The values in parentheses are the ohmic drop corrected cell potential. (Reproduced from Wang C, Mao ZQ, Xu JM, Xie XF. Preparation of a novel silica gel for electrode additive of PEMFCs. Journal of New Materials for Electrochemical Systems 2003;6(2):65–9, with permission from JNMES.)

Figure 6.21 shows the AC impedance spectra for the cathodic ORR of the cell electrodes prepared using the conventional method and the sputtering method. It can be seen that the spectra of electrodes 2 and 3 do not indicate mass transport limitation at either potentials. For electrode 1, a low-frequency arc develops, due to polarization caused by water transport in the membrane. It is also observable that the high-frequency arc for the porous electrode is significantly depressed from the typical semicircular shape. Nevertheless, the real-axis component of the arc roughly represents the effective charge-transfer resistance, which is a function of both the real surface area of the electrode and the surface concentrations of the species involved in the electrode reaction.

The spectra of electrode 2 do not exhibit a large difference in the kinetic arc in comparison with those of electrode 1. This was confirmed by polarization curve, through examining the difference in kinetic overpotential between the two electrodes. Comparing Figure 6.21*b* with Figure 6.21*c*, one may conclude that sputtering at a catalyst loading rate of 50 Å is superior to that at a rate of 100 Å.

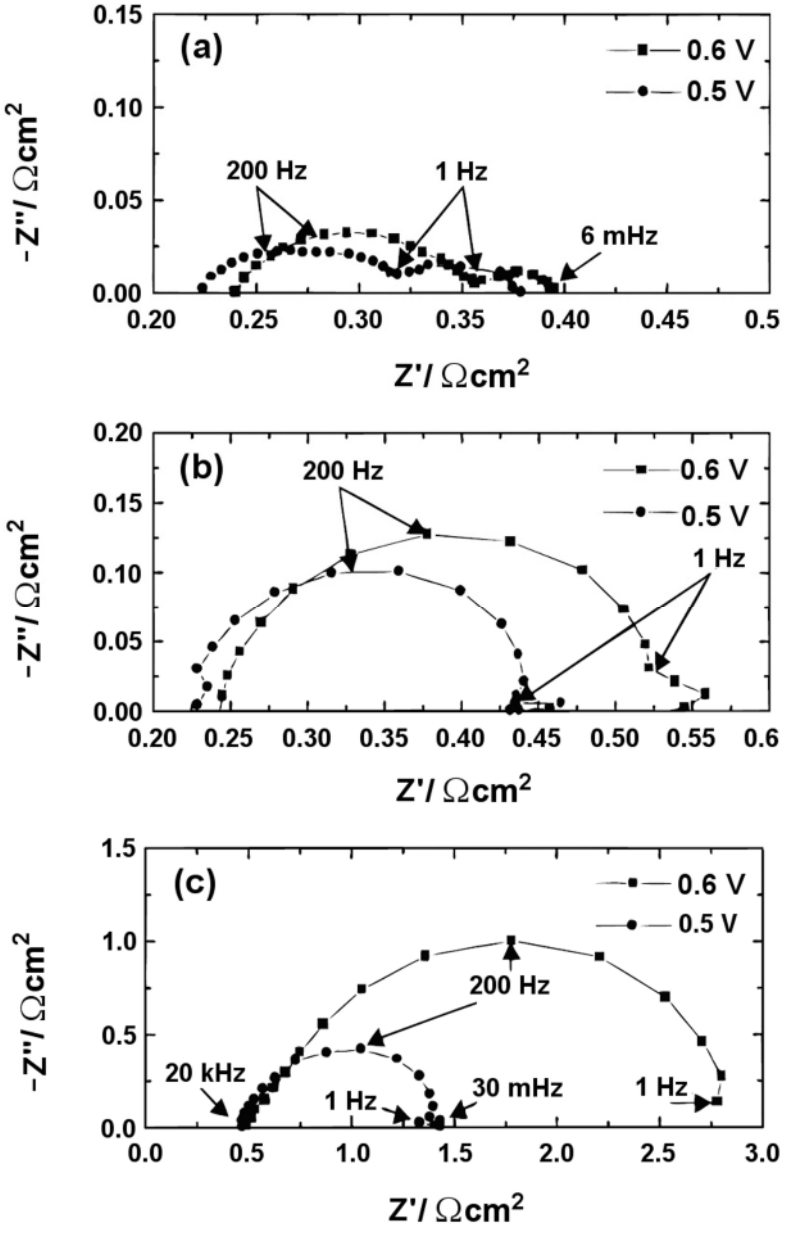

Figure 6.21. AC impedance spectra for the cathodic ORR of the cell incorporating electrodes prepared by *a* the conventional method (electrode 1), *b* the sputtering method with 50 Å rate (electrode 2), and *c* the sputtering method with 100 Å rate (electrode 3) [21]. (Reproduced by permission of ECS—The Electrochemical Society, from Cha SY, Lee WM. Performance of proton exchange membrane fuel cell electrodes prepared by direct deposition of ultrathin platinum on the membrane surface.)

6.1.1.7 Effects of the Composite Structure

Ahn et al. have developed fibre-based composite electrode structures suitable for oxygen reduction in fuel cell cathodes (containing high electrochemically active surface areas and high void volumes) [22]. The impedance data obtained at –450 mV (vs. SCE), in the linear region of the polarization curves, are shown in Figure 6.22. Ohmic, kinetic, and mass transfer resistances were determined by fitting the impedance spectra with an appropriate equivalent circuit model.

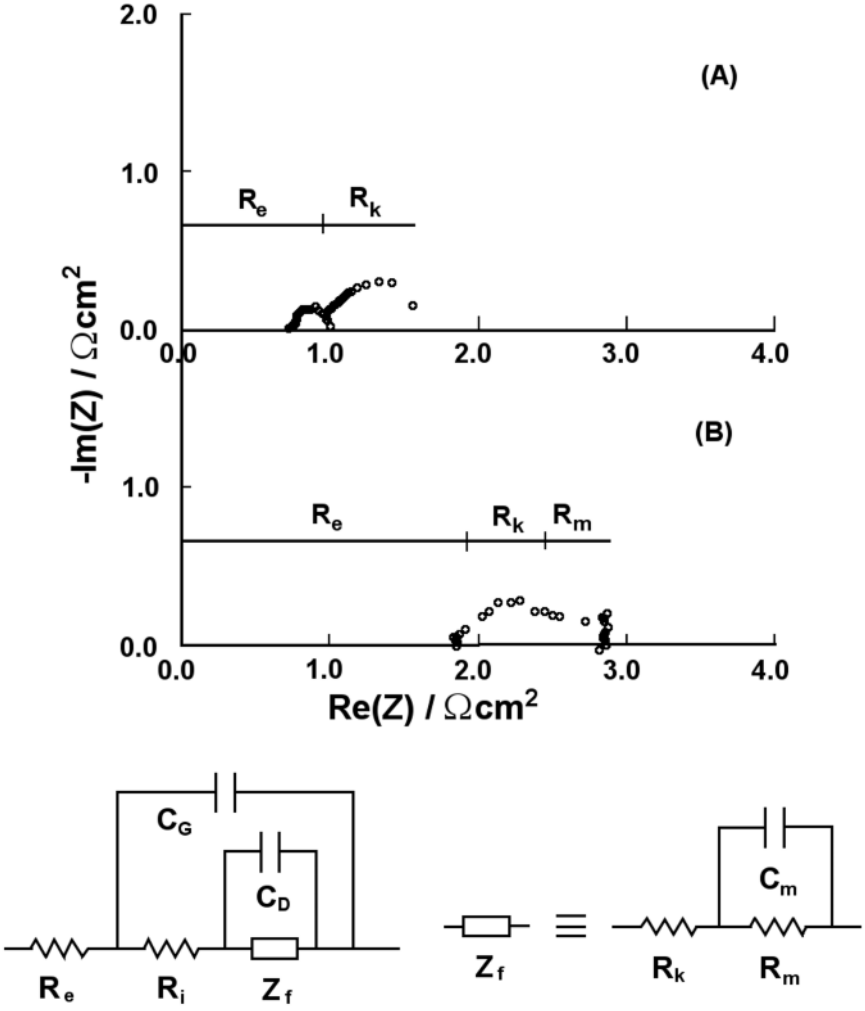

Figure 6.22. Nyquist plots for (A) a composite electrode at –450 mV vs. SCE and (B) a Prototech electrode at –450 mV vs. SCE [22]. (Reproduced from Ahn S, Tatarchuk BJ, Composite electrode structures for fuel cell applications. Proceedings of the 25th Intersociety Energy Conversion Engineering Conference, 1990;3:287–92, with permission from the American Institute of Chemical Engineers.)

Compared with a Teflon®-bonded commercial electrode, the composite electrode showed lower polarization losses at high current densities, even though the composite material did not contain Pt. The ohmic and mass transfer resistances were lower in the composite electrode than in the commercial electrode. The sintered contacts and interlocked networks formed in the composite structure permitted better electrical and physical contact between the carbon fibres and metal fibres, leading to a composite electrode with a high void volume and large macroscopic porosity, which increased the accessibility of carbon to the reactants [22].

6.1.2 Ionic Conductivity

MEA performance is mainly limited by ORR kinetics, as well as oxygen transport to the cathode catalyst. Another major loss is due to proton conduction, in both the membrane and the cathode catalyst layer (CL). Characterization of the ionic resistance of fuel cell electrodes helps provide important information on electrode structure optimization, and quantification of the ionomer degradation in the electrodes [23].

To increase fundamental knowledge about ionic resistance, it is important to develop a methodology to experimentally isolate the contributions of the various cell components. Electrochemical impedance spectroscopy has been widely used by Pickup's research group to study the capacitance and ion conductivity of fuel cell catalyst layers [24–27]; they performed impedance experiments under a nitrogen atmosphere, which simplified the impedance response of the electrode. Saab et al. [28] also presented a method to extract ohmic resistance, CL electrolyte resistance, and double-layer capacitance from impedance spectra using both the H_2/O_2 and H_2/N_2 feed gases. In this section, we will focus on the work by Pickup et al. on using EIS to obtain ionic conductivity information from operational catalyst layers.

When discussing the ionic conductivity of catalyst layers, one must mention the finite transmission-line equivalent circuit, which is widely used to model porous electrodes and was shown as Figure 4.33 in Chapter 4. For ease of discussion, the circuit is re-plotted here as Figure 6.23.

The finite transmission-line equivalent circuit is composed of two parallel resistive rails: electron transport through conducting carbon particles ($R_{\text{electronic}}$) and ion transport in the catalyst layer (R_{ionic}). As seen in Figure 6.23, the two rails are connected by capacitors uniformly distributed throughout the catalyst layer. According to this model, the Nyquist impedance plot of the electrode should consist of a 45° region at high to intermediate frequencies and a 90° region representing the full limiting capacitance and resistance at low frequencies [25]. Based on the model, the impedance response of a PEMFC electrode effectively characterizes the ionic conductivity profile because: (1) the charge-transfer resistance will be absent during cell operation in H_2/N_2 mode; (2) $R_{\text{electronic}}$ negligibly contributes to the impedance of the electrode, due to the excellent electronic conductivity of carbon particles in comparison with R_{ionic}; and (3) the electrolyte resistance can simply be subtracted from the response since it only shifts the plot along the real axis.

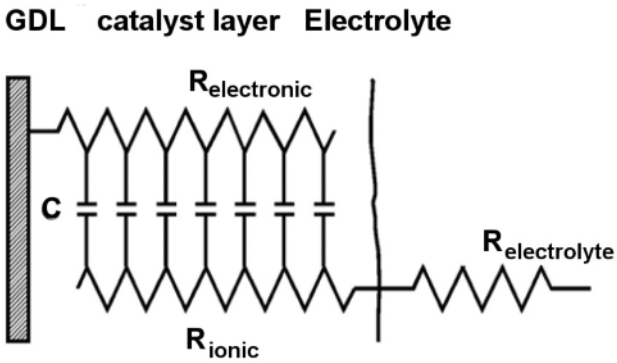

Figure 6.23. Finite transmission-line equivalent circuit describing the impedance behaviour of a PEMFC electrode [24]. (Reprinted from Electrochimica Acta, 50(12), Easton EB, Pickup PG. An electrochemical impedance spectroscopy study of fuel cell electrodes. Electrochim Acta, 2469–74, ©2005, with permission from Elsevier and the authors.)

Pickup et al. performed both ex situ and in situ experiments. Ex situ electrochemical measurements were carried out in a three-electrode configuration by exposing the 1 cm^2 test electrode to a 0.5 M H_2SO_4 electrolyte with a Pt wire counter electrode and a Ag/AgCl reference electrode. The working electrode was prepared by applying catalyst ink onto a glassy carbon electrode. For in situ measurements, a fuel cell with an active area of 1 cm^2 was operated in a two-electrode configuration with humidified hydrogen passing over the Pt black electrode, and nitrogen passing over the test electrode. Unlike other researchers, Pickup et al. applied capacitance plots in combination with the commonly employed Nyquist plots. They believed that the capacitance plot could better illustrate the variation in conductivity across the catalyst layer and that the measured total capacitance is relative to the electrochemically active area.

Nyquist plots from ex situ experiments are shown in Figure 5.4 of Chapter 5. Previous work by Pickup's research group [29, 30], showed that the high-frequency intercept with the real axis (R_{high}) is $1/(1/R_{electronic} + 1/R_{ionic})$, while the limiting low-frequency resistance is ($R_{electronic} + R_{ionic}/3$), which is the real axis intercept of the low-frequency region of the complex plane impedance plot, estimated by extrapolating the steep low-frequency region of the plot to the real axis. The ionic conductivity of the film, σ_{ionic}, is calculated from $\sigma_{ionic} = d / R_{ionic}A$, where A is the geometric area of the electrode and d is the film thickness. Therefore, it is obvious that the ionic resistance increases with the volume of ink applied and, as illustrated by the high-frequency region of Figure 6.24, the increase appears to be larger for electrodes containing 4–6 μL of catalyst ink, which is in agreement with the cyclic voltammetry results.

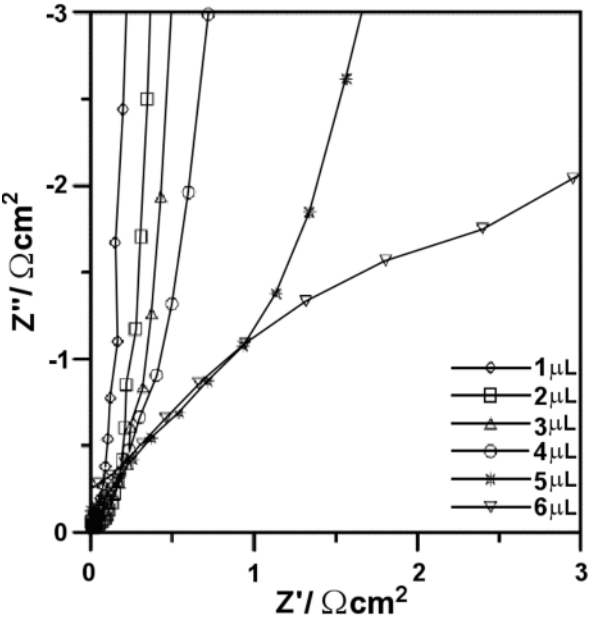

Figure 6.24. Expansion of the high-frequency region of Figure 5.4 [24]. (Reprinted from Electrochimica Acta, 50(12), Easton EB, Pickup PG. An electrochemical impedance spectroscopy study of fuel cell electrodes. Electrochim Acta, 2469–74, ©2005, with permission from Elsevier and the authors.)

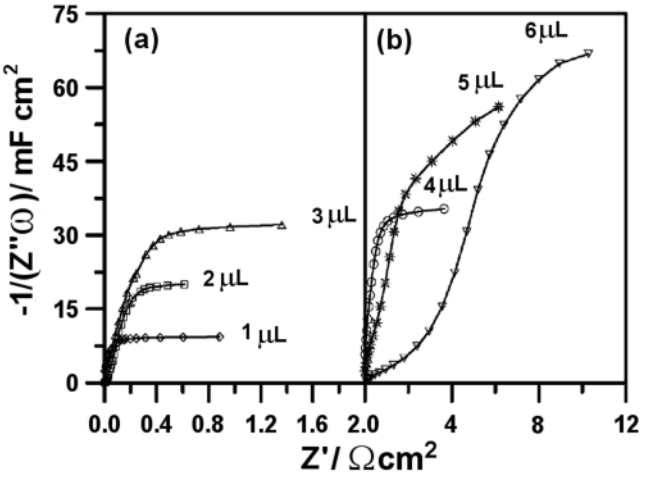

Figure 6.25. Capacitance plots obtained at a DC bias potential of 0.2 V vs. Ag/AgCl for electrodes with *a* 1–3 μL of catalyst ink applied and *b* 4–6 μL of catalyst ink applied [24]. (Reprinted from Electrochimica Acta, 50(12), Easton EB, Pickup PG. An electrochemical impedance spectroscopy study of fuel cell electrodes. Electrochim Acta, 2469–74, ©2005, with permission from Elsevier and the authors.)

By using the equation $C = 1/Z''\omega$, the capacitance plots in Figure 6.25, which effectively visualize the ionic resistivity increase, can be obtained from Figure 6.24. For 1–3 μL of ink, the initial slope of each plot is very similar, indicating similar resistivity in the samples. The slopes for 4–6 μL of ink are smaller, indicating higher resistivity. The increasing resistivity is better visualized by the normalized capacitances presented in Figure 6.26, which were obtained by dividing the capacitance by the mass of catalyst applied. In addition, comparison of the above results with those obtained in situ showed that they were very similar.

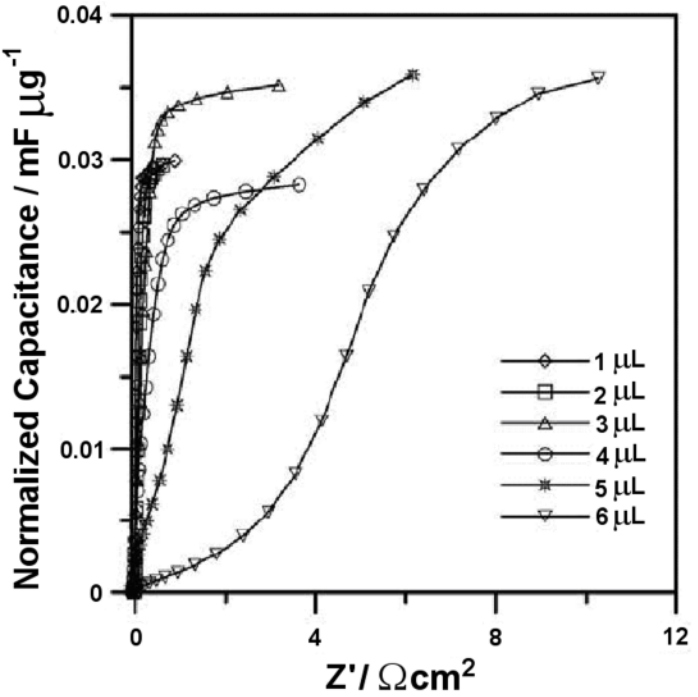

Figure 6.26. Mass normalized capacitance plots obtained for electrodes with different volumes of catalyst ink applied at a DC bias potential of 0.2 V vs. Ag/AgCl [24]. (Reprinted from Electrochimica Acta, 50(12), Easton EB, Pickup PG. An electrochemical impedance spectroscopy study of fuel cell electrodes. Electrochim Acta, 2469–74, ©2005, with permission from Elsevier and the authors.)

Another interesting ionic conductivity result obtained by Pickup's research group [25] is shown in Figure 6.27 (open symbols represent experimental data and solid symbols represent simulated impedance plots). The data clearly illustrates that the total resistance of the fuel cell cathodes given by ($R_{electronic}$ + R_{ionic}/3), as discussed above, decreases with increasing Nafion® content. This can be attributed to increasing ionic conductivity within the catalyst layer, since the electronic conductivity should remain constant or decrease as more non-electronically conductive Nafion® is added.

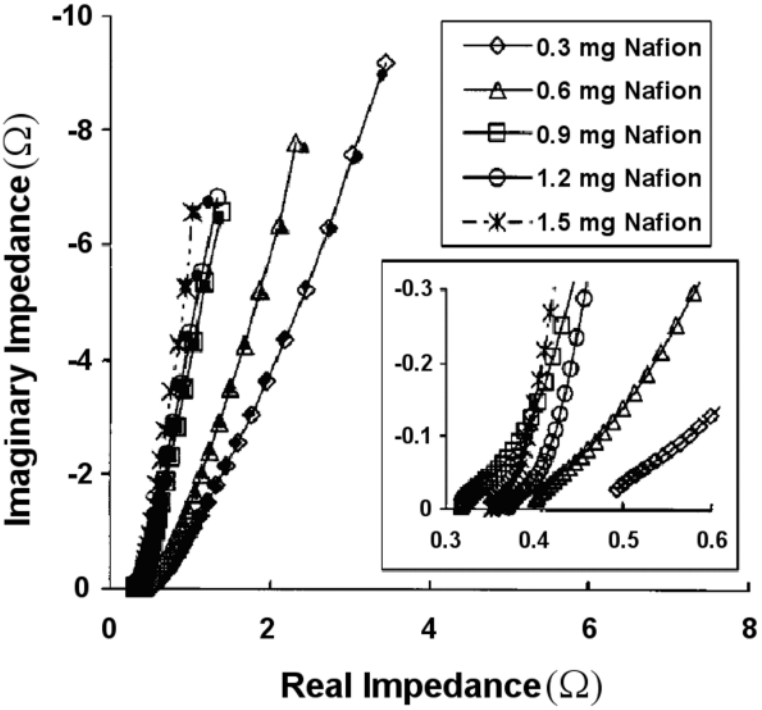

Figure 6.27. Nyquist plots (65000 to 0.82 Hz, 22 ± 2°C, 1.00 V vs. H_2) for nitrogen-bathed cathodes with various Nafion® loadings. The inset shows an expansion of the high-frequency region of the plots [25]. (Reproduced by permission of ECS—The Electrochemical Society, and the authors, from Li G, Pickup PG. Ionic conductivity of PEMFC electrodes.)

Based on the finite transmission-line equivalent circuit (consisting of 40 equal capacitors representing C, and 40 unequal resistors representing R_{ionic}) with $R_{electronic}$ set at zero, $R_{membrane}$ set at the experimental high-frequency intercept, and C set at the low-frequency limiting capacitance, the conductivity profiles were obtained, as shown in Figure 6.28. For those electrodes with higher Nafion® loadings, the conductivity is quite uniform at the side close to the membrane, and there is a sharp drop in conductivity close to the carbon paper backing side due to catalyst penetration of the pores in the carbon paper, which diminishes ionic contact with the rest of the layer. The electrodes with lower Nafion® loadings show lower conductivity because there is insufficient Nafion® to bind the catalyst particles, and the conductivity drops continuously with distance from the membrane.

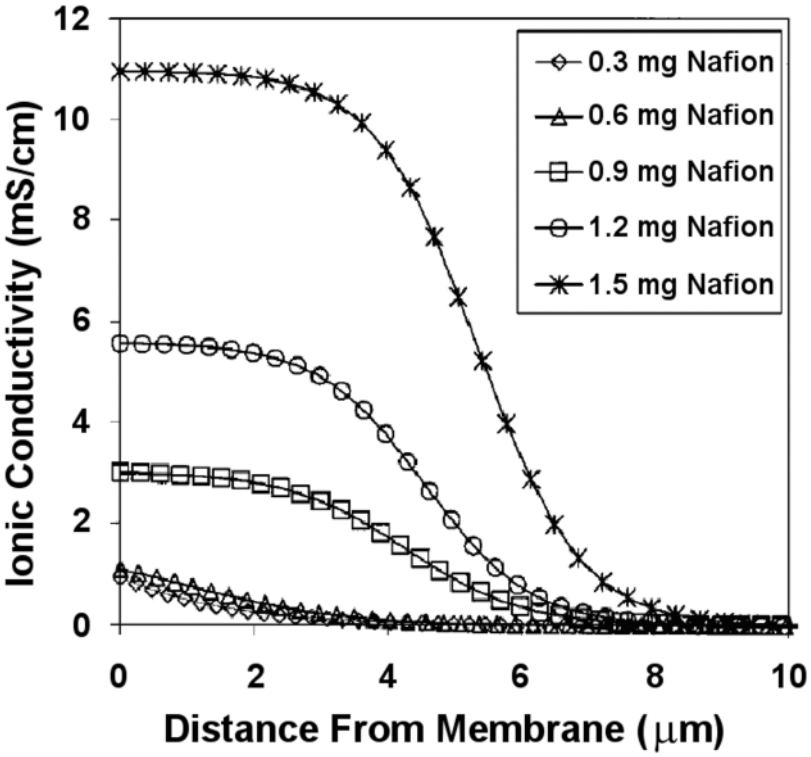

Figure 6.28. Conductivity profiles used to simulate the impedance data shown in Figure 6.27 [25]. (Reproduced by permission of ECS—The Electrochemical Society, and the authors, from Li G, Pickup PG. Ionic conductivity of PEMFC electrodes.)

Figure 6.29 is a good example of how the conductivity profile can assist with MEA fabrication optimization and provide reasonable explanations for the effect of conductivity on fuel cell performance. It can be seen that a uniform distribution of Nafion® produces the best performance, while higher Nafion® loading next to the carbon paper results in the worst performance. The conductivity profiles of these electrodes can provide the explanation. As shown in Figure 6.30, the electrode with more Nafion® next to the membrane exhibits the highest ionic conductivity close to the Nafion®; however, the conductivity does not remain stable, decreasing more rapidly with increasing distance from the membrane than the conductivity of the uniform electrode. The electrode with a low Nafion® loading next to the membrane shows lower conductivity close to the membrane, but conductivity also drops rapidly with distance. Neither bilayer electrode provides uniform ionic contact. However, the authors did not provide a clear explanation for why non-uniform ionic conductivity distribution results in inferior cell performance.

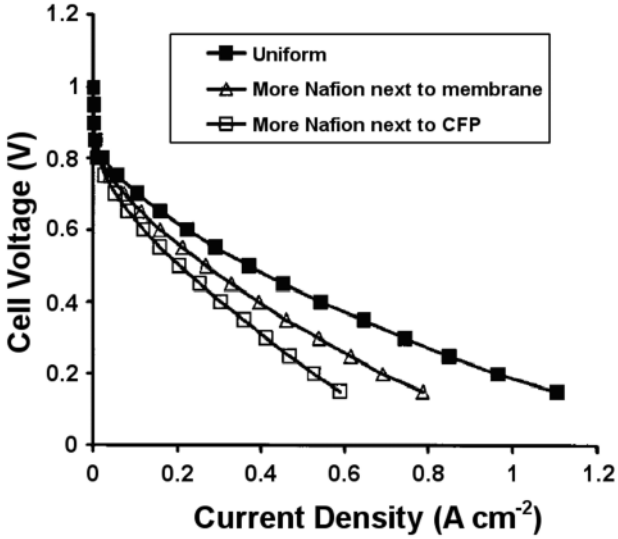

Figure 6.29. Polarization curves for PEMFCs with uniform and bilayer cathodes under H_2/O_2 operation at ambient temperature and pressure. All electrodes (1 cm^2) contained 0.9 mg of Nafion® [25]. (Reproduced by permission of ECS—The Electrochemical Society, and the authors, from Li G, Pickup PG. Ionic conductivity of PEMFC electrodes.)

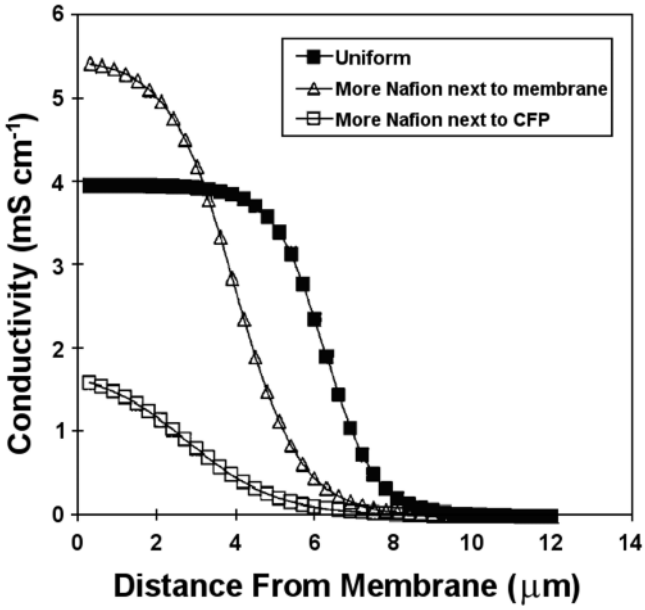

Figure 6.30. Conductivity profiles obtained from fitting of impedance data for uniform and bilayer cathodes. All electrodes (1 cm^2) contained 0.9 mg of Nafion® [25]. (Reproduced by permission of ECS—The Electrochemical Society, and the authors, from Li G, Pickup PG. Ionic conductivity of PEMFC electrodes.)

6.1.3 Contamination

Fuel cell contamination caused by impurities (such as CO, H_2S, NH_3, organic sulfur–carbon, and carbon–hydrogen compounds produced in the hydrogen production process) in the feed stream is an important issue investigated in fuel cell development and operation. These impurities lower cell performance and some can cause permanent MEA damage. The degradation mechanisms include: (1) the kinetic effect (poisoning of the electrode catalyst) and (2) the conductivity effect (increasing the resistance of the solid electrolyte, in both the membrane and the catalyst layer ionomer). CO poisoning is the most detrimental contaminant and is therefore widely studied by many researchers [31]. The dominant mechanism of CO contamination in relation to MEA performance is reported to be the kinetic effect, because the adsorbed CO not only affects the reactivity of the electrode surface by preventing hydrogen adsorption due to site exclusion, but also lowers the reactivity of the remaining sites through dipole interactions and electron capture [32]. CO poisoning can be investigated by various means, such as electrochemical techniques, in situ UV-visible and infrared reflectance spectroscopies, X-ray photoelectron spectroscopy (XPS), and thermal desorption spectroscopy (TDS). In this section, we will introduce the role of AC impedance in the study of CO poisoning. The impedance of the entire fuel cell can be obtained by feeding oxygen into the cathode side and simulated gas into the anode side. The anode impedance can be obtained by feeding hydrogen to the cathode and simulated gas to the anode.

Due to the poisoning effect of CO, it is logical that the impedance spectroscopy will change with time. A time-resolved 3D Nyquist plot is shown in Figure 6.31 [33]. The spectra were obtained under the following conditions. The test cell was a 23 cm^2 single cell with a (H_2+100 ppm CO)/O_2 gas feed, operated at 80°C and 2 bar pressure on both sides. The galvanostatic mode impedance measurements were performed under a constant load of 5A with a distortion amplitude of 200 mA. The potentiostatic mode impedance measurements were recorded at a constant voltage of 700 mV with a 10 mV distortion amplitude.

As seen in Figure 6.31, the cell impedance shows strong time dependence. However, such a measurement does not provide much information about CO poisoning since the current changes during the potentiostatic impedance measurements, and the differing current or current density, are present not only between two measurements but also during the recording of a single spectrum, especially in the low-frequency range. Therefore, while Figure 6.31 shows significant spectrum variation over time, it is difficult to isolate the CO poisoning at the anode.

The most useful impedance spectra are those obtained in a galvanostatic measurement mode because they offer a constant conversion rate with respect to the species involved in the electrochemical reaction. Figure 6.32 shows the Nyquist plots of the fuel cell impedance at different times under galvanostatic mode. The impedance can be seen to increase with time during the progressive CO poisoning of the anode. At the beginning of the measurements, the spectrum exhibits a single semicircle, representing the typically observed structure for cathode impedance. With increasing time, two semicircles (a full depressed semicircle followed by the

onset of a second at low frequencies) appear, indicating both anodic and cathodic behaviour resulting from the increasing anode impedance caused by CO poisoning at the anode. As time advances, the anodic impedance rises and becomes increasingly dominant, masking the cathodic cell impedance and developing a growing pseudo-inductive loop. The pseudo-inductive behaviour can be explained by a surface relaxation process arising from the competitive oxidation of hydrogen and CO at the anode.

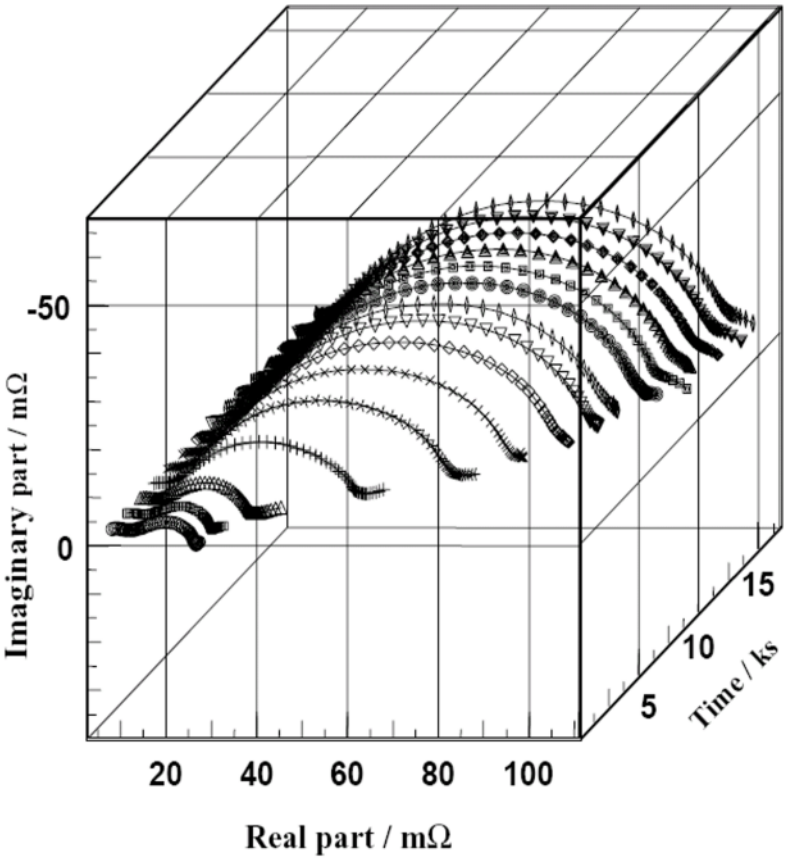

Figure 6.31. Nyquist plots of the interpolated impedance spectra measured at 700 mV and different times during the progressive poisoning of the anode with CO [33]. (Reprinted from Journal of Power Sources, 127(1–2), Wagner N, Gulzow E. Change of electrochemical impedance spectra (EIS) with time during CO-poisoning of the Pt-anode in a membrane fuel cell, 341–7, ©2004, with permission from Elsevier and the authors.)

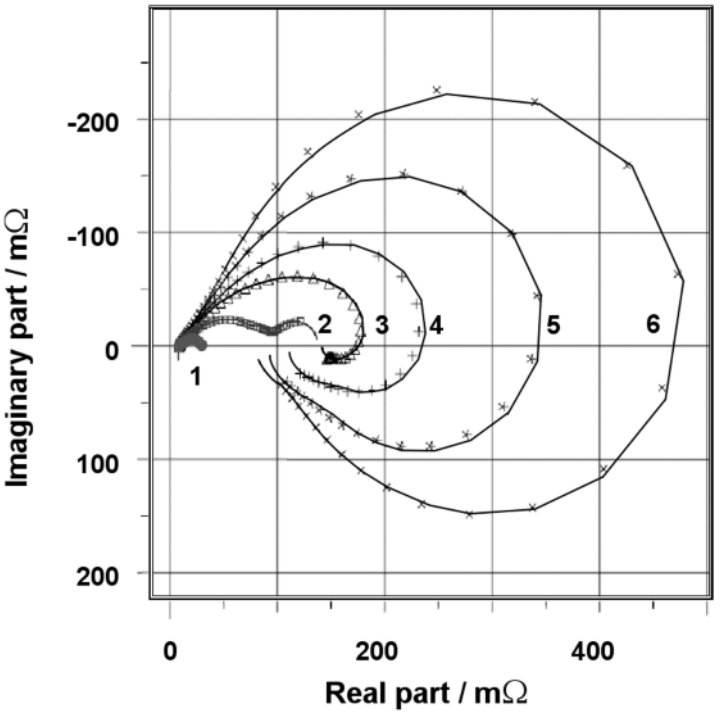

Figure 6.32. Nyquist plots of fuel cell impedance at different times under galvanostatic operation during progressive CO poisoning of the anode [33]. (Reprinted from Journal of Power Sources, 127(1–2), Wagner N, Gulzow E. Change of electrochemical impedance spectra (EIS) with time during CO-poisoning of the Pt-anode in a membrane fuel cell, 341–7, ©2004, with permission from Elsevier and the authors.)

To separate the contribution of the anode from that of the cathode, Wagner et al. provided a more general equivalent circuit, as shown in Figure 6.33. The anode, the cathode, and the membrane resistance were in series. A parasitic inductance due to the mutual induction effect was also included. The cathode impedance was given by charge-transfer resistance (R_{ct,O_2}) and constant phase element (CPE) in parallel. The anode impedance was complicated due to CO evolution and was described using double-layer capacitance (C_d) and Faraday impedance (Z_F) in parallel. The Faraday impedance is a surface relaxation impedance (which explains the development of the pseudo-inductive behaviour in the low-frequency range), where Z_k represents the relaxation impedance, which can be split into the relaxation resistance R_k and the relaxation inductivity X_k:

$$X_k = j\omega L_k = j\omega\tau_k R_k \tag{6.3}$$

where τ_k is the relaxation time constant. For the finite diffusion impedance Z_c, Nernst impedance was chosen to model the spectra. Based on this model, the anode

charge-transfer resistance increased by more than two orders of magnitude and the degradation in fuel cell performance was dominated by an increase in the anodic resistance from 3 to 500 mΩ, whereas the cathodic resistance remained nearly constant during the experiment. Ciureanu et al. [32, 34] and Kim et al. [35, 36] also investigated the relationship between impedance spectra and CO poisoning, but their measurements were based on the constant voltage mode.

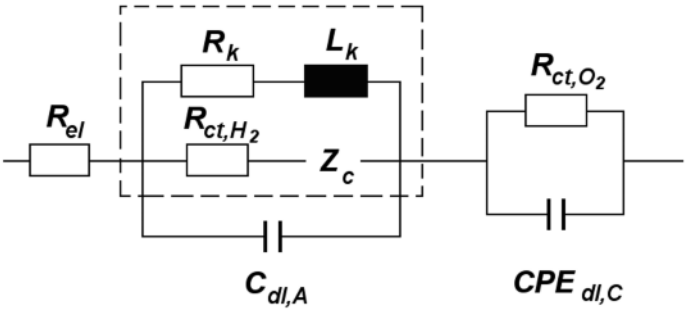

Figure 6.33. Equivalent circuit for evaluation of the interpolated impedance spectra measured in galvanostatic operation of a fuel cell during CO poisoning of the anode [33]. (Reprinted from Journal of Power Sources, 127(1–2), Wagner N, Gulzow E. Change of electrochemical impedance spectra (EIS) with time during CO-poisoning of the Pt-anode in a membrane fuel cell, 341–7, ©2004, with permission from Elsevier and the authors.)

6.1.4 Stack and Individual Cell Impedance

6.1.4.1 Indirect Determination

Numerous studies have been conducted on AC impedance in single cells. From a practical point of view, stack experiments provide more interesting data because a single cell is rarely used in real-world applications. With AC impedance it is possible to separate the impedances of each cell of the stack, to understand the gas distribution within the stack, and to detect a failure in the stack.

Diard et al. [37] studied the impedance of a commercial 10 W four-cell stack with individual cell geometric areas of 24 cm^2 (8 × 3 cm^2). The stack was operated on H_2/O_2 at 80°C, and the experiments were performed with equal flow rates of 20 mL/min and pressures of P_{H_2} = 0.5 bar and P_{O_2} = 0.2 bar at the stack inlet. The frequencies were swept over 10^5 ~ 1 Hz, from high to low frequencies, with eight points per decade being recorded.

Figure 6.34 shows the schematics of an EIS study of each element of a fuel cell stack under load. In positions a and e, the reference electrode (RE) and counter electrode (CE) were connected to the unipolar graphite plates of cells I and IV, respectively. By connecting b, c, and d to bipolar graphite plates, cells I and II, II and III, and III and IV were separated. The impedances of cells I, II, III, and IV were denoted as Z_I, Z_{II}, Z_{III}, and Z_{IV}, respectively. If connecting RE to a, b, c, d, and e, H_a, H_b, H_c, H_d, and Z_{II} will be measured, where H_b, H_c, and H_d are relative to Z_Ω

$+ Z_I$, $Z_\Omega + Z_I + Z_{II}$, and $Z_\Omega + Z_I + Z_{II} + Z_{III}$, respectively, and Z_{II} is the impedance of the fuel cell stack in parallel with the load. Z_{II} is given by

$$\frac{1}{Z_{11}(s)} = \frac{1}{Z_{stack}(s)} + \frac{1}{Z_{load}(s)} \tag{6.4}$$

where s is the Laplace complex variable.

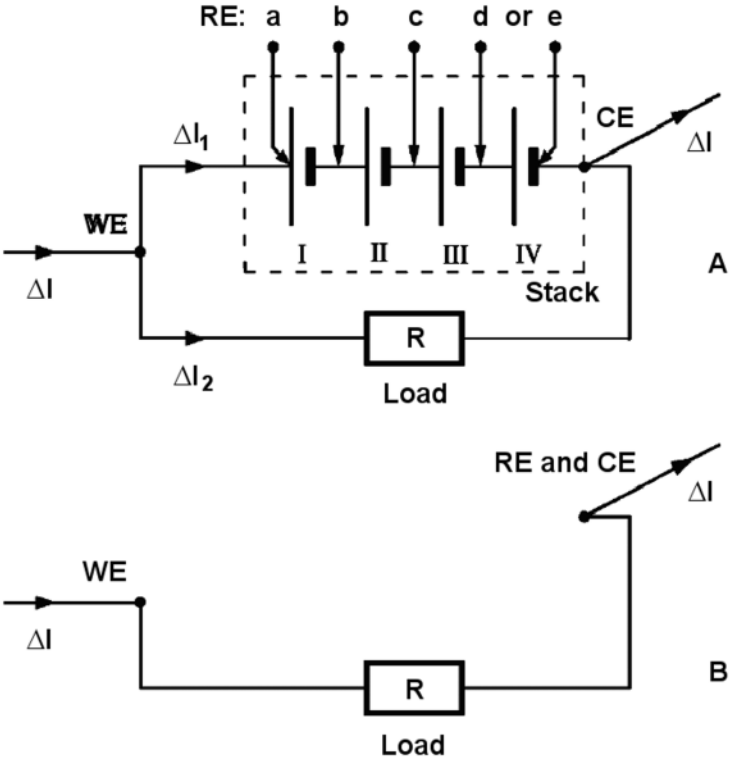

Figure 6.34. *A* Connections used for the EIS study of each element of a fuel cell stack running on a load. WE: working electrode; CE: counter electrode; RE: reference electrode. *B* Two-electrode arrangement used for the measurement of Z_{load} [37]. (Reproduced by permission of ECS—The Electrochemical Society, and the authors, from Diard JP, Glandut N, Le-Gorrec B, Montella C. Impedance measurement of each cell of a 10 W PEMFC stack under load.)

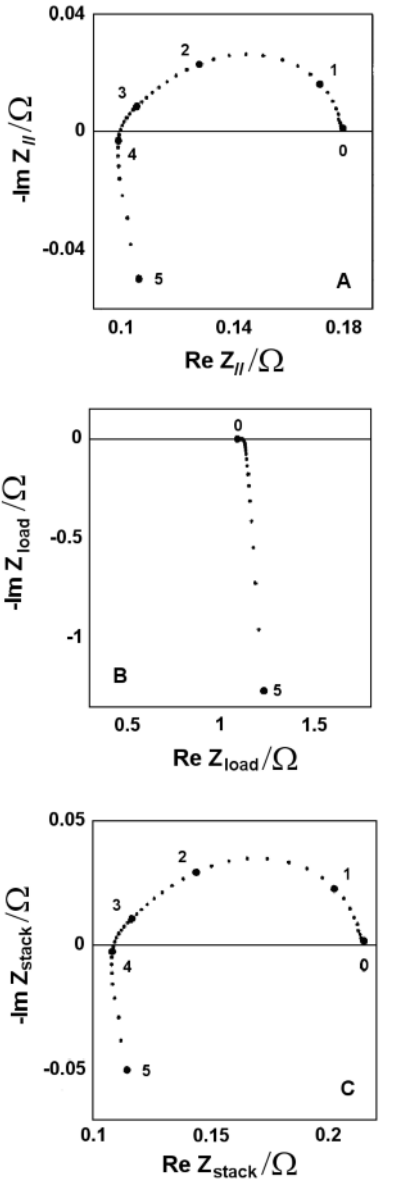

Figure 6.35. Nyquist representation of impedance diagrams measured *A* for the fuel cell stack in parallel with the load, and *B* for the load, using the connections of Figure 6.34A and B, respectively. *C* Impedance diagram of the fuel cell stack calculated from Z_{II} and Z_{load}. Flow rates: $Q_{H_2} = Q_{O_2} = 20$ mL min^{-1}; gas pressures: $p_{H_2} = 0.5$ bar and $p_{O_2} = 0.2$ bar. I_{dc} = 3 A and d_I = 10 mA [37]. (Reproduced by permission of ECS—The Electrochemical Society, and the authors, from Diard JP, Glandut N, Le-Gorrec B, Montella C. Impedance measurement of each cell of a 10 W PEMFC stack under load.)

Z_{stack} is the sum of the cell impedances plus the impedance of the wire connected to the unipolar plate of the first cell, Z_{Ω}:

$$Z_{stack}(s) = Z_{\Omega}(s) + Z_{\mathrm{I}}(s) + Z_{\mathrm{II}}(s) + Z_{\mathrm{III}}(s) + Z_{\mathrm{IV}}(s) \tag{6.5}$$

Then, the stack impedance can be written as

$$Z_{stack}(s) = \frac{Z_{\mathrm{II}}(s) Z_{load}(s)}{Z_{load}(s) - Z_{\mathrm{II}}(s)} \tag{6.6}$$

Figure 6.35 shows the stack impedance (Figure 6.35C) calculated from Z_{II} (Figure 6.35A) and Z_{load} (Figure 6.35B). Similarly, through measurements of H_a, H_b, H_c, and H_d, the values of Z_{I}, Z_{II}, Z_{III}, and Z_{IV} can be calculated. The calculation procedure is shown below.

(1) According to the measurement of H_a, $Z_{\Omega} / (Z_{\mathrm{I}} + Z_{\mathrm{II}} + Z_{\mathrm{III}} + Z_{\mathrm{IV}})$ can be calculated:

$$Z_{11}(s) = \frac{\Delta E_e(s)}{\Delta I(s)} = Z_{stack}(s) \frac{\Delta I_1(s)}{\Delta I(s)} \tag{6.7}$$

$$H_a(s) = \frac{\Delta E_a(s)}{\Delta I(s)} = Z_{\Omega}(s) \frac{\Delta I_1(s)}{\Delta I(s)} \tag{6.8}$$

$$K_a(s) = \frac{\Delta E_e(s) - \Delta E_a(s)}{\Delta I(s)}$$

$$= Z_{\mathrm{II}}(s) - H_a(s)$$

$$= [Z_{\mathrm{I}}(s) + Z_{\mathrm{II}}(s) + Z_{\mathrm{III}}(s) + Z_{\mathrm{IV}}(s)] \frac{\Delta I_1(s)}{\Delta I(s)} \tag{6.9}$$

Then $Z_{\Omega} / (Z_{\mathrm{I}} + Z_{\mathrm{II}} + Z_{\mathrm{III}} + Z_{\mathrm{IV}})$ is obtained by the division of Equation 6.9 by Equation 6.8:

$$\frac{Z_{\Omega}(s)}{Z_{\mathrm{I}}(s) + Z_{\mathrm{II}}(s) + Z_{\mathrm{III}}(s) + Z_{\mathrm{IV}}(s)} = \frac{H_a(s)}{Z_{\mathrm{II}}(s) - H_a(s)} \tag{6.10}$$

(2) Based on the measurements of H_b, H_c, H_d, $(Z_{\Omega} + Z_{\mathrm{I}}) / (Z_{\mathrm{II}} + Z_{\mathrm{III}} + Z_{\mathrm{IV}})$, and $(Z_{\Omega} + Z_{\mathrm{I}} + Z_{\mathrm{II}}) / (Z_{\mathrm{III}} + Z_{\mathrm{IV}})$, $(Z_{\Omega} + Z_{\mathrm{I}} + Z_{\mathrm{II}} + Z_{\mathrm{III}}) / Z_{\mathrm{IV}}$ can be calculated. The calculation process is similar to that of $Z_{\Omega} / (Z_{\mathrm{I}} + Z_{\mathrm{II}} + Z_{\mathrm{III}} + Z_{\mathrm{IV}})$:

$$\frac{Z_{\Omega}(s)+Z_{\mathrm{I}}(s)}{Z_{\mathrm{II}}(s)+Z_{\mathrm{III}}(s)+Z_{\mathrm{IV}}(s)}=\frac{H_b(s)}{Z_{\mathrm{II}}(s)-H_b(s)} \tag{6.11}$$

$$\frac{Z_{\Omega}(s)+Z_{\mathrm{I}}(s)+Z_{\mathrm{II}}(s)}{Z_{\mathrm{III}}(s)+Z_{\mathrm{IV}}(s)}=\frac{H_c(s)}{Z_{\mathrm{II}}(s)-H_c(s)} \tag{6.12}$$

$$\frac{Z_{\Omega}(s)+Z_{\mathrm{I}}(s)+Z_{\mathrm{II}}(s)+Z_{\mathrm{III}}(s)}{Z_{\mathrm{IV}}(s)}=\frac{H_d(s)}{Z_{\mathrm{II}}(s)-H_d(s)} \tag{6.13}$$

(3) Using the four equations containing $Z_{\Omega}/(Z_{\mathrm{I}}+Z_{\mathrm{II}}+Z_{\mathrm{III}}+Z_{\mathrm{IV}})$ (6.10), $(Z_{\Omega}+Z_{\mathrm{I}})/(Z_{\mathrm{II}}+Z_{\mathrm{III}}+Z_{\mathrm{IV}})$ (6.11), $(Z_{\Omega}+Z_{\mathrm{I}}+Z_{\mathrm{II}})/(Z_{\mathrm{III}}+Z_{\mathrm{IV}})$ (6.12), and $(Z_{\Omega}+Z_{\mathrm{I}}+Z_{\mathrm{II}}+Z_{\mathrm{III}})/Z_{\mathrm{IV}}$ (6.13), combined with Equation 6.5, the five unknown parameters, Z_{Ω}, Z_{I}, Z_{II}, Z_{III}, and Z_{IV} are therefore obtained separately.

Consequently, the impedance of the individual cell of a PEMFC stack and the total impedance of the stack have been determined separately. The results are shown in Figure 6.36.

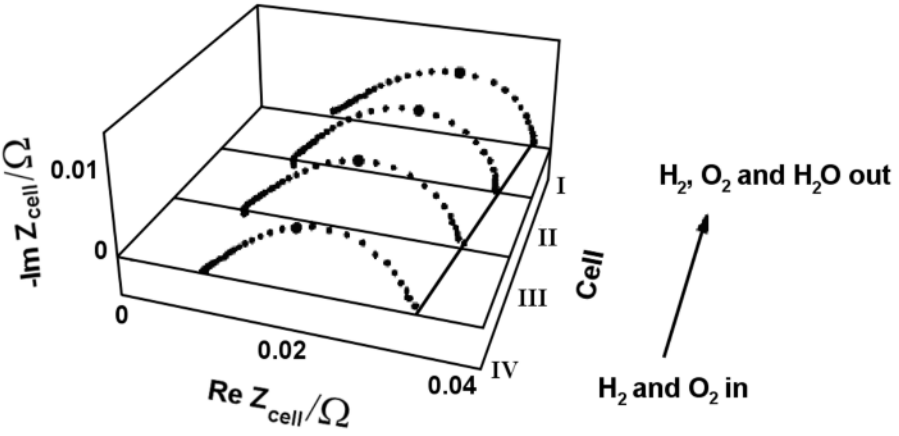

Figure 6.36. Three-dimensional representation of impedance diagrams calculated for each cell of the fuel cell stack. The solid line links the low-frequency limits (R_{LF}) of the diagrams. The large dots indicate the 100 Hz frequency for each diagram [37]. (Reproduced by permission of ECS—The Electrochemical Society, and the authors, from Diard JP, Glandut N, Le-Gorrec B, Montella C. Impedance measurement of each cell of a 10 W PEMFC stack under load.)

It is observable that the impedance increases from the cell at the gas inlet to the cell at the gas outlet (the gases having entered the stack on the cell IV side). This indicates that gas starvation occurs in the stack, cell by cell, from the inlet to the outlet. In addition, it is possible to foresee that a failure in a stack can be detected from one or any of the individual cells.

6.1.4.2 Direct Determination

As described in the previous section, the impedance of the stack and individual cells can be determined through a complicated calculation. Since integral measurements of the entire stack do not provide information about single cells, direct measurement of the individual cell impedance is of more interest. Impedance of individual cells under heavy load has been introduced in Section 5.3.3, but the spectra obtained were measured consecutively one by one. By using a multi-channel frequency response analyzer system, the impedance spectra of all single cells in a fuel cell stack can be measured simultaneously, which is suitable for evaluating the operating state of each cell concurrently and thereby explaining overall stack performance.

For the purpose of simultaneously obtaining EIS measurements of single cells, Hakenjos et al. [38] utilized a Solartron 1254 frequency response analyzer (FRA) with two 1251 multichannel extensions, which is capable of measuring the impedances of up to 19 single cells, to investigate their self-designed short stack consisting of four cells with an active area of 53 cm^2. A Kepco BOP 20-20M bipolar power supply was used for the load. The load was operated in current control mode with the AC perturbation above a DC bias analog programmed by the generator output of the 1254 FRA. The chosen amplitude of 250 mA for the current excitation was small enough to measure impedances up to 0.04 Ω. The stack was operated at a current of 4 A, and impedance spectra were taken approximately every 7 min. The duration required for the measurement of one spectrum was about 4.5 min.

The first impedance spectra were taken 12 min after the start of the experiment and are shown in Figure 6.37(M0). All four spectra are similar in shape, with the emergence of a second arc in the frequency range below 1 Hz suggesting minor mass transfer losses. There are no significant deviations in the high-frequency resistance. Cells 1 and 3 show larger charge transfer arcs causing slightly lower cell voltages, which is consistent with the voltage measurement results. Therefore, the lower performance of these two cells can be explained by lower electrochemical activity.

When the airflow rate is doubled to 2 L min^{-1}, the low-frequency arc vanishes, as shown in Figure 6.38. This can be explained by a change in the stoichiometry coefficient and a decrease in liquid water content in the GDL as more water is removed from the cell via the air stream. With an air flow rate of only 1 L min^{-1} there is no significant performance loss. Since the variations between the individual cell voltages do not vanish at higher airflow rates, the variations are not attributable to improper air distribution within the stack.

The second impedance measurement, taken after 30 min, is shown in Figure 6.37(M3). An increase in the low-frequency arc of the spectrum of cell 2 can be observed. This indicates an increase in diffusive losses.

In the third measurement, shown in Figure 6.37(M4), the spectrum of cell 2 indicates an almost linear 45° branch in the low-frequency range, suggesting Warburg diffusion behaviour. This severe diffusion loss causes a further decrease in cell voltage. The spectra of cells 1 and 3 also begin to show a rising low-frequency arc, which explains why cell 4 is the only one in which voltage is not decreasing.

As shown in Figure 6.37(M6), the impedance spectra eventually return to the shape observed at the beginning of the measurement. The charge transfer arcs are slightly smaller and the spectrum of cell 2 has shifted towards the lower real parts, which is a result of better membrane hydration after the flooding event.

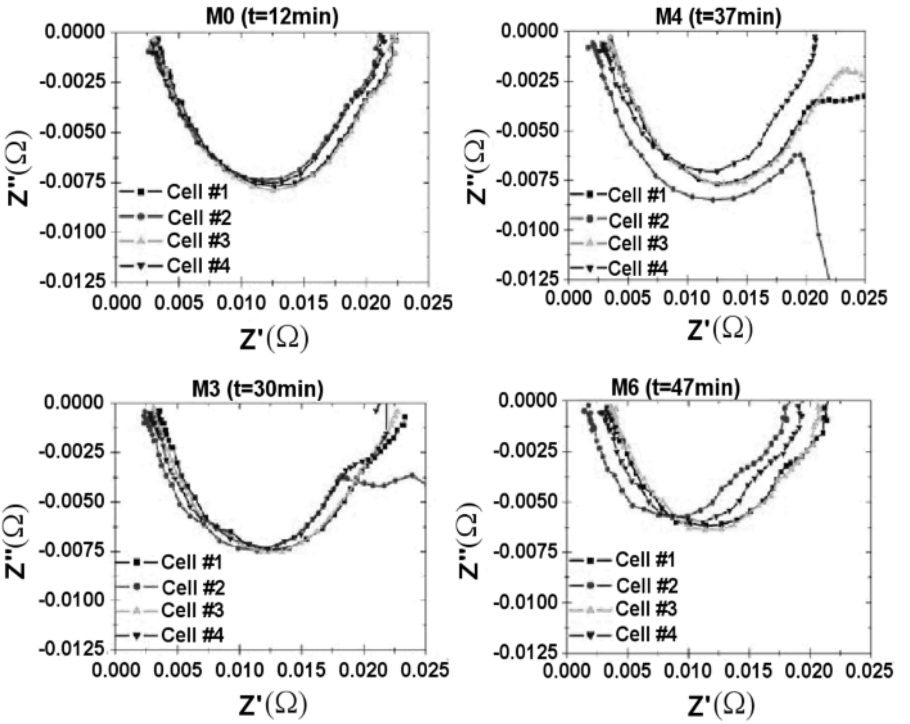

Figure 6.37. Impedance spectra measured at different times throughout the experiment. The gas flow rates are set to 0.3 L·min^{-1} dry hydrogen for the anode and 1 L·min^{-1} for the cathode [38]. (Reprinted from Journal of Power Sources, 154(2), Hakenjos A, Zobel M, Clausnitzer J, Hebling C. Simultaneous electrochemical impedance spectroscopy of single cells in a PEM fuel cell stack, 360–3, ©2006, with permission from Elsevier and the authors.)

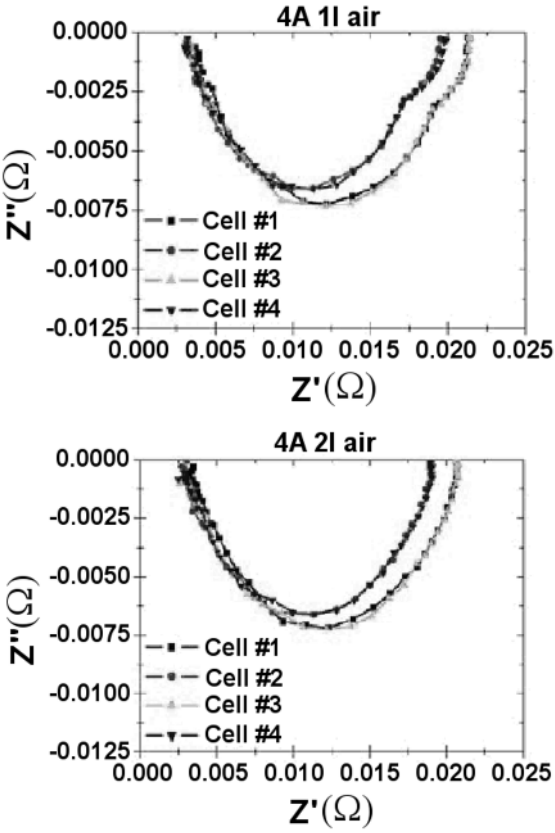

Figure 6.38. Impedance spectra at different airflow rates. Top: 1 L min^{-1}; bottom: 2 L min^{-1} [38]. (Reprinted from Journal of Power Sources, 154(2), Hakenjos A, Zobel M, Clausnitzer J, Hebling C. Simultaneous electrochemical impedance spectroscopy of single cells in a PEM fuel cell stack, 360–3, ©2006, with permission from Elsevier and the authors.)

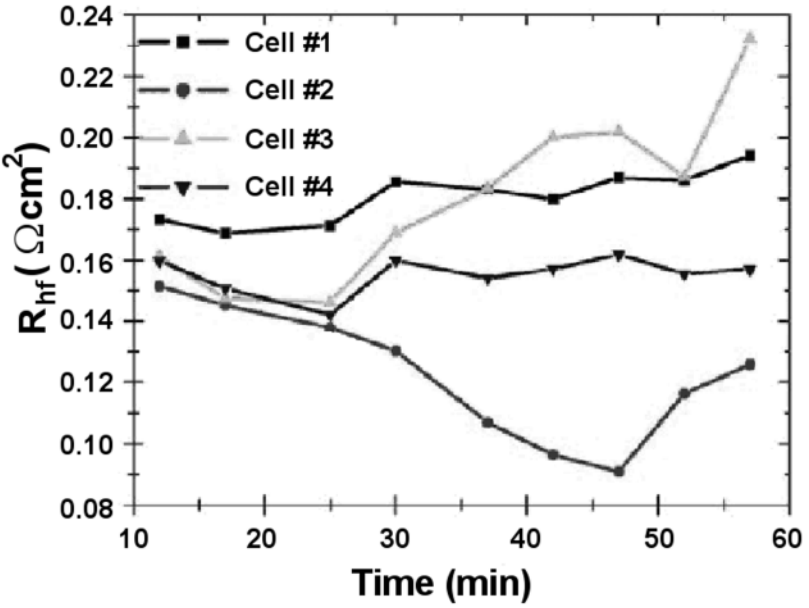

Figure 6.39. Progression of the high-frequency resistances over time [38]. (Reprinted from Journal of Power Sources, 154(2), Hakenjos A, Zobel M, Clausnitzer J, Hebling C. Simultaneous electrochemical impedance spectroscopy of single cells in a PEM fuel cell stack, 360–3, ©2006, with permission from Elsevier and the authors.)

The values of R_{hf} obtained through impedance measurements of individual cells (Figure 6.39) are valuable because they provide good evidence of the relationship between the proton conductivity of the membrane and water content, while also illustrating the relative deviations in resistances of the individual cells due to fabrication variations. The fluctuations in R_{hf} over time have been explained as follows: "Cell 1 initially has a slightly higher high-frequency resistance, which could be explained by a higher contact resistivity due to deviations in the fabrication process. However, there is no significant impact on the cell voltage. For the first three measurements, the high-frequency resistances show a slight decline due to membrane wetting with product water. For the measurement at 30 min this effect continues only for cell 2, whereas the resistance rises in the other cells. The parallel gas streams in the stack are one possible explanation. A complete blocking of the gas channels of cell 2 with water would increase the gas flow rates in the other cells, drying them. The pressure release impulse applied at a runtime of 44 min opens up the gas channels of cell 2 again and a dehydration of the membrane sets in 3 min later, raising the high-frequency resistance of cell 2 and lowering those of the other cells. The effect of drying and wetting is strongest in cell 3" [38].

6.1.5 Localized EIS

Brett et al. [39] first reported localized impedance measurement over a wide frequency range in a PEM fuel cell in 2003. Two years later Hakenjos et al. [40] published their work on localized EIS. Recently, Schneider and Scherer patented their fast, locally resolved EIS technique for PEMFCs [41]. Localized impedance measurement can illustrate reactant starvation along the flow channel. This AC impedance technique provides a new dimension of information, helps to monitor fuel cell performance, and is a useful tool for flow channel design. Localized AC impedance also has advantages over conventional EIS measurement because the latter is performed on the entire fuel cell, and the bulk impedance is measured under the assumption that there is an even distribution of reactant and current generation. In reality, the local conditions of the fuel cell can vary dramatically due to hardware issues (such as manufacturing inconsistencies and edge effects) and operating conditions (such as temperature, pressure, and flooding).

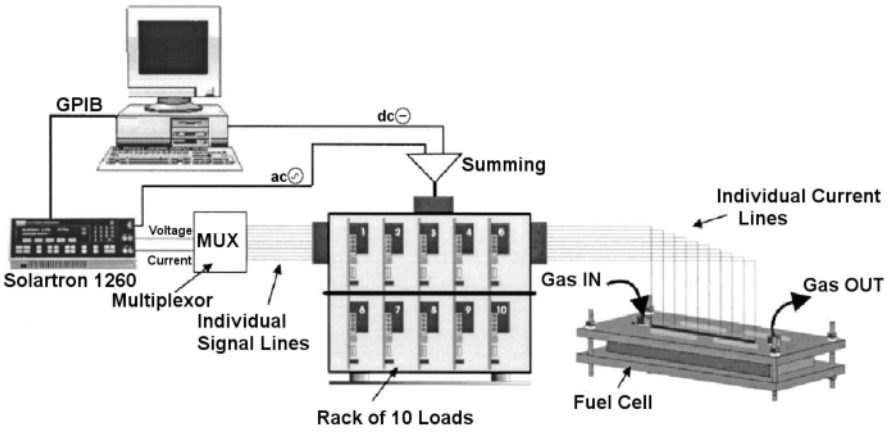

Figure 6.40. Diagram of experimental setup for making localized impedance measurements [39]. (Reproduced by permission of ECS—The Electrochemical Society, from Brett DJL, Atkins S, Brandon NP, Vesovic V, Vasileiadis N, Kucernak A. Localized impedance measurements along a single channel of a solid polymer fuel cell.)

Figure 6.40 shows the system configuration for making localized impedance measurements. The fuel cell is specially designed with a single flow channel (110 mm long, 2 mm wide, and 1 mm deep) at the cathode. The channel has 10-segment current collectors running through their own electric circuits. The experimental setup for localized impedance measurements requires sufficient channels for simultaneous impedance measurement of the local regions of the fuel cell and the local currents or potentials, and independent synchronized measurement of the response.

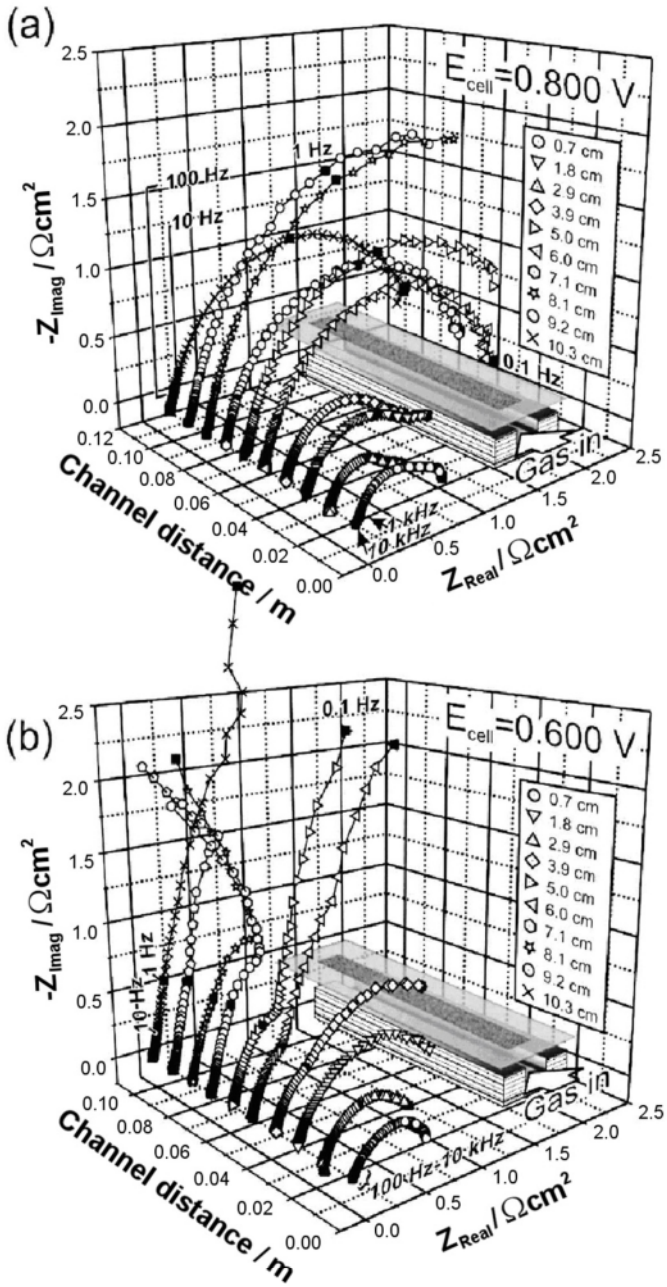

Figure 6.41. Complex plane EIS plots as a function of distance along the channel at cell potentials of *a* 0.8 V and *b* 0.6 V [39]. (Reproduced by permission of ECS—The Electrochemical Society, from Brett DJL, Atkins S, Brandon NP, Vesovic V, Vasileiadis N, Kucernak A. Localized impedance measurements along a single channel of a solid polymer fuel cell.)

Figure 6.41*a* and *b* shows the 3D Nyquist plots along channels operated at 0.8 and 0.6 V, respectively. It is obvious that the localized EIS response provides more detailed information than the conventional measurement. At 0.8 V, the arc radius increases with distance along the channel due to oxygen depletion, but the EIS profile at the end of the channel does not follow the trend due to edge effects. At 0.6 V, the first four arcs show the same trend as depicted at 0.8 V, but the subsequent arcs exhibit a directional change, with a vertical feature for the first arcs before these bend back, then shift again to the original direction due to edge effects. This deviation has been attributed to enhanced reactant starvation caused by excessive consumption of oxygen at the higher overpotentials at the beginning of the channel. The transformation of the impedance plot into a negative resistance loop (the seventh and eighth plots) was proven to correspond to a decrease in current, following a maximum current caused by acute oxygen starvation; during the measurement of the polarization curve, greater reactant consumption resulted in a current inversion at high overpotential. So it has been concluded that the high-frequency feature is attributable to the membrane conductivity and reaction kinetics, while the low-frequency feature is related to the oxygen diffusion limitation caused by fuel starvation, which corresponds to the reactant flow rate in the channel.

It is also observable that there is no notable difference between the membrane resistances along the channel at both potentials, which suggests that the external operating parameters either do not affect the membrane or affect the membrane uniformly along the channel (a thin Nafion® 112 membrane was used in Brett et al.'s work [39]).

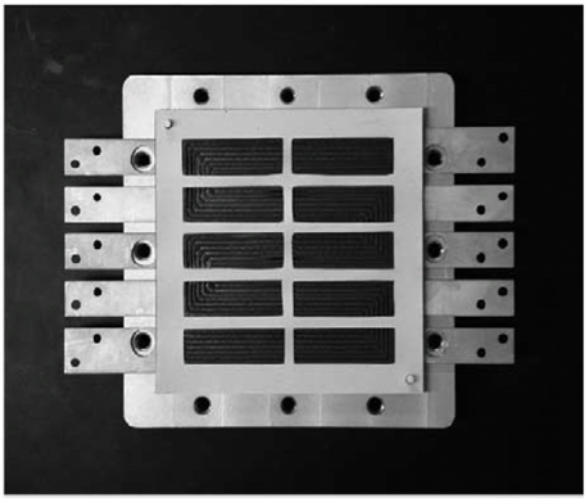

Figure 6.42. Picture of the anode configuration for the fourth-generation segmented cell designed by LANL [43]. (Reprinted from Journal of Power Sources, 123(2), Bender G, Wilson MS, Zawodzinski TA. Further refinements in the segmented cell approach to diagnosing performance in polymer electrolyte fuel cells, 163–71, ©2003, with permission from Elsevier and the authors.)

Another novel fuel cell design concept, similar to the above configuration, is the segmented cell. This contains several smaller electrodes instead of the traditionally used single larger electrode. The current, voltage, and resistance of each electrode can be measured independently. The segmented cell for PEMFCs was first introduced by Cleghorn et al. [42], and subsequent generations were designed by the German Aerospace Centre and Ballard Power Systems, Inc. [43]. Improvements of the fourth-generation segmented cell designed by LANL (Los Alamos National Laboratory) include the ability to measure the current, voltage, and resistance simultaneously rather than sequentially. This configuration aids in the diagnosis of the current distribution across the surface of an electrode, as well as the high-frequency resistance (HFR) distribution and spatial AC impedance spectroscopy. Figure 6.42 shows the anode configuration for the fourth-generation segmented cell. There are 10 anode segments, each with an active surface area of 7.71 cm^2, whereas the cathode consists of a single segment with an active area of 104 cm^2. The measurement setup of the segmented cell is presented in Figure 6.43.

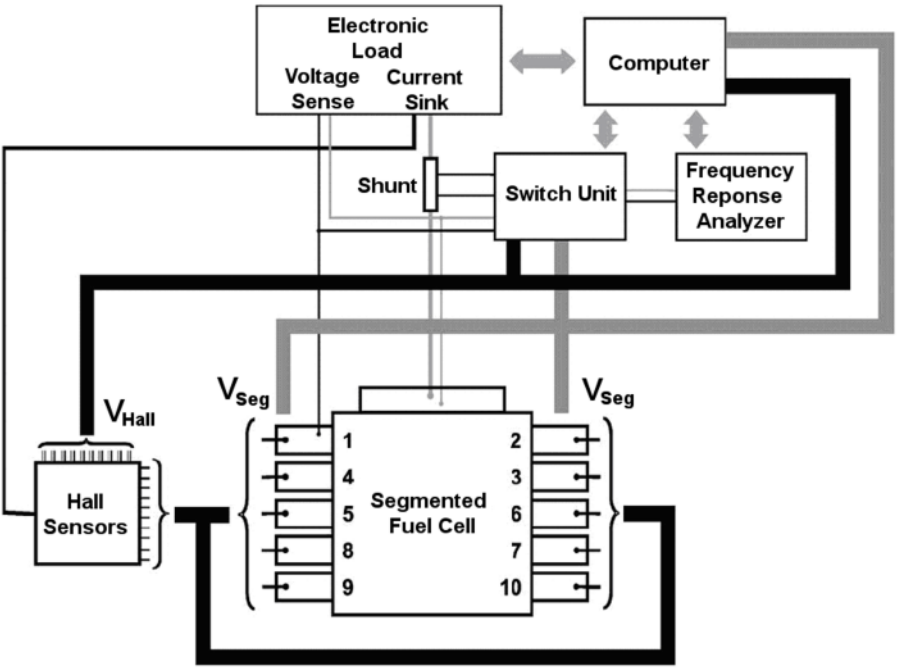

Figure 6.43. Schematic of a segmented cell measurement setup [43]. (Reprinted from Journal of Power Sources, 123(2), Bender G, Wilson MS, Zawodzinski TA. Further refinements in the segmented cell approach to diagnosing performance in polymer electrolyte fuel cells, 163–71, ©2003, with permission from Elsevier and the authors.)

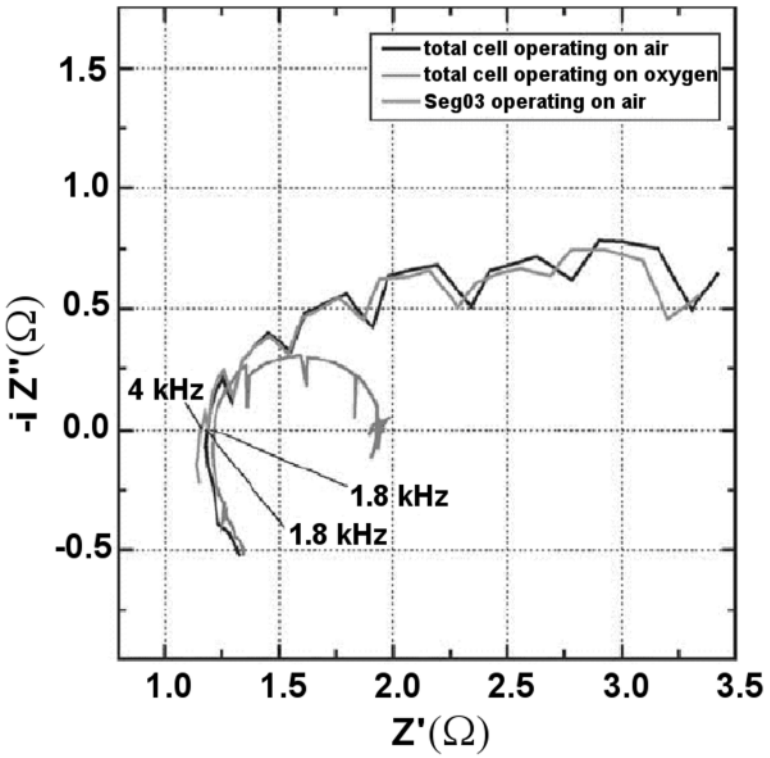

Figure 6.44. Nyquist plot of AC impedance spectra of the segmented cell measured during different operating conditions. The plotted data of the total cell and segment Seg03 is uncorrected for the employed voltage and current gains [43]. (Reprinted from Journal of Power Sources, 123(2), Bender G, Wilson MS, Zawodzinski TA. Further refinements in the segmented cell approach to diagnosing performance in polymer electrolyte fuel cells, 163–71, ©2003, with permission from Elsevier and the authors.)

The LANL segmented cell design represents a significant improvement over previous segmented cell systems. The measurement setup is very effective for spatial fuel cell measurements. Unfortunately, the LANL researchers did not provide ample impedance data. Figure 6.44 shows the Nyquist plots for the AC impedance of the total cell with air and pure oxygen over a frequency range 1 Hz to 10 kHz, and of the segmented cell with air, Seg03, which exhibits the individual segment. An explanation of the spectra was not provided by the LANL researchers. The zero-crossing frequencies for the total cell and the individual segment measurement were 1.8 and 4.0 kHz, respectively. This result indicates that there is an additional inductive component associated with individual segment impedances.

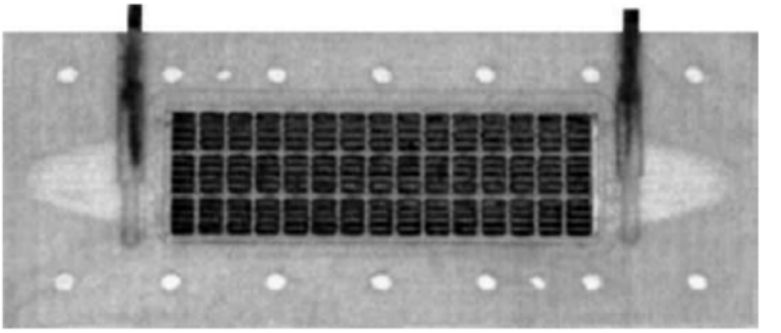

Figure 6.45. Test fuel cell with straight channel design [40]. (Reprinted from Journal of Power Sources, 145(2), Hakenjos A, Hebling C. Spatially resolved measurement of PEM fuel cells, 307–11, ©2005, with permission from Elsevier and the authors.)

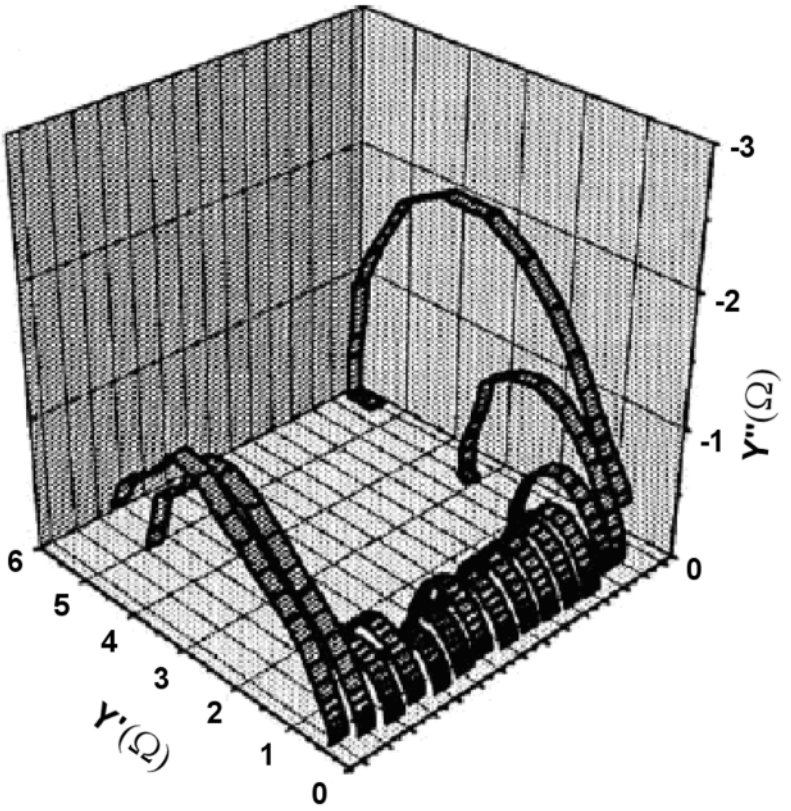

Figure 6.46. Local impedance spectra of the middle row of the straight channel cell [40]. (Reprinted from Journal of Power Sources, 145(2), Hakenjos A, Hebling C. Spatially resolved measurement of PEM fuel cells, 307–11, ©2005, with permission from Elsevier and the authors.)

Another example of localized EIS is the work of Hakenjos et al. [40]. The cell used is shown in Figure 6.45. To minimize boundary effects, the flow fields on both the anode and cathode were composed of 14 parallel straight channels. Each 100-mm-long channel was 1 mm wide with 1 mm ribs in between. This flow-field geometry had an active area of 29 cm^2. For current distribution measurements, one flow-field was segmented. Forty-five graphite segments, arranged in three rows of 15, were integrated into a plastic endplate. Each segment was connected with a separate current line and a voltage sensor. Figure 6.46 shows the local impedance spectroscopy for the middle row of segments. A row of impedance spectra is clearly seen. The high-frequency resistance of the measurement was evaluated and compared with the simulated membrane protonic resistivity at a 300 sccm flow rate, as shown in Figure 6.47, with very good agreement. Both the measurement and the simulation showed a high protonic resistance at the inlet that decreased along the channel due to increased membrane humidity.

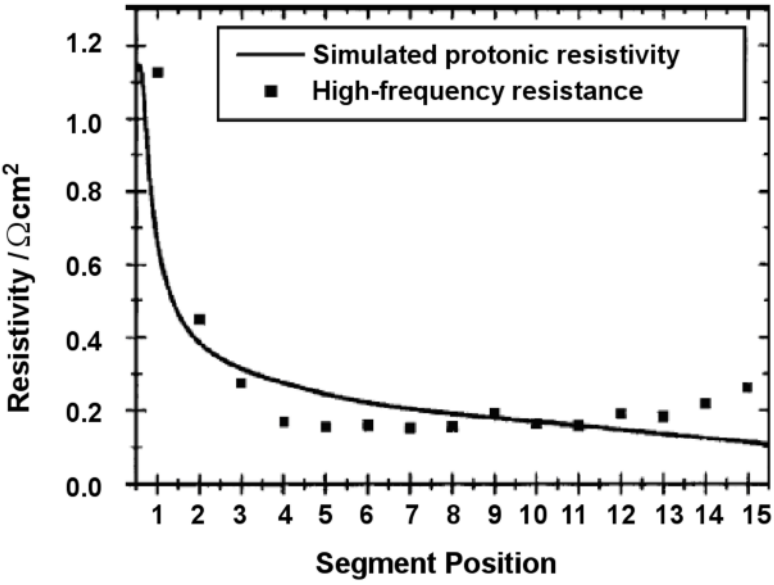

Figure 6.47. Extracted high-frequency resistivity of the impedance measurement shown in Figure 6.46, compared with the simulated membrane resistivity of the 300 sccm simulation [40]. (Reprinted from Journal of Power Sources, 145(2), Hakenjos A, Hebling C. Spatially resolved measurement of PEM fuel cells, 307–11, ©2005, with permission from Elsevier and the authors.)

6.1.6 EIS at High Temperatures

6.1.6.1 High PEM Fuel Cell Advantage and Characteristics of its AC Impedance

PEM fuel cells operated at high temperatures (> 100°C) have several advantages over those operated at lower temperatures: (1) faster electrochemical kinetics, (2) improved and simplified water management, (3) effective thermal management,

and (4) improved contaminant tolerance. From 100°C to 120°C, the saturated vapour pressure increases from 1 atm to 2 atm. So at high operating temperatures, the possibility of produced water condensation in PEM fuel cells is low; in addition, water flooding is not a problem at high current densities. However, several major challenges remain. For example, at higher operating temperatures, membrane dehydration and the consequent decrease in proton conductivity is a significant issue. MEA degradation is also accelerated because the size of platinum particles increases and carbon oxidation speeds up at high operating temperatures. AC impedance can be used to analyze conductivity, kinetics, and mass transport at high operating temperatures.

Figure 6.48 shows performance at 120°C under 100% RH and 30 psig back-pressure, along with the results at 80°C and 100°C for comparison. The performance visibly decreases with increasing operating temperature in the current density range being studied. The cell voltages at 1 A/cm^2 were 0.67 V at 80°C, 0.654 V at 100°C, and 0.637 V at 120°C. At higher current densities, performance decreased quickly at 80°C due to water flooding. Figure 6.49 shows a typical in situ AC impedance spectrum at the same three temperatures. The kinetic resistance increased from 0.095 Ω cm^2 to 0.101 Ω cm^2 when the temperature increased from 80°C to 120°C. However, the mass transfer resistance decreased from 0.077 Ω cm^2 to 0.072 Ω cm^2 over the same temperature range.

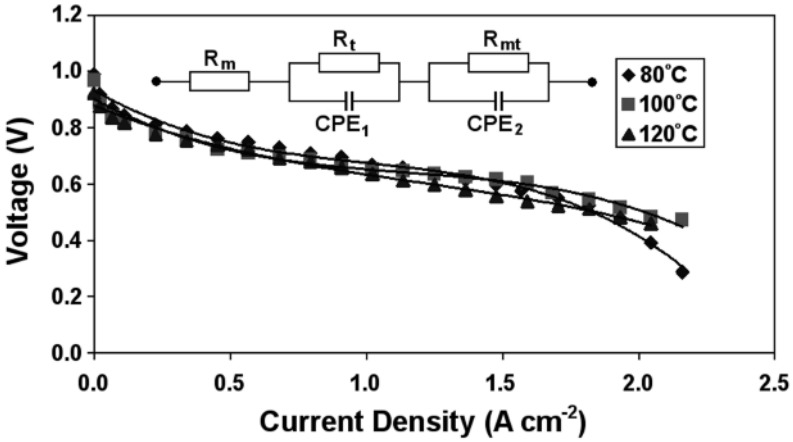

Figure 6.48. Performance at 80°C, 100°C, and 120°C under 100% RH and 30 psig [44]. (Reproduced by permission of ECS—The Electrochemical Society, and of the authors, from Tang Y, Zhang J, Song C, Liu H, Zhang J, Wang H, MacKinnon S, Peckham T, Li J, McDermid S, Kozak P, Temperature dependent performance and in situ AC impedance of high temperature PEM fuel cells using the Nafion112 membrane.)

For the Nafion®-based PEM fuel cells, the membrane conductivity decreased with increasing operating temperatures. The resistance points on the Re axis at the high-frequency end in Figure 6.49 can be treated approximately as the membrane through-plane resistance in PEM fuel cells; other resistances, including the ionic resistance of the Nafion® ionomer and the cell contact resistance, may have made

some minor contribution. Figure 6.50 shows the membrane resistance as a function of current density at different fuel cell operating temperatures. The membrane resistance remained roughly constant with current density, but it did increase with increasing temperature. For example, an increase in temperature from 80 to 120°C produced a 10–15% increase in membrane resistance.

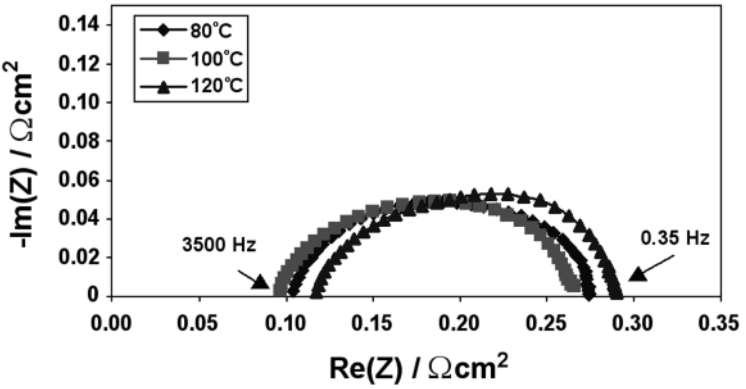

Figure 6.49. In situ AC impedance spectroscopy at a frequency range of 3500 to 0.1 Hz at 0.91 A/cm^2, 100% RH, and 30 psig pressure at 80°C, 100°C, and 120°C [44]. (Reproduced by permission of ECS—The Electrochemical Society, and of the authors, from Tang Y, Zhang J, Song C, Liu H, Zhang J, Wang H, MacKinnon S, Peckham T, Li J, McDermid S, Kozak P, Temperature dependent performance and in situ AC impedance of high temperature PEM fuel cells using the Nafion112 membrane.)

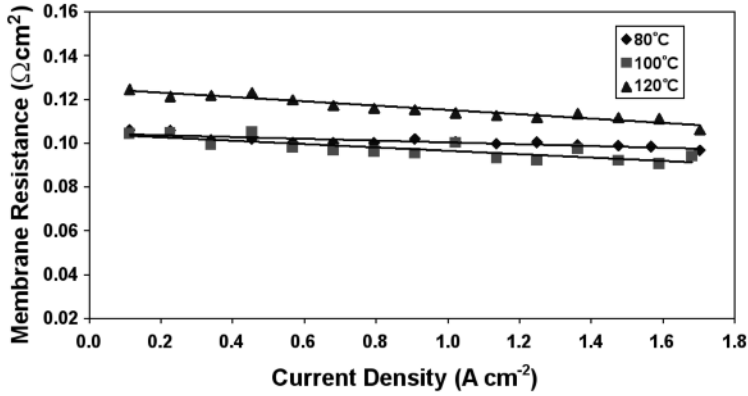

Figure 6.50. Nafion® through-plane resistance as a function of current density at three fuel cells operating at 80°C, 100°C, and 120°C; 100% RH for both anode and cathode, and 30 psig back-pressure with hydrogen and air feeding with a Nafion® 112-based baseline MEA [44]. (Reproduced by permission of ECS—The Electrochemical Society, and of the authors, from Tang Y, Zhang J, Song C, Liu H, Zhang J, Wang H, MacKinnon S, Peckham T, Li J, McDermid S, Kozak P, Temperature dependent performance and in situ AC impedance of high temperature PEM fuel cells using the Nafion112 membrane.)

Figure 6.51 shows the charge-transfer resistance as a function of current density at 80, 100, and 120°C. Initially, the charge resistance decreased rapidly with current density, which is the behaviour anticipated by AC impedance theory. The temperature also had a visible effect on charge-transfer resistance. According to electrochemical reaction kinetics, rising temperature should increase the rate of the electrode reaction, thus improving the kinetics, especially for oxygen reduction. However, Figure 6.51 depicts the opposite situation; the temperature increase caused a drop in performance. The measured electrochemical platinum surface area (EPSA) of the cathode catalyst layer decreased from 106 cm^2/cm^2 at 80°C to 59.3 cm^2/cm^2 at 120°C. This significant EPSA reduction may likely be responsible for the increase in charge-transfer resistance. Another possible cause could be the reduction of water content in the catalyst layer, especially in the Nafion® ionomer. Water content reduction at high temperatures could have had a major effect on performance; the proton supply to the electrochemical reaction sites might have become slower or insufficient, which could also have caused an increase in the charge-transfer resistance. Other effects, such as oxygen partial pressure reduction at higher temperatures and 100% RH, could also have affected oxygen reduction kinetics, resulting in an increase in charge-transfer resistance.

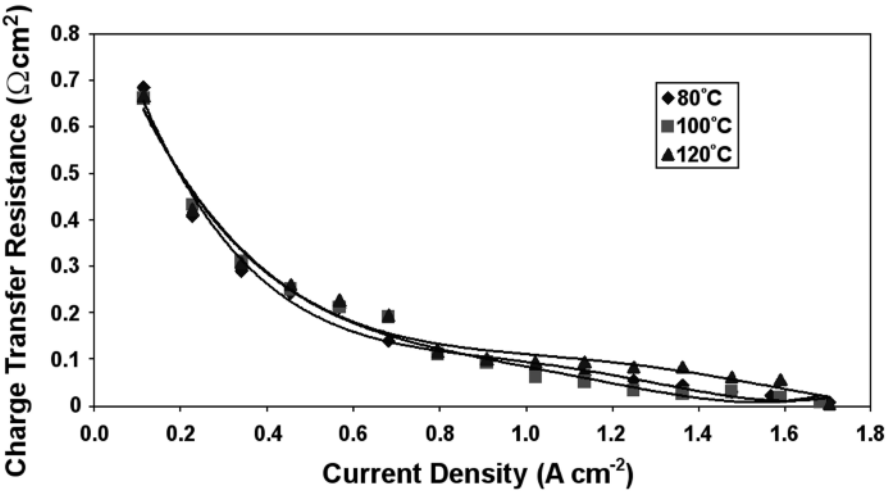

Figure 6.51. Charge-transfer resistance as a function of current density at 80°C, 100°C, and 120°C, 30 psig back-pressure, and 100% RH [44]. (Reproduced by permission of ECS—The Electrochemical Society, and of the authors, from Tang Y, Zhang J, Song C, Liu H, Zhang J, Wang H, MacKinnon S, Peckham T, Li J, McDermid S, Kozak P, Temperature dependent performance and in situ AC impedance of high temperature PEM fuel cells using the Nafion112 membrane.)

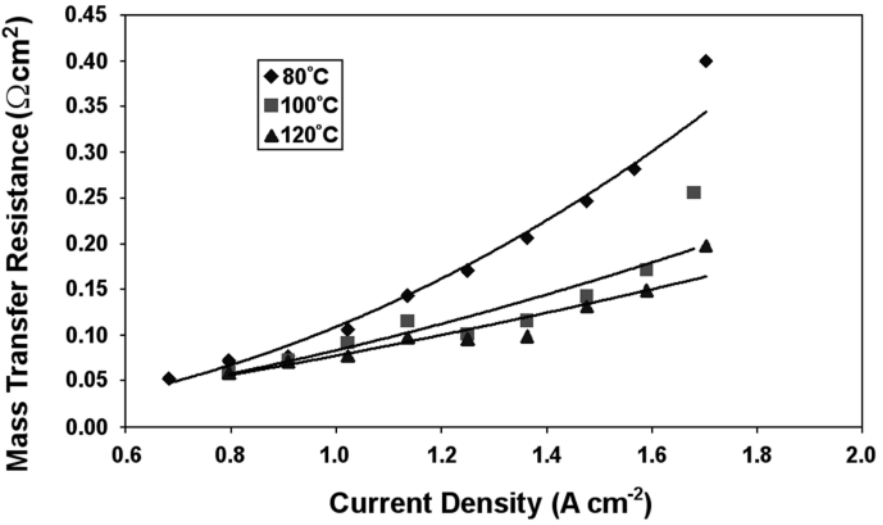

Figure 6.52. Mass transfer resistance as a function of current density at 80, 100, and 120°C, 30 psig back-pressure and 100% RH [44]. (Reproduced by permission of ECS—The Electrochemical Society, and of the authors, from Tang Y, Zhang J, Song C, Liu H, Zhang J, Wang H, MacKinnon S, Peckham T, Li J, McDermid S, Kozak P, Temperature dependent performance and in situ AC impedance of high temperature PEM fuel cells using the Nafion112 membrane.)

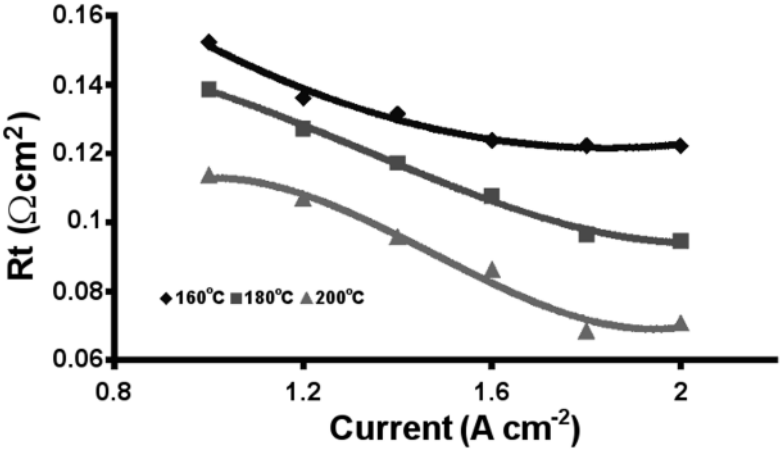

Figure 6.53. Charge-transfer resistance of a PBI-based PEMFC at different operating temperatures

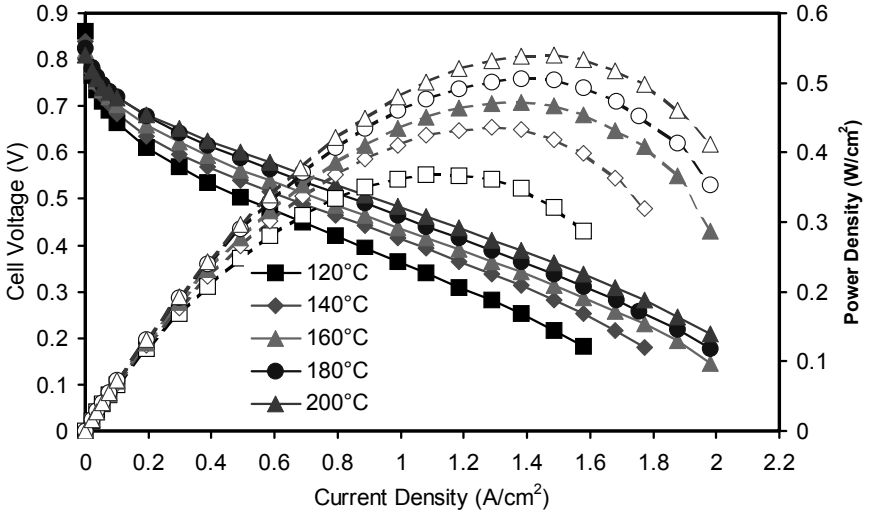

Figure 6.54. Performance of a PBI-based PEMFC at different operating temperatures [45]. (Reprinted from Journal of Power Sources, 172(1), Zhang J, Tang Y, Song C, Zhang J, Polybenzimidazole-membrane-based PEM fuel cell in the temperature range of 120–200°C, 163–71, ©2007, with permission from Elsevier.)

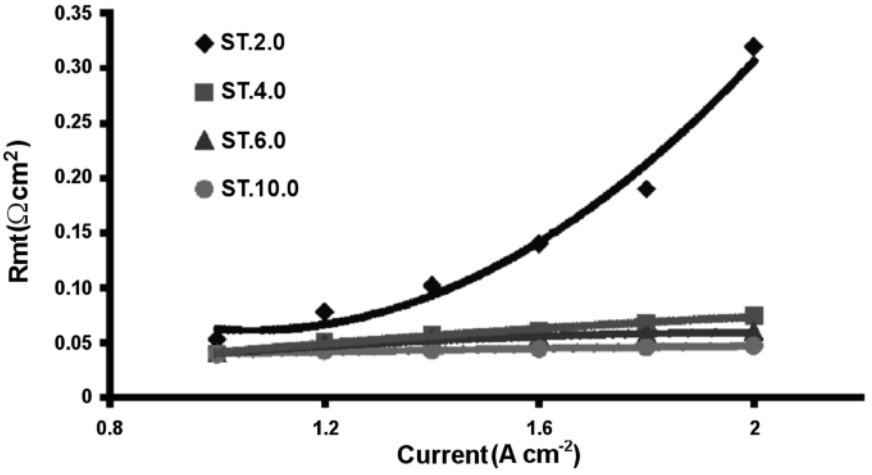

Figure 6.55. Mass transfer resistance of a PBI-based PEMFC at different air stoichiometries [45]. (Reprinted from Journal of Power Sources, 172(1), Zhang J, Tang Y, Song C, Zhang J, Polybenzimidazole-membrane-based PEM fuel cell in the temperature range of 120–200°C, 163–71, ©2007, with permission from Elsevier.)

Figure 6.52 shows mass transfer resistance as a function of current density at 80, 100, and 120°C. As the temperature increased from 80 to 120°C, mass transfer resistance decreased dramatically, which improved cell performance, especially in the high current density range. For example, at 1.36 A/cm^2, the difference in mass transfer resistance between 80°C and 120°C was about 0.1 Ω cm^2, which corresponds roughly to a performance improvement of 136 mV.

The PBI-based PEM fuel cell can operate from 120°C to 200°C without external humidification. AC impedance shows that kinetics resistance decreases at higher temperatures, as shown in Figure 6.53, which is different from the characteristics of Nafion®-based PEM fuel cells at high temperatures, but is consistent with the performance trend of the PBI-based PEM fuel cells, as shown in Figure 6.54. Although there is no humidification of the reactant streams in the operation of PBI PEM fuel cells, mass transfer issues are still observed through AC impedance, as shown in Figure 6.55.

6.1.6.2 Performance Diagnosis Based on AC Impedance

Assuming negligible anode polarization, the steady-state polarization curves can be described by a semi-empirical equation:

$$E = E_o - b\ln(I) - IR_m - m_{mt}\exp(n_{mt}I) \tag{6.14}$$

where E is the fuel cell voltage, E_o is the open circuit voltage (OCV) related constant of the fuel cell, b is the Tafel slope, I is the current density, R_m is the membrane resistance, m_{mt} is the mass transfer coefficient, and n_{mt} is the simulation parameter for curve fitting. In this equation, b ln(I) is the contribution of fuel cell reaction kinetics (dominated by oxygen reduction), IR_m is the contribution of membrane resistance, and $m_{mt}\exp(n_{mt}I)$ is the mass transfer contribution to the performance drop. These definitions may only be accurate for the special case where the AC frequency is very low. The CPE_1 and CPE_2 will become very large compared with the values of R_t and R_{mt}. Therefore, the sum of a series of R_m, R_t, and R_{mt} values could be considered the overall internal resistance of the fuel cell. Thus, the internal AC impedance of the cell at a constant temperature can be obtained by mathematical operation on Equation 6.14, assuming that E_o remains constant over the entire current density range:

$$-\frac{\partial E}{\partial I} = \frac{b}{I} + R_m + m_{mt}n_{mt}e^{n_{mt}I} \tag{6.15}$$

where $R_{cell} = \partial E/\partial I$ can be defined as the internal fuel cell AC impedance and b/I can be defined as the charge-transfer resistance, and expressed as

$$R_t = \frac{b}{I} \tag{6.16}$$

where b is the Tafel slope, and can be expressed as $\frac{RT}{\alpha n_\alpha F}$; R is the gas constant (8.314 J/(K·mol)), T is the temperature (K), α is the charge transfer coefficient of the electrode reaction, n_α is the electron number in the rate-determining step, and F is the Faradaic constant (96487 C). R_m in Equation 6.15 can be defined as the membrane resistance and $m_{mt} n_{mt} e^{n_{mt} I}$ can be defined as the mass transfer resistance, R_{mt}, and expressed as

$$R_{mt} = m_{mt} n_{mt} e^{n_{mt} I} \tag{6.17}$$

Using the above definitions, Equation 6.15 can be rewritten as

$$R_{cell} = R_t + R_m + R_{mt} \tag{6.18}$$

In Equation 6.18, R_t is a function of current density and temperature, R_m is less dependent on the current density but is strongly dependent on the temperature, and R_{mt} is the mass transfer impedance, which is strongly dependent on current density and temperature. Note that this equation is only accurate at an AC impedance frequency at or near zero.

The percentage of the cell voltage drop (ΔV_{cell}%) caused by an individual resistance ($R_i = R_t$, R_m, or R_{mt}) at a constant current density can be expressed as

$$\Delta V_{cell}\% = \frac{R_i}{R_{cell}} \tag{6.19}$$

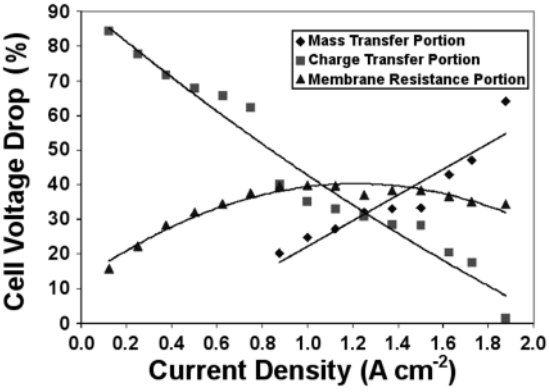

Figure 6.56. Percentage of cell voltage drop caused by charge-transfer, membrane, and mass transfer resistances, respectively, at 120°C [44]. (Reproduced by permission of ECS—The Electrochemical Society, and of the authors, from Tang Y, Zhang J, Song C, Liu H, Zhang J, Wang H, MacKinnon S, Peckham T, Li J, McDermid S, Kozak P, Temperature dependent performance and in situ AC impedance of high temperature PEM fuel cells using the Nafion112 membrane.)

Figure 6.56 shows the percentage of the cell voltage drop caused by the charge transfer, membrane, and mass transfer resistances at 120°C (see Figure 3.14 for 80°C). For both temperatures, the cell voltage reduction in the low current density range (< 0.5 A/cm^2) was dominated by charge transfer polarization, while the mass transfer polarization was dominant at high current densities (> 1.5 A/cm^2). In the current density range 1.0–1.3 A/cm^2, the three sources of polarization (charge transfer, membrane, and mass transfer) contributed almost equally to the overall voltage drop. It also shows that at 120°C, the percentage of mass transfer polarization was considerably lower than at 80°C, demonstrating that operating at high temperatures can effectively improve mass transfer in a PEM fuel cell.

The results also suggest that through AC impedance measurements, the performance drops caused by individual processes such as electrode kinetic resistance, membrane resistance, and mass transfer resistance can be correlated to either reduction or improvement in cell performance. If individual impedances are known, the contribution to the change in performance can be identified, which is very important in the design and optimization of high-temperature MEA catalyst layer components, structure down-selection, and MEA architecture.

At two different temperatures, T_1 and T_2, a rough approximation of Equation 6.18 could allow estimation of the AC impedance differences by

$$\Delta R_{cell}^{T_2-T_1} = \Delta R_t^{T_2-T_1} + \Delta R_m^{T_2-T_1} + \Delta R_{mt}^{T_2-T_1} \tag{6.20}$$

The fuel cell performance drop due to the change in internal resistance between two temperatures at a constant current density can also be estimated roughly based on Equation 6.20:

$$I\Delta R_{cell}^{T_2-T_1} = I\Delta R_t^{T_2-T_1} + I\Delta R_m^{T_2-T_1} + I\Delta R_{mt}^{T_2-T_1} \tag{6.21}$$

where $I\Delta R_t^{T_2-T_1}$ is the performance drop caused by charge-transfer resistance, $I\Delta R_m^{T_2-T_1}$ represents the drop induced by membrane resistance, and $I\Delta R_{mt}^{T_2-T_1}$ is the drop caused by mass transfer resistance. Because E_o is also temperature-dependent, the change in overall cell performance ($\Delta E_{cell}^{T_2-T_1}$) caused by a temperature increase should also include the change in E_o ($\Delta E_o^{T_2-T_1}$):

$$\Delta E_{cell}^{T_2-T_1} = \Delta E_o^{T_2-T_1} + I\Delta R_t^{T_2-T_1} + I\Delta R_m^{T_2-T_1} + I\Delta R_{mt}^{T_2-T_1} \tag{6.22}$$

As mentioned above, E_o includes several contributions, so it would not be feasible to estimate the contribution of $\Delta E_o^{T_2-T_1}$ to the overall performance drop at this time. A quantitative description of the polarization dependence of E_o would be very useful for a fundamental understanding of fuel cell performance.

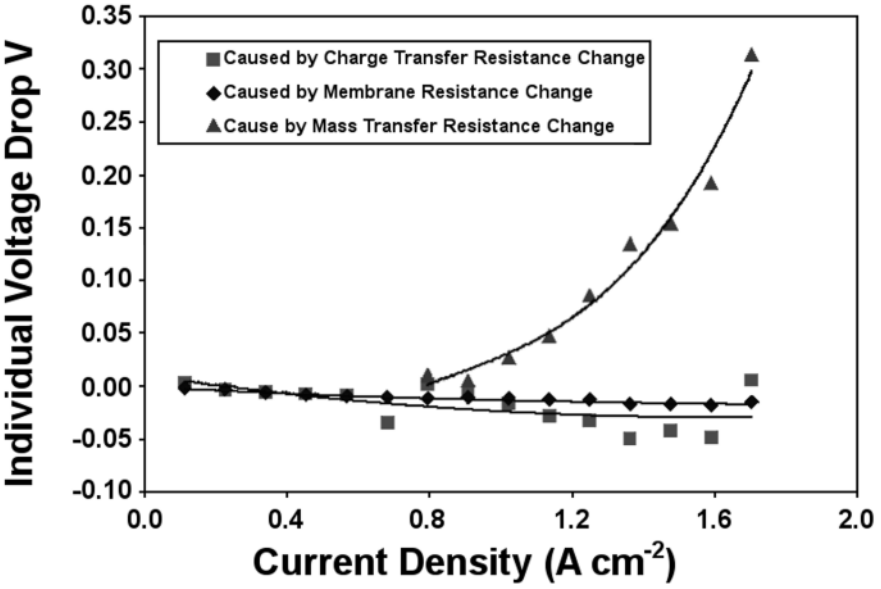

Figure 6.57. Individual performance drops within a fuel cell when the operating temperature was increased from 80°C to 120°C [44]. (Reproduced by permission of ECS—The Electrochemical Society, and of the authors, from Tang Y, Zhang J, Song C, Liu H, Zhang J, Wang H, MacKinnon S, Peckham T, Li J, McDermid S, Kozak P, Temperature dependent performance and in situ AC impedance of high temperature PEM fuel cells using the Nafion112 membrane.)

Figure 6.57 shows the fuel cell performance changes due to a temperature increase from 80°C to 120°C, based on Equation 6.22, as a function of current density. The calculation incorporates the assumption that $\Delta E_o^{T_2-T_1} = 0$. Positive values on the y-axis indicate a performance improvement at 120°C, while negative values represent a performance drop. The overall performance decline caused by the temperature increase is dominated by the membrane and charge-transfer resistances in the low current density range (< 0.9 A/cm^2). However, the mass transfer process is dominant in the high current density range (> 0.9 A/cm^2). The positive values indicate that the performance improvement is a result of improved mass transfer at high temperatures, which could be attributed to improved water management in the catalyst layers. Over the entire current density range, when the temperature is increased from 80°C to 120°C, the performance drop caused by charge-transfer resistance is less than 55 mV and the drop caused by membrane resistance is less than 20 mV. A significant overall improvement of ~350 mV can be observed at a current density of 1875 mA/cm^2 [44].

6.2 EIS Applications in DMFCs

6.2.1 Ex Situ Methanol Oxidation

6.2.1.1 Methanol Oxidation on a Polished Pt Electrode [46]
Methanol oxidation is a self-poisoning process, in which the intermediate adsorbate CO, formed from the dissociation of methanol, poisons the catalytic sites of Pt. The mechanism of methanol oxidation is as follows:

$$CH_3OH_{bulk} + Pt \rightarrow Pt\text{-}CO_{ads} + 4H^+ + 4e^- \tag{6.23}$$

$$H_2O + Pt \leftrightarrow Pt\text{-}OH_{ads} + H^+ + e^- \tag{6.24}$$

$$Pt\text{-}CO_{ads} + Pt\text{-}OH_{ads} \rightarrow CO_2 + 2Pt + H^+ + e^- \tag{6.25}$$

Understanding the oxidation mechanism is important. Impedance spectroscopy was recently used to study methanol electrooxidation, and kinetic parameters can be deduced from impedance spectra. Figure 6.58 shows an equivalent circuit that was developed for methanol oxidation on a Pt electrode, but which is common for all electrochemical reactions. In this circuit, a constant phase element was used rather than a double-layer capacitance, since a CPE is more realistic than a simple capacitor in representing the capacitive behaviour.

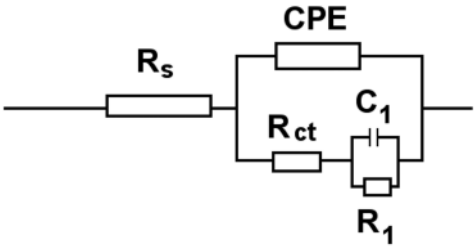

Figure 6.58. Equivalent circuit for the methanol oxidation reaction

In the circuit, R_s is the electrolyte resistance, CPE indicates the double-layer capacitance, R_{ct} is the methanol oxidation charge-transfer resistance, while R1 and C1 are the mass transfer related resistance and capacitance (mainly due to methanol adsorption or CO coverage). The physical expression of these parameters can be deduced from the reaction kinetics. In the methanol oxidation reaction, the overall charge transfer rate is the sum of each charge-transfer step (r_{ct}). The Faradaic resistance (R_f) equals the inverse of the DC polarization curve slope:

$$R_f^{-1} = \frac{di}{dE} = F\frac{dr_{ct}}{dE} \tag{6.26}$$

The dependence of the charge-transfer rate on the intermediate coverage and electrode potential gives

$$\frac{dr_{ct}}{dE} = (\frac{\partial r_{ct}}{\partial E})_{\theta} + (\frac{\partial r_{ct}}{\partial \theta})_{E} \frac{d\theta}{dE} \tag{6.27}$$

The first term in Equation 6.27 corresponds to the inverse of the charge-transfer resistance, and the second term represents the inverse of the intermediate coverage resistance (R_c):

$$R_{ct} = \frac{1}{F(\frac{\partial r_{ct}}{\partial E})_{\theta}} \tag{6.28}$$

$$R_{c} \equiv \frac{1}{F(\frac{\partial r_{ct}}{\partial \theta})_{E} \frac{d\theta}{dE}} \tag{6.29}$$

According to the equivalent circuit, at zero frequency the Faradaic resistance equals the sum of the charge-transfer resistance and the mass transfer resistance:

$$R_{f} = R_{ct} + R_{1} \tag{6.30}$$

Combining Equations 6.26 to 6.29, the following equation can be obtained:

$$R_{f}^{-1} = R_{ct}^{-1} + R_{c}^{-1} \tag{6.31}$$

Equations 6.30 and 6.31 can then be combined:

$$R_{c} = -\frac{R_{ct}(R_{ct} + R_{1})}{R_{1}} \tag{6.32}$$

where R_c indicates whether the change in coverage, induced by a change in electrode potential, increases or decreases the rate of charge transfer.

Another important parameter is the coverage relaxation time, τ, which indicates how quickly the coverage of the intermediate will relax back to its equilibrium value after a perturbation:

$$\tau \equiv \frac{R_{ct}R_{1}C}{R_{ct} + R_{1}} = \frac{-1}{\frac{N_{A}}{N}(\frac{\partial r_{\theta}}{\partial \theta})_{E}} \tag{6.33}$$

where $R_c\tau$ determines whether the second semicircle, observed in the complex plane for systems containing one adsorbed intermediate, is inductive or capacitive. Equation 6.33 is deduced from the current change associated with the voltage perturbation of a chemical reaction. A detailed deduction process can be found in reference [47].

Qualitatively, AC impedance spectra obtained at different potentials show that the phase angle, capacitance, and impedance spectra change with potential. Figure 6.59 presents the phase angle change with potential on a polycrystalline Pt electrode in 0.5 M H_2SO_4, with and without methanol. The presence of methanol leads to a change of phase angle with potential. Methanol oxidation on the unpoisoned electrode surface is followed by an abrupt decrease in the phase angle. A phase angle larger than 90° or less than 0° indicates the presence of pseudo-inductance due to a negative charge-transfer resistance, which usually results from passivation of the electrode surface. Passivation may be caused by the reversible formation of oxide species or chemisorbed hydroxyl radicals.

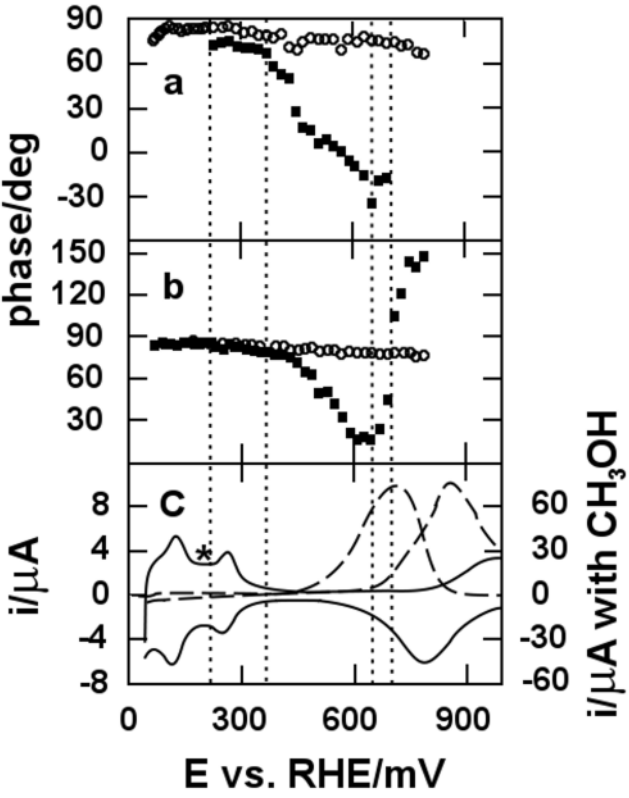

Figure 6.59. Comparison of the AC phase measured at *a* 0.06 Hz and *b* 1 Hz with *c* the cyclic voltammetry of smooth polycrystalline platinum in 0.5 M H_2SO_4 with (squares and dashed line) and without (circles and solid line) 0.5 M CH_3OH. Sweep rate: 50 mV/s [46]. (Reprinted with permission from Journal of Physical Chemistry B 2001:105(5):1012–25. ©2001 American Chemical Society.)

The change in capacitance with changing potential can also provide valuable information. The series capacitance is given by

$$C_s = -1/(Z''\omega) \tag{6.34}$$

where C_s is the series capacitance, Z'' is the imaginary impedance, and ω is the frequency.

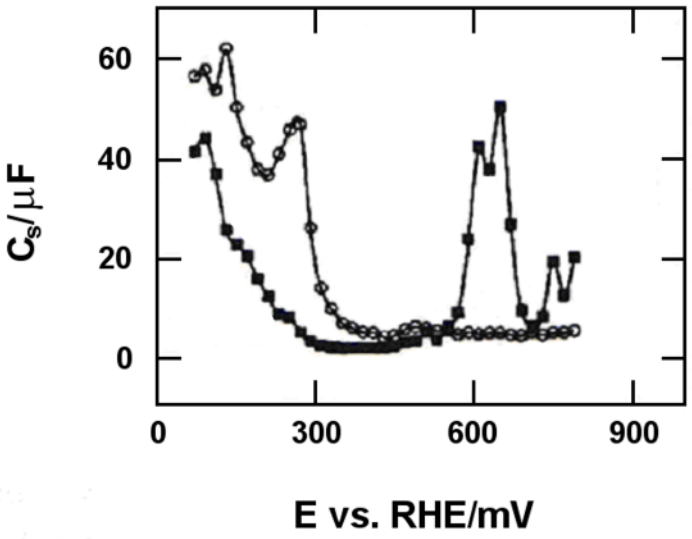

Figure 6.60. Series capacitance at 1 Hz obtained from the impedance of smooth polycrystalline Pt in 0.5 M H_2SO_4 with (squares) and without (circles) 0.5 M CH_3OH [46]. (Reprinted with permission from Journal of Physical Chemistry B 2001:105(5):1012–25. ©2001 American Chemical Society.)

Figure 6.60 shows the capacitance change with potential. In the presence of methanol, the capacitance due to hydrogen adsorption decreases abruptly at certain potentials (200–350 mV) because the adsorbed methanol blocks hydrogen adsorption. On the other hand, a capacitance increase at high potentials (430–650 mV) indicates dissociative methanol adsorption.

Figure 6.61 shows the four parameters (R_f, R_{ct}, R_c, and τ) with potential. In the region of 370–600 mV versus RHE, the inverse of the Faradaic resistance and charge-transfer resistance versus electrode potential gives the Tafel slope. The changing features in these plots indicate a change in the mechanism of methanol electrooxidation.

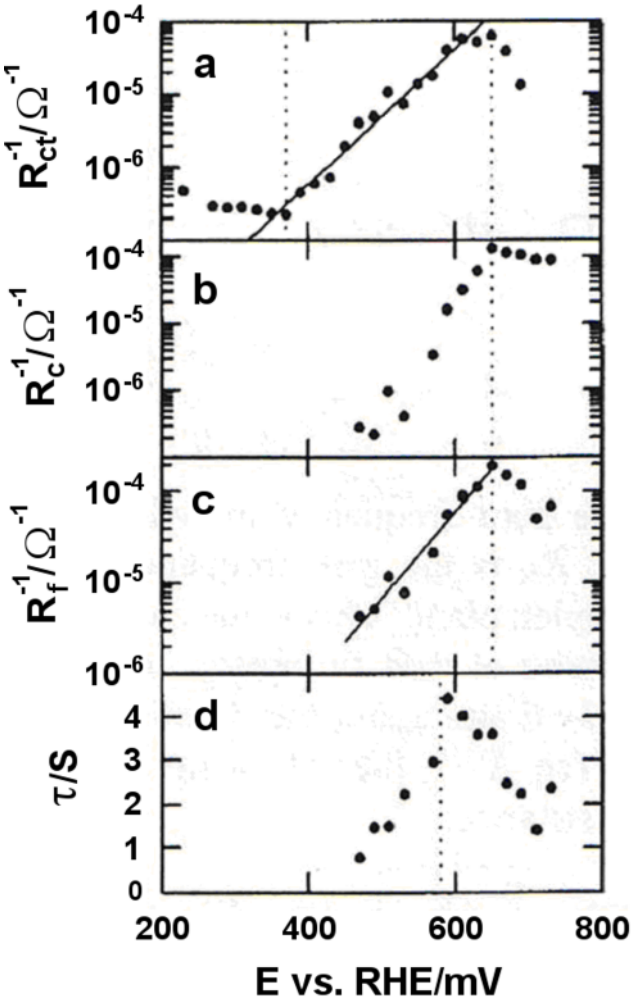

Figure 6.61. Parameters plotted as a function of electrode potential. Data were obtained by fitting the impedance spectra to Figure 6.58 [46]. (Reprinted with permission from Journal of Physical Chemistry B 2001:105(5):1012–25. ©2001 American Chemical Society.)

Quantitative results can also be obtained by fitting the impedance spectra using the equivalent circuit shown in Figure 6.58. Physical parameters obtained from the fitting are summarized in Table 6.1.

Table 6.1. Physical parameters obtained from impedance spectroscopy of the electrooxidation of methanol [46]. (Reprinted with permission from Journal of Physical Chemistry B 2001:105(5):1012–25. ©2001 American Chemical Society.)

	R_f^{-1}	R_{ct}^{-1}	R_c^{-1}	t
Physical expression	$\frac{di}{dE}$	$F\left(\frac{\partial r_{ct}}{\partial E}\right)_\theta$	$F\left(\frac{\partial r_{ct}}{\partial \theta}\right)_E \frac{d\theta}{dE}$	$-\frac{N}{N_A}\left(\frac{\partial r_\theta}{\partial \theta}\right)_E^{-1}$
Circuit definition	$\frac{1}{R_{ct}+R_1}$	$\frac{1}{R_{ct}}$	$-\frac{R_1}{R_{ct}(R_{ct}+R_1)}$	$\frac{R_{ct}R_1C}{R_{ct}+R_1}$

Impedance spectra can also be used to obtain the adsorption coverage of CO, the reaction rates for CO formation and oxidation, and the effect of CO adsorption on hydrogen oxidation. In the presence of CO adsorption, H adsorption and oxidation rate can be deduced:

$$H^+_{(aq)} + e^- \leftrightarrow H_{(ads)} \tag{6.35}$$

The charge-transfer resistance of this reaction is given by the following equation:

$$R_{ct} = \frac{1}{F(\frac{\partial r_{ct}}{\partial E})_{\theta_H}} \tag{6.36}$$

Assuming the Butler–Volmer equation and Langmuir adsorption isotherm hold for this reaction, the charge-transfer rate in the presence of CO adsorption is

$$r_{ct} = \frac{N}{N_A}\{k_{-1}\theta_H \exp[(1-\beta)fE] - k_1(1-\theta_H-\theta_I)c_{H^+}\exp(-\beta fE)\} \tag{6.37}$$

where $k_{-1}$and k_1 are the rate constants for adsorption and desorption, respectively, θ_H is the hydrogen coverage, θ_I is the CO coverage, β is the charge transfer coefficient, and $f = \frac{F}{RT}$.

The exchange rate constant is defined as

$$k_0 \equiv k_1 c_{H^+}\exp[-\beta f E_{0.5}] = k_{-1}\exp[(1-\beta)fE_{0.5}] \tag{6.38}$$

where $E_{0.5}$ is the electrode potential at a steady state in which half of the unblocked sites were occupied with hydrogen. Thus,

$$r_{ct} = k_0 \frac{N}{N_A}\{\theta_H \exp[(1-\beta) f(E-E_{0.5})] - (1-\theta_H-\theta_I)\exp[-\beta f[E-E_{0.5}]\} \tag{6.39}$$

At steady state, the hydrogen coverage can be expressed as

$$\theta_H = \frac{1-\theta_I}{1+\exp[f(E-E_{0.5})]} \tag{6.40}$$

The charge-transfer resistance of hydrogen oxidation is given as

$$R_{ct}^{-1} = Fk_0 f(1-\theta_I)(\frac{N}{N_A})\frac{\exp[(1-\beta) f(E-E_{0.5})]}{1+\exp[f(E-E_{0.5})]} \tag{6.41}$$

The coverage of CO can be obtained from the following reaction:

$$CH_3OH \rightarrow I \rightarrow \text{product} \tag{6.42}$$

$$\frac{d\theta_I}{dt} = k_a(1-\theta_H-\theta_I) - k_d(1-\theta_H-\theta_I)\theta_I \tag{6.43}$$

Together with Equation 6.40, solution of this equation gives CO coverage as follows:

$$\theta_I = \frac{1-\exp[\frac{\exp[(f(E-E_{0.5})]}{1+\exp[f(E-E_{0.5})]}(k_d-k_a)t]}{1-\frac{k_d}{k_a}[\frac{\exp[f(E-E_{0.5})]}{1+\exp[f(E-E_{0.5})]}(k_d-k_a)t]} \tag{6.44}$$

Combining the cyclic voltammogram, which provides the number of surface atoms, with fitting of the time-dependent impedance spectra obtained after adding methanol to the sulphuric solution (using Equations 6.41 and 6.44) produces the kinetic parameters of methanol oxidation. Figure 6.62 shows these values at different potentials.

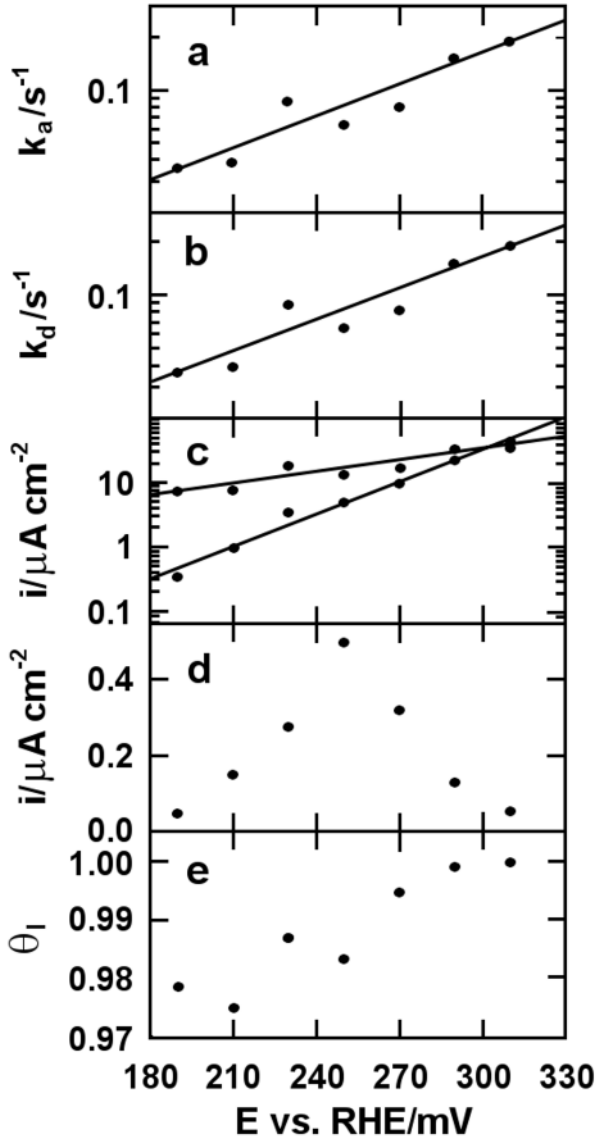

Figure 6.62. Kinetic parameters obtained by fitting the inverse charge-transfer resistance for hydrogen adsorption to the kinetic model [46]. (Reprinted with permission from Journal of Physical Chemistry B 2001:105(5):1012–25. ©2001 American Chemical Society.)

6.2.1.2 Methanol Electrooxidation on Pt/C Catalysts [48, 49]

Methanol oxidation by Pt/C catalysts more closely mimics the operating environment in a real DMFC. The impedance spectra characteristics of methanol oxidation on Pt/C thin films coated on a glassy carbon electrode are dependent on the potential, as shown in Figures 6.63 and 6.64. Below 0.4 V, the diameter of the semicircle decreases with increasing potential. However, the impedance spectra obtained at potentials larger than 0.4 V (0.41 and 0.415 V) show a different trend, where the diameters increase with increasing potential. Further increases in the applied potential lead to the presence of impedance spectra in quadrants II and III. Additionally, an inductance loop is observed at potentials larger than 0.3 V.

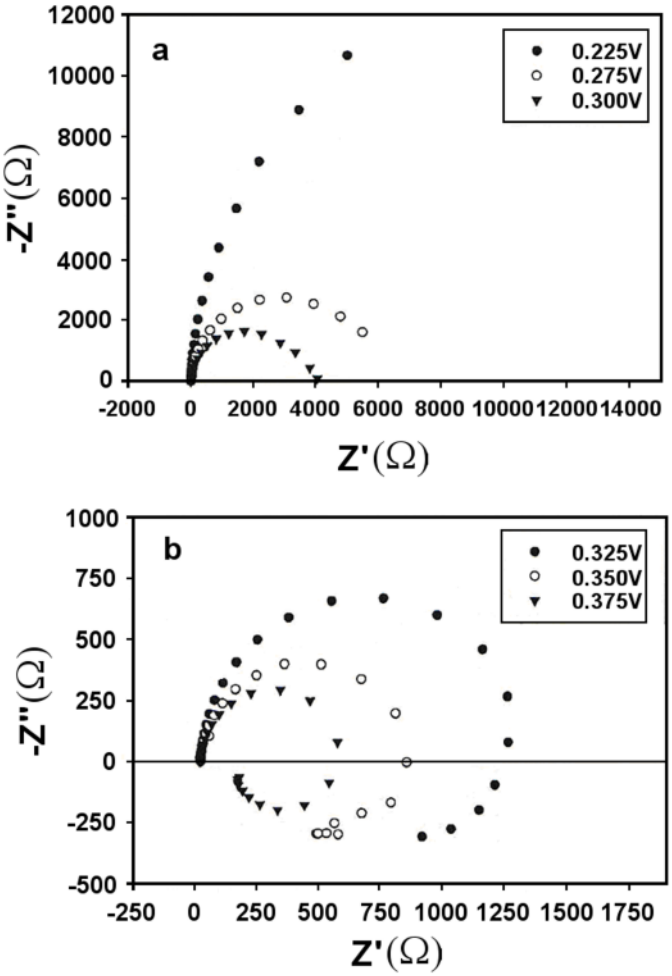

Figure 6.63. Impedance spectra as a function of applied potential *a* below 0.300 V and *b* at 0.325–0.375 V [48]. (Reproduced by permission of ECS—The Electrochemical Society, and of the authors, from Hsing IM, Wang X, Leng YJ. Electrochemical impedance studies of methanol electro-oxidation on Pt/C thin film electrode.)

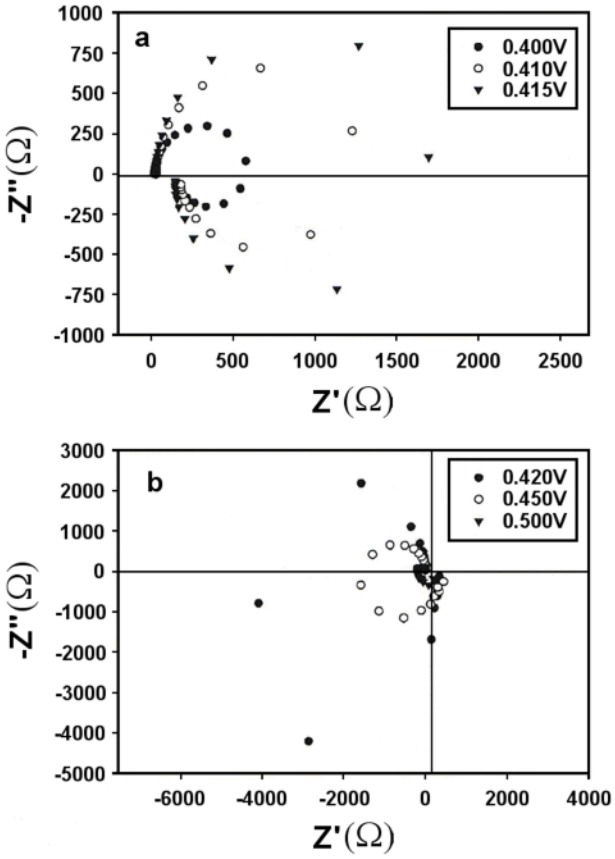

Figure 6.64. Impedance spectra as a function of applied potential at *a* 0.400–0.415 V and *b* above 0.420 V [48]. (Reproduced by permission of ECS—The Electrochemical Society, and of the authors, from Hsing IM, Wang X, Leng YJ. Electrochemical impedance studies of methanol electro-oxidation on Pt/C thin film electrode.)

The theoretical model for methanol electrooxidation on a Pt/C thin-film electrode is based on the model shown in the previous section. The competitive adsorption between hydrogen and CO was not considered in this case, as only anode potentials higher than 0.225 V were taken into account; the adsorbed species involved were CO_{ads} and OH_{ads}, defined as θ_1 and θ_2, respectively.

The reaction mechanism is the same as that shown in Section 6.2.1.1. According to Jarvi and Stuve [50], an exponent of 5 should be used for Reaction 1 in the case of there being one site for CO and one for H. Assuming the Tafel relation holds for all three steps (see the previous section), the reaction rate can be expressed as

$$\upsilon_1 = k_1 C_m (1 - \theta_1 - \theta_2 - \theta_0)^5 \exp(\frac{E}{b_1}) \tag{6.45}$$

$$\upsilon_2 = k_2 C_w (1-\theta_1-\theta_2-\theta_0)\exp(\frac{E}{b_2}) - k_{-2}\theta_2 \exp(\frac{-E}{b_2}) \tag{6.46}$$

$$\upsilon_3 = k_3 \theta_1 \theta_2 \exp(\frac{E}{b_3}) \tag{6.47}$$

where b_1, b_2, and b_3 are the Tafel slope for the three step reactions. The adsorbed CO and adsorbed OH production rates thus can be written as

$$q_1 \dot{\theta}_1 = q_1 \frac{d\theta_1}{dt} = \upsilon_1 - \upsilon_3 \tag{6.48}$$

$$q_2 \dot{\theta}_2 = q_2 \frac{d\theta_2}{dt} = \upsilon_2 - \upsilon_3 \tag{6.49}$$

At steady state, Equations 6.48 and 6.49 are equal to zero, and the total current of methanol oxidation is expressed as

$$i_F = 4\upsilon_1 + \upsilon_2 + \upsilon_3 \tag{6.50}$$

The equivalent circuit is the same as shown in the previous section. The total impedance is given as

$$Z_{total} = R_s + \frac{1}{(j\omega Y_0)^n + \frac{1}{Z_F}} \tag{6.51}$$

where R_s is the electrolyte solution resistance, Y_0 and n are two components of the constant phase element, and Z_F is the Faradaic impedance. The latter is written as

$$Z_F = \frac{\Delta E}{\Delta i_F} \tag{6.52}$$

The Faradaic current is dependent on the electrode potential as well as the fractional coverage of the surface by adsorbed species. At steady state, the change in current is approximated by the first-order Taylor expansion:

$$\Delta i_F = (\frac{\partial i_F}{\partial E})_{ss} \Delta E + (\frac{\partial i_F}{\partial \theta_1})_{ss} \Delta\theta_1 + (\frac{\partial i_F}{\partial \theta_2})\Delta\theta_2 \tag{6.53}$$

Thus,

$$Z_F = \frac{1}{(\frac{\partial i_F}{\partial E})_{ss} + (\frac{\partial i_F}{\partial \theta_1})_{ss} \frac{\Delta \theta_1}{\Delta E} + (\frac{\partial i_F}{\partial \theta_2})_{ss} \frac{\Delta \theta_2}{\Delta E}} \tag{6.54}$$

This equation can be rewritten in the following form, established by C.N. Cao [51]:

$$Z_F = \frac{1}{\frac{1}{R_{ct}} + \frac{A + j\omega B}{D - \omega^2 + j\omega T}} \tag{6.55}$$

Expressions for the parameters are given in Table 6.2.

Table 6.2. Expressions for the parameters in Equation 6.55 [48]. (Reproduced by permission of ECS—The Electrochemical Society, and of the authors, from Hsing IM, Wang X, Leng YJ. Electrochemical impedance studies of methanol electrooxidation on Pt/C thin film electrode.)

Parameter	Value	
$\frac{1}{R_{ct}}$	$\left(\frac{\partial i_F}{\partial E}\right)_{ss}$	
A	$m_1 b_2 J_{12} + m_2 b_1 J_{21} - m_1 b_1 J_{22} - m_2 b_2 J_{11}$	
B	$m_1 b_1 + m_2 b_2$	
D	$J_{11} J_{22} - J_{12} J_{21}$	
T	$-(J_{11} + J_{22})$	
m_i	$\left(\frac{\partial i_F}{\partial \theta_i}\right)_{ss}$	$i = 1,2$
b_i	$\left(\frac{\partial \theta_i}{\partial E}\right)_{ss}$	$i = 1,2$
J_{ik}	$\left(\frac{\partial \theta_i}{\partial \theta_k}\right)_{ss}$	$i,k = 1,2$
θ_i	$\frac{\partial \theta_i}{\partial t}$	$i = 1,2$

Table 6.3. Values of the parameters for model simulation of the studied system [48]. (Reproduced by permission of ECS—The Electrochemical Society, and of the authors, from Hsing IM, Wang X, Leng YJ. Electrochemical impedance studies of methanol electro-oxidation on Pt/C thin film electrode.)

Parameter	Value	Remarks
Pt loading	6 μg Pt/0.125 cm^2	
Pt real area	2 cm^2	112 m^2g^{-1} Pt (E-Tek Inc.) assuming 30% utilization efficiency
q_1	420 μC cm^{-2}	published result for CO adsorption on smooth Pt (111)
q_2	210 μC cm^{-2}	assuming OH occupies one Pt site
θ_0	0.07	published result
Y_0	1.1–0.85 mF	determined from experiment; assuming linear decrease with potential
n	0.95	determined from experiment
R_s	20 Ω	determined from experiment
b_1	0.055	
b_2	0.11	
b_3	0.055	
C_m	1 M	
k_1	0.5×10^{-5} A/cm^2M	
k_2	1.08×10^{-4} A/cm^2M	
k_3	0.5×10^{-8} A/cm^2	
k_{-2}	1000 A/cm^2	

Fitting the experimental spectra using the above model, kinetic parameters of the three step reactions can be obtained, as listed in Table 6.3.

6.2.2 In Situ Anode Reaction [52]

Methanol oxidation in DMFCs has also been investigated with impedance spectroscopy. The anode impedance spectrum was usually obtained using the cathode as a reference electrode, by supplying hydrogen to the cathode, or by using a reference electrode to separate the anode and cathode impedance spectra. The

impedance spectrum of a typical DMFC anode in the kinetically controlled potential region was shown in Chapter 5, Figure 5.38. The MEA was prepared using PtRu as the anode catalyst, Pt as the cathode catalyst, and a Nafion® membrane. The anode polarization was obtained by supplying the cathode with H_2.

Three arcs are observable in the impedance spectrum. The high-frequency arc, the diameter of which decreases with increasing temperature and remains unchanged as anode potential changes, is related not to methanol oxidation, but instead to membrane resistance, double-layer capacitance, and geometrical capacitance. The medium-frequency arc is attributable to methanol oxidation. The diameter shrinks significantly as anode potential increases, indicating a decrease in charge-transfer resistance with increasing overpotential. The diameter of the arc corresponds to the charge-transfer resistance; however, the kinetic parameters of methanol oxidation are not deducible from the charge-transfer resistance. The low-frequency arc grows as methanol flow rate or methanol concentration decreases. This arc is attributable to the mass transfer of methanol; thus, the equivalent circuit of methanol oxidation at a DMFC anode is illustrated in Figure 6.65. Three RC circuits connected in series denote the three processes.

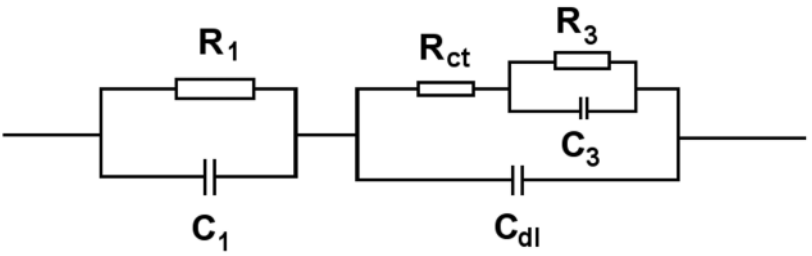

Figure 6.65. Equivalent circuit of a typical DMFC anode. R_1 and C_1 are membrane resistance and capacitance, R_{ct} and C_{dl} are charge-transfer resistance and double-layer capacitance, and R_3 and C_3 are mass-transfer-related resistance and capacitance.

The typical impedance spectra do not illustrate the inductance effect that is normally observed in DMFCs, especially at high overpotentials, where the methanol oxidation rate is higher and the CO coverage decreases with increasing potential. Figure 6.66 shows the DMFC anode impedance spectra at different current densities; the corresponding equivalent circuit is shown in Figure 6.67.

The inductance loop can be clearly seen in the spectra and the inductance should be considered in the equivalent circuit, as shown in Figure 6.67. However, the physical meaning of the parameters in Figure 6.67 is not as clear as that in Figure 6.66, except for C_d, the double-layer capacitance.

For simplification, the physical meaning of R_∞ is similar to the charge-transfer resistance, R_0 is the resistance related to CO adsorption, and the inductance (L) is related to CO adsorption and potential. For methanol oxidation, the simple mechanism can be written as follows

$$CH_3OH \rightarrow (CO)_{ads} \tag{6.56}$$

Assuming mass transfer did not occur, the net rate of production of electrons is

$$r_e = 4\upsilon_1 + 2\upsilon_2 = i/F \tag{6.57}$$

and the net rate of production of $(CO)_{ads}$ is

$$r_{CO} = \upsilon_2 - \upsilon_1 = \frac{q_{CO}}{F}\frac{d\theta}{dt} \tag{6.58}$$

where θ is the surface coverage of CO and q_{CO} is the charge required for CO adsorption to complete the coverage.

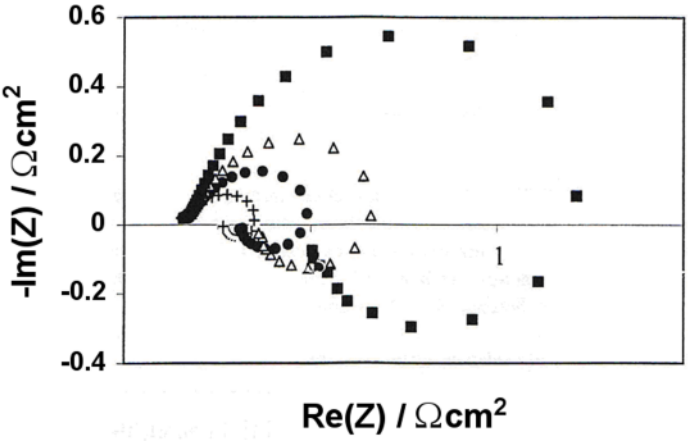

Figure 6.66. DMFC anode impedance plots obtained under pure kinetic control: (+) 500 mA/cm^2, (•) 300 mA/cm^2, (Δ) 200 mA/cm^2, (■) 100 mA/cm^2 [53]. (Reprinted from Journal of Power Sources, 84(2), Mueller JT, Urban PM, Holderich WM. Impedance studies on direct methanol fuel cell anodes, 157–60, ©1999, with permission from Elsevier.)

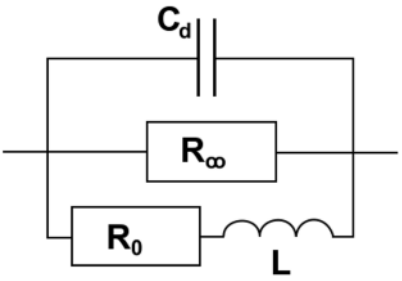

Figure 6.67. Equivalent circuit for modelling the Faradaic impedance of DMFC anodes [53]. (Reprinted from Journal of Power Sources, 84(2), Mueller JT, Urban PM, Holderich WM. Impedance studies on direct methanol fuel cell anodes, 157–60, ©1999, with permission from Elsevier.)

The Faradaic impedance is given by the following equation:

$$Z_{faraday} = \frac{i\omega + C}{A + B} = \left(\frac{1}{R_\infty} + \frac{1}{R_0 + i\omega L}\right)^{-1} \tag{6.59}$$

where

$$R_\infty = \frac{1}{A} \tag{6.60}$$

$$R_0 = \frac{C}{B} \tag{6.61}$$

$$L = \frac{1}{B} \tag{6.62}$$

$$A = F\left(\frac{\partial r_e}{\partial E}\right)_\theta \tag{6.63}$$

$$B = \frac{F^2}{q_{CO}}\left(\frac{\partial r_e}{\partial \theta}\right)_E \left(\frac{\partial r_{CO}}{\partial E}\right)_\theta \tag{6.64}$$

$$C = \frac{-F}{q_{CO}}\left(\frac{\partial r_{CO}}{\partial \theta}\right)_E \tag{6.65}$$

The simulation of the AC impedance spectrum obtained at 100 mA/cm^2 gives the following parameters: C = 0.135 F/cm^2, R_∞ = 1.705 Ωcm^2, R_0 = 0.863 Ωcm^2, and L = 0.716 L/cm^2.

6.2.3. Determination of the Ionic Resistance [54, 55]

As predicted from modelling based on the transmission line model, and as observed in experiments, the Nyquist plot of the AC impedance spectra of methanol oxidation at the anode shows a linear region at high frequencies. This region is due to ionic transport and double-layer charging in a porous structure; in addition, the frequency is higher than the so-called characteristic frequency, ω_c ($\omega_c = 1/R_{ct}C_{dl}$), where R_{ct} is the charge-transfer resistance of methanol oxidation in the anode catalyst layer and C_{dl} is the double-layer capacitance of the anode catalyst layer. The resistance of the linear region can be represented by the following equation:

$$Z = \sqrt{\frac{R_P}{C_{dl}}}\omega^{-1/2}\frac{\sqrt{2}}{2}(1 - i) \tag{6.66}$$

$$|Z| = \sqrt{\frac{R_P}{C_{dl}}}\omega^{-1/2} \tag{6.67}$$

When the impedance versus the reciprocal of the square root of the frequency is plotted, the slope gives $(R_p/C_{dl})^{1/2}$, where R_p is the ionic resistance of the anode catalyst layer. The double-layer capacitance can be obtained from the cyclic voltammogram. According to the definition of capacitance, the capacitance of the double layer equals the current divided by the scan rate ($C_{dl} = Iv^{-1}$). The ionic resistance can be obtained from the capacitance of the double layer.

6.2.4 In Situ Cathode Reaction [52, 56, 57]

The impedance spectra of the DMFC cathode electrodes are obtained by subtracting the anode impedance from the total cell impedance. The cell impedance, Z_{DMFC}, was obtained from normal operation of the DMFC (i.e., the cathode side was fed with air or O_2 and the anode side was fed with methanol solution). The anode impedance was measured by supplying H_2 to the cathode compartment, which was used as a dynamic hydrogen reference electrode. Since the impedance of the H_2 electrode is negligible, the measured impedance is considered to be the anode impedance, Z_{anode}. The cathode impedance is therefore

$$Z_{cathode} = Z_{DMFC} - Z_{anode} \tag{6.68}$$

Typical impedance spectra of a DMFC cathode operating on air and pure O_2 were shown in Chapter 5, Figure 5.39. Two arcs were observed when air was used as the oxidant, while only one arc was observed for O_2. According to the previous equation, the membrane resistance (or the arc at high frequencies caused by the membrane) was not present in the cathode impedance spectra. Since the membrane impedance was included in both the total cell impedance Z_{DMFC} and the anode impedance Z_{anode}, subtracting the two cancelled out the membrane impedance.

The arc in the medium-frequency range is due to the charge transfer of the ORR. The low-frequency arc is due to mass transport, especially in the case of air. To access the catalytic sites, oxygen needs to diffuse through nitrogen and water, which leads to mass transport resistance.

Unlike the cathode reaction in hydrogen/air PEM fuel cells, the cathode reaction in a DMFC also involves poisoning of the catalyst due to methanol crossover. Methanol oxidation on the electrode can lead to CO adsorption, which usually results in inductance at low frequencies. In some cases, an inductance loop is observed in cathode impedance spectra, as shown in Figure 6.68.

To elucidate methanol crossover at the DMFC cathode, the active electrode surface of the cathode was divided into two separate parts: one for oxygen reduction and the other for oxidation of crossover methanol. In this model, the methanol oxidation and oxygen reduction occur in parallel at different sites or pores because of the porous structure of the catalyst layer. The equivalent circuit for this model is presented in Figure 6.69.

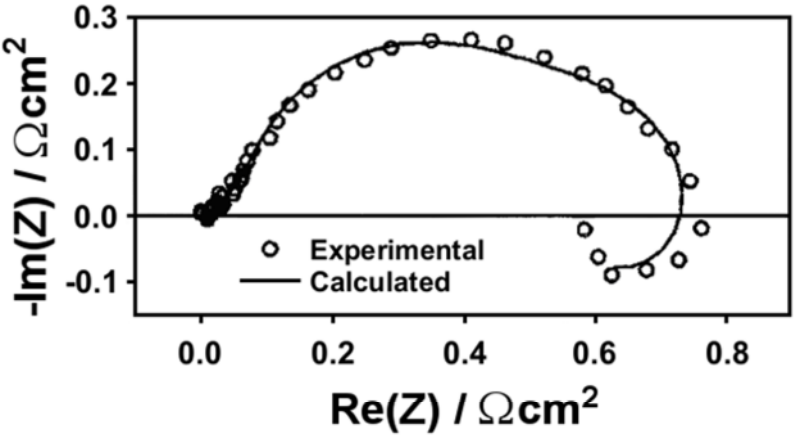

Figure 6.68. Impedance spectra of a DMFC cathode. Experimental conditions: 75°C, air stoichiometric ratio 10, 69 mA cm^{-2}, 0.879 V, and frequency range 10 kHz–0.1 Hz [57]. (Reproduced by permission of ECS—The Electrochemical Society, from Piela P, Fields R, Zelenay P. Electrochemical impedance spectroscopy for direct methanol fuel cell diagnostics.)

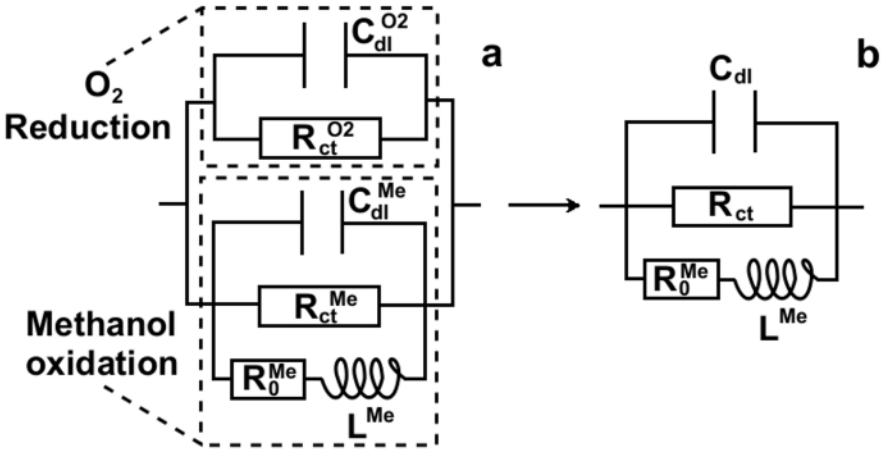

Figure 6.69. Equivalent circuit for the impedance of a pore wall in a DMFC cathode [57]. (Reproduced by permission of ECS—The Electrochemical Society, from Piela P, Fields R, Zelenay P. Electrochemical impedance spectroscopy for direct methanol fuel cell diagnostics.)

The charge-transfer resistances and double-layer capacitances of oxygen reduction and methanol oxidation can be simplified using the following equations:

$$R_{ct} = \frac{1}{\frac{1}{R_{ct}^{O_2}} + \frac{1}{R_{ct}^{Me}}} \tag{6.69}$$

$$C_{dl} = C_{dl}^{O_2} + C_{dl}^{Me} \tag{6.70}$$

By using the combined parameters, the equivalent circuit is simplified to Figure 6.69*b*. The catalyst layer is a porous structure and the impedance of each pore is given by the following equations:

$$Z_{pore} = \frac{\rho l}{\pi r^2} \Lambda^{-\frac{1}{2}} \coth(\Lambda^{\frac{1}{2}}) \tag{6.71}$$

and

$$\Lambda = \frac{2\rho l^2}{r Z_{el}} \tag{6.72}$$

where ρ is the specific resistance of the electrolyte in the pore, Ω cm; l is the pore length, cm; r is the pore radius, cm; and Z_{el} is the electrochemical impedance of the pore wall.

In spite of the bulk electrolyte resistance cancelling out in Equation 6.68, small differences between the series resistance in the measurements of Z_{DMFC} and Z_{anode} also contribute to cathode impedance. Considering the mass transport resistance of O_2 in the pores and the bulk electrolyte resistance, the cathode impedance is given by

$$Z_{cathode} = R_s + Z_{pore} \frac{2\pi r l}{a} + Z_w^{O_2} \tag{6.73}$$

and

$$Z_w^{O_2} = R_w \tanh(\sqrt{j\omega\tau_w}) / \sqrt{j\omega\tau_w} \tag{6.74}$$

where: τ_w is a time constant of oxygen transport through the backing, which can be approximated by $d^2 D^{-1}$; d is the thickness of the oxygen diffusion barrier in cm; and D is the effective oxygen diffusion coefficient in the oxygen transport barrier.

6.3 Chapter Summary

This chapter has examined a variety of EIS applications in PEMFCs, including optimization of MEA structure, ionic conductivity studies of the catalyst layer, fuel cell contamination, fuel cell stacks, localized impedance, and EIS at high temperatures, and in DMFCs, including ex situ methanol oxidation, and in situ anode and cathode reactions. These materials therefore cover most aspects of PEMFCs and DMFCs. It is hoped that this chapter will provide a fundamental understanding of EIS applications in PEMFC and DMFC research, and will help fuel cell researchers to further understand PEMFC and DMFC processes.

References

1. Brunetto C, Tina G, Squadrito G, Moschetto A (2004) PEMFC diagnostics and modelling by electrochemical impedance spectroscopy. Proceedings of the 12th IEEE Mediterranean electrochemical conference. IEEE Cat. No. 04CH37521 3:1045–50
2. Springer TE, Raistrick ID (1989) Electrical impedance of a pore wall for the flooded-agglomerate model of porous gas-diffusion electrodes. J Electrochem Soc 136:1594–603
3. Raistrick ID (1990) Impedance studies of porous electrodes. Electrochim Acta 35:1579–86
4. Paganin VA, Oliveira CLF, Ticianelli EA, Springer TE, Gonzalez ER (1998) Modelistic interpretation of the impedance response of a polymer electrolyte fuel cell. Electrochim Acta 43(24): 3761–6
5. Song JM, Cha SY, Lee WM (2001) Optimal composition of polymer electrolyte fuel cell electrodes determined by the ac impedance method. J Power Sources 94(1):78–84
6. Antolini E, Giorgi L, Pozio A, Passalacqua E (1999) Influence of Nafion loading in the catalyst layer of gas-diffusion electrodes for PEFC. J Power Sources 77(2):136–42
7. Guo Q, Cayetano M, Tsou Y, De-Castro ES, White RE (2003) Study of ionic conductivity profiles of the air cathode of a PEMFC by ac impedance spectroscopy. J Electrochem Soc 150(11):A1440–9
8. Ahn SY, Lee YC, Ha HY, Hong SA, Oh IH (2004) Effect of the ionomers in the electrode on the performance of PEMFC under non-humidifying conditions. Electrochim Acta 50:673–6
9. Freire TJP, Gonzalez ER (2001) Effect of membrane characteristics and humidification conditions on the impedance response of polymer electrolyte fuel cells. J Electroanal Chem 503:57–68
10. Springer TE, Zawodzinski TA, Wilson MS, Gottesfeld S (1996) Characterization of polymer electrolyte fuel cells using ac impedance spectroscopy. J Electrochem Soc 143(2):587–99
11. Bernardi DM, Verbrugge MW (1992) A mathematical model of the solid-polymer-electrolyte fuel cell. J Electrochem Soc 139:2477–91
12. Wilson MS, Valerio JA, Gottesfeld S (1995) Low platinum loading electrodes for polymer electrolyte fuel cells fabricated using thermoplastic ionomers. Electrochim Acta 40:355–63
13. Jordan LR, Shukla AK, Behrsing R, Avery NR, Muddle BC, Forsyth M (2000) Diffusion layer parameters influencing optimal fuel cell performance. J Power Sources 86:250–4

14. Passalacqua E, Squadrito G, Lufrano F, Patti A, Giorgi L (2001) Effects of the diffusion layer characteristics on the performance of polymer electrolyte fuel cell electrodes. J Appl Electrochem 31:449–54
15. Kong CS, Kim DY, Lee HK, Shul YG, Lee TH (2002) Influence of pore-size distribution of diffusion layer on mass-transport problems of proton exchange membrane fuel cells. J Power Sources 108(1-2):185–91
16. Fischer A, Jindra J, Wendt H (1998) Porosity and catalyst utilization of thin layer cathodes in air operated PEM-fuel cells. J Appl Electrochem 28:277–82
17. Bevers D, Wagner N, Von Bradke M (1998) Innovative production procedure for low cost PEFC electrodes and electrode/membrane structures**.** Int J Hydrogen Energy 23(1):57–63
18. Abaoud HA, Ghouse M, Lovell KV, Al-Motairy GN (2003) Alternative formulation for proton exchange membrane fuel cell (PEMFC) electrode preparation. J New Mater Electrochem Syst 6(3):149–55
19. Wang C, Mao ZQ, Xu JM, Xie XF (2003) Preparation of a novel silica gel for electrode additive of PEMFCs. J New Mater Electrochem Syst 6(2):65–9
20. Mukerjee S, Srinivasan S, Appleby AJ (1993) Effect of sputtered film of platinum on low platinum loading electrodes on electrode kinetics of oxygen reduction in proton exchange membrane fuel cell. Electrochim Acta 38(12):1661–9
21. Cha SY, Lee WM (1999) Performance of proton exchange membrane fuel cell electrodes prepared by direct deposition of ultrathin platinum on the membrane surface. J Electrochem Soc 146 (11):4055–60
22. Ahn S, Tatarchuk BJ (1990) Composite electrode structures for fuel cell applications. Proceedings of the 25th intersociety energy conversion engineering conference 3:287–92
23. Makharia R, Mathias MF, Baker DR (2005) Measurement of catalyst layer electrolyte resistance in PEFCs using electrochemical impedance spectroscopy. J Electrochem Soc 152(5):A970–7
24. Easton EB, Pickup PG (2005) An electrochemical impedance spectroscopy study of fuel cell electrodes. Electrochim Acta 50(12):2469–74
25. Li G, Pickup PG (2003) Ionic conductivity of PEMFC electrodes. J Electrochem Soc 150(11):C745–52
26. Lefebvre MC, Martin RB, Pickup PG (1999) Characterization of ionic conductivity profiles within proton exchange membrane fuel cell gas diffusion electrodes by impedance spectroscopy. Electrochem Solid-State Lett 2(6):259–61
27. Ren X, Pickup PG (2001) Simulation and analysis of the impedance behaviour of electroactive layers with non-uniform conductivity and capacitance profiles. Electrochim Acta 46:4177–83
28. Saab AP, Garzon FH, Zawodzinski TA (2002) Determination of ionic and electronic resistivities in carbon/polyelectrolyte fuel-cell composite electrodes. J Electrochem Soc 149(12):A1541–6
29. Duffitt GL, Pickup PG (1992) Enhanced ionic conductivity of polypyrrole due to incorporation of excess electrolyte during potential cycling. J Chem Soc Faraday Trans 88:1417–23
30. Pickup PG (1990) Alternating current impedance study of a polypyrrole-based anion-exchange polymer. J Chem Soc Faraday Trans 86:3631–6
31. Zhang J, Wang H, Wilkinson DP, Song D, Shen J, Liu ZS (2005) Model for the contamination of fuel cell anode catalyst in the presence of fuel stream impurities. J Power Sources 147(1-2):58–71
32. Ciureanu M, Wang H (2000) Electrochemical impedance study of anode CO-poisoning in PEM fuel cells. J New Mater Electrochem Syst 3(2):107–19

33. Wagner N, Gulzow E (2004) Change of electrochemical impedance spectra (EIS) with time during CO-poisoning of the Pt-anode in a membrane fuel cell. J Power Sources 127(1-2):341–7
34. Ciureanu M, Wang H (1999) Electrochemical impedance study of electrode-membrane assemblies in PEM fuel cells: I. Electro-oxidation of H_2 and H_2/CO mixtures on Pt-based gas-diffusion electrodes. J Electrochem Soc 146(11):4031–40
35. Kim JD, Park YI, Kobayashi K, Nagai M, Kunimatsu M (2001) Characterization of CO tolerance of PEMFC by ac impedance spectroscopy. Solid State Ionics. Diffusion and Reactions 140(3-4):313–25
36. Kim JD, Park YI, Kobayashi K, Nagai M (2001) Effect of CO gas and anode-metal loading on H_2 oxidation in proton exchange membrane fuel cell. J Power Sources 103(1):127–33
37. Diard JP, Glandut N, Le-Gorrec B, Montella C (2004) Impedance measurement of each cell of a 10 W PEMFC stack under load. J Electrochem Soc 151(12):A2193–7
38. Hakenjos A, Zobel M, Clausnitzer J, Hebling C (2006) Simultaneous electrochemical impedance spectroscopy of single cells in a PEM fuel cell stack. J Power Sources 154(2):360–3
39. Brett DJL, Atkins S, Brandon NP, Vesovic V, Vasileiadis N, Kucernak A (2003) Localized impedance measurements along a single channel of a solid polymer fuel cell. Electrochem Solid-State Lett 6(4):A63–6
40. Hakenjos A, Hebling C (2005) Spatially resolved measurement of PEM fuel cells. J Power Sources 145(2):307–11
41. Schneider I, Scherer G (2006) Fast locally resolved electrochemical impedance spectroscopy in polymer electrolyte fuel cells. European patent EP 1691438 A1
42. Cleghorn S, Derouin CR, Wilson MS, Gottesfeld S (1998) A printed circuit board approach to measuring current distribution in a fuel cell. J Appl Electrochem 28:663–72
43. Bender G, Wilson MS, Zawodzinski TA (2003) Further refinements in the segmented cell approach to diagnosing performance in polymer electrolyte fuel cells. J Power Sources 123(2):163–71
44. Tang Y, Zhang J, Song C, Liu H, Zhang J, Wang H, MacKinnon S, Peckham T, Li J, McDermid S, Kozak P (2006) Temperature dependent performance and in situ ac impedance of high temperature PEM fuel cells using the Nafion112 membrane. J Electrochem Soc 153:A2036–43
45. Zhang J, Tang Y, Song C, Zhang J (2007) Polybenzimidazole-membrane-based PEM fuel cell in the temperature range of 120–200°C. J Power Sources 172(1):163–71
46. Melnick RE, Palmore GT (2001) Impedance spectroscopy of the electro-oxidation of methanol on polished polycrystalline platinum. J Phys Chem B 105(5):1012–25
47. Armstrong RD, Henderson M (1972) Impedance plane display of a reaction with an adsorbed intermediate. J Electroanal Chem 39(1):81–90
48. Hsing IM, Wang X, Leng YJ (2002) Electrochemical impedance studies of methanol electro-oxidation on Pt/C thin film electrode. J Electrochem Soc 149(5):A615–21
49. Wang X, Hsing IM, Leng YJ, Yue PL (2001) Model interpretation of electrochemical impedance spectroscopy and polarization behavior of H_2/CO mixture oxidation in polymer electrolyte fuel cells. Electrochim Acta 46(28):4397–405
50. Jarvi TD, Stuve EM (1998) Fundamental aspects of vacuum and electrocatalytic reactions of methanol and formic acid on platinum surfaces. In: Lipkowski J and Ross PN (ed), Electrocatalysis. Wiley-VCH, New York
51. Cao CN (1990) On the impedance plane displays for irreversible electrode reactions based on the stability conditions of the steady-state—II. Two state variables besides electrode potential, Electrochim Acta 35 (5): 837-44

52. Mueller JT, Urban PM (1998) Characterization of direct methanol fuel cells by ac impedance spectroscopy. J Power Sources 75(1):139–43
53. Mueller JT, Urban PM, Holderich WM (1999) Impedance studies on direct methanol fuel cell anodes. J Power Sources 84(2):157–60
54. Havranek A, Wippermann K (2004) Determination of proton conductivity in anode catalyst layers of the direct methanol fuel cell (DMFC). J Electroanal Chem 567(2):305–15
55. Zhao X, Fan X, Wang S, Yang S, Yi B, Xin Q, Sun G (2005) Determination of ionic resistance and optimal composition in the anodic catalyst layers of DMFC using ac impedance. Int J Hydrogen Energy 30(9):1003–10
56. Furukawa K, Okajima K, Sudoh M (2005) Structural control and impedance analysis of cathode for direct methanol fuel cell. J Power Sources 139(1–2):9–14
57. Piela P, Fields R, Zelenay P (2006) Electrochemical impedance spectroscopy for direct methanol fuel cell diagnostics. J Electrochem Soc 153(10): A1902–13

Appendix A

Fourier Transform

The term "Fourier transform" usually refers to the continuous integration of any square-integrable function to re-express the function as a sum of complex exponentials. Due to the different types of functions to be transformed, many variations of this transform exist. Accordingly, Fourier transforms have scientific applications in many areas, including physics, chemical analysis, signal processing, and statistics. The continuous-time Fourier transforms are defined as follows [1–3]:

$$F(\nu) = F[f(t)](\nu) = \int_{-\infty}^{\infty} f(t)e^{-2\pi i\nu t}dt \tag{A.1}$$

$$f(t) = F^{-1}[F(\nu)](t) = \int_{-\infty}^{\infty} F(\nu)e^{2\pi i\nu t}d\nu \tag{A.2}$$

Equation A.1 is called the *forward* Fourier transform and Equation A.2 is called the *inverse* Fourier transform. If ν is defined as the oscillation frequency, the angular frequency is $\omega = 2\pi\nu$. Therefore, the *forward* Fourier transform can be used to express the function $F(\nu)$ in the frequency domain by the integral of function $f(t)$ in the time domain, whereas the *inverse* Fourier transform can be used to express the function $f(t)$ in the time domain by the integral of function $F(\nu)$ in the frequency domain.

Very often, $\hat{f}(\nu)$ and $\breve{f}(t)$ are used to denote the forward and inverse Fourier transforms, respectively. As described in Chapter 5, Section 4, $\hat{U}(\omega)$ is the Fourier transform of the applied AC voltage $U(t)$, and $\hat{I}(\omega)$ is the Fourier transform of the current response $I(t)$. We write the transform in terms of the angular frequency $\omega = 2\pi\nu$ instead of the oscillation frequency ν:

$$\hat{U}(\omega) = F[U(t)] = \int_{-\infty}^{\infty} U(t)e^{-i\omega t}dt \tag{A.3}$$

$$U(t) = F^{-1}[\hat{U}(\omega)] = \frac{1}{2\pi}\int_{-\infty}^{\infty} \hat{U}(\omega)e^{i\omega t}d\omega \tag{A.4}$$

However, this destroys the symmetry of the transform pair. To restore this symmetry, the following equations are conventionally used:

$$\hat{U}(\omega) = F[U(t)] = \frac{1}{\sqrt{2\pi}}\int_{-\infty}^{\infty} U(t)e^{-i\omega t}dt \tag{A.5}$$

$$U(t) = F^{-1}[\hat{U}(\omega)] = \frac{1}{\sqrt{2\pi}} \int_{-\infty}^{\infty} \hat{U}(\omega) e^{i\omega t} d\omega \tag{A.6}$$

Similarly,

$$\hat{I}(\omega) = F[I(t)] = \frac{1}{\sqrt{2\pi}} \int_{-\infty}^{\infty} I(t) e^{-i\omega t} dt \tag{A.7}$$

$$I(t) = F^{-1}[\hat{I}(\omega)] = \frac{1}{\sqrt{2\pi}} \int_{-\infty}^{\infty} \hat{I}(\omega) e^{i\omega t} d\omega \tag{A.8}$$

More commonly, the Fourier transform pair may be defined using two arbitrary constants *a* and *b*; thus,

$$F(\nu) = \sqrt{\frac{|b|}{(2\pi)^{1-a}}} \int_{-\infty}^{\infty} f(t) e^{ib\nu t} dt \tag{A.9}$$

$$f(t) = \sqrt{\frac{|b|}{(2\pi)^{1+a}}} \int_{-\infty}^{\infty} F(\nu) e^{-ib\nu t} d\nu \tag{A.10}$$

With different parameters $\{a,b\}$, Fourier transforms may be used in different fields, e.g., $\{0,1\}$ in modern physics, $\{1,-1\}$ in pure mathematics and systems engineering, $\{1,1\}$ in probability theory for computation of the characteristic function, $\{-1,1\}$ in classical physics, and $\{0,-2\pi\}$, which is used in signal processing and greatly simplifies transforms of common functions such as 1, $\cos(2\pi\nu t)$, etc.

In two dimensions, the Fourier transform becomes

$$F(x,y) = \int_{-\infty}^{\infty} \int_{-\infty}^{\infty} f(k_x,k_y) e^{-2\pi i(k_x x + k_y y)} dk_x dk_y \tag{A.11}$$

$$f(k_x,k_y) = \int_{-\infty}^{\infty} \int_{-\infty}^{\infty} F(x,y) e^{2\pi i(k_x x + k_y y)} dx dy \tag{A.12}$$

Similarly, the n-dimensional Fourier transform can be defined for *k* by ($x \in R^n$):

$$F(x) = \underbrace{\int_{-\infty}^{\infty} \cdots \int_{-\infty}^{\infty}}_{n} f(k) e^{-2\pi i k x} d^n k \tag{A.13}$$

$$f(k) = \underbrace{\int_{-\infty}^{\infty} \cdots \int_{-\infty}^{\infty}}_{n} F(x) e^{2\pi i k x} d^n x \tag{A.14}$$

Fourier transforms have many remarkable properties. If $f(t)$ and $g(t)$ have Fourier transforms $F(\nu)$ and $G(\nu)$, some of the resulting properties are as follows.

(1) Linearity, symmetry, shift, and scaling

Linearity:

$$F[af(t)+bg(t)] = aF[f(t)]+bF[g(t)] = aF(\nu)+bG(\nu) \tag{A.15}$$

Symmetry:

$$F(-\nu) = F[f(-t)](\nu) \tag{A.16}$$

Shift:

$$F[f(t-t_0)](\nu) = e^{-2\pi i \nu t_0} F(\nu) \tag{A.17}$$

Scaling:

$$F[f(\sigma t)](\nu) = F(\frac{\nu}{\sigma})/\sigma \tag{A.18}$$

$$F[f(t/\sigma)](\nu) = \sigma F(\sigma\nu) \tag{A.19}$$

(2) Transforms of convolutions of functions (here, $f * g$ denotes convolution)

$$F[f * g] = F[f]\,F[g] \tag{A.20}$$

$$F[fg] = F[f] * F[g] \tag{A.21}$$

$$F^{-1}[F(f)F(g)] = f * g \tag{A.22}$$

$$F^{-1}[F(f) * F(g)] = fg \tag{A.23}$$

(3) The extremely important relationship between autocorrelation and Fourier transforms ($\bar{f}$ denotes the complex conjugate of f)

$$F[|F(\nu)|^2](t) = \int_{-\infty}^{\infty} \bar{f}(\tau) f(\tau+t) d\tau \tag{A.24}$$

(4) The Fourier transform of the derivative

$$F[f'(t)](\nu) = 2\pi i \nu\, F[f(t)](\nu) \text{ (assuming } \lim_{t\to\pm\infty} f(t) = 0) \tag{A.25}$$

$$F[f^{(n)}(t)](\nu) = (2\pi i \nu)^n\, F[f(t)](\nu) \tag{A.26}$$

When using sine wave signals, the perturbation signal and the current response are

$$U(t) = U_0(\omega)\sin(\omega t) \tag{A.27}$$

$$I(t) = I_0(\omega)\sin[\omega t + \theta(\omega)] \tag{A.28}$$

Now let us consider the Fourier transform of the applied AC voltage, $U(t)$, and the current response, I(t). The transform of a sine function is a positive complex delta function at the appropriate positive frequency and a negative complex delta at the appropriate negative frequency:

$$F[\sin(2\pi\nu_0 t)](\nu) = \int_{-\infty}^{\infty} e^{-2\pi i\nu t}\left(\frac{e^{2\pi i\nu_0 t} - e^{-2\pi i\nu_0 t}}{2i}\right)dt$$

$$= \frac{1}{2} i \int_{-\infty}^{\infty} [-e^{-2\pi i(\nu-\nu_0)t} + e^{-2\pi i(\nu+\nu_0)t}]dt$$

$$= \frac{1}{2} i[\delta(\nu+\nu_0) - \delta(\nu-\nu_0)] \tag{A.29}$$

where $\delta(t)$ is the delta function; then,

$$F[U_0\sin(2\pi\nu_0 t)](\nu) = \int_{-\infty}^{\infty} U_0 e^{-2\pi i\nu t}\left(\frac{e^{2\pi i\nu_0 t} - e^{-2\pi i\nu_0 t}}{2i}\right)dt$$

$$= \frac{U_0}{2} i \int_{-\infty}^{\infty} [-e^{-2\pi i(\nu-\nu_0)t} + e^{-2\pi i(\nu+\nu_0)t}]dt$$

$$= \frac{U_0}{2} i[\delta(\nu+\nu_0) - \delta(\nu-\nu_0)] \tag{A.30}$$

The transform of a cosine function is a positive delta at the appropriate positive and negative frequencies:

$$F[\cos(2\pi\nu_0 t) f(t)](\nu) = \int_{-\infty}^{\infty} f(t)\cos(2\pi\nu_0 t) e^{-2\pi i\nu t} dt$$

$$= \frac{1}{2}\int_{-\infty}^{\infty} f(t) e^{2\pi i\nu_0 t} e^{-2\pi i\nu t} dt + \frac{1}{2}\int_{-\infty}^{\infty} f(t) e^{-2\pi i\nu_0 t} e^{-2\pi i\nu t} dt$$

$$= \frac{1}{2}\int_{-\infty}^{\infty} f(t) e^{-2\pi i(\nu-\nu_0)t} dt + \frac{1}{2}\int_{-\infty}^{\infty} f(t) e^{-2\pi i(\nu+\nu_0)t} dt$$

$$= \frac{1}{2}[F(\nu - \nu_0) + F(\nu + \nu_0)] \tag{A.31}$$

$$F[\cos(2\pi\nu_0 t)](\nu) = \int_{-\infty}^{\infty} \cos(2\pi\nu_0 t) e^{-2\pi i \nu t} dt$$

$$= \frac{1}{2}\int_{-\infty}^{\infty} e^{2\pi i \nu_0 t} e^{-2\pi i \nu t} dt + \frac{1}{2}\int_{-\infty}^{\infty} e^{-2\pi i \nu_0 t} e^{-2\pi i \nu t} dt$$

$$= \frac{1}{2}\int_{-\infty}^{\infty} e^{-2\pi i (\nu - \nu_0) t} dt + \frac{1}{2}\int_{-\infty}^{\infty} e^{-2\pi i (\nu + \nu_0) t} dt$$

$$= \frac{1}{2}[\delta(\nu - \nu_0) + \delta(\nu + \nu_0)] \tag{A.32}$$

$$F[I_0 \sin(2\pi\nu_0 t + \theta)](\nu) = F\{I_0[\sin(2\pi\nu_0 t)\cos\theta + \cos(2\pi\nu_0 t)\sin\theta]\}(\nu)$$

$$= F\{I_0[\sin(2\pi\nu_0 t)\cos\theta]\}(\nu) + F\{I_0 \cos(2\pi\nu_0 t)\sin\theta]\}(\nu)$$

$$= \frac{I_0 \cos\theta}{2} i[\delta(\nu + \nu_0) - \delta(\nu - \nu_0)] + \frac{I_0 \sin\theta}{2}[\delta(\nu - \nu_0) + \delta(\nu + \nu_0)] \tag{A.33}$$

Other commonly used Fourier transforms are listed in Table A.1.

Table A.1. Commonly used Fourier transforms

Function	$f(t)$	$F(\nu) = F[f(t)](\nu)$
1	1	$\delta(\nu)$
Sine	$\sin(2\pi\nu_0 t)$	$\frac{1}{2} i[\delta(\nu + \nu_0) - \delta(\nu - \nu_0)]$
Cosine	$\cos(2\pi\nu_0 t)$	$= \frac{1}{2}[\delta(\nu - \nu_0) + \delta(\nu + \nu_0)]$
Delta function	$\delta(t - t_0)$	$e^{-2\pi i \nu t_0}$
Gaussian	e^{-kx^2}	$\sqrt{\frac{\pi}{k}} e^{-\pi^2 \nu^2 / k}$
Exponential function	$e^{-2\pi\nu_0 \lvert t \rvert}$	$\frac{1}{\pi} \frac{\nu_0}{\nu^2 + \nu_0^2}$

In both scientific computation and digital signal processing, one must use the discrete Fourier transform (DFT), which is applied to a discrete complex valued series instead of continuous domains. The forward DFT is defined as

$$x(n) = \frac{1}{N}\sum_{k=0}^{N-1} x(k)e^{-jk2\pi n/N} \text{ for } n = 0...N-1 \tag{A.34}$$

and the inverse transform is defined as

$$x(n) = \sum_{k=0}^{N-1} x(k)e^{jk2\pi n/N} \text{ for } n = 0...N-1 \tag{A.35}$$

where x is a complex number

$$x_i = x_{real} + jx_{imag} \tag{A.36}$$

and $x(k)$ is a complex series with N samples: $x_0, x_1, x_2, x_3 ... x_k ... x_{N-1}$. It is obvious that the transform can also be applied to the real valued series by setting the imaginary part to 0.

When writing about Fourier transforms, we must also mention the fast Fourier transform (FFT), which is an efficient algorithm to compute the DFT and its inverse, making the FFT a practical and important computational operation [4]. The FFT is of great importance in a wide variety of applications, from digital signal processing, to solving partial differential equations, to calculating algorithms for quickly multiplying large integers [5]. If the length of x is a power of 2, a radix-2 FFT algorithm is used; that is, the FFT can reduce the number of computations by calculating N points from $2N^2$ to $2N\lg N$, where lg is the base-2 logarithm. If the length of x is not a power of 2, a transform can be performed on sets of points corresponding to the prime factors of N. Base-4 and base-8 FFTs can be made 20–30% faster than base-2 FFTs by using the optimized code [6].

References

1. Wolfram MathWorld (2009) Fourier transform. Wolfram Research, Inc. http://mathworld.wolfram.com/FourierTransform.html. Accessed 30 March 2009
2. Bracewell RN (1978) The Fourier transform and its applications. 2nd edn. McGraw-Hill, New York
3. Wikipedia (2009) Fourier transform. http://en.wikipedia.org/wiki/Fourier_transform. Accessed 19 May 2009
4. Brigham EO (1947) The fast Fourier transform. Prentice-Hall, Englewood Cliffs, NJ
5. Wikipedia. (2009) Fast Fourier transform. http://en.wikipedia.org/wiki/Fast_Fourier_transform. Accessed 16 May 2009
6. Wolfram MathWorld (2009) Fast Fourier transform. http://mathworld.wolfram.com/FastFourierTransform.html. Accessed 30 March 2009

Appendix B

Laplace Transform

When discussing diffusion, one inevitably needs to solve diffusion equations. The Laplace transform has proven to be the most effective solution for these differential equations, as it converts them to polynomial equations. The Laplace transform is also a powerful technique for both steady-state and transient analysis of linear time-invariant systems such as electric circuits. It dramatically reduces the complexity of the mathematical calculations required to solve integral and differential equations. Furthermore, it has many other important applications in areas such as physics, control engineering, signal processing, and probability theory.

The Laplace transform is an integral that transforms a function in the time domain into a new function of a complex variable. Assuming that there is a function $f(t)$, we define a new function:

$$\bar{f}(s) = L\{f(t)\} = \int_{0^-}^{\infty} f(t) e^{-st} dt \tag{B.1}$$

or

$$F(s) = L\{f(t)\} = \int_{0^-}^{\infty} f(t) e^{-st} dt \tag{B.2}$$

Here, $\bar{f}(s)$, $F(s)$, and $L\{f(t)\}$ are each the unilateral or one-sided Laplace transform of function $f(t)$, which is a linear operator of function $f(t)$; s is a complex argument ($s = \sigma + i\omega$) and t is a real argument ($t \geq 0$). Note that the low limit of integration is 0^-, as the use of 0^+ would exclude such direct analysis as the instantaneous energy transfer in the circuit (e.g., impulses at $t = 0$).

The Laplace transform can be alternatively defined as the bilateral Laplace transform or two-sided Laplace transform by extending the limits of integration to the entire real axis. In this case, the formulas become

$$\bar{f}(s) = L\{f(t)\} = \int_{-\infty}^{\infty} f(t) e^{-st} dt \tag{B.3}$$

or

$$F(s) = L\{f(t)\} = \int_{-\infty}^{\infty} f(t) e^{-st} dt \tag{B.4}$$

Generally, the default Laplace transform is unilateral or one-sided.

The one-sided Laplace transforms of commonly used functions and the main properties of the one-sided Laplace transform are listed in Tables B.1 and B.2, respectively. The two-sided Laplace transforms and their main properties can be found in Tables B.3 and B.4, respectively [1–4].

Table B.1. One-sided Laplace transforms

Time signal	Laplace transform	Comments
E	$\frac{E}{s}$	E, constant
t	$\frac{1}{s^2}$	
$\frac{1}{\sqrt{\pi t}}$	$\frac{1}{\sqrt{s}}$	
$2\sqrt{\frac{t}{\pi}}$	$\frac{1}{s\sqrt{s}}$	
e^{-at}	$\frac{1}{s+a}$	a, complex
$\frac{1}{a}(1-e^{-at})$	$\frac{1}{s(s+a)}$	a, complex
$\sin(at)$	$\frac{a}{s^2+a^2}$	a, real
$\cos(at)$	$\frac{s}{s^2+a^2}$	a, real
$e^{at}\sin(bt)$	$\frac{b}{(s-a)^2+b^2}$	a, b real
$e^{at}\cos(bt)$	$\frac{s-a}{(s-a)^2+b^2}$	a, b real
$\exp(a^2t)erfc(a\sqrt{t})$ *	$\frac{1}{s+a\sqrt{s}}$	a, real

* $erf(x)=\frac{2}{\sqrt{\pi}}\int_0^x e^{-y^2}dy$; $erfc(x)=1-erf(x)$

Property	Time signal	Laplace transform	Comments
Linearity	$af(t)+bg(t)$	$a\bar{f}(s)+b\bar{g}(s)$	a, b complex
Shift	$f(t-a)u(t-a)$	$e^{-sa}\bar{f}(s)$	a, real
Converse shift	$e^{-at}f(t)$	$\bar{f}(s+a)$	a, complex
Scaling	$f(ct)$	$\frac{1}{c}\bar{f}\left(\frac{s}{c}\right)$	c, real $c>0$
Differentiation	$\frac{d^n f(t)}{dt^n}$	$s^n\bar{f}(s)-s^{n-1}f(0)-s^{n-2}f'(0)-\ldots-f^{(n-1)}(0)$	$n = 1, 2, \ldots$
Integration	$\int_0^t f(\tau)d\tau$	$\frac{\bar{f}(s)}{s}$	
Convolution	$f(t) * g(t)$	$\bar{f}(s)\bar{g}(s)$	

Table B.2. Main properties of the one-sided Laplace transform

Table B.3. Two-sided Laplace transforms

Time signal	Laplace transform	Comments
$u(t)$*	$\frac{1}{s}$	
$\delta(t)$**	1	
$\delta^{(k)}(t)$	s^k	$k = 0, 1, 2, \ldots$
$e^{at}u(t)$	$\frac{1}{s-a}$	a, complex
$-e^{at}u(-t)$	$\frac{1}{s-a}$	a, complex
$\sin(at)u(t)$	$\frac{a}{s^2+a^2}$	a, real
$\cos(at)u(t)$	$\frac{s}{s^2+a^2}$	a, real
$e^{at}\sin(bt)u(t)$	$\frac{b}{(s-a)^2+b^2}$	a, b real
$e^{at}\cos(bt)u(t)$	$\frac{s-a}{(s-a)^2+b^2}$	a, b real

* Unit step function (or Heaviside step function): $u(x) = \begin{cases} 1, & x \geq 0 \\ 0, & x < 0 \end{cases}$

** Dirac delta $\delta(x)$ function: $\delta(x) = \begin{cases} \infty, & x = 0 \\ 0, & x \neq 0 \end{cases}$

Table B.4. Main properties of the two-sided Laplace transform

Property	Time signal	Laplace transform	Comments
Linearity	$af(t)+bg(t)$	$a\bar{f}(s)+b\bar{g}(s)$	a, b complex
Shift	$f(t-a)$	$e^{-sa}\bar{f}(s)$	a, real
Converse shift	$e^{at}f(t)$	$\bar{f}(s-a)$	a, complex
Scaling	$f(at)$	$\frac{1}{\lvert a\rvert}\bar{f}\left(\frac{s}{a}\right)$	a, real, $a\neq 0$
Differentiation	$\frac{df(t)}{dt}$	$s\bar{f}(s)$	
Integration	$\int_{-\infty}^{t} f(\tau)d\tau$	$\frac{\bar{f}(s)}{s}$	
Convolution	$f(t)*g(t)$	$\bar{f}(s)\bar{g}(s)$	

The main properties of the Laplace transform that can be used in solving diffusion equations are as follows:

(1) Linearity

$$L\{af(t)+bg(t)\}=a\bar{f}(s)+b\bar{g}(s) \tag{B.5}$$

(2) Laplace transform of a derivative

$$L\left\{\frac{df(t)}{dt}\right\}=s\bar{f}(s)-f(0) \tag{B.6}$$

(3) Laplace transform of a constant E

$$L\{E\}=\frac{E}{s} \tag{B.7}$$

Besides the above properties, an inverse Laplace transform is often applied by using convolution to solve the diffusion equations, thus,

$$L^{-1}\left\{\bar{f}(s)\bar{g}(s)\right\}=f(t)*g(t)$$

$$= \int_0^t f(t-\tau)g(\tau)d\tau = \int_0^t f(\tau)g(t-\tau)d\tau \tag{B.8}$$

Here is an example solving a non-steady diffusion equation using the Laplace transform and the inverse Laplace transform. According to Fick's second law, the diffusion equation can be expressed as

$$\frac{\partial C(x,t)}{\partial t} = D\frac{\partial^2 C(x,t)}{\partial x^2} \tag{B.9}$$

where D is the diffusion coefficient ($\mathrm{cm^2 s^{-1}}$). The initial conditions of the differential equation are as follows

$$C(x,0) = C^* \ (t = 0) \tag{B.10}$$

$$C(x,t) = C^* \ (t > 0, x \to \infty) \tag{B.11}$$

where C^* is the initial concentration or bulk concentration of the reactant. By applying the Laplace transform to both sides, Equation B.9 in one dimension can be written as

$$s\overline{C}(x,s) - C(x,0) = D\frac{d^2\overline{C}(x,s)}{dx^2} \tag{B.12}$$

Substituting into Equation B.12 the initial condition in Equation B.10, we obtain

$$\frac{d^2\overline{C}(x,s)}{dx^2} - \frac{s}{D}\overline{C}(x,s) + \frac{C^*}{D} = 0 \tag{B.13}$$

This is a two-order linear ordinary differential equation. The general solution of Equation B.13 can be written as

$$\overline{C}(x,s) = \frac{C^*}{s} + Ae^{-\lambda x} + Be^{\lambda x} \tag{B.14}$$

where $\lambda = \sqrt{s/D}$, A, and B are constants to be determined. To establish constant B, we transform Equation B.11 (initial condition) using Laplace transforms on both sides:

$$\overline{C}(x,s) = \frac{C^*}{s} \quad (x \to \infty) \tag{B.15}$$

Comparing Equations B.14 and B.15, we obtain

$$B = 0 \tag{B.16}$$

Thus, Equation (B.14) becomes

$$\overline{C}(x,s) = \frac{C^*}{s} + Ae^{-\lambda x} \tag{B.17}$$

Constant A can also be determined by the transform of the initial condition. For an electrode reaction,

$$O_x + e^- \Leftrightarrow R_d$$

if the exchange current is very large, the initial condition can be written as

$$C_O(0,t) = 0 \quad (t > 0) \tag{B.18}$$

where C_O represents the oxidant concentration. By applying the Laplace transform to both sides, Equation B.18 can be expressed as

$$\overline{C}_O(0,s) = 0 \tag{B.19}$$

Substituting $x = 0$ into Equation B.17, we obtain

$$A = -\frac{C^*}{s} \tag{B.20}$$

Then Equation B.17 becomes

$$\overline{C}_O(x,s) = \frac{C^*}{s} - \frac{C^*}{s}e^{-\lambda x} \tag{B.21}$$

Therefore, the solution can be obtained by the inverse Laplace transform:

$$C_O(x,t) = C^* - C^* erfc\left(\frac{x}{2\sqrt{Dt}}\right) \tag{B.22}$$

The following is another simple example solving a differential equation in a DC circuit, as shown in Figure B.1. This DC circuit contains a constant voltage source, a capacitor, a resistor, and a switch, connected in series. The question is: if the timing starts from the moment of turning on the switch, what will $V_c(t)$ be as a function of time?

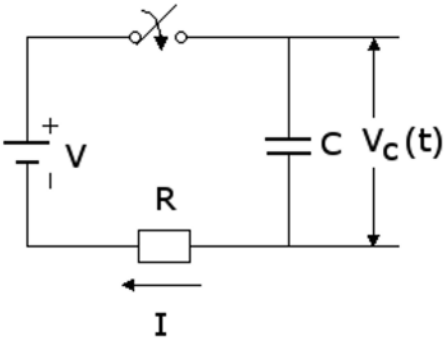

Figure B.1. A DC circuit contains a capacitor, a resistor, and a switch

Based on the circuit analysis, this DC circuit tells us

$$IR + V_c(t) = V \tag{B.23}$$

As

$$q = CV_c(t) \tag{B.24}$$

and

$$I = \frac{dq}{dt} \tag{B.25}$$

we obtain

$$I = \frac{d(CV_c(t))}{dt} = C\frac{dV_c(t)}{dt} \tag{B.26}$$

Then Equation B.23 becomes

$$CR\frac{dV_c(t)}{dt} + V_c(t) = V \tag{B.27}$$

The initial condition is

$$V_c(t) = 0 \quad (t = 0) \tag{B.28}$$

By applying Laplace transforms to both sides, we can rewrite Equation B.27 as

$$CRs\overline{V}_c(s) - V_c(0) + \overline{V}_c(s) = \frac{V}{s} \tag{B.29}$$

Substituting the initial condition into Equation B.29, we obtain

$$CRs\overline{V}_c(s) + \overline{V}_c(s) = \frac{V}{s} \tag{B.30}$$

Obviously, the solution of Equation B.30 is

$$\overline{V}_c(s) = \frac{V}{s(1+RCs)} = \frac{V}{RC} \cdot \frac{1}{s(s+\frac{1}{RC})} \tag{B.31}$$

From Table B.1 we know that the inverse Laplace transform of $\frac{1}{s(s+a)}$ is $\frac{1}{a}(1-e^{-at})$. Therefore, the solution of Equation B.27 can be obtained by the inverse Laplace transform of Equation B.31:

$$V_c(t) = \frac{V}{RC} \cdot RC(1-e^{-\frac{1}{RC}}) = V(1-e^{-\frac{1}{RC}}) \tag{B.32}$$

References

1. Verdult V (1997) Mathematical tables. Delft University of Technology. http://www.seminaire-sherbrooke.qc.ca/math/Pierre/Tables.pdf. Accessed 19 May 2009
2. Wikipedia (2009) Laplace transform. http://en.wikipedia.org/wiki/Laplace_transform. Accessed 19 May 2009.
3. Kreyszig E (1999) Laplace transform. In: Advanced engineering mathematics. 8th edn. John Wiley, New York
4. Jeffrey A (2002) The Laplace transform. In: Advanced engineering mathematics. Harcourt/Academic Press, San Diego

Appendix C

Kramers–Kronig Transform

Introduction

EIS measurement is generally carried out after alteration of an extensive parameter, e.g., temperature or pressure. In such cases, it takes time for the system to reach a new equilibrium state. To obtain a reliable complex non-linear least squares (CNLS) analysis of the impedance data, the system must be in equilibrium over the entire frequency range. Aging and non-linear effects can also seriously affect data analysis. A great advantage of EIS is that one can conduct an independent check of the validity of impedance data or demonstrate the compliance of a system within the constraints of linear systems theory (LST), an effective time-saving theory for linear systems. The secret is the use of Kramers–Kronig (K–K) transforms. K–K transforms were originally developed in the 1920s to deal with optical data. Many years later, researchers started to apply them to electrochemical and corrosion problems [1–4], and even material stability evaluation [5] and surface energy loss [6].

Kramers–Kronig transforms can be used in impedance data validation because the K–K relation links the real and imaginary parts of the impedance: if the real part of the impedance is known over the entire frequency range, its imaginary part is uniquely determined, and when the imaginary part is given, the real part is completely determined up to the additive constant Z_{re} (∞). Kramers–Kronig relations ensure that if one knows the real or imaginary part of a minimum-phase function over all frequencies, one can calculate the value of the other part at any frequency [7]. For example, Priyantha et al. [8] used K–K relations when they studied the corrosion behaviour of Alloy 22 in NaCl brine, transforming their impedance data in the complex plane to demonstrate that the system conformed to the constraints of linear systems theory. Kramers–Kronig data validation presents another powerful tool for impedance data analysis. This can lead to a more appropriate equivalent circuit model for the CNLS-fit routine.

During impedance data analysis it is sometimes difficult to obtain an acceptable match between the measurement and the model. Possible causes are an inappropriate model or corrupted data resulting from a systematic deviation. Systems, such as corrosion systems or fuel cell systems, change or age slowly as the spectra are being generated. The use of improperly large excitation voltage (or current), causing non-linear effects, may also lead to a corrupted data file. K–K transforms can be used to indicate whether the data are erroneous or whether the equivalent circuit is inappropriate. Thus, the K–K relations, which are based on the principle of causality, present us with a particularly useful tool for data validation [9].

Equations

Before performing K–K transformation, one needs to make sure that the data are obtained based on the following rules:

1. Causality: the measured response is merely due to the applied perturbation signal.
2. Linearity: this implies a small excitation voltage (typically < 10 mV for potentiostatic mode and < 5% for galvanostatic mode).
3. Stability: the system should not change with time or continue to oscillate after the excitation is stopped.
4. Finiteness: the calculation is applicable for all frequencies, including $\omega \to 0$ and $\omega \to \infty$.

Based on the above rules, the K–K relation indicates that the imaginary part of a dispersion is completely determined by the real part of the dispersion over the frequency range from $\omega = 0$ to $\omega = \infty$. Vice versa, the real part is determined by the imaginary dispersion over the frequency range $0 \le \omega \le \infty$. The transformation for the real part of the impedance, $Z_{re}(\omega)$, is expressed as [8]

$$Z_{re}(\omega) = Z_{re}(\infty) + \frac{2}{\pi}\int_0^{\infty} \frac{xZ_{im}(x) - \omega Z_{im}(\omega)}{x^2 - \omega^2} dx \tag{C.1}$$

The imaginary part, $Z_{im}(\omega)$, is expressed as [8, 10, 11, 12]

$$Z_{im}(\omega) = -\frac{2\omega}{\pi}\int_0^{\infty} \frac{Z_{re}(x) - Z_{re}(\omega)}{x^2 - \omega^2} dx \tag{C.2}$$

where ω is the frequency of transform and x is the frequency of integration. For the admittance, a similar set of equations can be obtained. It has been noted that the K–K transform is a purely mathematical relation so it does not depend on any physical condition of the system.

For a validated data set, the measured real part and transformed imaginary part, Equation C.1, will match. Similarly, the measured imaginary dispersion and the transformed real part, Equation C.2, will match. In contrast, for a corrupted data set neither the measured real part and transformed imaginary part, nor the measured imaginary dispersion and the transformed real part will match. For systems that are not completely stable, significant deviations between the experimental and transformed data are usually apparent at low frequencies due to the longer acquisition time.

Examples

A typical example of K–K transforms of electrochemical impedance data is depicted in Figure C.1, with both imaginary-to-real and real-to-imaginary axis transforms. The high fidelity between the experimental and transformed data for both real and imaginary axes demonstrates that the system (zinc in a borate

solution, pH = 10.5) complies with the linearity, causality, stability, and finiteness constraints of linear systems theory [13].

Another example of K–K transforms being used for impedance data validation is presented in Figure C.2. Figure C.2*a* shows a comparison between the measured real part and the transformed imaginary part, while Figure C.2*b* compares the measured imaginary dispersion to the transformed real part.

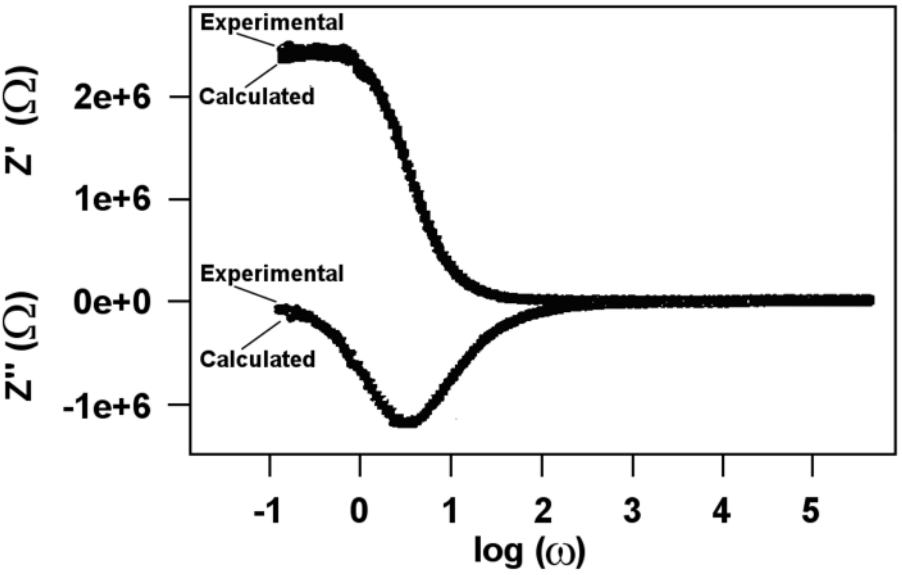

Figure C.1. K–K transforms of real and imaginary components of the electrochemical impedance for passive zinc in a borate solution of pH = 10.5, at 1.2 V (SCE) [13]. (Reproduced by permission of ECS—The Electrochemical Society, from Ismail KM, Macdonald DD. Characterization of the barrier passive film on zinc.)

As presented in Figure C.2*a*, the measured real part and transformed imaginary part (imaginary-to-real axis transformation) match quite well, with only a tiny deviation at extremely low frequencies due to the longer acquisition time. The measured imaginary dispersion and the transformed real part (real-to-imaginary axis transformation), as seen in Figure C.2*b*, show an obvious deviation, particularly at low frequencies. The deviations, which occur at the extremes of the frequency range, arise from the "tails problem", which tends to be more severe for the real-to-imaginary axis transform than for the imaginary-to-real transform. Priyantha et al. [8] nevertheless concluded that the K–K transforms in their studies demonstrated that the system (Alloy 22/brine) remained relatively stable during the time of the measurement, and was both causal and linear. Although the deviations are not significant, this interpretation is rather strained.

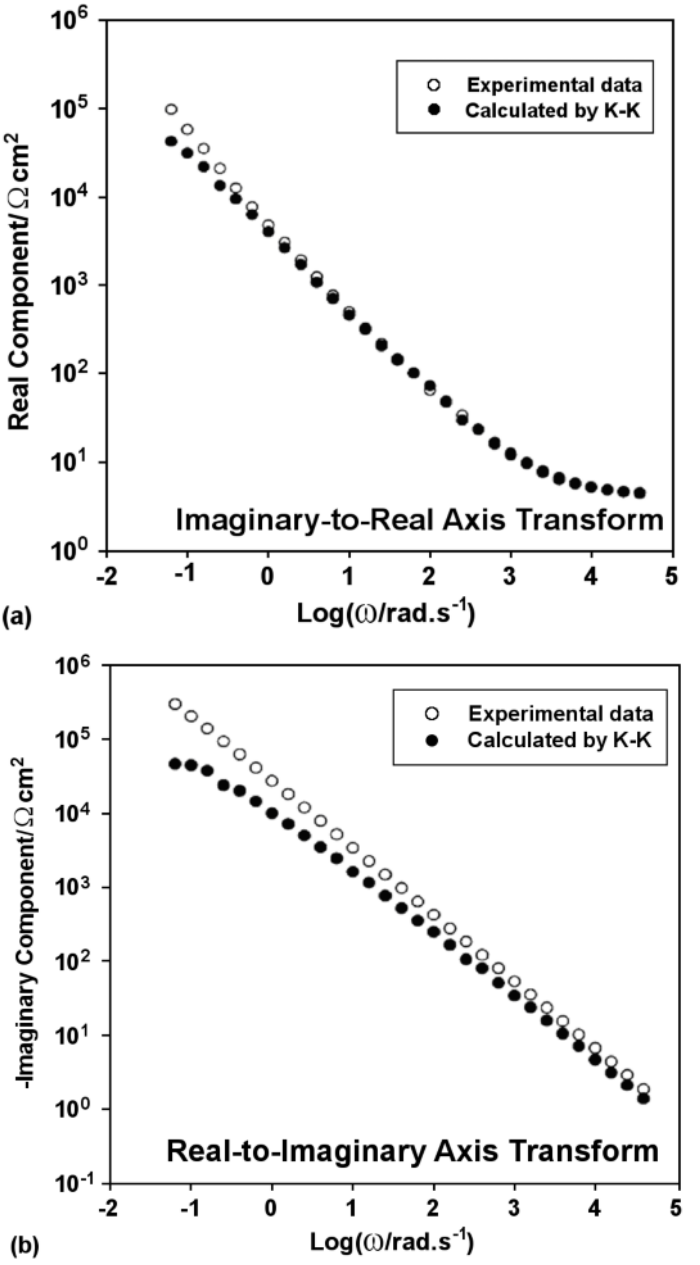

Figure C.2. Typical K–K transforms of the impedance data for Alloy 22 in acidified (pH = 3), saturated (6.2 M) NaCl solution at 80°C. *a* Real-to imaginary axis transformation; *b* imaginary-to-real axis transformation [8]. (Reprinted from Journal of Electroanalytical Chemistry, 572(2), Priyantha N, Jayaweera P, Macdonald DD, Sun A. An electrochemical impedance study of Alloy 22 in NaCl brine at elevated temperature. I. Corrosion behavior, 409–19, ©2004 with permission from Elsevier.)

An interesting example arises from the work of Polo et al., who validated the impedance fitting of 254SMO and AISI304 stainless steels under pitting conditions. The comparisons are presented in Figures C.3 and C.4. According to these figures, the impedance data satisfy K–K transforms for UNS S31254 SS but do not fulfil K–K relations for UNS S30400 SS [11].

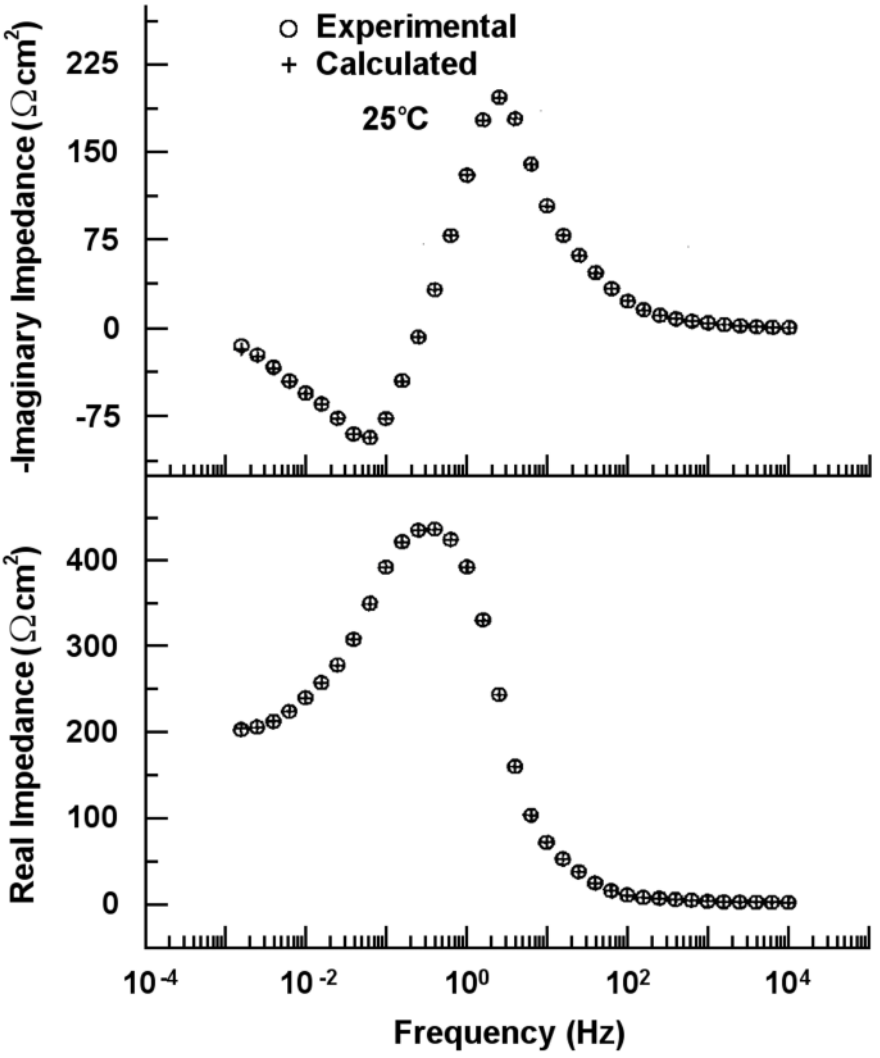

Figure C.3. Comparison of experimental impedance and impedance calculated using K–K relations for a UNS S31254 SS/diethylamine system at 0.840 V (SCE) and 25°C [11]. (Reproduced from Polo JL, Cano E, Kong DY, Bastidas JM. Impedance fitting of 254SMO and AISI304 stainless steels under pitting conditions. Corrosion 2002;58(8):670–4. With permission from the National Association of Corrosion Engineers.)

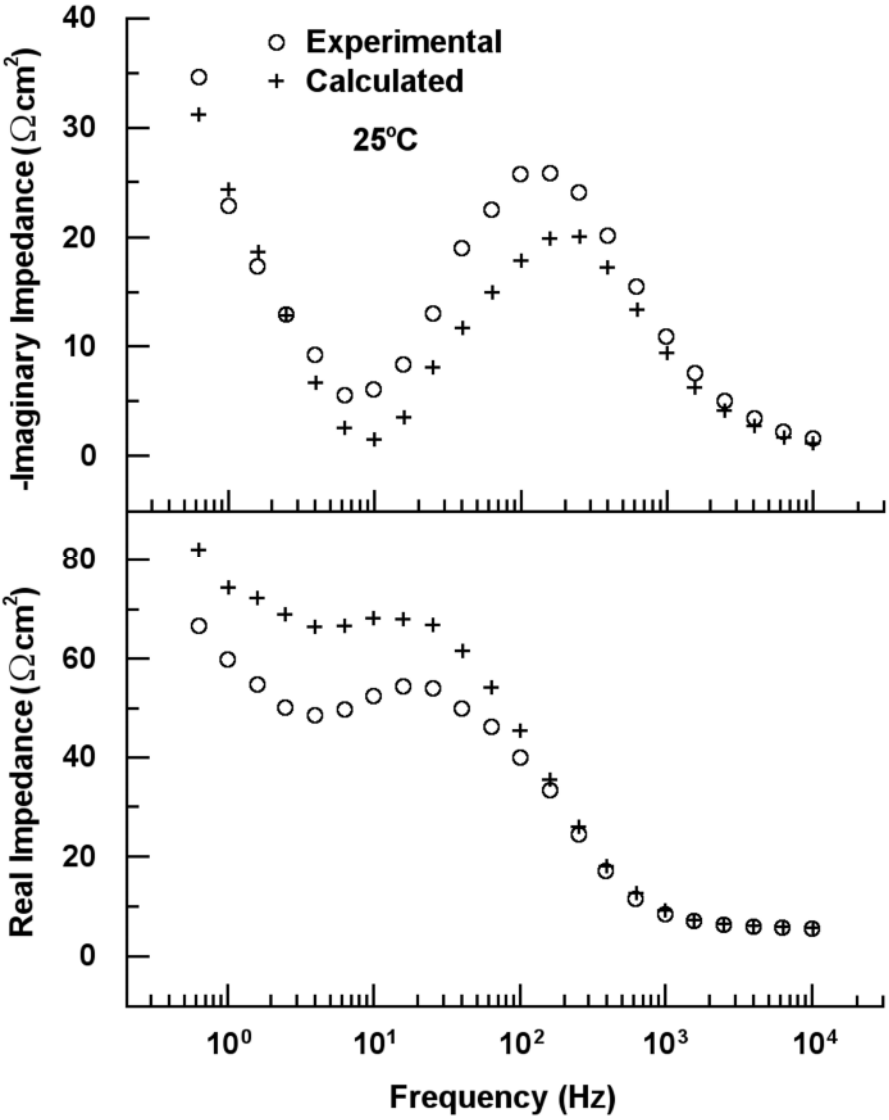

Figure C.4. Comparison of experimental impedance and impedance calculated using K–K relations for a UNS S30400 SS/NaCl system at 0.5 V (SCE) and 25°C [11]. (Reproduced from Polo JL, Cano E, Kong DY, Bastidas JM. Impedance fitting of 254SMO and AISI304 stainless steels under pitting conditions. Corrosion 2002;58(8):670–4. With permission from the National Association of Corrosion Engineers.)

The main problem with this method is that the requirement that integration be carried out from zero to infinite frequency is an experimental impossibility. Hence, the extensions have to be extrapolated to zero and infinite frequency from the tested frequency window. This could be achieved by the use of polynomial

extrapolation, suggested by Urquidi-Macdonald et al. [4]. When an end region can be modelled by a single time constant, i.e., by a simple equivalent circuit obtained through a partial CNLS-fit, a more realistic extrapolation can be obtained [14].

Another method, developed by Agarwal et al. [15], is to model the impedance data with an equivalent circuit consisting of a set of parallel RC circuits in series. The circuit parameters are obtained from CNLS fitting. If the residuals, defined as

$$\Delta_{re} = \frac{Z_{re,i} - Z_{re}(\omega_i, a_k)}{\left|Z(\omega_i, a_k)\right|} \tag{C.3}$$

$$\Delta_{im} = \frac{Z_{im,i} - Z_{im}(\omega_i, a_k)}{\left|Z(\omega_i, a_k)\right|} \tag{C.4}$$

exceed the preset error limit, additional parallel RC circuits can be added to the equivalent circuit, until no significant improvement can be obtained. The fitting procedures sometimes need to be repeated several times.

Summary

The application of K–K relations to the real or imaginary parts of actual experimental data does not often allow the measured values of the other parts to be calculated closely, as data over all frequencies is never available, and all experimental data are contaminated by error. Nevertheless, K–K analysis turns out to be very helpful when no appropriate mathematical model or equivalent circuit is available, and thus no NNLS fitting can be used [7].

References

1. Urquidi-Macdonald M, Real MS, Macdonald DD (1986) Application of Kramers-Kronig transforms in the analysis of electrochemical impedance data. J Electrochem Soc 133(10):2018–24
2. Macdonald DD, Urquidi-Macdonald M (1985) Application of Kramers-Kronig transforms in the analysis of electrochemical systems. J Electrochem Soc 132(10):2316–19
3. Macdonald DD, Urquidi-Macdonald M (1990) Kramers-Kronig transformation of constant phase impedances. J Electrochem Soc 137(2):515–17
4. Urquidi-Macdonald M, Real S, Macdonald DD (1990) Applications of Kramers-Kronig transforms in the analysis of electrochemical impedance data—III. Stability and linearity. Electrochim Acta 35(10):1559–66
5. Shi M, Chen Z, Sun J (1999) Kramers-Kronig transform used as stability criterion of concrete. Cem Concr Res 29(10):1685–8
6. Tan GL, DeNoyer LK, French RH, Guittet MJ, Gautier-Soyer M (2004) Kramers-Kronig transform for the surface energy loss function. J Electron Spectrosc Relat Phenom 142(2):97–103

7. Barsoukov E, Macdonald JR (2005) Impedance spectroscopy theory, experiment, and applications, 2nd edn. Wiley Interscience, Hoboken, NJ
8. Priyantha N, Jayaweera P, Macdonald DD, Sun A (2004) An electrochemical impedance study of alloy 22 in NaCl brine at elevated temperature. I. Corrosion behavior. J Electroanal Chem 572(2):409–19
9. Boukamp BA (2004) Electrochemical impedance spectroscopy in solid state ionics: recent advances. Solid State Ionics 169(1–4):65–73
10. Darowicki K, Kawula J (2004) Validity of impedance spectra obtained by dynamic electrochemical impedance spectroscopy verified by Kramers-Kronig transformation. Pol J Chem 78(9):1255–60
11. Polo JL, Cano E, Kong DY, Bastidas JM (2002) Impedance fitting of 254SMO and AISI304 stainless steels under pitting conditions. Corrosion 58(8):670–4
12. Song H, Macdonald DD (1991) Photoelectrochemical impedance spectroscopy. J Electrochem Soc 138(5):1408–10
13. Ismail KM, Macdonald DD (1994) Characterization of the barrier passive film on zinc. In: Proceedings of the seventh international symposium on oxide films on metals and alloys. Electrochemical Society, Pennington, NJ
14. Boukamp BA (1993) Practical application of the Kramers-Kronig transformation on impedance measurements in solid state electrochemistry. Solid State Ionics 62(1–2):131–41
15. Agarwal P, Orazem ME, Garcia-Rubio LH (1992) Measurement models for electrochemical impedance spectroscopy. J Electrochem Soc 139(7):1917–27

Appendix D

Effects of Equivalent Circuit Parameters on Nyquist Plots

Model D1

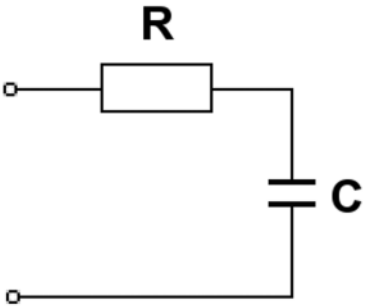

Figure D.1. Resistor and capacitor in series (Figure 4.2*a*)

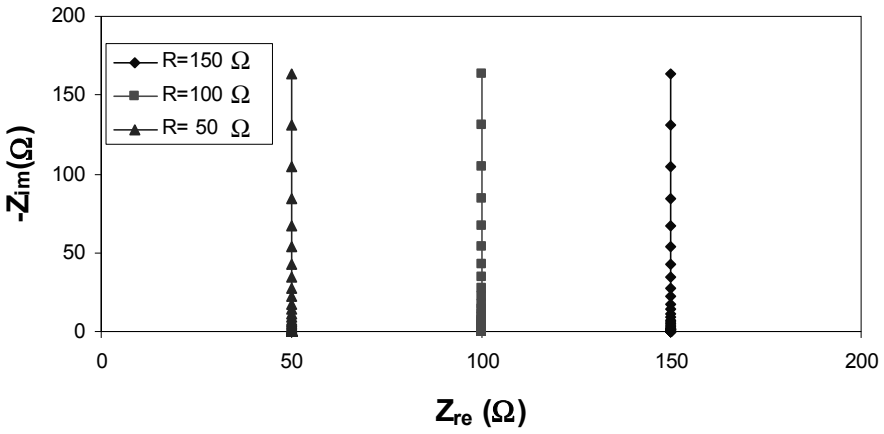

Figure D.2. Nyquist plot of resistor and capacitor in series over the frequency range 1 MHz to 1 mHz ($C = 1\,\mathrm{F}$)

Model D2

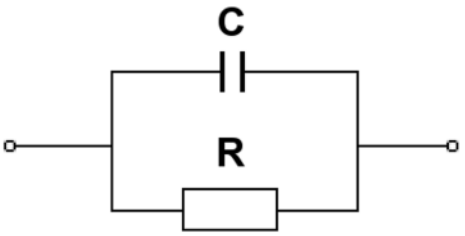

Figure D.3. A resistor and a capacitor in parallel (Figure 4.3*a*)

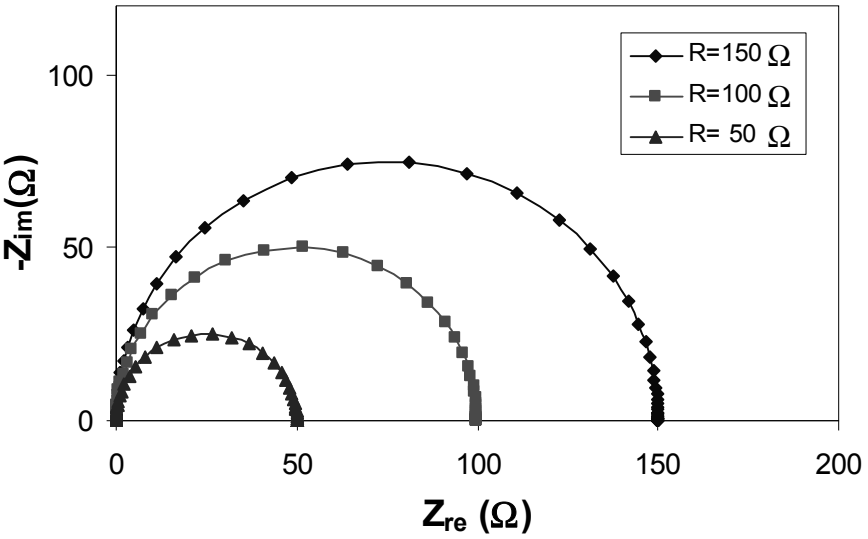

Figure D.4. Simulated Nyquist plot of a resistor and a capacitor in parallel over the frequency range 1 MHz to 1 mHz (C = 0.001 F)

Model D3

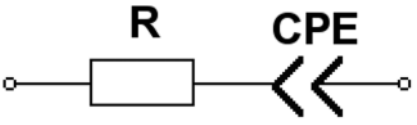

Figure D.5. A resistor and a CPE in series (Figure 4.4*a*)

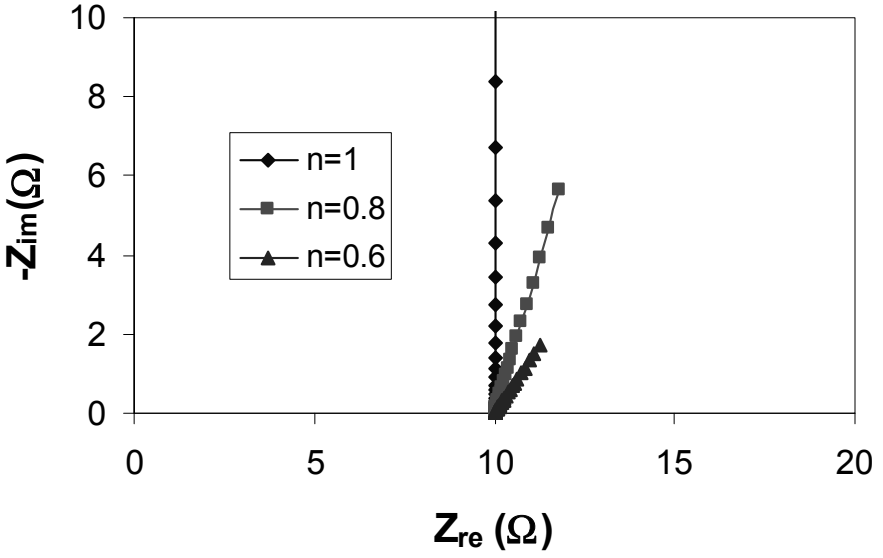

Figure D.6. Simulated Nyquist plot of a resistor and a CPE in series over the frequency range 1 MHz to 1 mHz ($R = 10\ \Omega$, $Q = 10\ \Omega^{-1}s^{n}$)

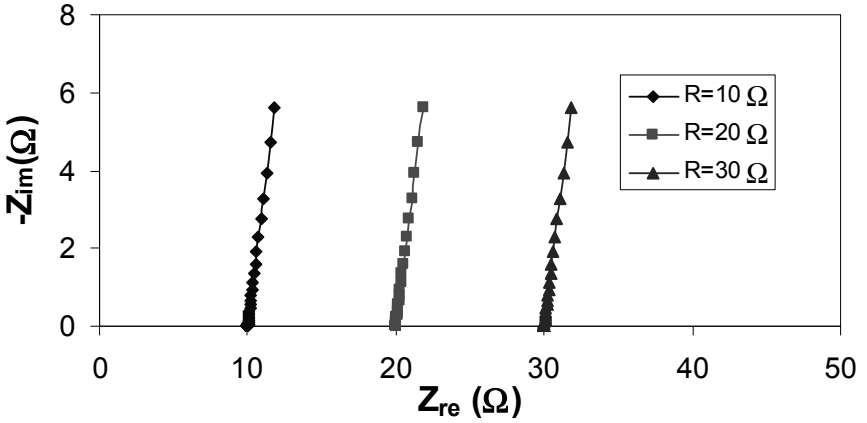

Figure D.7. Simulated Nyquist plot of a resistor and a CPE in series over the frequency range 1 MHz to 1 mHz ($n = 0.8$, $Q = 10\ \Omega^{-1}s^{0.8}$)

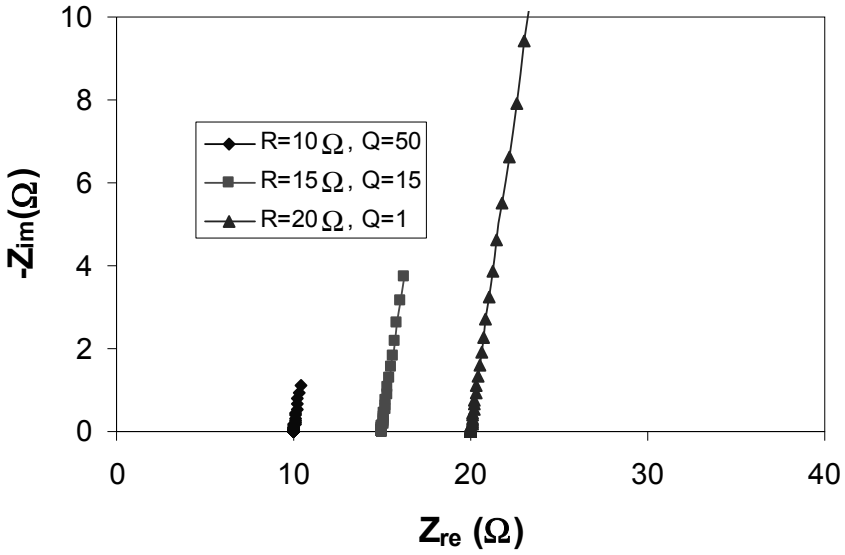

Figure D.8. Simulated Nyquist plot of a resistor and a CPE in series over the frequency range 1 MHz to 1 mHz ($n = 0.8$, the unit of $Q : \Omega^{-1}s^{0.8}$)

Model D4

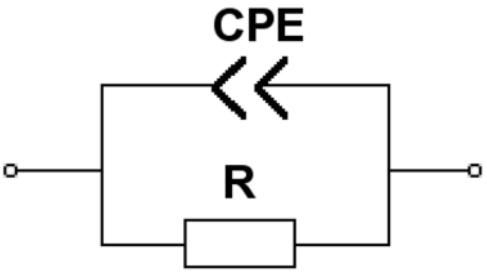

Figure D.9. A resistor and a CPE in parallel (Figure 4.5*a*)

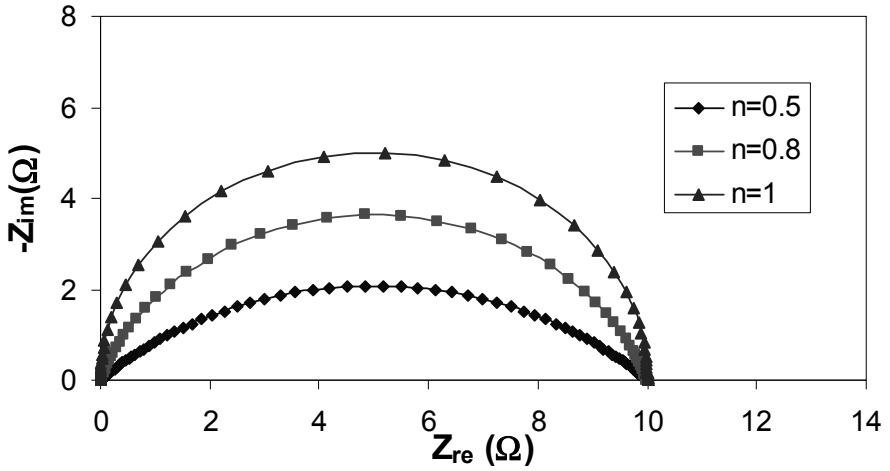

Figure D.10. Simulated Nyquist plot of a resistor and a CPE in parallel over the frequency range 1 MHz to 1 mHz ($R = 10\,\Omega$, $Q = 0.01\ \Omega^{-1}s^{n}$)

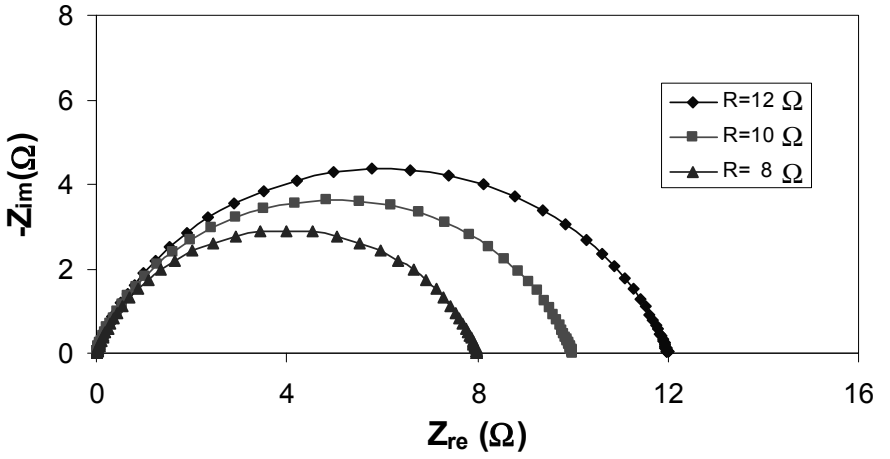

Figure D.11. Simulated Nyquist plot of a resistor and a CPE in parallel over the frequency range 1 MHz to 1 mHz ($n = 0.8$, $Q = 0.01\ \Omega^{-1}s^{0.8}$)

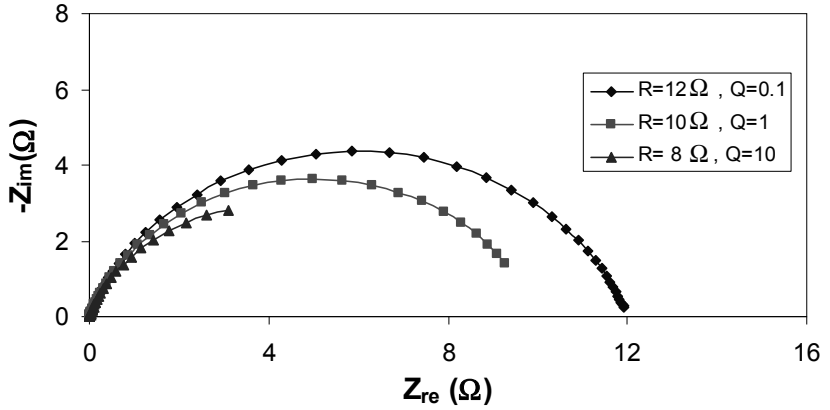

Figure D.12. Simulated Nyquist plot of a resistor and a CPE in parallel over the frequency range 1 MHz to 1 mHz ($n = 0.8$, the unit of Q : $\Omega^{-1}s^{0.8}$)

Model D5

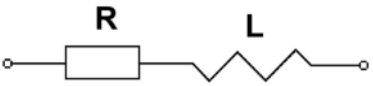

Figure D.13. A resistor and an inductor in series (Figure 4.6*a*)

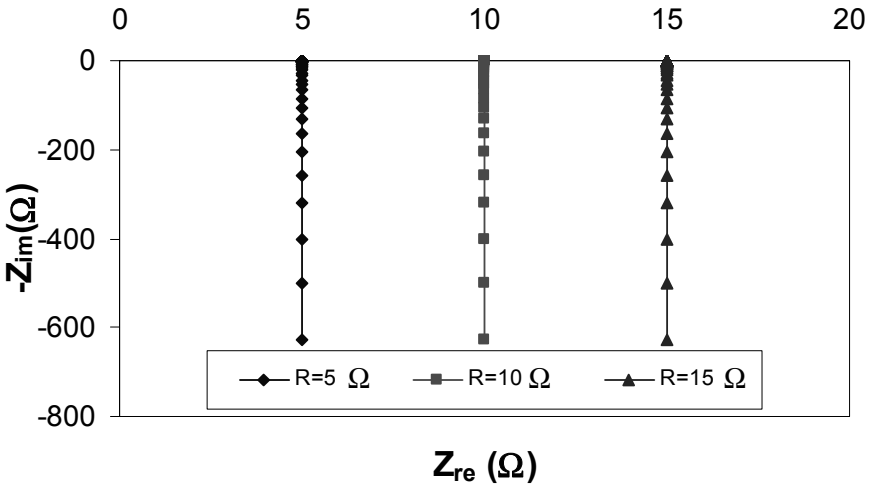

Figure D.14. Nyquist plot of a resistor and an inductor in series over the frequency range 1 MHz to 1 mHz ($L = 0.0001$ H)

Model D6

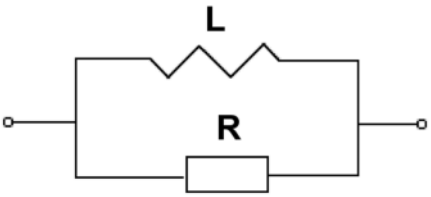

Figure D.15. A resistor and an inductor in parallel (Figure 4.7*a*)

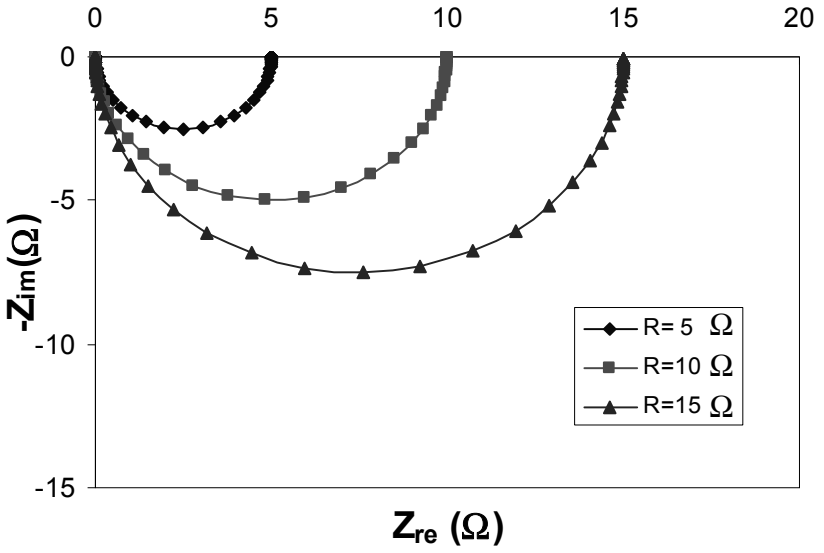

Figure D.16. Nyquist plot of a resistor and an inductor in parallel over the frequency range 1 MHz to 1 mHz (L = 0.001 H)

Model D7

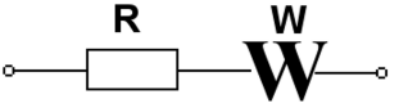

Figure D.17. A resistor and a Warburg element in series (Figure 4.8*a*)

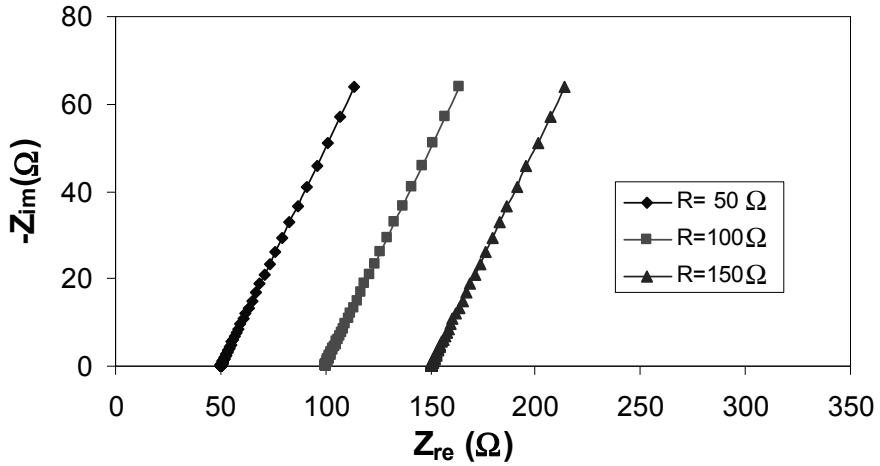

Figure D.18. Simulated Nyquist plot of a resistor and a Warburg element in series over the frequency range 1 MHz to 1 mHz ($\sigma = 5\ \Omega s^{-1/2}$)

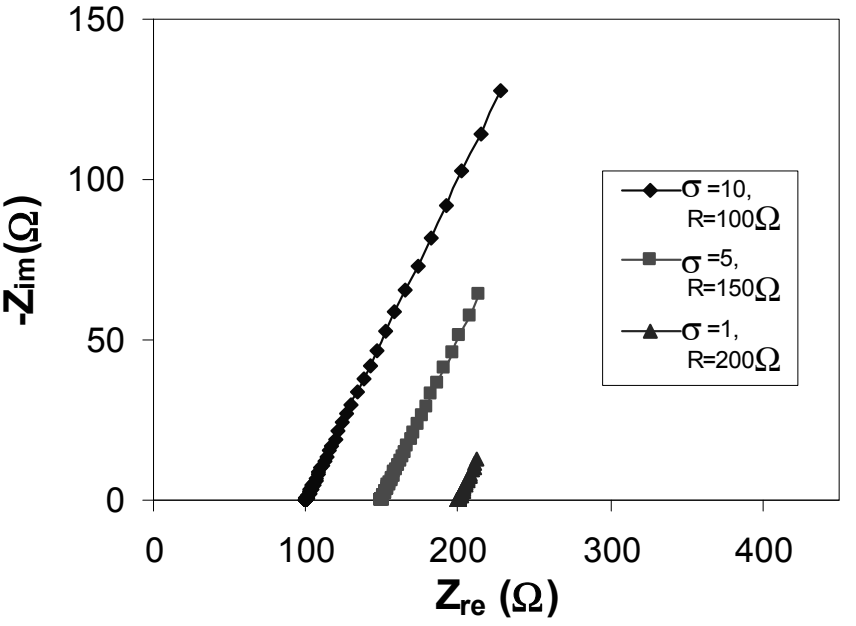

Figure D.19. Simulated Nyquist plot of a resistor and a Warburg element in series over the frequency range 1 MHz to 1 mHz (the unit of σ : $\Omega s^{-1/2}$)

Model D8

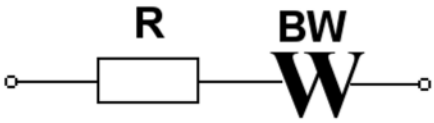

Figure D.20. A resistor and a bounded Warburg in series (Figure 4.9*a*)

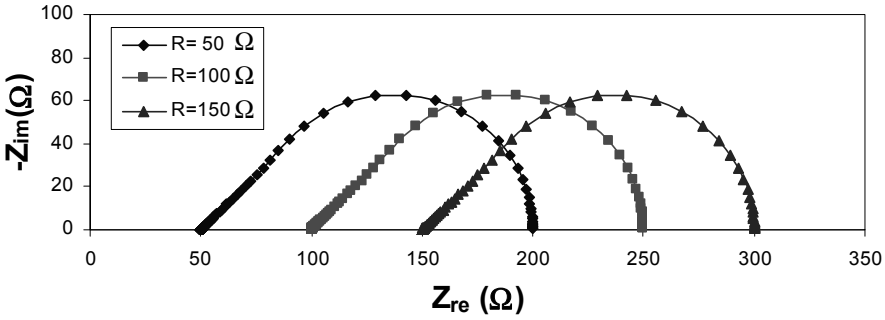

Figure D.21. Nyquist plot of a resistor and a bounded Warburg in series over the frequency range 1 MHz to 1 mHz ($R_0 = 150\ \Omega$, $\sigma = 100\ \Omega s^{-1/2}$)

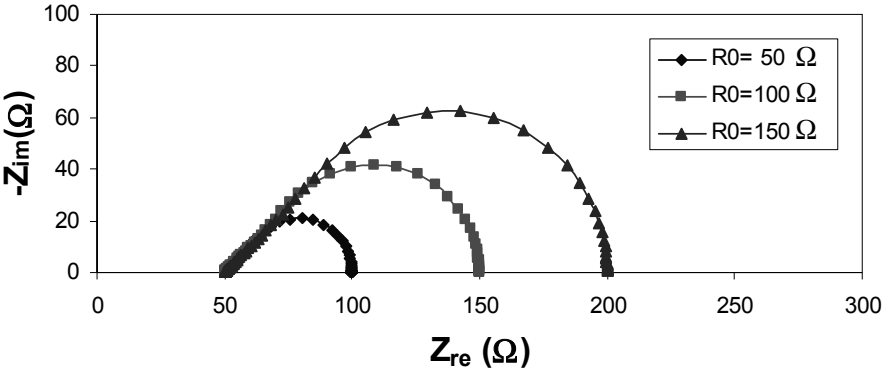

Figure D.22. Nyquist plot of a resistor and a bounded Warburg in series over the frequency range 1 MHz to 1 mHz ($R = 50\ \Omega$, $\sigma = 100\ \Omega s^{-1/2}$)

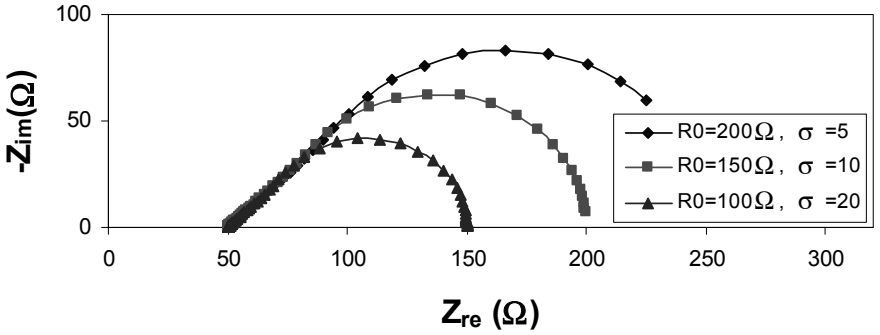

Figure D.23. Nyquist plot of a resistor and a bounded Warburg in series over the frequency range 1 MHz to 0.1 mHz ($R = 50\ \Omega$)

Model D9

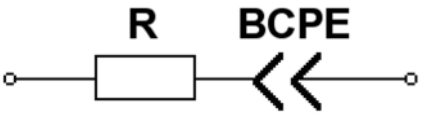

Figure D.24. A resistor and a bounded CPE in series (Figure 4.10*a*)

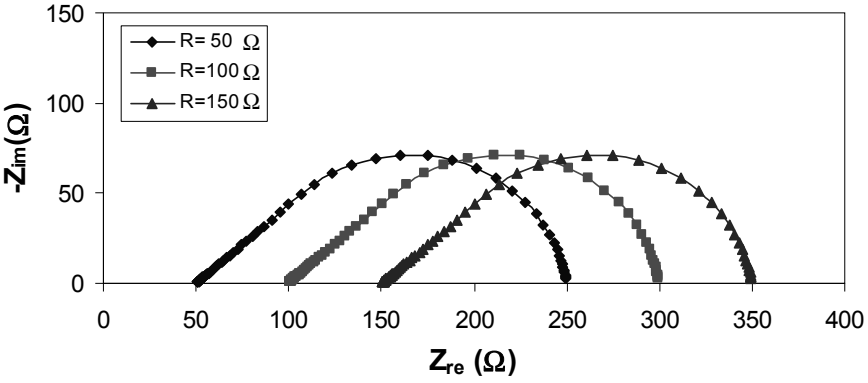

Figure D.25. Nyquist plot of a resistor and a bounded CPE in series over the frequency range 6 kHz to 1 mHz ($R_0 = 200\ \Omega$, $Q = 0.01\ \Omega^{-1}s^n$, $n = 0.45$)

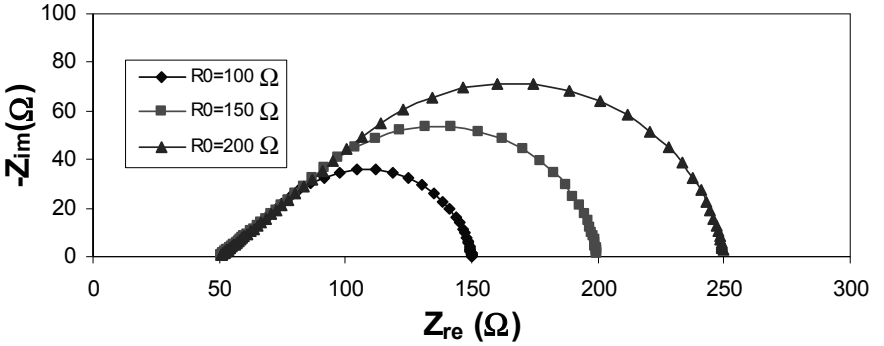

Figure D.26. Nyquist plot of a resistor and a bounded CPE in series over the frequency range 28 kHz to 1 mHz ($R = 50\ \Omega$, $Q = 0.01\ \Omega^{-1}s^{n}$, $n = 0.45$)

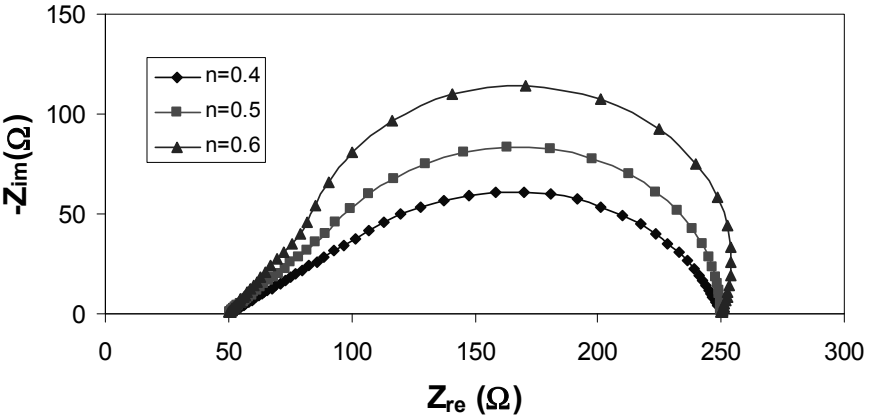

Figure D.27. Nyquist plot of a resistor and a bounded CPE in series over the frequency range 18 kHz to 1 mHz ($R = 50\ \Omega$, $R_0 = 200\ \Omega$, $Q = 0.01\ \Omega^{-1}s^{n}$)

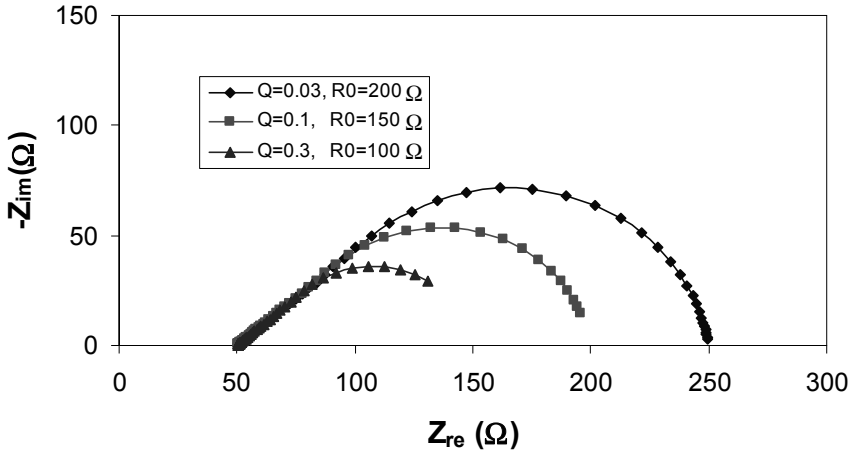

Figure D.28. Nyquist plot of a resistor and a bounded CPE in series over the frequency range 500 Hz to 0.1 mHz ($R = 50\ \Omega$, $n = 0.45$, the unit of $Q: \Omega^{-1}s^{0.45}$)

Model D10

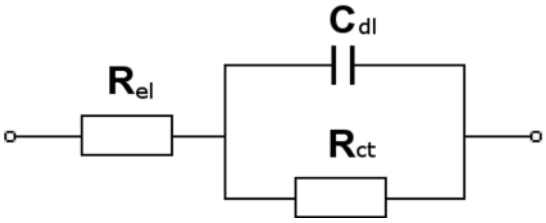

Figure D.29. Randles cell (Figure 4.11*a*)

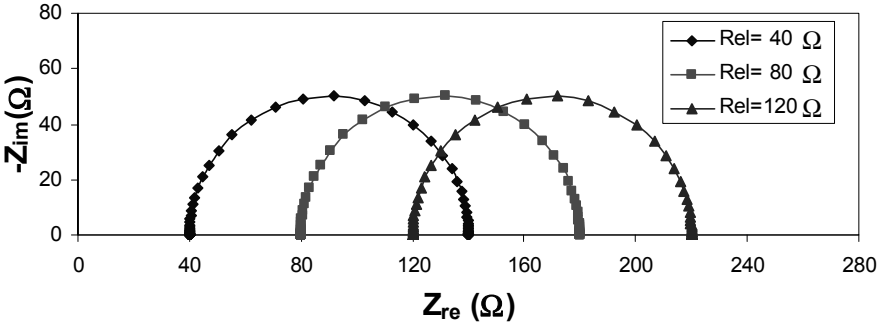

Figure D.30. Nyquist plot of Randles cell over the frequency range 1 MHz to 1 mHz ($R_{ct} = 100\ \Omega$, $C = 0.001\ F$)

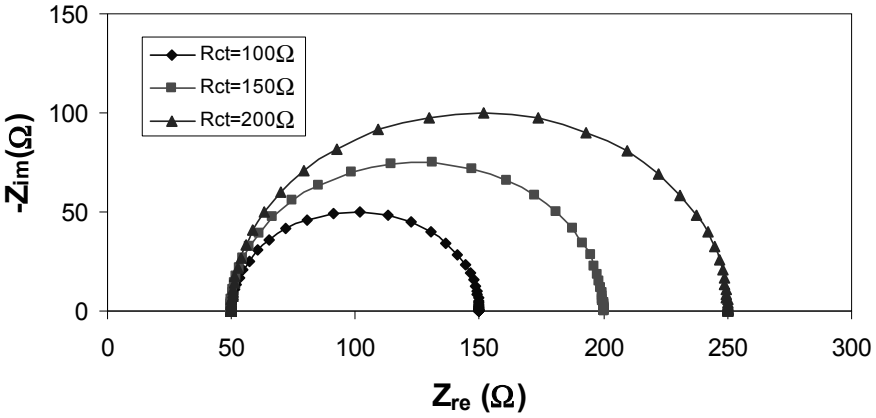

Figure D.31. Nyquist plot of Randles cell over the frequency range 1 MHz to 1 mHz ($R_{el} = 50\ \Omega$, $C = 0.001\ F$)

Model D11

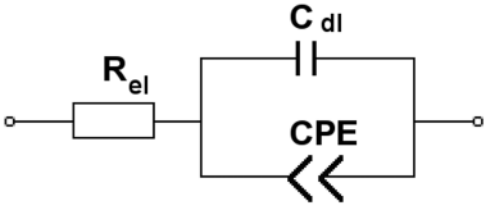

Figure D.32. Randles cell with R_{ct} replaced by CPE (Figure 4.12*a*)

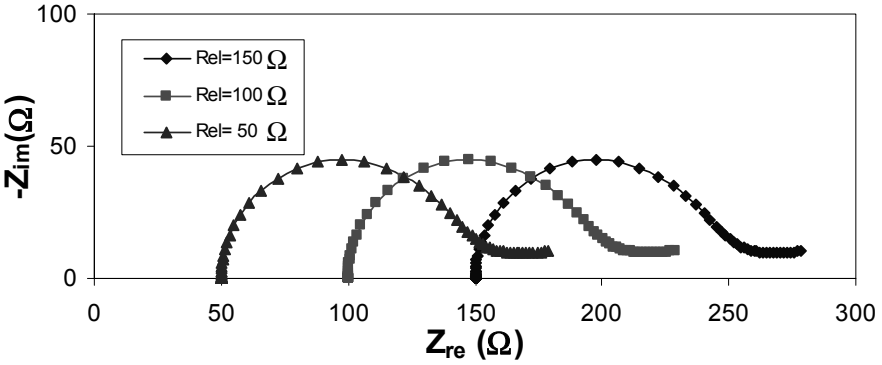

Figure D.33. Nyquist plot of Randles cell with R_{ct} replaced by CPE over the frequency range 1 MHz to 1 mHz ($C_{dl} = 0.001\ F$, $n = 0.05$, $Q = 0.01\ \Omega^{-1}s^{0.05}$)

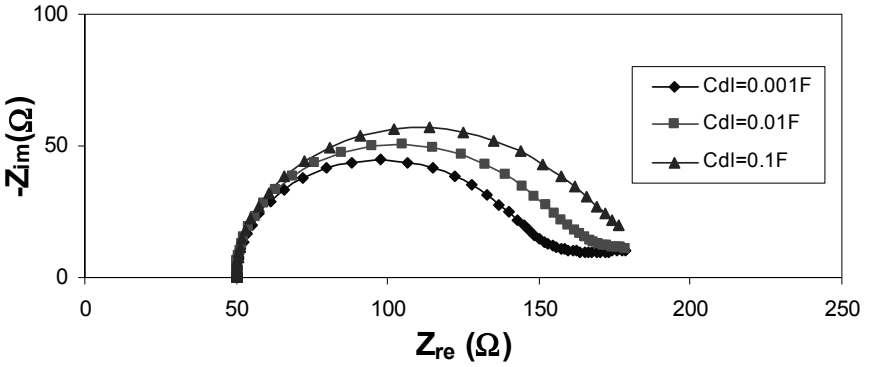

Figure D.34. Nyquist plot of Randles cell with R_{ct} replaced by CPE over the frequency range 1 MHz to 1 mHz ($R_{el} = 50\,\Omega$, $n = 0.05$, $Q = 0.01\,\Omega^{-1}s^{0.05}$)

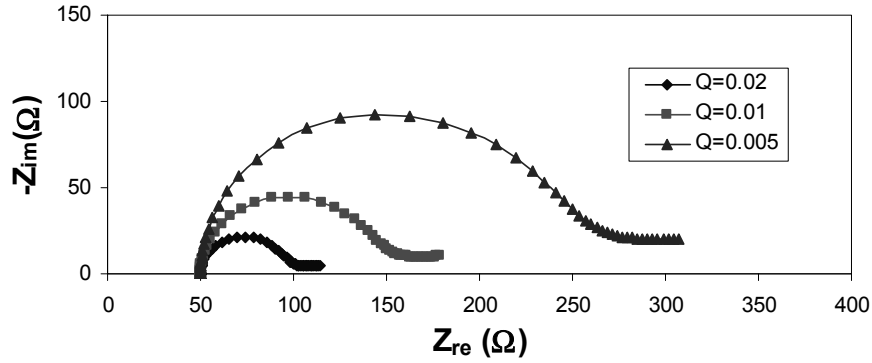

Figure D.35. Nyquist plot of Randles cell with R_{ct} replaced by CPE over the frequency range 1 MHz to 1 mHz ($R_{el} = 50\,\Omega$, $C_{dl} = 0.001\,F$, $n = 0.05$, the unit of $Q : \Omega^{-1}s^{0.05}$)

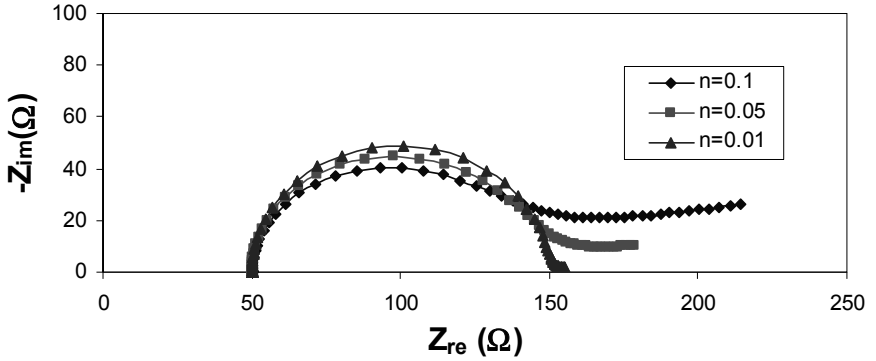

Figure D.36. Nyquist plot of Randles cell with R_{ct} replaced by CPE over the frequency range 1 MHz to 1 mHz ($R_{el} = 50\ \Omega$, $C_{dl} = 0.001\ F$, $Q = 0.01\ \Omega^{-1}s^{n}$)

Model D12

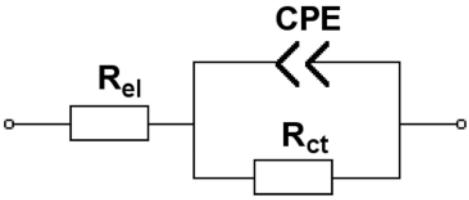

Figure D.37. Randles cell with capacitor replaced by CPE (Figure 4.13*a*)

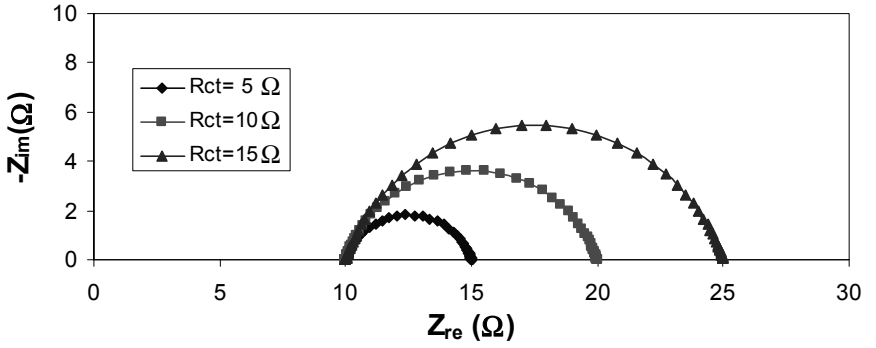

Figure D.38. Nyquist plot of Randles cell with capacitor replaced by CPE over the frequency range 1 MHz to 1 mHz ($R_{el} = 10\ \Omega$, $n = 0.8$, $Q = 0.01\ \Omega^{-1}s^{0.8}$)

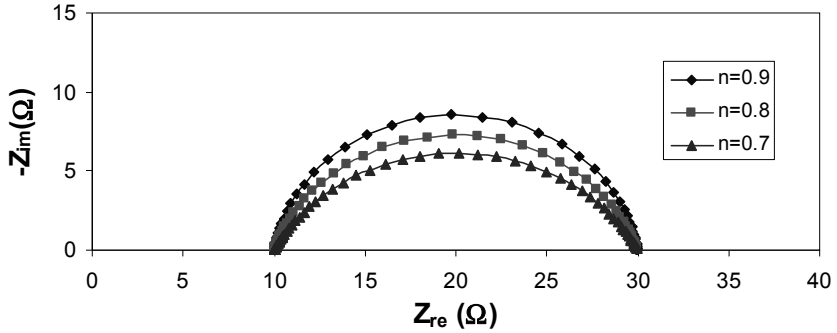

Figure D.39. Nyquist plot of Randles cell with capacitor replaced by CPE over the frequency range 1 MHz to 1 mHz ($R_{el} = 10\ \Omega$, $R_{ct} = 20\ \Omega$, $Q = 0.01\ \Omega^{-1}s^{n}$)

Model D13

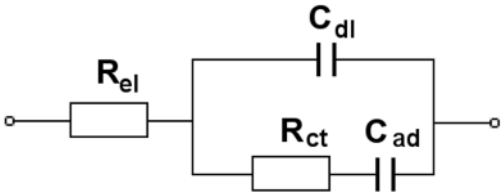

Figure D.40. Modified Randles cell with an extra capacitor in series with R_{ct} (Figure 4.14*a*)

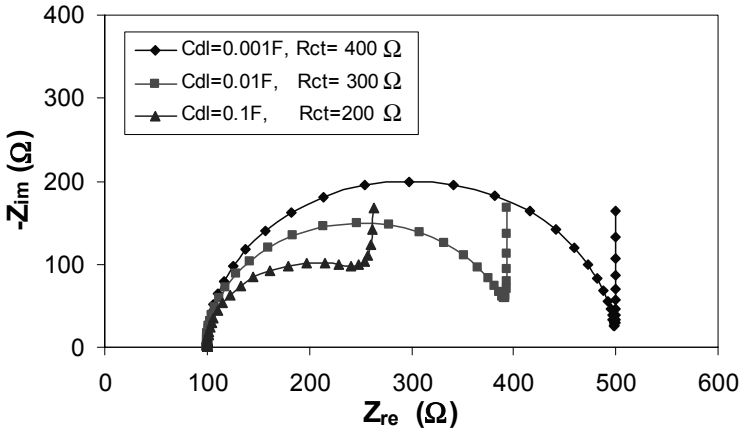

Figure D.41. Nyquist plot of modified Randles cell with an extra capacitor in series with R_{ct} over the frequency range 1 MHz to 1 mHz ($R_{el} = 100\ \Omega$, $C_{ad} = 1\ F$)

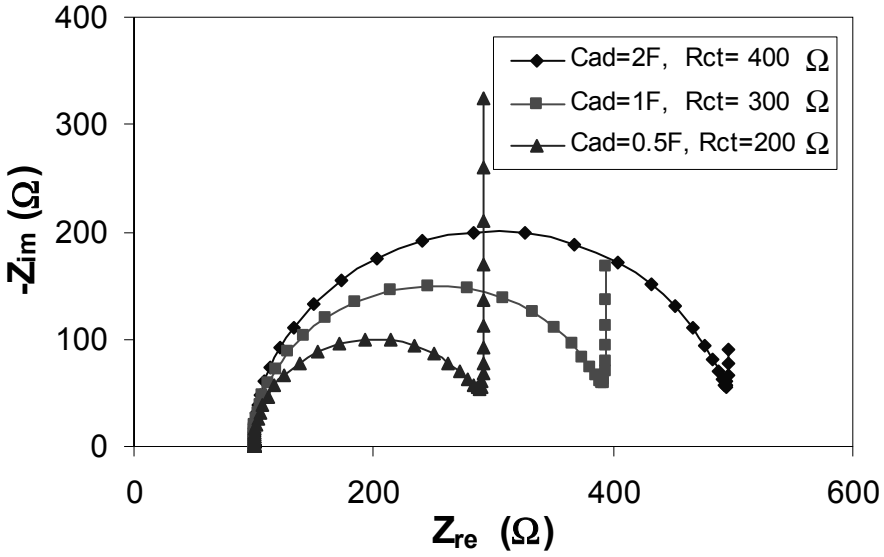

Figure D.42. Nyquist plot of Randles cell with an extra capacitor in series with R_{ct} over the frequency range 1 MHz to 1 mHz ($R_{el} = 100\ \Omega$, $C_{dl} = 0.01\ F$)

Model D14

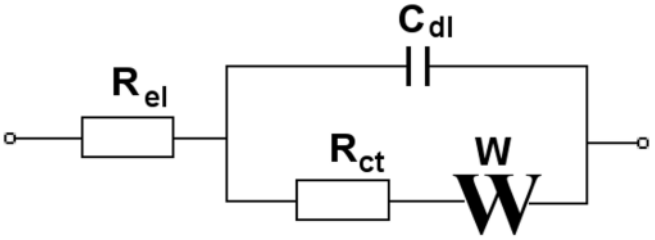

Figure D.43. Modified Randles cell with a Warburg element in series with R_{ct}. (Figure 4.15*a*)

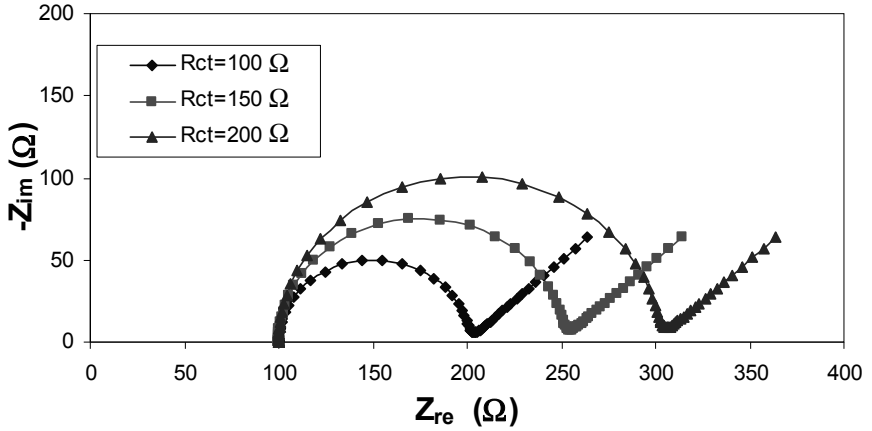

Figure D.44. Nyquist plot of Randles cell with a Warburg element in series with R_{ct} over the frequency range 1 MHz to 1 mHz ($R_{el} = 100\ \Omega$, $C_{dl} = 0.0001\ \mathrm{F}$, $\sigma = 5\ \Omega \mathrm{s}^{-1/2}$)

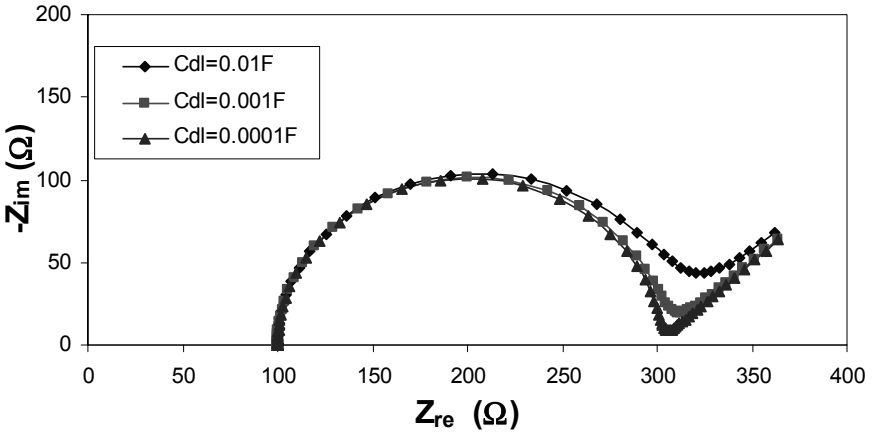

Figure D.45. Nyquist plot of Randles cell with a Warburg element in series with R_{ct} over the frequency range 1 MHz to 1 mHz ($R_{el} = 100\ \Omega$, $R_{ct} = 200\ \Omega$, $\sigma = 5\ \Omega \mathrm{s}^{-1/2}$)

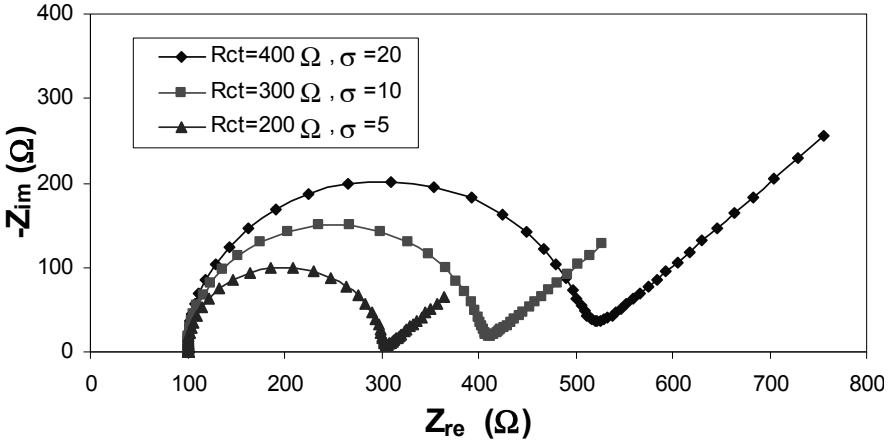

Figure D.46. Nyquist plot of Randles cell with a Warburg element in series with R_{ct} over the frequency range from 1 MHz to 1 mHz ($R_{el} = 100\,\Omega$, $C_{dl} = 0.0001\,F$, the unit of $\sigma : \Omega s^{-1/2}$)

Model D15

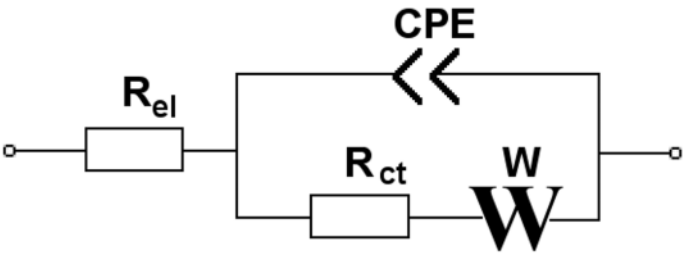

Figure D.47. Modified equivalent circuit of Model D14 with CPE in place of capacitor (Figure 4.16*a*)

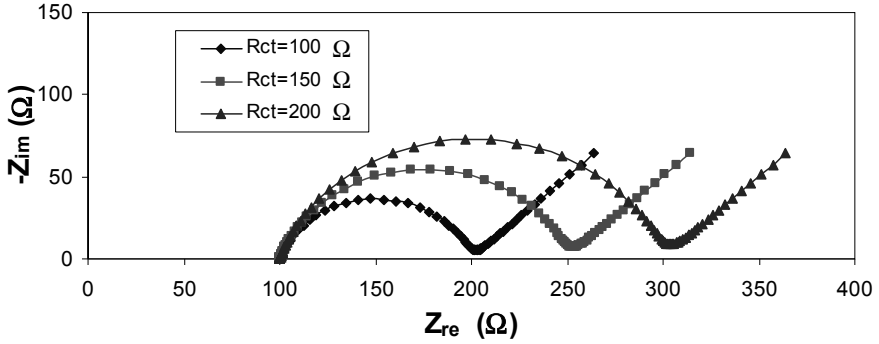

Figure D.48. Nyquist plot of a modified equivalent circuit of Model D14 with CPE in place of capacitor, over the frequency range 1 MHz to 1 mHz ($R_{el} = 100\ \Omega$, $Q = 0.0001\ \Omega^{-1}s^{0.8}$, $\sigma = 5\ \Omega s^{-1/2}$, $n = 0.8$)

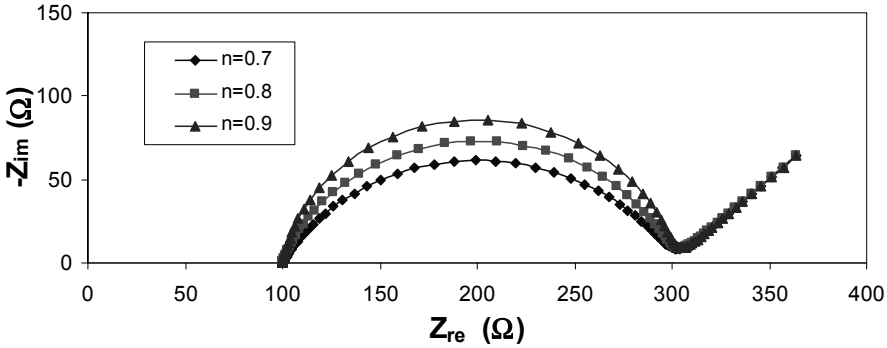

Figure D.49. Nyquist plot of a modified equivalent circuit of Model D14 with CPE in place of capacitor, over the frequency range 1 MHz to 1 mHz ($R_{el} = 100\ \Omega$, $R_{ct} = 200\ \Omega$, $Q = 0.0001\ \Omega^{-1}s^{0.8}$, $\sigma = 5\ \Omega s^{-1/2}$)

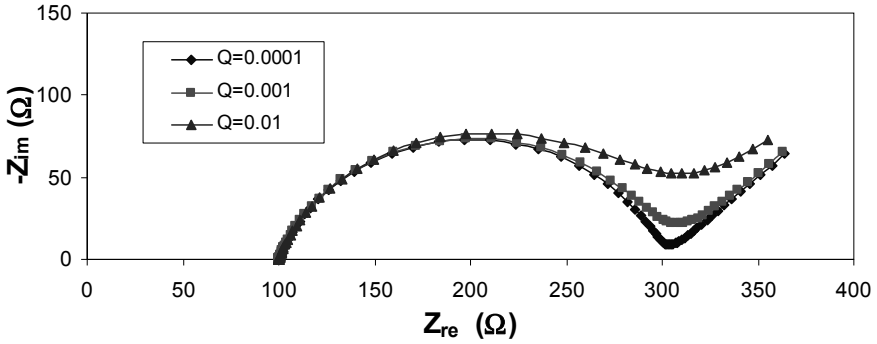

Figure D.50. Nyquist plot of a modified equivalent circuit of Model D14 with CPE in place of capacitor, over the frequency range 1 MHz to 1 mHz ($R_{el} = 100\ \Omega$, $R_{ct} = 200\ \Omega$, $\sigma = 5\ \Omega s^{-1/2}$, $n = 0.8$, the unit of $Q : \Omega^{-1}s^{0.8}$)

Model D16

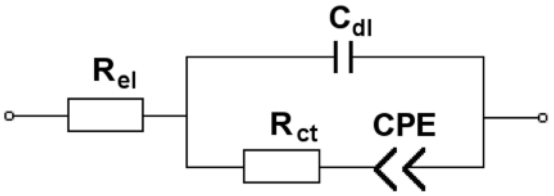

Figure D.51. Modified Randles cell with a CPE in series with R_{ct} (Figure 4.17*a*)

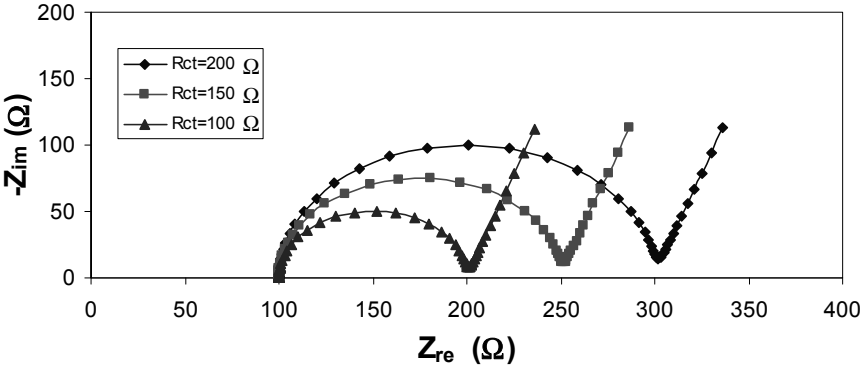

Figure D.52. Nyquist plot of the modified Randles cell with an extra CPE in series with R_{ct} over the frequency range 1 MHz to 1 mHz ($R_{el} = 100\ \Omega$, $C_{dl} = 0.001\ F$, $Q = 0.5\ \Omega^{-1}s^{0.8}$, $n = 0.8$)

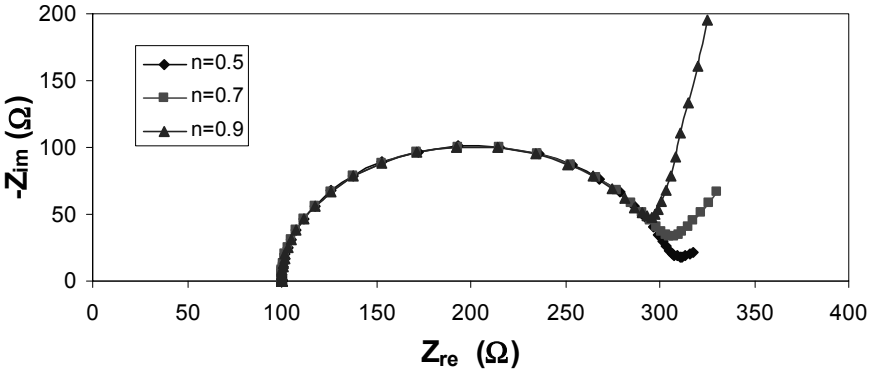

Figure D.53. Nyquist plot of modified Randles cell with an extra CPE in series with R_{ct} over the frequency range 1 MHz to 1 mHz ($R_{el} = 100\ \Omega$, $R_{ct} = 200\ \Omega$, $C_{dl} = 0.01\ F$, $Q = 0.5\ \Omega^{-1}s^{n}$)

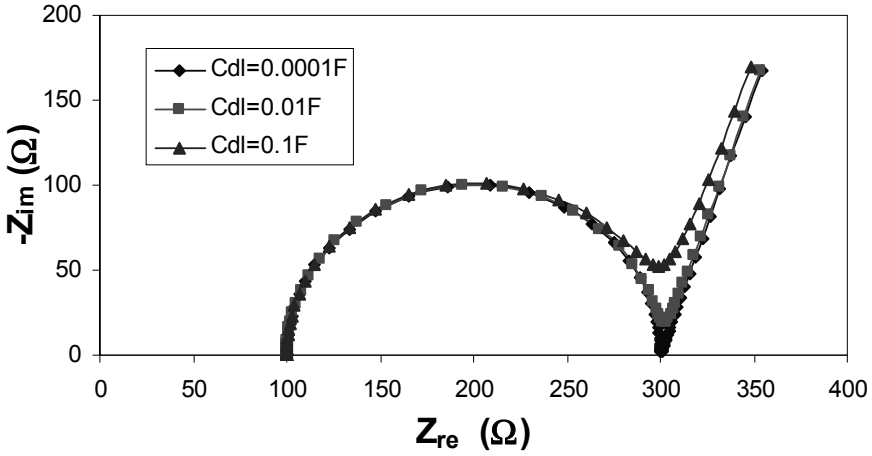

Figure D.54. Nyquist plot of modified Randles cell with an extra CPE in series with R_{ct} over the frequency range 1 MHz to 0.1 mHz ($R_{el} = 100\ \Omega$, $R_{ct} = 200\ \Omega$, $Q = 2\ \Omega^{-1}s^{0.8}$, $n = 0.8$)

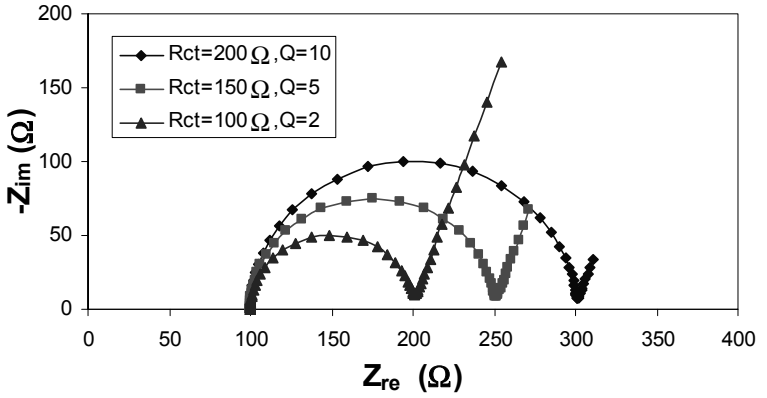

Figure D.55. Nyquist plot of modified Randles cell with an extra CPE in series, with R_{ct} over the frequency range 1 MHz to 0.1 mHz ($R_{el} = 100\,\Omega$, $C_{dl} = 0.01\,F$, $n = 0.8$, the unit of $Q: \Omega^{-1}s^{0.8}$)

Model D17

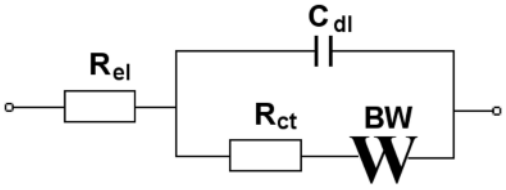

Figure D.56. Modified Randles cell with a bounded Warburg in series with R_{ct} (Figure 4.18*a*)

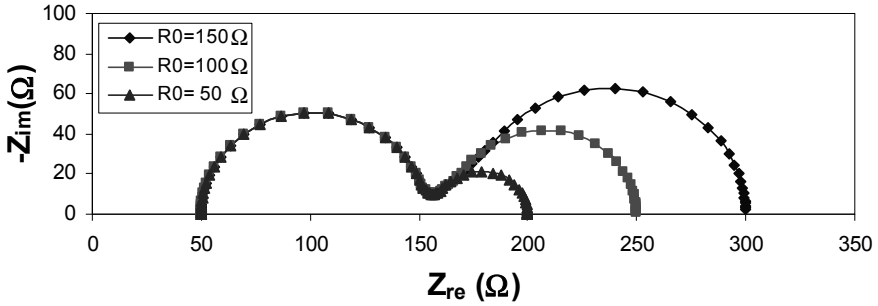

Figure D.57. Nyquist plot of modified Randles cell with a bounded Warburg element over the frequency range 1 MHz to 1 mHz ($R_{el} = 50\,\Omega$, $R_{ct} = 100\,\Omega$, $C_{dl} = 0.00001\,F$, $\sigma = 50\,\Omega s^{-1/2}$)

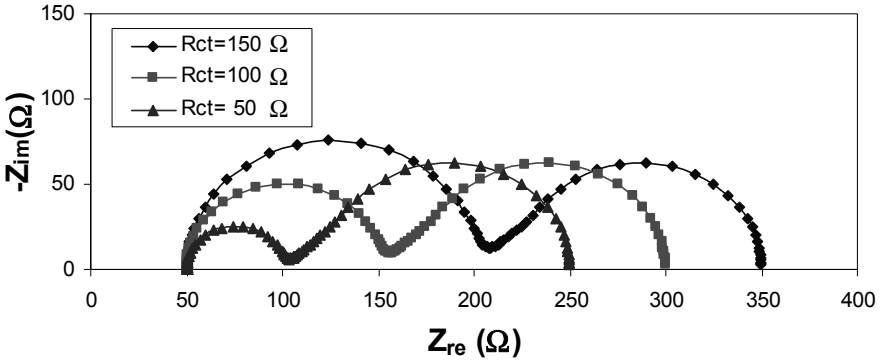

Figure D.58. Nyquist plot of modified Randles cell with a bounded Warburg element over the frequency range 1 MHz to 1 mHz ($R_{el} = 50\,\Omega$, $R_0 = 150\,\Omega$, $C_{dl} = 0.00001\,F$, $\sigma = 50\,\Omega s^{-1/2}$)

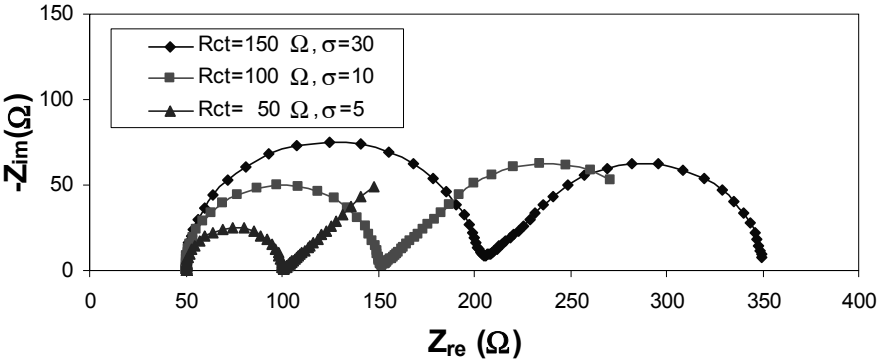

Figure D.59. Nyquist plot of modified Randles cell with a bounded Warburg element over the frequency range 1 MHz to 1 mHz ($R_{el} = 50\,\Omega$, $R_0 = 150\,\Omega$, $C_{dl} = 0.00001\,F$, the unit of σ : $\Omega s^{-1/2}$)

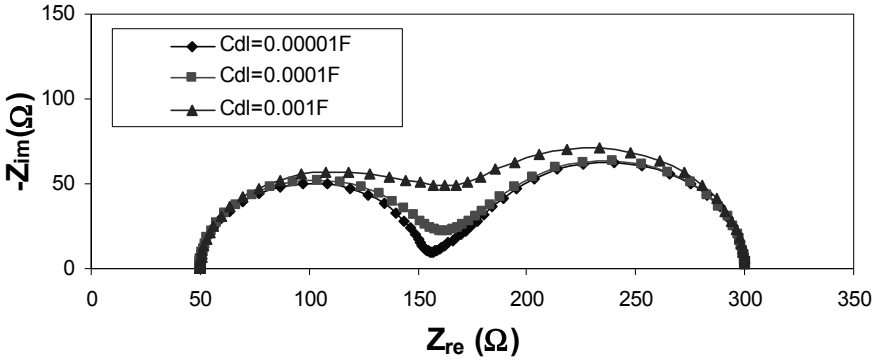

Figure D.60. Nyquist plot of modified Randles cell with a bounded Warburg element over the frequency range 1 MHz to 1 mHz ($R_{el} = 50\ \Omega$, $R_{ct} = 100\ \Omega$, $\sigma = 50\ \Omega s^{-1/2}$, $R_0 = 150\ \Omega$)

Model D18

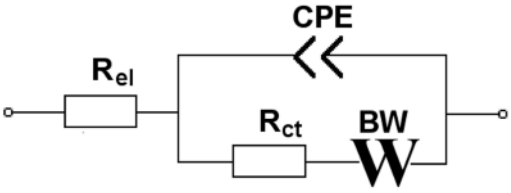

Figure D.61. Modified equivalent circuit of Model 17 with CPE in place of capacitor (Figure 4.19*a*)

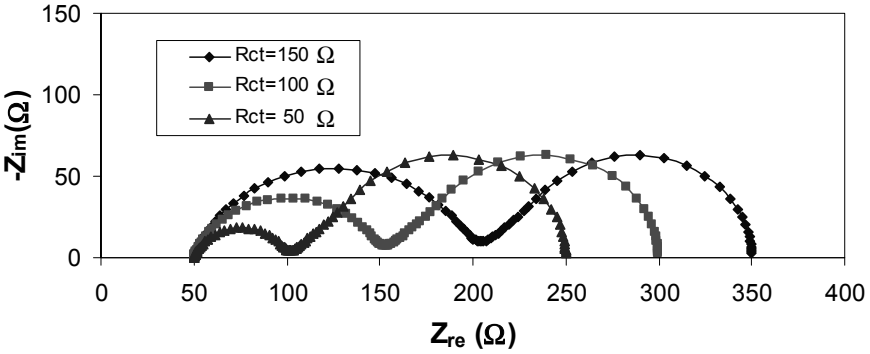

Figure D.62. Nyquist plot of the modified equivalent circuit of Model 17 with CPE in place of capacitor over the frequency range 1 MHz to 1 mHz ($R_{el} = 50\ \Omega$, $Q = 0.00001\ \Omega^{-1}s^{0.8}$, $n = 0.8$, $\sigma = 50\ \Omega s^{-1/2}$, $R_0 = 150\ \Omega$)

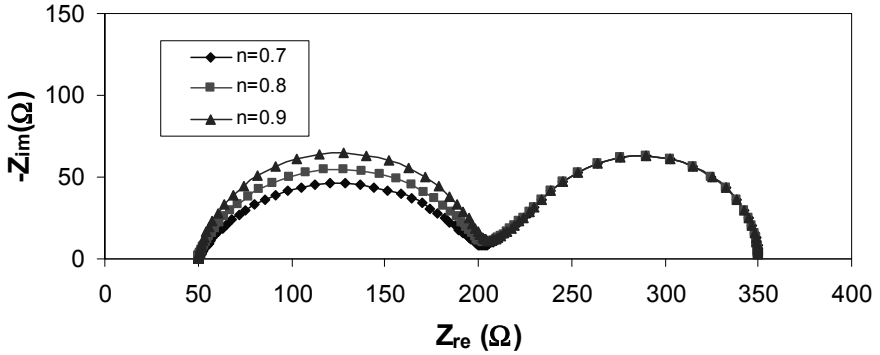

Figure D.63. Nyquist plot of the modified equivalent circuit of Model 17 with CPE in place of capacitor over the frequency range 1 MHz to 1 mHz ($R_{el} = 50\ \Omega$, $R_{ct} = 150\ \Omega$, $Q = 0.00001\ \Omega^{-1}s^{n}$, $\sigma = 50\ \Omega s^{-1/2}$, $R_0 = 150\ \Omega$)

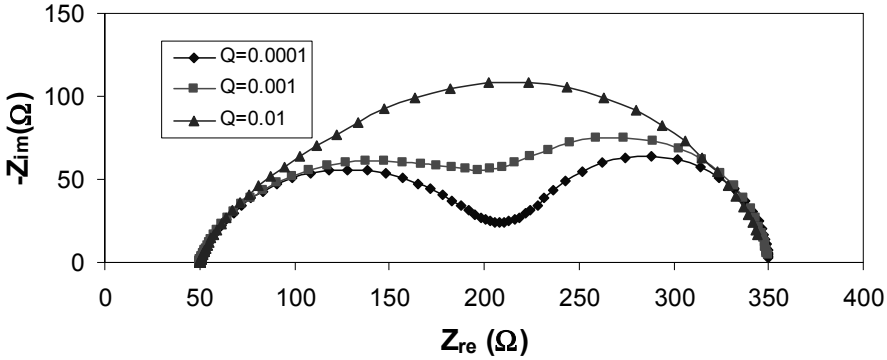

Figure D.64. Nyquist plot of the modified equivalent circuit of Model 17 with CPE in place of capacitor over the frequency range 1 MHz to 1 mHz ($R_{el} = 50\ \Omega$, $R_{ct} = 150\ \Omega$, $n = 0.8$, $\sigma = 50\ \Omega s^{-1/2}$, $R_0 = 150\ \Omega$, the unit of $Q: \Omega^{-1}s^{0.8}$)

Model D19

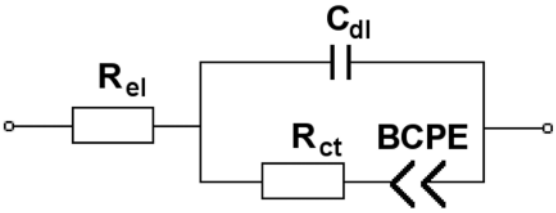

Figure D.65. Equivalent circuit of modified Randles cell with bounded CPE in series with R_{ct} (Figure 4.20*a*)

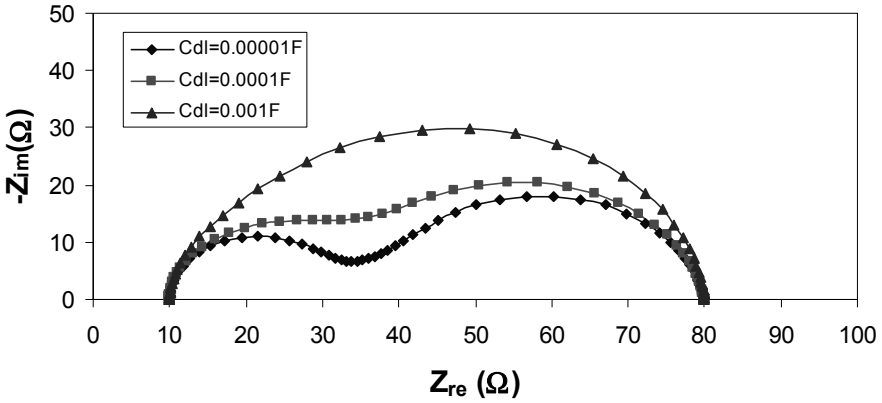

Figure D.66. Nyquist plot of modified Randles cell with bounded CPE in series with R_{ct} over the frequency range 6 kHz to 1 mHz ($R_{el} = 10\ \Omega$, $R_{ct} = 20\ \Omega$, $R_0 = 50\ \Omega$, $Q = 0.01\ \Omega^{-1}s^{0.45}$, $n = 0.45$)

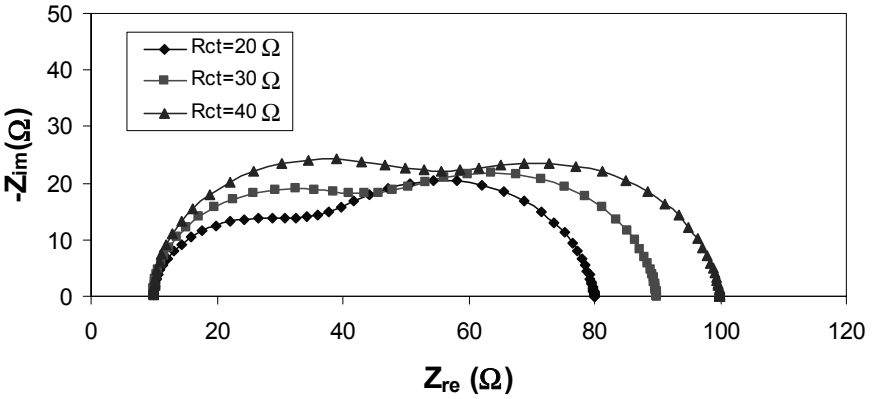

Figure D.67. Nyquist plot of modified Randles cell with bounded CPE in series with R_{ct} over the frequency range 6 kHz to 1 mHz ($R_{el} = 10\ \Omega$, $R_0 = 50\ \Omega$, $Q = 0.01\ \Omega^{-1}s^{0.45}$, $n = 0.45$, $C_{dl} = 0.0001\ F$)

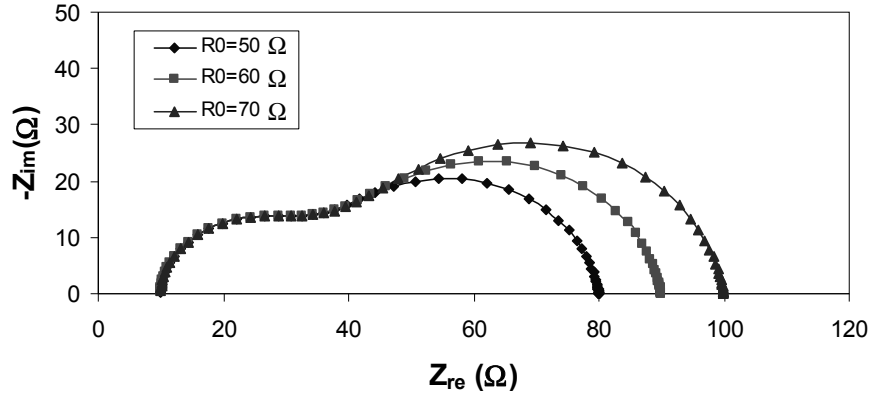

Figure D.68. Nyquist plot of modified Randles cell with bounded CPE in series with R_{ct} over the frequency range 6 kHz to 1 mHz ($R_{el} = 10\ \Omega$, $R_{ct} = 20\ \Omega$, $Q = 0.01\ \Omega^{-1}s^{0.45}$, $n = 0.45$, $C_{dl} = 0.0001\ F$)

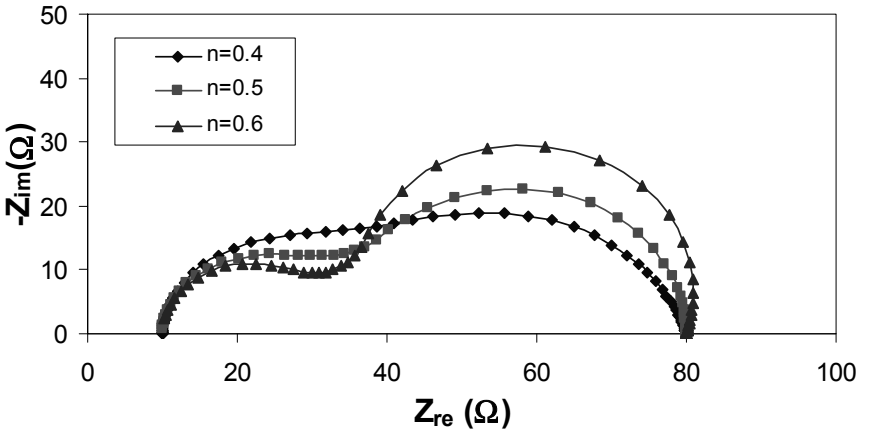

Figure D.69. Nyquist plot of modified Randles cell with bounded CPE in series with R_{ct} over the frequency range 6 kHz to 1 mHz ($R_{el} = 10\,\Omega$, $R_{ct} = 20\,\Omega$, $Q = 0.01\,\Omega^{-1}s^{n}$, $R_0 = 50\,\Omega$, $C_{dl} = 0.0001\,F$)

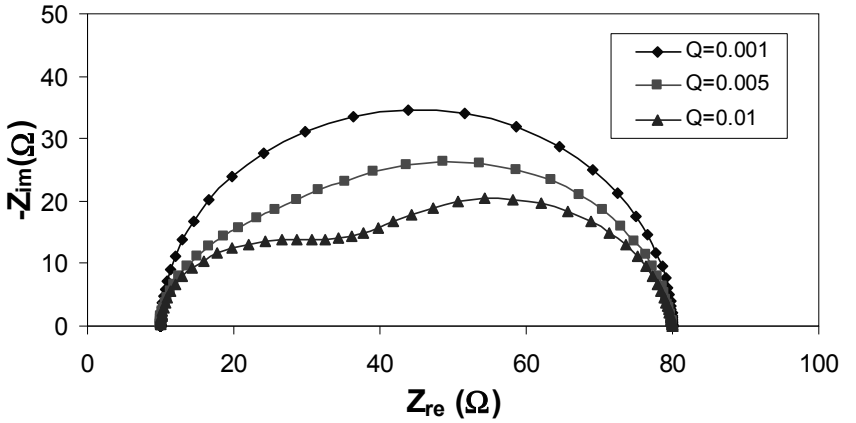

Figure D.70. Nyquist plot of modified Randles cell with bounded CPE in series with R_{ct} over the frequency range 6 kHz to 1 mHz ($R_{el} = 10\,\Omega$, $R_{ct} = 20\,\Omega$, $R_0 = 50\,\Omega$, $n = 0.45$, $C_{dl} = 0.0001\,F$, the unit of $Q: \Omega^{-1}s^{0.45}$)

Model D20

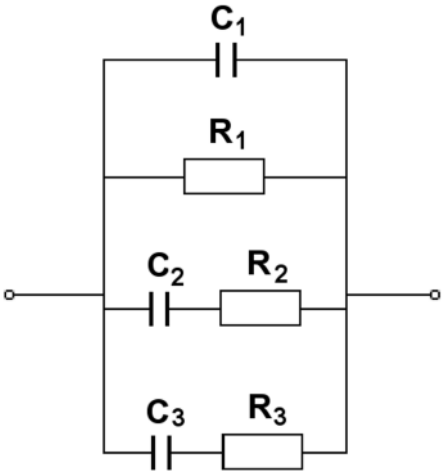

Figure D.71. A simple example of Maxwell's structure with two parallel processes (Figure 4.22*a*)

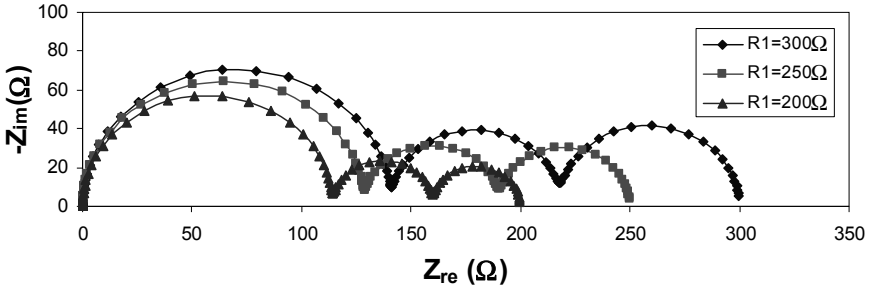

Figure D.72. Nyquist plot of simple Maxwell structure with two parallel processes over the frequency range 1 MHz to 1 mHz ($C_1 = 0.000001\,\mathrm{F}$, $R_2 = 400\,\Omega$, $C_2 = 0.0001\,\mathrm{F}$ $R_3 = 800\,\Omega$, $C_3 = 0.01\,\mathrm{F}$)

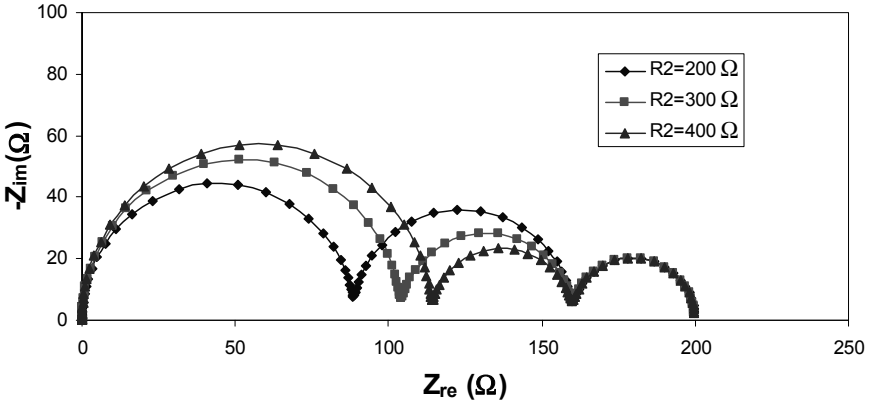

Figure D.73. Nyquist plot of simple Maxwell structure with two parallel processes over the frequency range 1 MHz to 1 mHz ($R_1 = 200\,\Omega$, $C_1 = 0.000001\,\mathrm{F}$, $C_2 = 0.0001\,\mathrm{F}$ $R_3 = 800\,\Omega$, $C_3 = 0.01\,\mathrm{F}$)

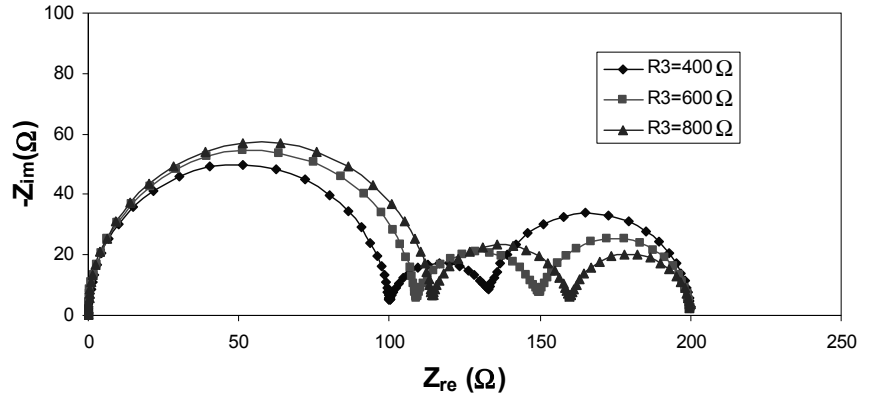

Figure D.74. Nyquist plot of simple Maxwell structure with two parallel processes over the frequency range 1 MHz to 1 mHz ($R_1 = 200\,\Omega$, $C_1 = 0.000001\,\mathrm{F}$, $R_2 = 400\,\Omega$, $C_2 = 0.0001\,\mathrm{F}$, $C_3 = 0.01\,\mathrm{F}$)

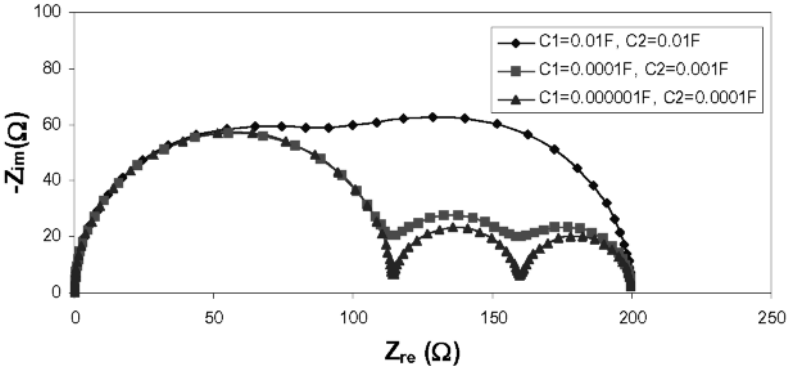

Figure D.75. Nyquist plot of simple Maxwell structure with two parallel processes over the frequency range 1 MHz to 1 mHz ($R_1 = 200\ \Omega$, $R_2 = 400\ \Omega$, $R_3 = 800\ \Omega$, $C_3 = 0.01\ F$)

Model D21

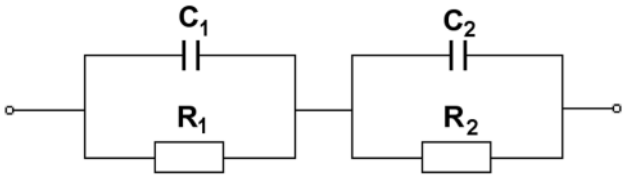

Figure D.76. Voigt's structure with two RC in series (Figure 4.24*a*)

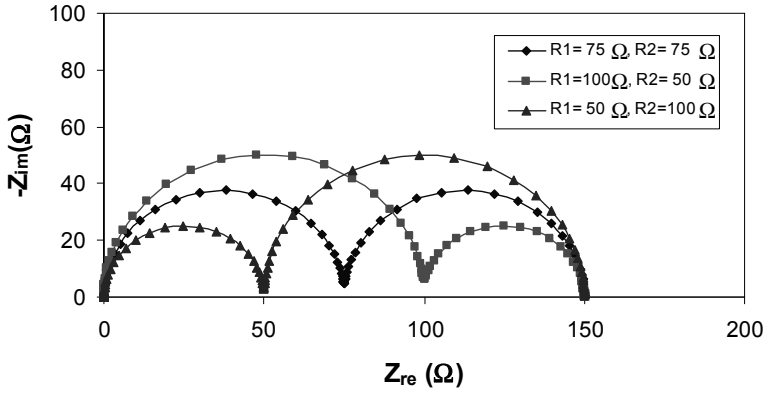

Figure D.77. Nyquist plot of Voigt's structure with two RC in series over the frequency range 1 MHz to 1 mHz ($C_1 = 0.00001\ F$, $C_2 = 0.01\ F$)

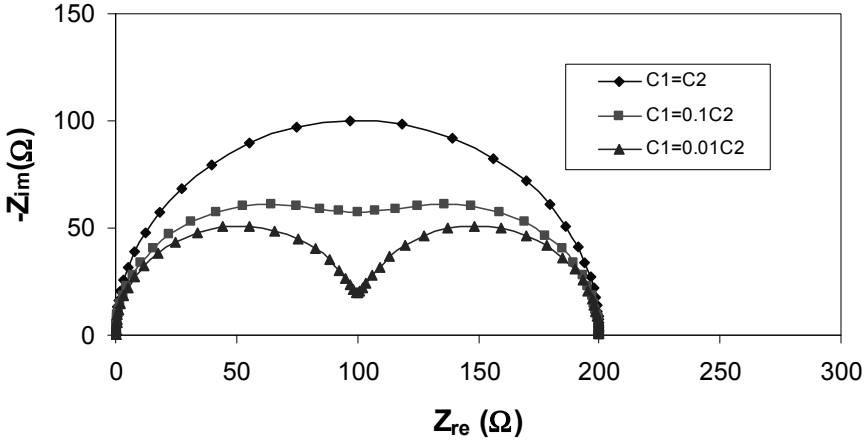

Figure D.78. Nyquist plot of Voigt's structure with two RC in series over the frequency range 1 MHz to 1 mHz ($R_1 = 100\ \Omega$, $R_2 = 100\ \Omega$, $C_2 = 0.01\ \text{F}$)

Model D22

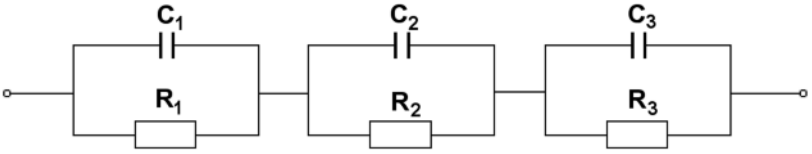

Figure D.79. Voigt's structure with three RC in series (Figure 4.25*a*)

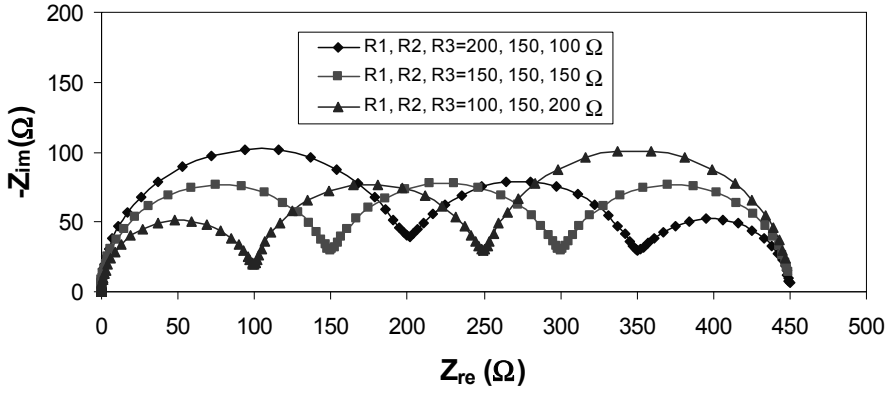

Figure D.80. Nyquist plot of Voigt's structure with three RC in series over the frequency range 1 MHz to 1 mHz. ($C_1 = 0.00001\ \text{F}$, $C_2 = 0.001\ \text{F}$, $C_3 = 0.1\ \text{F}$)

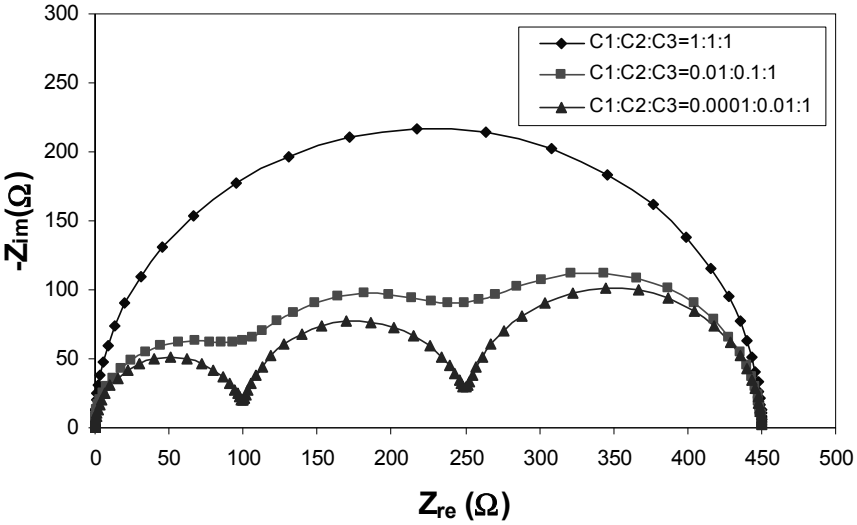

Figure D.81. Nyquist plot of Voigt's structure with three RC in series over the frequency range 1 MHz to 1 mHz. ($R_1 = 100\ \Omega$, $R_2 = 150\ \Omega$, $R_3 = 200\ \Omega$, $C_3 = 0.01\ \mathrm{F}$)

Model D23

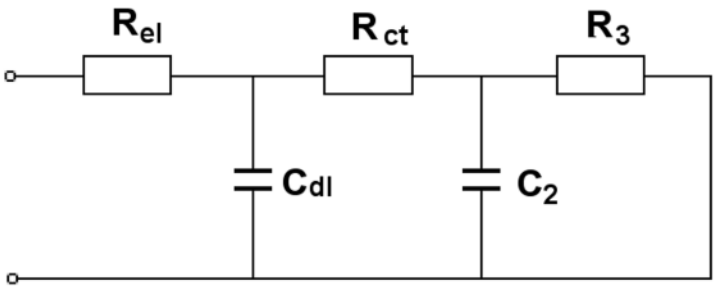

Figure D.82. Ladder structure for electrochemical systems known as Faradaic reactions involving one adsorbed species (Figure 4.27*a*)

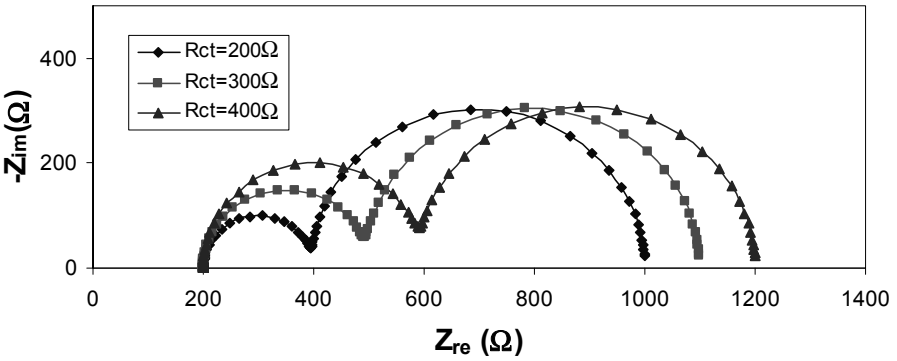

Figure D.83. Nyquist plot of a ladder structure for Faradaic reaction involving one adsorbed species over the frequency range 1 MHz to 1 mHz ($R_{el} = 200\,\Omega$, $R_3 = 600\,\Omega$, $C_{dl} = 0.0001\,F$, $C_2 = 0.01\,F$)

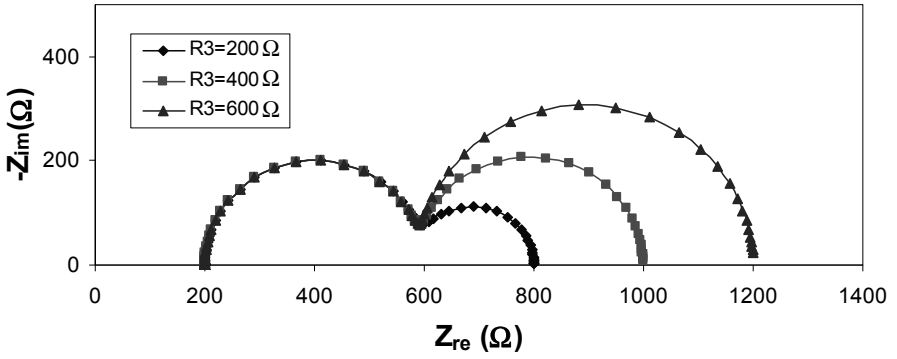

Figure D.84. Nyquist plot of a ladder structure for Faradaic reaction involving one adsorbed species over the frequency range 1 MHz to 1 mHz ($R_{el} = 200\,\Omega$, $R_{ct} = 400\,\Omega$, $C_{dl} = 0.0001\,F$, $C_2 = 0.01\,F$)

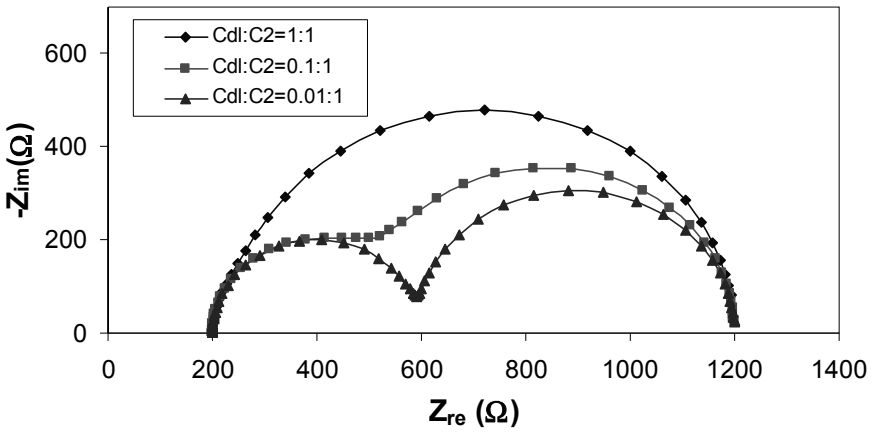

Figure D.85. Nyquist plot of a ladder structure for Faradaic reaction involving one adsorbed species over the frequency range 1 MHz to 1 mHz ($R_{el} = 200\,\Omega$, $R_{ct} = 400\,\Omega$, $R_3 = 600\,\Omega$, $C_2 = 0.01\,F$)

Model D24

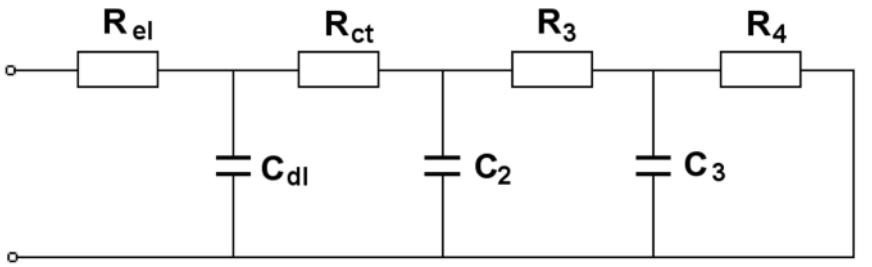

Figure D.86. A ladder structure with two adsorbed species in the absence of diffusion limitation (Figure 4.28*a*)

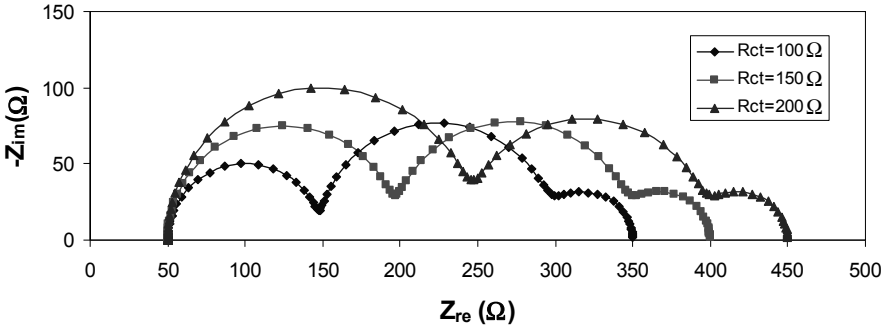

Figure D.87. Nyquist plot of a ladder structure with two adsorbed species over the frequency range 1 MHz to 1 mHz ($R_{el} = 50\,\Omega$, $R_3 = 150\,\Omega$, $R_4 = 50\,\Omega$, $C_{dl} = 0.00001\,F$, $C_2 = 0.001\,F$, $C_3 = 0.1\,F$)

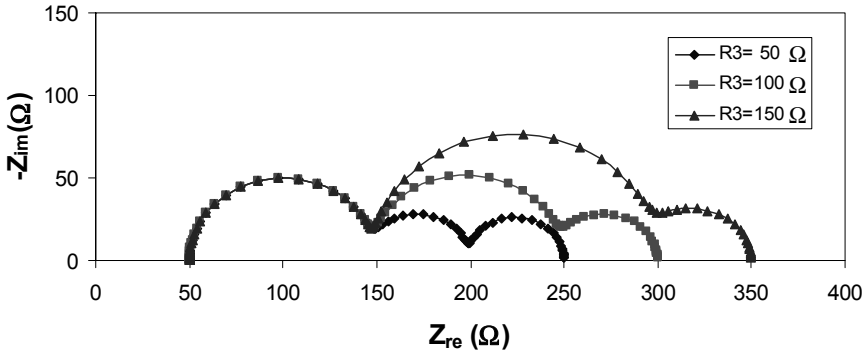

Figure D.88. Nyquist plot of a ladder structure with two adsorbed species over the frequency range 1 MHz to 1 mHz ($R_{el} = 50\,\Omega$, $R_{ct} = 100\,\Omega$, $R_4 = 50\,\Omega$, $C_{dl} = 0.00001\,F$, $C_2 = 0.001\,F$, $C_3 = 0.1\,F$)

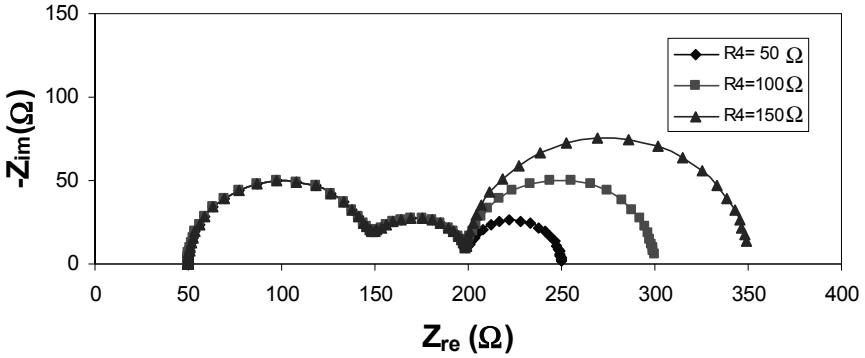

Figure D.89. Nyquist plot of a ladder structure with two adsorbed species over the frequency range 1 MHz to 1 mHz ($R_{el} = 50\,\Omega$, $R_{ct} = 100\,\Omega$, $R_3 = 50\,\Omega$, $C_{dl} = 0.00001\,F$, $C_2 = 0.001\,F$, $C_3 = 0.1\,F$)

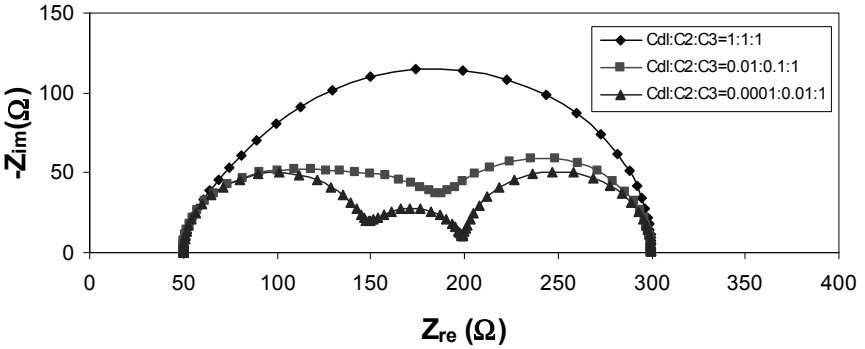

Figure D.90. Nyquist plot of a ladder structure with two adsorbed species over the frequency range 1 MHz to 1 mHz ($R_{el} = 50\,\Omega$, $R_{ct} = 100\,\Omega$, $R_3 = 50\,\Omega$, $R_4 = 100\,\Omega$, $C_3 = 0.01\,F$)

Model D25

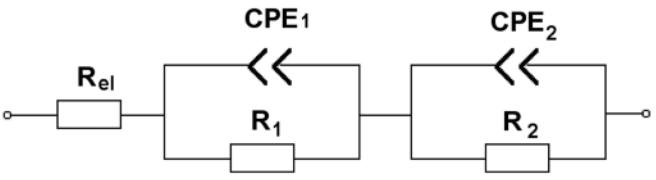

Figure D.91. Resistor and Voigt's structure in series with capacitor replaced by CPE (Figure 4.29*a*)

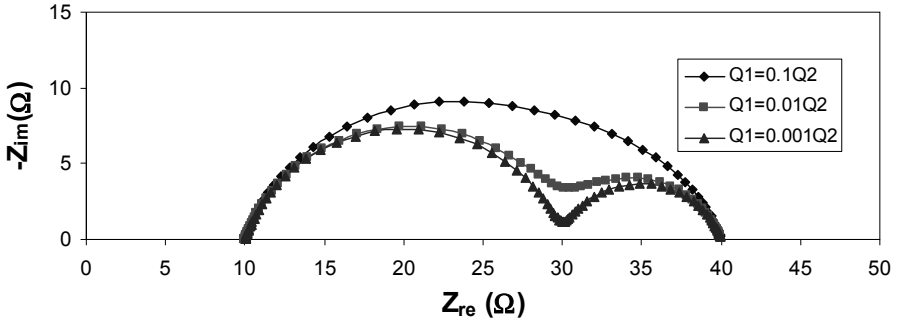

Figure D.92. Nyquist plot of modified Voigt's structure over the frequency range 1 MHz to 1 mHz ($R_{el} = 10\ \Omega$, $R_1 = 20\ \Omega$, $R_2 = 10\ \Omega$, $n_1 = 0.8$, $n_2 = 0.8$, $Q_2 = 0.1\ \Omega^{-1}s^{0.8}$)

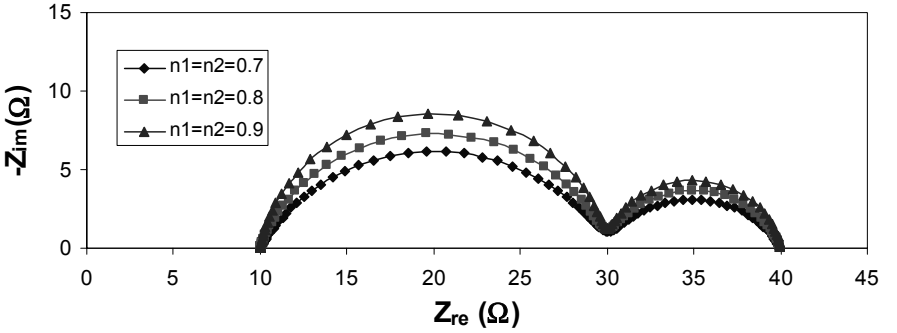

Figure D.93. Nyquist plot of modified Voigt's structure over the frequency range 1 MHz to 1 mHz ($R_{el} = 10\ \Omega$, $R_1 = 20\ \Omega$, $R_2 = 10\ \Omega$, $Q_1 = 0.0001\ \Omega^{-1}s^{n_1}$, $Q_2 = 0.1\ \Omega^{-1}s^{n_2}$)

Model D26

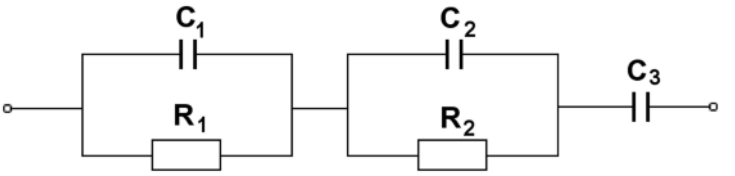

Figure D.94. Capacitor and Voigt's structure in series (Figure 4.30*a*)

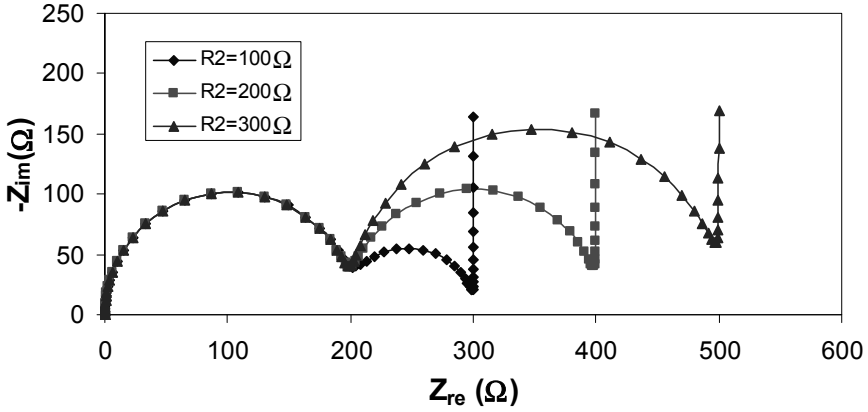

Figure D.95. Nyquist plot of a capacitor and Voigt's structure in series over the frequency range 1 MHz to 1 mHz ($R_1 = 100\ \Omega$, $C_1 = 0.0001\ \mathrm{F}$, $C_2 = 0.01\ \mathrm{F}$, $C_3 = 1\ \mathrm{F}$)

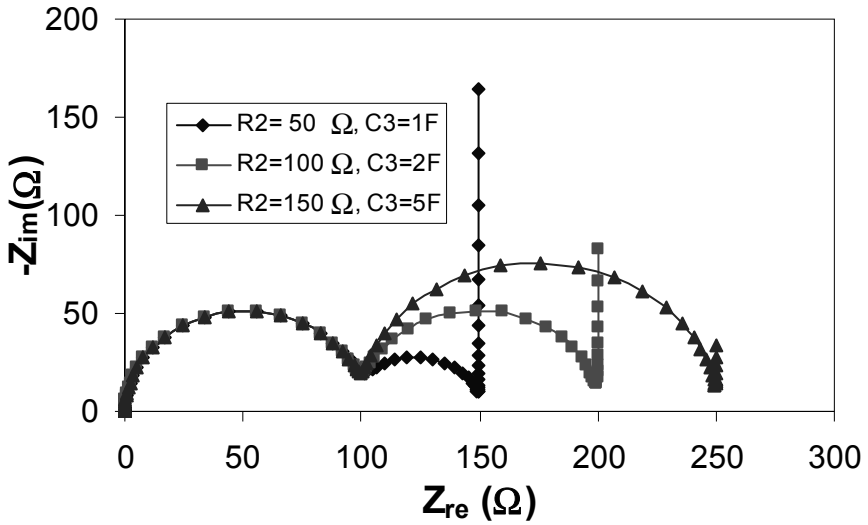

Figure D.96. Nyquist plot of a capacitor and Voigt's structure in series over the frequency range 1 MHz to 1 mHz ($R_1 = 100\ \Omega$, $C_1 = 0.0001\ \mathrm{F}$, $C_2 = 0.01\ \mathrm{F}$)

Contributor Biographies

Dr. Xiao-Zi Yuan is a research officer and a project leader of the Unit Cell Team at the Institute for Fuel Cell Innovation, National Research Council of Canada (NRC-IFCI). Dr. Yuan received her B.S. and M.Sc. in Electrochemical Engineering from Nanjing University of Technology in 1991 and 1994, respectively, under the supervision of Professor Baoming Wei, and her Ph.D. in Material Science from Shanghai Jiaotong University in 2003, under the supervision of Professor Zifeng Ma. After graduating with her M.Sc., she held a lecturer position at Nantong University for six years, and upon completing her Ph.D. was an associate professor there for one year. Beginning in 2005, she carried out a three-year postdoctoral research program at NRC-IFCI with Dr. Haijiang Wang. Dr. Yuan has over fifteen years of R&D experience in applied electrochemistry, including over nine years of fuel cell R&D (among these three years at Shanghai Jiaotong University, one year at Fachhochschule Mannheim, and five years, to date, at NRC-IFCI). Currently her research focuses on PEM fuel cell design, testing, diagnosis, and durability. Dr. Yuan has published more than forty research papers in refereed journals, produced over ten technical reports, given more than twenty conference papers or presentations, and holds five China patents.

Dr. Chaojie Song is a research officer at the Institute for Fuel Cell Innovation, National Research Council of Canada (NRC-IFCI). He received his B.Sc. in Chemistry from Lanzhou University (1984), and his M.Sc. in Electrochemistry from Hebei Normal University (1989) under the supervision of Professors Wenzhi Zhang and Xizun Wu. Dr. Song completed his Ph.D. in Inorganic/Analytical Chemistry at the University of New Brunswick (1997–2001) under the supervision of Professor Gilles Villemure, working on layered silicate clays, mesoporous molecular sieve silicas, and the use of these nanostructured materials in modified electrodes. He then conducted postdoctoral work under the supervision of Professors Kurt R. Hebert and Surya K. Mallapragada at Iowa State University (April–December 2001). In 2002, he joined Professor Peter G. Pickup's group at Memorial University of Newfoundland as a postdoctoral fellow, then in December 2003 as a research associate, working on fuel cell catalyst development. He joined the NRC-IFCI in 2004 under the supervision of Dr. Jiujun Zhang, working on

high-temperature PEM fuel cells and fuel cell catalyst development. Dr. Song has over seventy research publications, including journal papers, conference presentations, and industrial technical reports, and is an active member of The Electrochemical Society.

Dr. Haijiang Wang is a senior research officer, project manager of multi-projects, and the core competency leader of the Unit Fuel Cell Team at the Institute for Fuel Cell Innovation, National Research Council of Canada (NRC-IFCI). He leads a team of more than ten scientists carrying out R&D on novel fuel cell design and materials, as well as fuel cell diagnosis and durability. Dr. Wang received his Ph.D. in electrochemistry from the University of Copenhagen, Denmark, in 1993. He then joined Dr. Vernon Parker's research group at Utah State University as a postdoctoral researcher, to study electrochemically generated anion and cation radicals. In 1997 he began working with Natural Resources Canada as a research scientist, carrying out research on fuel cell technology. In 1999 he joined Ballard Power Systems as a senior research scientist to continue his investigations. After five years with Ballard, he joined NRC-IFCI in 2004. He is currently adjunct professor at five universities, including the University of British Columbia and the University of Waterloo. Dr. Wang has twenty-five years of professional research experience in electrochemistry and fuel cell technology. To date, he has published over seventy journal papers, forty industrial reports, and thirty conference papers or presentations, and has been issued three patents.

Prof. Jiujun Zhang is a senior research officer and PEM Catalysis Core Competency Leader at the Institute for Fuel Cell Innovation, National Research Council of Canada (NRC-IFCI). Dr. Zhang received his B.S. and M.Sc. in Electrochemistry from Peking University in 1982 and 1985, and his Ph.D. in Electrochemistry from Wuhan University in 1988. After completing his Ph.D., he took a position as an associate professor at the Huazhong Normal University for two years. Beginning in 1990, he carried out three terms of postdoctoral research at the California Institute of Technology, York University, and the University of British Columbia. Dr. Zhang has over twenty-seven years of R&D experience in theoretical and applied electrochemistry, including over thirteen years of fuel cell R&D (among which six years were at Ballard Power Systems and five years have been at NRC-IFCI), and three years of electrochemical sensor experience. Dr. Zhang holds several adjunct professorships, including one at the University of Waterloo and one at the University of British Columbia. His research is based on: fuel cell catalyst development; catalyst layer/cathode structure; fundamental understanding through theoretical approaches based on first-principles modeling; catalyst layer characterization and electrochemical evaluation; preparation of cost-effective membrane electrode assemblies for fuel cell testing and evaluation; and fuel cell contamination. To date, Dr. Zhang has co-authored 220 publications, including refereed journal papers, books and book chapters, conference proceeding papers, and invited oral presentations. He also holds more than ten US patents/patent publications, and has produced over seventy industrial technical reports. Dr. Zhang is an active member of The Electrochemical Society, the International Society of Electrochemistry, and the American Chemical Society.

Index

acid-doped polybenzimidazole, 7, 12, 317–19
active area, 20, 194, 231, 239, 250, 273, 276, 284, 289, 303, 310, 313
active elements, 39
active layer, 195–200
additivity, 134–5
admittance, 77–8, 118–21, 143–8, 168, 364
admittance matrix, 78
adsorption, 6, 19, 26–27, 34, 84, 95, 126, 135, 140, 158–63, 174–7, 180–1, 198, 201, 212, 223, 235, 295, 323, 326, 328–39
adsorption model, 158–63
adsorption resistance, 180
air shortage, 224, 241–2
alkaline fuel cells, 2–4, 10–11, 282
alternating current, 39, 50–71, 81–2, 89, 92–3, 102, 123, 126, 129, 131–4, 139, 183–4, 187, 197, 200–8, 219–22, 229, 237–40, 246–57, 268–76, 279, 285–8, 295, 300, 303, 307, 309–25, 339, 347, 350, 363
  AC impedance, 17, 26–28, 36, 55–71, 81–2, 89, 102, 123–34, 183–7, 204–7, 218–27, 236–39, 245–56, 266–74, 279, 284–6, 295, 298, 307, 310–25, 338
ammonia, 234–5, 297
angular frequency, 51–2, 347
anisotropism, 209–12
apparent electron number, 16, 19–20
apparent exchange current density, 17, 34
asymmetric system, 244
back-diffusion, 7, 133, 242, 279
bilateral Laplace transform. See two-sided Laplace transform
bilayer electrode, 188, 293
bipolar graphite plates, 298
Bode diagram. See Bode plot
Bode plot, 82–90, 216–22, 283
boundary condition, 100–1
boundary conditions, 314
bounded CPE, 85, 143, 152–4, 166–7
bounded Randles cell, 163–7
bounded Warburg, 85, 117, 142–3, 151–4, 164–6
branch, 19, 72–3, 76, 168–70, 228, 242, 266, 277, 303
  45° branch, 266, 277, 303
  45° branch distortion, 228–30
bulk concentration, 100–6, 358
Butler-Volmer equation, 15–16, 105, 328
capacitance, 27, 45–8, 84–5, 90, 96–8, 108–10, 128, 133, 138–4, 154–61, 164–6, 171, 175–6, 180–91, 197–8, 209, 217–18, 223–4, 227–30, 234, 239, 266–8, 288–2, 297, 323–6, 336–40
capacitor, 26, 39, 43, 45–9, 53, 56–71, 78, 81–2, 85, 90, 96, 115, 139–40, 144–5, 159–65, 171–9, 184, 222, 288, 292, 323, 359–60, 371–2, 385–391, 395–6, 408–10
carbon black, 197, 201–2
carbon fibre electrode, 201–2
carbon monoxide, 6, 10, 140, 180, 197, 212, 233, 235, 238
  adsorption, 180, 328, 335–39
  contamination, 6, 10, 212, 233–5, 238, 295
  poisoning, 295–298, 323, 339
carbon nanotubes, 201–2
carbon paper, 7, 12, 195–6, 201, 213
carbon supports, 5–7, 12, 182, 195–6, 201–2
carbon-supported PtRu, 6
Carnot efficiency, 35–6
Cartesian coordinates, 82, 118–20
catalyst coated membranes, 7
catalyst down-selection, 133, 193–5
catalyst ink, 195, 197–8
catalyst layer, 7–8, 31, 123–5, 128, 129, 133, 180–4, 191, 194–8, 201, 212,

219, 223, 228–29, 233, 243, 274–80, 288–92, 295, 316, 321–2, 338–43
catalyst loading, 5–6, 9, 133, 214, 244, 264–7, 275, 285
catalyst loading rate, 285
cation exchange, 97
causality, 134, 135, 363–5
characteristic frequency, 58, 116, 122–3, 146, 224, 338
charge transfer, 25–7, 31, 34, 85, 87, 96, 98–9, 104, 141, 144, 188, 198–201, 214, 218, 223, 232, 244
charge-transfer resistance, 17, 19–20, 27–8, 84–90, 96–7, 104, 107, 115–16, 122, 123, 129, 133–4, 139–40, 154, 155–67, 157, 175–7, 180, 196, 201, 214–18, 219, 223, 229, 232–3, 238, 266–75, 281–5, 288, 297–298, 317–30, 336–40
chronoamperometry, 21–2
circuit elements, 39–45, 48, 72–4, 78, 81, 84–5, 90, 93, 110, 141–3, 152
coaxial probe method, 208–12
competitive adsorption, 332
composite electrode structure, 287
complex admittance, 118–23
complex algebra, 39, 54–71
complex argument, 101, 353
complex expression, 104, 108
complex impedance, 55, 96, 118–20, 131, 141, 154, 256
complex nonlinear least squares, 89–91, 257
complex number, 54–7, 79
complex plane, 55–65, 68–71, 108, 113–18, 163, 248–9
complex variable, 263, 353
conductance, 41, 45
conductive polymer, 139, 182, 184–91
constant phase element, 26, 84–5, 91, 139, 141–3, 146–8, 152–4, 156–8, 161–7, 177, 180, 222, 232, 297, 319, 323, 333, 371–407
constant stoichiometry, 240–2
contact resistance, 31, 34, 129, 133, 203, 207, 219
contamination, 6–7, 10, 233–5, 238, 245, 295–298, 314. See also poisoning
continuous-time Fourier transforms, 347
convolution, 91–2, 101–2, 257, 349, 355, 357
Cottrell equation, 21
counter electrode, 193–4, 197–8, 244, 246
coverage relaxation time, 91, 128, 218, 223–4, 297, 324
coverage resistance, 324–8
Cramer's rule, 77
current density, 2–3, 15–20, 31, 33–4, 104–8, 124–5, 132, 155–6, 180, 198–200, 210, 217, 248–54
current distribution, 142, 154, 180, 218, 246–7
current interruption, 20–1, 123, 128–9, 203
cyclic voltammetry, 22–6
cyclic voltammogram, 23–6, 201
deconvolution, 89, 91–2, 257
delta function, 347–50
De Moivre's formula, 146
determinant, 77
diagnostic tools, 123, 128, 133
differential equation, 49, 78–80, 352–3, 358–9
diffusion coefficient, 21–5, 107, 134, 164, 202, 224
diffusion equation, 100–1, 353, 357–8
diffusion resistance, 180–1, 238
diluted hydrogen, 230–2
diluted oxygen, 232–3
direct coal fuel cells, 2
direct current, 27, 39–50, 52, 81, 92, 129, 131, 133, 198, 200, 238, 249–50, 255, 290–1, 303, 323
direct ethanol fuel cells, 8
direct formic acid fuel cells, 8
direct methanol fuel cells, 8–10, 92, 140, 180, 194, 235–7, 244, 249, 323–41
discrete Fourier transform, 351
dissociative methanol adsorption, 326
double-layer capacitance, 27, 81, 85–8, 90, 98, 129, 133–4, 154–67, 175–7, 180–1, 185–8, 191, 223, 229, 238, 264, 266, 288, 297–9, 323, 336, 339–40
double-layer capacitor, 85, 115–16
double-layer charging, 161, 196, 222, 228, 338
dual catalyst layers, 274
DuPont, 3, 97, 184, 203
dynamic hydrogen electrode, 235–6, 245–9
dynamic hydrogen reference electrode, 32
earthenware, 1
effective diffusion coefficient, 224

electric circuits, 26–7, 39–93, 96, 139, 142–80, 182–5, 191. See also equivalent circuits
AC circuits, 39, 50–5
DC circuits, 39–50
electric networks. See electric circuits; network analysis; network reduction; network topology
electrical double layer, 95
electroosmotic drag, 7, 242
electroceramic material, 171
electrochemical half-cell, 194–6
electrochemical interfaces, 85, 95–8, 117–18, 134–5, 139–40, 146, 170, 186–7, 191, 201, 205–7, 242, 264–8, 271–7. See also Randles cell
electrochemical surface area, 17, 201, 267, 287, 310, 316
electrochemical systems, 20–1, 27–8, 81–7, 92, 95–7, 109–23, 134, 139, 143–4, 174–80, 256
electrochemistry, 1, 5, 9, 13–30, 34–6, 95–7, 104
electrode active surface area, 3
electrode potential, 13–15, 19, 23–4, 29–33, 98–104, 125, 140, 155–6, 187–8, 196–202, 219, 227–8, 235, 238, 246–8, 272–3, 277–8, 333
electrode preparation methods, 193–5, 226, 282–6, 289
electrode reactions, 1, 5–6, 12, 16–18, 95, 104–8, 125, 170, 172, 238, 285, 316, 320. See also hydrogen oxidation reaction; oxygen reduction reaction
electrode/electrolyte interface, 27, 34, 95–7, 118, 140, 146, 170, 201
electrolysis, 1, 13
electrolyte conductivity, 12, 129
electrolyte/electrolyte interface, 95
electron transfer number, 16, 104–7, 155–8
electronic conductivity, 8, 97, 180, 182, 280, 288, 291–2
electronic conductor, 40, 95, 144, 182
electronic resistance, 139–40, 180–2, 187–8
elementary reaction, 15–16
empirical coefficient, 239
equilibrium electrode potential, 98–104
equivalent circuits, 26–8, 72, 74–6, 82–92, 287–89, 292–3, 297–9, 323–4, 328, 333, 336–7, 339–41, 371–410
See also electric circuits
Euler's formula, 56, 151, 153
ex situ diagnosis, 193–214, 289
exchange current density, 15–19, 34, 104–8, 155–6, 198, 217
exponential function, 351
external reference electrode, 246
Faradaic impedance, 96–112, 154, 176, 333, 337–8
Faradaic parameters, 110–11
Faradaic resistance, 156–7, 323–6
Faraday's constant, 101
fast EIS, 255–8
fast Fourier transform, 130, 255–6
fast Fourier transform algorithm, 255
Fick's second law, 142, 358
finite diffusion impedance, 297–299
finite transmission line, 185
finite transmission-line equivalent circuit, 233, 288–9, 292
finiteness, 364–5
flow channels, 8, 125, 218, 224, 264, 306–8, 312–13
forward Fourier transform, 347
four-probe method, 204–10
Fourier transforms, 130, 255–7, 347–52
frequency domain, 123, 139, 255–7
frequency response analyzer, 130–2, 237, 250, 264, 284–5, 303
frequency-rich perturbation, 255
fuel cell degradation, 133, 135, 234–5, 288, 295, 298, 314
fuel cell efficiencies, 10–13, 35–6, 241, 263
fuel cell stack, 1–3, 5–6, 10, 123, 193, 212, 240–3, 250–3, 298–300
fuel starvation, 302, 309
galvanostatic mode, 135, 214, 237–8, 251, 295–297
gamma function, 102
gas crossover, 10, 21, 30–1, 124–5, 339
gas diffusion electrode, 3, 10, 195–7, 199–201, 213, 263–4, 268, 271, 279
gas diffusion layers, 13, 124, 129–30, 133, 180, 191, 195–6, 244, 264, 268–70, 279–82
Gaussian Fourier transform, 350
Gemini space vehicles, 3
Gibbs free energy, 13, 29, 35
glassy carbon electrode, 195, 198, 289, 331

gold, 2, 193
gold foils, 2
gradient catalyst layer, 182
graphite carbon, 3, 8, 12, 195, 213, 298, 313
H_2/air fuel cells, 4–10, 12, 14, 17, 20, 28–30, 35–6, 123, 135, 180, 215–16, 217–30, 264–69, 275–8, 282–6, 290, 296, 300, 342
H_2S contamination, 233, 235, 295
half-wave potential, 25
heating/cooling system, 8
heavy duty conditions, 250–4, 258
heterogeneous reaction, 174
high frequency, 57, 82, 84, 87, 90, 114–16, 170, 188, 196, 198, 200, 217, 219, 226–35, 242, 251–3, 265–6, 276–9, 285, 289–92, 303, 306, 309–14, 336
high-frequency intercept, 87, 188, 242, 279, 292
high-frequency limit, 114–16
high-frequency resistance, 230, 234, 276–79, 303, 306, 310, 313
homogeneity, 134, 142–3, 164, 195
hydrogen adsorption, 201, 295, 326, 330
hydrogen crossover, 30–1
hydrogen oxidation reaction, 10, 13, 16–17, 30–3, 195, 198–202, 217, 230, 266
hydrogen shortage, 242
hydrophilicity, 97, 184, 244
hydrophobic channels, 264
hydrophobicity, 97, 184, 244, 264
impedance matrix, 76–7
impedance spectrum, 17, 28, 82–4, 87–90, 95, 123, 126–35, 142, 181–2, 184, 191, 197, 201, 205–10, 214–20, 235–46, 252, 255–7, 267–81, 286–90, 297–300, 303–5, 314–17, 326–35, 336–38
impurities, 2, 10, 135, 234–5, 295
in situ diagnosis, 193, 213–49, 257
in-plane conductivity, 203–9
in-plane direction, 180, 209
in-plane resistance, 203, 209, 212
inductance, 49–50, 84–5, 96, 140, 142–3, 148–50, 181, 297, 325, 331, 336, 339
inductor networks, 49–50
inductors, 39, 43, 49–50, 53–4, 56, 59–64, 78, 81–2, 140, 148–50
initial concentration, 100–7
in situ diagnosis, 200, 214–51
interlocked networks, 288
internal cell resistance. See ohmic resistance
internal combustion engine, 1, 35–6, 263
internal reference electrode, 213–14, 245–6, 249
intrinsic exchange current density, 17
inverse Fourier transform, 347
inverse Laplace transformation, 101
ionic conductors, 95, 182. See also Nafion®
ionic resistance, 133, 139–40, 182–8, 197, 202, 228, 233, 266, 288–89, 314, 338–9
ionized air reference electrode, 249
irreversible contamination, 235
irreversible system, 25–6
isotropic membrane, 209
Johnson Matthey, 201
kinetic arc, 219, 223, 239, 266, 268–72, 278, 285
kinetic loop, 218–26, 231–3, 239–42, 251, 270, 273–4
kinetic parameters, 16–17, 25, 33, 104–7, 109–13, 134, 283, 323, 329–30, 335–6. See also charge-transfer resistance; diffusion coefficient, double-layer capacitance; exchange current density; Tafel slope
Kirchhoff's laws, 42–3, 73, 78
  Kirchhoff's current law, 42–4, 48, 77
  Kirchhoff's voltage law, 42–4, 47–8, 76
Kramers–Kronig relation, 363–9
Kramers–Kronig transforms, 135–6, 257, 363–9
Langmuir adsorption isotherm, 328
Laplace complex variable, 299–301
Laplace transforms, 46, 101–2, 353–631
limiting low-frequency resistance, 289
line graph, 72
linear circuit, 73–8
linear systems theory, 134–5, 363
linearity, 134–6, 256, 349, 355–7, 364–5
link, 72–3
load bank, 130–2, 250–1, 254
localized impedance, 307–8
loop analysis, 76–7
loops, 73, 76–7, 140, 196–200, 218–9, 222–6, 231–3, 239, 242, 251–3, 270, 273, 279, 296, 309, 331, 336, 339

low frequency, 57, 82, 90, 126, 132, 157, 187, 272
low-frequency arc, 223–4, 235–6, 241, 266–7, 278–9, 284–5, 303–4, 339
low-frequency limit, 113, 302
low-temperature fuel cells, 4–5, 13, 203. See also polymer electrolyte membrane fuel cells
macroscopic porosity, 288
mass transfer, 23, 26–7, 31–5, 95, 116, 123–6, 129, 139–40, 205, 214, 222–3, 232–5, 239–4, 279–2, 287–88, 317, 318–5, 336–37
mass transfer coefficient, 319–20
mass transfer drop, 34–5
mass transfer resistance, 27, 125–6, 139, 282, 287–88, 314, 317–1, 324
mass transport limitation, 124, 226, 240, 271–2, 280–1, 285
matrix cofactor, 77
Maxwell's structure, 168–70
medium frequency, 157, 217–20, 223, 232–3, 235, 336, 339
membrane dehydration, 202, 246, 307, 314
membrane electrode assembly, 7, 20, 28, 129–30, 133, 191, 195–6, 212, 217–20, 228, 245–7, 265–89, 294–6, 314–15, 321, 336
membrane thickness, 203, 208, 211–13, 223, 243, 276–79
mesh, 72–3, 76–7
mesh analysis, 76–7
methanol crossover, 10, 339–40
methanol electrooxidation, 193, 235, 323, 326–7, 331–5
methanol oxidation, 9–10, 195, 323–40
methanol-tolerant catalysts, 10
microscopic structures, 117–18
mixed potential, 10, 30–1, 125
molten carbonate fuel cells, 2–4, 92
multi-electron transfer, 15–16, 19
Nafion®, 3, 6–7, 9, 97, 133, 139, 182–4, 195, 197, 202, 204–7, 209–13, 216–19, 230, 239, 243, 249, 264–7, 271–79, 283–5, 291–4, 309–19, 336
Nafion® content, 133, 264, 271–6, 291
Nafion® loading, 272–4, 292–3
nanoparticles, 196–200
Nernst equation, 13–15, 244
Nernst impedance, 224, 291–298
Nernst-Einstein equation, 203
network analysis, 39, 72–81
network reduction, 73–5
network topology, 72–3
nodal analysis, 77–8
node, 41–3, 72–3, 77–8
non-linear least squares, 89–90
non-polarizable electrode, 155
non-uniform adsorption, 162–3
normal hydrogen electrode, 193, 196
Norton impedance, 75
Norton's theorem, 74–5
novel silica gel additive, 283–5
nuclear magnetic resonance, 203
Nyquist plot, 27–8, 82–91, 141–89, 197–8, 201–2, 216–21, 224–42, 273–5, 278–97, 309–11, 338, 371–410
Ohm's law, 40–4, 52, 55, 81, 139, 210
ohmic drop, 20, 34, 129, 196, 230, 239, 264, 276–7, 285
ohmic loss, 97, 123–5, 128–9, 133, 254
ohmic resistance, 34, 116, 123–4, 128–9, 133, 196, 217, 219, 226, 230, 232, 240, 244, 251, 271, 275, 288
one-sided Laplace transform, 353–5
open circuit, 41, 46, 74, 117, 186
open circuit conditions, 125, 201–2
open circuit voltage, 11, 14, 17, 27, 29–33, 124–5, 155, 188, 201, 214, 216–17, 220, 237–8, 319
oscillation frequency, 347
overpotential, 15–21, 32–4, 104–7, 128, 140, 219–4, 238, 249, 266–70, 279–80, 285, 309, 336
oxidant, 2, 10, 28, 97, 99–100, 106, 133, 156, 218, 238–39, 264, 339
oxygen dilution, 218, 232–3
oxygen reduction reaction, 1, 7, 10, 13, 16–17. 19–20, 28–30, 33–4, 123, 193, 195–200, 215, 217–20, 224–5, 230–3, 239–44, 264, 266, 269–3, 278–81, 285–88, 316, 319, 339–41
oxygen starvation, 309
oxygenated species, 9–10
parallel circuits, 27, 41, 44–5, 48–50, 56–70, 75, 84–5, 90–1, 96, 98, 109–11, 120, 143–50, 154, 168–9, 184, 186, 208–9, 265, 289, 298–300, 306
parallel resistive rails, 288
passivation, 325
passive elements, 39
perfluorosulfonated polymer, 3, 6, 139
perforated platinum foil, 2

periodic wave, 50–1
phase angle, 51–2, 57–71, 87, 108, 198–200, 255, 325
phasor, 55
phosphoric acid fuel cells, 2, 4, 12
planar network, 73, 76, 98, 297
platinum black, 1–2, 5, 201, 289
platinum loading, 5–6, 9, 195, 201, 267–9, 276, 338
poisoning, 2, 6, 212, 232, 234, 237, 293–6, 320, 336
polar coordinates, 54, 82, 120–2
polarizable electrode, 144, 146, 154–8
polarization curves, 20, 31–2, 34–5, 123–8, 268–72, 282–7, 294, 310, 319, 324–5
polarization resistance, 85–7, 126–7, 264, 281–2
polybenzimidazole membranes, 7, 12, 318–20
polybenzimidazole-based PEM fuel cells, 318–20
polyethylene oxide, 282–3
polymer, 6, 39, 97, 117, 140, 182–91, 283–5. See also polymer electrolyte membrane fuel cell; polymer/electrolyte interface
polymer electrolyte membrane fuel cells, 3–9, 12, 20, 28, 31–6, 92–3, 97, 123–30, 133, 135, 139, 180–91, 193–258, 263–342
  EIS applications in, 263–342
  electrochemistry of, 13–28
  equivalent circuits in, 180–91
  performance of, 193–259
polymer/electrolyte interface, 187
polynomial equation, 353, 368–69
polypyrrole polystyrene sulfonate, 187–91
polytetrafluoroethylene content, 7, 133, 264, 268–71
pore former, 279–82
porosity, 224–5, 279–80, 284, 288
porous carbon paper, 12, 195
porous electrode, 72, 117–18, 161, 165, 180, 222, 228, 285–89
porous medium, 224
potential perturbation, 27, 92, 98–99, 105, 131, 134, 225, 237–8, 249–51, 255–6, 268, 273, 303, 324–5
potentiodynamic, 212
potentiostat, 130–1, 237–8, 244, 250, 268, 273, 284–5
potentiostatic, 201, 212, 214, 236–7, 273, 276, 284, 295
power density, 8, 124, 263
proton conductivity, 6–7, 28, 97, 133, 139, 203, 209, 239, 242, 266, 272, 275–6, 288, 306, 314
proton exchange membrane, 133, 184, 196, 2456, 263
proton migration, 272
pseudo-elementary reaction, 16
pseudo-inductive behaviour, 296–7
pseudo-reference electrode, 249
Pt/C catalysts, 10, 184, 195, 199, 265–7, 273, 331–5
PtRu, 6, 9–10, 336
quasi-reversible process, 26
R-CPE circuit, 148
Randles cell, 85–7, 152, 154–67, 186–7, 191, 214
Randles-Ershler electric equivalent circuit model, 26–7
Randles-Sevcik equation, 24
rate-determining step, 16, 19–20, 32, 155, 198, 266
RC circuit, 57–9, 69–70, 109–10, 120, 144–5, 154, 168–73, 177, 191, 336
reaction mechanism, 10, 15, 28, 92, 95, 125, 133, 193, 198–200, 212, 235, 263, 295, 324, 327–28, 332, 337–38
reductant, 99–101, 106, 156
reference electrode, 96, 193, 196–8, 209, 212–14, 230, 243–49, 289, 298–99, 338, 342. See also dynamic hydrogen reference electrode; normal hydrogen electrode; saturated calomel electrode
reflective finite diffusion, 117
relative humidity, 20, 123, 180, 209, 212–13, 315–18
relaxation time constant, 297
reliability/durability, 3, 13, 50
resistance
  adsorption, 180
  charge transfer, 17, 19–20
  contact, 31, 34, 129, 133, 203, 207, 219
  diffusion, 180–1, 238
  electronic, 139–40, 180–2, 187–8
  Faradaic, 156–7, 323–6
  high-frequency, 230, 234, 276–79, 303, 306, 310, 313
  in-plane, 203, 209, 212

ionic, 133, 139–40, 182–8, 197, 203, 228, 233, 266, 2914–92, 315, 338–40
limiting low-frequency, 289
mass transfer, 27, 125–6, 139, 282, 287–88, 315, 318–2, 324
ohmic, 34, 116, 123–4, 128–9, 133, 196, 218, 220, 226, 230, 232, 240, 244, 251, 273, 277, 288
polarization, 85–7, 126–7, 264, 281–2
through-plane, 203, 209–10, 212, 314–15
Warburg, 140–1, 180
resistor, 39, 42–5, 52–3, 55–60, 63–71, 74, 81–2, 90, 144–54, 177, 180, 184, 198, 279, 292, 371–82
reversibility, 23–6, 108, 124, 154–5, 233–4, 244, 326. See also quasi-reversible process; reversable hydrogen electrode
reversible system, 24–5
rotating disk electrode, 195, 198–9
rotating ring-disk electrode, 195
salt bridge, 245–49
saturated calomel electrode, 193, 196–8, 201–2, 209–11, 287
scaling, 351, 357, 359
screen printing, 283–5
segmented cell, 309–13
self-poisoning process, 323. See also methanol oxidation
semi-infinite diffusion, 101, 117, 166
semicircle rotation, 188–23
series circuit, 27, 41–4, 47–50, 58–70, 74, 84, 90–1, 96, 98, 107, 109–12, 143–54, 158–67, 170–3, 177–9, 191, 208–9, 297, 320, 327, 337, 342
shift, 16, 20, 26, 120, 134, 182, 288, 349, 355, 357
short circuit, 41, 49, 73–4
side chains, 97
signal/noise ratio, 134
simulation parameter, 319–20
single cell, 1, 6, 87, 123, 193, 212, 214, 218, 221, 228–30, 264, 276–7, 280–2, 295, 298, 303–7
single-walled carbon nanotubes, 201–2
sintered contacts, 288
sinusoidal perturbation, 98–9, 105, 250, 268
sinusoidal wave, 50–5, 81, 98, 251
Solartron, 130–2, 251, 264, 276, 303
solid electrolyte, 3, 4, 92, 95, 97, 118, 212, 247, 264, 295. See also Nafion®
solid oxide fuel cells, 4, 92
solid polymer electrolyte fuel cells, 3, 4. See also polymer electrolyte membrane fuel cells
spraying, 200, 275, 282–3
sputtering, 284–6
stability, 12, 97, 132, 134–6, 193, 196, 201, 244–6, 254–5, 363–5
stack, 1–3, 5–6, 10, 123, 193, 212, 240–2, 250–4, 298–307
stack impedance, 251, 301
stoichiometry, 231–2, 240–2, 303, 320, 341
superposition, 212
sulfonic group, 97
superposition, 73–4, 80, 243, 255
surface concentration, 21–3, 99, 285
surface relaxation impedance, 297
symmetrical gas feeding, 214–17, 237, 244
symmetrical gas supply, 214–17
symmetry, 347–49
symmetry factor, 15
Tafel equation, 238
Tafel kinetics, 128–9
Tafel relation, 332
Tafel slope, 18–20, 33–4, 128, 198, 239, 320–1, 326, 333
Taylor expansion, 333
Teflon®-bonded silicon carbide, 12
test station, 193, 251
thermal desorption spectroscopy, 295
thermoneutral voltage, 124
Thevenin impedance, 75
Thevenin's theorem, 74–5
thin-film/flooded agglomerate model, 264
three-electrode configuration, 193–4, 244–5, 247, 289
three-phase interface, 3
through-plane conductivity, 180, 203, 209–11
through-plane resistance, 203, 208–11, 314–15
time domain, 139, 255–7, 347, 353
time-resolved technique, 254, 295–6
Toray, 195, 201
traditional Nafion® polymer additive, 283–5
transfer coefficient, 15–17, 25, 32–5, 104, 156, 319–20, 329

transmission line, 182–3, 185–7, 338
transmissive finite diffusion, 117
tree, 72–3
two-probe method, 203–07, 212
two-sided Laplace transform, 354–5, 356–7
unipolar graphite plates, 298–301
universal gas constant, 105, 155, 203, 320
vectorgraph, 108
Voigt's structure, 170–9
voltage sensor, 313
Warburg diffusion, 84–5, 303
Warburg element, 87, 142–3, 150–1, 154, 160–1, 165, 232
Warburg impedance, 87, 96–7, 104, 113, 116–17, 141, 150–2, 167, 224–5, 228
Warburg resistance, 140–1, 180
water back-diffusion, 7, 242, 279
water flooding, 7, 132, 218, 224, 277–82, 304, 307, 314
water management, 7, 133, 239, 242–3, 246, 279, 313, 322
working electrode, 21–2, 96, 193–5, 198, 212, 244, 246–49, 289, 299
X-ray photoelectron spectroscopy, 295
Z-plot, 139
Zview, 84, 132